ISSN 0911-5730
UVSOR-26
May 1999

UVSOR
ACTIVITY REPORT
1998

Ultraviolet Synchrotron Orbital Radiation Facility
Institute for Molecular Science

CONTENTS

Preface

Status of UVSOR

Beam Physics

Instruments Developments

Studies using UVSOR

BL1A

BL1B

BL2A

BL2B1

BL3A1

BL3A2

BL3B

BL4A1

BL4B

BL5A

BL5B

BL6A1

BL6A2

BL6B

BL7A

BL8A

BL8B1

BL8B2

Appendix

UVSOR
ACTIVITY REPORT
1998

edited by

T. Kinoshita, M. Hosaka, S. Tanaka

Preface

This Activity Report covers the research activities done by over 800 users from about 60 institutions at the UVSOR facility in 1998. This is the fifth volume in the red-covered Activity Report series. For these five years, the improvement and upgrade projects of monochromators and end stations for the second 10 years of UVSOR are going well, where the first SR was emitted in November 1983. I would like to acknowledge various kinds of supports to the projects by the government and the outside users, and efforts of the UVSOR staff. The following are some of the highlights of monochromators in 1998.

BL2B2: Construction of the spherical grating monochromator for the energy range of 20-200 eV has reached its terminal stage. Available photon flux and resolution were evaluated by measuring the double excitation of He in the photon energy range from 59 to 67 eV; a series of Rydberg states were observed up to n=9+ in the case of the slit widths of 100 μm. After further improvement, we will start inner-valence and shallow core photoionization study of gas-phase molecules.

BL4A: A multilayered mirror monochromator was completed. This beamline is uniquely designed for the study of the excitation energy dependence in SR-stimulated photochemical processes. The first measurement shows that the photoexcitation around the Al 2p edge induces a very effective deposition of the Al thin film on the Si substrate from dimethylaluminium hydride .

BL5A: A new high-resolution monochromator called SGM-TRAIN (Spherical Grating Monochromator with Translational and Rotational Assembly Including a Normal incidence mount) was completed. The monochromator is combined with the helical undulator. The photoelectron spectroscopy for solids, solid surfaces, metal deposited Si surfaces, and quasi-crystalline solids has been carried out using the radiation from the bending magnet. The use of the undulator is now in preparation.

BL7A: The focusing mirror system was installed between the front-end and the soft X-ray double crystal monochromator chambers to obtain the higher performance. In conjunction with the use of the Wiggler radiation and a variety of the monochromator crystals, the experiment at the wide energy region (especially, lower than 2 keV) with high photon flux is now available.

BL7B: The 3m normal incidence monochromator (3m NIM; McPherson upgrade model of 2253) has replaced the 1m Seya-Namioka type monochromator for extended solid-state researches with the higher resolution and intensity, the wider wavelength region available and so on. The performance of the monochromator is now being checked. The throughput and resolution are achieved as expected in the design. The beamline will be opened to the users from April 1999.

The following are some of the highlights of end stations in 1998. We are now trying to develop new fields in molecular science towards the next century, by combining various detection systems and light sources, such as synchrotron radiation, laboratory laser and FEL (free electron laser).

BL2B1: Several groups are using the electron-ion coincidence apparatus for investigating the mechanism of the ion desorption from various types of solid induced by the core-level excitation and ionization. A modified apparatus is now completed. The coincidence signal intensity has been improved by about one order. We will get more reliable data to discuss the mechanism in detail.

BL4B: A scanning tunneling microscopy (STM) system is installed. The mechanism for SR-stimulated desorption of SiO_2 thin films on the Si(111) surfaces is investigated. An atomically flat and clean Si(111)-(7×7) surface was obtained after two hours SR irradiation at a surface temperature of 700 °C. The STM topograph shows that the desorption mechanism may be completely different between thermal and SR-stimulated desorption of the SiO_2 film.

BL8B1: We have applied the UV/ozone cleaning technique to two mirrors (M1 and M21) and two gratings (G2 and G3). After the cleaning, "dark holes" in the output spectra from the monochromator around 290 eV due to carbon-containing contaminations on the surfaces of the mirrors and gratings were successfully removed.

BL3A2: Pump-probe experiments combining synchrotron radiation and a mode-locked Ti:sapphire laser are performed to study the formation mechanism of N_2^+ ($X^2\Sigma^+$,v=0) from VUV photoexcitation of N_2 and N_2O. An RF ion trap is utilized to increase the effective density of ions. In the case of photoionization of N_2, rotational lines of the $(B^2\Sigma^+,v'=0) \leftarrow (X^2\Sigma^+,v''=0)$ transitions are well resolved. The rotational temperatures of N_2^+ ions from N_2 and N_2O are estimated to be ca. 300K and <250K, respectively.

BL3B: Photoionization dynamics of polarized rare gas atoms has been studied by photoelectron spectroscopy. Aligned Rydberg atoms were produced by the linearly polarized SR excitation and were subsequently ionized by a YAG laser whose electric vector can be rotated by means of a half-wave plate. Measuring the angular distribution of photoelectrons, as a function of the angle between the electric vector and the linear momentum vector of photoelectrons, allows us to perform complete experiments of photoionization, if a particular Rydberg state is chosen as the initial state.

BL6B: A new setup for time-resolved measurements in the far-infrared region was completed by combining a Michelson-type interferometer, a bolometer and a picosecond mode-locked Nd:YAG laser. A full one-to-one 90MHz synchronization between the laser pulse and synchrotron radiation is achieved and the delay time between pump (laser photoexcitation) and probe (FIR-SR) is controllable. The time-resolution is predominantly determined by the SR duration width of about 1 ns. The reflectivity change as small as 10^{-3} is detectable. Pump-probe measurements were carried out for an organic semiconductor, $\beta'\text{-(BEDT-TTF)}_2\text{ICl}_2$, and some spectral changes induced by laser irradiation were observed.

We hope much more breakthroughs in science will be brought by the users of the improved and upgraded beamlines.

The UVSOR facility has only two associate professors and three or two research associates in the beamline division. In FY98 one associate professor and one research associate were changed. In April 1998 Dr. Shin-ichi Kimura was promoted to an associate professor of Kobe University. In November 1998 Associate Professor Toyohiko Kinoshita moved to the University of Tokyo to join in the VSX project. In May 1999 Dr. Eiji Shigemasa will come as a new associate professor from the Photon Factory, the Institute of Material Structures Science. On the other hand, the UVSOR has only one associate professor and one or two research associates in the light source division. In August 1998 we could have Dr. Shigeru Kouda as a second research associate. The machine group is very important to propose the UVSOR-II project. Now we are discussing how to reinforce the light source division with the Ministry of Education, Science, Sports and Culture (Monbusho).

March, 1999

N Kosugi

Nobuhiro Kosugi
Director of UVSOR

Status of UVSOR

The UVSOR Accelerator Complex in 1998

Hiroyuki HAMA, Masahito HOSAKA, Shigeru KOUDA, Jun-Ichiro YAMAZAKI, Toshio KINOSHITA

UVSOR Facility, Institute for Molecular Science, Okazaki 444 Japan

1. General

In 1998, the beam supply for user synchrotron radiation experiments was started on Jan-12 after the new year vacation. The statistics of the ring performance in1998 is shown in Table 1. Since the operation with the single-bunch mode was assigned for only two weeks, most of the user machine time was consumed with the multi-bunch mode with 12-bunch filled. The continuous beam delivery was interrupted by an accidental failure of the booster synchrotron in October. This most serious troubles encountered in the year was occurred on a high voltage unit of the synchrotron power supply. Large capacitance chemical condensers were exploded due to an irregular high voltage. Because there was no apparent malfunction discovered in the system, it took a very long time to fix the power supply. We have concluded a break of a balance resistance might provoke a spike of the irregular high voltage. After three-week unscheduled shut-off, the system was restored. Consequently we lost approximately 200 hours of the user beam time. In addition to this major trouble, a couple of minor troubles occurred on various devices such as misfire of the fast kicker for the beam extraction from the booster was frequently happened in May. These minor troubles were fortunately fixed very rapidly and a serious situation was kept away.

Table. 1 1998 Ring Performance Statistics

	Multi(12)-Bunch	Single-Bunch	R&D
Ave. fill Current	248 mA	73 mA	-
Ave. Lifetime	5.2 hours@200mA	1.8 hours@30mA	-
Int. Current	200.1 A·hours	2.2 A·hours	43.4 A·hours
Total operation	1578 hours	100 hours	886 hours
Ave. Beam current	127 mA	22 mA	49 mA

Monthly statistics of significant operational performance in the user machine time are presented in Fig. 1 through 4. The unscheduled shutdown due to the trouble of the booster mentioned above caused decreases of the operation time in October and November. Large portion of shorter operation times of March, April and August was the scheduled shut-off terms.

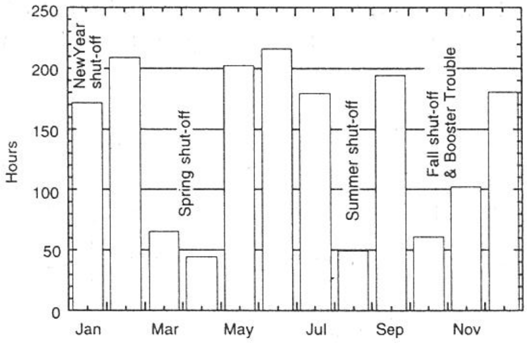

Fig. 1 The total integrated operation time for users accumulated each month.

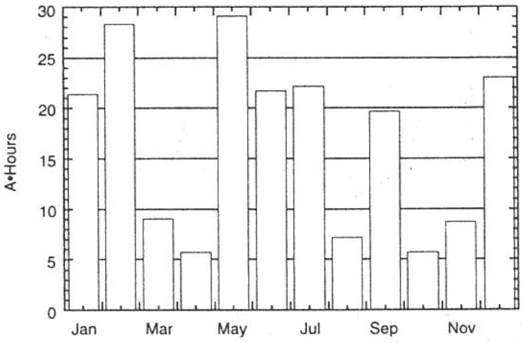

Fig. 2 The integrated beam current for users accumulated each month.

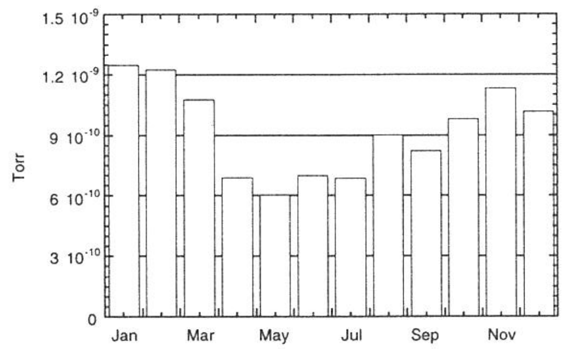

Fig. 3 The ring vacuum pressure at 200 mA beam current averaged over each month.

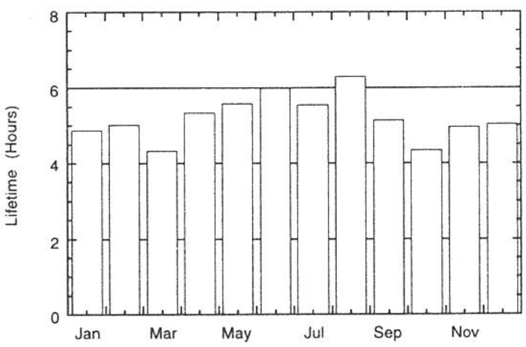

Fig. 4 The beam lifetime at 200 mA beam current with 12-bunch operation averaged over each month.

From April through Summer, good vacuum resulted from which the bake-out was done for a part of the ring vacuum chamber and all Ti sublimation pumps were maintained during the Spring shut-off term. From October, the higher vacuum resulted from the superconducting 4 T wiggler radiation, which was commissioned again after a long shut-down due to a malfunction of the 4 K refrigerator since the end of December, 1997.

2. Improvement

The lattice functions of the storage ring have been improved after the Spring shut-off term, then the operating point of betatron number was changed from (3.16, 2.64) to (3.16, 1.43) to expand the dynamic aperture. Furthermore the dispersion function on the straight sections for the insertions and the RF cavity has been reduced to be less than 7 3 cm (former value is approximately 30 cm). Since the vertical tune is kept away from the third order resonance, the beam handling became easier, so that the ramping (600 MeV to 750 MeV) speed was able to be two times faster than the pervious operation and it became possible to decelerate the beam from 750 MeV to 600 MeV without the beam lost, then the re-injection time has been greatly reduced because more than 130 mA beam current remains. After the beam re-injection and the energy ramping, the beam orbit is able to be corrected within an error of less than 30 μm (rms-value of 16 BPMs) from the default one .

This operating point became to be changed again after a shut-off term in October for the ring operation with the superconducting 4 T wiggler. Both operating points showing in Fig. 2(a) and (b) have no solution in case of introducing an additional focusing power of the 4 T wiggler at the beam injection energy, 600 MeV. Thus we had injected the beam with a 3 T excitation of the wiggler and the magnetic field had been increased up to 4 T by following the energy ramping so far. It was obviously inconvenient for a smooth beam injection procedure. The lattice function of Fig. 2(b) was modified to optimize for the 4 T wiggler by reducing

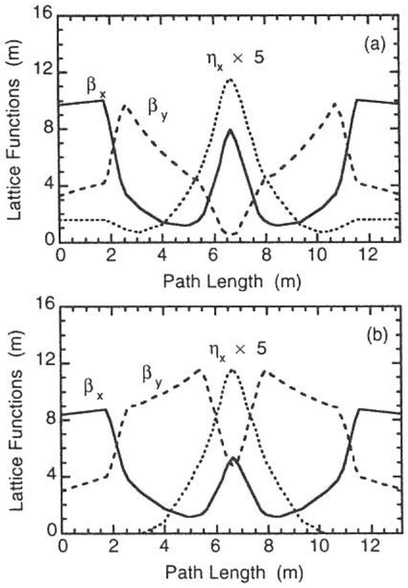

Fig. 5 (a)Pervious Lattice functions of the betatron numbers of (3.16. 2.64), and (b)developed Lattice functions of (3.16,1.43).

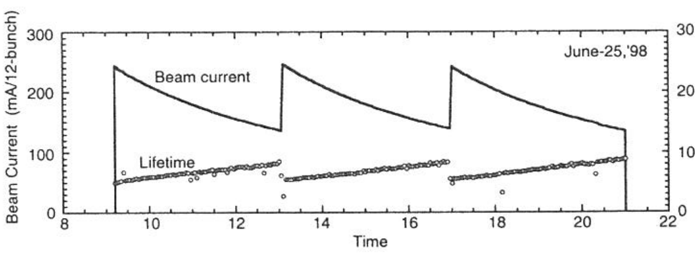

Fig. 6 Beam current and lifetime of a typical one-day operation.

the betatron length in the long straight section down to 1.7 m. Consequently the 600 MeV beam was able to be injected with the 4T excitation, and then the injection rate was not significantly reduced by completely correcting a closed orbit distortion due to the wiggler.

Power supplier and pulsers for the bump magnets in the booster synchrotron which had been used for more than 15 years were replaced. New ones employs IGBTs for fast switching of discharge, and the charging voltages of all three pulsers can be changed proportionately. It is apparently working well. However the pulse width is a bit longer than old one because of internal impedance of the IGBT, and then the beam current injected from the linac has decreased to approximately 60 % of the pervious current. The pulse width should be improved along with the beam injection scheme between the synchrotron and the linac.

An additional feedback system for the third harmonic RF cavity (HCV) used for suppression of the coupled-bunch instability was installed. In the HCV, the RF voltage should be kept at approximately one-third of that in the main RF cavity (MCV). Moreover the phase between the HCV and the MCV should be kept at a certain angle so as to introduce the Landau damping. Because the induced RF field due to the beam current is so large that the resonant frequency of the HCV should be widely detuned from the third harmonic of the main RF frequency to reduce the induced field and create the appropriate phase (approximately $\pi/2$ of the main RF). The external current is fed to keep a constant RF voltage in the HCV with the same phase of the beam induced field. This operation is not complete passive or active mode, and then called "semi-active" mode. In this mode, as the beam current decreases the external current must be increased to keep the RF voltage. However, because of the large detuning of the HCV and the finite output power of the power amplifier, most of the fed external power is usually reflected and it becomes impossible to keep the RF voltage. Therefore, as the beam current decreased the resonant frequency of the HCV had to be a bit tuned by manually moving the plunger in order to increase the RF voltage. Normally there are two feedback system required for the RF cavity. One is a power or RF voltage feedback applying to the power amplifier (or a low level circuit), and another is a phase or resonant frequency feedback applying to the plunger. In this case, a forward power feedback of the external current should be applied to the plunger. As a result of the new feedback system of which the external forward power level controls a phase shifter of the third harmonic oscillator, the bunches has been stabilized at a wide range from the fill current through a few tens mA and operators was released from an annoying plunger control.

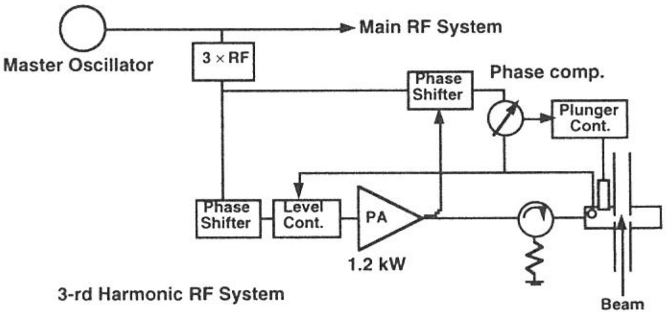

Fig. 7 Feedback loops of the third harmonic RF cavity system.

A new aluminum beam pipe for the storage ring has been testing by the accelerator group. Recent experimental studies of the ring impedance showed an evidence of which the inductive impedance dominates the bunch lengthening and the single-bunch instabilities. Estimated normalized broad-band inductive impedance has been 3 ~ 4 Ω which may resulted from many discontinuities of the beam pipe. In order to reduce the ring impedance, a new beam pipe has been designed. In addition, the vacuum system is also getting older and new one has been highly desired. The new beam pipe equips lumped NEG pumps containing 6 NEG modules, which has a pumping speed of more than 3000 *l*/s for the hydrogen gas. By using an appropriate auxiliary pump with a pumping speed 2 ~ 3 *l* / for inert gases and the methane gas, an excellent vacuum of less than 10^{-8} Pa was able to be achieved without baking of the beam pipe. Although the whole system is still under designing, the ring vacuum will be greatly improved in near future.

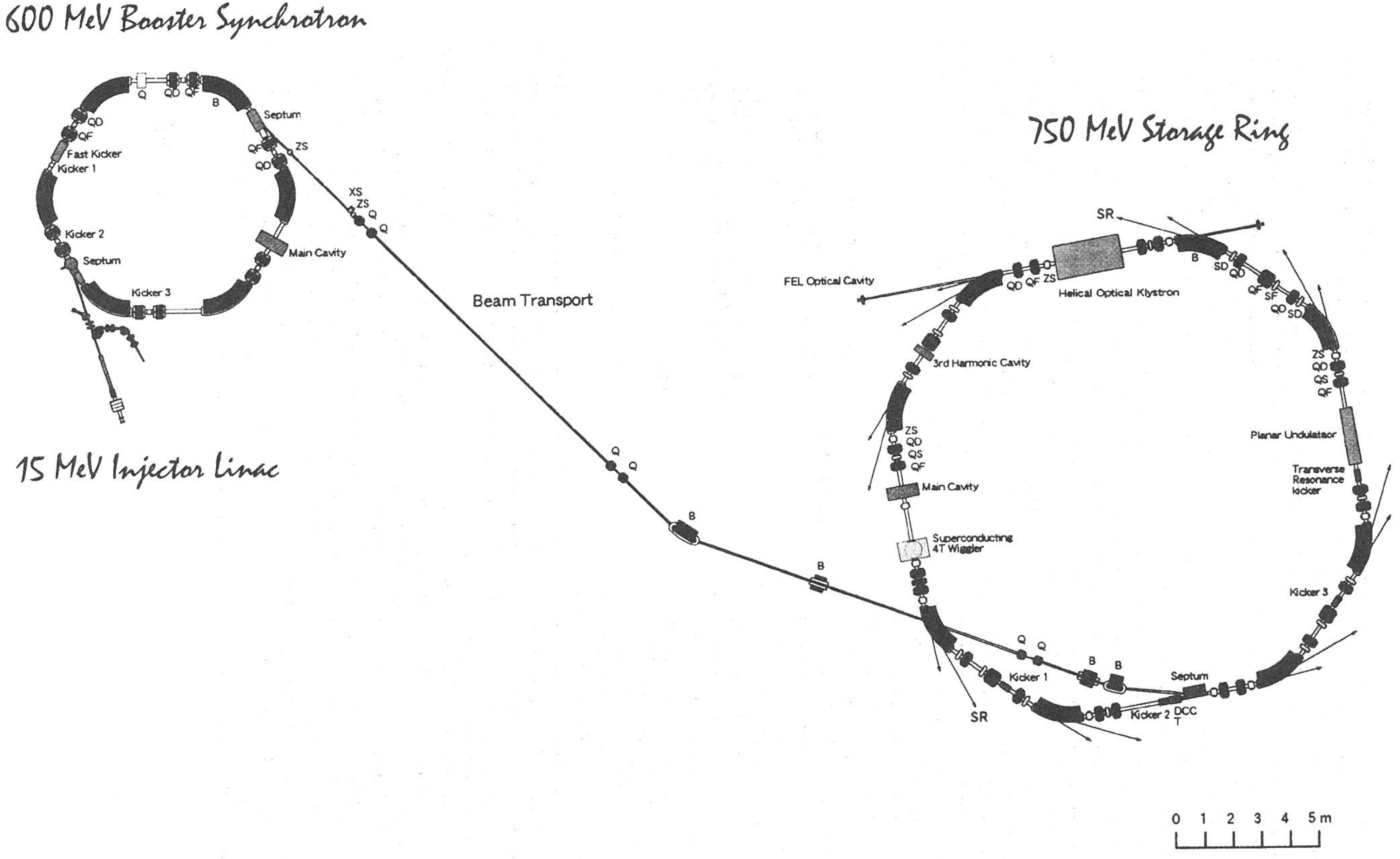

The UVSOR Accelerator Complex

ACCELERATOR COMPLEX

Injection Linac

Energy	15 MeV
Energy Spread	~ 1.6 MeV
Frequency	S-band 2856 MHz
Acceleration	$2\pi/3$ Traveling Wave
Length	2.5 m
Klystron Power	1.8 MW
Repetition Rate	2.6 Hz

Booster Synchrotron

Lattice Type	FODO
Energy	600 MeV
Beam Current	32 mA (8-bunch filled)
Circumference	26.6 m
Super Cell	6
Bending Radius	1.8 m
Betatron Tune	2.25 (horizontal) 1.25 (vertical)
Momentum Compaction	0.138
Harmonics	8
RF Frequency	90.115 MHz
Repetition Rate	2.6 Hz

Storage Ring

Lattice Type	Chasman-Green
Energy	750 MeV
Critical Energy	425 eV
Super Cell	4
Bending Radius	2.2 m
Betatron Tune	3.16 (horizontal) 1.43 (vertical)
Momentum Compaction	0.0264
Emittance	164 nm rad (horizontal)
RF Frequency	90.115 MHz
Harmonics	16
Beam Current	Multi-Bunch 200 mA Single-Bunch 70 mA
Life Time	4 h at 200 mA

Additional Equipment

Higher - Harmonic Cavity	3 × 90.115 Mhz
Superconducting Wiggler	4 T (maximum)
Undulator	for SR
Helical Optical Klystron	for FEL

Control System

Preface: Based on Dual-Host system with CAMAC loop and friendly man-machine interface

Architecture

CPU	VAX4000 (× 2)
OS	VMS
Connection	DECNET & Local Cluster
Operator Console	X - Servers (VXT200 × 3)
Status Monitors	VT286s + Macintosh
Interfaces	CAMAC serial loop GPIB for Beam Monitors RS232C for Host CPU of Wiggler
Languages	FORTRAN, C, Pascal

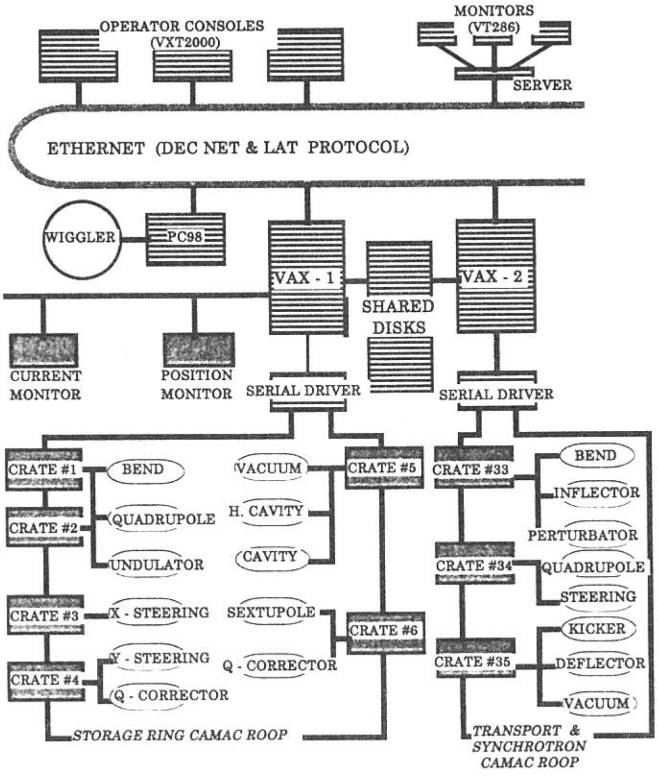

Scheme of Accelerator Control System “UCOSS”

Beam Lines in 1998

Masao KAMADA
UVSOR Facility, Institute for Molecular Science

About one third of beam lines has been upgraded in recent years. In May, we had a beer party to celebrate the commissioning of a 3-m normal-incidence monochromator at BL7B for solid-state researches. Before the party, each active working member had reported an initial planning, expected performance, ray tracing calculation, budget, troubles at test stages, and reason for delay in schedule. Also the future schedule was discussed in details during the party. In July, we had another beer party to celebrate the commissioning of a multi-layer monochromator at BL4A for photochemical reaction. The members in the Urisu group reported the initial calculation, construction procedures, and test experimental results. All of us joined them to expect future scientific achievements with these monochromators. In December, the Mitsuke group had announced the good high-resolution spectrum obtained by the Dragon-type monochromator at BL2B2, where the old Seya-Namioka monochromator was scrapped to expand the wavelength region and to achieve high-resolution for gaseous experiments in VUV and EUV ranges. In December, the new mirror system at BL7A was commissioned by Prof. T. Kinoshita. This mirror system is useful to change spectral range between soft and hard x-ray regions with 4T-superconducting wiggler.

Besides them, a 15-m SGM monochromator at BL8B1 was operational mainly for gaseous experiments in EUV region with a TOF-Mass spectrometer, besides the use for solid-state spectroscopy. A Bruker FT-IR interferometer and an old FT-FIR of a Martin-Puplett type at beam line 6A1 were used for solid-state experiments in the wide wavelength range from near infrared to millimeter wave. A SGM-TRAIN monochromator at beam line 5A, which has been constructed for the use of circularly polarized light from the helical undulator, was operational for photoemission experiments in EUV range. On the other hand, the photoelectron spectroscopy system at BL8B2 is under replacement by the Ueno group to achieve higher-resolution of angle-resolved UPS for organic materials.

Therefore, sixteen experimental stations excluding BL2B2, 4A, 7B, and 8B2 were operational in 1998. The UVSOR facility will soon have twenty stations operational; two soft-x-ray stations equipped with a double-crystal monochromator, eight extreme ultraviolet stations with a glancing incidence or a plane-grating monochromator, four vacuum-ultraviolet stations with a Seya-Namioka-type or a normal incidence-type monochromator, two (far) infrared stations equipped with a FT interferometer, a multi-layer monochromator, and three white-light stations without any monochromator.

In 1998, many and interesting results were obtained at UVSOR beam lines. For examples, combination experiments with SR and lasers were successfully carried out at BL1B, BL3A2, and BL6A2 for gaseous and solid/surface researches. New experiments with an electron-ion coincidence (EICO) method to investigate SR-induced desorption on solid surfaces were actively conducted at beam line 2B1. Resonant photoelectron experiments on organic and transition-metal compounds were carried out at BL1A, BL5B, and BL7A. Photoelectron microscopy experiments were also conducted at BL5B, and BL7A. Photoelectron experiments on semiconductor and metallic surfaces were conducted at BL2B2 and 5A. Two-dimensional photoemission experiments for solid and gaseous molecules at BL1A and BL3B, respectively. Photochemical reaction experiments on semiconductors and organic compounds were carried out at BL3A1, 4B, and 8A. Infrared reflection at high pressure and magnetic circular dichroism in high magnetic field were successfully studied with FT-IR and FT-FIR at BL6A1.

There were lots of troubles as usual in old facilities in the world. In August, a transformer of FT-IR at BL4B was burned, and a switching system at BL2A had electric leakage. In October, a rotary pump at BL8B1 was suddenly fired. These accidents pushed us to install a new alarm system for watching electric troubles in the experimental hall. Also, we did an evacuation drill for our security in November.

The UVSOR facility strongly asks all users to conduct their experimental procedures according to the beam line manuals and the guidebook. The persons who want to use the open and the in-house beam lines are recommended to contact with the following station master or supervisor and the representative, respectively. The persons who want to know updated information of the UVSOR facility are recommended to open http://www.uvsor.ims.ac.jp/.

Table I. Station masters and supervisors of open beam lines in 1998

Beam Line	Station Master	Sub Master	Supervisor
1B	M. Hasumoto	M. Kamada	M. Kamada
2B1	S. Tanaka	M. Kamada	M. Kamada
3A1	M. Kamada	K. Hayashi	M. Kamada
3A2	N. Kondo	T. Gejo	T. Kinoshita
5A	S. Tanaka	M. Hasumoto	M. Kamada
5B	M. Hasumoto	K. Hayashi	T. Kinoshita
6A1	K. Hayashi	O. Matsudo	M. Kamada
7A	T. Kinoshita	O. Matsudo	T. Kinoshita
7B	T. Kinoshita	M. Hasumoto	T. Kinoshita
8A	T. Gejo	N. Kondo	T. Kinoshita
8B1	T. Gejo	N. Kondo	T. Kinoshita

Table II. Representatives of in-house beam lines in 1998.

Beam Line	Representative	Department/Facility
1A	N. Kosugi	VUV Photo Science
2A	N. Kosugi	UVSOR
2B2	K. Mitsuke	VUV Photo Science
3B	K. Mitsuke	VUV Photo Science
4A	T. Urisu	VUV Photo Science
4B	T. Urisu	VUV Photo Science
6A2	M. Kamada	UVSOR
6B	K. Yakushi	Molecular Assemblies
8B2	N. Ueno	VUV Photo Science

BL1A

Soft X-Ray Beamline for Photoelectron-Photoabsorption Spectroscopy

BL1A is a soft x-ray beamline for photoelectron-photoabsorption spectroscopy. The beamline is equipped with a focusing premirror and a double crystal monochromator[1]. The monochromator serves soft x-rays in the energy range from 585 to 4000 eV by using several kind of crystals such as β-alumina, beryl, quartz, InSb and Si crystals. The throughput spectra of the beryl (10$\bar{1}$0) and InSb (111) crystals are shown in Fig.1. Typical energy resolution ($E/\Delta E_{h\nu}$) of the monochromator is about 1500 when we use a pair of beryl or InSb crystals.

For photoelectron-photoabsorption spectroscopy, an ultra-high-vacuum (UHV) apparatus is connected. The top view of the apparatus is shown in Fig. 2. It is equipped with a high-performance electron analyzer (SES-200, SCIENTA Co.). The pass energy (E_P) can be varied between 1 and 500 eV and typical resolving power ($E_P/\Delta E_{elec.}$) is more than 1000. Using the apparatus, resonant photoelectron spectra for solid samples can be obtained with the total energy resolution (ΔE_{total}) of ~0.7 eV around hν=1000 eV.

Reference

[1] A.Hiraya et al., Rev. Sci. Instrum.,63 (1992) 1264.

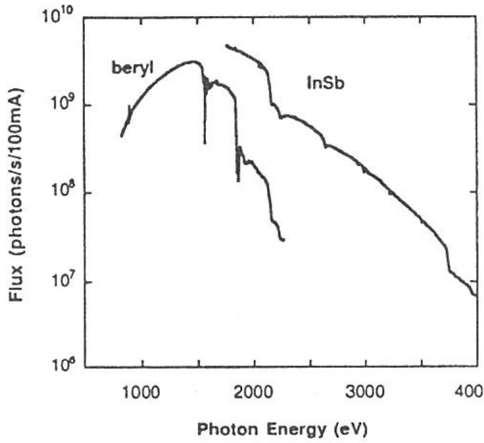

Figure 1. Throughput spectra of the double crystal monochromator at the BL1A.

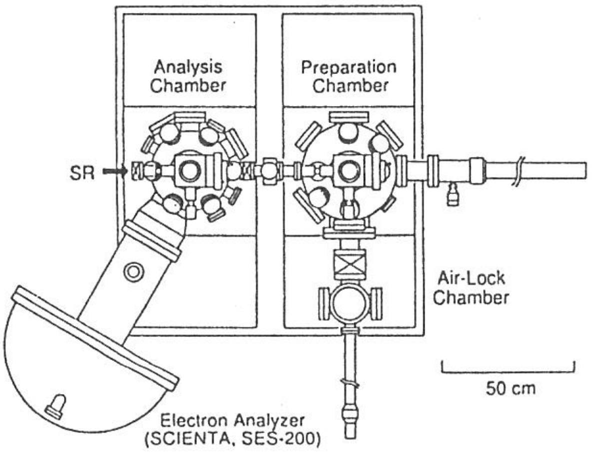

Figure 2. Top view of the UHV apparatus for photoemission-photoabsorption spectroscopy.

Specification

Monochromator : double crystal monochromator (θ_B=70-20°)
Monochromator crystals (2d value, energy range) : β-alumina (22.53Å, 585-1609eV), beryl (15.965Å, 826-2271eV), quartz (8.512Å, 1550-4000eV), InSb (7.481Å, 1764-4000eV), Si (6.271Å, 2104-4000eV)
Resolution : E/ΔE=1500 for beryl and InSb
Experiment : photoelectron-photoabsorption spectroscopy for solid

BL1B

Seya-Namioka Monochromator for General Purpose in VUV Region

The beam line 1B has been used for many experiments such as absorption, reflectivity, photo-ionization, and luminescence in condensed phase. The system consists of a pre-mirror, a 1-m Seya-Namioka type monochromator, and a post-mirror. Three gratings with 600, 1200, and 2400 gr/mm can cover the wavelength range from 40 nm to 650 nm, and two post mirror make it possible to change the focus point. A long-focus mirror is usually used with a LiF window to separate a main chamber for spectroscopy in liquids and biospecimens, while a short-focus mirror is suited to solid-state spectroscopy. The output flux from this monochromator is about 10^{10} phs/s around 200 nm with 0.1 mm slits. The spectral distributions obtained with three gratings are shown in the figure, although they are not the best data because of the contamination of the mirrors and gratings due to the recent careless accident.

A second monochromator (Spex 270M) and a LN-cooled CCD detector (Princeton Inc.) are available for luminescence experiments, together with a liquid helium-flow type cryostat. A time-resolved system to observe luminescence and excitation spectra with three time-gates is also possible. The decay measurement is one of the highlights of this station. A couple of weeks are supplied for the decay measurements under single bunch operation. A TAC system is therefore one of the standard instruments at this beam line.

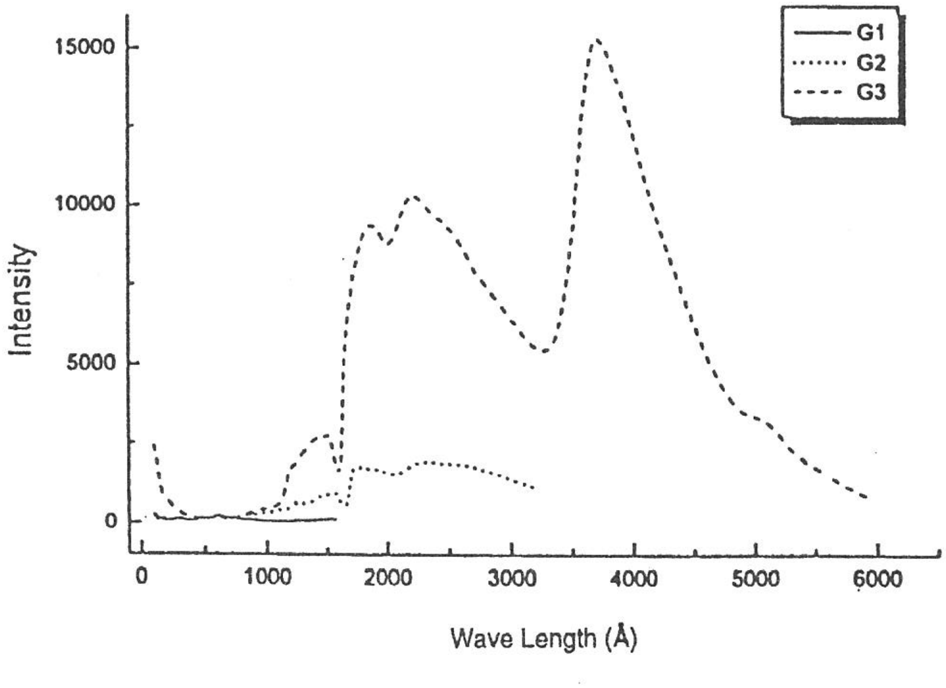

BL2A

Gas Phase Photoabsorption and Fluorescence Spectroscopy

Photoabsorption cross section and fluorescence excitation spectra of gaseous sample are simultaneously measured in a vacuum cell or effusive jet condition. The primary photons in the 30-400 nm region are dispersed by a 1-m Seya monochromator. Higher order light in the 80-120 nm range is suppressed by using a long channel with a cross section 2.5 × 5.0 × 170 mm long filled with argon gas at a pressure $\cong$0.3 Torr as shown in fig. 1. No filter is used between 30 and 80 nm since the photon flux at $\lambda<40$ nm is very weak (see fig. 1). The gas filter and cell are placed in a main chamber which is evacuated by a 5000 *l*/s diffusion pump (Varian, Model VHS10). A LiF window is used for the measurement at the $105<\lambda<210$ nm range as usual. Thus, the total photoabsorption cross section and fluorescence excitation spectra are available in the wide wavelength region 30-210 nm without or with little contamination by the higher order light.

Dispersed fluorescence and polarity of emission from the excited fragment are also measurable in addition to the total photoabsorption and emission cross sections. In the single bunch operation of synchrotron radiation with the period of 178 ns, a radiative life time can be measured.

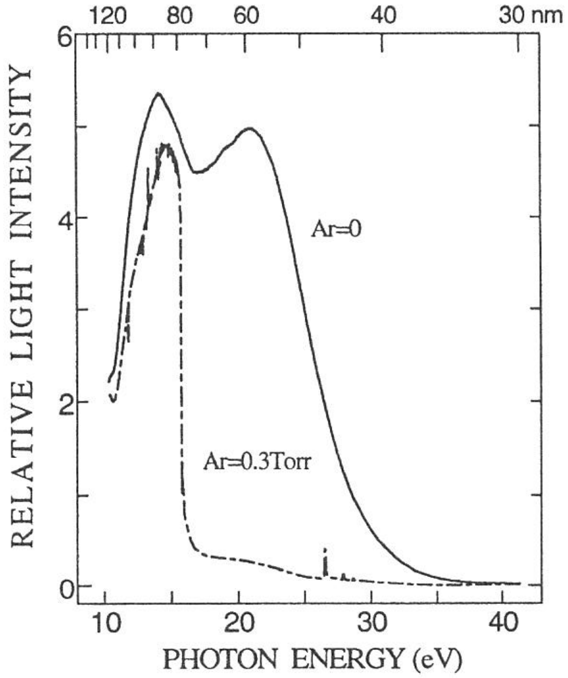

Fig. 1. Transmitted I_0 intensity with and without an Ar gas filter.

Specification

Monochromator : 1-m Seya
Wavelength range : 30-400 nm
Resolution : $\Delta E/E \cong 10^{-3}$ at 100 nm
Grating : 1200 *l*/mm blazed at 96 nm
Experiments :

- Vacuum cell or effusive jet
- Total photoabsorption cross section
- Fluorescence cross section
- Dispersed fluorescence
- Radiative lifetime
- Emission polarity

BL2B1

Soft-X ray beamline for solids and solid surfaces

BL2B1 is a beamline in order to study solids and solid surfaces by the use of photoabsorption and photoelectron spectroscopy. A 2-meter grazing incidence monochromator ('Grasshopper' type, Mark XV; Baker Manufacturing Co.) is installed. A 2400 l/mm grating has been installed since April 1994, and was replaced by a 1800 l/mm grating at March 1997. The resolving power is better than 600 at C-K edge (about 290 eV). Figure 1 shows the photoelectron yield from the Au mesh (10%-transmission) located near the position of a sample by the use of the 1800/mm grating. The dip around 300 eV is due to carbon contamination of optical elements.

The analyzing chamber is installed at the focusing point of the monochromized light. The pressure is less than 1×10^{-10} Torr. A double-pass CMA, a LEED optics, an ion-gun for sputtering, and a sample holder which can be cooled with liquid nitrogen and heated, etc. are equipped for the 'in-situ' measurements. The photoelectron spectroscopy including CIS (Constant initial state spectroscopy), CFS (Constant final state spectroscopy) can be measured using CMA, which is controlled by a personal computer. Samples can be transferred to the analyzing chamber from the air, through the preparation chamber in which sample treatments (e.g. cleaving, filing, and deposition) can be made.

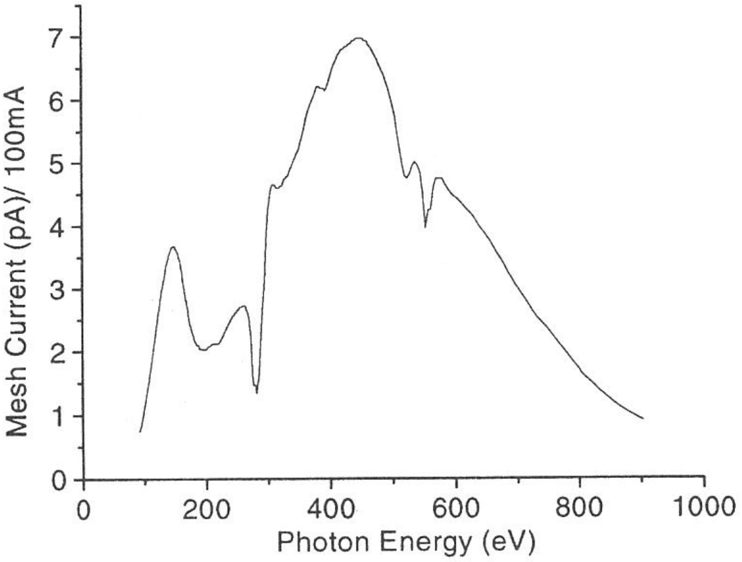

Figure 1. Photoelectron yield measured by the use of the Au mesh

Specification

Monochromator :2m grasshopper type
Energy range :95-1000 eV (1800 l/mm)
Resolution of photon :<0.4eV at 300eV (1800 l/mm)
Resolution of photoelectron :<0.3eV (hv=150eV)
Experiment : Photoelectron spectroscopy, X-ray absorption spectroscopy,

BL3A1

Irradiation Port with Undulator Radiation

The beam line 3A1 has been used for various kinds of experiments need intense undulator radiation. In recent years, photo-desorption, photo-chemical reaction, SR-CVD, photo-etching, irradiation damage effects in condensed phase, light amplification induced by core-level excitation, and so on have been carried out at this beam line. The luminescence from High-Tc superconductors and fullerens, the fluorescence yield of which is not high enough at beam lines for bending radiation, has been observed. A combination experiment with undulator radiation and a diode laser has been successfully conducted for time-response measurement of SR-induced desoprtion.

A planar-type undulator installed in a long straight section of the UVSOR storage ring provides an intense quasi-monochromatic radiation to beam lines 3A1 or 3A2. The undulator consists of 24 sets of magnets, a period length of which is 80 mm. The photon-energy range from 8 to 52 eV can be covered by the fundamentals with a K-value from 0.62 to 3.6, although higher harmonics are mixed into the spectral distribution in case of high K-values.

The beam line 3A1 has no monochromator between the undulator and a sample chamber. The radiation is introduced by a toroidal focusing mirror into sample chamber through a pinhole of 1 mm in diameter and metallic filter (Al, Sn, and In). A gold mesh is always installed in the sample chamber to monitor the incident photons. A typical spectrum distribution measured by the monochromator at BL 3A2 is shown in the figure, where the undulator gap is 60 mm and the photon flux is estimated to be about 10^{14}-10^{15} phs/s on the samples.

A differential pumping system can be provided for the users who want to use gaseous materials. A second monochromator (Jobin-Yvon HR-320), another VUV monochromator (home-made one of normal-incident type), and a helium storage-type cryostat are available for luminescence experiments. A TAC system is also one of the standard instruments of this beam line. For liquid- or gaseous-phase experiments, MgF_2 windows can be installed to separate the sample chamber from the beam line.

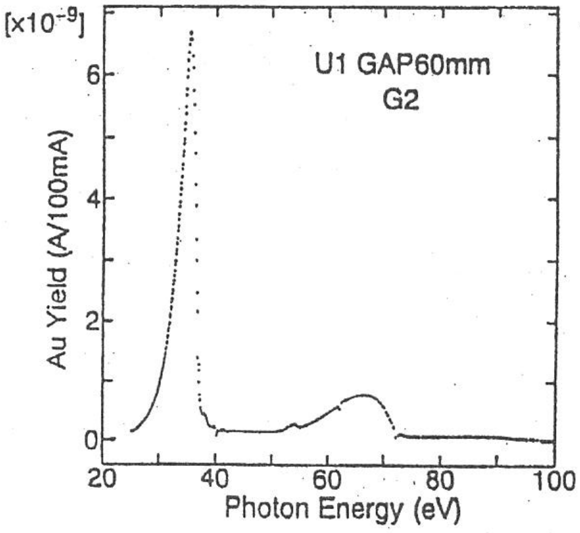

Fig. 2 Typical spectrum of undulator

BL3A2

Gas-Phase Dissociative Photoionization Apparatus

This machine has been constructed to study the formation of multiply-charged ions and their dissociation processes. The monochromator is constant-deviation grazing-incidence type with 2.2m focal length and covers wide wavelength region(10-100nm) where many kinds of molecules and multiply-charged ions are effectively measured. High intensity photon beam is available by introducing the radiation emitted from the undulator to the monochromator. The apparatus contains an angle-resolved time-of-flight mass spectrometer (TOFM) equipped with automatic data acquisition system for photoion-photoion coincidence measurements. For full understanding of dissociative multiple photoionization, we detect the coincidence signals of two fragment ions produced from a parent ion, evaluate the kinetic energy release in "Coulomb explosion", and measure the angular distributions for the fragment ions. The sensitivity with respect to high-speed ions (several tens of electron volts) is much improved in comparison with commercial TOFMS.

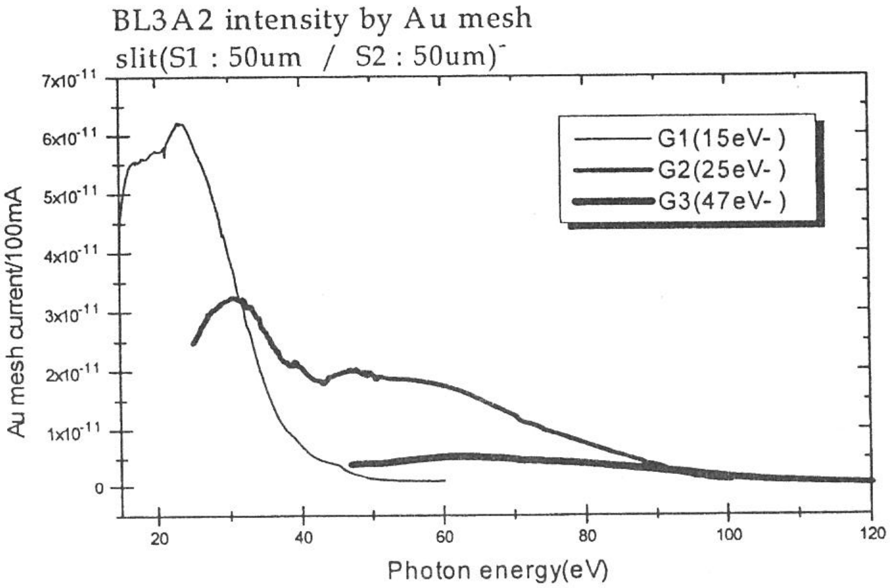

Specifications

monochromator : 2.2m Constant-Deviation Grazing-incidence

Spectral range : 10 - 100nm (15eV - 120eV)

Resolution : 550 - 800 (0.03eV - 0.18eV)

Mass spectrometer : 300

Length of the drift tube : 0.2 - 1m

Rotatable angle : 0 - 90° with respect to the photon beam

BL3B

Beam Line for Gas Phase Two-Dimensional Photoelectron Spectroscopy

This beam line is devoted to studies of elementary atomic and molecular processes induced by excitation of valence electrons. A monochromator is a vertically dispersed normal incidence type with 3m focal length and 10° angle between the incident and diffracted photon beams. The maximum wavelength resolution of 0.007nm is narrow enough to separate vibrational levels of excited states for various molecules. A main component in an experimental chamber is a spherical sector electrostatic energy analyzer which has been designed and setup for photoelectron spectroscopy. One can perform two-dimensional photoelectron spectroscopy with good resolution ($\leq$ 30meV) in which the photoelectron yield is measured as a function of both photon energy and electron kinetic energy (binding energy). A two-dimensional spectrum, usually represented as a contour plot (*e.g.* Fig. 1), contains rich information on photoionization dynamics and properties of superexcited states. A great variety of interesting high-lying states involved in autoionization have been studied as follows: (1) a bound valence state of nitric oxide whose autoionization gives rise to a number of irregularly spaced peaks in its photoionization efficiency curve,[1] (2) the $(3\sigma_g)^{-1}(3\sigma_u)^1$ valence state of acetylene which dominates photoionization cross section and leads to strong vibrational excitation,[2] (3) Rydberg states of nitric oxide which undergo dissociation into N** + $O(^1D^e, ^3P^e)$ followed by autoionizing transitions of the superexcited nitrogen atoms,[3] and (4) multiple-electron-excited Rydberg states of carbonyl sulfide which are primarily produced by conversion from the Rydberg states converging to $OCS^+(B^2\Sigma^+)$ and subsequently dissociate into S** + $CO(X^1\Sigma^+)$ giving rise to autoionizing transitions of the superexcited sulfur atoms.[4]

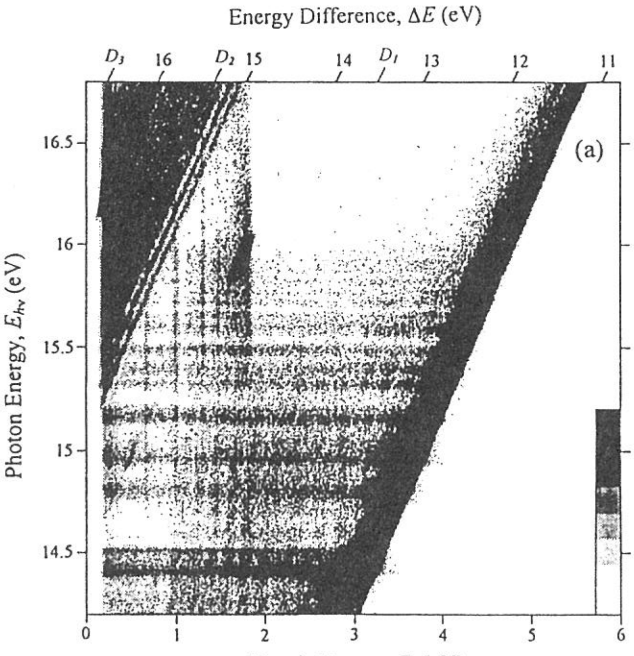

Figure 1. Two-dimensional photoelectron spectrum of OCS taken at the photon energy range from 14.2 to 16.8eV. The electron yield is presented by the plots with eight tones from light to dark on a linear scale.[4]

1) K. Mitsuke *et al.*, *J. Electron Spectrosc. Rel. Phenom.* **79**, 395 (1996).
2) H. Hattori and K. Mitsuke, *ibid.* **80**, 1 (1996); H. Hattori *et al.*, *J. Chem. Phys.* **106**, 4902 (1997).
3) Y. Hikosaka *et al.*, *ibid.* **105**, 6367 (1996).
4) Y. Hikosaka *et al.*, *ibid.* **107**, 2950 (1997).

Specification

Monochromator : 3 m normal incidence
Wavelength range : 30 - 200 nm
Resolution : 0.007 nm at 100 nm

BL4A

Multi-Layered Mirror Monochromator Beam Line for Synchrotron Radiation Stimulated Processing Study

This beam line is now under construction. Synchrotron radiation stimulated reaction has been studied actively during the last decade. The excitation energy dependence of the reaction, however, is a difficult data to obtain, due to that it requires a large number of monochromatised photons which is not supplied by the conventional monochromator beam lines. This beam line is designed to supply 10^{13} to 10^{14} monochromatised tunable photons/s with 3–5 % resolutions, by using a double crystal type multi-layered mirror monochromator. The multi-layered mirrors now considered are Mo/Si for 50–90 eV and Mo/C or Mo/B_4C for 90–150 eV ranges. The calculated reflectivities for a Mo/Si mirror is shown in Fig. 1. The background photons of the lower energy region can be removed by a metal thin film filter.The beam spot size at the focussed point (sample surface in the reaction chamber) is about 2x3 mm^2. For the energy range of 200–500 eV which is covered by this beam line, however, the reflectivity of the multi-layered mirror is generally low, and development of the high efficiency mirror is required.

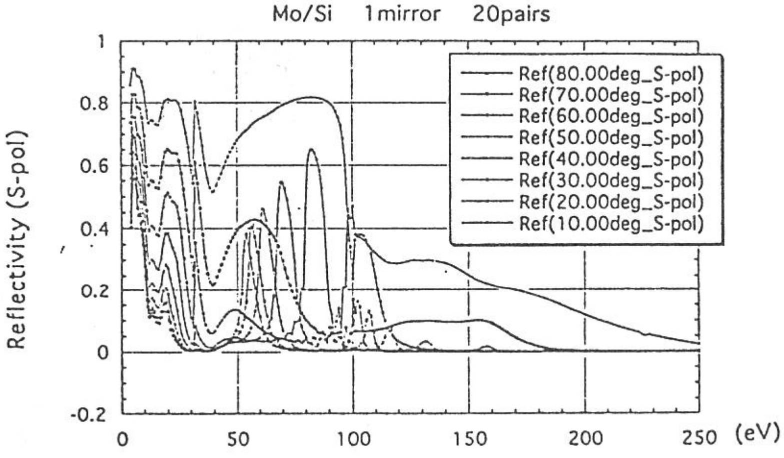

Fig. 1 Calculated reflectivities of the Mo/C multi-layered mirror.

Specifications

Monochromator :Multi-layered mirror monochromator
Wavelength range :50–150 eV
Resolution :3–5 %
Experiments :Excitation energy dependence of the SR processing

BL4B

Synchrotron Radiation Stimulated Processing Beam Line

Several kinds of synchrotron radiation stimulated processing experiments can be conducted using this beam line. The reaction gases up to about 0.1 torr can be used by the differential vacuum pumping. Reaction apparatus shown in Fig. 1 is consisted of four ultra high vacuum chambers, which is used for etching and chemical vapor deposition (CVD) experiments, Si gas source molecular beam epitaxy (MBE) experiments, sample storage, and air–locked sample introduction. The infrared reflection absorption spectrum measurement system is equipped to the reaction chambers to monitor the surface reaction *in situ*. The SR stimulated chemical reaction of surface submonolayer hydrogen on Si(100) have been successfully monitored recently [1].

[1] A.Yoshigoe, K.Mase, Y Tsusaka, T.Urisu, Y.Kobayashi, and T.Ogino, Appl. Phys. Lett. 67 (1995) 2364.

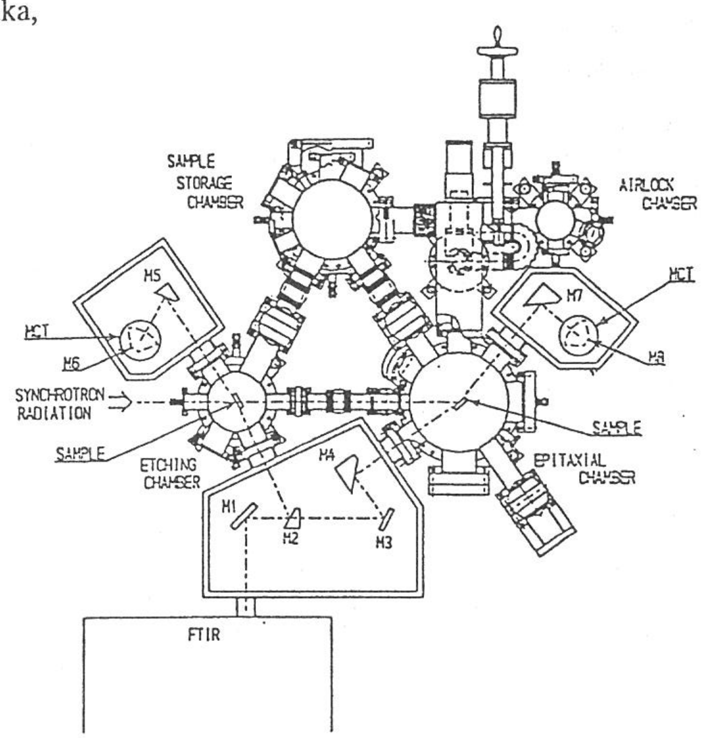

Figure 1. Reaction apparatus

Specification

Monochromater : white beam reflected by bent–cylindrical mirror with grazing incidence angle of 2 degrees.

Wavelength range : 1–100nm

Experiments : SR–stimulated processing

BL 5A

Photoelectron Spectrometer for Solids and Surfaces

The beamline 5A is designed for spin- and angle-resolved photoelectron experiments for solids and surfaces with the circularly polarized synchrotron radiation from a helical undulator and for high-resolution photoelectron experiments with bending magnet radiation. The beamline consists of a Spherical Grating Monochromator with Translational and Rotational Assembly Including a Normal incidence mount (SGM-TRAIN), a spin- and angle-resolved photoelectron spectrometer, and a high-resolution photoelectron spectrometer.

The SGM-TRAIN is an improved version of a constant-length SGM to aim the following points; (1) wide energy range of 5-250 eV, (2) high resolving power, (3) use of linear and circular polarization, (4) reduction of second-order light, and (5) two driving modes by a computer control. The second-order light is well suppressed by using laminar-profile gratings and combinations of mirrors and gratings.

Specifications

1)Monochromator

Type:SGM-TRAIN
(two glancing-incidence and one normal-incidence)
Energy Range: 5-250 eV
Resolution: 0.5-80 meV with slits of 0.01mm
Flux: 3×10^{10} phs/sec at 120 eV with slits of 0.1 mm
(for bending manget radiation)

2) Main Instruments

Two-levels UHV chamber (1×10^{-10} Torr)
Hemi-spherical electron-energy analyzer
(OMICRON HR-125)
Spin- and Angle-resolved spectrometer
(low-energy diffused scattering type)
LEED of reverse type (OMICRON)
Ion-gun (ULVAC-Phi)
He-lamp for UPS
Low-temperature cryostat (>30 K)

3)Helical Undulator (Optical Klystron)

Number of periods	18
Period length, □u	110 mm
Length of dispersive part	302.5 mm
Total length	2351.2 mm
Deflection parameter, Kx,y	0.07-4.6 (helical mode)
Deflection parameter, K	0.15-8.5 (planar mode)
Fundamentals	2-45 eV (Circular polarization)

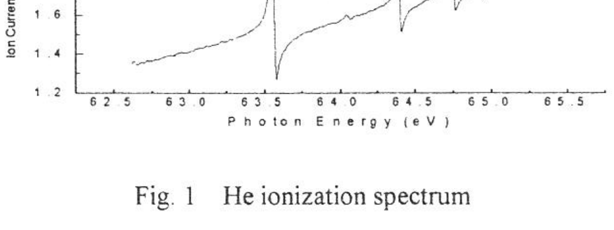

Fig. 1 He ionization spectrum

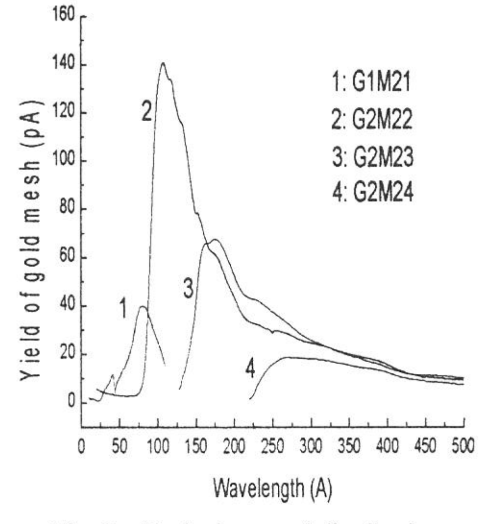

Fig. 2 Typical spectral distribution

Refs: M. Kamada et al., Rev. Sci. Instrum. 66, 1537 (1995), N. Takahashi et al., Jpn. J. Appl. Phys. 35, 6314 (1996).

BL5B

Calibration Apparatus of Optical Elements

BL5B has been constructed to calibrate optical elements. The beam line consists of a plane grating monochromator (PGM) and three chambers (Fig. 1). The chamber A is used for calibration of optical elements, the camber B for optical measurements of solids and the chamber C for photo-stimulated desorption (PSD) experiments. The chamber C is sometimes changed to a chamber for photoemission microscopy.

The calibration chamber is equipped with a goniometer. The goniometer, which was installed for the characterization of optical components, has six degrees for freedom; X-Y translation of a sample, and interchange of samples and filters. They are driven by vacuum pulse motors. Since the polarization of SR is essential for such measurement, axis of the rotation can be made in either horizontal or vertical direction (s- or p-polarization).

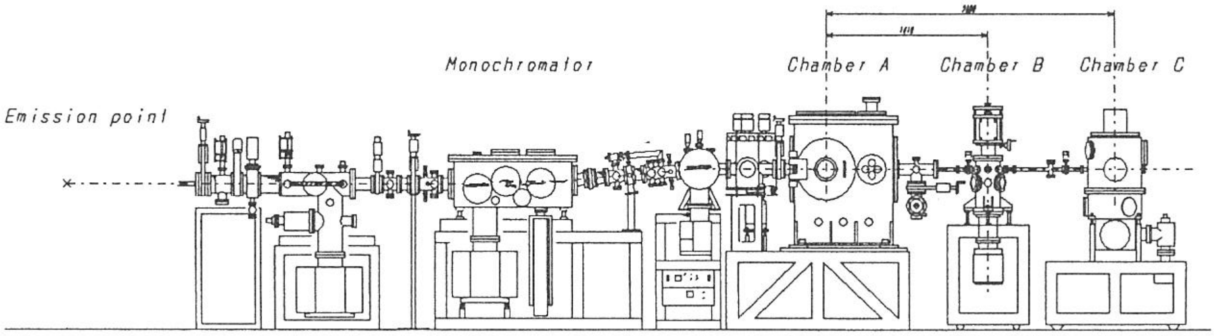

Figure 1. Schematic figure of BL5B spectrometer system.

Specification

Monochromator: Plane grating

Wavelength range: 2 - 200 nm (Fig. 2)

Resolution: $\lambda / \Delta\lambda = 300 \sim 500$

Experiments: Calibration of optical elements, absorption of solids, photo-stimulated desorption from rare gase solids, photoelectron microscopy.

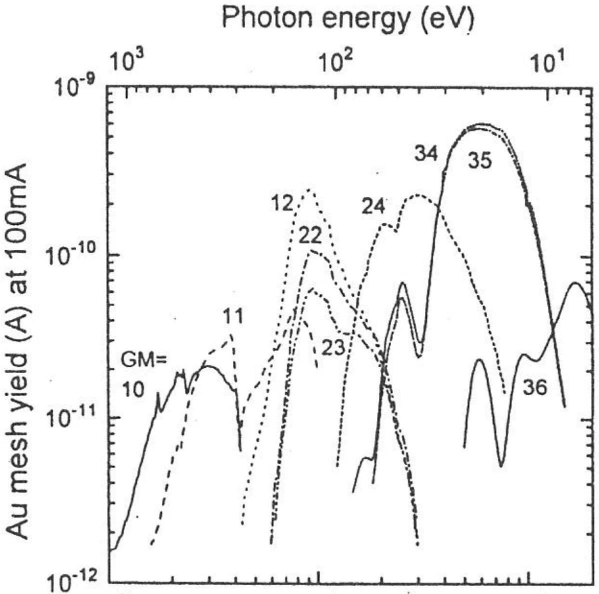

Figure 2. Throughput spectra of BL5B detected by a gold mesh (84% transmission).

BL6A1

Fourier-Transform Middle- and Far- Infrared spectrometers for solids

Synchrotron radiation of UVSOR covers a very wide energy region from soft-X ray to millimeter wave. BL6A1 was constructed in order to cover a long wavelength part in the spectral distribution from near infrared to millimeter wave. The beamline is composed of two kinds of interferometers, a Martin Puplett type and a Michelson type (Fig.1). The spectrum from 0.7 um to 2 mm is measureable by changing three kinds of detectors; MCT, Si-bolometer and InSb hot electron detector (Fig.2). Owing to the high brightness of the SR, the present spectroscopic system is especially favorable to the transmission and reflection measurements on tiny specimens.

In summer 1998, the control system for the Martin-Puplett type interferometer (SPECAC) was replaced owing to its lots of troubles. Most of the components in the control system were newly installed except the chopper controller and the PC. After some correction, the system is now under use regularly.

We have also installed new beamsplitters in the rapid scan type interferometer (Bruker IFS66V): Quartz(II) and myler(23 micron). It expands the measurable region.

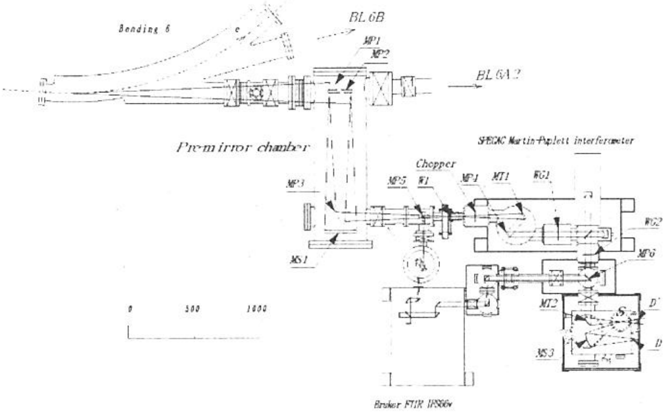

Fig.1 Top view of BL6A1.

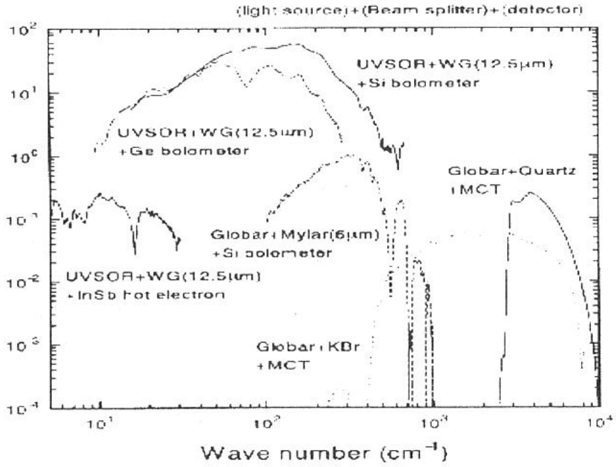

Fig.2 Throughput spectra of BL6A1.

Specification

Interferometers: a Martin-Puplett type and a Michelson type

Detectors: Si bolometer (20-1000 cm-1)
Ge bolometer (with polyethylene window, 30-300 cm-1)
Ge bolometer (with quartz window, 10-200 cm-1)
InSb bolometer (5-50 cm-1)
MCT (400-10,000 cm-1)
Photovoltaic type MCT (400-4000 cm-1, time response: 10 nsec)

Wavelength range: 5~300 cm-1 by the Martin-Puplett type interferometer
40~28,000 cm-1 by Michelson type interferometer

Experiments: Temperature dependence of reflectivity and transmission spectra, absorption under high pressure (up to 20 GPa), reflectivity under magnetic field (up to 8 T) and time-resolved spectroscopy.

BL6A2

Photoelectron Spectrometer for Solids and Surfaces

A Plane Grating Monochromator (PGM) consists of pre-mirrors, a plane grating, focusing mirror, and a post-mirror, with an exit slit only. It covers the wide spectral range from 2 to 130 eV with exchanging two gratings and 5 focusing mirrors. A typical spectral distribution is shown in the figure, where the numbering indicates the combination of the grating and the mirror. A typical photon flux is about 10^{11} phs/s/100 mA at 90 eV with a resolving power of 700. Angle-integrated and angle-resolved photoelectron spectrometers are available. The overall resolution of the integrated type analyzer is about 0.3 eV, while the angle-resolved hemispherical analyzer has a resolving power of 100 with an angular resolution of 1.1° in two axes. The optical system including an ICCD detector can be installed. The standard instruments for surface analysis such as Auger, LEED, Ion gun, and gas doser are installed in the analyzing chamber, the base pressure of which is 1.2×10^{-10} Torr. The samples are transferred from an air-lock chamber to the analyzing chamber through a preparation chamber.

Specifications

1) Monochromator
Type: Plane Grating Monochromator (no entrance slit)
Range: 2-130 eV
Resolution: 0.015-0.3 eV with slit of 0.3 mm
Flux: 10^{11} phs/s/100 mA at 90 eV with 0.1mm slit

2) Main Instruments
Angle-integrated Cylindrical Analyzer
(home made, ΔE=0.3 eV)
Angle-Resolved Hemi-Spherical Analyzer
(home made, $E/\Delta E$=100 $\Delta\theta$=1.1° Two-axes)
Second Monochromator (Jobin-Yvon HR-320)
ICCD (Princeton Instrum.)
Preparation Chamber
Air-lock chamber for quick insertion
LEED of Reverse type (OMICRON)
Ion-gun of Differential type (ULVAC-Phi)
Auger (ULVAC-Phi)

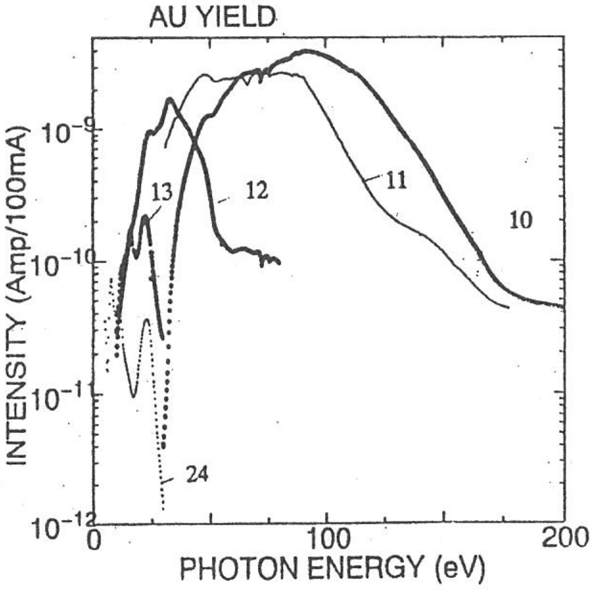

Fig. 1 Typical spectral distribution

BL7A

Soft X-ray Spectrometer for Solids

The beam line BL7A equipped with a double crystal monochromator (DXM) was constructed for the spectroscopic research of solids in the soft X-ray region, where both the bending magnet radiation and the 4T wiggler radiation are provided. Reconstruction of the beam line, such as installation of the focusing mirror system and the new software, improvement of the pumping system etc., has been almost completed. The focussing mirror system was installed between the front-end of the BL7A and the monochromator chamber to obtain the higher performance. The detail of the mirror system is described in this activity report (by Kinoshita et al.). By using the mirror system, procedure of the movement of the beamline between the wiggler line and the bending line has not become necessary. The schematic drawing of the beam line is shown in Figure 1. When we use the relatively lower photon energy light (less than 1.7keV), we use the pair of Si mirrors whereas the pair of Cr mirrors is used for higher energy experiments. The beamline covers the photon energy range from 0.8-5.5keV, by using several pairs of monochromator crystals.

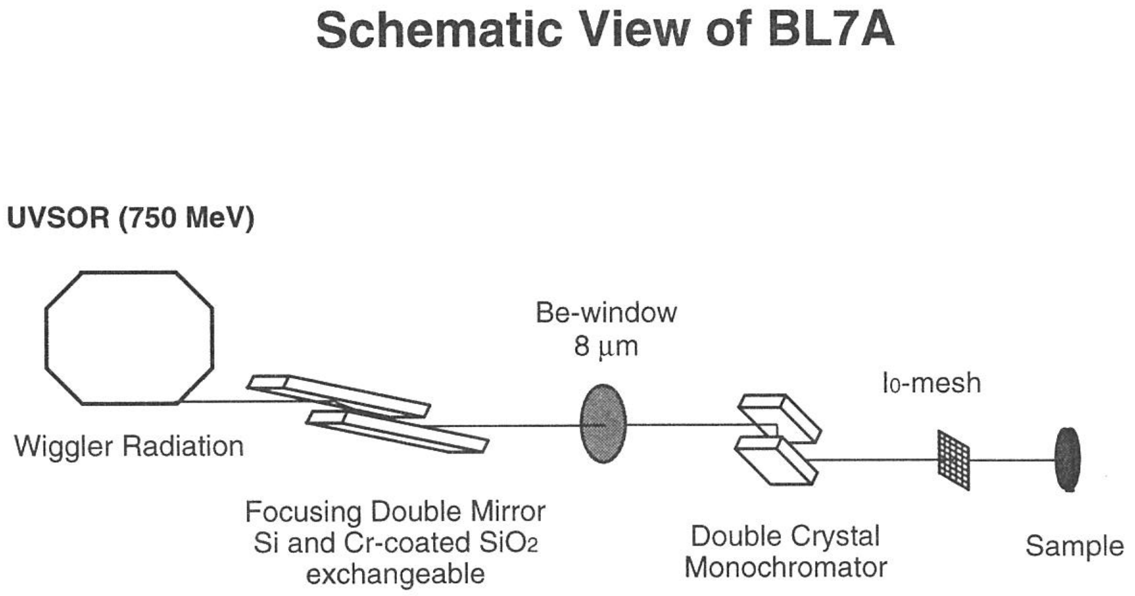

Figure 1. The schematic drawings of the beam line BL7A. The mirror system and the monochromator are located in the straight line downstream of the wiggler.

Specification

Monochromator : Double Crystal Monochromator

Monochromator crystals and covered photon energy:

Beryl(($10\bar{1}0$) (0.82-2.27keV), YB$_{66}$(400) (1.12-3.08keV), Quartz-Y(($10\bar{1}0$) (1.53-4.26keV),

InSb(111) (1.74-4.85keV), Ge(111) (2.00-5.55keV).

Typical resolution: 0.46eV (Beryl Crystal, E=860eV)

Experiments : X-ray absorption spectroscopy (by photoelectron total yield and/or fluorescence)

BL7B

3m Normal Incidence Monochromator for UV, VIS and IR Spectroscopy of Solids

The reconstruction of the beamline BL7B has been almost completed. The 1m Seya-Namioka type monochromator was replaced to the 3m normal incidence monochromator (3m NIM; McPherson upgrade model of 2253) for the extended researches of the highest level with the higher resolution and intensity, the wider wave-length region available and so on. It will be also possible to utilize the linear and circular polarization inherent in synchrotron radiation (SR) and to realize some combined experimental systems, for example, with the synchronized laser to SR pulse or with the extended field. The outline of the new beamline is shown in Figure 1. The main parts of the system are a pre-mirror focusing system, a 3-m NIM and a post-mirror focusing system. The light from 50 to 1000 nm wavelength region is covered by changing three gratings *in situ*. Each spherical grating is original laminar type fabricated on SiO_2 and has effective grooved area of $120x40mm^2$. The 2 focusing positions are available for the experiments. At the position between 2 positions, LiF or MgF2 window valve is installed. Therefore, the measurements for the organic materials, liquid and biochemical ones are possible at the 2nd focal position.

This beamline is used for absorption, reflection and fluorescence measurements on various materials with higher performance (high energy resolution, high intensity, well-polarized light, short repetitive pulse light) not only in the VUV region but also in the near UV, VIS and near IR region. The perfoemance of the beamline is presented in this activity report (by Fukui et al.). The beamline will be opened to the users from April, 1999.

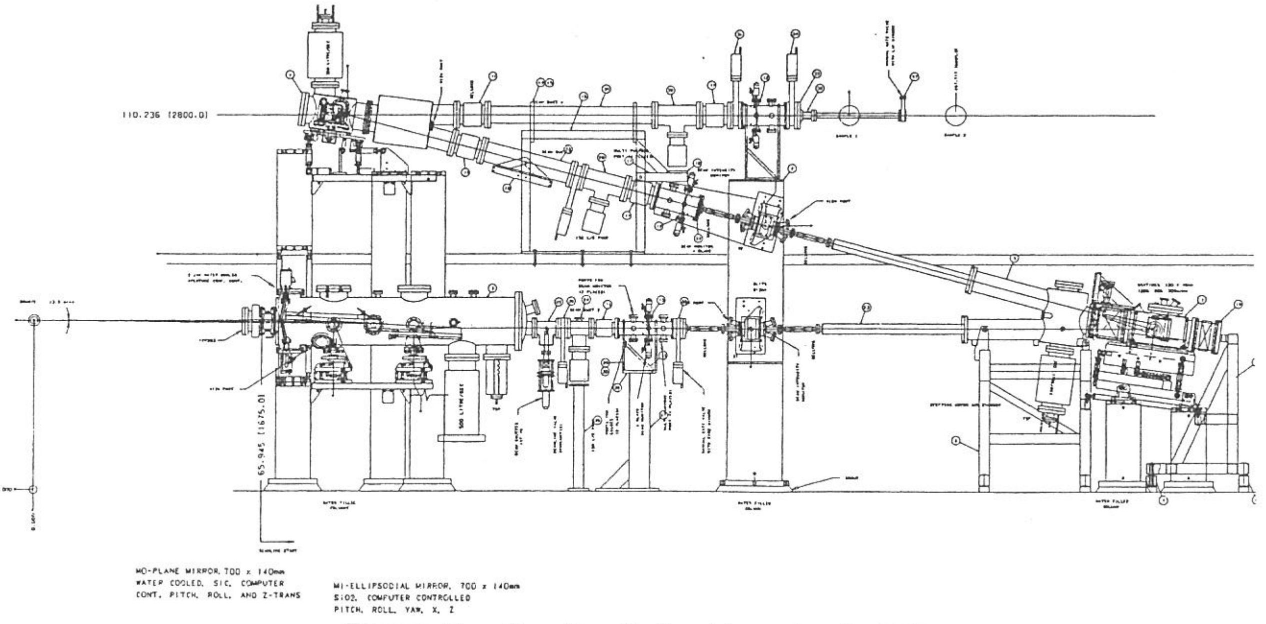

Figure 1. The outline of the side view of the new beamline BL7B.

Specification

Monochromator : 3m Normal Incidence Monochromator
Wavelength range : 50nm-1000nm
Typical resolution : $E/\Delta E$=4000-23000 for 0.01mm slit
Experiments : Absorption, reflection, fluorescence spectroscopy mainly for solids

BL8A

Free Port

This beamline was constructed as a free port to which user can connect their own instruments. The beamline consists of a front end, a focusing premirror chamber and a separation chamber. Both focused and unfocussed beam can be used. A general purpose reaction chamber and a two (or three) stage differential pumping system are available for the experiments that use gas samples without window. With using three stage differential pumping system, gas pressure at the reaction chamber upto 0.5 torr can be used while keeping ultra high vacuum at the premirror chamber.

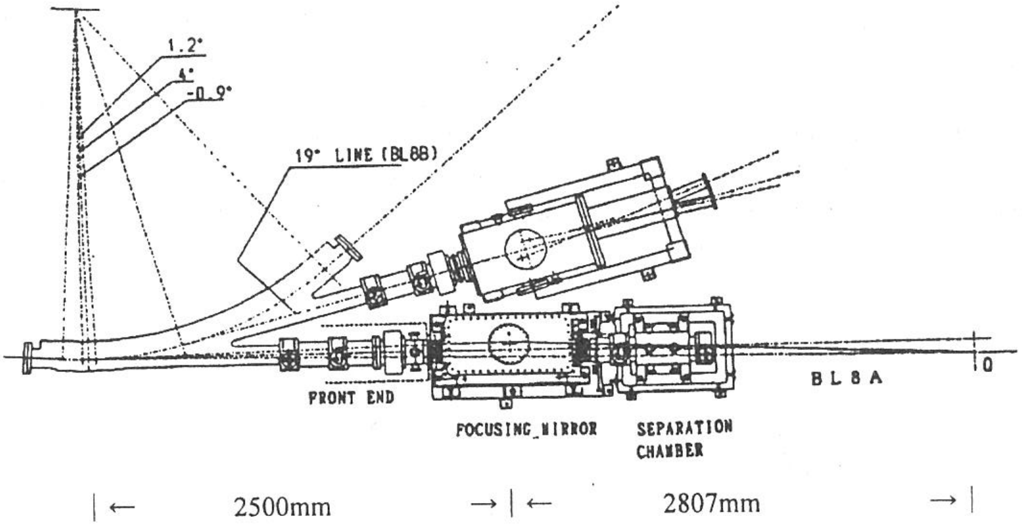

UP VEW OF BL8A

Specification

Spectral range : whole range of synchrotron radiation from UVSOR

Acceptance angle

Unfocused beam : 25 mrad (horizontal) × 8 mrad (vertical)
0.6 mrad (horizontal) × 0.6 mrad (vertical)
(with ϕ 3 mm aperture before sample)

Focused beam : 7.7 mrad (horizontal) × 8 mrad (vertical)
Beam spot size at focu : 3 mm (horizontal) × 2 mm (vertical)
Source - mirror distance : 2500 mm
Mirror - focus distance : 2807 mm

BL8B1

Photoabsorption and Photoionization Spectrometer

Last year a new beam line BL8B1 was constructed for observation of high resolution photoabsorption and photoionization experiments in the photon energy range from 30 to 800 eV, which includes the 1s core excitation energy of C, N and O atoms. For high resolution measurement among these energy, a constant-deviation constant-length spherical grating monochromator (CDCL-SGM) with three gratings (G1: R = 15 m; 1080 l/mm, G2: R = 15 m 540 l/mm, G3: R = 7.5 m; 360 l/mm) has been employed, whose entrance and exit slit positions and directions of incident and exit photon beams do not change during its scan. Consequently, it provides us with an resolution (E/ΔE) of 4000 at 400 eV and of 3000 at 245 eV. A drain current of gold foil reveals the absolute photon flux normalized by an ring current when two slit widths are 10 μm (Fig. 1).

Being Equipped at the downstream of the monochrometer, an chamber with a time-of-flight ion detector and a photoelectron detector allows us to measure photoelectron - photoion coincidence (PEPICO) and photoion - photoion coincidence (PIPICO) spectra. Measurements of absorption, electron yield and emission spectra of solid samples are also available.

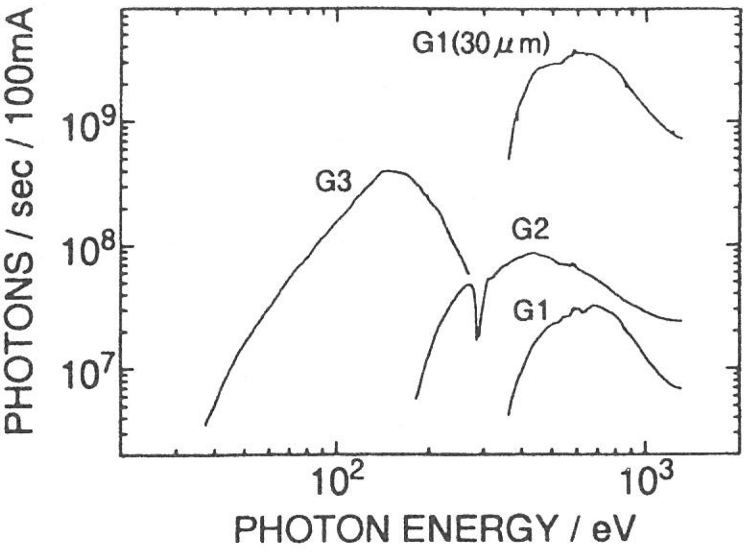

Figure 1. Absolute photon fluxes measured by a drain current of gold foil

Specification

Monochrometer	: 2.2 m constant-deviation grazing incidence
Wavelength range	: 30 to 800 eV
Resolution	: E/ΔE = 4000 at 400 eV and 3000 at 245 eV
Available Experiments	: Measurement of photoabsorption and photoionization spectra for gas and solid sample

BL8B2

Angle-Resolved Ultraviolet Photoelectron Spectrometer for solids

BL8B2 is a beamline for angle-resolved ultraviolet photoemission spectroscopy (ARUPS) system which is designed for measuring various organic solid such as molecular crystals, organic semiconductor, and conducting polymers. The beamline consists of a plane-grating monochromator (PGM), a sample preparation chamber with a fast entry Load-Lock chamber, a measurement chamber with an accurate manipulator for temperature dependence (base pressure 3×10^{-10} Torr), a cleaning chamber (base pressure 2×10^{-10} Torr), and a sample evaporation chamber (base pressure 3×10^{-10} Torr). The cleaning chamber is equipped with back-view LEED/AUGER, Ar^+ gun and an infrared heating units. The PGM consists of pre-mirrors, a plane grating, focusing mirror, and a post-mirror, with an exit slit. It covers the wide range from 2 to 150 eV with exchanging two gratings (G1; 1200 l/mm, G2; 450 l/mm) and five cylindrical mirrors. The toroidal mirror focuses the divergent radiation onto the sample in the measurement chamber. The spot size of the zeroth-order visible light at the sample surface is about $1\times1\mathrm{mm}^2$. The energy resolution at a slit width of 100 μm was found to be 0.004 - 0.3 eV in the wavelength range from 2 to 130 eV. A hemispherical electron energy analyzer of 25 mm mean radius with an angular resolution of 2° can be rotated around vertical and horizontal axes. The sample mounted on a manipulator can be also rotated around two axes.

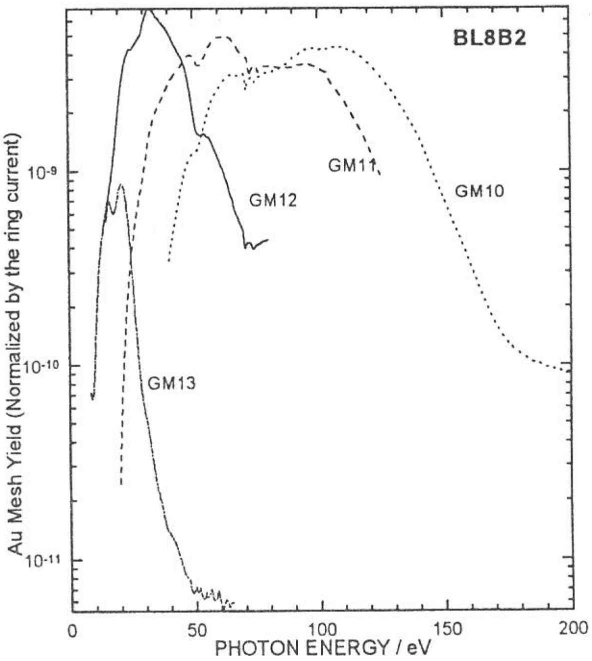

Figure Throughput spectra of plane-grating monochromator at BL8B2 with 100 μm exit slit.

Specification

Monochromator : plane grating monochromator

Spectral range : 2 - 130 eV

Resolution : 0.25 eV at 40 eV, as determined by the Fermi edge of gold.

Experiment : Ultraviolet Photoelectron Spectroscopy for various organic solids

Polarization : 85~91 % at 5000 Å

Open beam lines

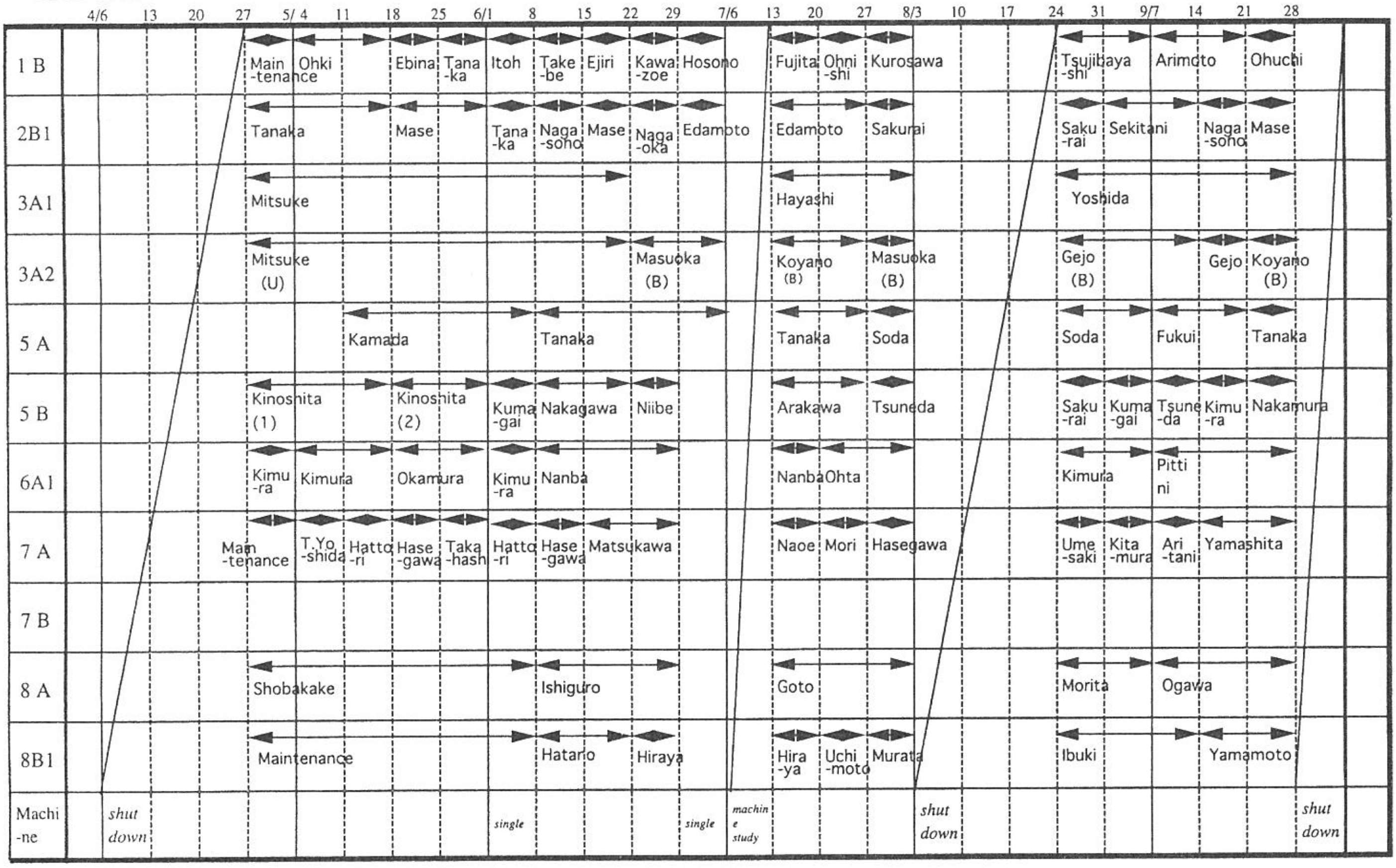

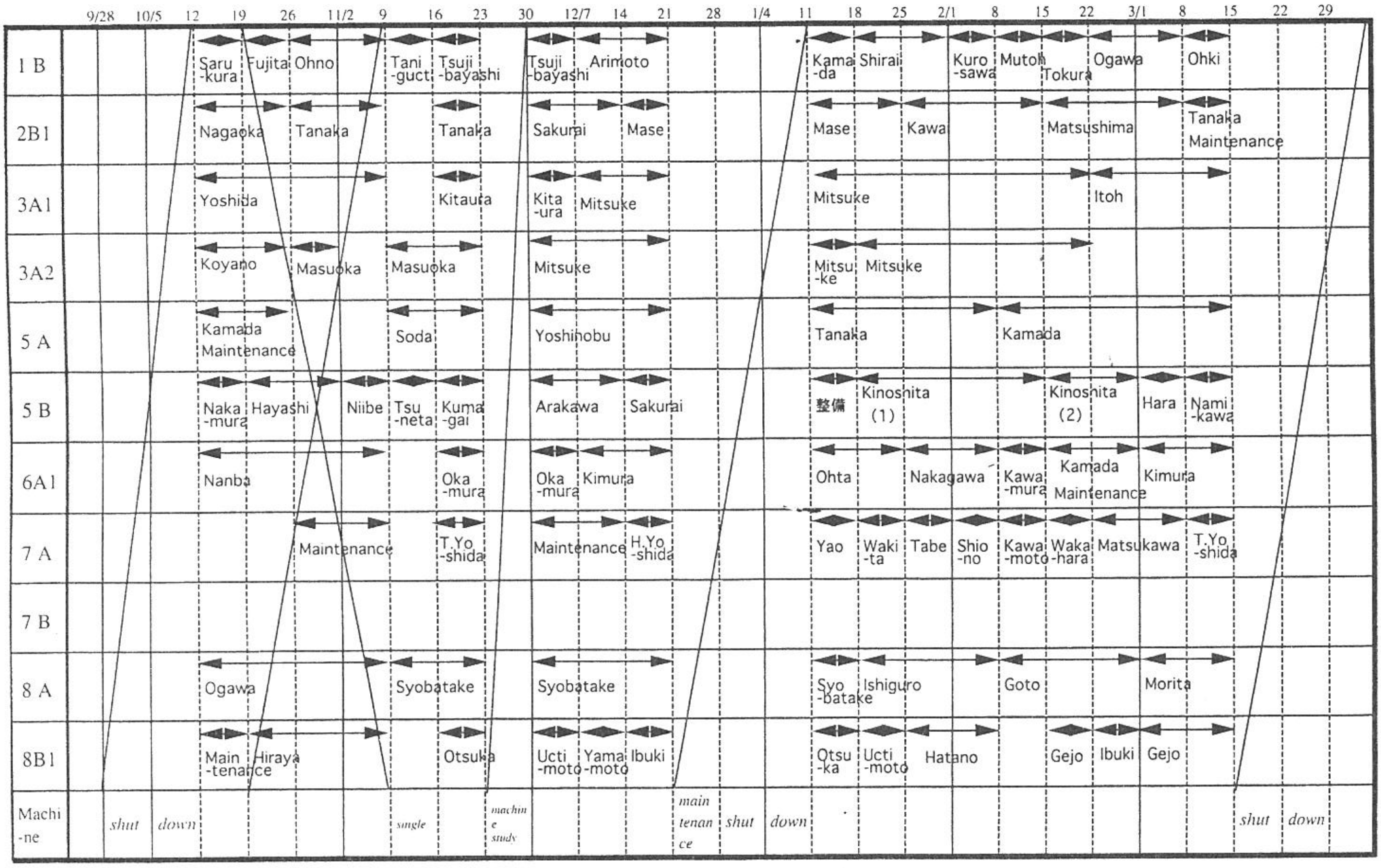

In-house beam lines

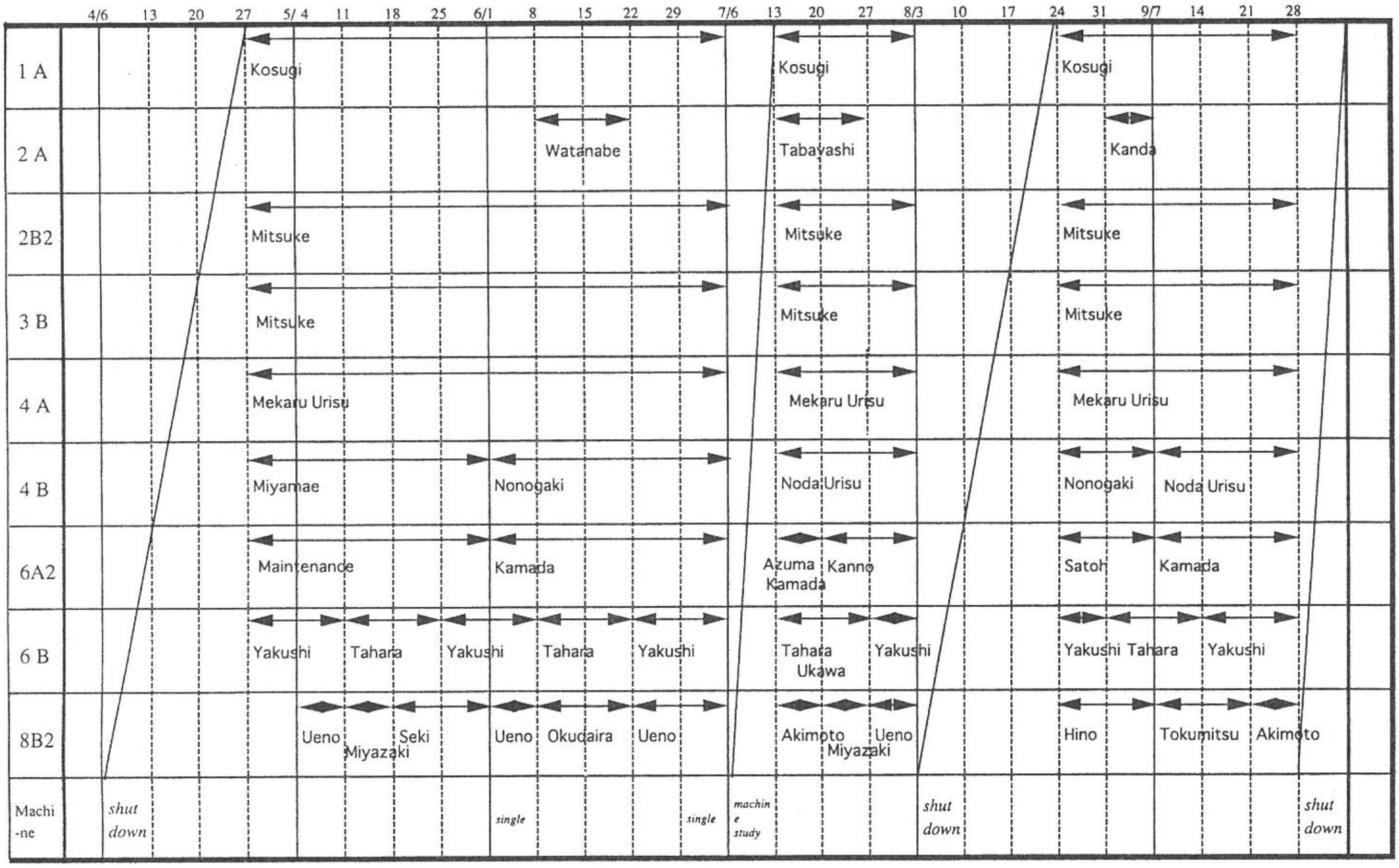

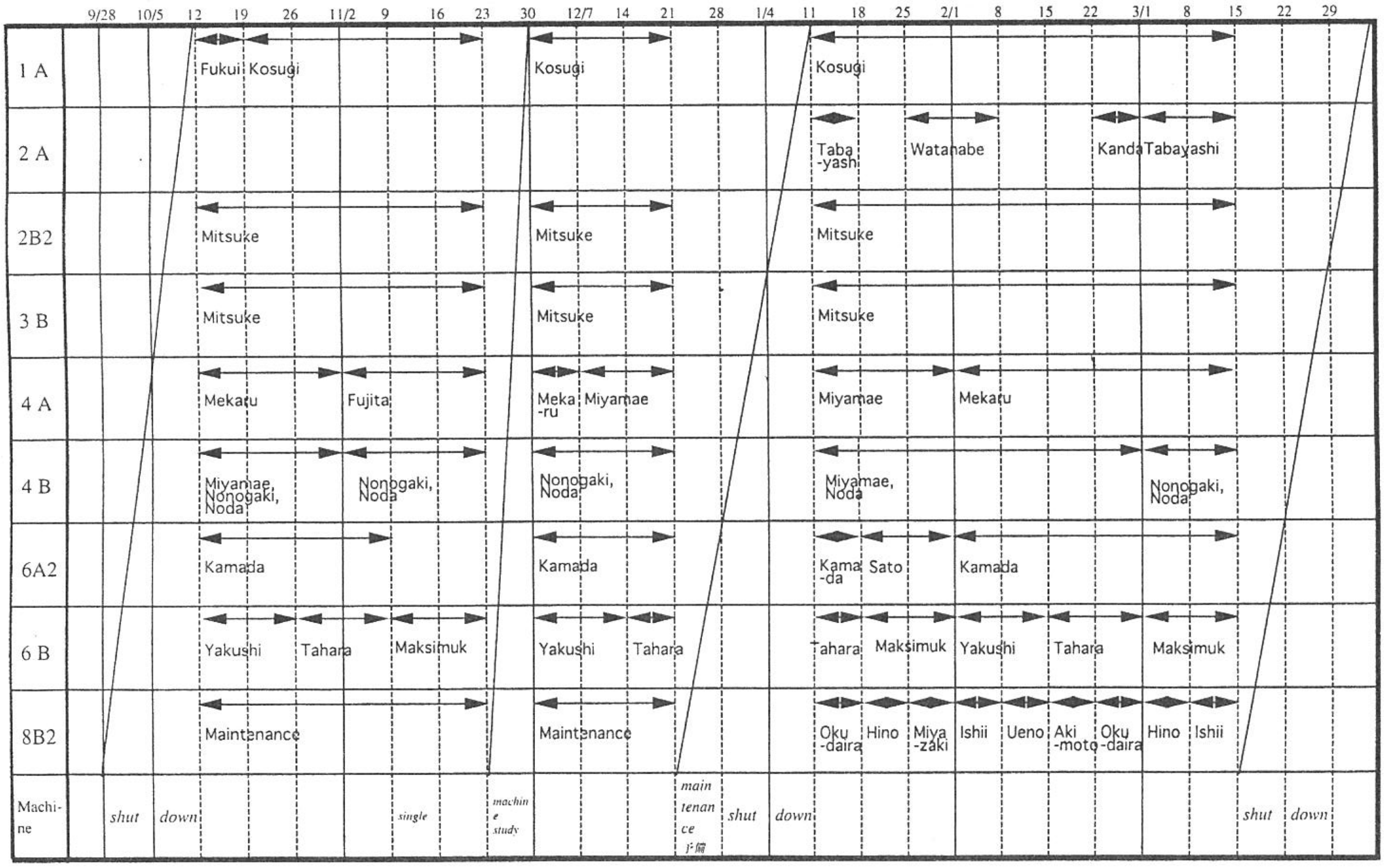

UVSOR

Beam Physics

Improvements of optical resonator and control system in the UVSOR-FEL

S. Koda, H. Hama, M. Hosaka, J. Yamazaki and K. Kinoshita
Institute for Molecular Science, Okazaki, 444-8585, Japan

Free Electron Laser (FEL) has been developed in the UVSOR. First lasing of the FEL was achieved in 1993 [1]. The wavelength of 239nm was attained in 1997 [2] and the UVSOR-FEL was temporally shutdown due to interference with development of the beam line BL5A.

As next step of the FEL research, we aim to provide feasibly stable FEL light for user experiments and to study further detailed mechanism of FEL. For the purpose, we are developing new optical resonator and control system. Schematic figure of the FEL system is shown in Fig. 1. The system consists of the resonator, an optical klystron and those control system.

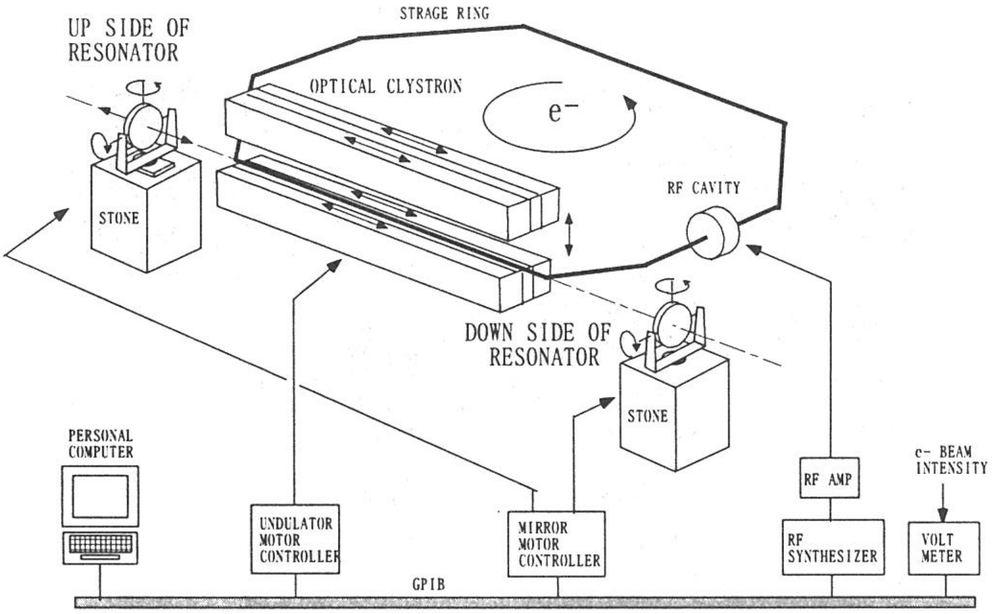

Fig. 1 Schematic view of improved FEL system in UVSOR.

In the development of the resonator, it is important to reduce mechanical movement, which produces directly instability of the FEL. In addition, it is required to be compact to avoid conflicting with the beam line of BL5A. Detail of the resonator is shown in Fig. 2. To escape complicated mechanical resonance and to decrease amplitude of mechanical oscillation, the structure of the resonators is simplified and heavy stones are employed as the resonator base. The control axes of mirrors are reduced from ten axes of an old FEL system to five axes. The bases of the resonator are changed from steel frames of the old FEL system to bulks of stone. The stones are heavy stones with density of 3.0 g/cm^3 . The stone weights of the up and down side in Fig. 2 are values of 2.2 t and 1.7 t, respectively. The stone of the down side in setting is shown in Fig. 4.

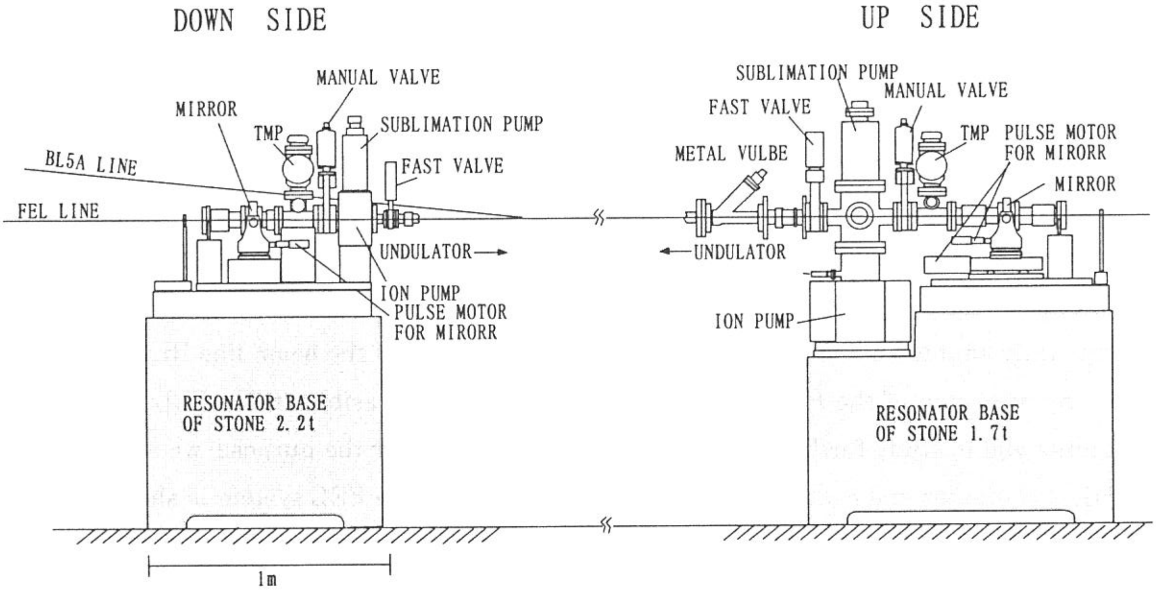

Fig. 3 Detail of FEL resonator.

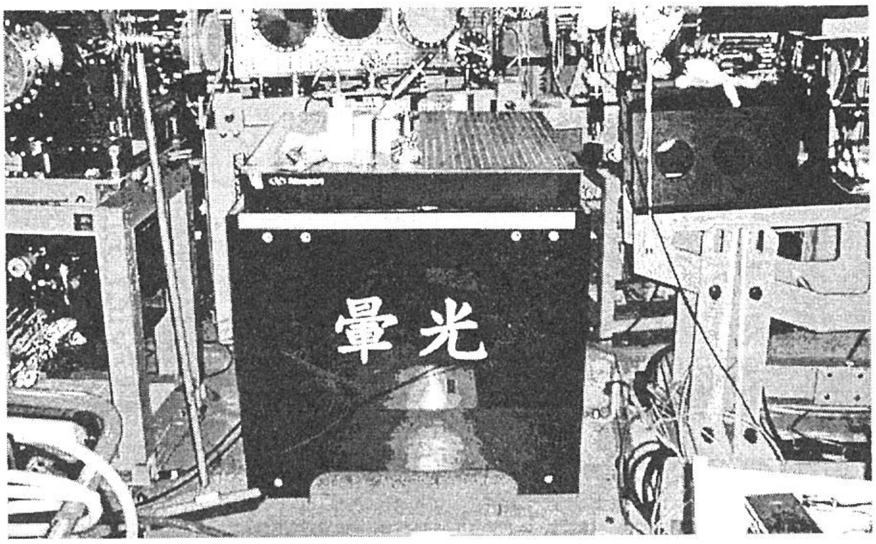

Fig. 4 The resonator base-stone of down side in setting

In development of control system, distributed and individual control of each devices in the old system are concentrated to a personal computer via a GPIB network (Fig. 1). The control system, which works on LabView, is finally going to control and monitor a RF synthesizer for the UVSOR cavity, five motors of the optical klystron, five motors of the resonator mirrors and a digital volt-meter for monitoring e^- beam intensity.

Construction of the resonator has almost completed. The control system is under construction but the system has been partially used for machine study using the optical klystron. First FEL experiment with wavelength of 270nm will be started in May, 1999.

[1] S. Takano, H. Hama and G. Isoyama, Nuclear Instruments and Methods A331 (1993) P. 20-36

[2] H. Hama, K. Kimura, M. Hosaka, Yamazaki and T. Kinoshita, Proceedings of the third Asian Symposium on Free electron Lasers, Ionics Publishin, Tokyo (1997) P. 17.

Measurement of misalignment of quadurupole magnets of the UVSOR storage ring

Masahito HOSAKA, Shigeru KODA, Jun-ichiro YAMZAKI and Hiroyuki HAMA

UVSOR Facility, Institute for Molecular Science, Myodaiji, Okazaki 444-0867

In order to improve the performance of the UVSOR storage ring, we are determining a 'golden orbit' in which the electron beam passes through the magnetic center of all the quadruple magnets. In the effort, we have deduced spatial relationships between beam position monitor (BPM) centers and quadrupole centers using a beam based technique.

The basic idea of the measurement comes from so called 'K-modulation' method used in different storage ring laboratories[1]. A beam passing through a quadrupole magnet in a storage ring with a horizontal (or vertical) displacement of x_0 gains a dipole kick of $B = klx_0$, where k and l are the focusing strength and the length of the quadrupole magnet, respectively. When the focusing strength is changed by Δk, the deviation in the i-th BPM is

$$\Delta x_i = \frac{\sqrt{\beta_Q \beta_i}}{2\sin(\pi\nu)}\cos(\pi\nu - |\Delta\psi|)\cdot l\Delta k x_0, \qquad (1)$$

where β_Q and β_i are the betatron functions in the quadrupole magnet and the i-th BPM, respectively, $\Delta\psi$ is the difference between the betatron phases and ν is the betatron tune. Accordingly, the mean square value of the closed orbit deviations measured by using all BPMs with which the storage ring is equipped is given by

$$\overline{\Delta x^2} = \frac{1}{n}\sum_i^n \Delta x_i^2 \propto x_0^2, \qquad (2)$$

as a function of x_0 where n is the total number of BPMs. If the horizontal difference between the center of the quadrupole and the BPM mounted into it is x_Q, an arbitrary value of x_0^2 is given by $(x_{BPM} - x_Q)^2$ where x_{BPM} is a value of a beam position measured using the BPM. The value of x_Q can be deduced by fitting a parabola to the data points of $\overline{\Delta x^2}$ for different x_{BPM}s.

In the UVSOR storage ring, however, it is not possible to measure x_Q directly, since a BPM is not mounted into each quadrupole but two BPMs are located upstream and downstream of a straight section which consists of 4 quadrupoles (Fig. 2). Then we have developed a modified method of deducing a quadrupole's magnetic center ; we measure a trajectory passing through the center of a quadrupole using the two BPMs located upstream and downstream of it. In a formulation of the transfer matrices method [2] a beam trajectory is described by a position vector $\vec{x} = (x, x')$ where x and x' are a deviation from a reference axis and its divergence angle, respectively. Thus, we can characterize a trajectory as a position vector at the upstream BPM; this position vector is transformed to a position vector at a position of a quadrupole with transfer matrices . We now define the reference axis as the line connecting the center of the upstream BPM and the downstream BPM; displacements of quadrupoles ($x_{Q1}, x_{Q2}, \ldots x_{Qm}$ for the 1-st, the 2-nd, ... the m-th quadrupole) are relative to it. Then a trajectory passing through the j-th quadrupole's center satisfies a relation:

$$x_{Qj} = \left[T_{up\to Qj}\right]_{11} x_{up}(j) + \left[T_{up\to Qj}\right]_{12} x_{up}(j)' + \sum_{i=1}^{j-1} K(i,j), \qquad (3)$$

where $\vec{x}_{up}(j) = (x_{up}(j), x'_{up}(j))$ is the position vector at the upstream BPM, $T_{l\to n}$ denotes transfer matrix from l-position to n-position and $K(i,j) = -\left[T_{Qi+1\to Qj}(T_{Qi} - E)\right]_{11} x_{Qi}$ is the displacement at the j-th quadrupole position due to misalignment of the i-th quadrupole. The value of $x_{up}(j)$ can be deduced using the upstream BPM and the technique mentioned above. However, the value of $x_{up}(j)'$ can not be deduced directly and we therefore deduce it using the downstream BPM and the following relation:

$$x_{up}(j)' = \left\{x_{down}(j) - \left[T_{up\to down}\right]_{11} x_{up}(j) - \sum_{i=1}^{m} K(i,m)\right\} / \left[T_{up\to down}\right]_{12}, \qquad (4)$$

where $x_{down}(j)$ is the beam position at the downstream BPM. Consequently, the set of values of x_{Qj} for $j = 1, 2, \ldots, m$ can be obtained solving eq. (3) and (4) for $j = 1, 2, \ldots, m$ simultaneously.

In the UVSOR storage ring, there are 28 quadupole magnets classified into four groups (Q1, Q2, Q3, Q4) and each group has its own power supply. In order to change focusing strength of an individual quadupole magnet, we installed an extra cabling and connected a quadupole magnet to an additional DC power supply. Closed orbit deviations due to the change of the strength of a quadrupole magnet were measured using all BPMs as a functions of the beam position measured using upstream BPM and the downstream BPM and an example is shown in Fig. 1. In figure 2, we present the result of the measurement for one of long straight sections. As seen in the figure, misalignment of the qudrupoles both in the horizontal and the vertical direction are considerably. Consequently, for future improvement of the UVSOR storage ring, accurate realignment of the quadrupole magnets will be necessary.

REFERENCES

[1] F. Tecker, B. Dehning, P. Galbraith, K. Hendrichsen, M. Placidi, R. Schmid, Proc. of the 1997 Part. Accel. Conf., Vancouver (1997).

[2] H. Wollnik, “Optics of Charged Particles”, Academic Press, London (1987).

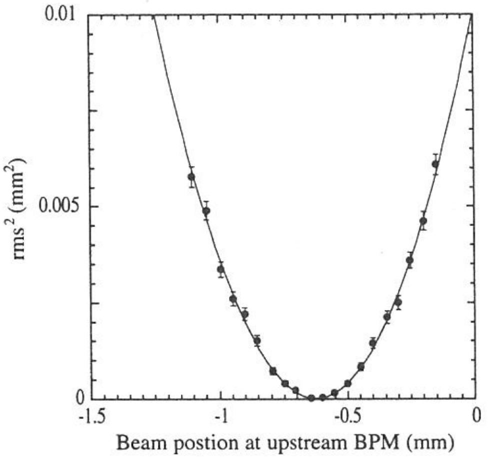

Figure 1 Measured mean square value of the closed orbit deviations due to change of the strength of QF1 as a function of beam positions measured using the upstream BPM. Fitting a parabola to data points , the trajectory passing through the center of QF1 was deduced.

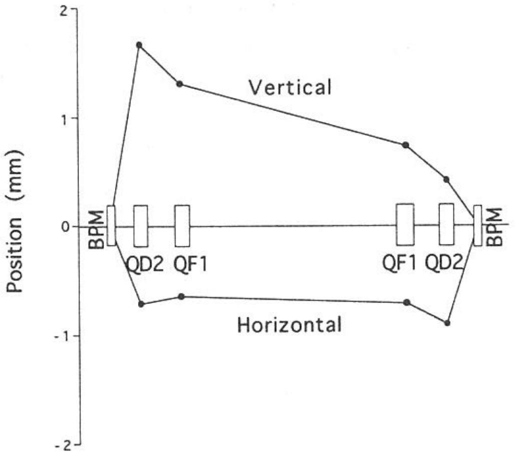

Figure 2 Measured misalignment relative to BPMs in the 3rd long straight section.

UVSOR

Instruments Developments

(BL2B2)

First performance test of the 18m Spherical Grating Monochromator

Hiroaki YOSHIDA[A] , Hideo HATTORI[B] , and Koichiro MITSUKE[B]

[A]*Department of Physical Sciences, Hiroshima University, Kagamiyama, Higashi-Hiroshima 739-8526, Japan*
[B]*Department of Vacuum UV Photoscience, Institute for Molecular Science, Myodaiji, Okazaki 444-8585, Japan*

An 18 m spherical grating monochromator (18 m SGM) with high resolution and high photon flux has been constructed at the bending-magnet beamline BL2B2 of the UVSOR [1]. The monochromator is designed to cover the energy range of 20–200 eV with the three gratings: G1 (2400 lines mm^{-1}, R = 18 m) at 80–200 eV , G2 (1200 lines mm^{-1}, R = 18 m) at 40–100 eV and G3 (2400 lines mm^{-1}, R = 9.25 m) at 20–50 eV. A resolving power of 5000 and photon flux of more than 10^{10} photons s^{-1} are expected at a 100 mA ring current. The including angles are 160° for G1 and G2. A small including angle of 140° is adopted for G3 and two plane mirrors coated with aluminium are located between G3 and the exit slit as optical filters. These geometrical devices may contribute significantly to reduction of the high-order lights.

Figure 1 shows a doubly excitation spectrum of He obtained by using G2. Sample gas was introduced as an effusive jet into the reaction chamber with a pressure of 3×10^{-6} Torr. The spectrum was obtained by extracting ions from the interaction region by applying a highly negative voltage to the cathode of a microchannel plate detector. Entrance and exit slit widths are set to 100 μm and the position of the exit slit is fixed at 4230 mm away from the center of the grating, which is close to the focusing length of the diffracted light with the energy of 60 eV. A series of the Rydberg states up to n = 9+ are clearly observed. The observed full width of the 9+ Rydberg transition is about 27 meV. The resolving power is thus estimated to be more than 2400 at 65 eV with the slit widths of 100 μm.

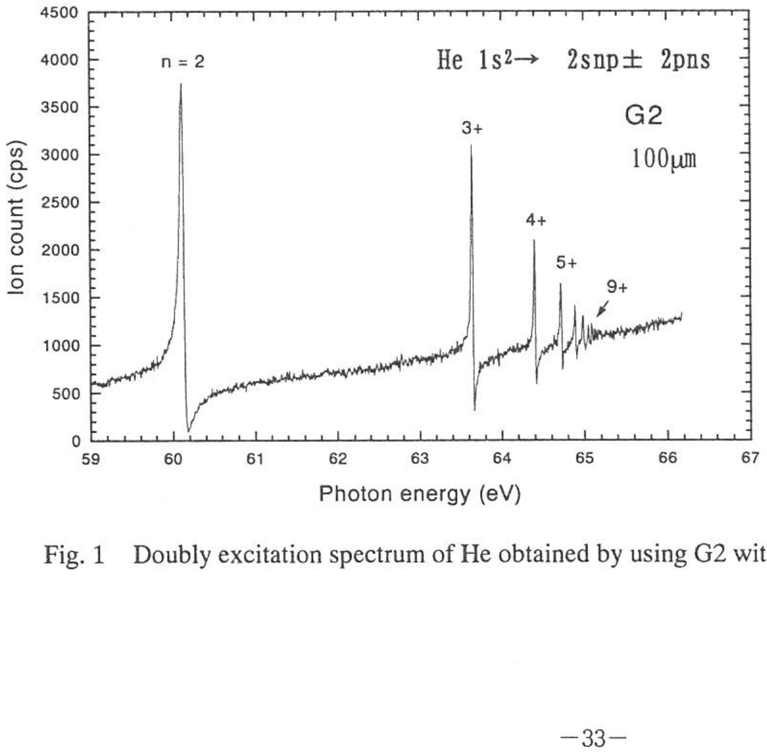

Fig. 1 Doubly excitation spectrum of He obtained by using G2 with slit widths of 100 μm.

Reference

[1] H. Yoshida and K. Mitsuke, J. Synchrotron Radiation, 5, 774 (1998).

(BL1B)

Construction of Nonlinear Spectroscopic System using CW Mode-Locked Ti:Sapphire Laser Synchronized with Synchrotron Radiation

S. Asaka, T. Tsujibayashi[a], M. Watanabe[b], O. Arimoto[c], S. Umemoto[c], S.Nakanishi[d], H. Itoh[d],
M. Itoh[e], Y. Bokumoto[c], J. Murakami[c], M. Iwanaga[f], J. Azuma[g], M. Kamada[h]

Equipment Development Center, Institute for Molecular Science, Okazaki 444-8585
[a]Department of Physics, Osaka Dental University, Hirakata 573-1121
[b]Department of Fundamental Sciences, Kyoto University, Kyoto 606-8501
[c]Department of Physics, Okayama University, Okayama 700-8530
[d]Department of Advanced Materials Science, Kagawa University, Takamatsu 760-8526
[e]Department of Electrical and Electronic Engineering, Shinshu University, Nagano 380-8553
[f]Graduate School of Human and Environmental Studies, Kyoto University, Kyoto 606-8501
[g]Department of Physics, Faculty of Science, Kyoto University, Kyoto 606-8502
[h]UVSOR Facility, Institute for Molecular Science, Okazaki 444-8585

We have newly developed a spectroscopic system combining cw mode-locked Ti:Sapphire laser with synchrotron radiation (SR), in which the laser pulse is synchronized with SR pulse. The present system has advantages of the peak power, repetition rate and time resolution in the visible/UV region derived from cw mode-locked laser as well as that of wide spectral range of photon energy in the VUV region derived from SR. These features are especially suited for nonlinear spectroscopy such as two-photon spectroscopy and pump-probe spectroscopy focused on inner-shell electronic states of solids. In this report we concentrate on a description of the measurement system. Physical aspects of the measured data obtained with our system will be reported elsewhere.

The present system was constructed at BL1B of UVSOR facility. We set up two types of measurement configuration. The first configuration is for two-photon spectroscopy, and its schematic diagram is shown in Figure 1. This configuration resembles the experimental set up reported earlier[1, 2]. The laser is a cw mode-locked Ti:Sapphire laser (Coherent Mira 900-F/P) pumped by a diode-pumped frequency-doubled Nd:Vanadate laser (Coherent Verdi, cw power 5 W). The tuning range, average power, pulse width, and repetition rate of this Mira 900 laser is 720-820 nm (with short wave optics set), 500 mW, 160 fsec, and 90 MHz, respectively, in the femtosecond configuration. The second and third harmonics of the laser output can be obtained by a harmonic generator (Coherent 5-140 UltraFast Harmonic Generator), generating average powers of 390 mW in second harmonics, and 260 mW in third harmonics. The synchronization of the laser and SR pulses is achieved by a phase-lock loop circuit (Coherent Mira Synchro-lock 9300). We used the 90-MHz RF from the UVSOR master oscillator as a reference frequency to which the laser pulse is synchronized.

We investigated the timing jitters between the laser and SR pulses by using a MCP-type photomultiplier and TAC-MCA system. The result showed that the jitter is well below a few tens of picosecond, which is the time resolution of the measurement system employed. We adopted an external voltage-controlled phase shifter (R&K PS-3 90 MHz) to make an arbitrary time delay between the two light pulses. The Synchro-lock system also has an internal voltage-controlled phase shifter. However, a quick phase change with the internal shifter, for example by 180 degrees (5.5 nsec) in 1 msec, resulted in a failure of phase locking loop.

In two-photon spectroscopy experiment we detected luminescence under two-photon excitation of the samples by photon counting method. To distinguish this signal from the background we used phase modulation method. In the first duration (e.g. 1 sec) the phase shifter is set so that the laser and the SR pulses reach the sample at the same time, and the photon numbers detected are accumulated in counter channel 1. In the next 1 sec, the phase shifter is set so that the two pulses does not overlap in time, and the photon numbers detected are accumulated in counter channel 2. After proper accumulation time, subtracting the count in channel 2 from that in channel 1 gives the nonlinear part of the emission signals.

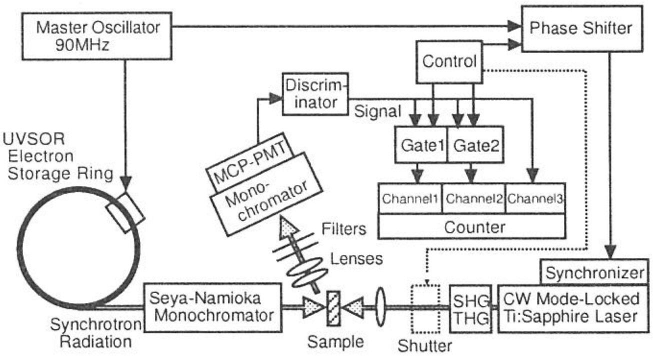

Figure 1. Schematic diagram of experimental system for two-photon spectroscopy.

We also tried an ON/OFF method for extracting desired signals. In the first duration an electronically controlled mechanical shutter for the laser is open, while in the second duration the shutter is closed. Thus the difference between the counts of the two channels gives desired signals, provided that the scattering from the laser alone can be neglected. The latter method is not suitable to the case where there exists a thermal effect due to heating of the sample by the laser, but also has a merit that it can reveal a relatively slow time dependence of the emission signals.

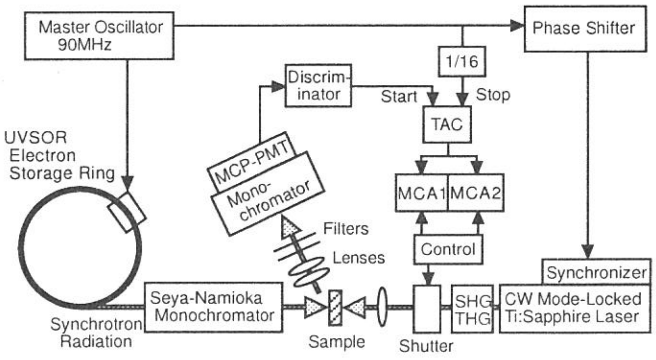

Figure 2. Schematic diagram of experimental system for measurement of laser induced emission change.

In addition to two-photon spectroscopy we performed laser-induced emission experiment. In this experiment we measured a variation of the emission intensity induced by laser irradiation under constant excitation of SR. Since the emission from the sample was expected to have a short lifetime and a low yield, we adopted dual TAC-MCA configuration (Figure 2). The pulse timing was adjusted so that the laser pulse (width 160 fsec) was at the center of the SR pulse (width 1 nsec). We used a mechanical shutter for the laser in the same way as in the above. The emission was detected by a MCP-type photomultiplier and time-to-amplitude-converted signals were fed to MCA 1 in the first duration and to MCA 2 in the second duration. By subtracting the accumulated count in MCA 2 from that in MCA 1, we obtained a time resolved emission change induced by the laser.

During the above experiment we noticed that there exist dark counts synchronized with the SR pulses. We found that they are caused by circulating electron bunches in the storage ring, having an electromagnetic nature, and are neither removed by repositioning electronics nor by adjusting the discrimination level. Fortunately since several empty bunches existed in the 16 bunch positions under the multi-bunch operation of UVSOR, we could find a low noise area of about 40 nsec within a single period of 176 nsec.

In conclusion we have developed an experimental system for nonlinear spectroscopy, which is based on the combined use of cw mode-locked Ti:Sapphire laser and SR. The synchronization of the pulses has been found satisfactory. Several measurement techniques have been developed and performed for this system to investigate inner-shell electronic states of solids. There were an electromagnetic noise from the electron storage ring, which should be carefully avoided in measuring very low level photon signals.

The present work was supported by Grant-in-Aid for Scientific Research from the Ministry of Education, Sports and Culture.

References

[1]S. Asaka et al., Rev. Sci. Instrum. **69** (1998) 1931.
[2]O. Arimoto et al., UVSOR Activity Report **25** (1998) 116.

(BL4A1)

Construction of the Multilayered-mirror monochromator and the beam line BL4A1

Harutaka Mekaru[A], Takayuki Miyamae[B], Tsuneo Urisu[B],
Shin Masui[C], Eijiro Toyota[C], and Hisataka Takenaka[D]

[A]*The Graduate University for Advanced Studies,*
[B]*Institute for Molecular Science, Myodaiji, Okazaki 444-8585*
[C]*Sumitomo Heavy Industries. Ltd., Yato, Tanashi, Tokyo 188-0001 Japan*
[D]*NTT Advanced Technology Corporation, Midori, Musashino, Tokyo 180-0012 Japan*

We proposed to use a multilayered-mirror (MLM) monochromator which is expected to provide an energy-tunable, high-photon-flux monochromatized light. A practical MLM monochromator has never been developed so far for the low energy region (decades to hundreds eV) that is especially important for SR process experiments. When considering a MLM monochromator for use in SR stimulated processes, technical problem is to remove the background existing in the low energy region caused by the total reflection.

Our focus in this work is on the energy region of 60 - 120 eV, in which fairly high reflectivity is known to be obtainable, for example, by Mo/Si and Mo/C MLMs. This energy region covers the core electron binding energy of Al (2s: 118.6 eV, 2p: 80.9 eV) and Si (2s: 150.8 eV, 2p: 108.2 eV), important materials in semiconductor processes. As mentioned above, it is important to reduce the background at the low energy region (<40 eV) caused by the total reflection and that at the high energy region caused by the higher order photons. In the present case, the C filter (120±24 nm thick) is used to reduce the low energy background. It is also effective to use MLMs at low incident angles in reducing this background because the total reflection component decreases as the incident angle to the MLM decreases. Use of two MLMs is effective not only in keeping the output beam position constant, but also in reducing the intensity of the higher order photons. The Mo/Si MLM structures were designed by assuming that a high reflectivity and a symmetric reflectivity curve would be obtained, and synthesized by sputter deposition techniques. The transmission electron microscope (TEM) cross-sectional image of the Mo/Si MLM fabricated for the present monochromator is shown in Fig. 1.

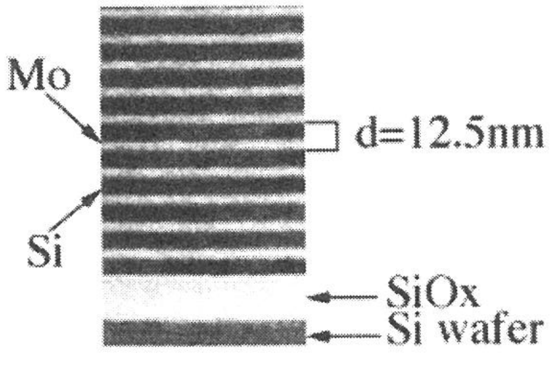

Fig. 1. Cross-Sectional TEM image of one of the Mo/Si MLMs fabricated for the present experiments (number of layers: 20, thickness ratio: Mo/Si = 3.75 nm/8.75 nm).

Figure 2 shows a schematic diagram to explain the mechanism of the mirror driving system. The rotating centers of the first and the second MLMs (A and B in Fig. 2, respectively) are set on the XY and YZ lines which form a rigid right angle XYZ with the first MLM parallel to the XY line and the second MLM perpendicular to the YZ line, as shown in Fig. 2. The pulse motor drive slides the rotational axis (A) of the first mirror parallel to the incident beam axis on the linear motion stage, with the rotational axis (B) position of the second mirror fixed. The first and the second mirrors are mechanically linked to each other and slide on the XY and YZ bars of the right angle XYZ, respectively, so that the apex Y translates in parallel with the linear motion of the first mirror. It is designed so that two kinds of mirror pairs can be exchanged with each other in the ultra high vacuum (UHV) by rotating half the mirror holders using ultrasonic motors. The driving system fabricated in this work has the feature that it covers the wide MLM beam incident angle (θ) range of 10 - 80 degrees. Fine adjustment of the first mirror is made in atmosphere and that of the second mirror can be made in the UHV by piezoelectric actuators. These adjustments suppress the horizontal and vertical shakinesses of the output beam axis, respectively, less than 0.4 mrad and 1.7 mrad over the full scanning range. The monochromator chamber is evacuated to 5.0×10^{-10} Torr by a 300-L/s turbo molecular pump.

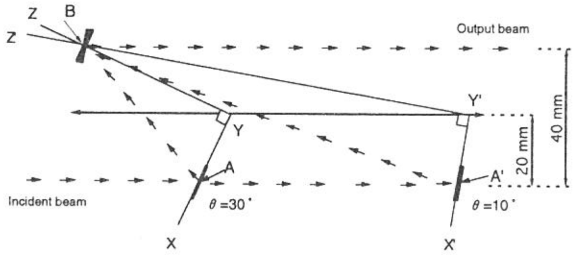

Fig. 2. The mirror driving mechanism of the MLM monochromator. The distance between the sliding surfaces of axis A and the apex Y is 20 mm, and that between the sliding surfaces of axis A and axis B is 40 mm.

Figure 3 shows the drawings of BL4A1, which consists of a pre-mirror chamber, a double crystal type MLM monochromator, a white beam chamber, a filter chamber, a detector chamber, and an X-ray photoelectron spectrometer (XPS) chamber. The pre-mirror is an elliptically-bent cylindrical quartz mirror with a Pt coating on its surface. (The radius of the cylindrical curvature is 236.2 mm and the longer and shorter radii of the elliptical curvature are, respectively, 2111 mm and 132 mm.) It is set at 2.35 m downstream from the light source point of the bending magnet with a grazing incident angle of 4 degrees. The horizontal and vertical acceptance angles of the pre-mirror are, respectively, 16.56 mrad and 12.79 mrad.

The reflected beam is focused at a point 6.1 m downstream from the center of the pre-mirror and has an elliptical spot size of about 5 mm×2 mm. When the MLM is not used, the SR beam is reflected by a pair of Pt coated plane mirrors with grazing incident angles of 2 degrees in the white beam chamber to keep the output beam at the same height as that of output beam from the MLM monochromator. Two filters, one consisting of a thin film of C and the other consisting of a thin film of Al, are set in the filter chamber, and a Au vapor-deposited detector and a Si photodiode detector (International Radiation Detectors Inc., AXUV-100) are set in the detector chamber to measure photo-current. A differential pumping system is set at the end of the beamline to maintain a high vacuum in the white beam chamber during the experiments using reaction gases in the XPS chamber.

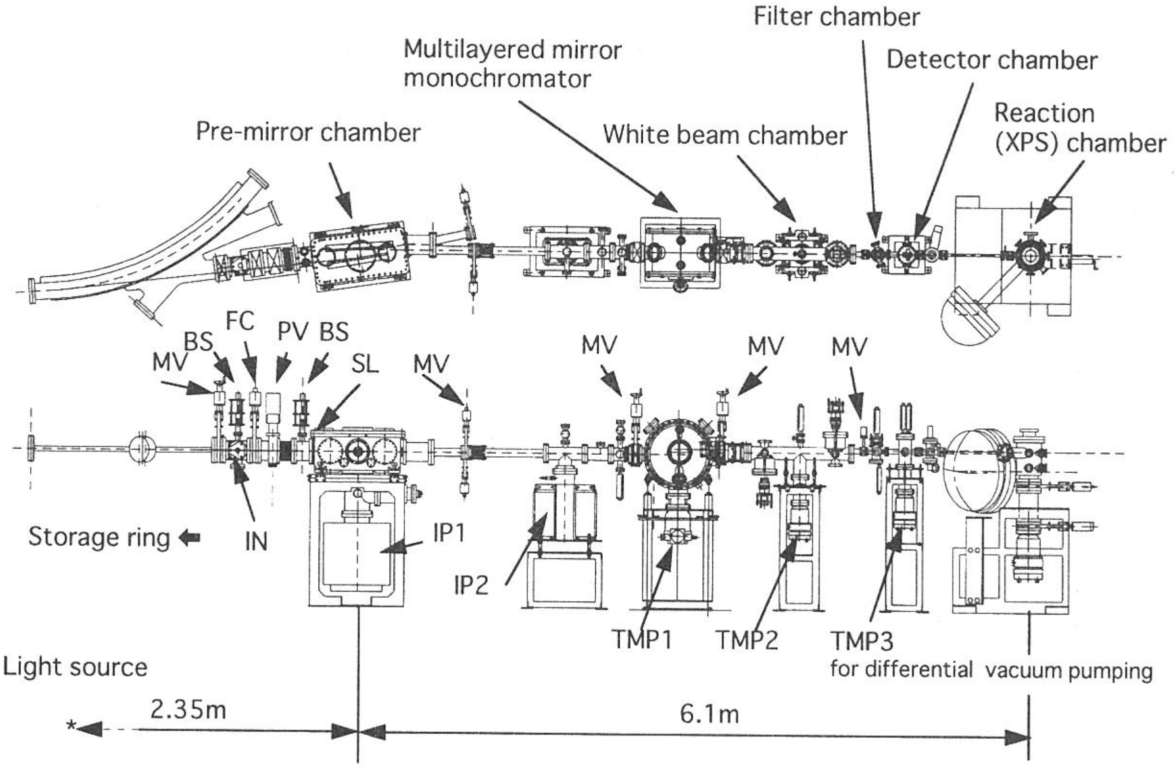

Fig. 3. Top and side views of the MLM monochromator beamline (BL4A1) constructed at the UVSOR facility in the IMS. MV: manual valve, IN: insulator pipe, FC: fast closing valve, PV: pneumatic valve, BS: beamline shutter, SL: slit, IP1: 400-L/s ion pump, IP2: 150-L/s ion pump, TMP1: 300-L/s turbo molecular pump, TMP2: 340-L/s turbo molecular pump, TMP3: 150-L/s turbo molecular pump.

(BL5A)

Measurements at the BL5A

Shin-ichiro Tanaka, Jun-ichi Murakami, Masami Hasumoto and Masao Kamada

Institute for Molecular Science, Okazaki, 444-8585, Japan

The beam line 5A has been constructed in order to measure the electronic structure of solid and solid surfaces, and consists of a monochromator for the synchrotron radiation and electron spectrometers for the photoelectron spectroscopy. It was constructed so that the radiation from a bending magnet and a helical undulator can be used for the monochromator (SGM-TRAIN[1]). However, the operation of the helical undulator interfere with the electron motion in the bending magnet at other beamlines of UVSOR, and the radiation from the bending magnet is mainly used currently. For the photoelectron spectroscopy, two kinds of electron spectrometers are installed. One is angle- and spin- resolved photoelectron spectrometer[2] for spin-resolved photoelectron spectrometer. It consists of electron lenses, an energy selector and spin detector. Electron lenses and the energy selector are commercial one (VSW HA54), and the spin detector of diffused scattering type is home-made. The other one is Omicron EA-125 analyzer, and used for conventional photoelectron spectroscopy without spin resolving. The performance of these apparatus has been presented in previous UVSOR activity reports.

The monochromator (SGM-TRAIN) is controlled by a PC with a home-made program written in Visual Basic (Microsoft) of 16-bit version on the windows 3.1. The EA-125 electron spectrometer is controlled by another PC with a commercial program written in Borland Pascal (DOS). The spin resolved electron spectrometer is controlled by the other PC with a home-made program written in Visual Basic of 32-bit version on the windows 95. Three computers are connected via the RS-232 cables, and the photon energy of the monochromator can be set according to the request of the program for the electron spectrometer. This system enables us to measure the constant initial state spectroscopy, in which the photon energy and the electron energy are changed simultaneously to keep the difference of them to be constant. It also enables the constant final state spectroscopy, in which the photon energy is changed and the electron energy was kept to be constant.

An upper curve in the figure bellow shows an example of the spectrum measured in the constant final state spectroscopy mode. The sample was Xe film depsosited at 30K. The kinetic energy of the photoelectron was fixed to be corresponding to the Xe-NOO Auger electron. The short escape depth of the Auger electron enabled us to detect the surface core exciton (a and a') at the Xe-4d edge, which were not observed in the ordinal total electron yield spectrum (lower curve).

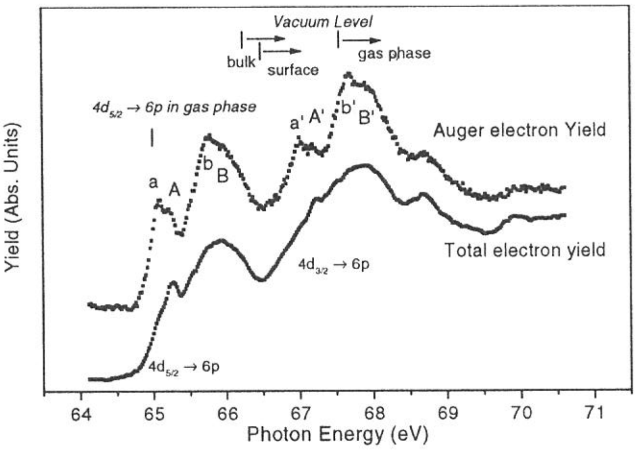

---

[1] M. Kamada, K. Sakai, S. Tanaka, S. Ohhara, S. Kimura, A. Hiraya, M. Hasumoto, K. Nakagawa, K. Ichikawa, K. Soda, K. Fukui, Y. Fujii and E. Ishiguro, Rev. Sci. Instrum. 66 (1995) 1537. ;M. Kamada, M. Hasumoto, N. Mizutani, T. Horigome,S. Kimura, S. Tanaka, K. Fukui and K. Sakai, J. Synchrotron Radiation, 5 (1998) 766.

[2] N. Takahashi, S. Tanaka, M. Ichikawa, S. Ohara, Y. Fujii, K. Nakanishi and M. Kamada, J. Jpn. Appl. Phys., 35 (1996) 6314.

(BL6A1)

Replacement of the control system for a Martin-Puplett type interferometer at BL6A1

Kenji Hayashi and Shin-ichi Kimura

UVSOR, Institute for Molecular Science, Myodaiji-cho, Okazaki-shi 444-8585
Kobe University

BL6A1 was constructed for spectroscopy in infrared region. We have two interferometers at BL6A1: a Martin-Puplett type (SPECAC Co.) and a Michelson type (Bruker IFS66V). The Martin-Puplett type interferometer has gone through with various experiments for more than fifteen years. We replaced the control system for the Martin-Puplett type interferometer (SPECAC) because of repeated troubles.

A new control system for SPECAC is schematically drawn in Fig.1. A control box outputs digital signals to a stepping motor and manages the limiter (photointerrupter) signals. A lock-in amplifier extracts the signals from the detectors which is synchronous with a chopper. Both of the control box and the lock-in amplifier are controlled by a PC/AT compatible computer. Most of the components for the control system, including the control software, were newly installed excepting the chopper controller and the PC.

We utilized the programming language LabVIEW for the control software. The readily-made instrument drivers (VIs) save time of programming and the easy-to-follow nature of the "graphical programming" seems to improve the re-productivity of the software. The top window of the SPECAC control software is shown in Fig.2. The software consists of three routines: "Main" (configuration, data acquisition and display), "ZPD"(adjustment of zero path difference position) and "FFT"(fast Fourier transform of the interferogram data). To fulfill the specification, the wait time before data acquisition and the elimination way for back rush of the lead screw were carefully implemented.

After the installation of the system, we carried out several tests for total reliability. For example, the interferometer was scanned for ten times and the aberration of the position of the ZPD peak was compared. One of the results is shown in Fig.3. It is clear that the motor slip did not occur and the position error was less than 1 micron.

After debugging of the software, the system has been adopted to the user time regularly. We will continuously improve its function for users' convenience.

The preparation time needed for both of the hardware and the software was about two month.

We are very grateful to all of the UVSOR staff for their kind support.

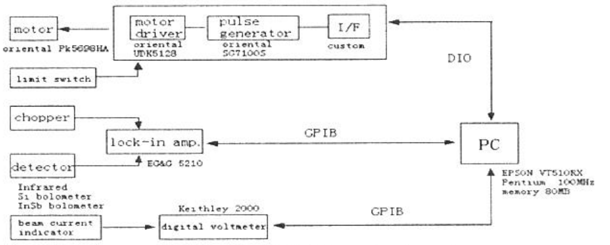

Fig.1 Diagram of the SPECAC control system.

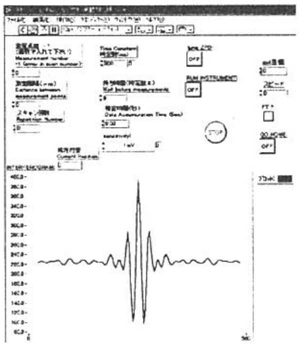

Fig.2 Top windows of the SPECAC control system.

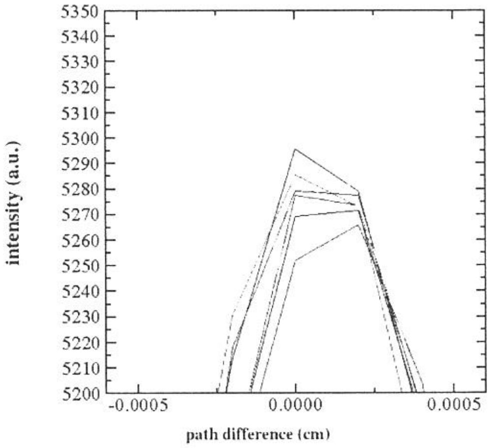

Fig.3 A result of tests for mirror movement.

(BL7A)

Performance of the focussing mirror system for the double crystal monochromator beamline BL7A

Toyohiko Kinoshita[1, 2], Tokuo Matsukawa[3], Tsutomu Kurisaki[4], Hikoshiro Ichihashi[4], Takashi Watanabe[5], Tetsunori Taninaka[6], Masazumi Ishida[6], Yuichi Haruyama[1], Yasutaka Takata[1] and Hiroaki Yoshida[7]

[1]*Institute for Molecular Science, Okazaki 444-8585*
[2]*Institute for Solid State Physics, University of Tokyo, Tokyo 106-8666*
[3]*Departmment of Science, Naruto University of Education, Naruto 772-8502*
[4]*Department of Chemistry, Faculty of Science, Fukuoka University, Fukuoka 814-0180*
[5]*Graduate School of Science and Technology, Kobe University, Kobe 657-8501*
[6]*Graduate School of Science and Engineering, Shizuoka University, Hamamatsu 432-8561*
[7]*Department of Physical Sciences, Hiroshima University, Higashi-Hiroshima 739-8526*

As described in the UVSOR Activity report in 1997, the reconstruction of the soft X-ray beamline BL7A, such as installation of the focusing mirror system and the new software, improvement of the pumping system etc., has been performed [1]. The focussing mirror system was installed between the front-end of the BL7A and the monochromator chamber to obtain the higher performance. The design detail of the mirror system was described previously [1]. By using the mirror system, we may not need to move the beamline from the wiggler line to the bending line. Although the bending magnet radiation is still available, this is for only the case when a trouble of the wiggler occurs. When we use the relatively lower photon energy light (less than 1.7keV), the pair of Si mirrors is used to prevent the radiation damage of the crystal owing to higher energy photons whereas the pair of Cr mirrors is used for higher energy experiments. In this activity report, we report the performance of the system.

Figure 1 shows the picture of the X-ray spot observed at the end station of the beamline, where the fluorescent screen with MCP (micro-channel plate) was attached. This is the spot obtained in the combination of Cr mirrors and the InSb monochromator crystals. The width of the spot is about 7mm and the height is 5mm. The spot size is larger than that expected from the ray tracing results presented in Fig. 2 of ref.1. This may be due to the slope error of the mirrors and the small misalignment of the mirror holder. By reducing the width of the (horizontal) diaphragms located in the upstream of the mirror, the small spot size of less than 1mm ϕ can be achieved.

Figure 2 shows the throughput of the BL7A for the several combinations of the focussing mirrors and the monochromator crystals. It is noted from the comparison with the previous result [2] that the intensity in all energy regions becomes stronger. Especially, due to the high cut Si mirrors, the wiggler radiation becomes available even in lower energy region, which may not damage the beryl and/or quartz crystals. As a result, the throughput from the beryl crystals becomes about 300 times than the previous one without the mirror system. It is also noticed that the glitches for YB_{66}(400) reflection around 1.4keV can be reduced by using the Si mirrors. The use of the focussing mirror system gives us a lot of advantages for performing the soft X-ray spectroscopy.

References

1. T. Kinoshita et al., UVSOR Activity Report 1997 p.62.
2. UVSOR Activity Report 1997, p. 21.

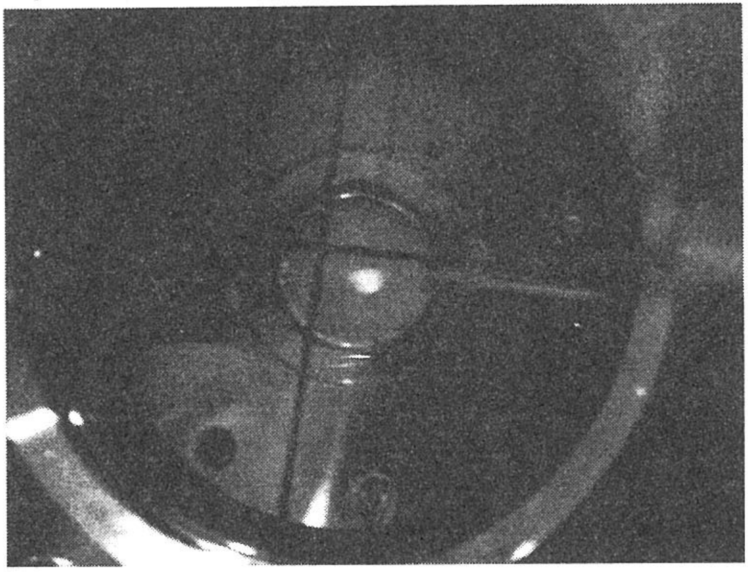

Figure 1. Observed light spot at the end station of BL7A. The acceptance angle of the beamline was set at about 4.5mrad.

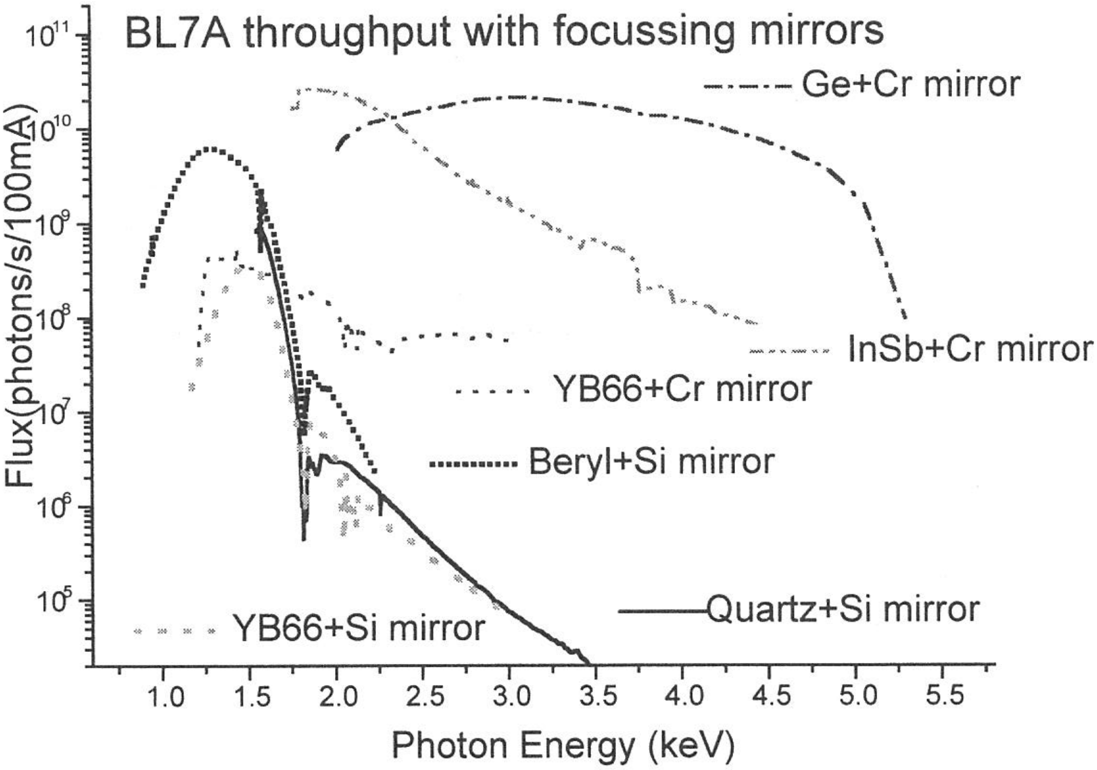

Figure 2. Throughput of the BL7A for the several combinations of the focussing mirrors and the monochromator crystals. 4T wiggler radiation is used as a light source.

(BL7B)

Present Performance of BL7B 3m Normal Incidence Monochromator

Kazutoshi FUKUI, Hideyuki NAKAGAWA
Faculty of Engineering, Fukui University, Fukui 910-8507, Japan
Iwao SHIMOYAMA, Kazumichi NAKAGAWA
Faculty of Human Development, Kobe University, Kobe 657-8501, Japan
Hidekazu OKAMURA, Takao NAMBA
Faculty of Science, Kobe University, Kobe 657-8501, Japan
Masami HASUMOTO and Toyohiko KINOSHITA
UVSOR Facility, Institute for Molecular Science, Okazaki 444-8585, Japan

The reconstruction of the beamline BL7B has been almost completed. The 1m Seya-Namioka type monochoromator was replaced to the 3m normal incidence monochromator (3m NIM) for the extended researches of the highest level with the higher resolution and intensity, the wider wavelength region available and so on. It will be also possible to utilize the linear and circular polarization inherent in SR and to realize some combined experimental systems, for example, with the synchronized laser to SR pulse or with the extended field.

The outline of the new beamline is illustrated at BL7B page of Status of UVSOR in this report. The optical design is also shown in Fig. 1. The design parameters of the optical elements are summarized in Table 1, 2 and 3. The 3 m NIM is a modified

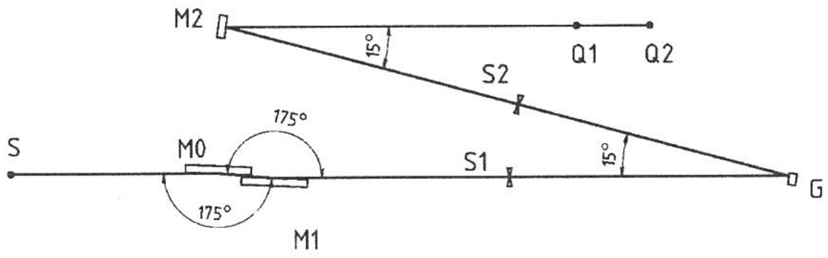

Fig. 1

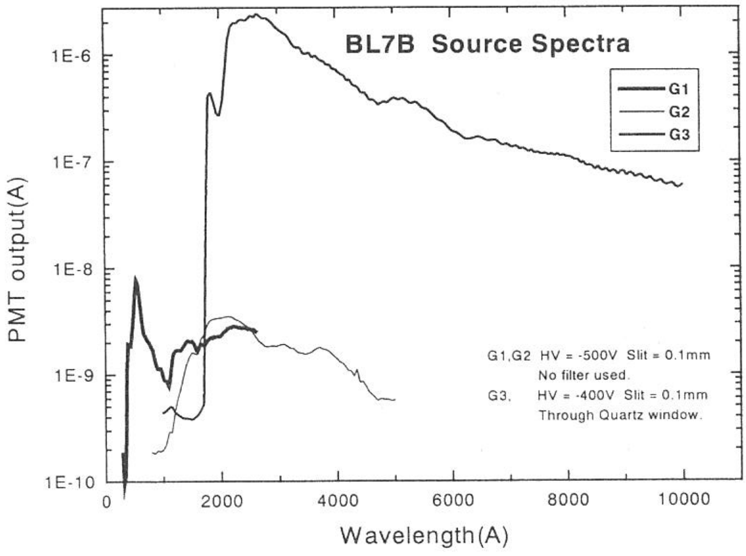

Fig. 2

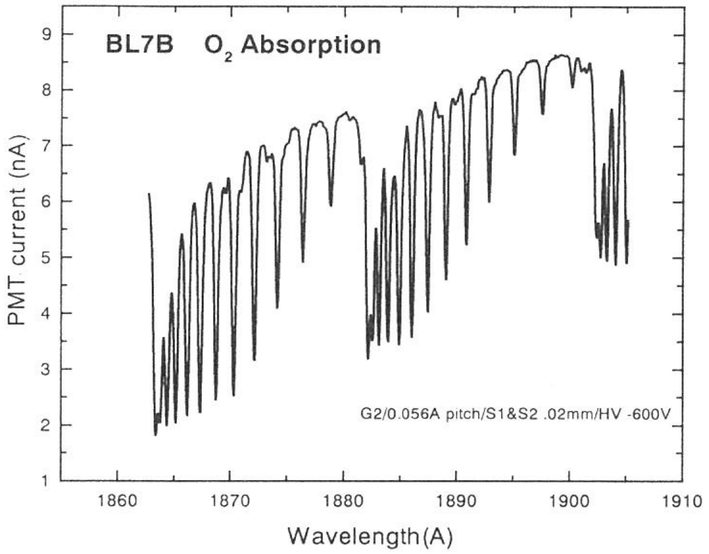

Fig. 3

version of the McPherson model 2253. The coverange of the three gratings in design is 50 – 150 nm for G1, 80 – 300 nm for G2 and 150 – 1000 nm for G3.

Figure 2 shows the source spectra of BL7B which are direct outputs from the photomultiplier with a sodium salicylate energy converter for G1 and G2, and through quartz window for G3. The lower limits of G1 and G3 are almost same as the desigin values, but that of G2 is not clear. Though the intensity of each spectrum can not compare with each other, whole range of BL7B is covered by G1 and G3. It is due to misfit of the actual blazing angle. The grating G2 will be replaced in near feature. The actual focus positions (Q1 and Q2 in Fig. 1) are almost same as design values. The spot size at Q2 is about 3 (H) x 0.8 (V) mm at present. Since spot size is strongly depend on the configuration of M0 and M1, the precise configuration adjustment of both M0 and M1 should be carried out.

Figure 3 shows the absorption spectrum of O_2 gas between 186.2 and 190.5 nm using G2 grating. The slit width of both entrance and exit slits are 0.02 mm. $E/\Delta E$ is more than 5000. It is not so difficult to measure such a spectrum, so that this beamline has enough resolution for solid state measurements.

Table 1

Pre-mirrors	Incidence angle (deg)	Radius (mm)	Dimensions (mm)	Coat	Material
M0	87.5	- (plane)	700 x 140	Au	SiC
M1		60568 x 115 (Toroidal)			SiO_2

Table 2

Grating	Deviation angle (deg)	Radius (mm)	Dimensions (mm)	Coat	Material	Grooves (mm^{-1})
G1	15	3000	40 x 120	Au	SiO_2	1200
G2				Al		600
G3				Al		300

Table 3

Post-mirrors	Incidence angle (deg)	Radius (mm)	Dimensions (mm)	Coat	Material
M21	7.5	3483 x 3348	120 x 120	Au	SiO_2
M22		3786 x 3633		Al + MgF_2	

(BL8B2)

A new angle-resolved UPS system for organic thin films at BL8B2

Nobuo UENO[A], Sinji HASEGAWA[A], Yasushi AZUMA[B], Koji K. OKUDAIRA[B], Yoshiya HARADA[B], Hisao ISHII[C], Daisuke YOSHIMURA[C] and Kazuhiko SEKI[C]

[A] *Institute for Molecular Science, Myodaiji, Okazaki 444-8585*
[B] *Faculty of Engineering, Chiba University, Chiba 263-8522*
[C] *Department of Chemistry, Nagoya University, Nagoya 464-8602*

Angle-resolved photoelectron spectroscopy (ARUPS) is a well-known technique to investigate the electronic structure of surfaces. One can in principle determine the orientation and electronic states of molecules adsorbed on crystal surfaces by the quantitative analysis of the photoelectron angular distribution. For thin films of functional organic molecules, which are promising candidates to realize new electronic devices, the determination of molecular orientation and the electronic structure in the ultrathin films is of fundamental importance, since the molecular orientation is different from that in a bulk crystal, and thus new electronic states appear owing to the molecule/substrate, molecule/overlayer and molecule/molecule interactions which depend on the molecular orientation. Although ARUPS experiments have been widely performed on such thin films, the quantitative analysis of the ARUPS intensity and the determination of molecular orientation have little been realized due to the difficulty of quantitative analysis of the photoelectron angular distribution. We have recently succeeded to analyze the photoelectron angular distributions from thin films of large functional organic molecules. The goal of our project is to obtain very precise information on both geometrical and electronic structure typical of ultrathin films of functional organic molecules by the quantitative analysis of photoelectron angular distribution, and open a door to realize quantitative chemical analysis of organic ultrathin films using ARUPS with synchrotron radiation.

For these studies, a new ARUPS spectrometer, which enable us to measure accurate photoelectron angular distributions from functional organic thin films with high energy-resolution and high sensitivity, were required. We constructed the new ARUPS system at the BL8B2 of the UVSOR facility. VG-ARUPS-10 spectrometer was introduced with a μ-metal measurement chamber. The angle-resolving spectrometer consists of a 75 mm hemispherical sector analyzer with two-axes rotations, electrostatic lens of various operation offering various angles of acceptance, and a high speed multi-channel detection system. A high-precision sample manipulator was also constructed to realize precise ARUPS measurements. Furthermore, a new simplified organic-sample preparation chamber with a liquid N_2 trap, which was designed to be cleaned up easily and to keep the UHV pump free from organic contamination, was constructed to realize ARUPS measurements of wide variety of organic thin films. The previous sample preparation chambers with LEED/Auger optics were also connected to the new measurement chamber. The new spectrometer station is shown in Fig. 1.

Although the new system is dedicated to organic materials, it will be also used in investigating inorganic materials.

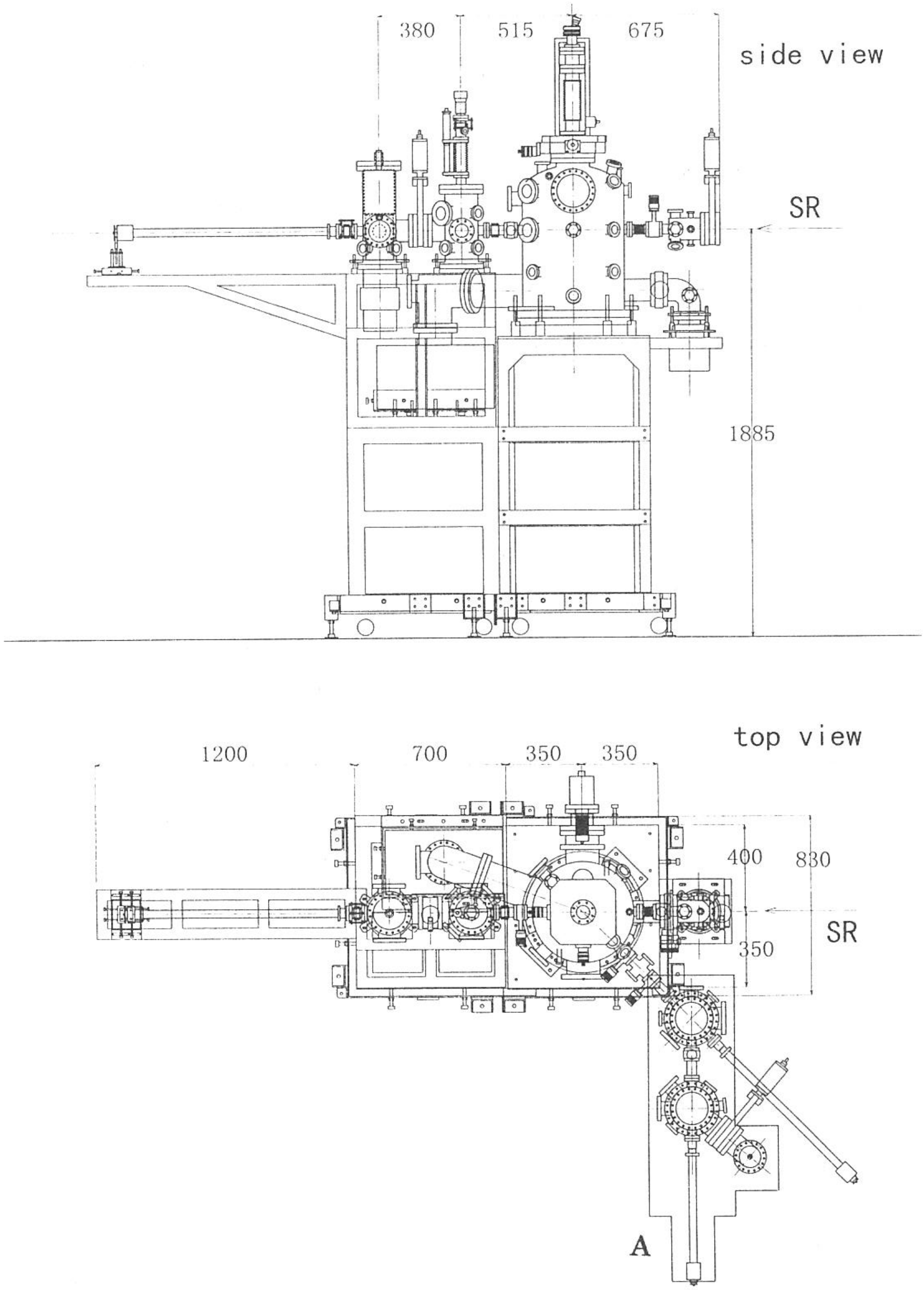

Fig. 1 The new ARUPS apparatus for organic thin films at the BL8B2. In the top-view drawing, the previously constructed sample preparation chambers (A) are also shown.

(BL8B1)

Cleaning mirrors and gratings at BL8B1 with UV/Ozone

Tatsuo GEJO and Eiken Nakamura[A)]
Institute for Molecular Science, Myodaiji, Okazaki 444-8585, Japan
[A)]Japan Advanced Institute of Science and Technology
1-1 Asahidai Tatsunokuchi Nomi Ishikawa, 923-1292, Japan

In the measurement with Soft X ray monochrometer, existence of carbon on mirror surfaces often give arise the problem: During the use of monochrometer, residual hydrocarbon reacts photochemicaly and gradually sticks on the surfaces. Since the residue contains carbon, it absorbs the photon, especially, one in the C K-edge energy region (290 ~ 310 eV). Consequently, it makes "a dark hole" in the output spectra of monochrometer. When the absorbance becomes more than 50 %, this may affect the absorption spectra obtained, because UV photon beam in stray light, which should be subtracted, become significant.

Since ozone is high reactive with hydrocarbon, UV/Ozone cleaning technique has been used to remove residual hydrocarbon and clean surfaces, mainly those of semiconductors: Ozone attack to the surface and make reactions with photochemicaly. We have applied this UV/ozone cleaning technique to mirrors and gratings in BL8B1. The UV apparatus (Nippon Laser Denshi, UV/Ozone cleaner) are used for generation of ozone. We flowed air to this apparatus and pumped by funs. At the exit, ozone were removed on the copper warmed up by heater. Typically, the mirrors were kept in this apparatus for 3 hours. Tow mirrors (M1 and M21) and two gratings (G2 and G3) were cleaned with the above procedure.

Fig 1 shows the output spectra of BL8B1 (200-600 eV) before and after ozone cleaning. The dip around 290 eV in fig. 1a) is due to the carbon on the surface of mirrors and gratings. After the cleaning,, we were successfully able to regain the throughput at 290 eV from 10% to 80 %. This provides the reasonable measurement in this energy region at Bl8B1.

We thank Mrs. Hayashi and Kondo at IMS for their technical support.

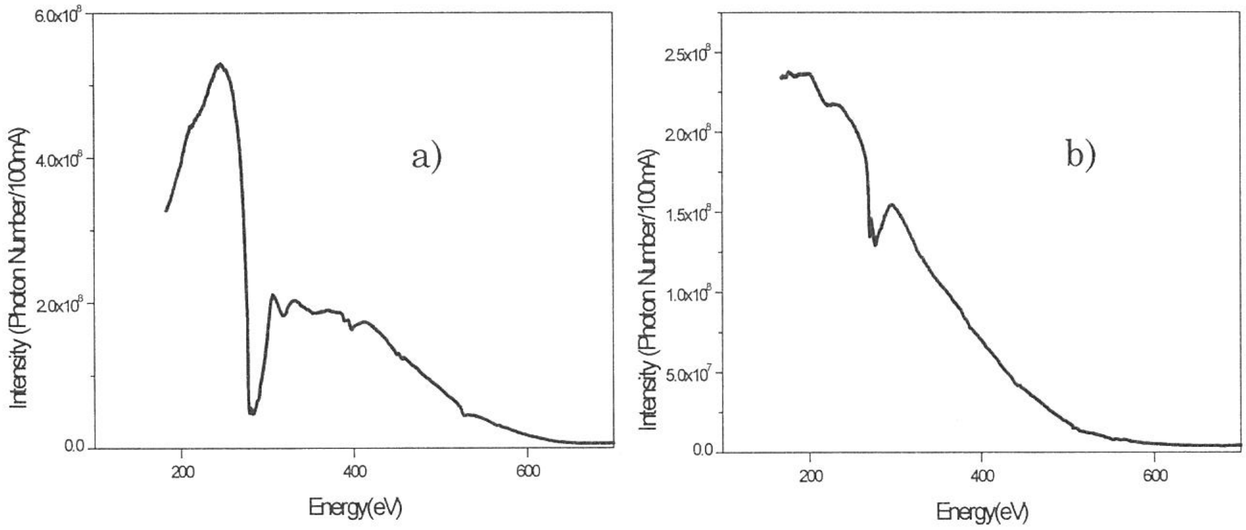

Fig. 1: Output spectra at BL8B1 when using the G2 grating (540 l/mm: R =15m).
a) and b) show the spectra before and after ozone cleaning, respectively.

(BL1A)

Characteristics of Resonant Photoemission of Metallic, Molecular, and Correlated Solid Systems

Yasutaka Takata, Takaki Hatsui and Nobuhiro Kosugi

The Graduate University for Advanced Studies, Institute for Molecular Science,
Myodaiji, Okazaki 444-8585

Inner-shell photoabsorption spectroscopy and photoemission spectroscopy are powerful tools to investigate the origin of electronic and magnetic properties in transition metal compounds. In the present study, we have investigated Ni 3p and 3s photoemission at the Ni 2p edge of some Ni-containing solid systems with different electronic properties to get a unified view for the resonant behavior. The systems chosen are NiO as a correlated system, Ni as a metallic system, and $K_2Ni(CN)_4$ as a molecular system.

Experiments were performed at BL1A soft x-ray beamline. A pair of beryl $(10\bar{1}0)$ crystals were used in the double crystal monochromator. The Ni 2p photoabsorption spectra were measured by monitoring the total electron yield. A SCIENTA SES200 electron energy analyzer was used to measure the photoelectron spectra. The total energy resolution in the photoelectron spectra was about 0.7 eV.

The Ni 2p photoabsorption spectra for the three systems are different as shown in Fig.1. In NiO the shoulder and weak features arise from correlation and multiplet effects [1]. In Ni metal the absorption is dominated by the broad conduction band. In $K_2Ni(CN)_4$ the strong extra features arise from the single electron transition MLCT (Metal-to-Ligand Charge Transfer) [2]. Fig. 2 shows off- and on-resonant Ni 3p, 3s photoemission spectra at the photon energy marked in Fig. 1. The on-resonant photoemission spectra of Ni metal and $K_2Ni(CN)_4$ are nearly the same and resemble the normal Auger spectra. That is, the correlation and multiplet interaction seem to be reduced in the metallic and molecular systems. On the other hand, the on-resonant spectra of NiO show more complicated features than those of Ni metal and $K_2Ni(CN)_4$, due to strong correlation and multiplet interaction [3].

The resonant behavior (photon energy vs. kinetic energy of the enhanced satellite bands) is quite different in the three systems as shown in Fig. 3. The resonant photoemission features in Ni metal and $K_2Ni(CN)_4$ nearly coincide with the normal Auger lines in energy. In $K_2Ni(CN)_4$ the resonantly enhanced satellite states have a character of combination of the normal Auger final state with the one-electron (excitonic electron) state, which is localized within a unit of $Ni(CN)_4^{2-}$ ion and is bound by the core holes, forming a series of core excitons converging to the Ni 2p ionized state in the photoexcitation and to the normal Auger final state in the resonant photoemission [4]. The binding energy of the one-electron state by the double holes in the Auger final state is larger than that by the single hole in the photoexcitation. Therefore, the resonantly emitted satellite electron decreases its kinetic energy for the higher excitation energy.

In Ni as a metallic system, the intermediately photoexcited, resonantly enhanced satellite, and normal Auger states are embedded in the continuum band and are well screened by the conduction electron. Therefore, the resonantly emitted satellite electrons show nearly the same kinetic energy as the normal Auger electrons. This is true in the broad band metallic system even if there should be several photoexcited and satellite states near the threshold due to multiplet and/or excitonic effects.

On the other hand, since in NiO the correlation and multiplet interaction are very important, there is neither clear one-to-one correspondence between the photoexcited states and the resonantly enhanced satellite states nor relation between the satellite electrons and the normal Auger electrons as shown in Fig. 3(a).

References

[1] G. van der Laan, J. Zaanen, G. A. Sawatzky, R. Karnatak and J.-M. Esteva, Phys. Rev., **B33** (1986) 4253.
[2] T. Hatsui, Y. Takata, and N. Kosugi, Chem. Phys. Lett., **284** (1998) 320.
[3] M. Nakamura, Y. Takata, and N. Kosugi, J. Electron Spectrosc., **78** (1996) 115.
[4] Y. Takata, M. Nakamura, and N. Kosugi, Chem. Phys. Lett., **287** (1998) 35.

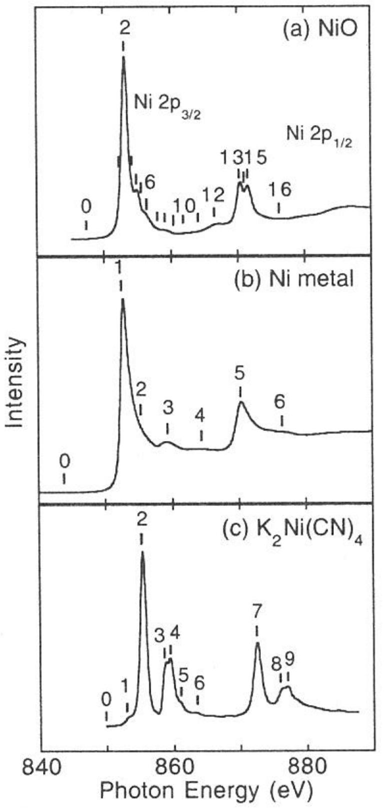

Fig. 1. Photoabsorption spectra at the Ni $2p_{3/2}$ and $2p_{1/2}$ edges for (a) NiO, (b) Ni metal, and (c) $K_2Ni(CN)_4$.

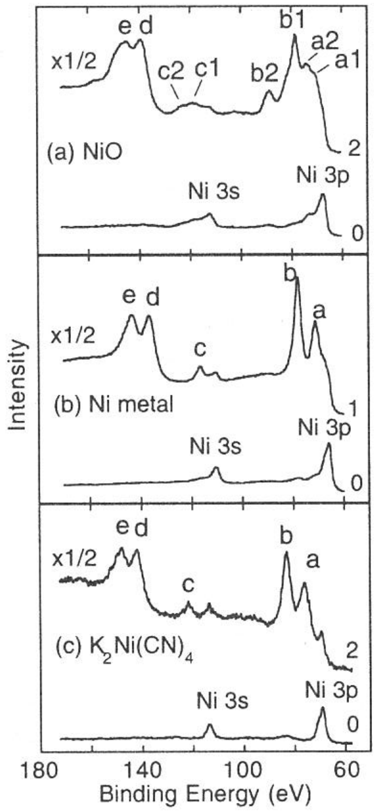

Fig. 2. Off-resonant and on-resonant photoemission spectra in the Ni 3p and 3s region at the Ni $2p_{3/2}$ absorption edge marked in Fig. 1 for (a) NiO, (b) Ni metal, and (c) $K_2Ni(CN)_4$.

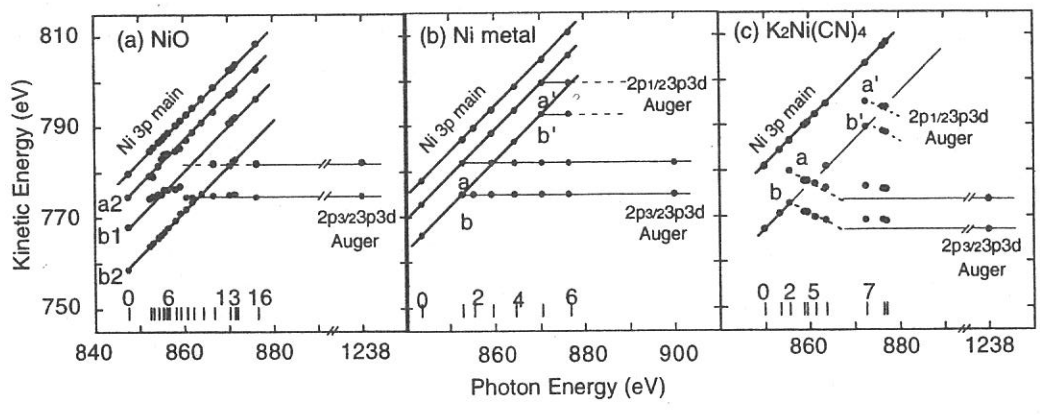

Fig. 3. Resonant behavior of satellite photoelectrons in the Ni 3p region at the Ni 2p excitation for (a) NiO, (b) Ni metal, and (c) $K_2Ni(CN)_4$. Photon energy dependence of the electron kinetic energy, ΔK.E./Δhν. The energy uncertainty is about 0.2 eV.

(BL1A) Ni-Ni chemical bond in $[Ni_2(napy)_4Br_2][B(C_6H_5)_4]$ studied by Ni $2p$ photoabsorption

Takaki Hatsui, Yasutaka Takata, and Nobuhiro Kosugi

The Graduate School for Advanced Studies, Myodaiji, Okazaki, 444-8585, Japan

Institute for Molecular Science, Myodaiji, Okazaki, 444-8585, Japan

Since the recognition of the structural and theoretical significance of the Re-Re bond [1], various complexes containing metal-metal bonding have been synthesized and a large number of experimental and theoretical studies have been done to characterize the metal-metal bonding [2,3]. In contrast to the metal-metal bonds of early transition elements, such as Cr, Mo, W, Re, and Ru, the Ni-Ni bonding is not well characterized [3]. In order to elucidate character of the Ni-Ni chemical bond, linearly polarized Ni $2p$ photoabsorption spectra of $[Ni_2(napy)_4Br_2][B(C_6H_5)_4]$ (napy: 1.8-naphthyridine), which has Ni-Ni bond (2.415 Å) being shorter than Ni-Ni bond in Ni metal (2.50 Å).

The sample was prepared as described in ref. [4]. A single crystal (about 1 x 5 x 5 mm) was obtained by slow recrystallization from acetone solution. The structure consists of binuclear complex cations $[Ni_2(napy)_4Br_2]^{1+}$ and $[B(C_6H_5)_4]^{1-}$ anions (Fig. 1) [4]. The molecular axis z chosen as Fig. 1 was determined by the X-ray diffraction analysis. Ni $2p$ photoabsorption spectra were measured at the BL1A soft x-ray beamline with a pair of beryl $(10\bar{1}0)$ crystals by monitoring total electron yields.

Fig. 2 shows the Ni $2p$ photoabsorption spectrum of powder $[Ni_2(napy)_4Br_2][B(C_6H_5)_4]$. The intensity ratio of the Ni $2p_{3/2}$ region to the Ni $2p_{1/2}$ region is larger than statistical value 2, indicating that the complex cation has unpaired electrons. This is consistent with the effective magnetic moment, 4.19 BM, for a $[Ni_2(napy)_4Br_2]^{1+}$unit [4].

In a simple diatomic system Ni_2, the Ni $3d$-$3d$ chemical bonding gives bonding and antibonding orbitals, σ and σ^* (d_{z2}), π and π^* (d_{xz}, d_{yz}), δ and δ^* (d_{xy}, d_{x2-y2}), where the degeneracies of the π, π^*, δ, and δ^* orbitals are removed in $[Ni_2(napy)_4Br_2]^{1+}$ because of imperfect eclipsed ligand geometry (Fig. 1). For the $[Ni_2(napy)_4Br_2]^{1+}$ cation, there are 3 holes in these '$3d$' orbitals ('$3d$' is not purely atomic), since the Ni atoms have the formal oxidation number +1.5. In order to elucidate the symmetries of the holes, the linearly polarized Ni $2p$ photoabsorption was measured. As shown in Fig. 2, distinct polarization dependence is observed. The lowest band A is strong in the $E\perp z$ direction, where E denotes the electric vector of incident photon, and very weak in the $E//z$ direction. Therefore, the band A is clearly assigned to the transition of d_{xy} or d_{x2-y2} symmetry. This indicates that some holes are located in 'δ' orbitals. On the contrary, the band B is strong in the $E//z$ direction and weak in the $E\perp z$ direction. This implies that the other holes are located in the σ^* orbital with d_{z2} symmetry.

The intensity ratio of band A to B is estimated to be about 2 from the curve fitting of the spectrum of the powder sample. Based on the polarization dependence and intensity of band A and B, it is reasonable to say that one hole is located in the σ^* orbital and two holes in δ-symmetry orbitals, though we cannot distinguish between $\delta^3\delta^{*3}$ and $\delta^4\delta^{*2}$ configurations.

References

[1] F. A. Cotton, N. F. Curtis, C. B. Harris, B. F. G. Johnson, S. J. Lippard, J. T. Mague, W. R. Robinson, and J. S. Wood, *Science*, **145** (1964) 1305.

[2] F.A. Cotton, and R.A. Walton, *Multiple bonds between metal atoms* (John Wiley & Sons, New York, 1982).

[3] F.A. Cotton, and G. Wilkinson, *Advanced Inorganic Chemistry*, 5th ed. (John Wiley & Sons, New York, 1988).

[4] L. Sacconi, C. Mealli, and D. Gatteschi, *Inorg. Chem.*, **13** (1974) 1985.

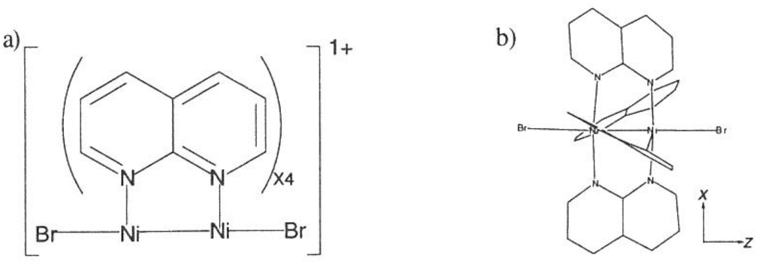

Fig. 1 The molecular structure of [Ni$_2$(napy)$_4$Br$_2$]$^{1+}$ (a) and the structure determined by X-ray diffraction analysis (b) [4].

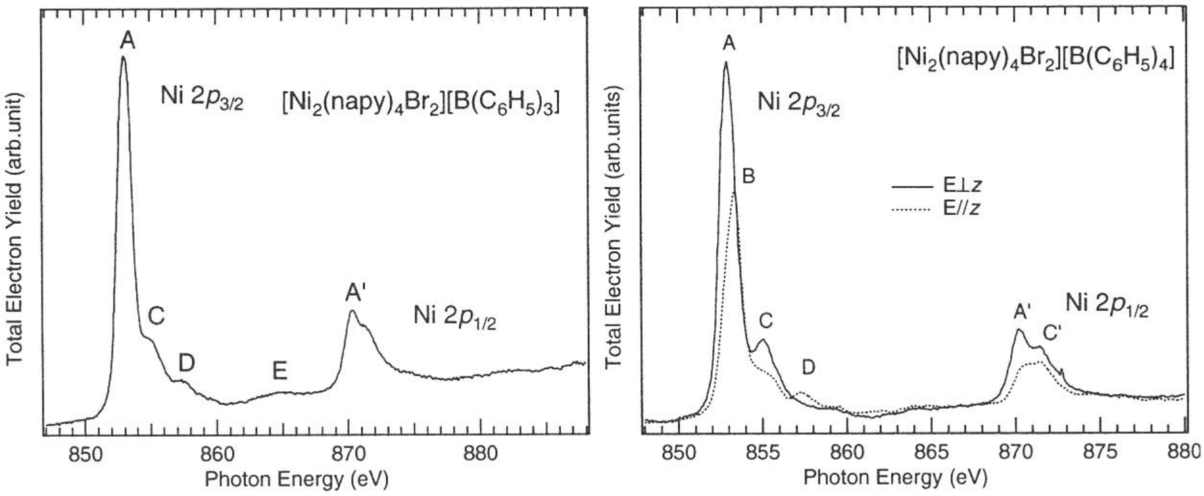

Fig. 2. Ni 2*p* photoabsorption spectrum of powder [Ni$_2$(napy)$_4$Br$_2$][B(C$_6$H$_5$)$_4$] (left) and polarized Ni 2*p* photoabsorption spectra of a single crystal for the E//*z* and E⊥*z* directions (right), where E and *z* denote the electric vector of the incident photon, and the molecular axis chosen as Fig. 1, respectively.

(BL1A)(BL7A)

Al-K XANES Spectra of Al1-xGaxN Solid Solusions

Shin-ichi NAOE
Faculty of Engineering, Kanzawa University, Kanazawa 920-8667, Japan
Kazutoshi FUKUI and Ryousuke HIRAI
Faculty of Engineering, Fukui University, Fukui 910-0017, Japan
Yasutaka TAKATA and Nobuhiro KOSUGI
Institute for Molecular Science, Myodaiji, Okazaki 444-0864, Japan

Introduction

AlN and GaN are becoming to be fundamental compound semiconductors which have a large band gap to give new promising electronic devices. On designing these devices, the knowledge of electronic structure is necessary to make the best of these materials. Electron correlation is not main phenomena in semiconductors. Its electronic structure will be explained by using the idea of density of states (DOS). In this study, Al-K edge spectra give directly p type unoccupied partial density of states (PDOS) at Al site, which will constitute one set of DOS information with that at N site. How is the rate of covalent bond in these materials, in comparison with the typical covalent bonding in Si and Ge.

Anisotropic spectra in regard to c-axis is expected on Al-K edge, because AlN takes wurtzite crystal structure. The measured spectra will be decomposed into polarized components which will reveal the relation of remarkable peaks between the decomposed components and an original spectra.

Spectral change of Al-K edge in Al1-xGaxN by increasing concentration of Ga element gives the local arrangement of wave function at Al site, which shows the rate of bonding in these materials. Putting all accounts together the results from the above mentioned points of view in our study, a better understanding of the electronic structure in AlN will be obtained.

Experimental

The sample takes a film form where c-axis of single crystal is perpendicular to the surface. The polarized ($c \perp E$ and $c \parallel E$) and non-anisotropic components were obtained by decomposing the spectra measured at various tilt angle of c-axis from the direction of incident light.

The measurement were carried out at BL7A and BL1A beam lines of UVSOR. Absorption measurements were done by the method of total electron yield, using qurtz crystal as a monochromator crystal. Samples with small content of Al were measured during a period of good machine stability, when the noise level of drain current is the order of 10^{-2} pA. The obtained signals were averaged to get reliability. The correct positions of the edge were determined by comparison with Al_2O_3 as a standard at BL1A beam line, where the high brightness of the monochromator system allows a rapid scan.

Results and Discussion

The summary of our results is mentioned as follows, including also the content of the previous report [1]. Al-K edge spectra (c⊥E) of Al1-xGaxN were obtained as shown in Fig. 1. Main peaks in the spectra (a, c and f) are retained, though the percentage of Al changes from100 to 5 %. This result and a small (0.2 eV) difference of edge position (chemical shift) suggest that PDOS at Al site is almost composed of Al wave functions and that the bonding character around Al is ionic. As shown in Fig.2, c⊥E and c ∥ E polarized components (XY and Z) and non-anisotropic component (NA) were obtained by the numerical decomposition using the method of the least square fitting. The result of the decomposition is supported by the fact that the synthesized spectrum from the three components (XY, Z and NA) at a magic angle (where the anisotropy of spectrum disappears in wurtzite structure) fairly coincides with p type PDOS calculated by a band theory [2]. Therefore, the obtained three components give us a new step for the further precise study of Al-K edge in this material.

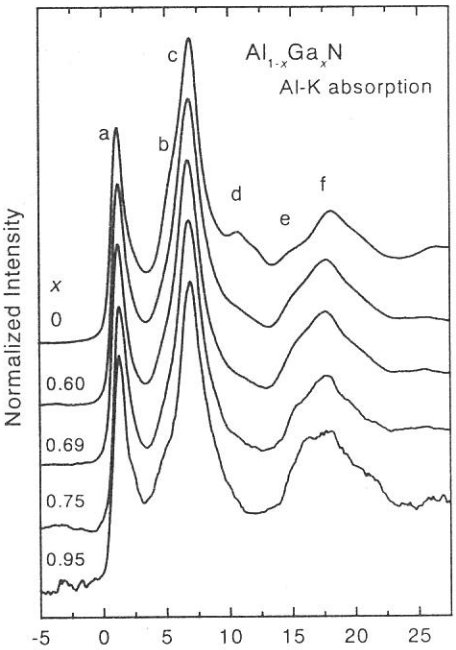

Fig. 1

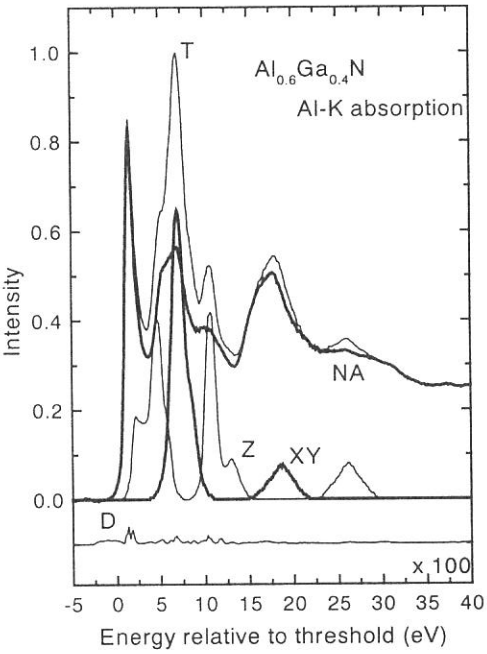

Fig. 2

The authors would like to thank Dr.S.Tanaka, Dr.Aoyagi (RIKEN) for supply of AlN and AlGaN samples.

References

1. K.FUKUI, R.HIRAI and S.NAOE : UVSOR Activity Report (1997) 172.

2. L.-C.Duda, C.B.Stagarescu, J. Downes, K.E.Smith, D.Korakakis, T.D.Moustakas, J. Guo, J.Nordgren : Phys. Rev. B **55** (1998) 1928., Y.-N.Xu and W.Y.Ching : Phys. Rev. B **48** (1993) 4335.

(BL-1B)

Vacuum Ultraviolet Reflection Spectra of Sulfide Glasses

Hiromichi Takebe

Department of Applied Science for Electronics and Materials,
Graduate School of Engineering Sciences,
Kyushu University, Fukuoka 816-8580

Sulfide glasses are prospective candidates for new fiber lasers and non-linear optical switches in near infrared and infrared regions. We have been studying Ge-S and Ga_2S_3-based glasses as alternatives of As-S glass with toxicity. All of sulfide glasses have high refractive indexes over 2 in the visible and near infrared regions [1]. The refractive index are related to the reflection properties of glass in the ultraviolet vacuum region. There are, however, to my knowledge, no reports on the reflection spectra of sulfide glasses except for As-S glass. In this work the reflection spectra of As-S, Ga_2S_3, and Ge-S based glasses were measured.

Spectral measurements were performed using a $As_{40}S_{60}$ glass for comparison, a typical Ga_2S_3-based glass with a composition of $70Ga_2S_3{\cdot}30La_2S_3$, and a series of Ge-S glasses with various S concentrations. Figure 1 shows the representative reflection spectra of sulfide glasses. The reflection bands due to the glass networks of M-S (M = As, Ga, Ge) are observed at 100 - 500 nm. The peaks of the reflection bands due to sulfur ions are located at longer wavelengths than those of the bands due to oxygen ions in oxide glasses [2]. These positions of the reflection bands correspond to the characteristics of refractive index dispersion; sulfide glasses have higher refractive index and dispersion than oxide glasses. Refractive indexes n_d of the sulfide glasses are 2.650 for $As_{40}S_{60}$, 2.493 for $70Ga_2S_3{\cdot}30La_2S_3$ (GLS), and 2.156 for $Ge_{33}S_{67}$. The highest n_d of As_2S_3 glass is related to the relatively-longer resonance wavelength of the reflection band located at 300 - 400 nm, compared with those of GLS and Ge-S glasses. GLS glass has relatively-high refractive indexes and low dispersion characteristics in sulfide glasses [3]. This feature of GLS glass corresponds to the higher reflection intensity of the band in spite of its shorter wavelength by comparison with $As_{40}S_{60}$ glass.

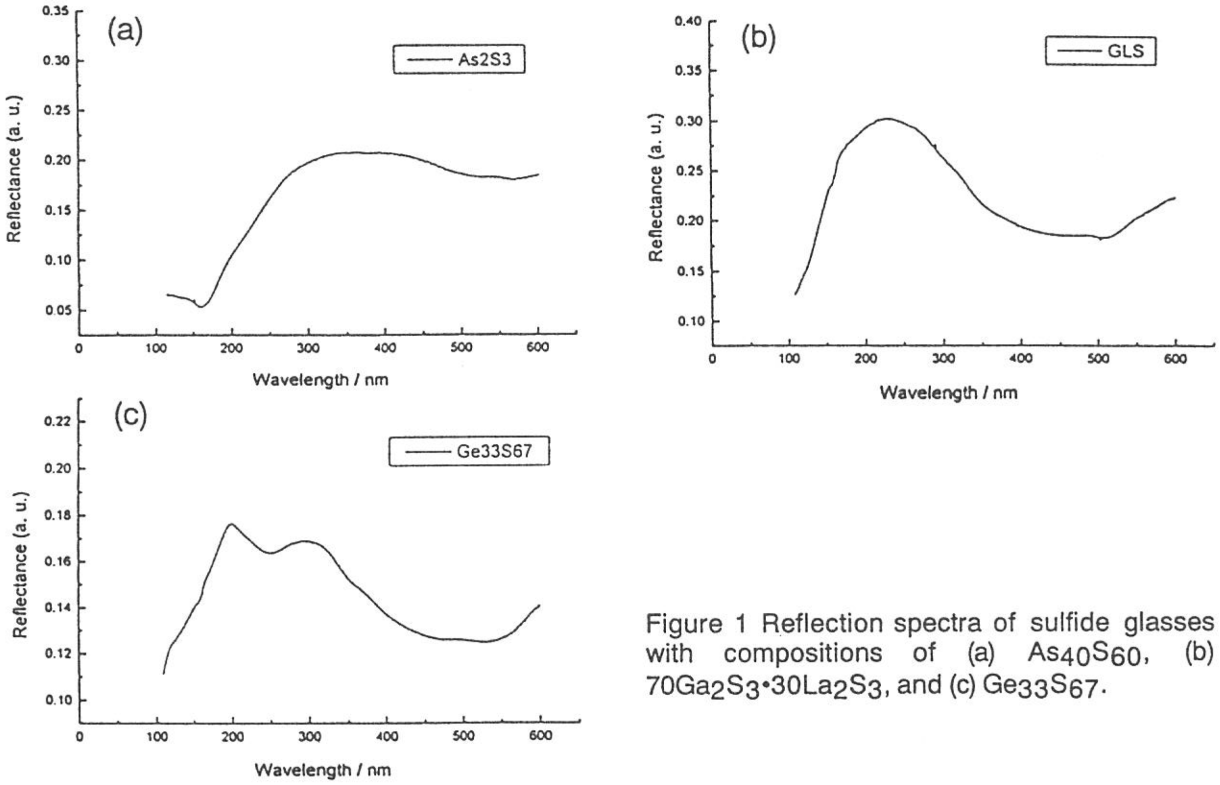

Figure 1 Reflection spectra of sulfide glasses with compositions of (a) $As_{40}S_{60}$, (b) $70Ga_2S_3{\cdot}30La_2S_3$, and (c) $Ge_{33}S_{67}$.

[1] H. Takebe, EMIS DATAREVIEWS SERIES No. 22, IEE (1998), pp. 294-297.

[2] T. Mito, S. Fujino, H. Takebe, K. Morinaga, S. Todoroki, S. Sakaguchi, J. Non-Cryst. Solids, 210 (1997) 155-162.

[3] H. Yayama, S. Fujino, K. Morinaga, H. Takebe, D. W. Hewak, and D. N. Payne, J. Non-Cryst. Solids (1998).

(BL1B)

Optical properties of cerium-doped LiCAF and LiSAF crystals for vacuum ultraviolet optical materials

Masahiro SAKAI, Zhenlin LIU[a], Hideyuki OHTAKE[a], Nobuhiko SARUKURA[a],
Yusaburo SEGAWA[b], Yoshikazu MIYAZAWA[c], Kiyoshi SHIMAMURA[d],
Sonia L. BALDOCHI[d], Kenji NAKANO[d], Na MUJILATU[d], and Tsuguo FUKUDA[d]

Research Center for Molecular Materials,
Institute for Molecular Science (IMS), Myodaiji, Okazaki 444-8585, Japan
[a] *Laser Center for Molecular Science,*
Institute for Molecular Science (IMS), Myodaiji, Okazaki 444-8585, Japan
[b] *Photodynamics Research Center, The Institute of Physical and Chemical Research (RIKEN),*
Nagamachi Koeji 19-1399, Aoba-ku, Sendai, Miyagi 980-0868, Japan
[c] *Research and Development Department, Optron Inc.*
Hakusan 7-5-16, Toride, Ibaraki 302-0032, Japan
[d] *Institute for Materials Research, Tohoku University,*
Katahira 2-1-1, Aoba-ku, Sendai 980-8577, Japan

Various new fluoride crystals have been developed as the host crystals for new solid-state tunable ultraviolet and infrared laser materials. Among them, $LiCaAlF_6$ (LiCAF) and $LiSrAlF_6$ (LiSAF) are the successful material for Chromium [1] or Cerium [2], doping. For Cerium doping in particular, Ce:LiCAF and Ce:LiSAF are attractive solid-state lasers with their practical tuning region from 288 to 315 nm [3]. In spite of similar tunability and laser efficiency, Ce:LiCAF is even more attractive because of its reduced solarization effects compared with Ce:LiSAF. However, the reason for this difference has not been studied well, and to further improve laser performance, spectroscopic studies of these materials will be necessary, including accurate band-gap measurement. In addition, optical material for the ultraviolet and vacuum ultraviolet region has become much more important for the deep ultraviolet lithographic technology required for the semiconductor processing technology of the next century and vacuum ultraviolet spectroscopy using synchrotron orbital radiation.

Crystals of Ce:LiCAF, Ce:LiSAF and LiF were grown by the CZ method. The preparation of raw powder material under a reactive atmosphere was the same for all of these fluoride crystals. All crystals ware about 1-mm thick. To measure the transmission spectra of various fluoride materials at room temperature, an experiment was performed at the beam line BL1B of UVSOR using a 1-m focal-length Seya-Namioka monochromator. The transmission at wavelengths from 100 to 200 nm was detected by a photo multiplier (Hamamatsu R105). All of the fluoride samples were mounted on sample holders separately, and introduced into a sample chamber. Figure 1 shows the transmission spectrum of various fluoride samples. The transmission edge of our LiF was slightly longer than that (102 nm) of the very best sample ever reported in ref. 4. The transmission edge of LiCAF was measured to be 112 nm and that of LiSAF was 116 nm. This difference may explain the solarization free nature of Ce:LiCAF compared with Ce:LiSAF. The absorption at around 125 nm might be attributed to the color center or impurity. Therefore, after the crystal quality is improved, this absorption should disappear. The problems of the commonly used optical materials for the ultraviolet and vacuum ultraviolet region such as LiF are the limitation of transmission wavelength, solarization of the material with irradiation of high power ultraviolet light, and the difficulty of material processing and polishing due to the cleavage or the hydroscopic nature. LiCAF does not have the cleavage or hydroscopic characteristics [5]. Therefore, LiCAF will be a suitable optical material for the ultraviolet and vacuum ultraviolet region, becoming much more important for the next generation lithographic technology.

In conclusion, superior transmission characteristics of $LiCaAlF_6$ (LiCAF) down to 112 nm were found for the first time. From the transparent wavelength shorter than that of conventional LiF, the non hydroscopic nature of LiCAF, and the better mechanical properties compared with LiF, LiCAF was shown to be an ideal optical material for the vacuum ultraviolet region.

The authors are grateful to Mr. M. Hasumoto and Prof. M, Kamada for their experimental support.

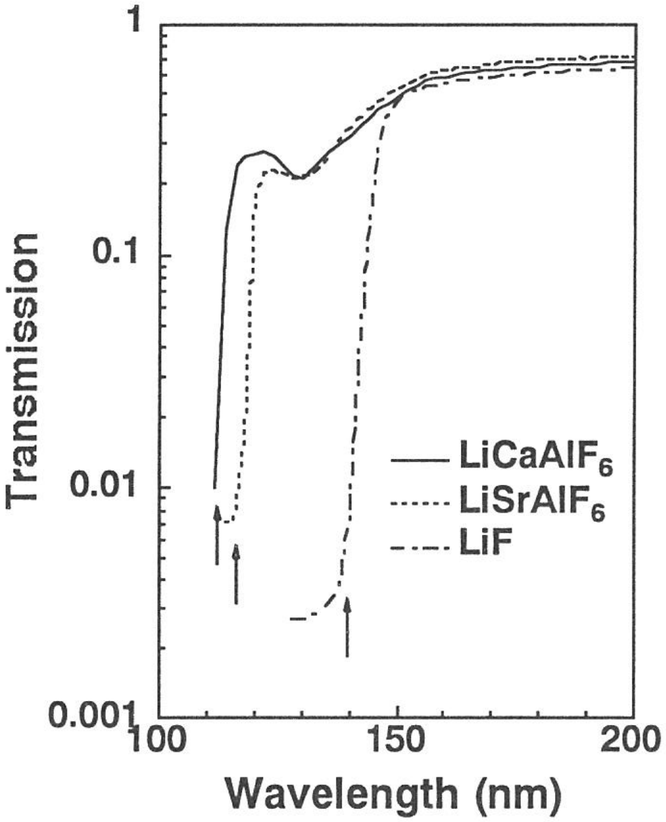

Fig. 1. Transmission characteristics of LiCAF, LiSAF and LiF at room temperature. The arrows show transmission edge wavelengths of various fluoride crystals. According this figure, transmission edge of LiCAF, LiSAF and LiF were 112 nm, 116 nm and 136 nm, respectively.

References

[1] S. A. Payne, L. L. Chase, H. W. Newkirk, L. K. Smith, and W. F. Krupke, IEEE J. Quant. Electron. 24, 2243 (1988); S. A. Payne, L. L. Chase, L. K. Smith, W. L. Kway, and H. W. Newkirk, J Appl. Phys. 66, 1051 (1989).
[2] M. A. Dubinskii, V. V. Semashko, A. K. Naumov, R. Y. Abdulsabirov, and S. L. Korableva, OSA proceedings on Advanced Solid-State Lasers, A. A. Pinto and T. Y. Fan, eds. (OSA 1993), vol. 15, 195; M. A. Dubinskii, V. V. Semashko, A. K. Naumov, et al. J. Mod. Opt., 40, 1, (1993); J. F. Pinto, G. H. Rosenblatt, L. Esterowitz, and G. J. Quarles, Electron. Lett. 30, 240 (1994); C. D. Marshall, S. A. Payne, J. A. Speth, W. F. Krupke, G. J. Quarles, V. Castillo, and B. H. T. Chai, J. Opt. Soc. Am. B. 11, 2054 (1994).
[3] See, for example, Z. Liu, S. Izumida, H. Ohtake, N. Sarukura, K. Shimamura,, N. Mujilatu , S. Baldochi, and T. Fukuda, Jpn. J. Appl. Phys., 37, L1318 (1998)
[4] E. D. Palik, "Handbook of Optical Constants of Solids", Academic Press, Inc. 1985.
[5] M. J. Weber, "Handbook of Laser Science and Technology", Supplement 2, CRC Press, Inc., 1994.

(BL1B) VUV Excited Photoluminescence in Multilayer Structures of Alkali Earth Fluorides

Arisato Ejiri, Akira Urasaki, Sinobu Kinjou, Tetsuya Tamaki and Asamitsu Taminato

Dept. of Science Education, College of Education, Univ. of the Ryukyus. Okinawa 903-0219 Japan.

It is well known that STE(self trapped exciton) luminescence in alkali earth fluorides (CaF_2, SrF_2, BaF_2) crystal can be strongly observed even at room temperature.[1] VUV excited luminescence in multilayer structures with 5 periods of LiF(200Å)-CaF_2(100Å) and of LiF(200Å)-BaF_2(100Å) were previously obseved [2], and a line series of luminescence was found in the former specimen at longer wavelength region than that of the original luminescence in CaF_2 crystal.

This phenomena were analyzed in terms of a multimode interference in a cavity made of the multilayer structure.

Present paper will report on the results of the similar measurement of VUV excited luminescence in multilayer structure of LiF-CaF_2 nad LiF-BaF_2. Sample specimen were deposited on the both of LiF single crystal and of Ag coated LiF single crystal and had compositions with commonly 5 periods in respect of LiF(200Å)-CaF_2(100Å), LiF(100Å)-CaF_2(50Å), LiF(200Å)-BaF_2(100Å), and LiF(100Å)-BaF_2(50Å). Typical results of the present measurement are shown in Fig. 1 -Fig. 3. In Fig. 1, STE luminescence spectra excited with 1050 Å light in single crystal specimens CaF_2 and BaF_2 at room temperature and a low temperature are shown. STE luminescences of these single crystals seem to become very large at the low temperature

In Fig. 2, the luminescence of the multilayer specimen and in Fig. 3, the excitation spectra of the multilayer luminescence are shown.

It is interesing phenomena that the multilayer luminescence at room temperature shows a much larger intensity than that at the low temperature contrarily to the case of the single crystals.

From these experimental studies, it was clearly revealed that the intensity of the multilayer luminescence was enhanced at around 300 nm as an effect of silver coating on the substrate as can be seen in Fig. 2. It should be also noted that the luminescence spectra have a doublet structure in the both of CaF_2 multilayer and BaF_2 one as can be seen in Fig. 2. This phenomena would be very interesting, because it can be expected that STE state likely confined in the well layer. Structures of the excitation Spectra having a large peak around 10 eV (Fig. 3) are strongly depended on the multilayer compositions.

References

1) A. Ejiri, A. Hatano, and K. Arakaki; UVSOR Act. Rep. 1995 68 (1996)

2) A. Ejiri, E. Chin, A. Urasaki, T. Yonamine and T. Yokozawa; UVSOR Act. Rep. 1997 106 (1998)

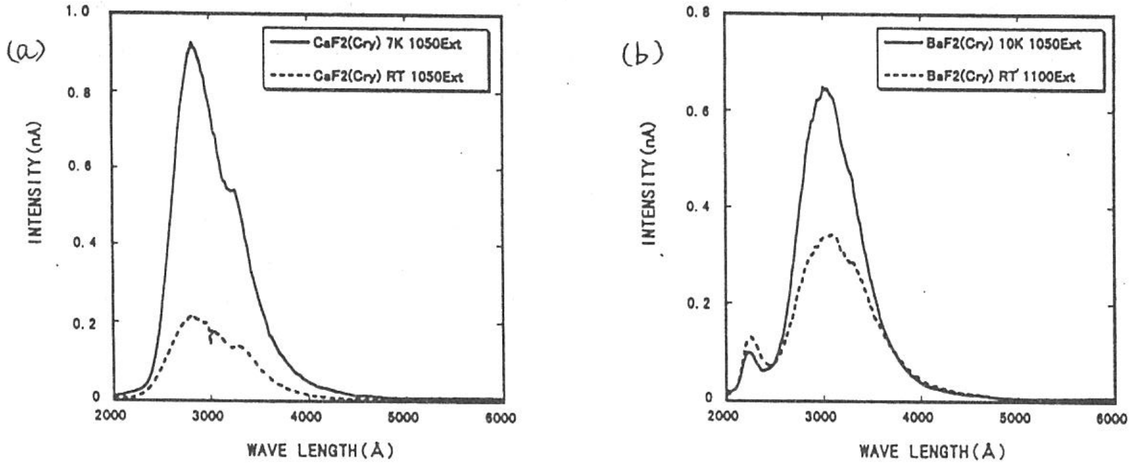

Fig. 1 STE luminescence spectra of (a) CaF_2 single crystal excited at 1050 Å and of (b) BaF_2 single crystal excited with 1050 Å at 10K and with 1100Å at RT.

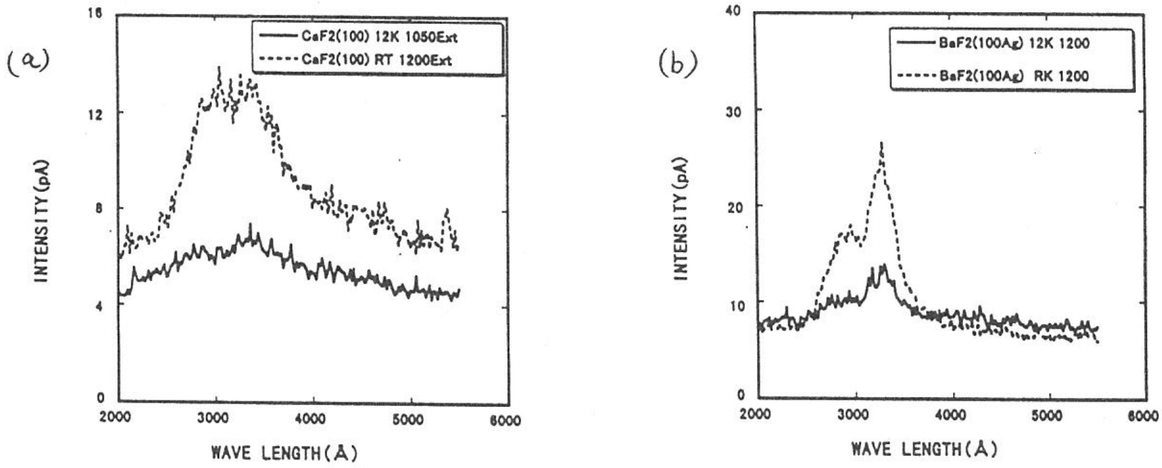

Fig. 2. Luminescence spectra of (a) the CaF_2 multilayer with 100 Å well width excited with 1050 Å at 12K and RT, and of (b) the BaF_2 multilayer on the Ag coated substrate.

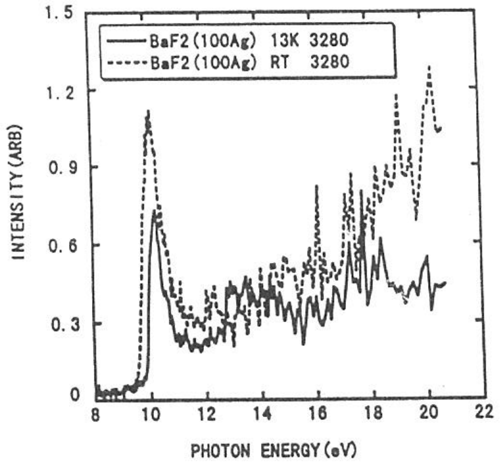

Fig. 3 Excitation spectra of the BaF_2 multilayer luminescence of 3280Å at RT and 13K.

(BL1B)

Two-Photon Spectroscopy of Excitons in CaF_2 by Using Synchrotron Radiation and Laser

Toru TSUJIBAYASHI[A], Masayuki WATANABE[B], Osamu ARIMOTO[C], Hiroshi NAGASAKI[C], Minoru ITOH[D], Jun-ichi MURAKAMI[D], Yoshizumi BOKUMOTO[D], Syunsuke NAKANISHI[E], Hiroshi ITOH[E], Shuji ASAKA[F], and Masao KAMADA[G]

[A]*Department of Physics, Osaka Dental University, Hirakata 573-1121*
[B]*Department of Fundamental Sciences, Kyoto University, Kyoto 606-8501*
[C]*Department of Physics, Okayama University, Okayama 700-8530*
[D]*Department of Electrical & Electronic Engineering, Shinshu University, Nagano 380-8553*
[E]*Department of Advanced Materials Science, Kagawa University, Takamatsu 760-8526*
[F]*Equipment Development Center, Institute for Molecular Science, Okazaki 444-8585*
[G]*UVSOR Facility, Institute for Molecular Science, Okazaki 444-8585*

Two-photon spectroscopy (TPS) is an important technique in optical measurements for investigation of electronic structures in condensed matters because of the difference in the parity-selection rules between one- and two-photon absorption transitions. The transition probability of two-photon absorption is much lower than that of one-photon absorption. Therefore, intense light from high-power lasers has been used for TPS. The restriction of laser wavelengths prevents TPS from being applied to wide-band gap materials.

Synchrotron radiation (SR) is one of the most important light sources since it provides continuous distribution in a wide energy range from X-ray to infrared. It is an exciting project to develop a novel technique of TPS using SR and laser, since the combination of the wide spectral range of SR and the high-power of lasers will give us fruitful information of the electronic structures of many materials. We measured the valence excitons of BaF_2 by using a time-gated photon counting method [1-5]. The obtained value of the binding energy of the exciton was larger by 50% than that reported in a previous paper [6]. In order to check the previous binding energy in another system, the measurement of the valence exciton in CaF_2 was performed. We report the experimental result in this paper.

The crystal of CaF_2 has wide band gap of about 12 eV. It is used as a material for optical windows. Under optical excitation around band gap or higher energies, luminescence due to radiative decay of self-trapped excitons (STEs) is observed around 4.4 eV.

The optical system for TPS was constructed at Beam-line 1B. Figure 1 shows a schematic diagram of the apparatus. A cleaved specimen of CaF_2 was mounted on a cold finger of a conduction-type cryostat. The SR light

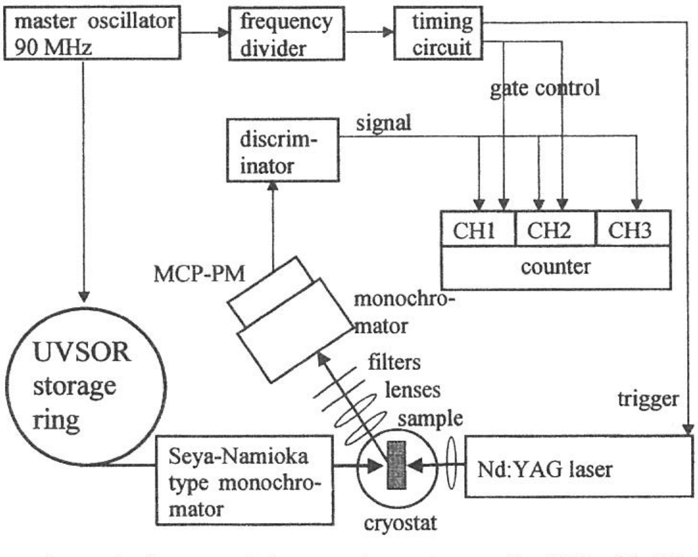

Fig. 1 Schematic diagram of the experimental setup for TPS with SR and laser.

was monochromatized through a 1-m Seya-Namioka-type monochromator. The pulse duration of the SR light was about 1.6 ns. The second harmonic light of a Nd:YAG laser ($\hbar\omega_{\mathrm{laser}} = 2.33$ eV) was introduced in the opposite direction. The averaged power of the laser was about 10 W. The trigger signal for the laser was provided by the master oscillator of a RF cavity of the storage ring through a divider which lowered the frequency of the pulses down to about 5 kHz. The time interval between successive SR pulses was about 11 ns, while the duration of the laser pulse was about 800 ns.

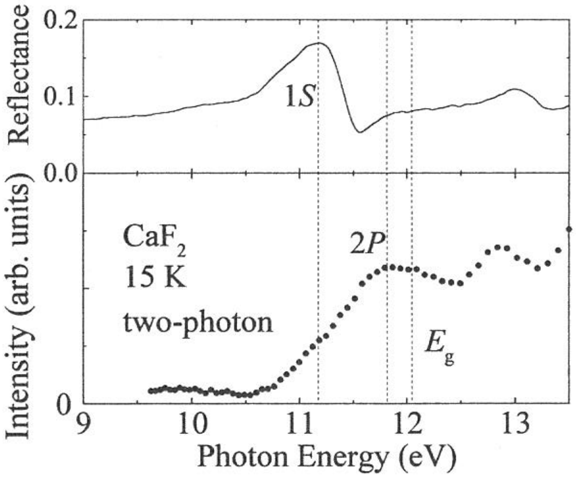

Fig. 2 Lower panel: TPS spectrum of CaF$_2$ at 15 K. Upper panel: Reflection spectrum.

We detected STE luminescence as the TPS signal by using a micro-channel plate photomultiplicr tube (MCP-PM) with narrow-band filters and a monochromator for eliminating the scattered light from the laser. The signal from the MCP-PM was fed to a three-channel time-gated photon counter. The photon signals just before and after the incidence of the laser pulses were counted at Channels 1 and 2, respectively: Channel 1 (CH1) counts the background signal induced only by the SR light, while CH2 counts the signal due to the simultaneous irradiation with SR and laser. The gate widths for both counters were set to be 4 μ s. CH3 counts the signal all the time for reference. The net luminescence signal induced by two-photon excitation was obtained by subtracting the count at CH1 from that at CH2. A few tens of seconds were required to accumulate the signal at a fixed wavelength. It is noteworthy that our experimental technique is a kind of zero method, and therefore it will be more sensitive than the transmission method that was applied to observe two-photon absorption of KI, KCl and NaCl by an Italian group [7].

Solid circles in the lower panel of Fig. 2 show the TPS spectrum of CaF$_2$ at 15 K. The abscissa of the figure represents the sum of photon energies of the SR and laser. The reflection spectrum is drawn by a solid line in the upper panel for comparison. The 1*S* peak at 11.2 eV in the reflection spectrum is indicated by an arrow. The TPS signal intensity rises at about 10.6 eV, and reaches a peak at 11.8 eV. We assign the peak to the TPS signal due to the 2*P* state of the Γ exciton because of the parity-selection rule. The reflection spectrum also has a shoulder at that energy position. We assign the shoulder to the 2*S* state of the exciton on the basis of the observation of the 2*P* peak in the TPS spectrum.

Assuming the simple hydrogen-like energy levels or Wannier exciton picture, the *n*th level (*n*=1,2,3...) of the exciton, E_n, is given by

$$E_{\mathrm{n}} = E_{\mathrm{g}} - \frac{R^*}{n^2}, \qquad (1)$$

where E_g is the band gap, and R^* the exciton binding energy. By using eq. (1), we estimate the binding energy of the exciton in CaF$_2$ at 0.8 eV. It is about 0.2 eV smaller than that in Ref. 6. In the case of BaF$_2$ our value is 0.9 eV, and it is about 0.3 eV larger than that in Ref. 6. These previous values are based on band gap energies determined by analysis of reflection and one-photon absorption spectra. On the other hand, the present analysis based on clear peaks due to 2*P* excitons. This makes the present result more reliable than the previous values.

This work was partially supported by the Grant-in-Aid for Scientific Research from the Japanese Ministry of Education, Science, Sports and Culture.

References

[1] T. Tsujibayashi *el al.*: UVSOR Activity Report **24** (1997) 52.
[2] O. Arimoto *el al.*: UVSOR Activity Report **25** (1998) 116.
[3] S. Asaka *el al.*: Rev. Sci. Instrum. **69** (1998) 1931.
[4] M. Kamada *el al.*: J. Synchrotron Radiation **5** (1998) 1035.
[5] O. Arimoto *el al.*: J. Electron Spectrosc. Relat. Phenom. **92** (1998) 219.
[6] T. Tomiki and T. Miyata: J. Phys. Soc. Jpn. **27** (1969) 658.
[7] M. Casalboni *el al.*:Phys. Rev. B **44** (1991) 6504.

(BL1B)

VUV excitation spectra of long persistent phosphorescence in $SrAl_2O_4$:Eu,Dy

M. Kamada, J. Murakami,[A] N. Kida,[B] N. Ohno,[B] T. Hasegawa,[C] J. Azuma,[C] and K. Tanaka[C]

UVSOR Facility, Institute for Molecular Science, Myodaiji, Okazaki 444-8585
[A]Faculty of Engineering, Shinshu University, Nagano 380-8553
[B] Division of Elector. and Appl. Phys., Osaka Electro-Commun. Univ., Neyagawa 572-8530
[C] Faculty of Science, Kyoto University, Sakyo, Kyoto 606-8224

In recent years, a new type of long persistent phosphors has been synthesized. The phosphors, for examples $SrAl_2O_4$:Eu, Dy and $CaAl_2O_4$:Eu,Nd, are much different from previous sulfide phosphors. The brightness and persistent time of the new phosphors are more than 10 times larger than the previous ones. Although the new long persistent phosphors attract much interest from application points of view, they are also very interesting materials for basic science. The carriers to provide the new long persistent phosphorescence are seemed to be holes, while those in the previous sulfide phosphors are electrons. The purpose of the present study is to know the long persistent phosphorescence induced by vuv excitation in order to investigate energy storage of vuv light.

The experiments were carried out at BL1B, where a 1-m Seya-Namioka type monochromator provides vuv light for excitation. Powders of pure and Eu-and Dy-doped $SrAl_2O_4$ were kindly supplied from Nemoto-Chem. Co. Ltd. The emission spectra were obtained by using a Princeton CCD system with a Spex 270M monochromator. The excitation spectra of $SrAl_2O_4$:Eu, Dy were measured in the range from 50 to 420 nm. The emission and excitation spectra of pure $SrAl_2O_4$ were also measured for comparison. Special cares were taken to separate long phosphorescence and short luminescence. After glow was also obtained with the vuv beam shutter being closed.

Figure 1 shows the emission spectra of $SrAl_2O_4$and $SrAl_2O_4$:Eu,Dy at 15 K under excitation by 180 nm. Strong emission bands are observed at about 450 and 520 nm in $SrAl_2O_4$:Eu,Dy. Weak bands are also appreciable around 250 and 360 nm. On the other hand, emission bands are observed around 250 and 360 nm in $SrAl_2O_4$. This indicates that the emission bands at about 450 and 520 nm are attributed to the impurity (Eu, Dy), while the bands around 250 and 360 nm are due to the host material ($SrAl_2O_4$).

Figure 2 shows excitation spectra of the emission bands mentioned above. The 450-nm and 520-nm emission bands in $SrAl_2O_4$:Eu,Dy are seen in the short-wavelength region below 400 nm. The 250-nm and 360-nm emission bands are observed in the wavelength region shorter than 190 nm. It should be noticed that the spectral profiles of the 450-nm and 520-nm emission bands in the wavelength region shorter than 190 nm are very similar with those for the 250-nm and 360-nm emission bands. This indicates that the 450-nm and 520-nm emission bands in $SrAl_2O_4$:Eu,Dy can be produced by energy transfer from host $SrAl_2O_4$. The mechanism of this host-sensitization is under consideration

The authors would like to express their sincere thanks to Mr. Y. Murayama of Nemoto Chem. Co.Ltd. for his kind supply of the present samples.

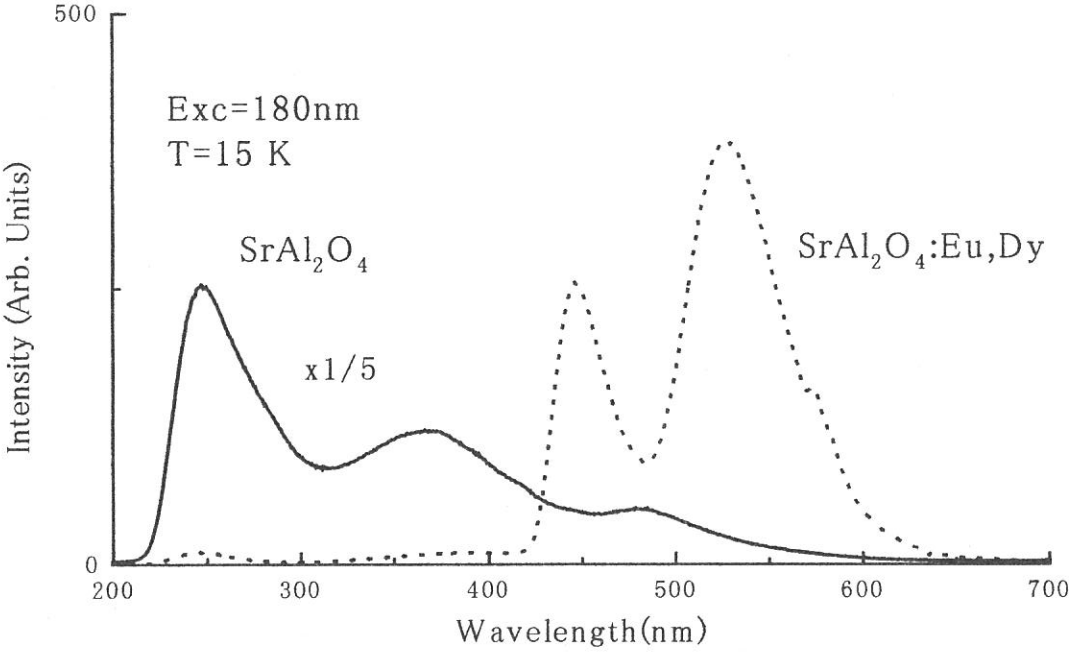

Fig. 1. Emission spectra of $SrAl_2O_4$ and $SrAl_2O_4$:Eu,Dy

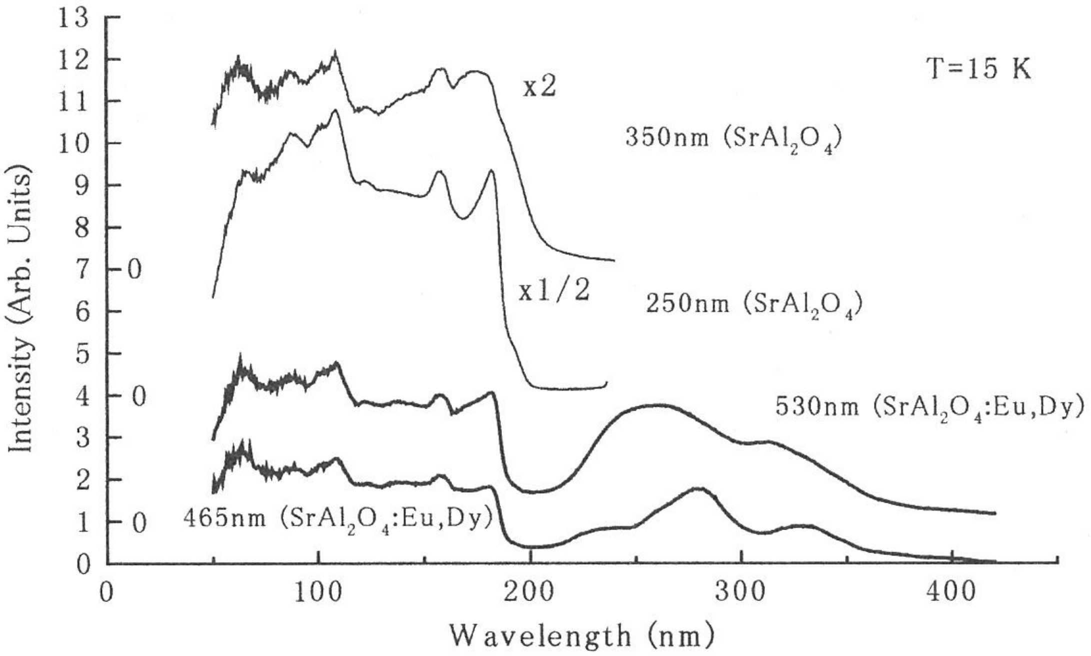

Fig. 2. Excitation spectra of $SrAl_2O_4$ and $SrAl_2O_4$:Eu,Dy

(BL1B)

Formation Processes of Secondary Excitons and Electron-Hole Pairs by Vacuum Ultraviolet Radiation in $PbCl_2$ Crystal

M. Kitaura[1], M. Itoh[2], Y. Bokumoto[2] and M. Fujita[3]
[1]*Department of Physics and Mathematics, Fukui National College of Technology, Sabae 916-8507*
[2]*Department of Electrical and Electronics Engineering, Shinshu university, Nagano, 380-8553*
[3]*Maritime Safety Academy, Kure, 737-8512*

The use of synchrotron radiation (SR) allows us to obtain information on relaxation processes of elementary electronic excitations (EE's) in ionic crystals over a wide energy region. For example, Lushchik *et al.* have measured excitation spectra for intrinsic luminescence of alkali halides in a vacuum ultraviolet (vuv) region, and succeeded in discriminating several relaxation processes accompanied with multiplication of EE's (MEE's) [1]. We are interested in relaxation and migration of elementary EE's under conditions of MEE's in lead chloride ($PbCl_2$). The $PbCl_2$ crystal contrasts well with alkali halides with respect to the following points. First, the exciton absorption has features of the intra-ionic $6s^2 \rightarrow 6s6p$ transition in Pb^{2+} ions [2]. Second, the intrinsic defect is described as a dimer Pb_2^{3+} ion in which an electron is self-trapped at a pair of adjacent lead ions [3]. Third, the valence band is wider than the band gap and consists of lead $6s$ and chlorine $3p$ orbitals [4]. The aim of the present study is to investigate the interrelation between the electronic band structures and the relaxation of primarily created EE's in $PbCl_2$.

Optical properties of $PbCl_2$ have been studied extensively so far. In especial, luminescence studies have been carried out energetically because they give complementary information on the initial process of the photolysis in this material. Two types of luminescence are known to be observed in $PbCl_2$ [5,6]. The one is the UV luminescence produced under excitation in the lowest exciton band, which has been attributed to radiative decay of the self-trapped excitons at Pb^{2+} ion sites. The other is the BG luminescence stimulated by photons with energies above the band gap, which originates from tunneling recombination of a hole released from some trapping center with an electron trapped at the Pb_2^{3+} self-trapped electron (STEL) center. Formation processes of secondary excitons and *e-h* pairs by high energetic EE's will be, therefore, easily distinguished by measuring excitation spectra for the UV and BG luminescence in a vuv region.

In the present work, we have measured reflectance spectrum and excitation spectra for the UV and BG luminescence up to 30 eV. A similar measurement has been undertaken independently by Kink *et al* [7]. For the excitation spectra, reflection losses of an excitation light by the crystal surface were corrected by referring to the reflectance spectrum. The excitation spectra for the UV and BG luminescence, thus obtained, are shown in Fig. 1 (a) and (b), respectively. In spite of the correction for reflection losses by the surface, both the excitation spectra exhibit prominent dips at reflectance peaks in the energy region below 15 eV. The dips should be connected with nonradiative annihilation of EE's at the crystal surface, because optical excitation at the reflectance peaks with high absorption coefficient creates EE's at the crystal surface.

The UV luminescence yield η_{UV} begins to increase sharply at 9.6 eV, similarly to the reflectance. Such an increase in η_{UV} takes place around twice the value of the band gap energy, and thus originates from formation of secondary excitons by inelastic scattering of hot photoelectrons. The threshold energy for the secondary exciton formation $E_{th}^0 = 9.6$ eV exceeds the sum of the minimum energies required for creation of an exciton and of an *e-h* pair, namely, $E_{ex} + E_g = 9.2$ eV. The excess energy $E_{th}^0 - (E_{ex} + E_g) = 0.4$ eV would be gained by a valence hole created primarily. The condition $E_{th}^0 > E_{ex} + E_g$ has been satisfied in most of ionic crystals. We suppose that the spectral region of 9.6 - 20 eV, where η_{UV} is relatively flat, is characterized by creation of a photohole in the valence band and a hot photoelectron in a higher conduction band. Our cluster calculation of $PbCl_2$ well explains the reflectance spectrum by considering the higher conduction band to be of the lead $6d$ orbital. The value of η_{UV} does not almost change as the photon energy increases up to 30 eV. Therefore, it is most likely that, in the whole spectral range investigated here, the formation of secondary excitons arises from creation of hot photoelectrons in the lead $6d$ conduction band.

We observe a stepwise increase of the BG luminescence yield η_{BG} around integral multiples of the band gap energy. The value of η_{BG} is gradually enhanced in the range 14 - 20 eV, reaching almost twice as high as at 14 eV where one photon creates one *e-h* pair. These results undoubtedly satisfy conditions for multiplication of *e-h* pairs; therefore, excitation with photons of 14 - 20 eV leads to formation of secondary *e-h* pairs. Although self-trapping of electrons is observed in $PbCl_2$, photoelectrons get high kinetic energy in the secondary *e-h* pair formation. The kinetic energy of the photoelectrons nearly equals to the excess energy $E_{th}^{\pm} - 2E_g = 4.4$ eV, which is gained by a photohole. On the basis of this result, we suppose that at low temperatures the $PbCl_2$ crystal exhibits both electron and hole self-trapping in the absence of an exciton effect. In the 17 - 20 eV range, we remark a slight increase in η_{BG}, which may arise from the electronic transition between the chlorine 3*s* outermost core band and the lead 6*p* conduction band. The value of η_{BG} takes the minima at 21.4 eV, 22.7 eV, and 23.9 eV at which three peaks appear sharply in the reflectance spectrum. These reflectance peaks have been ascribed to creation of core excitons which consist of a hole in the lead 5*d* core states and an electron in the lead 6*p* conduction band. Such "cationic" core excitons will decay nonradiatively to produce an effective electron emission (i.e., Auger-decay process), resulting in the decrease of radiative recombination of a hole with the STEL center, i.e., the decrease of η_{BG}. This interpretation is based on the fact that the quantum yield of photoelectron emission in $PbCl_2$ has the maxima at the same energies as the reflectance peaks [8]. A further increase in the excitation photon energy brings about the treble value of η_{BG} at 30 eV, that is, the energy at which one photon creates three *e-h* pairs. In this case, we expect that secondary valence excitations are generated through the following two processes. One is inelastic scattering of a hot photoelectron in the lead 6*p* conduction band, being described above. The other is nonradiative Auger-decay of a photohole in the chlorine 3*s* core band, which kicks up a valence electron into the high-lying conduction band.

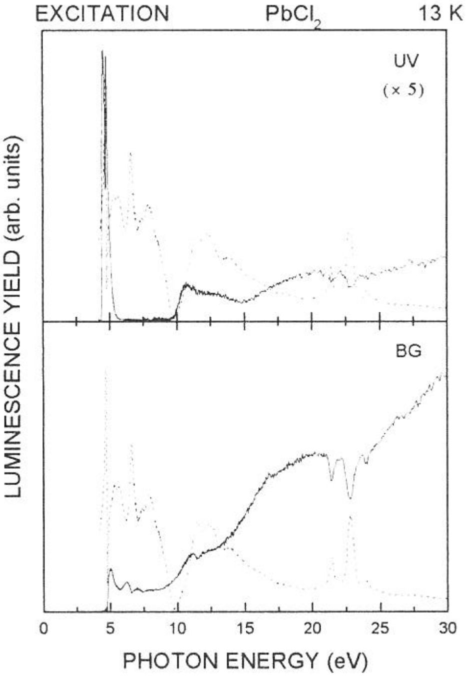

Fig. 1. Excitation spectra for the UV and the BG luminescence bands in $PbCl_2$ measured at 13 K The reflectance spectrum of $PbCl_2$ at 13 K is also shown by a broken curve for reference.

References

[1] A.Lushchik, E.Feldbach, Ch.Lushchik, M.Kirm, and I.Martinson: Phys. Rev. B **50**, (1994) 6500.

[2]M.Fujita, H.Nakagawa, K.Fukui, H.Matsumoto, T.Miyanaga, and M.Watanabe: J. Phys. Soc. Jpn., **60** (1991) 4393.

[3] S.V.Nistor, E.Goovearts, and D.Schoemaker: Phys. Rev. B **48**, (1993) 9575.

[4] M.Itoh, T.Shiokawa, K.Sawada, and M.Kamada: J. Phys. Soc. Jpn., **67** (1998) 2140.

[5] M.Kitaura and H. Nakagawa: J. Electron Spectrosc. and Relat. Phenom., **79** (1996) 171.

[6] M.Kitaura and H. Nakagawa: J. Lumi. **72-74** (1997) 883.

[7] R.Kink, T. Avarmaa, V.Kisand, A.Lohmust, I.Kink, and I.Martinson: J. Phys.: Condense. Matter **10** (1998) 693.

[8] M.Itoh: J. Fac. Eng. Shinshu University, (1998) 19.

(BL-1B)

Vacuum Ultraviolet Absorption Spectra of Amino Acids

M. Tanaka, Y. Kishigami, I. Shimoyama[1)], K. Ebina[2)] and K.Nakagawa[2)]

Graduate school of Cultural Studies and Human Science, Kobe University, Tsurukabuto, Nada-Ku, Kobe 657-8501

[1)]Graduate school of Science and Technology, Kobe University, Rokkohdai, Nada-Ku, Kobe 657-8501

[2)]Faculty of Human Development, Kobe University, Tsurukabuto, Nada-Ku, Kobe 657-8501

Vacuum ultraviolet absorption spectra of aspartic acid (Asp) and phenylalanine (Phe) were measured in the region of 40 nm to 250 nm.

Evaporated thin films of Asp and Phe was carefully prepared with a new technique developed by our group, in which amino acids were evaporated on the sodium salycilate (SS) films. Thickness *d* of the films were 42 nm for Asp and 33 nm for Phe. Measurements of spectra were performed at the beamline BL-1B at room temperature. Measuring the fluorescence intensity of SS without amino acids as the reference spectra $I_0(\lambda)$ and that with amino acids as $I(\lambda)$, absorption coefficient $\mu(\lambda)$ were calculated from the Lambert-Beer's law $I(\lambda) = I_0(\lambda)\exp(\mu(\lambda)d)$.

Absorption spectral shape obtained for Asp was in a good agreement with that reported by Nakagawa et al.[1], in which spectrum was measured in the region of 140 nm to 250 nm. But absolute values of $\mu(\lambda)$ obtained in this work were smaller than that by Nakagawa et al.[1] by a factor of 2.1 in the region of 140 nm to 250 nm. We assumed that the thickness of our films on the SS was not uniform because substrates of our experiment were non-flat SS, and we multiplied a factor of 2.1 to the $\mu(\lambda)$ obtained in this work. The curve A in Fig. 1 shows the absorption spectrum of Asp after this correction at λ=147 nm.

With a similar procedure we obtained absorption spectra of Phe. In the case of Phe, since the strong fluorescence was observed around 190 nm, we connected our spectrum with that by Nakagawa et al.[1] at λ=147 nm. The curve B in Fig. 1 shows the absorption spectrum of Phe after this correction. Curve B' in the figure is the spectra reported by Nakagawa et al.[1].

Assignment of peaks in these spectra are of great interest and we have a plan to make a quantum mechanical calculation of energy levels of these amino acids together with some theorists.

Reference

[1]K. Nakagawa et al., in "The Role of Radiation in the Origin and Evolution of Life", ed. by M. Akaboshi et al., Kyoto University Press (1999), Kyoto Japan, in press.

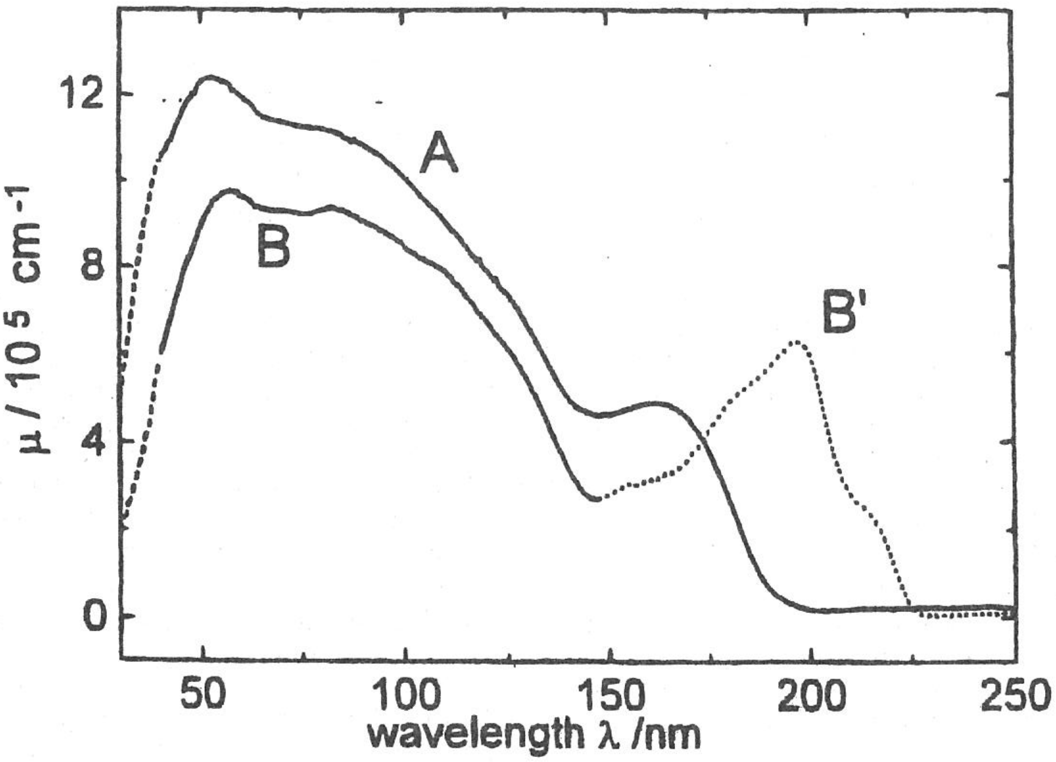

Fig. 1. Absorption spectra of aspartic acid (Curve A) and Phenylalanine (Curve B and B').

(BL1B)

Self-Trapped Exciton Luminescence in BaF_2 Stimulated under Simultaneous Irradiation of Synchrotron Radiation and Laser

M. Watanabe, M. Iwanaga[a], S. Asaka[b], T. Tsujibayashi[c], O. Arimoto[d], M. Itoh[e],
S. Nakanishi[f], H. Itoh[f] and M. Kamada[g]

Department of Fundamental Sciences, Kyoto University, Kyoto 606-8501
[a]*Graduate School of Human and Environmental Studies, Kyoto University, Kyoto 606-8501*
[b]*Equipment Development Center, Institute for Molecular Science, Okazaki 444-8585*
[c]*Department of Physics, Osaka Dental University, Hirakata 573-1121*
[d]*Department of Physics, Okayama University, Okayama 700-8530*
[e]*Department of Electrical & Electronic Engineering, Shinshu University, Nagano 380-8553*
[f]*Department of Advanced Materials Science, Kagawa University, Takamatsu 760-8526*
[g]*UVSOR Facility, Institute for Molecular Science, Okazaki 444-8585*

BaF_2 is a widely-used material as a scintillator in many fields such as high-energy physics and nuclear medicine. Therefore, its fundamental information about radiation damages due to defect formation is important for practical uses. Recently we have developed a spectroscopic system utilizing synchrotron radiation (SR) and laser as light sources, and applied it to two-photon spectroscopy of BaF2 [1]. In the present work we apply our system to photostimulated-luminescence method which is a very sensitive tool to detect radiation damages generated in samples. We report that photostimulation occurs for self-trapped exciton (STE) luminescence under simultaneous irradiation of SR and laser. The present result indicates that lattice defects are generated in BaF_2 even under the irradiation with relatively weak light beam compared to γ-ray or neutron.

Single crystal of BaF_2 obtained from the Horiba Ltd. was used here. Experiments were performed with a combination of the SR and a cw mode-locked Ti:sapphire laser (wavelength 780 nm, pulse width 100 fs, repetition rate 90 MHz, average power 500 mW). In our experiments, both the SR and the laser were used as cw light sources. The sample with a cleaved (111) surface was mounted on a copper finger of a temperature-variable cryostat. The SR beam, dispersed by a 1m Seya-Namioka type monochromator, irradiated the sample surface under normal incidence configuration, and the laser beam was incident from an opposite direction of the SR beam. Luminescence was detected through a monochromator equipped with a photomultiplier.

Figure 1 shows luminescence spectra under the SR excitation (○), and the simultaneous irradiation of the SR and the laser (●). The sample was irradiated with the SR at 19.5 eV, which corresponds to the transition from the Ba^{2+} 5p core band to the conduction band [2]. Two emission bands centered at 5.5 eV and 4.1 eV are assigned to the Auger-Free and the STE luminescence, respectively [3]. One can see that emission intensity increases by the simultaneous irradiation. Difference between the two spectra, i.e., net signal intensity induced by the simultaneous irradiation is shown by closed squares. It is evident that the laser irradiation stimulates only the STE luminescence. The signal intensity was found to increase linearly with the laser power.

Figure 2 shows the dependence of the signal intensity induced by the simultaneous irradiation on the SR photon energy. As the photon energy is increased from the valence excitation at around 10 eV, the signal intensity begins to increase and becomes remarkable in a region from 16 to 21 eV, followed by the decrease in the higher energy region. The energy region from 16 to 21 eV is mainly characterized by several core-exciton transitions [2]. It is suggested that the photostimulation effect observed by us is related to the formation of core excitons.

In order to investigate the mechanism of the photostimulation effect, we measured the stimulated signal intensity as a function of temperature. The result is presented in Fig.3. The signal intensity gradually increases with increasing temperature, but abruptly decreases above 100 K. Beaumont *et al* reported that, in BaF_2, a V_k center (self-trapped hole) is thermally released above 100 K [4]. Then it is reasonable to consider that the photostimulation effect is ascribed to the generation of V_k centers.

In alkali halides, it is well known that photostimulation of the STE luminescence occurs under simultaneous irradiation of UV and red light [5]. The photostimulated STE luminescence arises from the recombination of a V_k center and an electron released from some trapped center by the red light. Since formation process of the STE luminescence in BaF_2 is quite similar to that in alkali halides, we conclude that the photostimulation effect in BaF_2 is due to the capture of an optically released electron by the V_k center. We also measured the time response of the photostimulated signal, when the laser beam was periodically turned on and off during steady irradiation of the SR. Whenever the laser beam was turned on, the signal rose instantaneously in our time resolution, and decayed with a time constant of a few ms to a stationary value. The peak height of this short-lived spike was found to increase with the period of the SR irradiation. This fact indicates that the steady irradiation of the SR continues to generate trapping centers of electrons and holes. That is, lattice defects are generated even under the irradiation of weak light beam such as the SR. The experimental result in Fig.2 may suggest that the dissociation of core exciton is effective for defect formation in BaF_2. Further studies are in progress.

This work is supported by a Grant-in Aid for Scientific Research from The Ministry of Education, Science, Sports and Culture of Japan.

References

[1] O. Arimoto *et al* : J. Electron Spectroscopy and Related Phenomena **92** (1998) 219.
S. Asaka *et al* : Rev. Sci. Instrum. **69** (1998) 1931.
[2] G. W. Rubloff : Phys. Rev. B**5** (1972) 662.
[3] M. Itoh *et al* : Rev. Solid State Sci. **4** (1990) 467.
[4] J. H. Beaumont *et al* : Proc. R. Soc. London A **315** (1970) 69.
[5] M. Itoh : J. Phys. Soc. Jpn. **53** (1984) 1191.

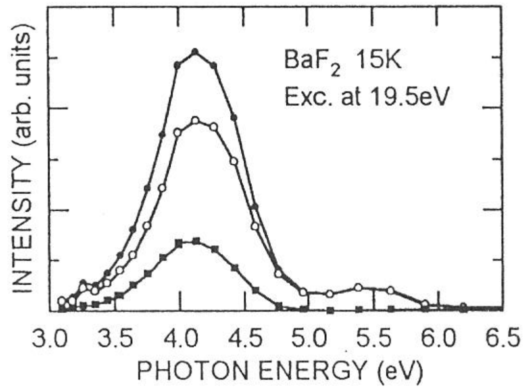

Fig.1 Luminescence spectra of BaF_2 under the excitation with SR (○), and the simultaneous irradiation with SR and laser (●). Difference between the two spectra is also shown by closed squares.

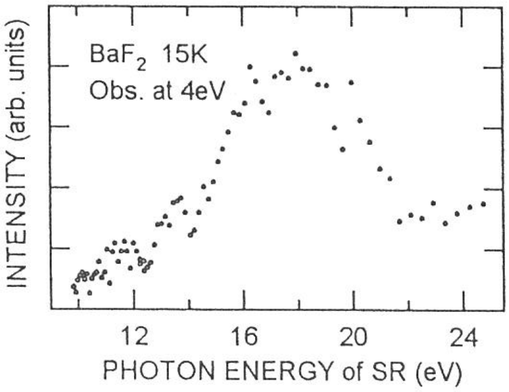

Fig.2 Dependence of the photostimulated signal on the photon energy of SR.

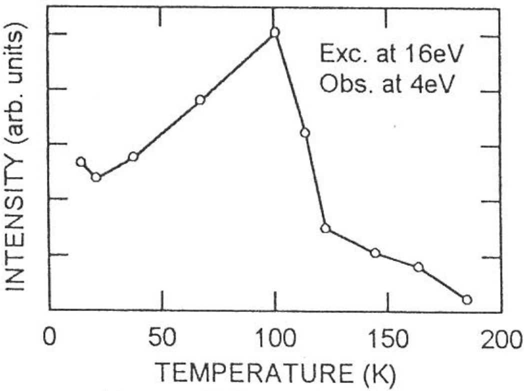

Fig.3 Temperature dependence of the photostimulated signal intensity.

(BL1B) One-Photon Photoionization Thresholds of Aromatic Molecules at Water/Air Surface

Teiichiro Ogawa[A], Shinya Sasaki, Manabu Tokeshi[B], Takanori Inoue[C], and Akira Harata[A]

Department of Molecular Science and Technology, Kyushu University
Kasuga-shi, Fukuoka, 816-8580

Photoionization behavior at the solution surface is different from that in the bulk solution. Photoionization threshold in solution has been determined in a single-photon process using synchrotron radiation or hydrogen discharge lamp, and in a two-photon process using laser radiation. Although there are a few measurements on photoionization threshold of aromatic molecules on solution surface using laser two-photon excitation, no measurements have been carried out using one-photon excitation on solution surface. We have tried to measure one-photon ionization spectra (energy dependence of photoionization efficiency) and photoionization thresholds of aromatic molecules on water surface using synchrotron radiation.

The experimental apparatus is shown in Fig. 1. Synchrotron radiation of energy from 4.7 to 7.5 eV was used as an excitation source. The beam power was monitored using a photomultiplier to calibrate its energy dependence. It was about 10^{10} photon/s at 6.2 eV, and varied as shown in Fig. 2. The beam was softly focused through a sapphire lens and irradiated the solution surface at 85° to the surface normal. The solution was kept in a stainless-steel vessel (0.1 mL) of 8 mm in diameter, and the vessel was served as the current collecting electrode. A disk electrode was located 5 mm above the solution surface and was connected to a high-voltage power supply unit. The photoionization current was measured using a current meter (Keithley, 617). The perylene (guaranteed grade, Nacalai Tesque) was used as recieved. The water was distilled, deionized, filtered and distill again in a quartz vessel.

The one-photon ionization spectra of perylene on the water surface have been measured and its intensity was linearly proportional to its concentration for 10^{-6} - 10^{-8} M. The photoionization spectrum was nomalized by beam power and solution concentration. The blank signal (signal of pure water) was relatively small and was not dependent of the excitation energy.

The photoionization current near threshold can be represent by a power law,

$$I = c(E_{excess})^{5/2} = c(h\nu - I_{th})^{5/2}$$

where E_{excess} is the excess energy of the ionized pair, $h\nu$ is the photon energy and I_{th} is the ionization threshold. A plot of the (2/5)th power of the normalized photoionization current versus the photon energy should give a straight line, and its onset on the abscissa should give I_{th}, because there would be no photoionization current below I_{th}. Figure 3 shows the photoionization spectra of perylene molecules on water surface, and I_{th} of perylene has been determined to be 5.9 eV. I_{th} of perylene was determined to be 5.95 eV by a two-photon process using a Ti-sapphire laser and agree with the present value within experimental errors.

The photoionization threshold on the surface has been related with the ionization potential in gas phase, I_p, as:

$$I_{th} = I_p + P^+$$

where P^+ is the polarization energy of the positive ion. This equation should be applicable to these molecules in this study, because the electron escapes directly from the surface and so the electron affinity of the solvent is able to be negligible. P^+ of perylene on water can be determined as -0.9 eV. The value of P^+ can be obtained from Born equation using the dielectric constant and the radius of the molecule. The observed value of P^+ was about half as much as the calculated value, this indicates that the effective dielectric constant of water surface should be much smaller than that of bulk water, 80.4 at 20°C.

[A] Present address: Department of Molecular and Material Sciences , Kyushu University, Kasuga-shi, Fukuoka, 816-8580

[B] Present address: Integrated Chemistry Project, Kanagawa Academy of Science and Technology, Kawasaki-shi, Kanagawa, 213-0012

[C] Present address: Department of Applied Chemistry, Ohita University, Dannoharu, Ohita, 870-1124

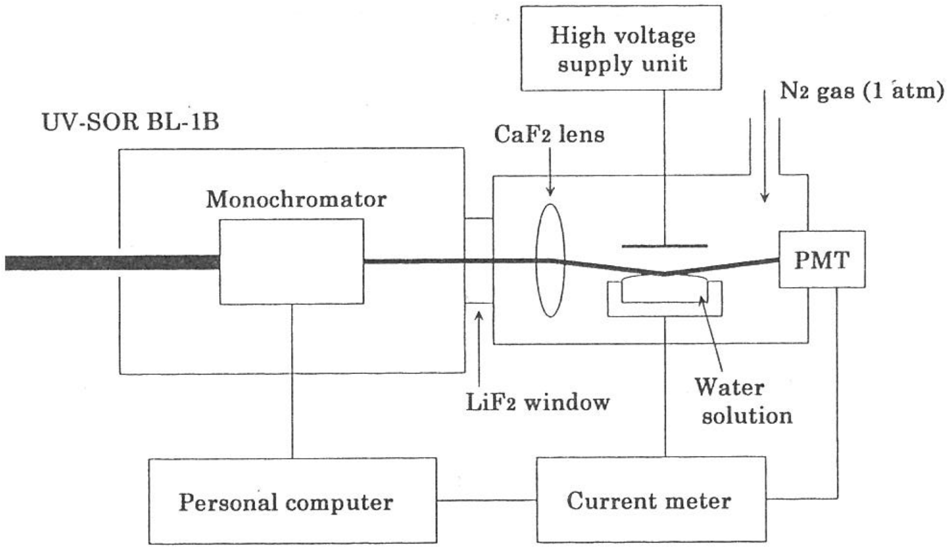

Fig. 1 Schematic diagram of the experimental apparatus.

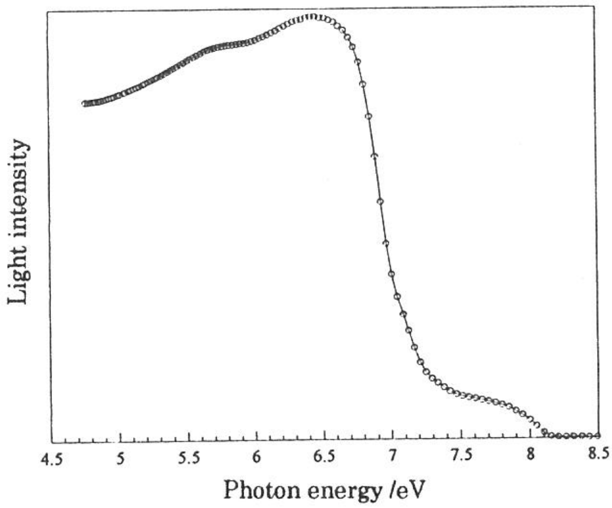

Fig.2 The intensity of the excitation light.

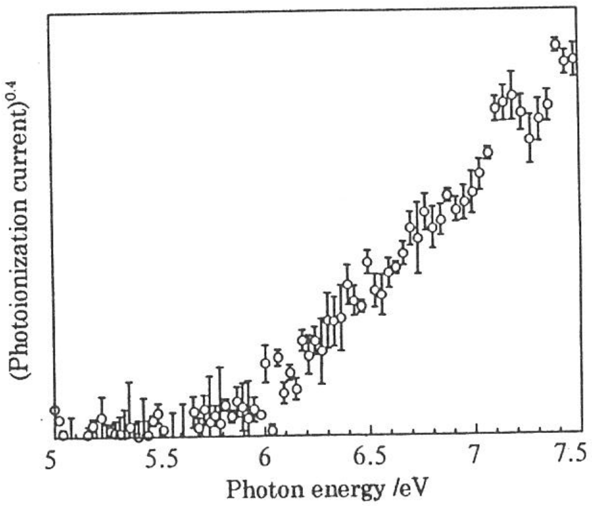

Fig.3 Photoionization spectra of perylene.

Reference
1. Inoue, T.: Sasaki, S.: Tokeshi, M.: Ogawa, T., *Chem. Lett.*, 1998, 609
2. Holroyd, R. A.: Preses, J.M.: Zevos, N., *J. Chem. Phys.*, 79 (1983) 483.
3. Ogawa, T.: Chen, H-T.: Inoue, T.: Nakashima, K., *Chem. Phys. Lett.*, 229 (1994) 328.
4. Watanabe, I.: Ono, K.: Ikeda, S., *Bull. Chem. Soc. Jpn.*, 64 (1991) 352.
5. Born, M., *Z. Physik*, 1 (1920) 45

(BL1B)

Optical Spectra of PbF_2 Crystals in the VUV Region

Masami FUJITA, Minoru ITOH[A], Jun-ichi MURAKAMI[A], Yoshitoshi BOKUMOTO[A]
Mamoru KITAURA[B], Hideyuki NAKAGAWA[C] and Dmitri L. ALOV[D]

Maritime Safety Academy, Wakaba, Kure 737-8512
[A]*Department of Electrical and Electronic Engineering, Faculty of Engineering, Shinshu University, Wakasato, Nagano 380-8553*
[B]*Fukui National College of Technology, Geshi, Sabae 916-8507*
[C]*Department of Electrical and Electronics Engineering, Faculty of Engineering, Fukui University, Bunkyo, Fukui 910-8507*
[D]*Institute of Solid State Physics, Chernogolovka, Moscow 142432 Russia*

Lead fluoride is an interesting material because it has two structural modifications which coexist at normal conditions. The orthorhombic phase (α-PbF_2) is more stable below 320℃, but the cubic phase (β-PbF_2) is also metastable at low temperatures. Optical spectra of β-PbF_2 have been measured previously using polished surface and evaporated film[1], because flat surface cannot be obtained by the cleavage of the cubic crystal. It is known that the phase transition of β-PbF_2 into α phase is caused by application of pressure. In the present experiment, reflection spectra have been measured in order to examine the effect of surface treatment on the optical spectra and to investigate the electronic structure in lead fluoride.

Single crystals of α-PbF_2 were grown from aqueous solution. Reflection spectra were measured using the as-grown surface which contains the *ab*-plane. Single crystals grown by the Bridgman method were used for the measurement of β-PbF_2. Experiments were performed at BL1B of UVSOR.

Reflection spectra of α-PbF_2 crystal at LHeT are shown in Fig. 1(a) for ***E*//*a*** and ***E*//*b*** polarization. Figures 1(b) and 1(c) show the reflection spectra of β-PbF_2 for a polished surface and for a cleaved surface, respectively. The peak at 5.7 eV in each spectrum is due to the lowest exciton transition. The exciton band in Fig. 1(a) exhibits dichroism and the exciton band in Fig. 1(c) has three fine structures[2]. It was found that the spectral shape of the exciton band in Fig. 1(b) can be fitted well by the average of the spectra for ***E*//*a*** and ***E*//*b*** in Fig. 1(a). The spectrum in the 6-7 eV region in Fig. 1(b) exhibits intermediate features between Fig. 1(a) and (c). These facts indicate that the phase transition on the surface of cubic crystal into orthorhombic phase is induced by the stress during mechanical polishing. We regard the spectrum of the cleaved surface as intrinsic to β-PbF_2.

Figure 2 shows reflection spectra of α- and β-PbF_2 up to 30eV. In the 10-13 eV region, several sharp peaks are observed in β-PbF_2. They are attributed to the transitions from both F^- 2*p* valence band and Pb^{2+} 6*s* valence band. The structures in the 14-19 eV region are due to the transition from the valence band to the Pb^{2+} 6*d* conduction band, according to our cluster calculation. On the other hand, broad structures are observed in α-PbF$_2$ in 10-19 eV region. The cluster calculation shows that the F$^-$ $2p$ valence band of α-PbF$_2$ is rather wide and complicated compared to β-PbF$_2$, because of the lower symmetry of the crystal structure. The difference in the valence band structure would be reflected in the optical spectra in 10-19 eV region.

Sharp peaks observed in the 20-25eV region are due to the exciton transition from Pb^{2+} $5d$ core level to the $6p$ level. The peaks 1, 2 and 3 are assigned to the transitions from $^1S_0$ ground state to the $J=1$ excited states of $^3P_1$, $^1P_1$ and $^3D_1$, as is the case of PbCl$_2$ and PbBr$_2$[3]. In addition to these main peaks, a small peak 0 is observed in both crystals and a peak 3' is observed in β-PbF$_2$. Some of the $J \neq 1$ excited states, which are optically forbidden in a free-ion state, can couple with the $J=1$ states through the crystal-field potential in each crystal. The additional peaks 0 and 3' are probably due to the transitions to such excited states. The appearance of these peaks in β-PbF$_2$ indicates that the crystal-field interaction in Pb^{2+} $5d$ core level plays an important role as is the case of Tl$^+$ $5d$ core exciton in thallous halides[4], because the cubic crystal-field does not lift the degeneracy of $6p$ orbitals.

References

[1]J. H. Beaumont, A. J. Bourdillon and J. Bordas: J. Phys. C Solid State Phys. **10**(1977)761.

[2]M. Fujita, M. Itoh, H. Nakagawa, M. Kitaura and D. L. Alov: J. Phys. Soc. Jpn. **67**(1998)3320.

[3]M. Fujita, H. Nakagawa, K. Fukui, H. Matsumoto, T. Miyanaga and M. Watanabe: J. Phys. Soc. Jpn. **60**(1991)4393.

[4]M. Fujita, N. Ohno, Y. Kiyama and K. Nakamura: J. Electron Spectrosc. Relat. Phenom. **79**(1996)59.

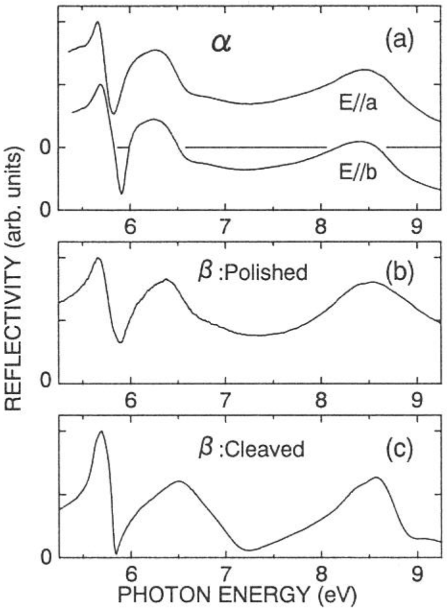

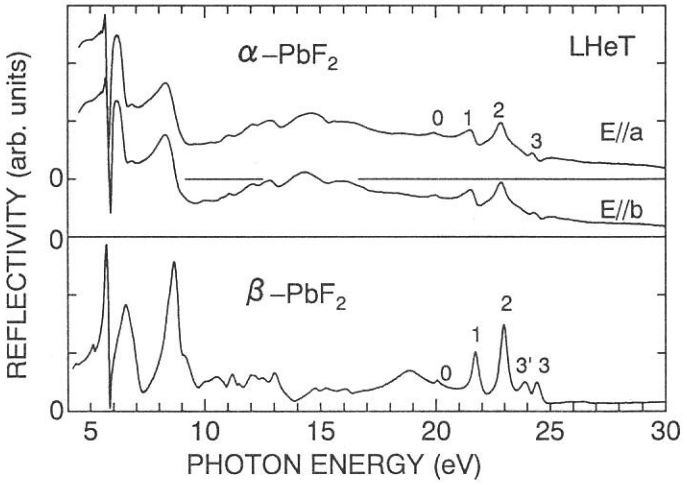

Fig. 2. Reflection spectra of α- and β-PbF$_2$ crystals in the 5-30 eV region at LHeT.

Fig. 1. Reflection spectra of (a) α-PbF$_2$, (b) β-PbF$_2$ for polished surface, and (c) β-PbF$_2$ for cleaved surface at LHeT.

(BL-1B)

Photoluminescence from Quasi One Dimensional Crystal Piperidinium Tribromoplumbate

Junpei Azuma, Koichiro Tanaka and Ken-ichi Kan'no
Department of Physics, Kyoto University
Sakyo, Kyoto 606-8205, Japan

Piperidinium trihaloplumbate $C_5H_{10}NH_2PbX_3$ [X=I,Br] (abbreviated as PLX hereafter) is well known to have a self-organized 1D structure; two consecutive lead ions are bridged by three halogen ions to form polymeric chains. In other words, $[PbX_6]^{4-}$ octahedra connect to each other by sharing their faces. The piperidine cations, which connect two adjacent columns, isolate these polymeric chains.[1,2] These materials are suitable for the study of nano-scale quantum wires, which are difficult to synthesize in semiconductors by artificial methods.[3,4]

$C_5H_{10}NH_2PbBr_3$ (PLB) complex is synthesized from piperidine hydrobromide $C_5H_{10}NH_2Br$ and lead bromide $PbBr_2$ in dimethylformamide. Transparent and colorless single crystals were grown for 2-3 weeks by evaporating the solvent slowly at room temperature. Typical sizes of crystals are 1.0x1.0x7.0mm^3.

Reflectivity and luminescence excitation measurements were performed at beam line BL-1B of UVSOR. The absolute value of reflectivity was determined by using reflectivity in the transparent region measured by a He-Ne laser.

Figure 1 shows polarized reflection spectra of PLB at 15K. There is strong anisotropy that the reflectivity for E//b polarization is several times as large as that for E⊥b polarization. This indicates that electrons and holes are confined within the polymeric chains. A peak with large oscillator strength appears at 3.9eV only for the light polarized parallel to the chains, which is assigned to the lowest exciton transition. The piperidine cations filling between chains are supposed to act as the barrier against the 3.9eV exciton, because the intramolculer absorption edge of the piperidine vapor is known to be located at 4.8eV. The lowest exciton peak of PLI is located at 3.3eV.[3] The band gap energy increases by 0.6eV through substitution of bromine ions for iodine ions of PLI.

It is well known that in alkali halide the highest occupied state of Pb^{2+} impurity is the 6s orbital and those of halogen ions are np orbitals (Br: n=4, I: n=5).[5] These orbitals are mixed to form molecular orbitals, in which antibonding state is considered as HOMO of $[PbX_6]^{4-}$ octahedra. The lowest unoccupied state of lead ion is the 6p orbital and those of halogen ions are (n+1)s orbitals. LUMO of $[PbX_6]^{4-}$ octahedra should be the lead 6p orbital because the energy of (n+1)s orbitals are much higher than that of the lead 6p orbital. The substitution of bromine ions for iodine ions, therefore, makes the energy of HOMO decrease, resulting in the increase of the band gap energy.

The effect of substitution of bromine ions for iodine ions of PLI is almost the same as that of the $[PbX_6]^{4-}$ system in alkali halide, so that np orbiatls of halogen ions must be mixed strongly in the valence band of PLX system. (See inset in Fig. 1.)

Figure 2(a) shows a luminescence spectrum at 15K under 3.9eV excitation. Two emission bands appear at 3.0eV and 1.8eV, which are denoted as V emission and R emission respectively. Their large Stokes-shifts indicate strong exciton-lattice interaction in the excited states. A contour map of the emission efficiency at 15K is shown in Fig. 2(b), which is obtained by summarizing the luminescence spectra under various excitation energies. V and R emission can be stimulated above 3.8eV. Above 4.2eV the peak energy of R emission spectra shifts for the higher energy side around 1.85eV. It suggests that R emission band must be a composite emission band. In the low energy region below 3.8eV two luminescence bands are observed instead of V and R emission. These bands located around 2.6 and 1.9eV have extrinsic natures because they strongly depend on the sample preparation. Figure 2(c) shows excitation spectra for emission intensities at 3.0eV and 1.9eV. Above 4.2eV R emission is stimulated more

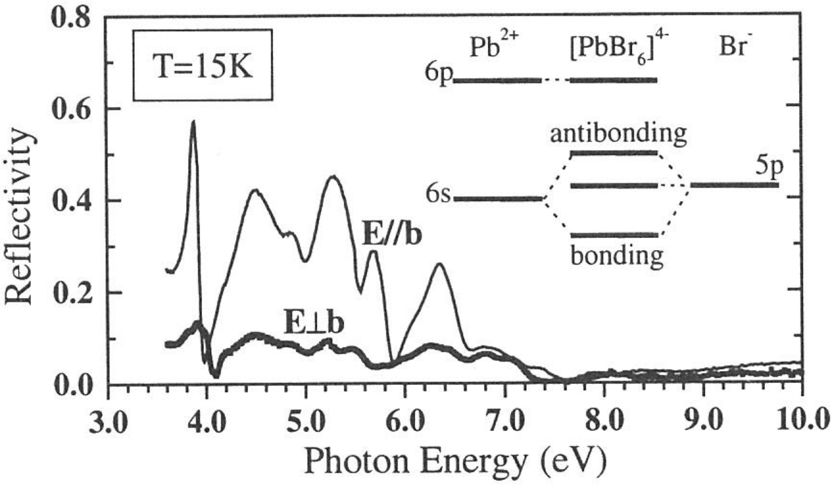

FIG. 1: Polarized reflection spectra of $C_5H_{10}NH_2PbBr_3$ at 15K. The indexes on the spectra show the polarization of the incident light. Inset shows schematic energy level diagram of $[PbBr_6]^{4-}$ octahedra.

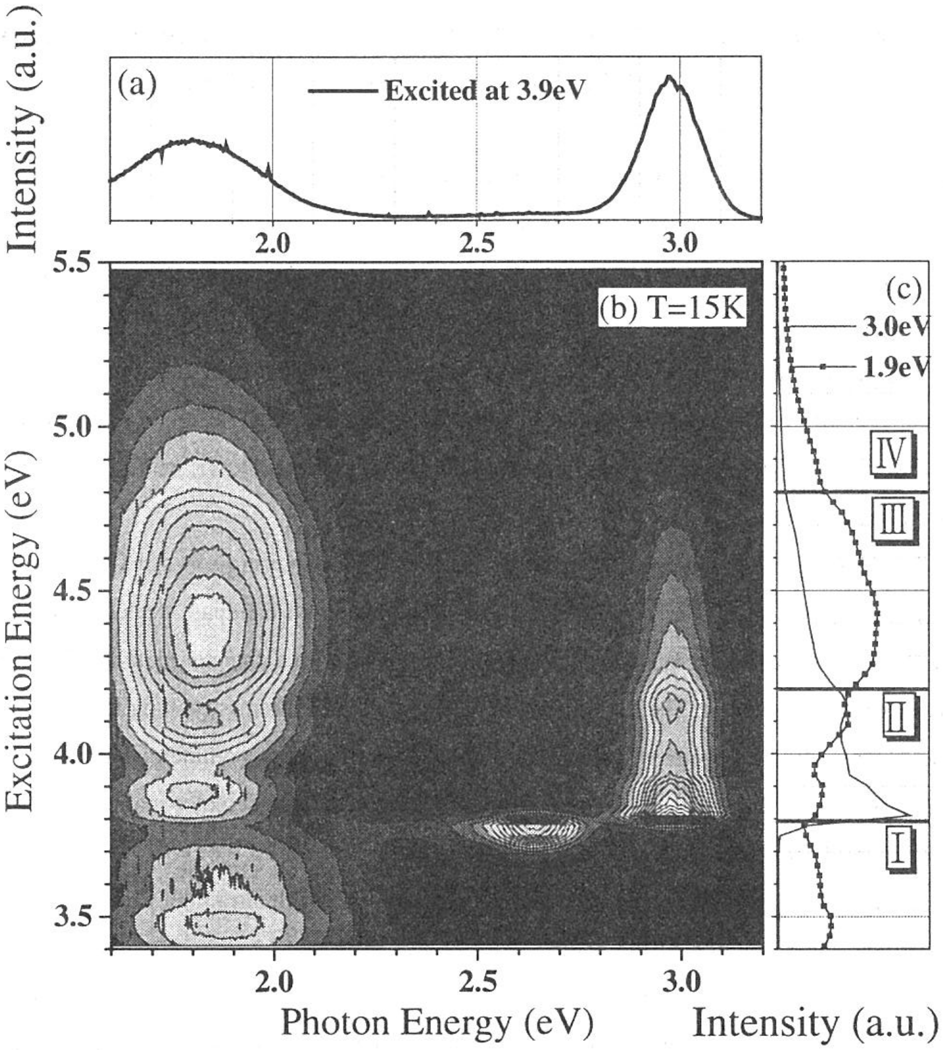

FIG. 2(a): Luminescence spectrum of $C_5H_{10}NH_2PbBr_3$ at 15K under 3.9eV excitation. Excitation light is polarized parallel to the b-axis. (b): Contour map representation of luminescence spectra under various excitation energies. (c): Excitation spectra detected at 3.0 and 1.9eV. This figure shows vertical cross sections of the contour map at 3.0 and 1.9eV. Four qualitative excitation regions are indicated. (See text.)

efficiently than V emission while below 4.2eV the R emission intensity is weaker than the V emission intensity. The excitation energy region higher than 4.8eV all emission efficiency becomes lower. Four distinct regions, therefore, can be recognized as I to IV in Fig. 2(c).

In conclusion, several emission bands were found under excitation in the intrinsic absorption region. It suggests that multi-stability exists in the photo-excited state of PLB.

References

1. G. V. Gridnova, E. A. Ziger, V. M. Koshkin, S. V. Lindeman, Yu. T. Struchkov and V. E. Shklover, Doklady Akademii Nauk, 278, 414 (1984).
2. A. B. Corradi, S. Bruni, F. Cariati, A. M.Ferrari, A. Saccani, F. Sandrolini and P. Sgarabotto, Inorg. Chim. Acta., 254, 137 (1997).
3. A. Nagami, K. Okamura and T. Ishihara, Physica B, 227, 346 (1996).
4. G. C. Papavassiliou and I. B. Koutselas, Synth. Metals, 71, 1713 (1995).
5. T. Tsuboi, Phys. Status Solidi B, 96, 321 (1979).

(BL1B)

Improvement of resolution of the detector for inverse photoemission spectrometer by coating KCl thin film on bandpass detector

Hiroshi YANAGI, Kazushige UEDA, Sakyo HIROSE, Syuntaro IBUKI, Tomomi HASE, Hideo HOSONO and Hiroshi KAWAZOE

Materials and Structures Laboratory, Tokyo Institute of Technology, Yokohama 226-8503

Inverse photoemission spectroscopy (IPES) is the most convenient technique to probe unoccupied electronic states of solids. Electron energy loss spectroscopy (EELS) and X-ray absorption spectroscopy (XAS), which also observe unoccupied states, give the partial density of states (PDOS), while IPES generally gives the total density of states (DOS).

IPES, which observes photons emitted from a sample by capturing electrons with a specified kinetic energy, has two different types; one detects isochromatic photons with bandpass detector and the other detects photons that have a variety of energies through a monochrometer with a channel plate amplifier and a position-sensitive resistive anode detector. The former type of IPES called BIS (bremsstrahlung isochromat spectroscopy) includes the Geiger-Müller counter with a CaF_2 entrance window or a commercial photomultiplier with an entrance window as a bandpass detector. The Geiger-Müller counter type detector realizes a resolution of 0.6eV as a full width at half maximum (FWHM) centered at the photon energy of 9.8eV. However, the photomultiplier type has advantages in high stability, no dead time and compatibility with ultra high vacuum. Ueda et al. reported that the sensitivity and resolution of the photon detector were improved by coating a KCl film of over 100nm thickness on the Cu-BeO first dynode [1]; the FWHM of 0.47eV centered at the photon energy of 9.8eV. In this article, we describe the results of application of this technique for improvement of resolution in our instrument.

The detector of photons installed in our BIS instrument is a commercial photomultiplier (Hamamatsu Photonics: R595) with a SrF_2 entrance window, which is a bandpass photon detector with FWHM of 0.75eV centered at 9.39eV. The constitution is as almost the same as the instrument used by Ueda et al. except that their first dynode of photomultiplier was coated with a KCl film. All components are mounted in ultra high vacuum chamber under the base pressure below 4×10^{-8}Pa.

The KCl film of 210nm was evaporated onto the Cu-BeO first dynode (Hamamatsu Photonics: E5055) of the photomultiplier under a vacuum of 7×10^{-4}Pa. The thickness of the film was evaluated by a quartz thickness monitor. The estimation of bandpass characteristics of the new bandpass photon detector was carried out on BL1B of UVSOR in Institute for Molecular Science.

Figure 1 shows the characteristics of the bandpass photon detector before and after the deposition of KCl film on the first dynode: the dashed and dotted curves are characteristics obtained before the deposition and the solid curve is that after deposition. Peak heights of the dotted curve and the solid curve are adjusted to each other for comparison of FWHM. The FWHM is reduced from 0.75 to 0.45eV by the deposition of the KCl film on the Cu-BeO first dynode. Furthermore, the intensity of the peak top of the solid curve is about 34 times as high as that of the dashed curve. The sensitivity was increased by about one order on the deposition of KCl thin film on Cu-BeO first dynode. Consequently, the improvement of the bandpass photon detector for our instrument was successful.

Reference

[1] Y. Ueda, K. Nishihara, K. Mimura, Y. Hari, M. Taniguchi and M. Fujisawa, Nucl. Instrum. and Methods in Phys. Research, **A330**, 140(1993)

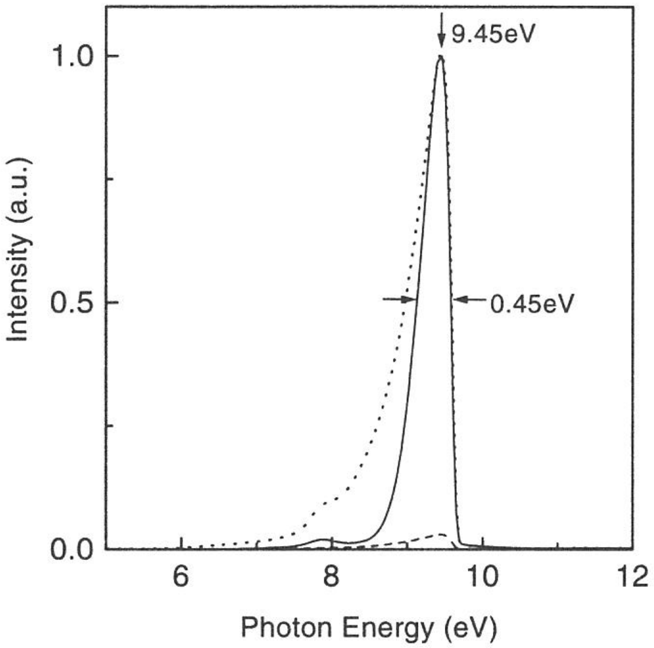

Fig. 1 Characteristics curves of bandpass detectors without (a dotted curve and a dashed curve) and with the KCl film (a solid curve) on the Cu-BeO first dynode of the photomultiplier. Peak heights of dotted curve and solid curve are adjusted to each other for comparison of FWHM.

(BL1B)

VUV excitation spectra of a trace of impurities in CaF_2 single crystals for ArF excimer laser lithography

M. Mizuguchi, T. Ogawa, H. Yanagi and H. Hosono

Materials and Structures Laboratory, Tokyo Institute of Technology, 4259 Nagatsuta, Midori-ku,
Yokohama 226-8503, Japan

INTRODUCTION

Calcium fluoride single crystals are now attracting much interested as a lens material for ArF excimer laser (emission wavelength = 193 nm) lithography because of a large band gap of ~12 eV, an isotropic optical property and excellent chemical stability. Since investigations on laser damage of this crystal by irradiation of the ArF excimer laser have been just started, elucidation of the predominant factors and mechanism of laser damage is an important issue. A small number of impurities in the crystal strongly influence the color center formation at room temperature, particularly trivalent ions such as yttrium and lanthanoid (Ln) ions. A trivalent yttrium ion is a common and persistent impurity in the CaF_2 single crystal because the ionic radius of Y^{3+} (102 pm) is close to that of Ca^{2+} (99 pm). We have reported that the time-resolved photoluminescence (PL) measurement is highly appropriate to detect a trace of Ln ions which have a close relation with degradation of CaF_2 single crystals because its sensitivity can be extremely enhanced by using pulsed laser light as an excitation source and the overlapping spectral components can be separated in time region.[1] Then VUV excitation bands of the PL due to a trace of Ln ions are important to discuss the reaction between the ArF laser pulses and the Ln ions. In this work, the VUV excitation bands of CaF_2 single crystals irradiated and unirradiated with ArF excimer laser pulses were measured at beam line BL1B at 10 K and room temperature.

EXPERIMENTAL

Commercially available three types of CaF_2 single crystals, UV grade, excimer grade (A) and (B) showing yellow-green, no visible and blue PL during irradiation of ArF excimer laser, respectively, were measured. Each sample was cut into a piece with 20 mm diameter x 3 mm thickness. The 20 mm diameter surfaces were cleaved along the (111) plane and polished to an optical grade. Table 1 summarizes the impurity contents (error range is ~ 100 %) chemically analyzed by inductively coupled plasma (ICP)-mass spectroscopic method. Although there was no significant difference in iron content among any samples, the yttrium concentration in the UV grade specimen was fairly high comparing with those of the other samples. Ln ion contents of each sample were estimated as 0.1 ppm or less than 0.1 ppm.

Table 1 Chemically analyzed impurity contents (mass ppm) in the samples

	Impurity									
Sample	Al	Fe	Sr	Ba	Mg	Y	La	Ce	Eu	Tb
Excimer grade (A)	7	<0.5	370	1.9	2	<1	<0.1	<0.1	<0.1	<0.1
Excimer grade (B)	10	<0.5	10	4	20	<1	<0.1	<0.1	<0.1	<0.1
UV grade	1	<0.1	10	5	<0.2	5	0.1	0.1	<0.1	0.1

RESULTS and DISCUSSION

Before the measurements at the beam line BL1B, the transmission spectra of the samples was observed with the conventional spectrometer at room temperature. Excimer grade (A) and (B) showed no absorption after the irradiation. On the other hand, irradiated UV grade specimen showed intense absorption which was ascribed to the yttrium-associated *F* center (YFC).[1] However since the sample chamber of BL1B was baked at ~500 K for ~ 8 h in order to get the high vacuum, the defects induced by the ArF laser light were relaxed. Then transmission spectra measured at BL1B did not have the difference between irradiated and unirradiated samples. In the following paragraph, irradiated and unirradiated samples are not distinguished.

In the all samples, PL bands due to self-trapped excitons (STE) peaking at 2810 Å were observed at 10 K and room temperature. The excitation spectrum of the 2810 Å PL band and absorption spectrum observed in the UV grade specimen are showed in figure 1. These spectra were measured at ~10 K.

Weak PL of a trace of Tb^{3+} peaking at 5410 Å, which was a most intense band among the PL bands due to f-f transition of Tb^{3+} and a potential index for estimation of laser toughness, was observed in the UV grade specimen at ~10 K. Figure 2 shows the excitation spectrum of the 5410 Å PL band. Excitation bands were observed at 3300 Å and around 1930 Å. The signals were so weak that the life time of the PL peaking at 5410 Å was not able to be measured. These results suggests that the defects (YFC) were generated via one photon (1930 Å pulse) absorption and the STEs were generated via two photon (1930 Å pulse) absorption, as reported in the previous paper.

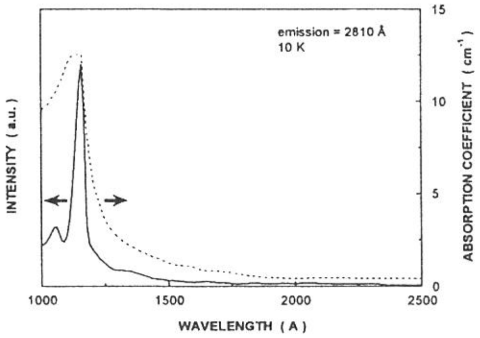

Fig.1 Absorption and Excitation Spectrum (Emission = 281 nm) observed in UV grade.

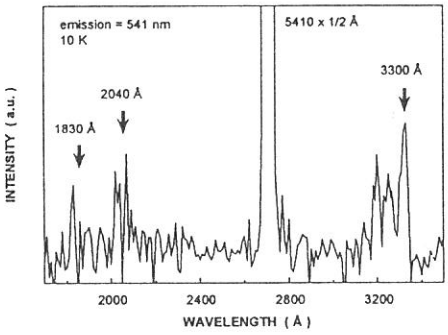

Fig. 2 Excitation Spectrum of Tb^{3+} observed in the UV grade.

REFERENCE

[1] M. MIZUGUCHI et.al., Proc. SPIE **3424**, 60 (1998)

(BL-1B)

Optical Absorption Spectra of $(C_2H_5NH_3)_2CdCl_4$ Single Crystal

Akimasa OHNISHI, Ken-ichi TANAKA and Takehisa YOSHINARI
Department of Physics, Yamagata University, Yamagata 990-8560

Recently, Ohnishi *et al.* 1) studied recombination luminescence from $(C_nH_{2n+1}NH_3)_2CdCl_4$; n = 1, 2 and 3 crystals with VUV lights and found the largely Stokes-shifted luminescence band at 2.50 eV under excitation into the excitonic absorption range. The result suggests strongly that the excitons created by photo-excitation in those crystals relax to the self-trapped exciton (STE) states. In the present study, the tail spectra in $(C_2H_5NH_3)_2CdCl_4$ have been measured in the temperature range from 100 K to 440 K to confirm the excitonic relaxation process.

$(C_2H_5NH_3)_2CdCl_4$ single crystals were grown at RT by evaporating the aqueous solution containing stoichiometric amounts of $C_2H_5NH_2{\cdot}HCl$ and $CdCl_2{\cdot}5/2H_2O$. Samples were cleaved in a plane perpendicular to the *c*-axis, mounted on a Cu holder of a He flow-type cryostat and then were cooled by thermal-conduction. The reflection and absorption spectra were measured using synchrotron radiation (SR) from a BL-1B beam line of UVSOR. The SR was dispersed with a 1 m Seya-Namioka monochromator of which slits were kept open to a band-pass of 0.2 nm.

Figure 1 shows the fundamental absorption spectrum of $(C_2H_5NH_3)_2CdCl_4$ single crystal at 9 K which is obtained from the Kramers-Kronig analysis of the reflection spectrum. The first exciton absorption band is observed around 6.4 eV with a shoulder at 6.2 eV, which is well fitted by two Lorentzian functions at 6.23 eV and 6.38 eV shown by dotted curves. The splitting of the two bands is 0.15 eV and is almost equal to the spin-orbit splitting of a chlorine atom. From this fact the valence bands are supposed to have strong chlorine *p*-character. No excitonic absorption band was observed at about 5.5 eV, different from the previous report.2) As seen by broken curve, since the absorption edge spectrum measured at 9 K rises with a threshold at 5.4 eV, there should be some problem in the experimental conditions or the analytical method in the previous work.

Figure 2 shows that the low energy tails of the first exciton absorption band measured in the temperature range of 100 – 440 K are semi-logarithmically plotted by thick curves as a function of photon energy. The tail spectra for different temperatures depend exponentially on photon energy over the range of 2 – 3 orders of absorption coefficient. The extrapolated thin lines of those spectra cross at one point as shown in the figure. These features indicate that the tail spectra in $(C_2H_5NH_3)_2CdCl_4$ obey the Urbach rule, expressed by the following formula,3)

$$\alpha = \alpha_0 \exp\left(-\sigma \frac{E_0 - E}{kT} \right), \tag{1}$$

where α is the absorption coefficient, E is the photon energy, α_0 and E_0 are constants, T is the temperature, k is the Boltzmann constant and σ is the temperature dependent steepness parameter. Here, the convergence point (E_0, α_0) is (6.2 eV, 5.1×10^9 cm^{-1}).

Temperature dependence of the steepness parameters obtained from the slope of the each straight line shown in Fig.2 is plotted by solid circles in Fig. 3. The solid curve represents the best fitted one calculated with eq. (2), 4, 5)

$$\sigma = \sigma_0 \frac{2kT}{\hbar\omega} \tanh\left(\frac{\hbar\omega}{2kT} \right), \tag{2}$$

where σ_0 is the limit of σ at high temperatures and $\hbar\omega$ is the effective energy of the phonons interacting with the excitons. We obtained σ_0 = 0.60 and $\hbar\omega$ = 46 meV from the fitting. The value of σ_0 indicates that the

STE is stable. Therefore it is concluded that the excitons in the present system are self-trapped because of the strong exciton-phonon interaction. This conclusion is consistent with the luminescence measurement by Ohnishi *et al.*[1)]

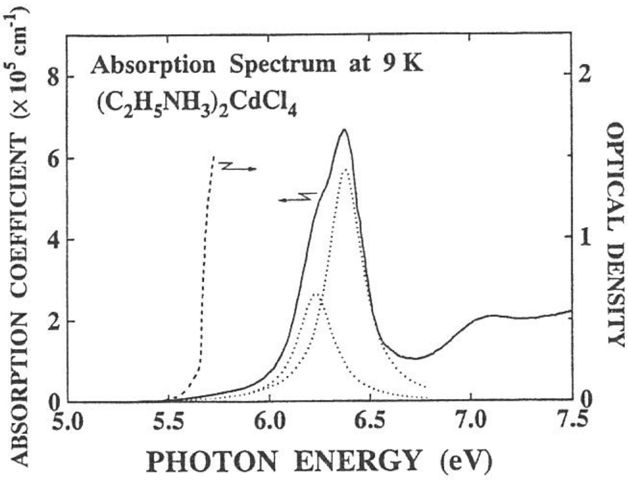

Fig. 1 Absorption spectrum of $(C_2H_5NH_3)_2CdCl_4$.

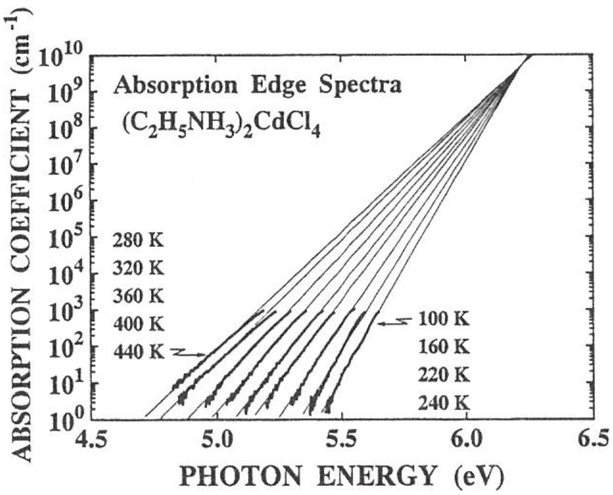

Fig. 2 Logarithmic plot of the low energy tail of the first exciton band.

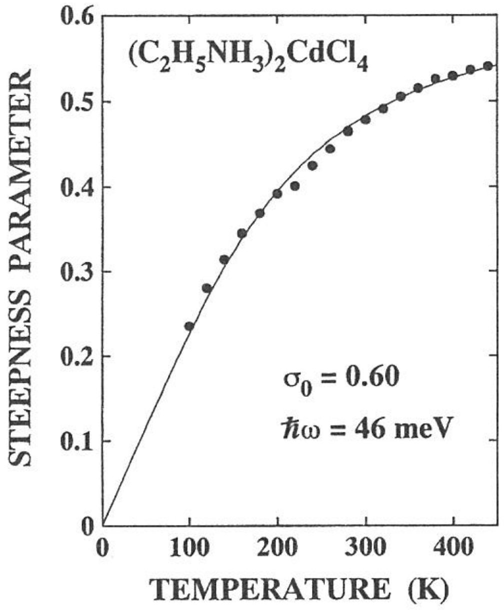

Fig. 3 Temperature dependence of the steepness parameter σ.

References

1) A. Ohnishi, T. Yamada, T. Yoshinari, I. Akimoto, K. Kan'no and T. Kamikawa, J. Electron Spectrosc. Relat. Phenom. **79** (1996) 163.

2) T. Yoshinari, T. Nanba, S. Shimanuki, M. Fujisawa, T. Matsuyama, M. Ikezawa and K. Aoyagi, J. Phys. Soc. Jpn. **58** (1989) 2276.

3) F. Urbach, Phys. Rev. **92** (1953) 1324.

4) H. Sumi and Y. Toyozawa, J. Phys. Soc. Jpn. **31** (1971) 342.

5) M. Schreiber and Y. Toyozawa, J. Phys. Soc. Jpn. **51** (1982) 1544.

(BL1B)

Effects of ion implantation and thermal annealing on the photoluminescence in amorphous silicon nitride

Kwang Soo SEOL, Tsuyoshi FUTAMI, Takashi WATANABE, Hiromitsu KATO, and Yoshimichi OHKI*

Department of Electrical, Electronics, and Computer Engineering, Waseda University,
3-4-1 Ohkubo, Shinjuku-ku, Tokyo 169-8555

**Present address: Applied Laser Chemistry Lab., The Institute of Physical and Chemical Research (RIKEN),*
2-1 Hirosawa, Wako-shi, Saitama 351-0198

Category: 4. Solid- & liquid- phase spectroscopy 1 (IR, VUV, etc)

I. EXPERIMENTAL PROCEDURES

The amorphous silicon nitride (a-SiN_x) film investigated in this paper was deposited on a p-type (100) silicon substrate by Low Pressure Chemical Vapor Deposition with a mixture of SiH_2Cl_2 and NH_3 gases with a pressure of 65 Pa around 700 °C. The flow rate of NH_3/SiH_2Cl_2 was 15 for sample A and 10 for sample B. The hydrogen content and the atomic ratio of N/Si, investigated by Rutherford back-scattering, are respectively 6 mol% and 1.52 for sample A deposited at 650 °C, and 4 mol% and 1.44 for sample B. Some films were implanted by Ar^+ ions with an acceleration energy of 70 keV up to a dose of 1×10^{12} - 5×10^{14} ions/cm^2. Both the as-deposited and the ion-implanted films were annealed in N_2 (1 atm) or in vacuum (4.0×10^{-2} Pa) by a rapid thermal annealing apparatus for 20 min.

Chemical change induced by thermal annealing was examined by Fourier-transform infrared absorption (FT-IR) and thermal desorption spectroscopy (TDS). The photoluminescence (PL) spectra were measured at room temperature using a monochromator equipped with a multichannel detector under excitation by a KrF excimer laser [wavelength: 248 nm (5.0 eV); pulse width: ~20 ns; pulse energy: ~100 mJ/cm^2]. The PL excitation (PLE) spectra were obtained at 77 K using synchrotron radiation (SR) at the BL1B line of UVSOR facility (Institute for Molecular Science, Okazaki, Japan). The PL lifetime was measured with a single-photon counting technique using SR at 13 K.

II. RESULTS AND DISCUSSION

When a-SiN_x film is irradiated by a KrF excimer laser, it exhibits a broad PL band centered at about 2.4 eV. The PL intensity gradually decreases and the PL peak energy shifts to a lower energy with an increase of the implanted dose of Ar^+ ions. From the result of the Gaussian fitting, this clearly indicates that the PL spectrum observed before ion-implantation is composed of two PL bands centered at 2.66 and 2.15 eV. The PL intensity decreases according to a power law with an increase in dose, and the exponent is larger for the 2.66 eV PL than the 2.15 eV PL. This is the reason that the PL shape shifts toward red.

In a-SiO_2 films, several PL bands such as the ones due to the oxygen vacancies and the non-bridging oxygen hole centers are induced by ion implantation. The intensities of these PLs become larger with an increase in implantation dose. In some a-SiO_2 films such as the one synthesized by plasma-enhanced chemical vapor deposition or the method called SIMOX (Separation by IMplanted OXygen), these PLs are seen without ion implantation. From these results, the PLs are considered to be associated with oxygen-deficient or oxygen-rich defects and that the ion implantation has an action of manifesting weak sites such as strained bonds by converting them into PL-detectable defects. However, the PL observed in the present study decreases its intensity with an increase of implanted dose of ions. This is the exact opposite of the result of a-SiO_2. Therefore, the PL in a-SiN_x is considered not to be due to implantation-induced defects such as vacancies or bond-breaks.

The two PL bands that had been quenched by ion-implantation are recovered by thermal annealing done at 900 °C for 20 min in N_2. But the recovered intensity is about one third of the intensity before ion-implantation. In a-SiO_2, the increased intensity by ion-implantation decreases by similar thermal annealing. This is also the opposite result of the present case of a-SiN_x.

The PL intensities of the 2.66 and 2.15 eV bands observed in non-implanted sample decrease abruptly by thermal annealing in vacuum at temperatures above 700 °C. Figure 1 shows the PL decay excited by 5.0 eV photons from SR, observed in the as-deposited sample A. It is clear that the decay is expressed by a stretched exponential function,

$$I(t)\propto(\tau/t)^{1-\beta}\exp\{-(t/\tau)^{\beta}\},$$

where I is the PL intensity, t the time, τ the effective lifetime, and β is a parameter which has a value between 0 and 1. When this sample is thermally annealed in vacuum, τ decreases at above 700 °C, which β hardly changes.

From the result of FT-IR, it is clear that the absorption at 3340 cm^{-1} due to N-H bonds and the one at 2200 cm^{-1} due to Si-H bonds abruptly decrease by thermal annealing at temperatures above 700 °C. Both the 2.66 and 2.15 eV PL bands clearly show a linear relationship with the hydrogen-related bonds. The above IR result indicates that hydrogen is released by the annealing. From the measurement of TDS, it is confirmed that the desorption of hydrogen starts around 700 °C.

The above-mentioned results suggest that the PL is related to the desorption of hydrogen. Therefore, the non-implanted sample A was thermally annealed at 900 °C for 20 min in vacuum or in 100 % hydrogen at 1 atm, and PL spectra were observed. While no change is seen for the H_2 annealing, the PL intensity decreases significantly by the vacuum annealing. This clearly supports the above assumption that the PL in SiN_x is related to hydrogen desorption.

Shown in Fig. 2 are the PL excitation spectra of sample A monitored at 2.66 and 2.15 eV, measured at 77 K using SR. It is clear that the PL bands are excited by the photons with energies above 4.5 eV. The energy of 4.5 eV is close to the value of optical band gap for the near-stoichiometric SiN_x. Therefore, the PL bands are considered to be related to recombination of electrons and holes, generated by interband photon absorption.

Previous studies reported several PL bands between 1.8 and 4.0 eV in near-stoichiometric or silicon- or nitrogen-rich a-SiN_x. Among those, a broad PL centered around 2.5 eV is commonly observed in near-stoichiometric or nitrogen-rich SiN_x. Based on the fact that the peak energy of the PL is similar to the calculated energy between the state of silicon dangling bond and valence or conduction band edge, the PL was previously attributed to the radiative recombination at the silicon dangling bond. However, the present results suggest that the PL is not due to implantation-induced defects, and that the PL intensity decreases if hydrogen is released. Furthermore, the properties of the PL observed in the present study are very similar to those of the PL observed in hydrogenated amorphous silicon (a-Si:H). In a-Si:H, the PL intensity also decreases if hydrogen is desorbed. The reason for this is considered that hydrogen in a-Si:H effectively eliminates the non-radiative sites relating to Si dangling bonds. Furthermore, the PL in a-Si:H is quenched by ion-implantation that could easily break Si-H bonds and Si-Si regular bonds. This similarity suggests that the ion-induced defects such as Si dangling bonds are not the origin of PL in a-SiN_x but non-radiative recombination centers that quench the PL. Hydrogen is thought to eliminate the recombination centers.

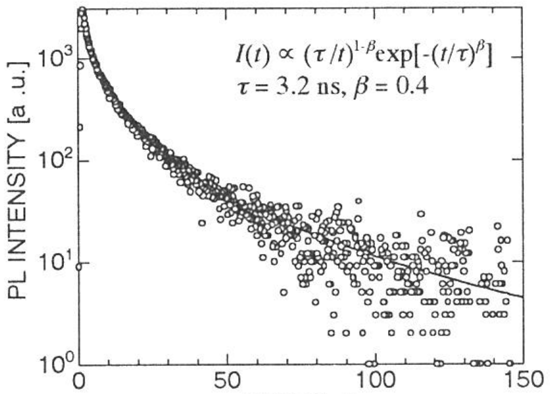

Fig. 1 PL decay excited by 5.0 eV photons from SR observed in the as-deposited sample A. I is the PL intensity, t the time, τ the effective lifetime, and β is a parameter which has a value between 0 and 1.

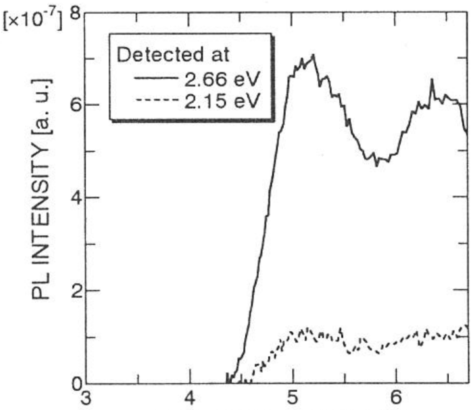

Fig. 2 PL excitation spectra for the 2.66 and 2.15 eV PL bands observed in sample A.

(BL1B)

Optical Spectra of PbF_2 Crystals in the VUV Region

Masami FUJITA, Minoru ITOH [A], Jun-ichi MURAKAMI [A],
Hideyuki NAKAGAWA [B], Mamoru KITAURA [C] and Dmitri L. ALOV [D]

Maritime Safety Academy, Wakaba, Kure 737-8512
[A] *Department of Electrical and Electronic Engineering, Faculty of Engineering,*
Shinshu University, Wakasato, Nagano 380-8553
[B] *Department of Electrical and Electronics Engineering, Faculty of Engineering,*
Fukui University, Bunkyo, Fukui 910-8507
[C] *Fukui National College of Technology, Geshi, Sabae 916-8507*
[D] *Institute of Solid State Physics, Chernogolovka, Moscow 142432 Russia*

Lead fluoride is an interesting material because it has two structural modifications which coexist at normal conditions. The orthorhombic phase (α-PbF_2) is more stable below 320℃, but the cubic phase (β-PbF_2) is also metastable at low temperatures. Optical spectra of β-PbF_2 have been measured previously using polished surface and evaporated film[1], because flat surface cannot be obtained by the cleavage of the crystal. It is known that the phase transition of β-PbF_2 into α phase is caused by application of pressure. In the present experiment, reflection spectra of α- and β-PbF_2 have been measured in order to study the effect of surface treatment on the optical spectra and to investigate the electronic structure of Pb^{2+} $5d$ core exciton state in lead fluoride.

Single crystals of α-PbF_2 were grown from aqueous solution. Reflection spectra were measured using the as-grown surface which contains the *ab*-plane. Single crystals grown by the Bridgman method were used for the measurement of β-PbF_2. Experiments were performed at BL1B of UVSOR.

Reflection spectra of α-PbF_2 crystal at low temperature are shown in Fig. 1(a) for $\boldsymbol{E}/\!/\boldsymbol{a}$ and $\boldsymbol{E}/\!/\boldsymbol{b}$ polarization. Figure 1(b) and (c) show the reflection spectra of β-PbF_2 for a polished surface and for a cleaved surface, respectively. The peak at 5.7 eV in each spectrum is due to the lowest exciton transition. The exciton band in Fig. 1(a) exhibits dichroism and the exciton band in Fig. 1(c) has three fine structures[2]. It was found that the spectral shape of the exciton band in Fig. 1(b) can be fitted well by the average of the spectra for $\boldsymbol{E}/\!/\boldsymbol{a}$ and $\boldsymbol{E}/\!/\boldsymbol{b}$ in Fig. 1(a). The spectrum in the 6-7 eV region in Fig. 1(b) exhibits intermediate features between Fig. 1(a) and (c). These facts indicate that the phase transition on the surface of cubic crystal into orthorhombic phase is induced by the stress during mechanical polishing. We regard the spectrum of the cleaved surface as intrinsic to β-PbF_2.

Figure 2 shows reflection spectra of α- and β-PbF_2 up to 30eV. In the 10-18eV region, several sharp peaks are observed in β-PbF$_2$, while broad structures are observed in α-PbF$_2$. The structures below 18 eV are attributed to the transitions from both F$^-$ $2p$ valence band and Pb^{2+} $6s$ valence band. Sharp peaks observed in the 20-25eV region are due to the exciton transition from Pb^{2+} $5d$ core level to the $6p$ level. The peaks 1, 2 and 3 are assigned to the transitions from $^1S_0$ ground state to the J=1 excited states of $^3P_1$, $^1P_1$ and $^3D_1$, as is the case of PbCl$_2$ and PbBr$_2$[3]. In addition to these main peaks, a small peak 0 is observed in both crystals and a peak 3' is observed in β-PbF$_2$. Some of the $J\neq1$ excited states, which are optically forbidden in a free-ion state, can couple with the J=1 states through the crystal-field potential in each crystal. The additional peaks 0 and 3' are probably due to the transitions to such excited states. The appearance of these peaks in β-PbF$_2$ indicates that the crystal-field interaction in Pb^{2+} $5d$ core level plays an important role as is the case of Tl$^+$ $5d$ core exciton in thallous halides[4], because the cubic crystal-field does not lift the degeneracy of $6p$ orbitals.

References

[1]J. H. Beaumont, A. J. Bourdillon and J. Bordas: J. Phys. C Solid State Phys. **10**(1977)761.

[2]M. Fujita, M. Itoh, H. Nakagawa, M. Kitaura and D. L. Alov: J. Phys. Soc. Jpn. **67**(1998)3320.

[3]M. Fujita, H. Nakagawa, K. Fukui, H. Matsumoto, T. Miyanaga and M. Watanabe: J. Phys. Soc. Jpn. **60**(1991)4393.

[4]M. Fujita, N. Ohno, Y. Kiyama and K. Nakamura: J. Electron Spectrosc. Relat. Phenom. **79**(1996)59.

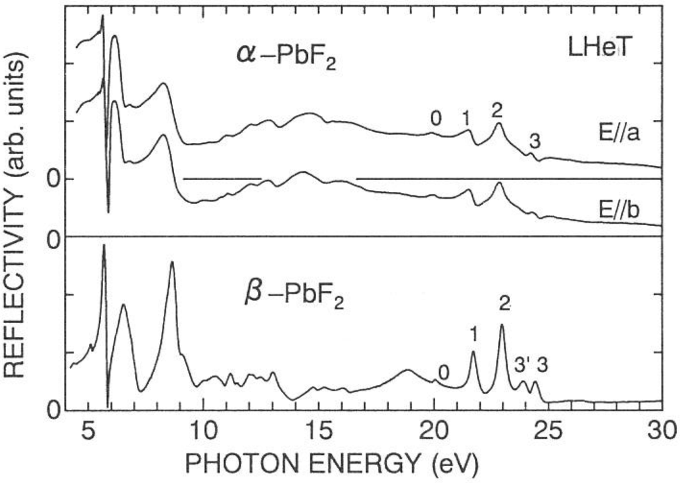

Fig. 2. Reflection spectra of α- and β-PbF$_2$ crystals in the 5-30 eV region.

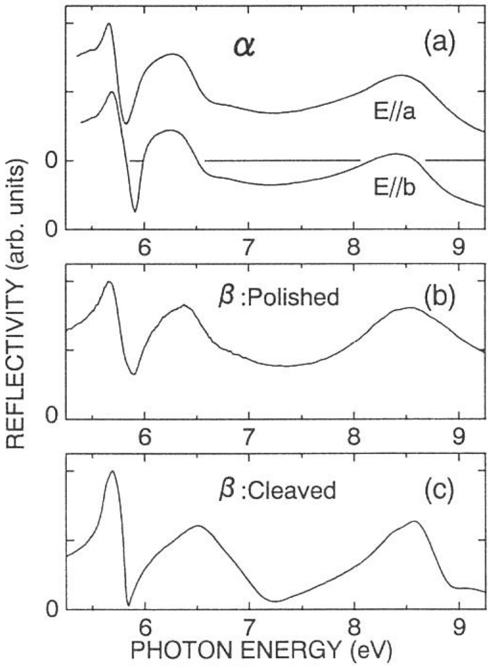

Fig. 1. Reflection spectra of (a) α-PbF$_2$, (b) β-PbF$_2$ with polished surface and (c) β-PbF$_2$ with cleaved surface.

(BL1B)

Far-Infrared to Vacuum-Ultraviolet Reflectivity Spectrum of $La_{0.70}Sr_{0.30}MnO_3$: Evidence Against Small Drude Weight

Koshi TAKENAKA,* Suguru KASHIMA, and Shunji SUGAI

Department of Physics, Nagoya University, Chikusa-ku, Nagoya 464-8602

Optical reflectivity study can make an essential role in the both fundamental and practical researches on the double-exchange ferromagnetic-metal manganites showing "colossal magnetoresistance (CMR)" because it enables us to not only deduce dielectric functions but also examine separately two key-elements of charge transport – carrier density (or Drude weight) and scattering time. The charge transport is one of the central concerns among the both studies.

The previous reflectivity studies on $La_{1-x}Sr_xMnO_3$ [1] have revealed the outline of the systematic change of the electronic structure with Sr-substitution. One of the significant implications is such small Drude weight that we cannot attribute it to mass-enhancement. However, the origin or truth of the small Drude weight is not well-investigated because the experiments did not cover the sufficient energy region or/and did not have the sufficient accuracy. We report here the established optical reflectivity spectrum $R(\omega)$ of $La_{0.70}Sr_{0.30}MnO_3$ measured on the *cleavage* surface of single crystal for a wide energy range (0.005–40 eV). The present result demonstrates that the small Drude weight originates from the distortion of the spectrum caused by the damages introduced into the surface by polishing and the true Drude weight is large and consistent with the Hall effect [2] and specific heat studies [3].

Single crystals of $La_{0.70}Sr_{0.30}MnO_3$ were grown by a floating zone method. The Curie temperature T_C=362 K. In order to obtain defect-free surfaces we cleaved the single-crystalline rod. Near-normal incident reflectivity measurements were made using a Fourier-type interferometer (0.005-2.2 eV), a grating spectrometer (1.2-6.5 eV), and a Seya-Namioka type spectrometer for vacuum-ultraviolet synchrotron radiation (4.0-40 eV) at BL1B of the UVSOR facility, Institute for Molecular Science. All data were taken at room temperature.

We show in Fig. 1 the reflectivity spectrum of $La_{0.70}Sr_{0.30}MnO_3$ measured on the cleavage surface of single crystal (solid line). It is characterized by a sharp edge at about 1.6 eV and a large weight below it. The implication of the reflectivity data becomes clearer when the optical conductivity spectrum is deduced via the Kramers-Kronig transformation of the reflectivity data. The optical conductivity spectrum exhibits a pronounced Drude-like component with large spectral weight below the edge (solid line in Fig. 2).

The main purpose in this study is the precise estimation of the "Drude weight". In a simple Drude model, $N^*_{\rm eff}(\omega_{\rm ps})=n(m_0/m^*)$, where $N^*_{\rm eff}(\omega)$ is the effective carrier number defined as

$$N^*_{\rm eff}(\omega) = \frac{2m_0V}{\pi e^2}\int_0^{\omega} \sigma(\omega')d\omega' \tag{1}$$

(n: carrier number per Mn-atom; m_0: a bare electron mass; m^*: effective mass; $\omega_{\rm ps}$; plasma frequency; V: the volume per Mn-atom). $N^*_{\rm eff}(\omega_{\rm ps})$ is so-called Drude weight. It is difficult, however, in the present case to estimate Drude weight because a simple Drude model seems not valid; the decay rate is too slow compared with $\propto\omega^{-2}$ to be interpreted within the Drude model.

However, the present result clearly demonstrates at least the following fact that the Drude weight is much larger than that previously reported [1]. For example, we assume ω_{ps}=1.6 eV (reflectivity edge), then $N^*_{\text{eff}}(\omega_{\text{ps}})$=0.346. Using $n\sim1$ per Mn-atom estimated from Hall effect study [2], mass-enhancement m^*/m_0 is estimated to be 2.9, which is consistent with the result of specific heat measurement [3].

The discrepancy to the previous result originate from the damages of the sample surface introduced by polishing. In Fig. 1 is shown also the reflectivity spectrum measured on the surface polished with diamond powder of diameter 0.3 μm (dashed line). It is found that polishing distorts drastically $R(\omega)$ of $La_{0.70}Sr_{0.30}MnO_3$. The previous data by Okimoto *et al.* [1] resembles closely this distorted spectrum. The damage of the surface probably localizes the carriers. However, as the wavelength of the incident light becomes longer, light reaches the inner, not damaged part, and hence $R(\omega)$ recovers the true spectrum, which is consistent with that the discrepancy almost disappears below 0.03 eV. "Small Drude weight" originates from the above restoration process (dashed line of Fig. 2).

The authors would like to thank Professor M. Kamada and Dr. M. Hasumoto for the useful advice and skillful technical assistance to use SOR beam. They are also grateful to Professor Y. Moritomo for many discussions and for the help in the visible-ultraviolet spectroscopy.

References
* Electronic address: k46291a@nucc.cc.nagoya-u.ac.jp
[1] Y. Okimoto *et al.*, Phys. Rev. B **55**, 4206 (1997).
[2] A. Asamitsu and Y. Tokura, Phys. Rev. B **58**, 47 (1998).
[3] J. M. D. Coey *et al.*, Phys. Rev. Lett. **75**, 3910 (1995).

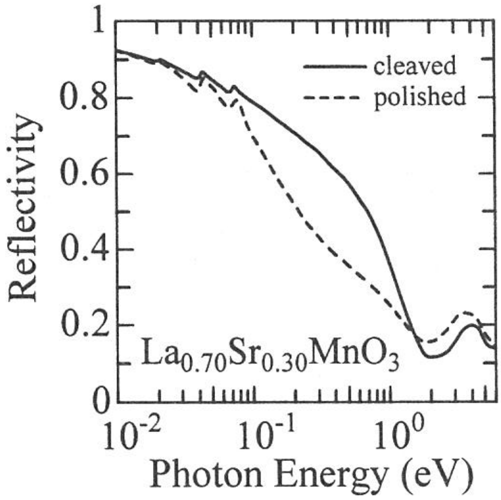

FIG. 1 Optical reflectivity spectra of $La_{0.70}Sr_{0.30}MnO_3$ measured on the cleavage surface (solid line) and the polished surface (dashed line).

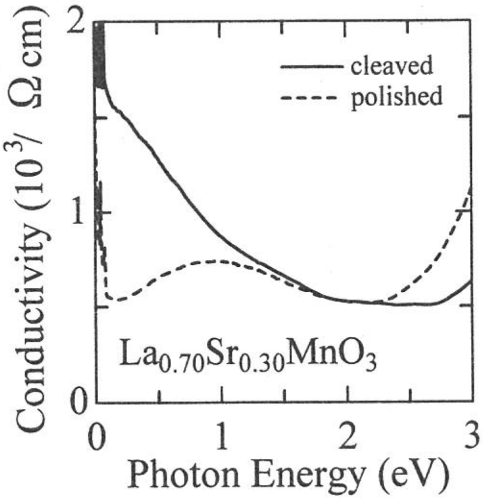

FIG. 2 Optical conductivity spectra of $La_{0.70}Sr_{0.30}MnO_3$ deduced from the reflectivity spectra measured on the cleavage (solid line) and polished (dashed line) surfaces via Kramers-Kronig transformation.

(BL1B)

Reflection Spectra of Hydrogen-Bonded Ferroelectrics $PbHPO_4$ and $PbHAsO_4$

Noriaki KIDA, Nobuhito OHNO and Masao KAMADA^A

Division of Electronics and Applied Physics, Graduate School of Enginnering
Osaka Electro-Communication University, Neyagawa 572-8530, Japan.
^{A}*UVSOR Facility, Institute for Molecular Science, Okazaki 444-8585, Japan.*

Lead monohydrogen phosphate $PbHPO_4$ (LHP) and its isomorphs $PbHAsO_4$ (LHA) are quasi-one dimensional ferroelectrics that have been classified as a second order structural phase transition from a monoclinic with a space group Pc to a paraelectric $P2/c$ at T_C=310 K and 312 K, respectively. The PO_4 or AsO_4 tetrahedra in both materials are linked to linear chains by short O-H-O bonds and not cross-linked to one another, in contrast to well studied KH_2PO_4 (KDP). This simple crystal structure has been taking an appeal to many researchers as a reference material to understanding of proton ordering in hydrogen-bonded ferroelectrics.

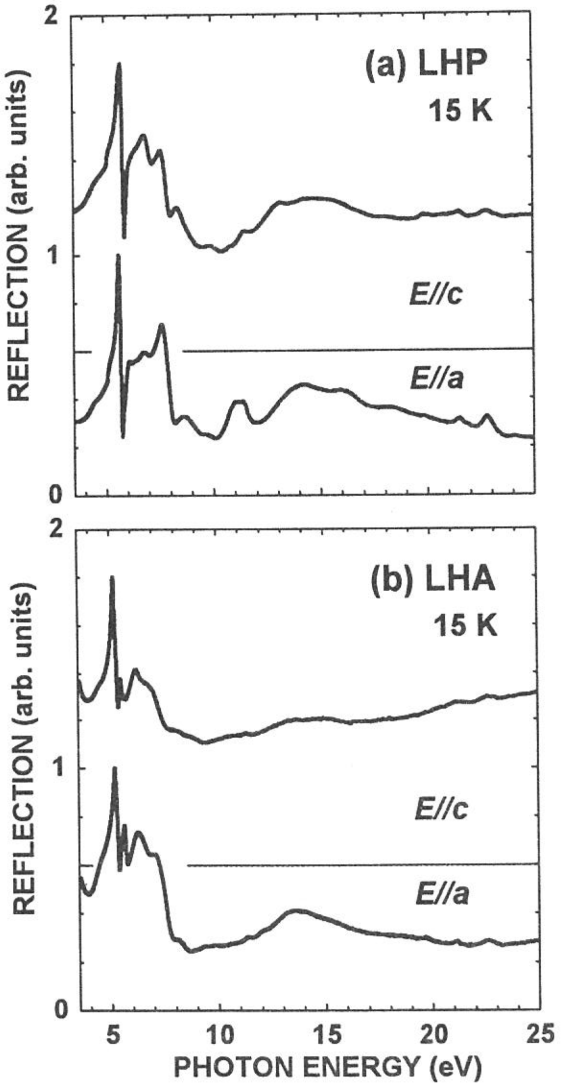

Figure 1. Polarized reflection spectra of (a) LHP and (b) LHA for E//a and E//c at 17 K.

In the present study, reflection spectra of single crystals of LHP and LHA have been investigated for the first time in the VUV region up to 25 eV by using polarized synchrotron radiation at BL1B beamline.

The specimens of LHP and LHA grown from the conventional gel-growth method [1] were used for optical measurements.

Figure 1 shows the reflection spectra of a single crystals of (a) LHP and (b) LHA for polarization parallel to the crystallographic a-axis ($E//a$) and the c-axis ($E//c$), respectively, measured at 17 K. The direction of P_S is in the ac plain, close to the a-axis. Distinguished sharp peaks with dispersive structure are observed at the absorption edge at 5.62 eV for $E//a$ and at 5.77 eV for $E//c$ in LHP. In LHA, these structures are located at 5.14 eV for $E//a$ and at 5.18 eV for $E//c$. They could be assigned as the first exciton transitions. The polarized reflection spectra of KDP and KH_2AsO_4 (KDA) have been reported [2, 3]. The reflection peaks of KDP and KDA at the absorption edge are observed at 8.2 and 7.0 eV, respectively, which have been ascribed to the transitions mainly due to the anions. No exciton transition is observed at the absorption edge in KDP and KDA. Therefore, we deduce the lowest transition of LHP and LHA as due to cationic excitation in Pb^{2+}; the upper valance bands are mainly composed of Pb^{2+} $6s$ states, and the lowest conduction bands are Pb^{2+} $6p$ states in its origin.

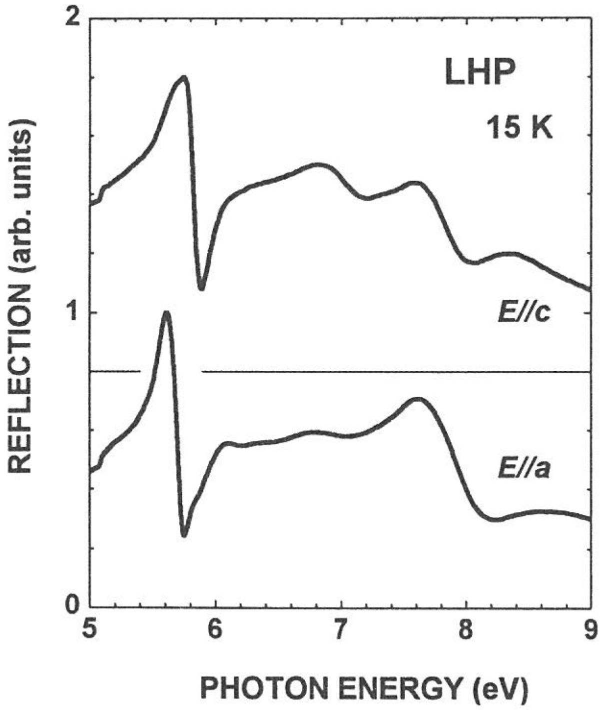

Figure 2. Expanded views of the reflection spectra near the first direct exciton region of LHP for $E//a$ and $E//c$ at 15 K.

Figure 2 shows expanded view of the reflection spectra of LHP near the first direct exciton region at 15 K. A clear shoulder structure at higher energy side of first direct exciton transtion is observed for $E//a$ at 6.0 eV for LHP. We tentatively assigned it to the n=2 state of exciton Rydberg series that permits an estimate of the binding energy (E_b) of the exciton. We obtain $E_b \simeq 670$ meV, which is comparable with $E_b = 680$ meV for the first exciton of β-PbF_2 [4]. However, recent experimental investigation for β-PbF_2 shows that such a n=2 exciton structure is not observed [5]. Bands around 7 eV are attributed to the transition from the valence band to the conduction bands, which are mixed by the spin-orbit interaction of Pb ions. With increasing of temperature, the first direct excition transition is shift to low energy side and visible even above T_C, indicating that the excitions are stable in paraelectric phase of LHP and LHA.

Sharp peaks at 21.7 eV and 22.9 eV are observed in LHP at 15 K, which may attribute to the Pb^{2+} $5d$ core excitons as observed in the lead halides [6, 7]. In LHA, these structures are barely discernible. Their energy positions are close to $^3P_1$ and $^1P_1$ levels of the free Pb^{2+} ion. Preliminarly experiment on the photoelectoron spectroscopy of LHP using Al K_α radiation at 300 K indicates that the Pb^{2+} $5d_{3/2}$ and $5d_{5/2}$ levels are located at ~22 and ~25 eV below the top of the valance band. An estimate of the core exciton binding energies is ~5 eV for $^3P_1$ state and ~8 eV for $^1P_1$ state. These values are comparable with that of β-PbF_2 [4]. Further analysis of electronic strucutures is now in progress.

We thank Prof. K. Deguchi for kindly providing single crystals of LHP and LHA.

---

[1] K. Deguchi, *J. Phys. Soc. Jpn.* **65**, 4076 (1996).

[2] S. Saito and R. Onaka, *Ferroelectrics* **21**, 553 (1978).

[3] S. Matsumoto, M. Fujisawa and S. Suga, *J. Electron Spectrosc. Relat. Phenom.* **79**, 51 (1996).

[4] J. H. Beaumont, A. J. Bourdillon and J. Bordas, *J. Phys. C: Solid State Phys.* **10**, 761 (1977).

[5] M. Fujita, M. Itoh, H. Nakagawa, M. Kitaura and D. L. Alov, *J. Phys. Soc. Jpn.* **67**, 3320 (1998).

[6] T. Hayashi, K. Toyoda and M. Itoh, *J. Phys. Soc. Jpn.* **57**, 1861 (1988).

[7] M. Fujita, H. Nakagawa, K. Fukui, H. Matsumoto, T. Miyanaga and M. Watanabe, *J. Phys. Soc. Jpn.* **60**, 4983 (1991).

(BL1B)

Reflection Spectra of Oriented Polyethylene Terephthalate Films in the Ultraviolet and Vacuum Ultraviolet Regions

Isuke OUCHI, Ikuo NAKAI[A], Masao KAMADA[B], Shin-ichiro TANAKA[B] and Masami HASUMOTO[B]

Faculty of Engineering, Tokushima Bunri University, Shido, Kagawa 769-2193
[A] *Faculty of Engineering, Tottori University, Koyama, Tottori 680-8552*
[B]*Institute for Molecular Science, Myodaiji, Okazaki 444-8585*

Ultraviolet spectra of polyethylene terephthalate (PET) have been studied in detail by one of the authors[1)] and other researchers[2)] since long ago; core electron spectra of this polymer have also been examined by ourselves[3,4)] and others.[5,6)] However, the photo absorption of valence electrons in the deeper levels have not been reported except some by XPS.[7,8)] The purpose of the present study is to investigate the deeper electronic structure of PET by use of ultraviolet and vacuum ultraviolet absorption of synchrotron radiation, whose polarized nature makes it possible to examine the effect of molecular orientation and helps to determine the character of the energy levels.

In the actual measurements, reflection spectra of thick films were taken and their Kramers-Kronig conversion was made to obtain the absorption spectra. PET films are very transparent in the visible region but absorb light strongly in the ultraviolet region; in the previous study[1)], films as thin as 0.1 μ m was utilized for the measurement of ultraviolet absorption but these are not thin enough for the measurement in vacuum ultraviolet region. On the other hand, it was proven there that the Kramers-Kronig conversion of reflection spectra of thick films gave rise to almost identical absorption spectra as directly measured by transmission method by use of the thin film.

We utilized the 1m Seya-Namioka type monochromator installed at the BL-1B of UVSOR. Five pieces of film samples were fixed on a copper plate, which was then attatched to the holder; the sample chamber was evacuated overnight before the measurement. The incidence angle was set as 12.5°. Actual measurements were made between 500A and 6000A.

Thick PET films were obtained from the Film Research Laboratory of Teijin Limited: amorphous undrawn films of 100 μ m thickness, uniaxially drawn films of 60 μ m and biaxially drawn films of 100 μ m.

An example of the reflection spectra is shown in Fig. 1; this spectrum is already corrected for multiple reflection. The method of the correction was taken from Kato[9)]and was the same as the previous paper.[1)]

The phase of reflected light was calculated from the reflection spectra by the Kramers-Kronig relation; contributions from the outside of the measured wavelength region were calculated by use of Roessler's approximation[10)] as in the previous work.[1)]

Using Fresnel equations, diffractive index, extinction coefficients and absorption coefficients were calculated. Examples of absorption spectra obtained in this way are shown in Fig, 2.

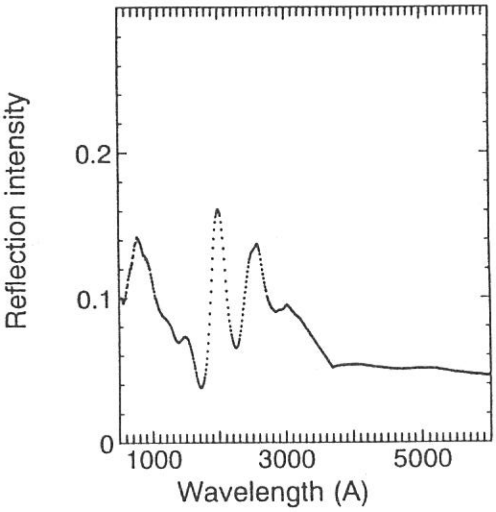

Fig. 1. Reflection spectra of an undrawn PET film. Multiple scattering is already corrected.

In the absorption spectrum of an undrawn PET film, which is shown in Fig. 2 (a), there are absorption peaks at 300 - 290 nm (4.13 - 4.26 eV), 254 - 244 nm (4.88 - 5.09 eV), 197 nm (6.29 eV), 145 nm (8.55 eV) and 91 - 83 nm (13.6 - 14.9 eV) with a broad shoulder at around 120 nm (ca.10.5 eV). The first three peaks in the ultraviolet region are the same as reported before and correspond to $^1A_g \rightarrow {}^1B_u$ transitions; according to Pariser-Parr-Pople approximation, the third peak at 197 nm consisted of two peaks of opposite polarity.[1] The absorption spectrum of a biaxially drawn PET film is displayed also in Fig. 2 (a). A slight disagreement in the peak positions must be due to technical handlings; negative absorption is also due to poor handling in some approximation and corrections, which must be improved.. The nature of the peaks at smaller wavelengths is also still to be studied.

Fig. 2 (b) shows the spectra of an uniaxially drawn PET film; their molecular orientation is either parallel or perpendicular to the electric vector of incident light and the dichroic nature is very clear. The double peak at 300 - 290 nm and a large peak at the shortest wavelength are of ⊥ polarity, the peak at 254 - 244 nm is very strongly polarized along ‖ direction, the other two are slightly ‖ polarized. Those in the longer wavelengths region agree to the previous result.1)

Relative resemblance of the spectral shape between a biaxially drawn film and an uniaxially drawn film with its draw axis parallel to the electric vector of the incident light, and also between an undrawn film and an uniaxially drawn film with perpendicular direction may be understandable from the structure change of the film by means of the stretching and heat-treatment. This, however, is still to be examined.

The authors are indebted to Mr. N. Takagi, Film Research Laboratory, Teijin Limited, who kindly sent us the film samples.

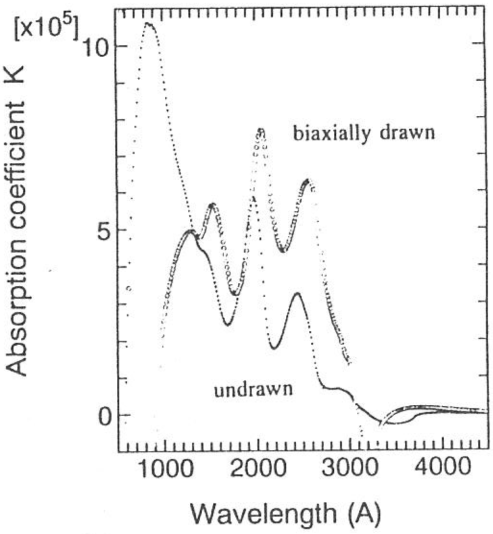

Fig. 2 (a) Converted absorption spectra of undrawn and biaxially drawn PET films.

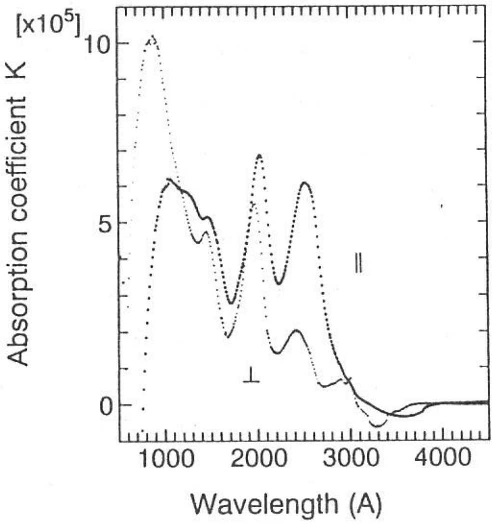

Fig. 2(b). Converted absorption spectra of an uniaxially drawn PET films. The symbols ‖ and ⊥ mean that the drawing direction is parallel or perpendicular to the electric vector of incident light, respectively.

1) I. Ouchi, Polym. J., 15 (1983) 225. 2) J.P. LaFemina and G. Arjavalingam, J. Phys. Chem., 95 (1991) 984. 3) I. Ouchi et al., Polym. J., 27 (1995) 127. 4) I. Ouchi et al., J. Electr. Spectr. Rel. Phenom., 78 (1996) 363. 5) E.G. Rightor et al., J. Phys. Chem., B 101 (1997) 1950. 6) S.G. Urquhart et al., ibid. 2267. 7) M. Chtaib et al., Phys. Rev. B, 44 (1991) 10816. 8) P. Boulanger et al., J. Electr. Spectr. Rel. Phenom., 63 (1993) 53. 9) R. Kato, J. Phys. Soc. Jpn., 16 (1961) 2525. 10) D.M. Roessler, Brit. J. Appl. Phys., 16 (1965) 1119.

(BL2A)

Photochemistry of Cyanogen Chloride in the 40 - 120 nm Region

Kazuhiro KANDA, Mitsuhiko KONO[1], Kosuke SHOBATAKE[2] and Toshio IBUKI[3]

Department of Fundamental Science, College of Science and
Engineering, Iwaki Meisei University, Iwaki 970-8551
[1] *Institute for Molecular Science, Myodaiji, Okazaki 444-8585*
[2] *Department of Materials Chemistry, School of Engineering,*
Nagoya University, Chikusa-ku, Nagoya 464-8603
[3] *Kyoto University of Education, Fukakusa, Fushimi-ku, Kyoto 612-0863*

In the vacuum UV photodissociation of ClCN, CN($B^2\Sigma^+$) and CN($A^2\Pi_i$) are produced as excited photofragments and subsequent CN(B-X) and CN(A-X) emissions have been observed in the UV and visible region and in the near infrared region, respectively. For the wavelength range shorter than 105 nm, little has been known about the high-lying electronic states of ClCN because of the lack of a radiation source available for the photoabsorption measurements. In the present study, by taking advantage of the window-less experimental configuration at BL2A of UVSOR, absolute cross section for the formation of CN(B) are determined in the wavelength range 40-120 nm. The relative cross section for the CN($A^2\Pi_i$) production was also measured. In the 90-120 nm region, the photoabsorption spectrum and photoexcitation spectrum have been measured by use of an Ar gas filter, instead of a LiF window, which was mounted in front of the absorption cell, in order to eliminate the secondary light of a incident SOR beam. Typical pressure of Ar in the gas filter was 270 mTorr. For the measurement in the 40-90 nm region, any gas was not introduced to the gas filter.

The electronic configuration of ClCN in the ground electronic state is[2]

$$(1\sigma)^2(2\sigma)^2(3\sigma)^2(1\pi)^4(3\sigma)^2(2\pi)^4;\ ^1\Sigma^+.$$

The first ionization potential (IP) of ClCN is reported to be 99770 cm^{-1} (100.2 nm) for the production of ClCN$^+$ in the $^2\Pi_{1/2}$ manifolds. The second IP associated with the $^2\Sigma^+$ ionic state is located at 111300 cm^{-1} (89.8 nm). In Fig. 1, the absolute cross section is plotted against the excitation wavelength in the range 30-150 nm, respectively. A broad, structureless continuum was observed below 90 nm, above the second IP. Numerous peaks have been observed in the wavelength region $\lambda > 90$ nm. The absorption peaks, in the 90-100 nm region have been assigned to the transitions to the super-excited states. These super-excited states have been associated with the Rydberg series converging to the second IP. As a result, almost absorption bands below the second IP can be assigned to the Rydberg transitions converging to these first and second IPs or intravalence transitions.

The absolute cross section for the production of CN(B) was determined by a comparison of the intensity of the CN(B-X) emission produced in the photodissociation of HCN.[3] The quantum yield was calculated as the ratio of the emission cross section to the absorption cross section. As shown in Fig. 2, the quantum yield for the production of CN(B) takes maximum value ~0.13 at 119 nm. It appears that the dominant photodissociation channels in the wavelength region $\lambda > 119$ nm lead to the production of CN fragments in $X^2\Sigma^+$ and/or $A^2\Pi_i$ states. As shown in Figs. 2 and 3, the cross section for the production of excited CN fragment decreases drastically down around 100 nm, due provably to the preferential operation of ionization in the energies above the first ionization potential.

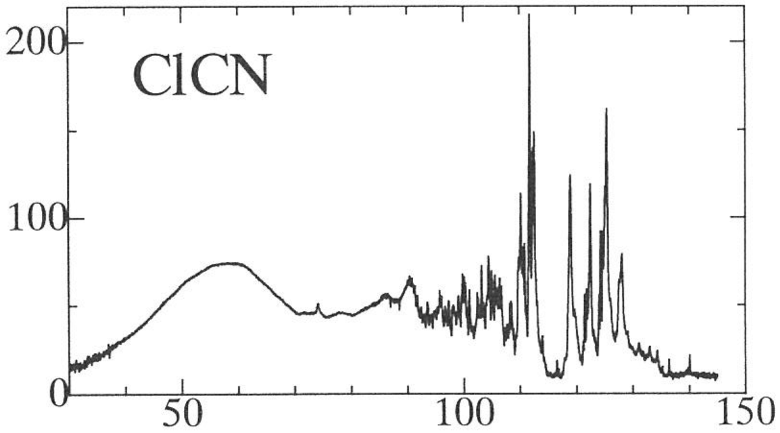

Fig.1 The absorption cross sections of ClCN in the 30-150 nm region. The spectral solution was 0.1 nm.

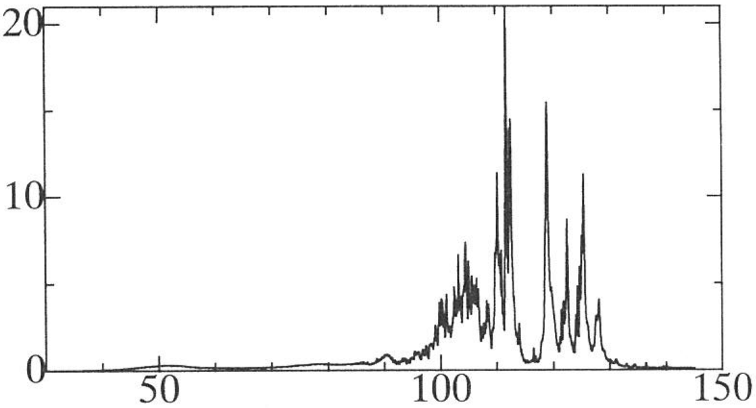

Fig.2 Absolute cross section for the production of CN(B) from ClCN.

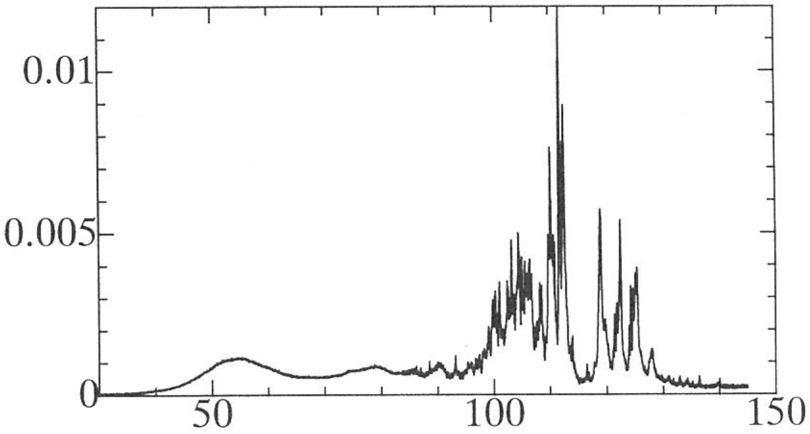

Fig.3 Absolute cross section for the production of CN(A) from ClCN

Reference

[1] E. Heilbronner, V. Hornung, K. A. Muszkat, Helv. Chem. Acta 53 (1970) 347.

[2] L. C. Lee, Chem. Phys., 72, 6414 (1980).

(BL2A)

Dissociative Excitation of HCOOH by Single- VUV and Two- UV Photon at 124 nm Region.

Kiyohiko TABAYASHI, Jun-ichi AOYAMA, Masafuyu MATSUI, Takashi HINO, Ko SAITO, and Toshio IBUKI*

Department of Chemistry, Faculty of Science, Hiroshima University,
Kagamiyama, Higashi-Hiroshima 739-8526
**Kyoto University of Education, Fukakusa, Fushimi-ku Kyoto 612-0863*

Dissociative excitation of HCOOH was studied by single- VUV photon absorption at 124.5 nm with SR source, and by two- UV photon absorption at 249 nm with KrF laser. Nascent rotational and vibrational (V/R) state distributions of $OH(A^2\Sigma^+)$ produced via the photodissociation, $HCOOH + nh\nu\ (n=1, 2) \rightarrow HCO + OH(A^2\Sigma^+)$ were determined by computer simulation analysis of the dispersed fluorescence spectra. The internal state distributions were found to be of the relaxed type, and rotational distribution could be approximated by a Boltzmann distribution.(Fig.I) One- VUV photon excitation gave the best-fit rotational temperature $T_r(v'=0)= 3000$ K and vibrational population ratio $N_{v'=1}/N_{v'=0}=0.14$, while two- UV photon excitation showed $T_r(v'=0)=2000$ K with $N_{v'=1}/N_{v'=0}=0.12$. Possible mechanisms for the OH(A) formation by both excitation sources were examined based on simple theoretical models. The degree of internal excitation is not consistent with a direct dissociation on a repulsive surface, and a dissociation from a long-lived intermediate state, neither. The formation of $OH(A\Sigma^+)$ is interpreted as dissociation of an electronically excited intermediate state leading to the formation of OH(A)+CHO, populated competitively via an electronic predissociation process. The substantially different V/R distributions observed are dependent on the excited precursor state initially accessed, and may result from the constraint in the competing predissociation step that follows.

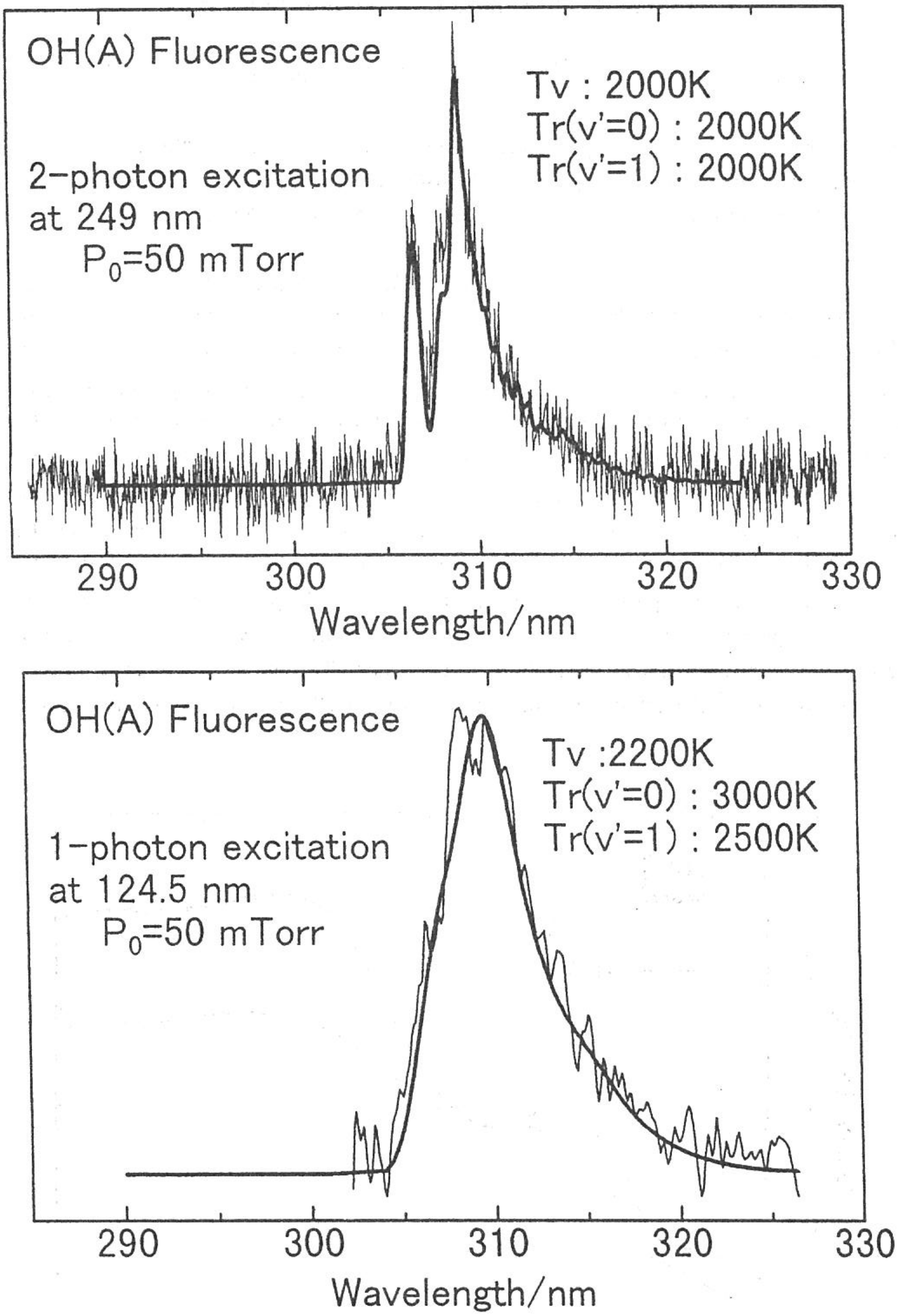

Fig. I. Experimetal and computer simulated spectra of OH(A-X) produced with one-VUV and two-UV photon excitation of HCOOH at 124.5 nm. Upper spectrum; spectral resolution was 0.83 nm. Lower spectrum; spectral resolution was 2.4 nm.

(BL2A)

Fundamental Absorption Spectra of Solid HBr

Makoto WATANABE 1), Kazumasa OKADA 2) and Toshio IBUKI 3)

1. *Research Institute for Scientific Measurements, Tohoku University*, Sendai 980-8577
2. *Department of Chemistry, Faculty of Science, Hiroshima University*, Higashi-Hiroshima 739-8526
3. *Department of Chemistry, Kyoto University of Education*, Kyoto 612-8522

Absorption spectra have been obtained for solid HBr films deposited on LiF single crystals at liquid nitrogen temperature(−177°C) in the 5−10 eV region. The base pressure of the sample chamber was 2×10^{-6} Torr. The absorption measurements were carried out warming the sample from −177°C to −82°C. The preliminary result is shown in Fig. 1. The thin and thick curves show the spectra for the samples as deposited(−177°C) and at −118°C, respectively. The optical density of the spectrum at −118°C is larger than that at −177°C. This may be due to the contamination of the sample with residual gases. Both spectra show broad spectral shapes, which are not found in gaseous HBr showing complicated vibronic structures 1). This feature is different from that in usual molecular crystals, in which the spectral profile of the individual molecule remains well. Two peaks around 6.5eV became clearer in the sample at −118°C than in the sample as deposited. The energy separation of the peaks is 0.5eV, which corresponds to the spin-orbit splitting of Br^- ion. These peaks are regarded as excitonic peaks. The electronic structure of solid HBr seems not to resemble that of gaseuos HBr, but to resemble to those of NaBr crystal2) and solid Kr3) though the excitonic peaks in solid HBr are not as sharp as those in these materials.

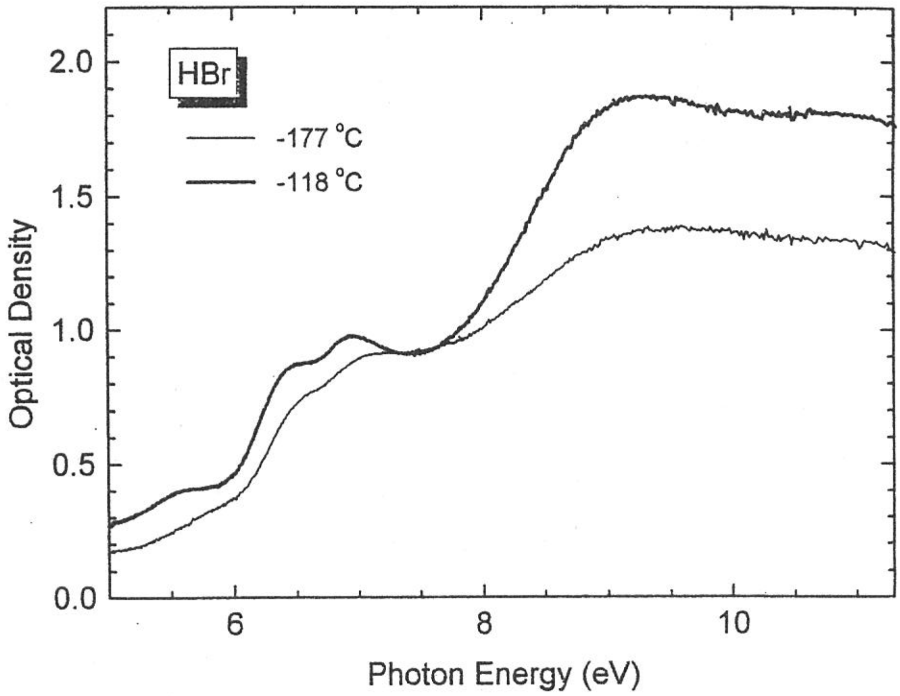

Fig.1 Absorption spectra of solid HBr.

References
1. J. B. Nee, M. Suto and L. C. Lee, J. Chem. Phys. **85** (1986) 4919.
2. J. E. Eby, K. J. Teegarden and D. B. Dutton, Phys. Rev. **116** (1959) 1099.
3. G. Baldini, Phys. Rev. **128** (1962) 1562.

(BL2B1)

Adsorbed states of chemisorbed and physisorbed N2 on Pd(110)

Jun Yoshinobu[1,2], Hiroyuki Kato[1], Hiroshi Okuyama[1], Hirohito Ogasawara[1], Tadahiro Komeda[1], Maki Kawai[1], Shin-ichiro Tanaka[3] and Masao Kamada[3]

1) The Institute of Physical and Chemical Research (RIKEN), 2-1 Hirosawa, Wako 351-0198. 2) The Institute for Solid State Physics, The University of Tokyo, 7-22-1 Roppongi, Minato-ku, Tokyo 106-6666. 3) Institute for Molecular Science, Myodaiji-cho, Okazaki 444-8585 .

Adsorption states of N_2 on Pd(110) at low temperature (20-100K) have been studied by means of high resolution electron energy loss spectroscopy (HREELS), photoelectron spectroscopy (PES), thermal desorption spectroscopy (TDS), low energy electron diffraction (LEED) and near edge X-ray absorption fine structure (NEXAFS)

At ~0.1 ML (monolayer) at 20K, two losses at 30 and 280 meV are observed in the specular direction in addition to the Pd(110) surface resonance peak at 18 meV [1]. According to the previous study [2], these peaks were attributed to Pd-N_2 stretching mode and N_2 stretching mode, respectively. By the off-specular mode, a hindered rotational mode is newly observed at ~25 meV. A p(2x1) LEED is observed at 0.5 ML [2]. The structure is a upright linear configuration according to the NEXAFS experiments.

With increasing the coverage, a peak assigned to the hindered rotational mode becomes visible at ~25 meV in the specular direction. At the saturation with adsorbed N_2 on Pd(110) at 50 K, loss peaks are observed at 24, 29 and 278 meV. Thus, the orientation of the molecule is tilted above 0.5 ML due to the intermolecular interaction.

From the TDS results, the desorption peaks are observed at ~85 K and 105 K. These N_2 species are chemisorbed on Pd(110) since the hybridization occurs between N_2 orbitals (mainly 1π, 5σ and 2π) and Pd valence band according to the PES results.

With increasing the coverage at 30 K, the desorption peaks from physisorbed and multilayer N_2 are observed at ~50 K and 35 K, respectively. The PES results shows less perturbed N_2 orbitals where the binding energy difference between $3\sigma_g$, $1\pi_u$ and $2\sigma_u$ is similar to that of gaseous N_2 .

REFERENCE

[1] J. Yoshinobu et al., Phys. Rev. B **38**, 1520 (1988).

[2] Y. Kuwahara et al., Surf. Sci. **180**, 421 (1987).

(BL-2B1)

Effective Escape Depth of Photoelectrons for Hydrocarbon Films in Total Electron Yield Measurement at C *K*-edge

Hideaki Ohara[1], Yasushi Yamamoto[1], Kotaro Kajikawa[1], Hisao Ishii[1], Kazuhiko Seki[1,2] and Yukio Ouchi[1]

[1]*Department of Chemistry, Graduate School of Science, Nagoya University, Chikusa-ku, Nagoya 464-8602, Japan*
[2]*Research Center for Materials Science, Nagoya University, Nagoya 464-8602, Japan*

When investigating molecular conformations and orientations in organic thin films by Near Edge X-ray Absorption Fine Structure (NEXAFS), we often need to pay attention to the escape depth L of materials, which depends on an electron-detection method. In the case of Auger electron yield mode, the escape depth of the Auger electron can be easily estimated since an electron energy dependence of the escape depth has been measured[1][2][3]. On the other hand, in total electron yield (TEY) mode of detection, which is also commonly used, photoelectrons suffer multiple scattering and exact escape depth is difficult to obtain due to the lack of information for secondary photoelectrons. Reliable information on L_{eff} for C *K*-edge TEY mode is still lacking.

In this study, we performed NEXAFS and AFM measurements for multilayer systems to deduce the L_{eff} at C *K*-edge TEY mode. The sample used in our experiment was a HTC (hexatriacontane, n-$C_{36}H_{74}$) /polyimide (biphenyl-3,3',4,4'-tetracarboxylic dianhydride type) / Si multilayer. Quantitative degrees of superposition of C *K*-edge spectra of HTC and polyimide with aromatic rings were evaluated to obtain L_{eff}.

The multilayer-sample were prepared as follows : To begin with, polyimide / NMP (N-methyl-2-pyrolidone) solution was spin-coated on a Si substrate. Then, HTC was evaporated on the polyimide. Three samples with different HTC thicknesses (#0 : 0 Å, #1 : 70 Å and #2 : 94 Å) monitored by a quartz oscillator were prepared. C *K*-edge NEXAFS spectra were taken at BL-2B1. Measurements were performed in TEY mode with normal incidence under a vacuum of 10^{-8} Pa range. AFM images of the sample were taken in dynamic force mode (DFM) not to damage the HTC layers. Ten AFM images ($10\mu m \times 10\mu m$) at different positions of each sample were taken and then averaged.

In Fig.1, we summarize C *K*-edge NEXAFS spectra for various HTC thicknesses. Peak (a) has already been assigned as $C1s \rightarrow \pi^*(C=C)$ resonance[4][5], so this peak is originated from the polyimide layer. Figure 2 shows a typical example of AFM images of sample #1. Evaporated HTC molecules onto polyimide formed islands (or domains) with different thickness and the height of one step was nearly equal to 47 Å corresponding to a full length of HTC molecule. The values of L_{eff} were determined with use of a following formula ;

$$I/I_0=\sum_{i=0} S_i \exp\left(-d\cdot i/L_{eff}\right)$$

where d is the thickness of one HTC layer (47 Å) and i is the number of the layers in the domain, respectively. S_i refers to the ratio of the domain size of corresponding thicknesses. Peak (a) intensity of samples #1 and #2 normalized by that of #0 (no HTC evaporated) gives I/I_0. Values obtained are listed in Table.1. As is shown in Table.1, L_{eff} range from 30 Å to 39 Å. An experimental error of L_{eff} ; mainly due to the inaccuracy in the evaluation of the domain size. These values are still quite reasonable when we consider NEXAFS studies on the surface freezing effect of pentacontane (PC, n-$C_{50}H_{102}$)[6], where a inclined PC monolayer is formed on top of the PC liquid phase for a couple of degrees. The tilt angle of PC deduced from TEY measurement is greater than those determined by X-ray diffraction. However, when account is taken of L_{eff}, the agreement between the X-ray diffraction and TEY measurements improve considerably demonstrating the importance of determining escape length of photoelectrons which are used in detection method.

References

[1]Cartier, E., Pfluger, P., Pireaux. and Rei Vilar, M. (1987). Appl. Phys. A44, 43-53.
[2]Bain, C. D., Whitesides, G. M. (1989). J. Phys. Chem. 93, 1670-1673.
[3]Laibinis, P. E., Bain, C. D. and Whitesides, G. M. (1991). J. Phys. Chem. 95, 7017-7021.

[4]Schedel, Th. - Niedrig et al. (1991). Ber. Bunsenges. Phys. Chem. 95, 1385.
[5]Jordan, J. L. - Sweet et al. (1988). J. Chem. Phys. 89, 2482.
[6]Yamamoto, Y., Mitsumoto, R., Ito, E., Araki, T., Ouchi, Y., Seki, K. and Takanishi, Y. (1996). J. Electron Spectrasc. 78, 367-370.

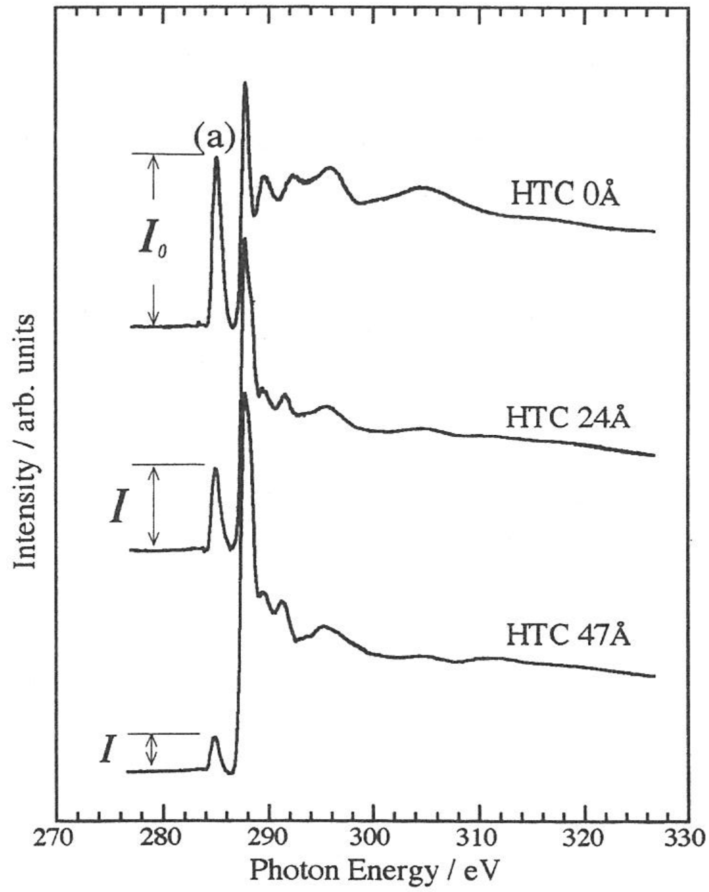

Fig.1. C K-edge NEXAFS spectra for various HTC thicknesses. Thicknesses are monitored by quartz oscillator.

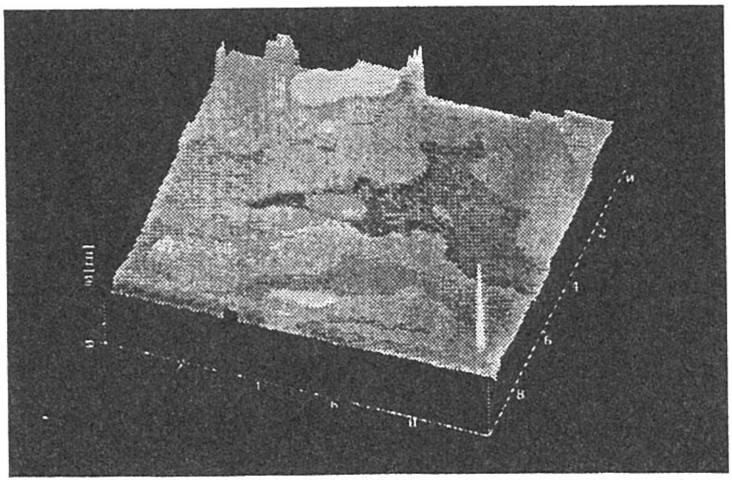

Fig.2 A typical example of AFM images of sample #1.

Table 1. Obtained effective escape depths.

Sample	I / I_0	L_{eff} / Å
#1	0.107	**39**
#2	0.065	**30**

(BL2B1)

Study of ion desorption induced by resonant core–electron excitations of condensed water using Auger electron–photoion coincidence spectroscopy

Kazuhiko Mase, Shin–ichiro Tanaka, Tsuneo Urisu, Eiji Ikenaga[1], and Kenichiro Tanaka[1]

Institute for Molecular Science, Okazaki 444–8585, Japan
[1]*Faculty of Science, Hiroshima University, Higashi Hiroshima 739, Japan*

Ion desorption mechanism in the region of resonant excitations of Oxygen 1*s* core–electron of condensed water is studied using Auger electron–photoion coincidence (AEPICO) spectroscopy. A newly developed coincidence analyzer was used for which the resolution of the electron kinetic energy was improved to $E/\Delta E = 100$. Figure 1 shows Auger electron yield (AEY, electron kinetic energy: 490 eV), total ion yield (TIY) and TIY/AEY spectra of condensed H_2O in the oxygen K–edge region. The TIY/AEY spectrum exhibited a characteristic threshold peak at the $4a_1 \leftarrow$ O:1*s* resonance ($h\nu = 532.3$ eV) and a suppression at the $3p \leftarrow$ O:1*s* resonance ($h\nu = 535.5$ eV). Figure 2 shows the electron kinetic energy dependence of the AEPICO yield (AEPICO yield spectra) at $h\nu = 532.6$, 533.6, 335.4, 540.6, 547.6, and 557.8 eV. At the $4a_1 \leftarrow$ O:1*s* resonance ($h\nu = 532.6$ eV) and $2b_2 \leftarrow$ O:1*s* resonance ($h\nu = 533.6$ eV), the AEPICO yield spectrum exhibited major, medium and minor peaks at the electron kinetic energies of 502.5, 482.5, and 465 eV, which are assigned to $(\mathrm{O}{:}2p)^{-2}(4a_1(\text{or } 2b_2))^1$, $(\mathrm{O}{:}2s)^{-1}(\mathrm{O}{:}2p)^{-1}(4a_1(\text{or } 2b_2))^1$, and $(\mathrm{O}{:}2s)^{-2}(4a_1(\text{or } 2b_2))^1$ spectator Auger final states, respectively. These results shows that ultrafast ion desorption mechanism is predominant at the $4a_1$ and $2b_2$ resonances. The enhancement of the H^+ AEPICO yield was attributed to the strongly O–H antibonding character of the $4a_1$ and $2b_2$ orbitals. At the $3p$ resonance ($h\nu = 535.4$ eV), the AEPICO yield spectrum exhibited major, medium and minor peaks at the electron kinetic energies of 460, 475, and 490 eV, which are assigned to $(2a_1)^{-2}(3p)^1$, $(2a_1)^{-1}(1b_2)^{-1}(3p)^1$, and $(1b_2)^{-2}(3p)^1$ spectator Auger final states, respectively. This result indicates that spectator Auger stimulated ion desorption mechanism is responsible at the $3p$ resonance. The suppression of the H^+ AEPICO yield was attributed to the reduction of the hole–hole Coulomb repulsion due to the $3p$ electron. At $h\nu = 540.6$, 547.6 and 557.8 eV, the AEPICO yield spectrum exhibited three peaks at the electron kinetic energies of 460, 475, and 490 eV, which are assigned to $(2a_1)^{-2}$, $(2a_1)^{-1}(1b_2)^{-1}$, and $(1b_2)^{-2}$ normal Auger final states, respectively. This result

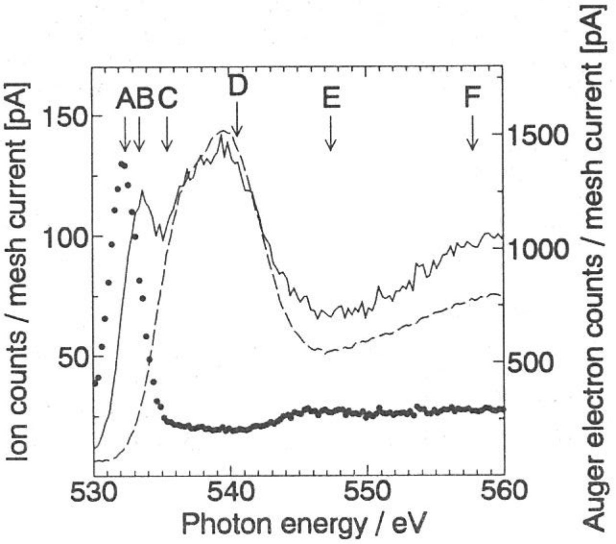

Figure 1. Total ion yield (TIY) spectrum (——), Auger electron yield (AEY) spectrum (- - - -), and TIY/AEY spectrum of condensed H_2O (⋯⋯).

indicates that the normal Auger stimulated ion desorption mechanism is responsible at photon energies above the O:1*s* ionization. These results and conclusions are consistent with the previous study carried out by low-resolution AEPICO spectroscopy [1].

Reference

[1] K. Mase, M. Nagasono, S. Tanaka, T. Urisu, E. Ikenaga, T. Sekitani, and K. Tanaka, *J. Chem. Phys.* **108**, 6550 (1998).

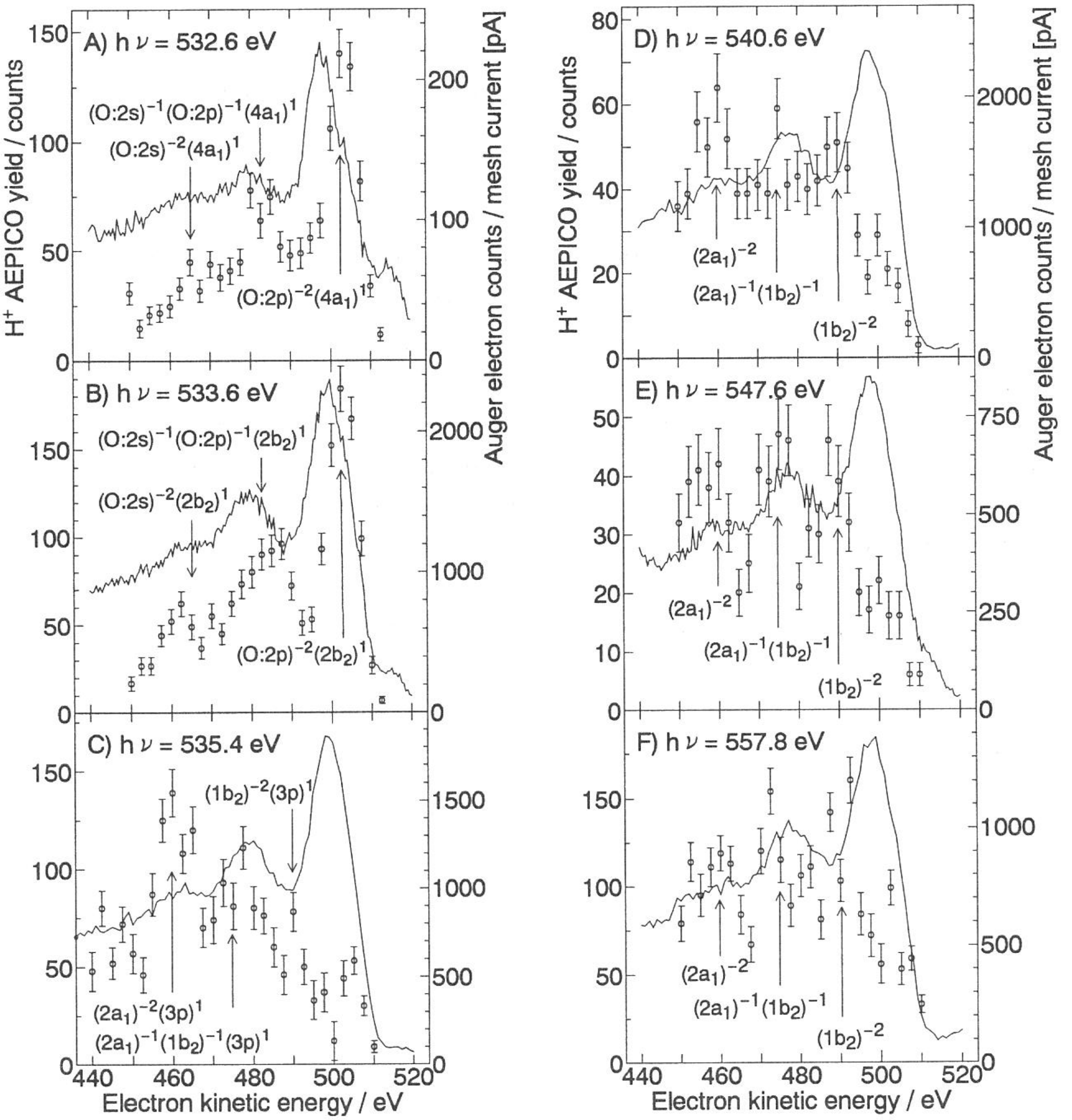

Figure 2. H⁺ AEPICO yield spectra at *hν* = A)532.6, B)533.6, C)535.4, D)540.6, E)547.6, and F)557.8 eV. The solid lines show typical Auger electron spectra.

(BL2B1)

Site-specific fragmentation following C:1*s* core-level photoionization of $CF_3CH(OH)CH_3$ adsorbed on a Si(100) surface

Arinobu Nakamura, Shin-ichi Nagaoka, Kazuhiko Mase,[A] Shin-ichiro Tanaka[A] and Tsuneo Urisu[A]
Department of Chemistry, Faculty of Science, Ehime University, Matsuyama 790-8577
[A]Institute for Molecular Science, Okazaki 444-8585

Synchrotron radiation has provided a powerful means to obtain information about core-level excitations, and the dynamic processes following the core-level excitations in molecules have long been a subject of interest. In contrast to valence electrons that are often delocalized over the entire molecule, the core electrons are localized near the atom of origin. Although core electrons do not participate in the chemical bonding, the energy of an atomic core-level in the molecule depends on the chemical environment around the atom. A shift in the energy levels of core electrons that is due to a specific chemical environment is called a chemical shift.

Monochromatized synchrotron radiation can excite core electrons of an atom in a specific chemical environment selectively, discriminating the core electrons from those of like atoms having different chemical environments. This site-specific excitation often results in site-specific fragmentation, which is of importance in understanding localization phenomena in chemical reactions and which is potentially useful for synthesizing materials through selective bond breaking. Synchrotron radiation can indeed play the part of an optical knife for molecules. When bond dissociation around an atomic site is required in the synthesis, one can use the optical knife that has the photon energy corresponding to the specific excitation of that site.

To elucidate the site-specific fragmentation, we have studied the spectroscopy and dynamics following core-level photoionization of various molecules condensed on surfaces [1,2]. To observe the dissociation processes following core-level ionization of a site selectively, we use the energy-selected-photoelectron photoion coincidence (ESPEPICO). The measurements of fragment ions coincidentally produced with energy-selected photoelectrons allow selective observation of the processes initiated by the electron ejection.

In the present work, we have used photoelectron spectroscopy and the ESPEPICO method to study the site-specific fragmentation following C:1*s* photoionization of $CF_3CH(OH)CH_3$ (TFIP) adsorbeded on a Si(100) surface. TFIP is expected to be adsorbed on Si(100) like $CF_3CH(OSi\{substrate\})CH_3$ [3]. The chemical environments of a C atom bonded to three F atoms (C[F]), of C bonded to three H atoms (C[H]) and of C bonded to H and OSi (C[OSi]) are different from one another, so it seems likely that TFIP will show site-specific fragmentation. In a monolayer regime, competition between surface reactions and electronic relaxation is expected to make the site-specific phenomena complex.

Figure 1 shows the photoelectron spectrum of TFIP in the region of C:1*s* electron emission. The low-resolution photoelectron spectrum shown in the main panel has two peaks in this region.

The peak at the higher-energy side is thought to correspond to C[F]:1*s* electron emission. The high-resolution spectrum of the peak at the lower-energy side is shown in the inset. The peak at the lower-energy side is found to be a doublet. The shoulders at the lower- and higher-energy sides in the inset are thought to correspond to C[OSi]:1*s* and C[H]:1*s* electron emissions, respectively.

Figures 2a, b and c show the ESPEPICO spectra obtained with emissions of the C[OSi]:1*s*, C[H]:1*s* and C[F]:1*s* electrons, respectively. These spectra were obtained with emissions of the C:1*s* electrons whose binding energy are indicated by arrows in Fig. 1. H^+ ion is predominantly desorbed coincidentally with the C[H]:1*s* and C[OSi]:1*s* electrons. In contrast, F^+ ion is predominantly desorbed coincidentally with the C[F]:1*s* electron. The ionic fragmentation occurs selectively around the C atom where the photoionization has taken place: synchrotron radiation can indeed play the part of an optical knife for molecules.

[1] S. Nagaoka, K. Mase, M. Nagasono, S. Tanaka, T. Urisu and J. Ohshita, J. Chem. Phys. 107, 10751 (1997).

[2] S. Nagaoka, K. Mase and I. Koyano, Trends Chem. Phys. 6, 1 (1997).

[3] J. Yoshinobu, S. Tanaka, and M. Nishijima, Appl. Phys. 60, 1196 (1991).

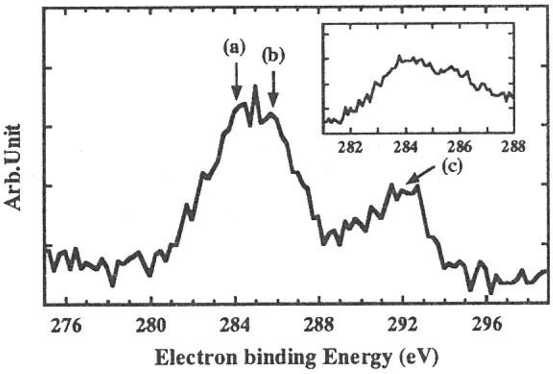

Figure 1

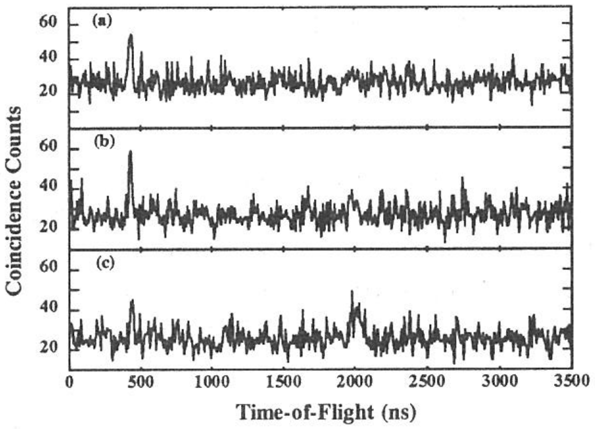

Figure 2

Figure 1 (left-hand side). Photoelectron spectrum of TFIP adsorbed on a Si(100) surface. The low-resolution photoelectron spectrum in the region of C:1*s* electron emission is shown in the main panel. The high-resolution spectrum of the peak at the lower-energy side is shown in the inset. The spectra in the main panel and the inset were taken at photon energies of 404.1 and 310.9 eV, respectively. Each of the channels in the main panel was measured for 2 s at a step 0.25 eV and each of those in the inset was measured for 8 s at 0.1 eV. An electronic field across the ionization region was applied during the measurement of the main panel.

Figure 2 (right-hand side). ESPEPICO spectra of TFIP adsorbed on a Si(100) surface. These spectra were obtained with emissions of the C:1s electrons whose binding energy are indicated by arrows in Fig. 1. The spectra were taken at a photon energy of 404.1 eV and the data collection time was 11700 s. (a) C[OSi]:1*s* electron emission. (b) C[H]:1*s* electron emission. (c) C[F]:1*s* electron emission.

(BL2B1)

ORIENTATION OF OXYGEN ADMOLECULES ON STEPPED PLATINUM(133) AND (335) SURFACES

Manami Sano*, Yoshiyuki Seimiya, Toshiro Yamanaka, Yuichi Ohno, Tatsuo Matsushima, Shin-ichiro Tanaka** and Masao Kamada**

*Catalysis Research Center and *Graduate School of Environmental Earth Science, Hokkaido University, Sapporo 060-0811, Japan,*

*** Institute for Molecular Science, Myodaiji Okazaki 444-8585, Japan*

The orientation of oxygen ad-molecules was studied on stepped Pt(133)=(s)[3(111)x(111)] and Pt(335) =(s)4(111)x(001) surfaces by using thermal desorption spectroscopy (TDS) and near edge X-ray absorption fine structure (NEXAFS). Three ad-molecule desorption peaks were commonly found at around 230 K(α_1-O_2), and below 200 K (α_2-O_2 and α_3-O_2). The ad-molecules yielding α_1-O_2 on Pt(133) lie along surface troughs, and those yielding α_2-O_2 and α_3-O_2 lie on declining three-atom-wide terraces of a (111) structure and are largely rotated from the surface trough direction. On the other hand, four-atom-wide terraces on Pt(335) seem too wide to yield definitely-oriented molecules except for a small coverage range.

Experiments;

TDS was carried out in a conventional UHV chamber. NEXAFS experiments were conducted in a chamber equipped with a Beam Line 2B1 using a grasshopper monochromator. The spectra were recorded by an Auger electron yield mode with the kinetic energy of the oxygen KLL Auger electrons at 520 eV. The angle of X-ray incidence (θ) was varied by rotating the sample crystal.

Results;

Pt(133); α_1-O_2 was oriented along the trough because the σ * resonance was maximized and no π * resonance appeared at the normal incidence of X-ray with the electric vector (Ē) oriented in the $[\bar{1}10]$ direction, and no σ * was confirmed for Ē in a plane perpendicular to it. The cross section ratio ($A_{\sigma/\pi}$) of the σ * resonance to the π * was estimated to be 3 from the incidence angle dependence of α_1-O_2. This value was used to determine the rotation angles of the other species. α_2-O_2 rotated 40° from the trough and α_3-O_2 60°.

Fig. 1 NEXAFS cross section.
The relative NEXAFS intensity ($A_{\sigma/\pi}$) of the π * and σ * resonance was determined from the incident angle dependence by assuming the definite orientation of α_1-O_2 along the trough on Pt(133). θ is the incidence angle of X-ray.

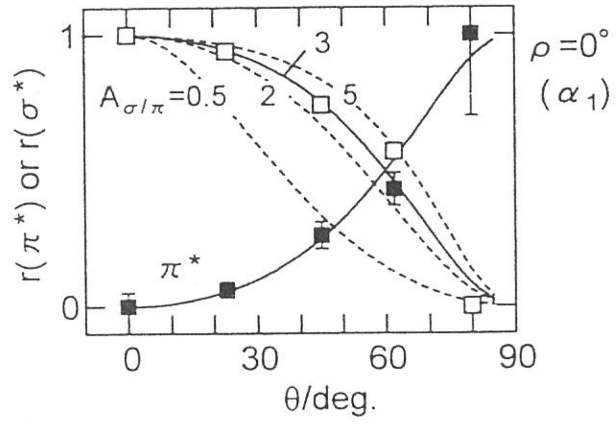

Pt(335); Oxygen ad-molecules were highly oriented along the trough at low coverages. NEXFAS spectrum showed that when the coverage (Θ_{O2}) was less than 0.17, the π * resonance was much less than the σ * at the normal incidence of X-ray with Ē in the $[\bar{1}10]$ direction. The fraction of the π * resonance was less than 10 % when Ē was oriented in the $[\bar{1}10]$

direction. The incidence angle dependence was plotted in Fig. 2b. The simulation with the ratio of $A_{\sigma/\pi}=3$ yielded the rotation angle of 20° from the trough direction. A comparison with the above results on Pt(133) suggests that α_1-O_2 limited at lower coverages is more oriented along the trough. This coverage may exceed the threshold value of α_1-O_2.

The additional oxygen molecules above this level showed enhanced π^* resonance and reduced σ^* signal as shown in Fig. 3. The contribution from these molecules was estimated as the difference between the signal at $\Theta_{O2}=0.17$ and that at saturation. The π^* resonance shared about 20 % of the total yield. The incidence angle dependence is shown in Fig. 2c. This dependence would yield the rotation angle of 40° from the trough direction if these ad-molecules are assumed to be equally oriented only into two directional ways in the opposite manner (likely as $\pm\beta$°) from the trough direction. However, this orientation is not conclusive yet, because at least two forms of oxygen may be involved in these molecules. The surface modification method should be applied to prepare each oxygen ad-molecule separately.

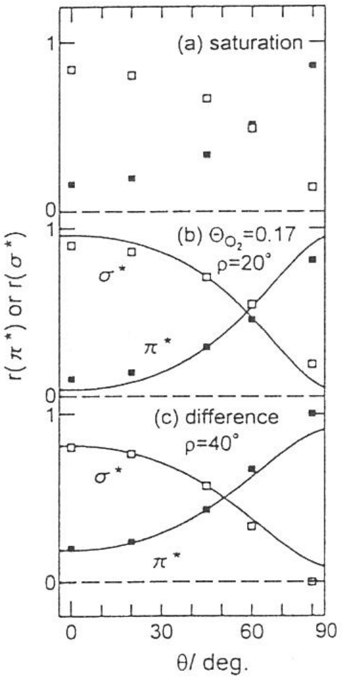

Fig. 2 NEXAFS intensity simulation.
The relative NEXAFS intensities of r(π^*) and r(σ^*) of oxygen at (a) saturation, (b) $\Theta_{O2}=0.17$, and (c) coverage higher than this level are plotted as a function of the **E** orientation in a plane parallel to the step edge. The solid and open squares are from experimental results. The curves in (b) and (c) were calculated at $A_{\sigma/\pi}$(cross-section ratio) = 3 and at ρ = 20 and 40°. ρ is the angle between the molecular axis and the trough direction. The declining terrace angle was assumed to be 14.5° .

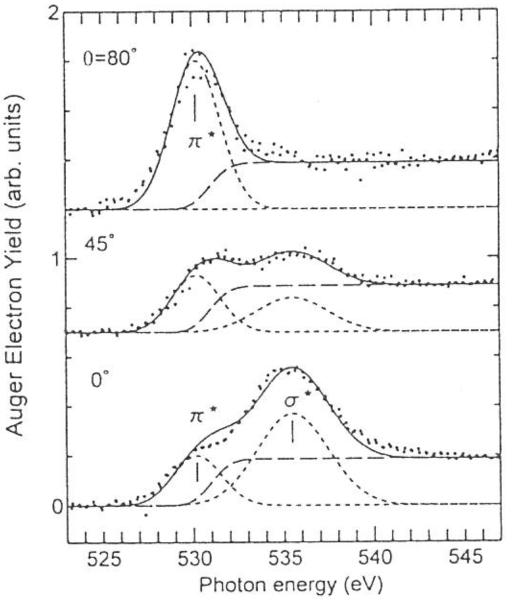

Fig. 3 NEXFAS of oxygen ad-molecules on Pt(335) at a high coverage and various incidence angles. The signal at $\Theta_{O2}=0.17$ was subtracted from that at saturation.

1. Manami Sano, Yoshiyuki Seimiya, Yuichi Ohno, Tatsuo Matsushima, Shin-ichiro Tanaka, Masao Kamada, Appl. Surf. Sci. 130-132 (1998) 518.
2. Manami Sano, Yoshiyuki Seimiya, Yuichi Ohno, Tatsuo Matsushima, Shin-ichiro Tanaka, Masao Kamada, Surf. Sci. (1999) in press.

(BL2B1)

Ion desorption from $TiO_2(110)$ surface

Shin-ichiro Tanaka, Kazuhiko Mase, Mitsuru Nagasono and Masao Kamada

Institute for Molecular Science, Okazaki, 444-8585, Japan

Desorption induced by the electronic transition (DIET) from the solid surfaces has been extensively studied for these decades, not only because it could be utilized as a tool for studying the atomic and electronic structures of solid surfaces, but also it is an important process of the photochemical reaction on the solid surface[1]. The mechanism of the ion desorption induced by the core-level excitation has been understood in a framework of the Knotek-Feibelman (KF) model[2]. Knotek and Feibelman observed the electron stimulated desorption (ESD) yield for the O^+ desorption from TiO_2 as a function of the incident electron energy, and found that the threshold of the desoprtion was corresponding to the threshold of the excitation from the Ti-3p level (not the O-2s level). In their model, the interatomic double Auger decay of the Ti-3p level results in the creation of the O^+ ion (it is O^{2-} in TiO_2), and the desorption occurs as a result of the repulsive force due to the Mardelung energy.

The electron –ion coincidence spectroscopy has been recently developed, and proved to be a very powerful tool for investigating the dynamics of the ion desorption induced by the core-level excitation and decay process[3]. In the present report, the ion desorption induced by the core-level excitation is investigated by using the synchrotron radiation and the electron-ion coincidence technique. All the experiments were carried out at the BL-2B1. The $TiO_2(110)$ surface was cleaned by a number of cycles of Ar^+ ion sputtering and annealing. For avoiding the vacancy of oxygen at the surface, the sample was heated in the 10^{-6} Torr of oxygen jus before every measurement.

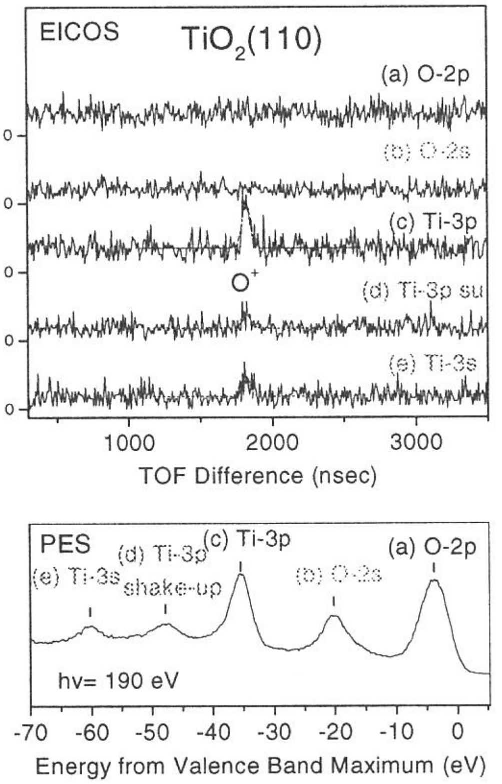

Figure 1 shows the coincidence spectra (upper part) and photoelectron spectrum (lower part) taken at hν=190 eV. The photoelectron spectrum shows the emission from the valence band (mainly O-2p) and from core levels of O-2s, Ti-3p and Ti-3s. A satellite peak due to the shake-up excitation of the Ti-3p level is also observed. The electron-ion coincidence spectra shows coincidence between ions and photoelectrons of the peaks indicated in the photoelectron spectrum. It is obvious that there are no peaks in the coincidence spectra of the valence (O-2p) and O-2s peaks [Fig. 1(a) and (b)] while O^+ peaks are observed for Ti-3p(c), Ti-3p shake-up (d) and Ti-3s(e) peaks. These results indicate that hole created via the photo-excitation of the valence and O-2s levels, meanwhile, the excitation of Ti-3p and Ti-3s levels yields the O^+ desorption. This is in agreement with the result of the electron stimulated desorption spectorscopy(ESDS) by Knotek et. al[2]. The desorption as a result of the direct process due to the excitation and decay can be distinguished from the desorption induced by the secondary electrons by using the coincidence technique, which was impossible in the ESDS technique. Father discussion will be made in a forthcoming paper.

---

[1] M. L. Knotek, Rep. Prog. Phys. **47**, 1499(1984); R.A. Rosenberg and V. Rehn, in *Synchrotron Radiation Research: Advances in surface and Interface Science, Vol. 2: Issues and Technology*, Ed. R.Z. Bachrach (Plenum Press, New York, 1992), p267.

[2] M.L. Knotek and P.J. Feibelman, Phys. Rev. Lett. **40**, 964(1978).; Surf Sci. **90**, 78(1979).

[3] K. Mase and M. Nagasono and S. Tanaka and M. Kamada and T.Urisu and Y. Murata, Rev. Sci. Inst., **68**, 1703(1997).

(BL3A1)

Photoinduced Effects on the Total Photoyield of Amorphous Chalcogenide Films by VUV light

Koji HAYASHI

Department of Electrical and Electronic Engineering, Gifu University, Gifu 501-1193

It is well-known that amorphous materials show a variety of photoinduced phenomena. Although a large number of studies have been made on photoinduced phenomena, little is unknown about the details of these mechanism. These phenomena were studied by exciting outer core electrons with the irradiation of the visible light with the energy corresponding to the optical bandgap or sub-bandgap. Little attention has been given to photoinduced effects by exciting inner core electrons with the irradiation of higher energy photon. To obtain a wide knowledge of the photoinduced effects, it is necessary to investigate the photoinduced effects on wide energy range. In the previous reports[1,2], we have reported the photoinduced effects on the optical bandgap and the photoconductivity of amorphous chalcogenide films by the irradiation of vacuum ultra-violet (VUV) light. In the present study, we performed an in-situ study of photoinduced effects by exciting inner core electrons and observed photoinduced changes on the total photoyield in amorphous chalcogenide (a-As_2S_3) films by VUV light.

Thin films of a-As_2S_3 used for the measurements of the total photoyield were prepared onto quartz substrates by conventional evaporation technique. The thickness of the films was around 6000 Å. An electrode using Al contact was fabricated first on the substrate for the measurements of the total photoyield, before depositing the amorphous films. The experiments were performed at a BL3A1 beam line of the UVSOR facility of the Institute for Molecular Science in Okazaki. VUV light that is filtered through an Al film from undulator radiation was used to measure the total photoyield. Before illumination, the samples were annealed at 443K (near the glass transition temperature) for two hours in a vacuum. To eliminate visible lights of synchrotron radiation and higher harmonics of undulator radiation, Al film was inserted between undulator and samples. The samples were fixed in sample chamber which were evacuated below 10^{-8} Torr. The photon flux of undulator radiation through Al film was estimated from the total photoelectric yield of gold mesh.

Figure 1 shows the photoinduced change on the total photoyield as a function of number of incident photon for a-As_2S_3 films. As shown in the figure, the total photoyield is slightly decreased, but it is gradually increased and it is seems to be finally saturated. The point of the saturation in the total photoyield is dependent on the energy of the excitation light. This is a new photoinduced effect caused by exciting inner core electron. It seems that the decrease and the increase in the total photoyield are related with the light induced metastable defects creation and photodarkening.

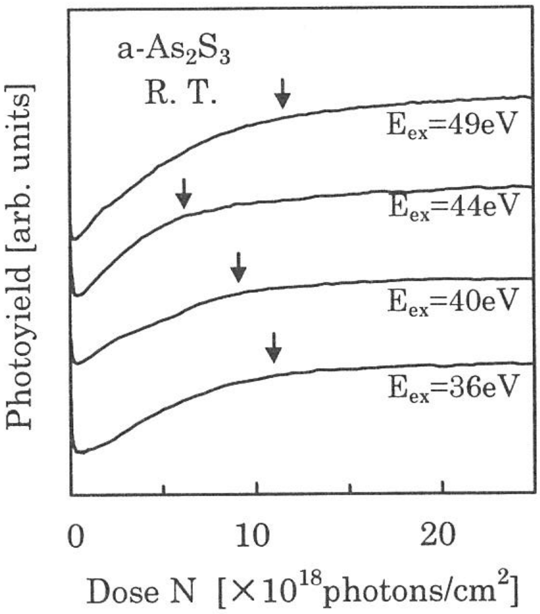

Fig.1 Photoinduced change on the total photoyield for a-As_2S_3 measured at room temperature.

REFFERENCES

[1] K. Hayashi, D. Kato, and K. Shimakawa, J. Non-Cryst. Solids., 198-200(1996)696.

[2] K. Hayashi, A. Hirai, and K. Shimakawa, UVSOR Activity Report 1996, p116.

(BL3A1)

Thermal Behavior of Holes in Lead Chloride Crystal

Mamoru KITAURA
Department of Applied Physics, Fukui National College of Technology, Sabae, 916-8507

Excitation with x-rays or ultra-violet (uv) lights induces intrinsic self-trapping of electrons at cation sites in $PbCl_2$. The self-trapped electron (STEL) center is represented by a Pb_2^{3+} diatomic molecular ion, which consists of an electron trapped at a pair of nearest neighbor Pb^{2+} ions in the direction along the *a* axis of the $PbCl_2$ crystal [1]. On the other hand, since the valence band of $PbCl_2$ is composed of lead 6*s* and chlorine 3*p* orbitals [2,3], possibility of self-trapped holes (STH's) at lead and chlorine sites is also expected. There seems to be, however, to our knowledge, few informations on structural and electronic features, or thermal behavior of holes in $PbCl_2$ so far. They are to be a subject of extensive studies with respect to photochemical decomposition in lead halides. In the present study, thermoluminescence (TL) from the $PbCl_2$ crystal pre-irradiated by a vacuum ultra-violet (vuv) light was investigated at the temperature range from 10 K to 150 K. The TL from the x-rayed $PbCl_2$ crystal has been studied by Bettinali *et al* [4]. They measured the TL glow curve in the temperature region above 80 K and found two peaks at 126 K and 180 K. The luminescent mechanism responsible for the two peaks has not been made clear yet.

Experiments were performed at BL3A1 of UVSOR. Quasi-monochromatic light from an undulator was used as an excitation light. The $PbCl_2$ specimens were mounted on the copper holder of a variable temperature cryostat of He-flow type. TL glow curves were observed at a constant heating rate of 0.1 K/sec. The TL intensity was detected by a photomultiplier without passing it through a monochromator. TL spectra at glow peaks were measured by using a monochromator (Spex 270M) equipped with a CCD camera (Princeton LN/CCD-1152B), and were corrected for the dispersion of the monochromator and for the spectral response of the detecting system.

Figure 1 shows a glow curve of the TL from the $PbCl_2$ crystal pre-irradiated by a vuv light at 36 eV. The dotted curve in Fig. 1 is calculated one, the detail of which will be described later. The TL intensity is normalized to unity at the maximum. The TL glow curve presents newly two peaks at 51 K and 71 K, besides the peak at 126 K, but does not exhibit the peak at 180 K. From electron spin resonance (ESR) experiments by Nistor *et al.*, the STEL centers are known to be stable below 130 K. Such thermal stability of the STEL centers

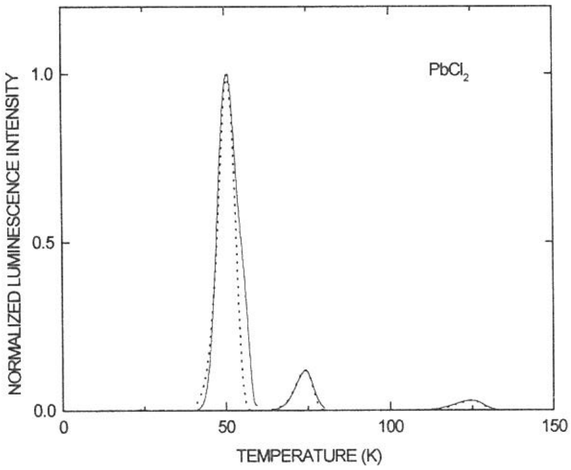

Fig. 1. Themoluminescence glow curve of $PbCl_2$.

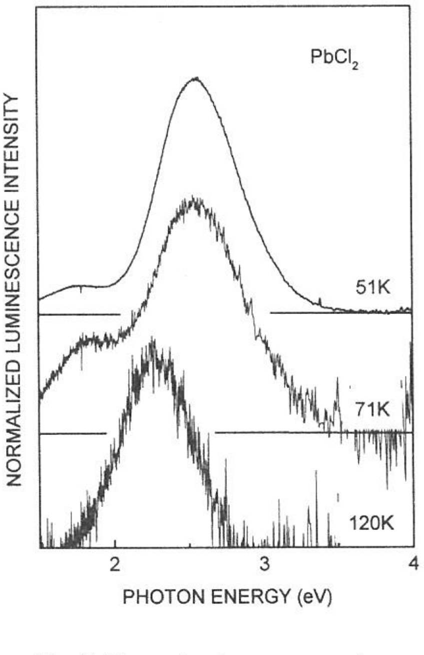

Fig. 2. Thermoluminescence spectra observed at 51 K, 71K, and 120 K

Table 1. Frequency factor ν_0 and activation energy E for each glow peak.

Peak (K)	51	71	120
ν_0 (s^{-1})	1.66×10^{9}	1.1×10^{11}	6.3×10^{11}
E (meV)	105	190	330

suggests that the two peaks at 51 K and 71 K originate from migration of holes thermally released from trapping centers. This is consistent with photoconduction studies [5] that revealed photoholes to be more movable carriers than photoelectrons in $PbCl_2$. On the other hand, the peak at 126 K would be reasonably connected to thermal decay of the STEL centers.

If de-excitation processes of electrons or holes captured by recombination centers are negligible, it is known that the TL intensity is given by

$$I(T) = n_0 \nu_0 \exp\left(-\frac{E}{\kappa T}\right) \exp\left\{-\int_{T_0}^{T} \frac{\nu_0}{\beta} \exp\left(-\frac{E}{\kappa T}\right) dT\right\}$$

where n_0 is the number of recombination centers at the temperature T_0 at which thermal stimulation is started, and β the heating rate; moreover, E and ν_0 are the activation energy and the frequency factor, respectively, for thermal migration of holes or electrons. The dotted curve in Fig. 1 is obtained by substituting the values in Table 1 for the parameters in the formula. It reproduces the TL glow curve observed, except the high-energy side of the peak at 51 K. Such deviation from the experimental data evidences the presence of a hole trapping center with slightly different structures.

The TL spectra observed at the three peaks are shown in Fig. 2. The intensity of the TL spectra is normalized to unity at the maximum of each spectrum. Two bands appear at 2.60 eV and 1.90 eV in the TL spectra at 51 K and 71 K, in which the 2.60 eV band is dominant. It was confirmed that glow curves for the two bands have peaks at 51 K and 71 K similarly. The 2.60 eV band, which is called as BG band, has been attributed to radiative recombination of a hole with an electron trapped at the STEL center [6]. This band is regarded as a intrinsic luminescence band in $PbCl_2$. The 1.90 eV band depends sensitively on sample conditions; therefore, it may be assigned to an extrinsic origin. On the other hand, another band is predominantly observed at 2.31 eV in the TL spectrum at 120 K. The origin of the 2.31 eV band is not clear at present.

Appearance of the BG band in the TL spectra at 51 K and 71 K suggests that, at least, two kinds of intrinsic hole trapping centers, that is, STH centers are created with the STEL centers. Furthermore, as far as electronic structures of the valence band of $PbCl_2$ are considered, it seems natural to expect self-trapping of holes at lead and chlorine sites in this material. Judging from these presumptive evidences, molecular ions of Cl_2^- and Pb^{3+} type are supposed to be plausible candidates for the STH centers in $PbCl_2$. The $PbCl_2$ crystal has several pairs of adjacent chlorine ions with slightly different separation and orientation, so slightly different Cl_2^- centers should be formed in $PbCl_2$. Thermal decay of the Cl_2^- centers will result in a TL glow peak which does not conform to the formula above. Actually in Fig.1, such a TL glow peak was observed at 51 K. It is, therefore, reasonable to connect thermal decay of the Cl_2^- centers to the TL glow peak at 51 K. On the other hand, the TL glow peak at 71 K probably arises from thermal decay of the Pb^{3+} centers. It is expected that, similarly to the case of alkali chlorides containing Pb^{2+} ions, the Pb^{3+} centers are formed when the Cl_2^- centers decay thermally.

REFERENCES

[1] S. V. Nistor, E. Goovaerts, and D. Schoemaker: Phys. Rev. B **48** (1993) 9575.

[2] J. Kanbe, H. Onuki, and R. Onaka: J. Phys. Soc. Jpn. **43** (1977) 1280.

[3] M. Itoh, T. Shiokawa, K. Sawada, and M. Kamada: J. Phys. Soc. Jpn. **67** (1998) 2140.

[4] C. Bettinali, G. Ferraresso, and E. Pacelli: J. Chem. Phys. **40** (1968) 3725.

[5] A. F. Halff and J. Schoonman: Phys. Stat. Sol. (a) **40** (1977) 511.

[6] M. Kitaura and H .Nakagawa: J. Electron Spectrosc. and Relat. Phenom. **79** (1996) 171.

[7] "*Structure Inorganic Chemistry*", ed. by A. F. Wells, (Clarendon Press, 1975) p. 222.

(BL3A-1)

The Initial Stage of Excitation Process by Undulator Radiation Light Using Scanning Tunneling Microscope

T.Hayakawa, H.Sato, A.Wakahara and A.Yoshida

Toyohashi University of Technology, Toyohashi 441-8580

In recent years, photo-enhanced chemical vapor deposition method (photo-CVD) using vacuum-ultra-violet-light (VUV-light) attracts much attention as a process technology in the following generation. However, since VUV-light in the photo-CVD process has a high photon energy, some influences to the substrate should be taken account. In order to obtain high quality functional thin films by using VUV-light excited CVD, it is important to know the initial stage on the film growth. Further investigations on the photon energy dependence are required. Scanning Tunneling Microscopy (STM) is a direct instrument working in real space on an atomic scale, and can give much information of surface reaction.

We have already clarified that the two kinds of images are observed on the sample irradiated with the Undulator Radiation (UR) : one is a dark spot and the other is a bright spot located at the center of dark circular image. The number of the patterns increased with increasing the UR light irradiation dose.

In the present work, we have investigated an effect of UR irradiation on substrate surface in vacuum with an in-situ UHV-STM.

In this experiment, we used MoS_2 as a substrate, because a clean surface can easily be obtained by the cleavage and the surface is not oxidized in air at room temperature. The UR irradiation was performed inside a reaction chamber with a base pressure below 3.0×10^{-8}torr. The undulator gap of 60mm corresponding to the 1st order photon energy of 36eV was used. Total dose was in the range of $5.0\times10^{18}\sim1.0\times10^{20}$photons/cm^2.

The surface structure was investigated on the UR light-induced defects by STM with constant height mode. The image was measured with the tip bias range of ±150mV.

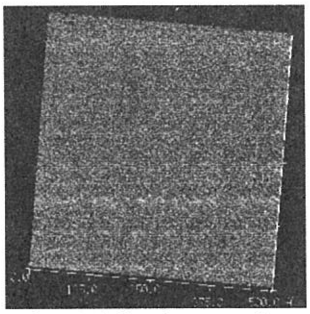

Fig.1 MoS_2 clean surface (500Å×500Å)

Figure 1 shows the STM image of MoS_2 clean surface on the 500Å×500Å scale with the sample bias voltage of -150mV and the tunneling current of 1nA.

Figure 2(a), (b), and (c) show the STM images of MoS_2 surface irradiated by UR light for 5.0×10^{18}, 3.1×10^{19}, and 1.0×10^{20}photons/cm^2 in vacuum, respectively. These images were observed on the 500Å×500Å scale, and the tip bias was +150mV. From these images, the

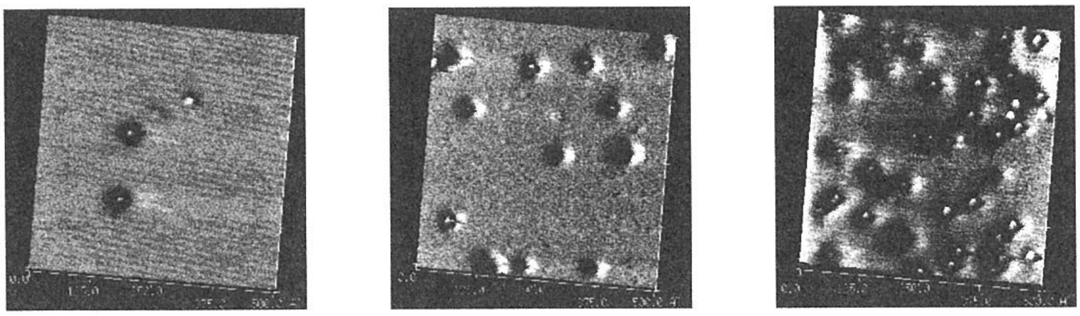

(a) 5.0×10^{18} photons/cm^2 (b) 3.1×10^{19} photons/cm^2 (c) 1.0×10^{20} photons/cm^2

Fig.2 MoS_2 surface reaction by UR light (500Å×500Å) depression region and the ring structure were found at the initial stages of irradiation. The number of the two kinds of patterns increased with increasing the irradiated dose.

The tip bias voltage dependence of two kinds of images is shown in a Fig. 3. The sample bias voltage in Fig. 3(a-1), and 3(b-1) was 150mV, and in Fig. 3(a-2), and 3(b-2) was -150mV. These images were observed on the 80Å×80Å scale. From Fig. 3(a-1) and 3(a-2), the dark circular region did not show voltage dependence. Therefore, the dark regions in the outside and at the center of VUV photon-induced defects are considered to ablated on the surface. From Fig. 3(b-1), and 3(b-2), the bright ring pattern in the dark region was observed. The bright ring pattern in the dark region are due to the positive charge localized at the center, so it is considered that some dark regions have some electrons trapped at the center of dark region.

In summary, effects of UR light irradiation on the MoS_2 surface have been investigated using STM. With the UR irradiation, the MoS_2 surface is modified, showing the initial stages of VUV photon-induced change on the irradiated surface on the atomic scale.

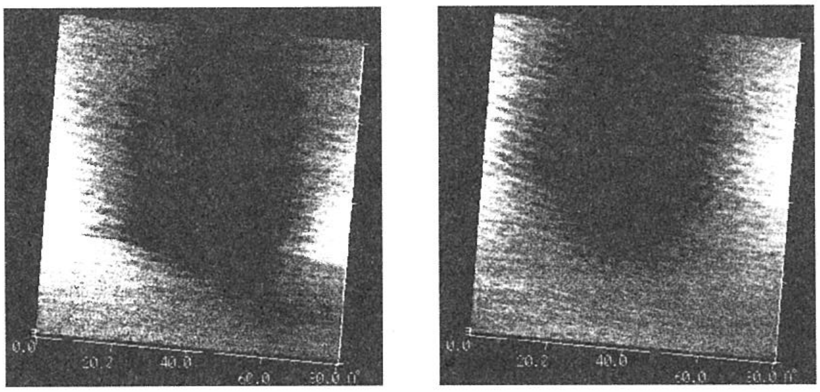

(a-1) tip bias voltage : 150mV (a-2) tip bias voltage : -150mV

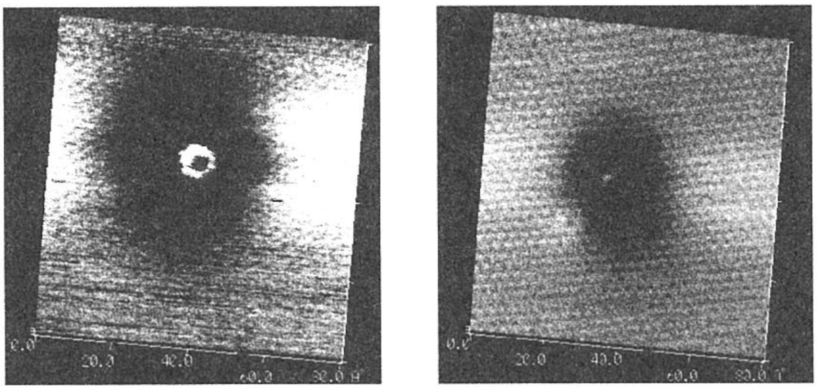

(b-1) tip bias voltage : 150mV (b-2) tip bias voltage : -150mV

Fig.3 STM images of the MoS_2 irradiated by UR light (80Å×80Å)

(BL3A2)

Dissociative photoionization of CF_4 from 23 to 120 eV

Toshio MASUOKA, Yoshikazu OGAKI, and Ataru KOBAYASHI

Department of Applied Physics, Faculty of Engineering
Osaka City University, Sugimoto 3-3-138, Sumiyoshi-ku, Osaka 558-8585

Using synchrotron radiation as a continuum light source, dissociative photoionization of CF_4 has been studied in the photon-energy region of 23-120 eV. The data were measured at UVSOR, Okazaki. Ion branching ratios were obtained by analyzing time-of-flight (TOF) mass spectra and were converted to the absolute cross sections for the production of singly charged CF_3^+, CF_2^+, CF^+, F^+, and C^+ ions as well as doubly charged CF_3^{2+} and CF_2^{2+} ions by using the reported total absorption cross sections[1] of CF_4.

TOF mass spectrometers are widely used to measure the ion branching ratios. However, it is not easy to measure ion branching ratios accurately at excitation energies where molecular and dissociative single and double photoionization take place concomitantly. Usually, the photoelectron signal is used as a start pulse for a time-to-amplitude converter (TAC) and the ion signal provides the stop pulse. With this arrangement, the different numbers of ejected electrons in single and double photoionization cause an overestimation of the number of the ions produced in double photoionization because the probability of forming one output pulse in the electron detector is higher for two electrons hitting simultaneously than that for one electron. This problem was overcome by using the rf signal of the storage ring as the start signal of the TAC.[2] Another problem is that when dissociative double photoionization occurs (e.g., $CF_4^{2+} \rightarrow F^+ + CF_3^+$), the heavier ion ($CF_3^+$) is not counted if the ion-detection efficiency is high. This is because the lighter F^+ ion stops the TAC. Since the ion-detection efficiency in the present study is of the order of a few percent, the heavier ion is detected with almost the same efficiency as the lighter ion.

The ion branching ratios are shown in Fig. 1 and the partial cross sections for the observed ions in Fig. 2. The absolute partial cross sections were obtained by the following equation:

$$\sigma_j(E) = [N_j(E) / \sum N_j(E)]Y(E)\sigma_t(E),$$

where σ_j is the partial cross section for a specific ionization process that produced the ion j, N_j is the number of ions of type j, $N_j(E)/\Sigma N_j(E)$ is the branching ratio, Y is the ionization yield (the number of ions produced/the number of photons absorbed in unit time), and σ_t is the total absorption cross section. Although the ionization yield in the region of dissociative double ionization is usually greater than unity, the yield in this region is not known at present and was assumed to be unity throughout the energy region studied. The overall agreement between the present data (●) and those of Brion *et al.*[1] (□) is excellent. Ion branching ratios were differentiated with respect to the incident photon energy. The results obtained by this analytical photoion spectroscopy show dissociation pathways of the CF_4^+ and CF_4^{2+}. These pathways will be discussed elsewhere by comparing them with the reported electronic states of the ions.

References
1) W. Zhang, G. Cooper, T. Ibuki, and C. E. Brion, Chem. Phys. **137**, 391 (1989).
2) T. Masuoka, Phys. Rev. A **48**, 1955 (1993).

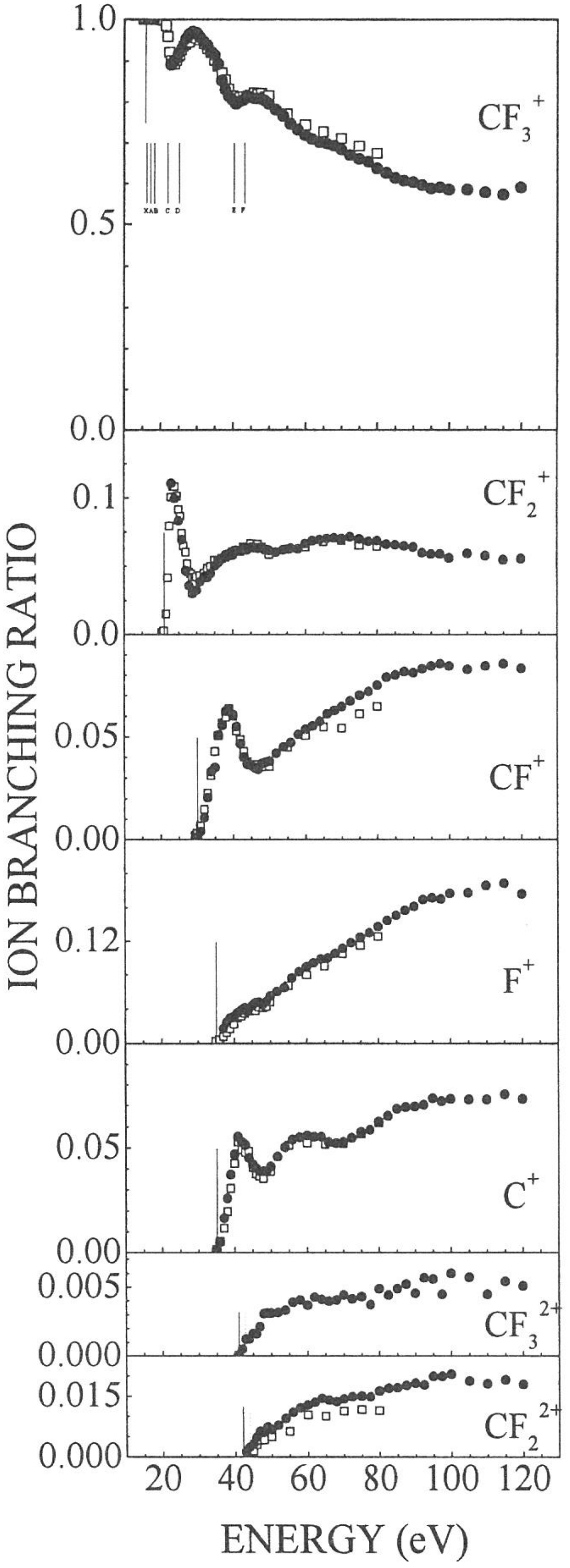

Fig. 1. Ion branching ratios of CF_4. ●, present data; □ from Ref. 1.

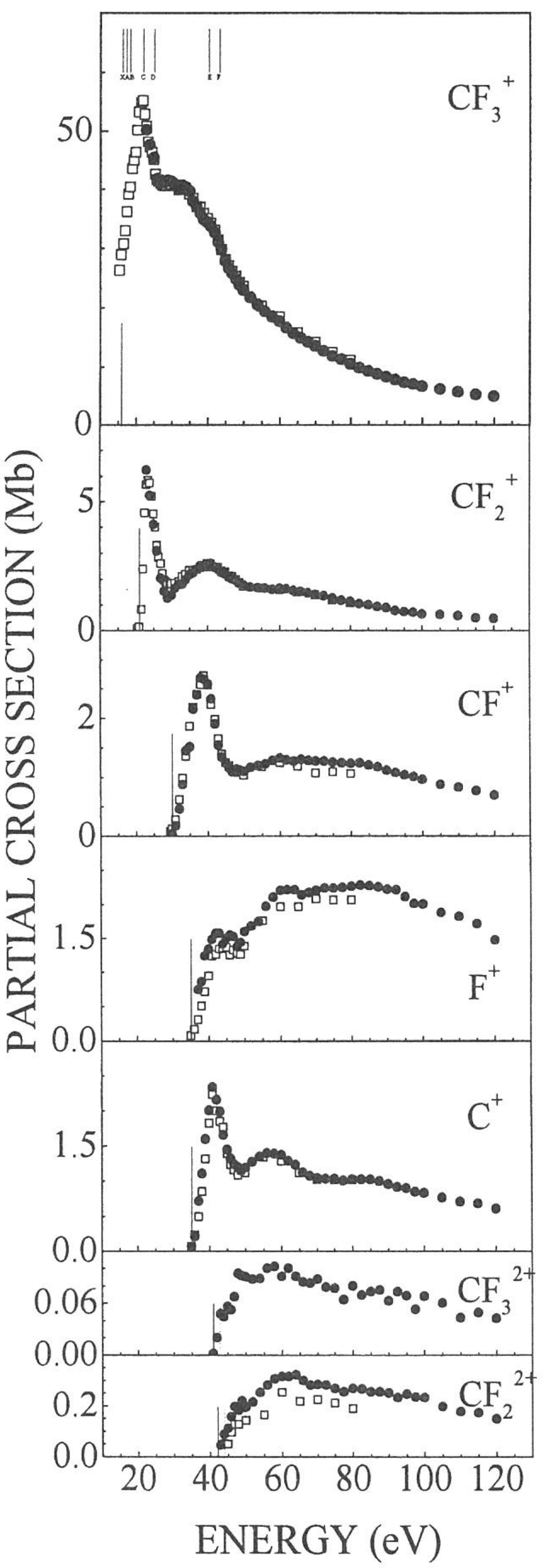

Fig. 2. Partial cross sections for the production of the observed ions.

(BL3A2)

Angular Distribution of Ionic Fragments in the Dissociation of SO_2^{2+}

Toshio MASUOKA, Yasuyuki KONISHI, and Ataru KOBAYASHI

Department of Applied Physics, Faculty of Engineering, Osaka City University
3-3-138 Sugimoto, Sumiyoshi-ku, Osaka 558-8585, Japan

Photoion-photoion coincidence (PIPICO) technique has been used to measure the angular distributions of $O^+ + SO^+$ and $O^+ + S^+$ fragments in the dissociative double photoionization of SO_2 in the 37-120eV region with linearly polarized synchrotron radiation.

For electric dipole transitions induced by linearly polarized radiation, the transition probability depends on the orientation of molecules with respect to the direction of polarization of the incident light, consequently this dependence gives rise to the anisotropic orientation of the molecular axes even though the distribution of the ground state molecules is isotropic. Therefore, the angular distributions of ionic photofragments provide detailed information on ionization and dissociation dynamics in terms of the symmetry of the dissociating parent states involved as well as the ejected electrons.

For molecules of cylindrical symmetry, asymmetry parameter β characterizing the angular distribution of the photofragments is given by the expression:

$$\frac{d\sigma}{d\Omega} = \frac{\sigma}{4\pi}\left(1 + \frac{\beta}{4}\left[1 + 3p\cos(2\theta)\right]\right),$$

where σ corresponds to the double ionization cross section, and the molecular axis is oriented along the direction Ω. θ is the angle between the molecular axis and the polarization of the incident light, or equivalently the angle between the direction of photofragment detection and the polarization direction. p is the degree of polarization of the light. In the present case, $p = 0.9$ was assumed.

According to the fact that, even though a molecule dissociates with any value of the asymmetry parameter, the PIPICO spectrum of the fragments detected at the magic angle of 54.7^0 gives the same plofile as that of the isotropic dissociation ($\beta = 0$), the kinetic energy distribution for a given photon energy is derived from the PIPICO spectrum at the detection angle of 54.7^0 by simulating the spectrum with $\beta = 0$. With the kinetic energy distribution thus obtained, the PIPICO spectra taken at two different detection angles ($\theta = 0^0$ and 90^0) are simulated by treating β as the fitting parameter. Practically the β value is determined so as to minimize the difference between the measured and calculated profiles. It should be mentioned here that in the present case the detection angle of 55^0 serves as "pseudo-magic angle" in the measurements where the angular dependence of the cross section almost vanishes. Energy variations of β thus derived are shown in Fig. 1 for $O^+ + SO^+$ and in Fig. 2 for $O^+ + S^+$.

In general, for a molecule undergoing a dipole transition involving a change of orbital angular momentum by +1 (Π tansition), the transition moment is perpendicular to the dipole axis, which gives a β value of -1. On the other hand, for a transition involving no change in orbital angular momentum (Σ transition), transition moment is parallel to the dipole axis, which gives a β value of 2. Thus, for a mixed transition where multi-states are involved, each component will contribute to an angular distribution, which in turn means that an experimental value for β provides the intensity ratio between the Σ and the Π components.

The overall feature of β values is a slight change in positive and negative sense around $\beta = 0$ in the whole energy range, indicating that the fragmentation is isotropic in the both cases of $O^+ + SO^+$ and $O^+ + S^+$. This shows a remarkable contract to the results of CO_2^{2+} where the anisotropic fragmentation is dominant in the low energy range less than 80eV.

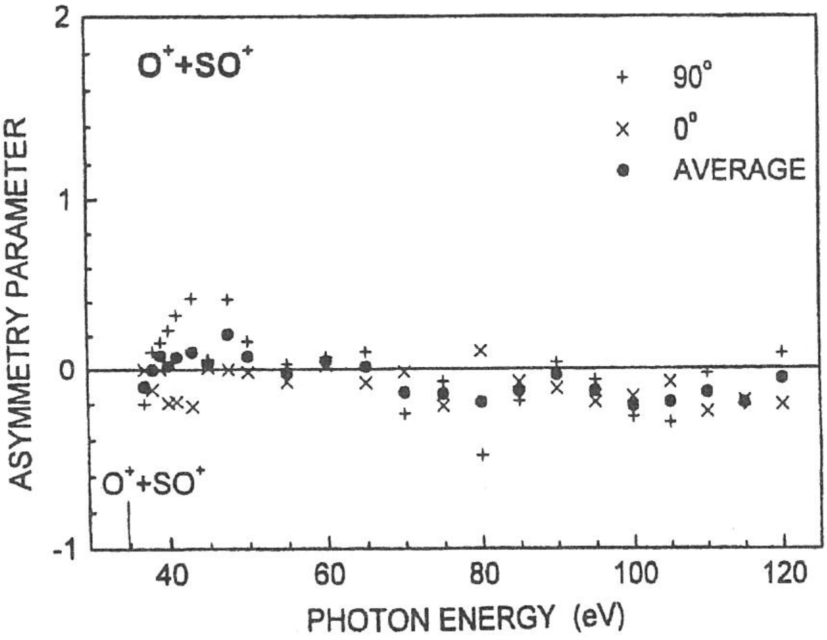

Fig. 1 The asymmetry parameter β for $O^+ + SO^+$ as a function of photon energy. The solid line marks the $\beta = 0$ isotropic reference. The averaged values are derived from the results at two different detection angles of 0^0 and 90^0. See text in more details.

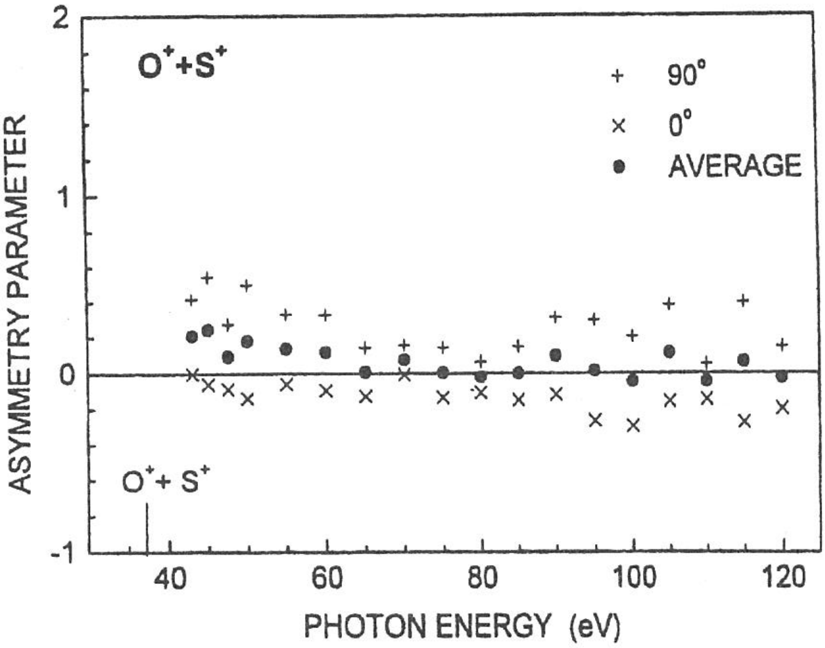

Fig. 2 The asymmetry parameter β for $O^+ + S^+$ as a function of photon energy. The solid line marks the $\beta = 0$ isotropic reference. As in the case of Fig. 1, the averaged values are derived from the results at two different detection angles of 0^0 and 90^0. See text in more details.

(BL3A2)

Laser Induced Fluorescence Excitation Spectroscopy of $N_2^+(X\ ^2\Sigma_g^+, v = 0)$ Produced by VUV Photoionization of N_2 — Rotational State-Resolved Spectrum

Masakazu MIZUTANI, Hiromichi NIIKURA[A] and Koichiro MITSUKE

Department of Vacuum UV Photoscience, Institute for Molecular Science,
Okazaki 444-8585, Japan
[A]The Graduate University for Advanced Studies, Okazaki 444-8585, Japan

The pump-probe experiment combining synchrotron radiation and a laser is expected to be a feasible method for probing ionic and neutral fragments resulting from VUV photoexcitation. We have developed laser induced fluorescence (LIF) excitation spectroscopy of products prepared by VUV excitation of gas phase molecules with synchrotron radiation.[1,2] Sample gases, N_2 and N_2O, expanded from a multi-capillary nozzle were photoionized with an undulator radiation supplied from the beam line 3A2. Formed N_2^+ ($X\ ^2\Sigma_g^+$, $v''=0$) ions were excited to the $B\ ^2\Sigma_u^+$, $v'=0$ state by irradiation of the second harmonic of a mode-locked Ti:sapphire laser, whose repetition rate is 90.115 MHz, and the fluorescence due to the transition ($B\ ^2\Sigma_u^+$, $v'=0$) → ($X\ ^2\Sigma_g^+$, $v''=1$) was detected. The rotational temperature of N_2^+ ($X\ ^2\Sigma_g^+$, $v''=0$) could be evaluated by simulating an LIF excitation spectrum. Previously, it had taken a long time for data acquisition because of an extremely low rate of fluorescence counts. The low count rate was considered to result from the short residence time of produced ions which escape from the laser-irradiation region in a few microseconds. Short residence time decreased the effective number density of N_2^+ ions. In order to lengthen the residence time we newly introduced a quadrupole RF ion trap composed of a central ring electrode and two end electrode.

The undulator radiation monochromatized by a grazing-incidence monochromator is introduced into an ion trap through one of 4 apertures which are equispaced on the side of the central ring electrode. The laser is introduced through the opposite aperture so as to counterpropagate the undulator light. The effusive beam of sample gas is injected through the other aperture and crosses perpendicularly with the two photon beams. The fluorescence from laser-excited N_2^+ is collected through an aperture drilled on the end electrode. A secondary monochromator equipped with a color filter glass is used to eliminate the scattering laser light. An RF voltage with an amplitude of 300 $V_{P\text{-}P}$ and a frequency of 1 MHz is applied to the central ring electrode. The fluorescence count rate is 40 times as high as that without the ion trap. Data acquisition time is reduced to one tenth of the previous acquisition time.

Figure 2 shows an LIF excitation spectrum of the ($B\ ^2\Sigma_u^+$, $v'=0$) ← ($X\ ^2\Sigma_g^+$, $v''=0$) transition of N_2^+ which is prepared by photoionization of N_2 at the photon energy of the synchrotron radiation, E_{SR} = 15.983 eV. In the report of the fiscal year of 1997, the spectral resolution of the laser was set to about 15 cm^{-1} and the rotational structure of the ($B\ ^2\Sigma_u^+$, $v'=0$) ← ($X\ ^2\Sigma_g^+$, $v''=0$) transition cannot be resolved. In the present spectrum, the pulse duration of the laser is expanded and the spectral resolution is improved to about 1.7 cm^{-1}, though the laser intensity is a tenth as high as the previous set up. The rotational lines at wavelengths shorter than 391.15 nm are well resolved and assigned to transitions for the R branch. In contrast, the lines at longer wavelengths, which comprise the P branch, are overlapped with each other because the band-head lies in the P branch and spacings between the lines are narrower than the spectral resolution.

The synchrotron radiation energy E_{SR} = 15.983 eV is equal to the resonance energy for the formation of $4d\sigma_g\ {}^1\Pi_u$ state converging to $N_2^+(A\ {}^2\Pi_u, v=0)$. Hence, most N_2^+ ions are considered to be produced by autoionization of this Rydberg state. The LIF excitation spectrum is simulated on the assumption that the rotational temperature of $N_2(X\ {}^1\Sigma_g^+, v=0)$ is 300 K and the propensity rule of rotational excitation accompanied by autoionization, $K_{mol.} = K_{ion}, K_{ion} \pm 1, \ldots, K_{ion} \pm l$, where $K_{mol.}$, K_{ion} and l denotes the total angular momentums apart from spin of neutral superexcited molecule, formed molecular ion and the orbital angular momentum of the ejected electron [3]. The experimental spectrum is similar to that obtained by the simulation. Details of this simulation will be described in a forthcoming paper.

References

1) M. Mizutani, H. Niikura, A. Hiraya and K. Mitsuke, *J. Synchrotron Rad.* **5** (1998) 1069-1071.
2) K. Mitsuke, M. Mizutani, H. Niikura and K. Iwasaki, *Rev. Laser Eng.* **27** (1998) 458-462.
3) G. Herzberg, *Molecular Spectra and Molecular Structure, I. Spectra of Diatomic Molecules,* (1966) p. 419

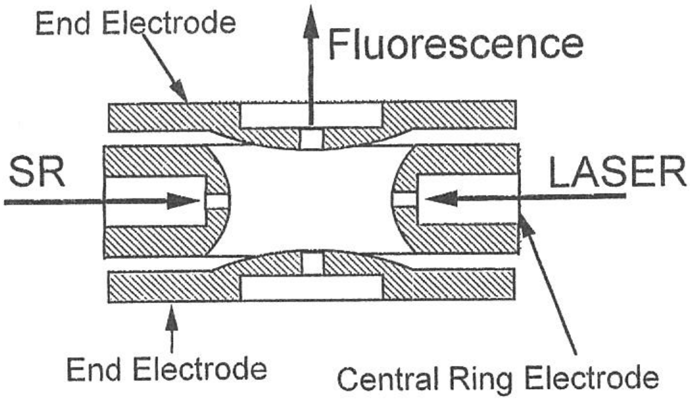

Figure 1. Schematic diagram of the ion trap.

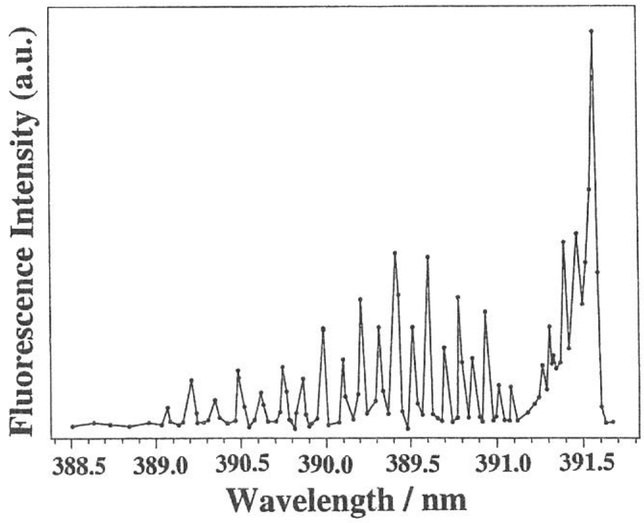

Figure 2. Laser induced fluorescence excitation spectrum of the $(B\ {}^2\Sigma_u^+, v'=0) \leftarrow (X\ {}^2\Sigma_g^+, v''=0)$ transition of N_2^+ which is prepared by photoionization of N_2 at E_{SR} = 15.983 eV. The monitored fluorescence is ascribed to the transition $(B\ {}^2\Sigma_u^+, v'=0) \rightarrow (X\ {}^2\Sigma_g^+, v''=1)$.

(BL3A2)

Laser Spectroscopy of Neutral Fragments from Superexcited States Prepared by Synchrotron-Radiation Photoexcitation

Hiromichi NIIKURA[A] , Masakazu MIZUTANI[B], Kota IWASAKI[B] and Koichiro MITSUKE[B]

[A]*Graduate Univ. for Advanced Studies,*[B] *Institute for molecular science, Myodaiji, Okazaki 444-8585, Japan.*

We have developed pump-probe spectroscopy making use of the combination of UV laser and synchrotron radiation to investigate the dynamics of neutral dissociation of superexcited molecules. For detecting neutral species, a resonance enhanced multiphoton ionization (REMPI) technique is invoked. The schematic experimental setup is shown in Fig. 1. Undulator radiation emitted from beamline BL3A2 of UVSOR is crossed perpendicularly with a molecular beam discharged from a pulsed nozzle. Produced ions are extracted toward electrode 1 by a retarding filed between electrodes 1 and 2. A part of neutral fragments produced by VUV excitation are sampled through an aperture of electrode 2 and ionized by a frequency-doubled dye laser (1 - 2 mJ pulse^{-1}) focused with an f = 500 mm lens on the space between electrodes 2 and 3. Ions produced by (2+1)-REMPI of neutral fragments are detected with a quadrupole mass filter equipped with a channeltron electron multiplier.

We have measured a REMPI spectrum of S ($3s^2 3p^4$ $^3P_{J''}$, J'' = 0, 2) dissociated from superexcited states of OCS prepared by photoexcitation with undulator radiation (BL3A2, UVSOR) whose photon energy ranges from 13 to 17 eV. The spectral resolution of the second harmonic of a probe laser was estimated to be 0.003 nm. Figure 2 shows a REMPI spectrum of S ($3s^2 3p^4$ $^3P_2$) atom as a function of the probe laser wavelength in the region including the two-photon transition, S ($3s^2 3p^3 5p$ $^3P_{J'}$) ← S ($3s^2 3p^4$ $^3P_2$). The undulator photon energy was fixed at 16.5 eV. The maximum at 269.290 nm is considered to comprise two peaks resulting from transitions from S ($3s^2 3p^4$ $^3P_2$) to S ($3s^2 3p^3 5p$ $^3P_1$ and $^3P_2$), though they are not separated because of a low signal-to-background ratio. As well as S ($3s^2 3p^4$ $^3P_2$), we have observed the REMPI signal of S ($3s^2 3p^4$ $^3P_0$) at 271.375 nm; this wavelength corresponds to a two-photon transition from S ($3s^2 3p^4$ $^3P_0$) to S ($3s^2 3p^3 5p$ $^3P_0$). Next, we fixed the laser wavelength at the maximum of the curve in Fig. 2, *i.e.*, 269.290 nm, and measured the REMPI signal intensity as a function of the energy of the undulator radiation in the range of 13 - 17 eV. The resultant spectrum is considered to represent a relative photodissociation cross section curve for the formation of S ($3s^2 3p^4$ $^3P_2$) from OCS. Peak features existing at 13 - 16 eV and

16 - 17 eV are ascribed to the Rydberg series converging to the $B\ ^2\Sigma^+$ and $C\ ^2\Sigma^+$ states, respectively, of OCS$^+$. In summary, we can obtain direct evidence for the first time for the formation of nonfluorescing and non-autoionizing neutral species dissociated from molecular superexcited states, by means of pump-probe spectroscopy combining synchrotron radiation and laser.

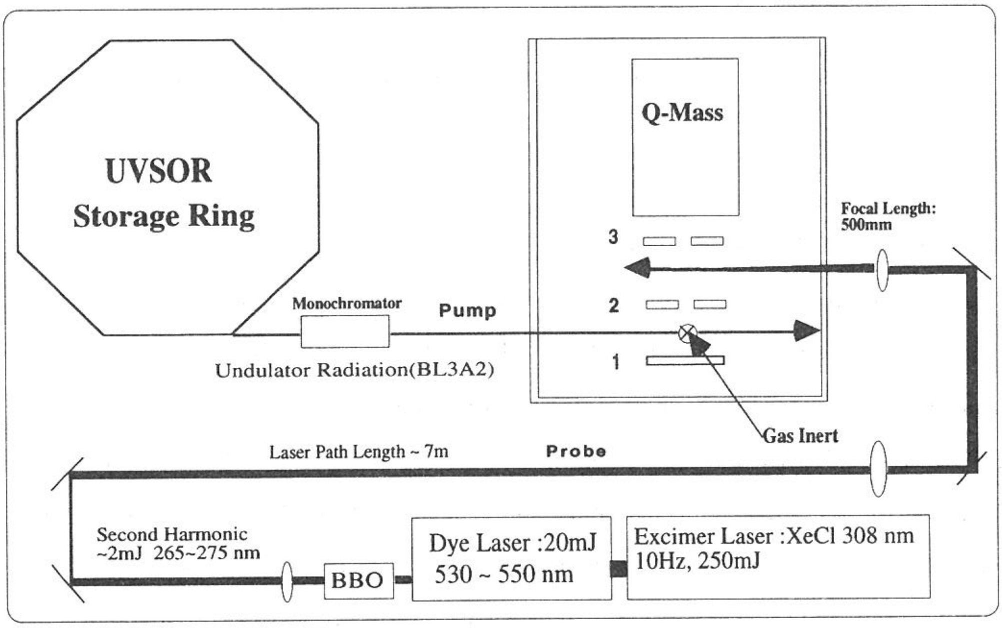

Figure 1. Schematic experimental setup for the REMPI spectroscopy of neutral fragments produced by synchrotron radiation excitation.

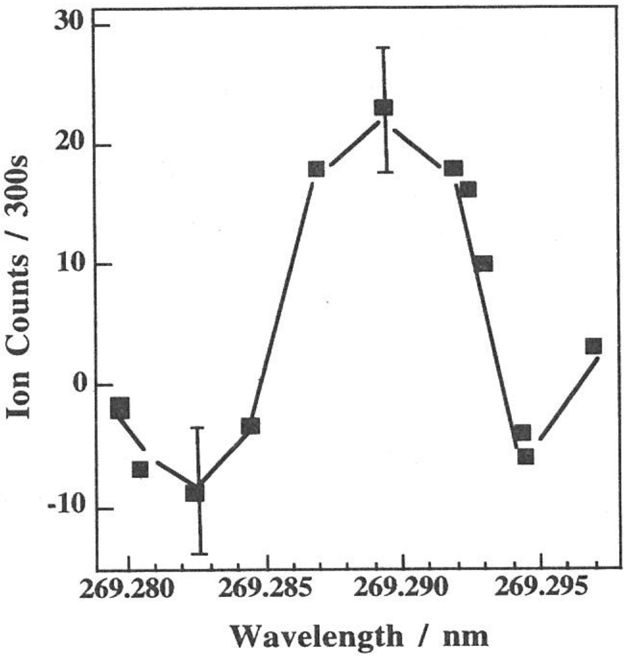

Figure 2. Laser REMPI spectrum of S ($3s^2 3p^4\ {}^3P_2$) produced by photoexcitation of OCS at the undulator photon energy of 16.5 eV.

(BL3A2)

Rotational and Vibrational Distributions of N_2^+ Produced from Superexcited States of N_2 and N_2O

Hiromichi NIIKURA[A], Masakazu MIZUTANI[B], Kota IWASAKI[B] and Koichiro MITSUKE[B]
[A]*Graduate Univ. for Advanced Studies,* [B]*Institute for Molecular Science,*
Myodaiji, Okazaki 444-8585, Japan.

Vibrational Distribution of $N_2^+(X\ ^2\Sigma_g^+)$ from N_2

The electronically ground state of N_2^+ is produced from N_2 or N_2O by direct ionization or autoionization using synchrotron radiation and observed by laser induced fluorescence (LIF) excitation spectroscopy. The experimental setup and procedures have been described in the preceding report of Mizutani *et al.* Figure 1 shows the yield curves of $N_2^+(X\ ^2\Sigma_g^+$, v", N") for (a) v" = 0 and (b) v" = 1, measured as a function of the photon energy of the synchrotron radiation. The spectral resolution was set to 2.4 Å. The wavelength of the probe laser were tuned to 391.54 nm and 388.53 nm in Panels (a) and (b), respectively, where the transitions $(B\ ^2\Sigma_u^+$, v' = 0) ← $(X\ ^2\Sigma_g^+$, v" = 0) and $(B\ ^2\Sigma_u^+$, v' = 1) ← $(X\ ^2\Sigma_g^+$, v"= 1), respectively, give rise to the band head in the *P* branch of concomitant rotational structures. The fluorescence was dispersed and detected by a second monochromator with a maximum transmission at 427 and 423 nm, in agreement with the central wavelengths in the rotational distributions of the transitions $(X^2\Sigma_g^+$, v" = 1) ← $(B^2\Sigma_u^+$, v' = 0) and $(X\ ^2\Sigma_g^+$, v" = 2) ← $(B\ ^2\Sigma_u^+$, v' = 1), respectively. Resonance peaks in Fig. 1 can be identified to Rydberg states converging to the ionization threshold of $N_2^+(A\ ^2\Pi_u)$; their assignments are given in Fig.1. The two spectra in Fig. 1 exhibit similar peak features, though obvious differences in the relative peak intensity are recognized. One of the most marked features is that the relative intensity of the $4d\delta g\ ^1\Pi_u$, v = 1 state at 771.6Å is enhanced in Panel (b). This result is consistent with the relative partial photoionization cross sections for the formation of $N_2^+(X^2\Sigma_g^+$, v = 0 and 1) from N_2 reported by Haworth *et al.* [1)] They have concluded that 75 % of Rydberg molecules in the $4d\delta g\ ^1\Pi_u$, v = 1 state undergo autoioniation into $N_2^+(X\ ^2\Sigma_g^+$, v = 1).

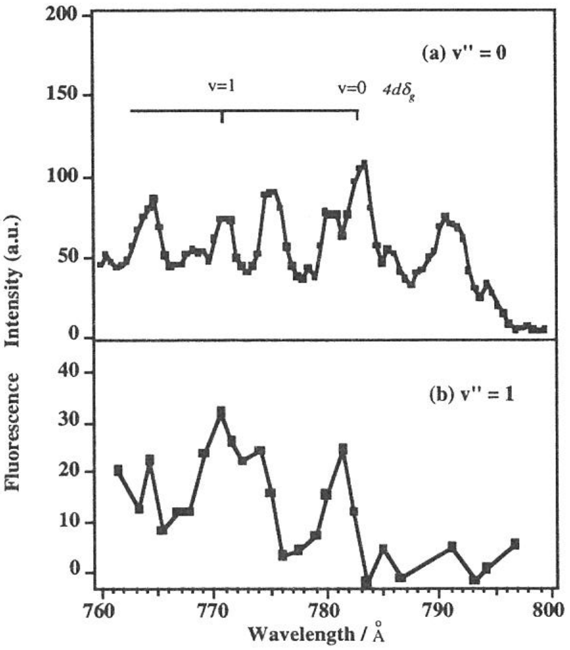

Figure 1. Yield curves of $N_2^+(X\ ^2\Sigma_g^+$, v", N") for (a) v" = 0 and (b) v" = 1.

Rotational Distribution of $N_2^+(X\ ^2\Sigma_g^+, v = 0)$ from N_2O

Figure 2 shows an LIF spectrum of $N_2^+(X\ ^2\Sigma_g^+, v'' = 0)$ produced from N_2O by synchrotron radiation photoexcitation at 18.987 eV. The two maxima centered at 391.54 nm and 390.8 nm are ascribed to the *P* and *R* branches, respectively, for the $(B\ ^2\Sigma_u^+, v' = 0, N') \leftarrow (X\ ^2\Sigma_g^+, v'' = 0, N'')$ transitions. Since the spectral resolution of the laser was approximately 15 cm^{-1}, the rotational lines are heavily overlapped. The rotational temperature of $N_2^+(X\ ^2\Sigma_g^+, v'' = 0)$ can be roughly estimated by comparing the ratio between the peak heights of the *P* and *R* branches, as long as the relative intensities of the rotational levels of N_2^+ produced by autoionization obey the Boltzmann distribution. The obtained value is 200 - 300 K. The solid line in Fig. 2 represents a spectrum at 250 K calculated by using the theoretical intensity distribution of rotation bands convoluted with a laser spectral width of 13 cm^{-1}.

[1] A. Haworth, D. G. Wilden and J. Comer, J. Electron Spectrosc. Relat. Phenom. **37** (1985) 291.

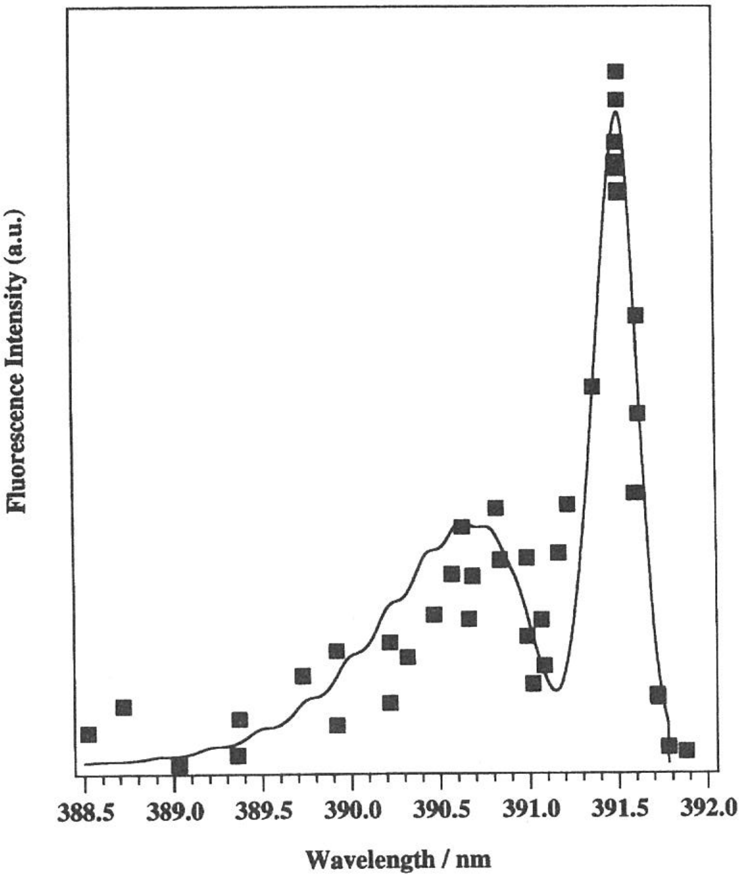

Figure 2. LIF spectrum of $N_2^+(X\ ^2\Sigma_g^+, v'' = 0)$ produced from N_2O. Photon energy of synchrotron radiation is fixed at 18.987 eV.

(BL3A2)

Dissociative Photoionization of $Mn(C_5H_5)(CO)_3$ in the Mn 3p Inner-Valence Region.

Yusuke Tamenori and Inosuke Koyano

Department of Material Science, Himeji Institute of Technology, Kamigori 678-1297

In previous X-ray absorption and electron energy loss measurements on various transition metal compounds, it has been suggested that a strong photoionization resonance can be found in the vicinity of metal np ionization threshold, which can be attributed to the transition from metal np orbital to an unoccupied molecular orbital. However, there has been little information about ion fragmentation following such resonance transition. We are performing a series of detailed studies of dissociative photoionization of various transition metal compounds in the inner valence region by use of the TOF mass spectrometry and photoion-photoion coincidence (PIPICO) technique. [1,2] In the present work, the dissociative photoionization of $Mn(C_5H_5)(CO)_3$ is studied in the vicinity of Mn 3p inner-valence region (55eV).

Figure 1 shows an example of TOF mass spectrum of $Mn(Cp)(CO)_3$ ($Cp = C_5H_5$) at 58eV of incident photons and with 20.0cm of flight tube length. The most intense fragment ion is Mn^+. Ions having a formula $Mn(Cp)(CO)_n^+$ (n=0,1,3) also show high abundance. On the other hand, the fragment ions having a formula $Mn(CO)_n^+$ are seldom observed. This fact shows that the Mn-CO bond cleavage occurs before the Mn-Cp bond cleavage. These results indicate that ion fragmentation dominantly proceeds by primary loss of the CO molecules. The CO elimination is followed by cleavage of Mn-Cp bond, and finally, Mn^+ is formed.

$$\begin{aligned} Mn(Cp)(CO)_3 + h\upsilon \quad &\rightarrow \quad Mn(Cp)(CO)_n^+ + (3-n)\,CO \\ &\rightarrow \quad Mn(Cp)^+ + 3\,CO \\ &\rightarrow \quad Mn^+ + Cp + 3\,CO \end{aligned}$$

The fragment ions Cp^+ and $C_3H_m^+$ are also abundant. This observation is in good agreement with the results of the previous investigation of ferrocene. [1] However, the abundance of CO^+ is relatively small and those of C^+ and O^+ are almost null in the ion fragmentation of $Mn(Cp)(CO)_3$. This result contrasts strikingly with that of ion fragmentation in the transition-metal carbonyl compounds. [2] It may indicate that the positive hole created in a CO ligand is quickly filled by electron transfer from Mn(Cp) before CO^+ elimination or C-O bond cleavage.

As the photon energy increases from below to above the Mn 3p ionization threshold (55eV), the intensities of the doubly charged ions of the formula $Mn(Cp)(CO)_n^{2+}$ show an increase. However, these ions amount to only a few percent in the mass spectra and thus the variation of these ions are very small. We can not find any remarkable variation in ion mass spectra when photon energy is tuned at the Mn 3p ionization threshold.

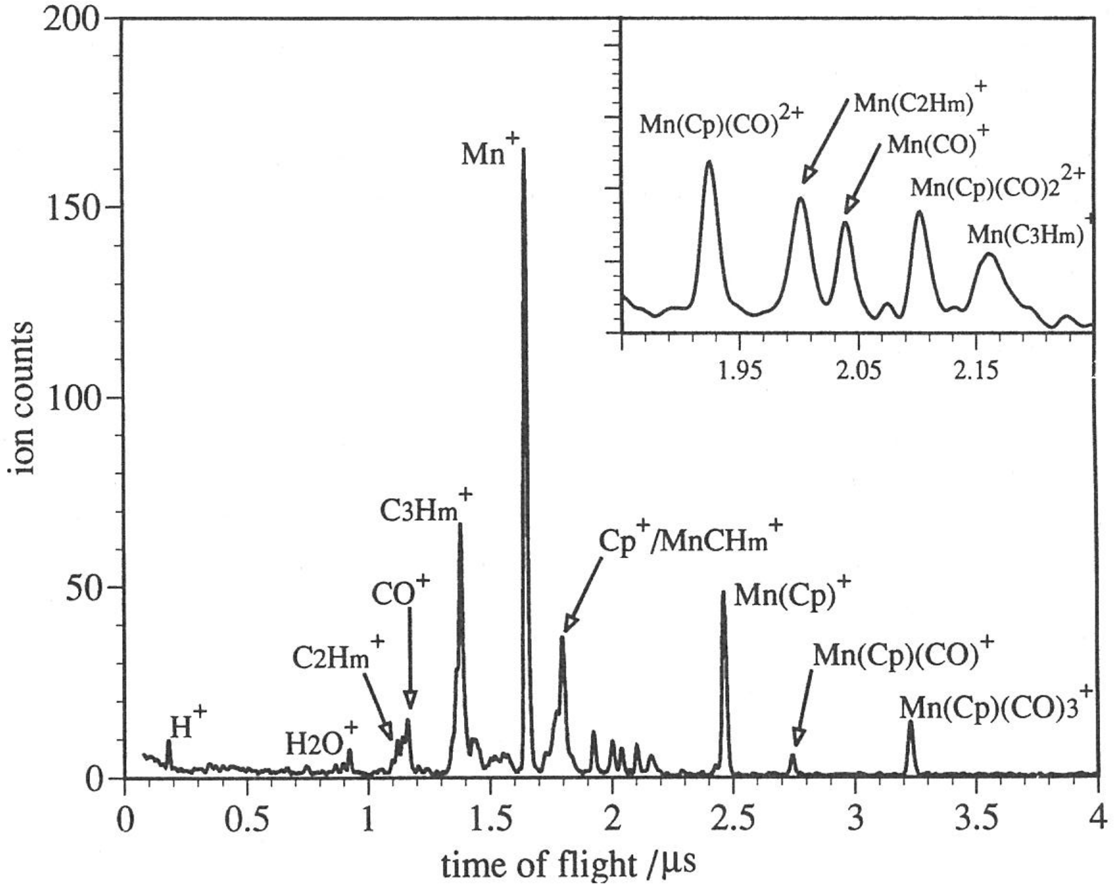

Figure 1; A PEPICO (TOF mass) spectrum of $Mn(Cp)(CO)_3$ taken at 58eV of incident photon energy and 20.0cm of flight tube length.

References

1, Y. Tamenori, and I. Koyano, UVSOR Activity Report (1997), P74

2, Y. Tamenori, K. Inaoka, and I. Koyano, J. Electron. Spectros. Rela. Phenom. 79, 503 (1996); Y. Tamenori, and I. Koyano, J. Phys. Chem. A101, 368 (1997)

(BL-3B)

Laser photoionization electron spectroscopy of polarized rare gas atoms excited with synchrotron radiation

Kota IWASAKI[A], Yasumasa HIKOSAKA[B] and Koichiro MITSUKE[A]

[A] *Institute for Molecular Science, Myodaiji, Okazaki 444-8585 , Japan*
[B] *Institute for Materials Structure Science, oho, Tsukuba 305-0801, Japan*

We have performed laser photoionization spectroscopy of polarized rare gas atoms in order to study spin-orbit interactions of many electron systems and exploit the possibility of the complete photoionization experiment. Rare gas atoms in a gas cell are excited by linearly polarized synchrotron radiation (85-100nm) supplied from the beamline BL3B and aligned toward the electric vector. The light beam of a Nd:YAG laser (532nm) intersects with the synchrotron radiation at a right angle and ionize the aligned targets. The electric vector of the laser can be rotated by using a half wave plate. Photoelectrons, emitted in the direction perpendicular to both the laser and synchrotron radiation, are detected with a 160° hemispherical electrostatic analyzer.

A two-dimensional spectrum of Kr is shown in Fig. 1. Major spots due to high photoelectron yield are aligned on two straight lines with a slope of unity; these spots are assigned to two final ionic states of Kr^+ $[^2P_{1/2,\ 3/2}]$. Since electronic states of excited Kr atoms are designated by a J_c- ℓ coupling scheme, a total angular momentum of the product ion J_f can be expected to be equal to that of a core ion of an excited state J_c. However, this picture seems to disagree with the present results in some cases. There are two possible explanations for this disagreement: the excited states designated by the J_c- ℓ coupling are influenced by mixing of J_c of 1/2 and 3/2, or an ejected electron exchanges angular momenta with the ion core during the photoionization process.

In Fig 2(a), the photoelectron yield for $Ar(5s'[1/2]_1) \rightarrow Ar^+(^2P_{1/2}) + e^-$ ($\ell=1$; $j=1/2, 3/2$) is plotted as a function of the angle ψ_e between the electric vector of the laser and the direction of the linear momentum of photoelectrons. The angular distribution should be interpreted in terms of a p wave from excited Ar aligned toward the electric vector of synchrotron radiation. We have obtained an asymmetry parameter ß of 1.96 from this result. The angular distributions have also been measured for photoelectrons produced by the process $Ar(3d[1/2]_1) \rightarrow Ar^+(^2P_{Jf}) +$ e^- ($\ell=1$ or 3; $j=1/2, 3/2$ or $5/2, 7/2$) with $J_f=1/2$ and 3/2. As shown in Fig. 2(b), the ß values for these distribution curves are much smaller than that for photoelectrons from the $5s'[1/2]_1$ state. We are planning the complete photoionization experiment to determine dipole matrix elements and a phase shift difference of each partial wave.

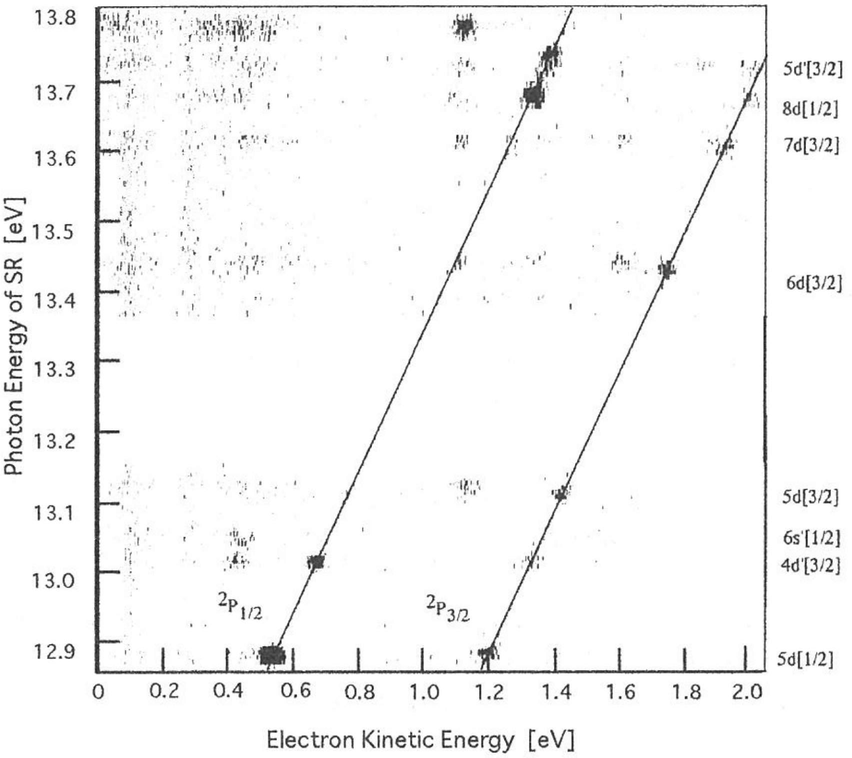

Fig 1. Two-dimensional spectrum of Kr. The electric vector of the laser is parallel to the direction of photoelectrons

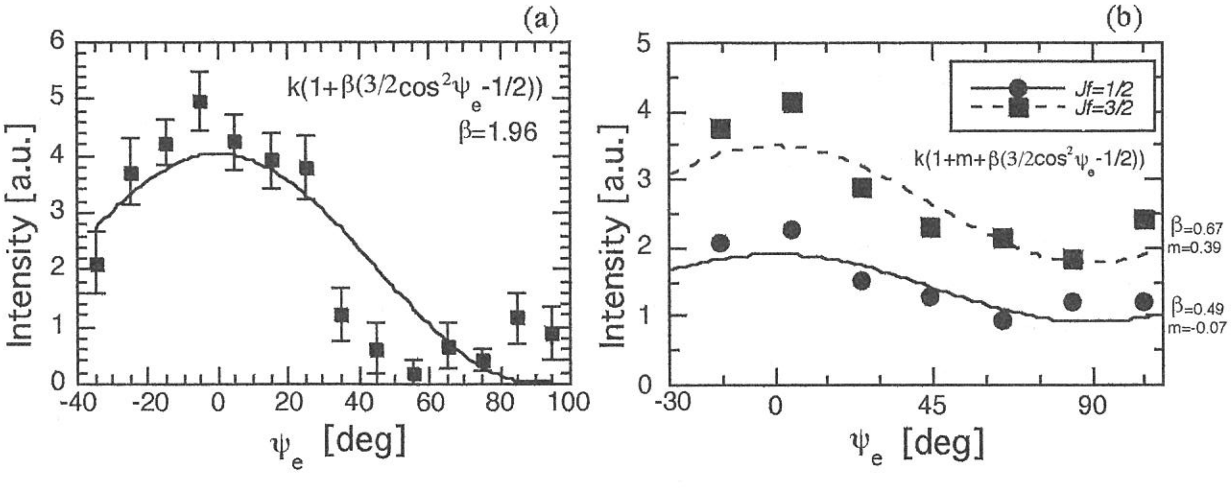

Fig. 2. Angular distributions of photoelectrons: (a) Ar(5s'$[1/2]_1$)→Ar$^+$($^2P_{Jf}$) and (b) Ar(3d$[1/2]_1$) →Ar$^+$($^2P_{Jf}$). Photoelectron yields were measured as a function of ψ_e.

(BL3B)

Spectator- and Participant-Like Behavior of a Rydberg Electron on Predissociation of Superexcited States of OCS

Yasumasa Hikosaka[A],Hideo Hattori and Koichiro Mitsuke

Institute for Molecular Science, Myodaiji, Okazaki 444-8585, Japan
[A] *Present address: Inst. of Mater. Struct. Sci., Oho, Tsukuba 305-0801, Japan*

Predissociation of superexcited states of OCS is studied by two-dimensional photoelectron spectroscopy using synchrotron radiation in the photon energy range of 15 - 16.5 eV.[1)] A two-dimensional photoelectron spectrum exhibits two kinds of characteristic patterns both of which are ascribed to autoionization of sulfur atoms. To clarify the point, we show a photoelectron spectrum of Figure 1 which is obtained as a cut through the two-dimensional spectrum along the electron kinetic energy axis at the phootn energy of 15.95 eV.[2)] The superexcited atom S* is produced by predissociation of a Rydberg state OCS*(R_B) converging to OCS$^+$($\tilde{B}\,^2\Sigma^+$). The pattern of the first kind results from predissociation processes in which the effective principal quantum number n of the Rydberg electron is almost conserved. This suggests that the Rydberg electron behaves as a spectator because of its negligibly weak interaction with the ion core (spectator predissociation). On the contrary, n of S* does not accord with that of OCS*(R_B) in the pattern of the second kind, indicating that the Rydberg electron participates directly into the electron exchange mechanism controlling conversion from OCS*(R_B) to a predissociating state (participant predissociation). With increasing n, OCS*(R_B) decays more preferentially by the spectator than by the participant predissociation. The spectator predissociation of OCS*(R_B) proceeds through a two-step conversion which involves Rydberg states converging to OCS$^+$($\tilde{A}\,^2\Pi$ and $\tilde{X}\,^2\Pi$) and a dissociative multiple-electron-excited state OCS*(*SAT*) asymptotically correlating with S* + CO($\tilde{X}\,^1\Sigma^+$). In contrast, the participant predissociation may be accounted for by a direct conversion from OCS*(R_B) to OCS*(*SAT*). The quantum yields are estimated from Figure 1 to be 0.07 and 0.02 for the participant and spectator predissociation, respectively, at the incident photon energy of 15.95 eV where OCS*(R_B) states with $n \sim 12$ lie. A simulation is performed to reproduce the partial cross section curve for the spectator predissociation by using a model in which the decay rates for the participant and spectator predissociation are assumed to be proportional to n^{-3} and n^0, respectively. The simulated and experimental cross section curves are in good agreement with each other at the photon energy higher than 15.8 eV.

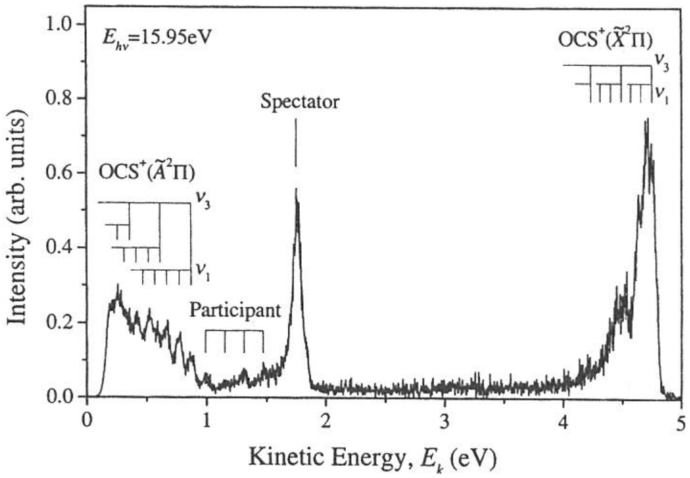

Figure 1. Photoelectron spectrum of OCS at the photon energy of 15.95 eV where OCS*(R_B) states with $n \sim$ 12 are located.

References

1) Y. Hikosaka, H. Hattori, T. Hikida, and K. Mitsuke, *J. Chem. Phys.* **107,** 2950 - 2961 (1997).
2) Y. Hikosaka, H. Hattori, and K. Mitsuke, *ibid.* **110,** 335-344 (1999).

(BL4A1)

Al thin film deposition on Si substrate surface stimulated by monochromatized SR

Harutaka Mekaru[A], Tsuneo Urisu[B]

[A]*The Graduate University for Advanced Studies,*
[B]*Institute for Molecular Science, Myodaiji, Okazaki 444-8585*

We constructed a multilayered-mirror (MLM) monocromator beam line at the UVSOR for the purpose of SR stimulated process studies. Based on our previous experiments of Al thin film deposition using dimethylaluminum hydride (DMAH),[1] we consider a total photon flux density higher than 10^{18} photons/cm^2 as a criterion for the necessary total flux, in the SR stimulated process experiments. This means that a monochromatized-photon flux larger than 10^{13}-10^{14} photons/s is needed, if we consider a reasonable irradiation time (a few tens of minutes to a few hours) and an irradiation area ($\geqq 3 \times 3$ mm^2) on the substrate surface applicable even to the device fabrications.

The output beam of the constructed beam line was applied to the Al thin film deposition using DMAH low temperature condensed layer. Details about the sample treatments are described in ref. 1. Si (100) substrate treated by conventional wet process was introduced into the reaction chambe. After cooling to about 100K, the DMAH gas was introduced and deposited on the substrate (10 –20 monolayers), then, the monochromatized SR beam (θ =50° , 84 eV) tuned to the Al 2p core electron excitation was irradiated for about 56 minutes at the average ring current of 100 mA. (This corresponds to the calculated total photon flux of 5×10^{17} photons/cm^2 on the sample surface). After the irradiation, the substrate temperature was increased to the room temperature to remove the unreacted DMAH, the composition of the deposited film was measured by XPS. As shown in Fig. 1, the deposited Al thin film was observed visually, although the thickness was not measured. An interesting point is the C concentration of the deposited film. The XPS spectra observed for the DMAH low temperature condensed layer is shown in Fig. 2A, and those for the deposited Al film is shown in Fig. 2B. By assuming C/Al=2 for DMAH condensed layer, the composition C/Al of the deposited film is estimated to be about 0.5. This value is quite small compared with those of films obtained by the white or filtered white SR beams irradiations. This may be due to that the Al-C bond is preferntially broken by the Al core electron excitations. To discuss the excitation energy dependence, much more detailed experiments are necessary. The data shown in Fig. 2, however, indicates clearly that the MLM monochromator beam line constructed have a sufficient performance as an SR stimulated process beam line.

Reference

1) Y. Imaizumi, Y. Tusaka, T. Urisu, and T. Ibuki, *Jan. J. Appl. Phys.* **35**, 6588 (1996)

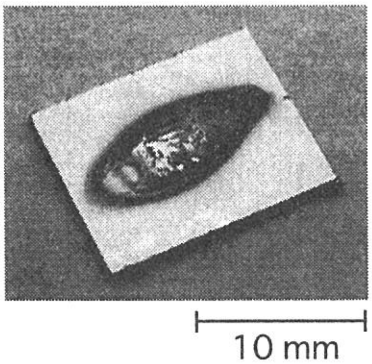

Figure 1. Photograph of the deposited Al thin film.

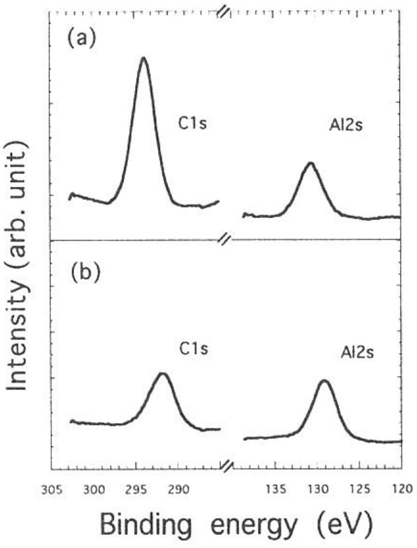

Figure 2. The observed XPS spectra for (A) the DMAH condensed layer at 105K and (B) the deposited Al thin film.

(BL4A1)

Performance of the Multilayered-mirror monochromator and the beam line BL4A1

Harutaka Mekaru[A], Toyohiko Kinoshita[B], Tsuneo Urisu[B].

[A]The Graduate University for Advanced Studies,
[B]Institute for Molecular Science, Myodaiji, Okazaki 444-8585

In this paper, we describe the performance of a double crystal type MLM monochromator combined with an appropriate thin-film filter that reduces the total reflection component, developed for SR stimulated process experiments. The MLM monochromator was installed in a beamline (BL4A1) of the UVSOR storage ring in the Institute for Molecular Science (IMS). The photon flux and the monochromaticity of the output beam were experimentally evaluated for the case of using Mo/Si MLMs combined with a C filter.

We first calculated the photon flux of the output beam as a function of photon energy, as shown in Fig. 1, taking into consideration the acceptance angles and reflectivity of the pre-mirror, the reflectivity of two MLMs calculated by assuming an ideal structure, and the transmission of the C filter. The transmission (84.4%) of the mesh holding a thin C film was also considered in addition to the transmission of the 120-nm-thick C filter. The characteristics of the output beam from the MLM monochromator beamline were estimated using Mo/Si MLMs and the C filter. A 120±24-nm-thick C filter was set behind the MLM monochromator to reduce the low energy background existing less than 40 eV. A 150±30-nm-thick Al filter was set at the downstream of the C filter to evaluate the monochromaticity of the output beam by measuring the transmission spectrum of the Al filter near the Al $L_{2,3}$ absorption edge. The intensities of the beam at the downstream of the C and the Al filter were measured by the Si photodiode detector as well as by the Au detector.

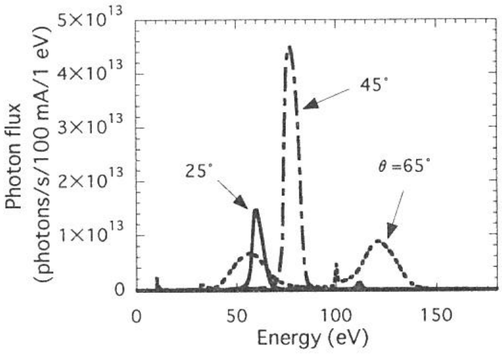

Fig. 1. Calculated spectra of the photon flux of output beam of the MLM monochromator beamline (BL4A1) using Mo/Si MLMs and a C filter (thickness 120nm).

Next, we measured the dependence of the photon flux on θ using the Si photodiode detector and compared it to the calculation, as shown in Fig. 2. The calculated flux is obtained by integrating the photon flux spectrum in the photon energy range from 0 to 2 keV for various θ values in Fig. 1. The monochromator does not operate at the normal incident angle side ($\theta \leqq 10^\circ$) because of the significant reductions of the MLM reflectivity and the transmission of the C filter. It also dose not operate at the grazing incident angle side ($\theta \geqq 55^\circ$) because of the significant increase of the background. If we require for the photon flux to be more than 1.0×10^{12} photons/s and for the background to be less than 15% (in the case of using Mo/Si MLMs combined with the C filter), the incident angle range which gives a practical output beam is determined to be between 10° (55 eV) and 55° (93 eV), as shown by dotted lines a and b in Fig. 3. The maximum intensity of the

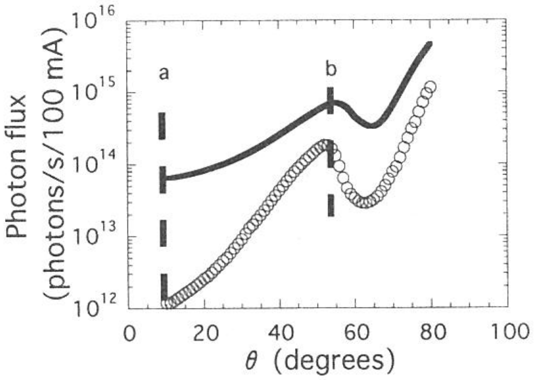

Fig. 2. The dependence on the incident angle θ of the photon flux of output beam. The solid line shows calculated values and "○" shows measured values. The dotted lines a and b show the working region of the monochromator.

photon flux of the output beam is obtained at about $\theta = 55^\circ$. The reduction of the photon flux over $\theta = 55^\circ$ is due to the absorption of Si (Si $L_{2,3}$) used as a MLM material. The measured photon flux at 55° was about 24% of the calculated value as shown in Fig. 3. If we attribute this difference of the measured value and the ideal value equally to the incompleteness of the pre-mirror and two MLMs and possible cut of the beam edge by the C filter, then the MLM's reflectivity would be estimated to be about 10% of the ideal value. We think this is a reasonable value, considering that we did not pay special attention to obtain MLMs with high reflectivity.

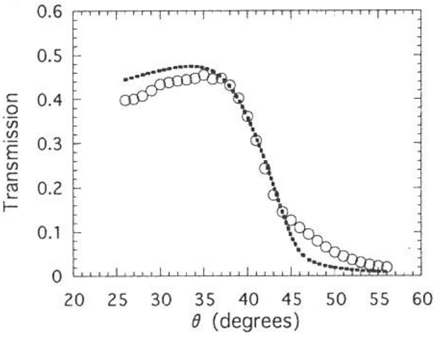

Fig. 3. The transmission of the Al filter in the vicinity of the Al $L_{2,3}$ absorption edge measured ("○") by using output beam of the monochromator as a function of θ. The dotted line represents calculated values. (An Al filter thickness of 180 nm and the transmission of 74.8% for the mesh holding the thin Al film are assumed.)

To evaluate the spectrum width, the contribution of the higher-order photon, and the low-energy background caused by the total reflection, the transmission characteristics of the monochromator output beam for the Al filter near the Al $L_{2,3}$ absorption edge were measured as a function of θ. The results are compared with the calculation in Fig. 3. The calculated transmission was obtained by taking the ratio between the integrated photon flux behind the C filter and that behind the Al filter for each θ value. In the calculation, the thickness of the Al filter was varied within the catalog value 150±30 nm to fit the calculation to the experiments. The broken curve in Fig. 3 was calculated for a thickness of 180 nm. Considering the error of the optical constants with MLM and filter materials and the structural incompleteness of the MLM, for which precise evaluations are difficult, the calculated results agree well with the experimental results. Thus, we conclude that the spectrum width should be almost equal to the calculated width (5 - 9 eV in 55 - 93 eV peak energy range), and the background is almost equal to the level predicted by the calculation.

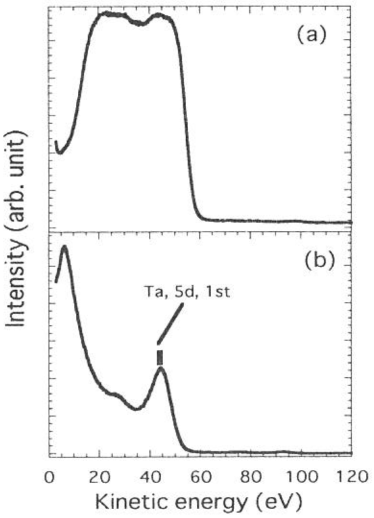

Fig .4. The photo-emission spectra of Ta excited by the output beam from the MLM monochromator. Mo/Si MLMs are used and $\theta = 20$ degrees: (a) the case without the C filter and (b) the case with the C filter. "1st" means the peak excited by the first-order photon component of the MLM monochromator output.

To confirm these conclusions, we measured the photo-emission spectra of Ta, which is expected to give two dominant peaks (4f and 5d) close to the Fermi edge for an excitation energy of 50 - 100 eV,using the monochromator output photons as an excitation light source. A CL150 analyzer and a HAC300 controller (VSW Inc.) equipped in the XPS chamber were used in this measurement. After acetone and methanol washing, the Ta substrate was introduced into the XPS chamber and heated up to about 850 K for 4 hours. The observed photo-emission spectra, excited by an output beam of $\theta = 20^\circ$, without filters (a) and with the C filter (b), are shown in Fig. 4. The clear peak assigned to the Ta 5d bands is observed in Fig. 4 (b), but not in (a). This indicates that the C filter sufficiently reduces the low-energy background. We confirmed that the present MLM monochromator using a Mo/Si MLM in combination with a C filter works well as predicted by the calculation in the energy range from 55 eV ($\theta = 10^\circ$) to 93 eV ($\theta = 55^\circ$). In this range, the photon flux of output beam was 1.0×10^{12} - 1.5×10^{14} photons/s, the spectrum width was 5 eV ~ 9 eV, the low-energy background was less than 7.2%, and the higher-order (second-order) photon background was less than 12%. We conclude that the MLM monochromator beamline (BL4A1) constructed here performs sufficiently well for studying the excitation-energy dependence in the SR stimulated processes.

(BL4B)

Synchrotron-radiation stimulated desorption of SiO_2 thin films on Si(111) surfaces observed by scanning tunneling microscopy

T. Miyamae [a], H. Uchida [b], I. H. Munro [a,c], and T. Urisu [a]

[a] *Institute for Molecular Science, Myodaiji Okazaki, 444-8585, Japan*

[b] *Electrical and Electronic Engineering, Toyohashi University of Technology, Tempaku-cho, Toyohashi, 441-8580, Japan*

[c] *Department of Physics, University of Manchester Institute of Science and Technology (UMIST), Manchester M6010D, UK*

Synchrotron radiation (SR), which involves wavelengths ranging from infrared to x-ray, is thought to be a suitable light source in photo-excitation. Recently, scanning tunneling microscopy (STM) is a powerful tool to obtain the information about the surface morphology and the local electronic structures. STM should give us various information about the SR-irradiated surfaces with atomic scale resolution. On the other hand, silicon dioxide films are also known to be removed during SR-irradiation at elevated temperatures in an ultrahigh vacuum (UHV).[1] Therefore, SR-stimulated desorption of SiO_2 films have been the target of intense research in the field of surface science and the semiconductor devices.

A STM system was constructed at BL4B of UVSOR. During STM measurement, the STM chamber was covered by a soundproof mat because of the elimination of the acoustic noise from the rotary pumps, turbomolecular pumps, and compressors of other beamlines in the UVSOR.

The sample (3×8 mm^2) was an *n*-doped Si(111) wafer with a thickness of 0.5 mm and a resistivity of about 1 Ω/cm. The thickness of the native oxide layer treated by the above method was about 1 nm. Mechanically ground Pt/Ir tips were used without any special cleaning for the STM measurements.

Figure 1 (a) shows the LEED pattern observed after 2 h SR-irradiation, which gave a 19200 mA·min dose, to the sample at a surface temperature of 700°C. At a sample temperature of 700°C, the 7×7 spots were observed, even for the 0.5 h SR-irradiation, although the intensities of the 1/7-order diffraction were fairly weak compared with those of the thermally cleaned Si surface. Notice that the SR non-irradiated region, LEED spots were not observed, and meaningful changes were not observed in the Auger spectra before and after the SR-irradiation at this temperature.

In Fig. 2, we show a topograph of the occupied states of the Si(111) surface after 2 h SR-irradiation to the samples at a temperature of 700°C. The morphology of the SR-irradiated surface seems to be rather inhomogeneous, and quite different from that in the usual thermal desorption process.[2-4] The bright grains in Fig. 2 (a) indicate areas of residual oxide and the dark regions correspond to the exposed Si surfaces. The grain height is uncertain since we have not determined the barrier height difference for the clean and oxide covered surfaces. Figure 2 (b) shows a magnified topograph of the dark region in Fig. 3 (a). Atomic image of Si(111)-7×7 surface was clearly observed and several bright sites were found in the STM topograph of the Si surface. The most important result in the present study is that the nanometer-size void structures, which are observed in the thermal desorption process, are not formed on SR-stimulated surfaces. In the case of the thermal desorption of thin SiO_2 films, the nanometer-size holes (voids) were created.[3,4] These void formations can be explained by Si atoms, which are supplied from the substrate lattice, migrating to the edge of the residual oxide. Such voids were not found in the SR-stimulated surface, indicating that the desorption mechanism is completely different from that associated with the thermal desorption processes of the SiO_2 films.

Next we consider the mechanism of SR-stimulated desorption of SiO_2. When a SR beam is irradiated to a SiO_2 film, the valence and core electrons of both Si and O atoms are excited.[1] SR induces Si-O bond breaking [5] and the photo-stimulated oxygen atom or ion desorption takes place on the oxide surface. High Si-content regions are formed as a result of oxygen desorption from the oxide surface. In the SiO_2, SR also forms numbers of defects such as non-bonding oxygen (Si-O), peroxyl bridges (Si-O-O-Si), peroxyl radicals (Si-O-O), and Si dangling bonds in the SiO_2 film.[6] By heating the sample, these defects dissociates and desorbs the oxygen, and volatile SiO, which can be thermally desorbed, is formed over the whole SR-irradiated area. Consequently, an atomically flat surface is obtained. From this model, it is predicted that the desorption of oxide film by SR-irradiation proceeds preferentially at the defect rich regions such as grain boundaries. This is consistent with the observation of inhomogeneous STM images shown in Fig. 2 (a). The model is also consistent with the observation of atomically flat SR-irradiated surfaces.

References

1 H. Akawaza, J. Takahashi, Y. Utsumi, I. Kawashima, and T. Urisu, J. Vac. Sci. Technol., A 9, 2653 (1991).

2 R. Trump, G. W. Rubloff, P. Balk, F. K. LeGoues, and J. Van Loenen, Phys. Rev. Lett., 55, 2332 (1985).

3 K. E. Johnson and T. Engel, Phys. Rev. Lett., 69, 339 (1992).

4 H. Watanabe, K. Fujita, and M. Ichikawa, Appl. Phys. Lett., 70, 1095 (1997).

5 D. E. Ramaker, J. Vac. Sci. Technol., A 1, 1137 (1983).

6 E. P. O'Reilly and J. Robertson, Phys. Rev. B 27, 3780 (1983).

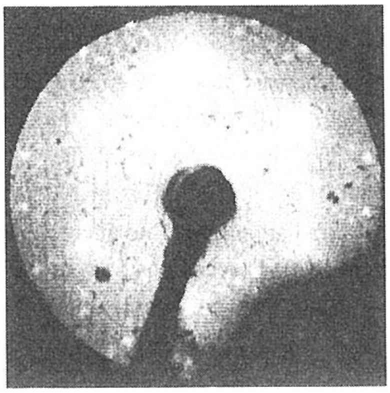

Fig. 1. (a) The LEED pattern for the SR-irradiated native oxide film on Si(111) surface. The primary electron energy is set at 50 eV. The SR-irradiation was made for 2 h at a sample temperature of 700°C.

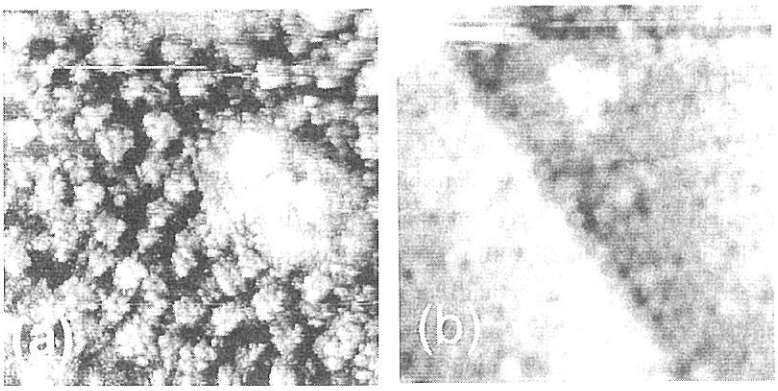

Fig. 2. (a) STM image of the SR-irradiated sample surface. The SR-irradiation was made for 2 h at a temperature of 700°C. The image is 250 × 500 nm. (b) Magnification of topograph in (a). The image is 20 × 20 nm.

(BL-4B)

Annealing and Synchrotron Radiation Irradiation Effect on Hydrogen Terminated Si(100) Surfaces Investigated by Infrared Reflection Absorption Spectroscopy

Shinya Hirano[a], Hideyuki Noda[a] and Tsuneo Urisu[b]

[a]The Graduate University for Advanced Studies, Myodaiji, Okazaki, 444-8585
[b]Institute for Molecular Science, Myodaiji, Okazaki, 444-8585

We are considering the application of synchrotron radiation (SR) stimulated processes, which have characteristics of high spatial resolution and low damage, to nano structure fabrications on semiconductor surfaces. From this viewpoint, the understanding and the control of the chemical nature of chemisorbed hydrogen on Si(100) surfaces are extremely important research subjects in SR processes as they are commonly occurring processes. In this work, the structure of the D-Si(100) 1x1 surface formed at 400 K and its change by annealing and SR irradiation have been investigated by measuring the high resolution IR spectrum by the BML-IRRAS method using a $CoSi_2$ BML Si(100) substrate, and reflective high-energy electron diffraction (RHEED).

The SiD stretching vibration band[1)] and its change by annealing observed by BML-IRRAS are shown in Fig. 1. The observed change of the SiD stretching vibration band due to the annealing plus SR irradiation is shown in Fig. 2. The change of the integrated absorbance (IA) and the peak position of the SiD stretching vibration band, with increasing annealing temperature are shown in Figs. 3(A) and 3(B), respectively.

The rapid decrease of the IA at around 700 K (Figs. 1 and 3(A)) and the corresponding peak shift to the lower frequency side (Fig. 3(B)) is explained by the decrease of the dipole-dipole coupling interaction.[1)] It is known that monohydride phase desorption occures through preparing mechanism, i.e., desorbs through the precursor form of H-Si-Si-H (D-Si-Si-D). Therefore, it is concluded that the surface after the annealing at 650 K or higher is covered only by D-Si-Si-D, if there exist no defects on the surface, and the sharp SiD stretching vibration band observed in Fig. 1 (spectrum D and E) is assigned to the D-Si-Si-D symmetric stretching vibration. On the other hand, the increase of the IA with annealing temperature increase from 570 to 650 K is explained by the thermal decomposition of $2SiD_2$ to D-Si-Si-D. It is reported that the SR irradiation decomposes di- and trihydrides but not the monohydride.[1)] In the present case, a slight increase of the IA of the SiD stretching vibration band is observed upon 570 K annealing plus SR irradiation (Fig. 3(A)▲). This increase is explained by the decomposition of dideuteride to monodeuteride by the SR irradiation, since no increase is observed only upon 570 K annealing (Fig. 3(A)○). Concerning this dideuteride decomposition by SR irradiation, not only desorption of deuterium atom by breaking the Si-D bond, but also the possibility of the etching (desorption of SiD or SiD_2) must be considered. By comparing Figs. 1 and 2, we can discuss this etching effects from a different viewpoint. By annealing at 650 K or higher, if there is no defect on the Si(100) surface, the existing surface deuteride species become only D-Si-Si-D (preparing mechanism) as experimentally verified by STM.[2)] Therefore, the IRRAS SiD stretching vibration band shape becomes sharp and symmetric as observed in Fig. 1 (D and E). However, the observed results are quite different in the case of SR irradiation plus annealing. The SR irradiation effects clearly appear in the shape of the IRRAS SiD stretching vibration band i.e., at the annealing temperature higher than 650 K, where only monodeuteride exists, the band shape becomes broad and asymmetric as shown in Fig. 2 (D, E and F), and as more clearly shown in Fig. 4, where the band shapes are compared for the cases of annealing only (670 K) and annealing (670 K) + SR irradiation. This asymmetric shape can be explained by the etching of the Si(100) surface by the SR irradiation. If there are no defects on the Si(100) surface, the surface hydride species should be, as already mentioned, only D-Si-Si-D, which are thermodynamically stable in the high temperature region where the surface migration of deuterium atoms frequently occurs. But, the observed SiD stretching vibration band shape shows that the surface species are not just D-Si-Si-D. Therefore, it is concluded that some defects are generated by SR irradiation on D-Si(100)1x1 surface which consists of D-Si-Si-D and D-Si-D, and it is concluded that the defects are generated by SR stimulated desorption (etching) of D-Si-D, since monodeuteride is not decomposed by SR irradiation. Since only monodeuteride exists on the surface after 650 K annealing, the component of the low frequency side tail of the SiD stretching vibration band in the high temperature region above 650 K in Figs. 2 or 4 is assigned to the stretching vibration of Si-D at the defect site generated by the etching. This means that the SR irradiation induces not only the desorption of D by breaking the Si-D bond, but also the desorption of SiD and/or SiD_2 by breaking the backbonds of D-Si-D.

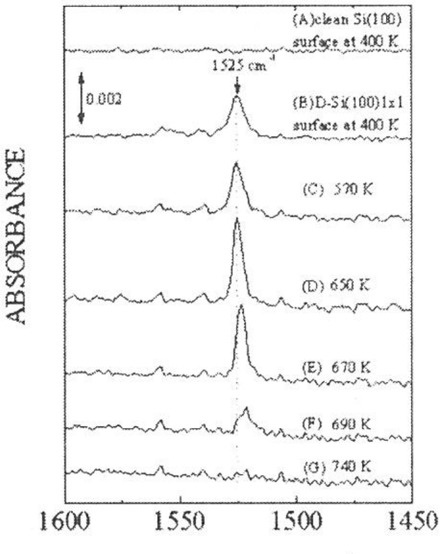

Figure 1. The change of the IRRAS spectrum of the SiD stretching vibration band with increase in annealing temperature.

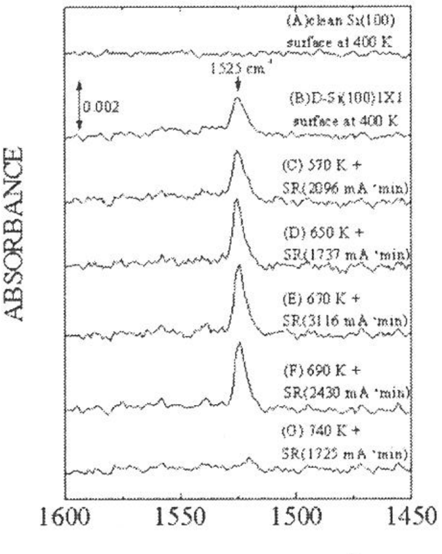

Figure 2. The change of the IRRAS spectrum of the SiD stretching vibration band annealing plus SR irradiation.

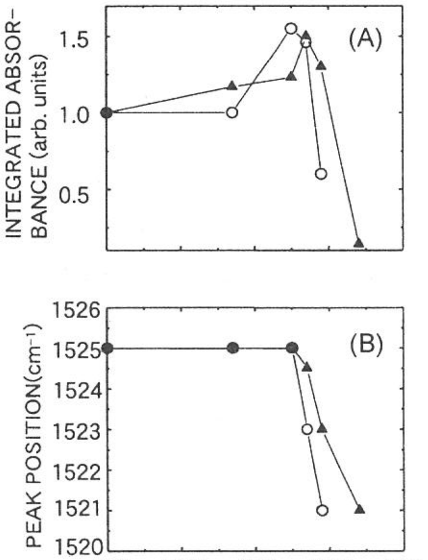

Figure 3. The change of the IA (A) and peak position (B) of SiD stretching vibration band upon annealing (○) and upon annealing plus SR irradiation (▲).

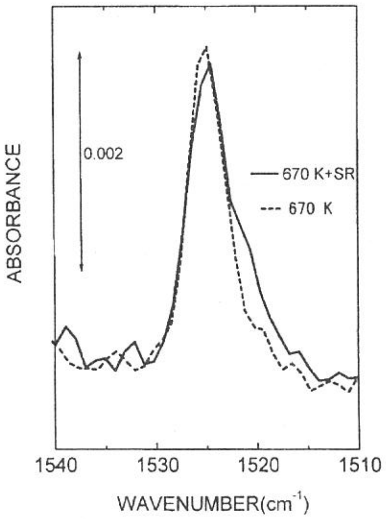

Figure 4. The band shapes of the SiD stretching vibration are compared for 670 K annealing only and the annealing + SR irradiation. Here, peak positions coincide between the two data sets.

1) S. Hirano, H. Noda, A. Yoshigoe, S. I. Ghyas and T. Urisu : Jpn. J. Appl. Phys. (in press).
2) J. J. Boland : J. Vac. Sci. Technol. A **10** (1992) 2458.

(BL-4B)

Fabrication of $CoSi_2$ buried metal layer substrates of IRRAS for *in situ* monitoring of synchrotron stimulated surface reactions

Hideyuki Noda[a], Mineo Hiramatsu[b] and Tsuneo Urisu[c]

[a]*The Graduate University for Advanced Studies, Myodaiji, Okazaki, 444-8585*
[b]*Faculty of Science and Technology, Meijo University, Tempaku-ku, Nagoya, 468-8502*
[c]*Institute for Molecular Science, Myodaiji, Okazaki, 444-8585*

The $Si/CoSi_2/Si$ structure which consisted of a semiconductor–metal–semiconductor is very useful for such high-speed devices as the metal base transistor and the permeable base transistor. Furthermore, this buried metal layer (BML) structure can be applied to the substrate for the high sensitive infrared reflection absorption spectroscopy (IRRAS) on Si surfaces. BML-IRRAS is a well-established technique for monitoring submonolayer amount adsorbates on Si surface and excellent in the point of no limitation with applicable wavelength by the substrate material. It is especially suitable for in situ monitoring of the surface reactions induced by synchrotron radiation (SR) irradiation.[1)] In comparison with conventional IR techniques using bulk Si, however, it is more important to control the surface and interface structure of the Si epitaxial layer on the BML. Typical techniques of $CoSi_2$ layer formations are ion beam synthesis (IBS), solid phase epitaxy (SPE) and codeposition of Si and metal using molecular beam epitaxy (MBE). The way of silicides growth by IBS and SPE are compared schematically in Figure 1. The IBS technique employs high–dose ion implantation into heated substrates and subsequent annealing to produce buried epitaxial $CoSi_2$ layers under a single–crystal Si overlayer (about 50～100 nm). In SPE, on the other hand, cobalt is deposited on the Si wafer by sputtering and a subsequent anneal forms the silicide. In this work, we used a Si_2H_6 gas source MBE (GSMBE) to grow epitaxial Si(100) layer on samples synthesized by IBS and SPE methods. Surfaces and interfaces of BML-Si(100) were evaluated by reflection high energy electron diffraction (RHEED) and scanning electron microscopy (SEM).

The surface cleaning of the substrates was achieved by the conventional wet method, followed by annealing to remove the surface oxide. Figure 2 shows RHEED patterns of IBS and SPE samples after surface cleaning, removal of the surface oxide and after epitaxial growth. The RHEED patterns changed from spotty to clear 2x1 by the epitaxial growth, as shown in photographs (Fig. 2(a) → (b) / Fig. 2(c) → (d)). Change from 2(a) to 2(b) indicates reconstructions of surface by homoepitaxial Si(100) growth. The 2x1 streak pattern of Fig. 2(d) indicates that heteroepitaxial Si(100) was successfully grown on a $CoSi_2$ layer. As compared to 2(b), however, the RHEED pattern 2(d) had a slightly weak 2x1 pattern, together with ring patterns. It is considered that this ring patterns of weak intensity indicates the growth of polycrystalline Si. Figure 3 shows the cross sectional SEM photographs obtained before and after Si(100) epitaxial growth. The buried $CoSi_2$ layer formed IBS method was continuous and had a nearly uniform thickness (Fig. 3(a)). And also, interfaces and surfaces of $Si/CoSi_2/Si$ structure were maintained smooth and continuous after epitaxial growth, as shown in Fig. 3(b). On the other hand, in the case of SPE, structures of Si epitaxial layer and interfaces of $Si/CoSi_2/Si$ were rough as shown in Fig. 3(d).

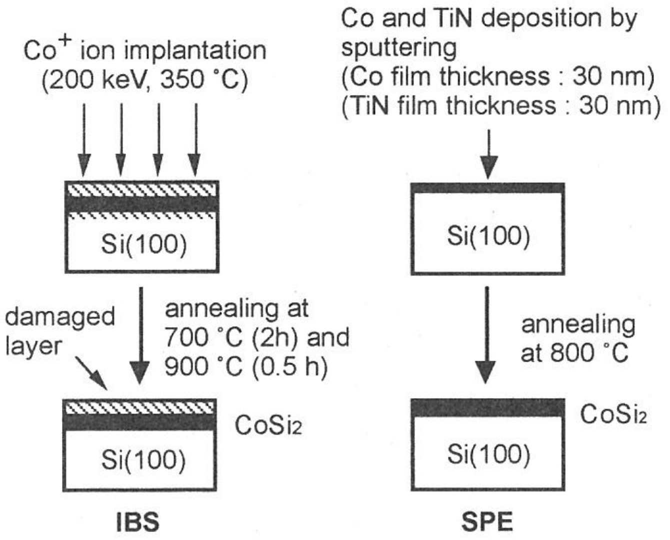

Fig. 1. The fabrication processes of CoSi2 layer. Comparison of IBS and SPE.

(a) annealing (950 °C) (b) GS-MBE (750 °C)

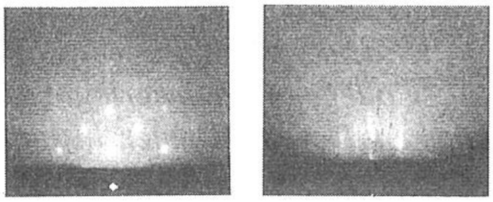

(c) annealing (850 °C) (d) GS-MBE (750 °C)

Fig. 2. RHEED patterns of IBS (a and b) and SPE (c and d) sumples : after removal of the surface oxide (a and c), after Si epitaxial growth (b and d).

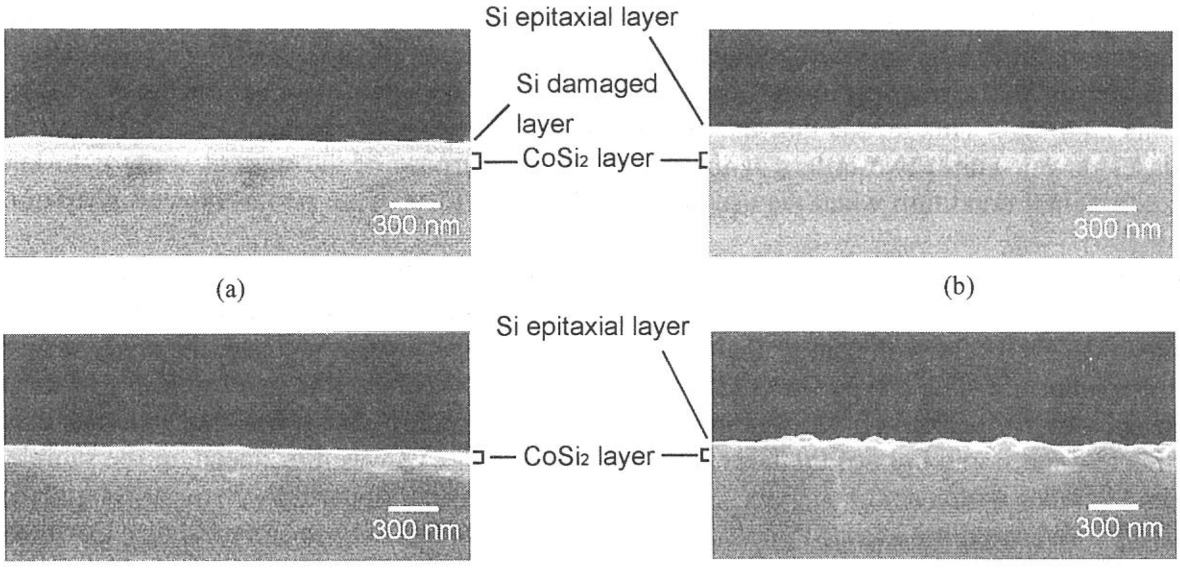

Fig. 3. Cross sectional SEM photographs of IBS (a and b) and SPE (c and d) samples : before (a and c), after (b and d) Si epitaxial growth.

1) S. Hirano, A. Yoshigoe, M. Nagasono, K. Mase, J. Ohara, Y. Nonogaki, Y. Takeda and T. Urisu, J. Synchrotron Rad. **5**, 1363 (1998).

(BL5A)

Photo-induced change in GaAs (100) surface

Masao Kamada, Jun-ichi Murakami[A], Senku Tanaka[B], Sam Dylan More,
Shuji Asaka[C], Minoru Itoh[A], and Yasuo Fujii[B]

UVSOR Facility, Institute for Molecular Science, Okazaki 444-8585
[A]Faculty of Engineering, Shinshu University, Nagano 380-8553
[B]College of Engineering, Osaka City University, Osaka 558-8585
[C]Equipment Develop Center, Institute for Molecular Science, Okazaki 444-8585

In recent years, photo-induced phenomena such as color-transition, magnetic-transition, and structural-transition have attracted much interest. The transition or change in electronic structures is closely related to these photo-induced transitions. However, most of works have been carried out using optical spectroscopy, but few have been conducted using photoelectron spectroscopy. As it is well known, the photoelectron spectroscopy is so surface sensitive that it may be powerful to investigate small change or transition on the photo-irradiated surfaces. Laser-induced change in photoelectron spectra has been reported by Long *et al.*, who have first observed the transient surface photo-voltage on Si (111) using synchrotron radiation (SR) and laser pulses.1) They used a high-power laser in the experiments, for examples, the repetition rate and time-width of their laser was 6 kHz and 0.1 mJ/cm^2, respectively. The average power of the laser was 0.6 W in 20 ns. They have also reported the laser-induced photochemical decomposition of GaAs(110), where metallic Ga was observed on the surface irradiated by laser pulses of 3.9 mJ/cm^2.2) In this case the average power was 23.4 W. This means that the photo-induced phenomena have much variety depending on the laser power within two-orders of magnitude. The purpose of the present study is to know good experimental condition when we use powerful lasers to investigate photo-induced phenomena on GaAs(100).

Experiments have been carried out at BL5A, UVSOR facility. A high-resolution monochromator SGM-TRAN, which was recently constructed,3) was used to excite samples at 100 eV. The OMICRON electron energy analyzer (EA-125HR) was used to measure the angle-resolved photoelectron spectra. The p-type GaAs (100) doped with Zn was installed in a liquid-nitrogen type cryostat without Ne-sputtering. Low-repetition and high-power Q-switched Nd:YAG laser was used. Second-harmonic light of the laser (photon energy 2.33 eV) was introduced on the sample in a vacuum chamber with a set of mirrors. The repetition rate and time-width were 20 Hz and 5 ns, respectively. We used the average power of 0.2-1 W without focusing in the present experiments. These conditions correspond to the pulse energy of 10-50 mJ/cm^2.

Figure 1 shows photoelectron spectra with 0.2-W laser excitation at 90 K. It is clearly observed that the photoelectron spectra were changed drastically by laser irradiation, for examples, the As-3d peak of oxide As around 55 eV disappeared after laser irradiation. This indicates that laser irradiation is useful to get clean surface of GaAs.

Figure 2 shows the photoelectron spectra with 1-W laser excitation at room temperature. The spectrum before laser irradiation has been already irradiated due to the experimental alignment. The As-*3d* peak increases after laser irradiation. This indicates that GaAs surface is easily decomposed by laser irradiation. We have carefully checked the threshold power to avoid the decomposition, and obtained the value of 0.28 W.

This work was partially supported by a Grant-in-Aid from the Ministry of Education, Science, Culture, and Sports.

References

1) J.P.Long et al., Phys. Rev. Lett. 64 (1990) 1158.
2) J. P. Long et al., Phys. Rev. Lett., 68 (1992) 1014.
3) M. Kamada et al., Rev. Sci. Instr., 66 (1995) 1537.

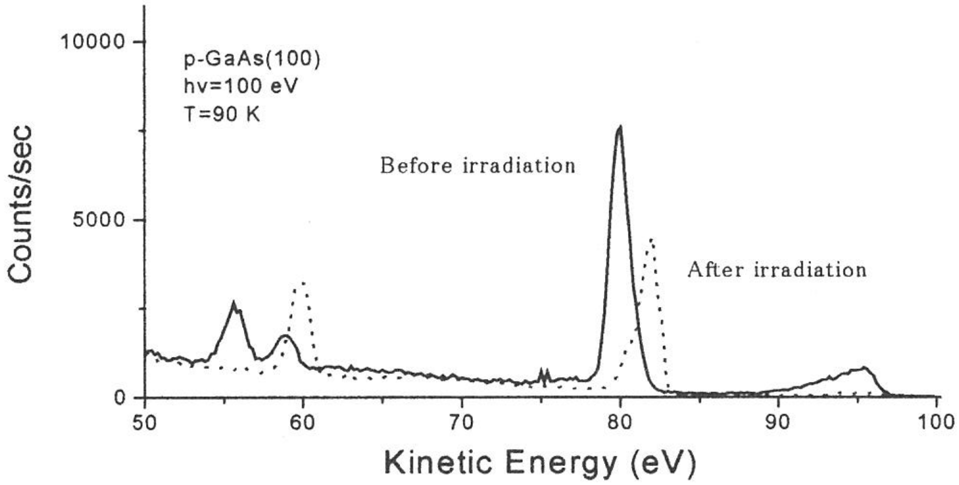

Fig. 1. Photoelectron spectra of GaAs with 0.2- W laser excitation at 90 K.

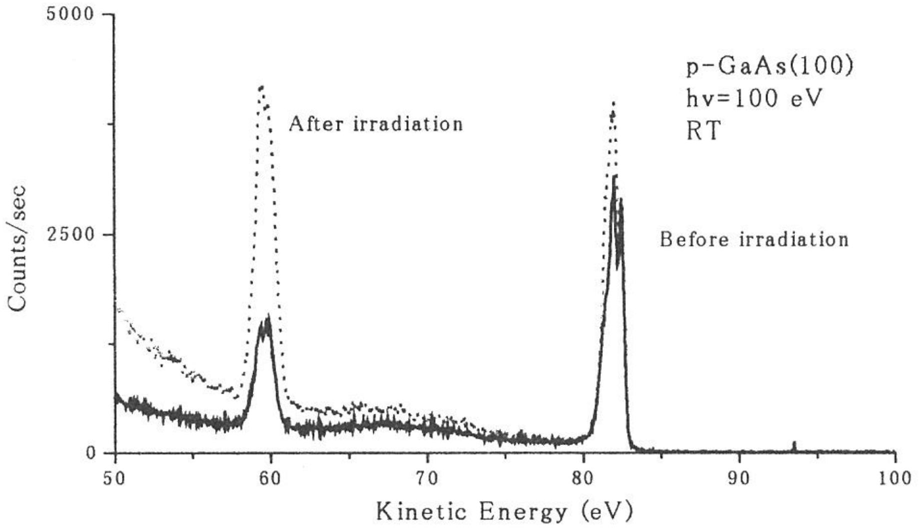

Fig. 2. Photoelectron spectra of GaAs with 1-W laser excitation at RT.

(BL5A)

Photoelectron Spectra of $Zn_{60}Mg_{30}Ho_{10}$ Icosahedral Quasicrystal

K. Soda, T. Nomura*, M. Kato, O. Yoshimoto*, Y. Yanagida, K. Morita,
T. Shimizu, T. Ishimasa*, S. Tanaka†, and M. Kamada†

Graduate school of Engineering, Nagoya University, Furo-cho, Chikusa, Nagoya 464-8603
**School of Engineering, Nagoya University, Furo-cho, Chikusa, Nagoya 464-8603*
†UVSOR Facility, Institute for Molecular Science, Okazaki 444-8585

The small electrical conductivity and its negative temperature dependence of quasicrystals (QCs) have been considered to partly arise from the existence of a pseudo-gap near the Fermi level as the Hume-Rothery phases [1]. The Al-based QCs composed of the Mackay icosahedron clusters seems to be stabilized near the electron per atom ratio $e/a \approx 1.75$, and some of them reveal the spectroscopic evidence of the pseudo-gap. On the other hand, icosahedral Zn-Mg-R (R = heavy rare earth element) QCs have attracted much interest because of the possibility to show the magnetic property intrinsic in the quasiperiodicity [2]. They also show the relatively high electrical conductivity [3] and the quasiperiodic structure consisting of the rhombic triacontahedron clusters with $e/a \approx 2.1$. These are somewhat different from the Al-based Mackay-icosahedron-type QCs. Thus, we have measured the photoelectron spectra of an icosahedral Zn-Mg-Ho QC for clarifying its electronic structure.

Ingots of poly-grain F-type icosahedral $Zn_{60}Mg_{30}Ho_{10}$ QCs were synthesized with use of a programmable electric furnace. The detailed sample preparation and its structural characterization are described elsewhere [4]. Specimens were cut from the ingot into a typical size of 5 x 5 x 3 mm^3 and attached on a copper plate by conductive epoxy glue. Clean surfaces for the photoelectron measurement were prepared by *in situ* scraping the specimen with a diamond file. Photoelectron spectra were taken under an ultrahigh vacuum of 2 x 10^{-8} Pa at room temperature with a hemispherical energy analyzer at BL5A. Total energy resolution including the thermal broadening was estimated to be 0.2 eV at the photon energy $h\nu$ of 45 eV from the measurement of the Fermi edge of gold. The origin of the binding energy E_B was also determined by the Fermi edge of Au.

Figure 1 shows typical photoelectron spectra near the valence band region. The excitation photon energies $h\nu$ are indicated in the figure. The spectra are enlarged below E_B = 8 eV by a factor of 20. The large peak with a shoulder around E_B = 9 eV is attributed mainly to the Zn 3d states. The structures seen in the binding energy region between 5 and 7 eV are ascribed to a part of the Ho 4f^9 final state multiplets, the rest of which probably overlap with the Zn 3d peaks [5]. These 4f^9 multiplets indicate the 4f^{10} configuration of Ho, *i.e.* Ho^{3+}. This is consistent with the magnetization measurement reported for the Zn-Mg-Ho QC [3].

Detailed spectral profiles near the Fermi level (close circles) are shown in Fig.2 in comparison with the spectrum of Au (open circles). The obtained valence band spectrum of the $Zn_{60}Mg_{30}Ho_{10}$ QC is peaked around E_B = 0.6 eV. However, its edge profile resembles much that of Au. This suggests no or weak pseudo-gap in this QC, although the unoccupied states cannot be probed in the photoelectron spectroscopy. Absence or weakness of the pseudo-gap may be related to the above-mentioned relatively high conductivity and the fact that the electron diffraction patterns show no intense spots near the wavevector of 0.470 Å^{-1}, which is double the Fermi wavevector, 2k_F, estimated on the assumption of the density of 5.4 ± 0.1 g/cm^3 and the valence of Zn^{2+}, Mg^{2+} and Ho^{3+} with the nominal composition of $Zn_{60}Mg_{30}Ho_{10}$. This seems to be in contrast to the Al-based Mackay- icosahedron-type QCs.

Further studies are intended with the higher energy resolution at the low temperature. Inverse photoelectron spectroscopy and soft X-ray emission spectroscopy of the $Zn_{60}Mg_{30}Ho_{10}$ QC are also in progress now, and their results will be reported elsewhere.

References

[1] *Physical Properties of Quasicrystals*, ed. Z. M. Stadnik (Springer-Verlag, Berlin, 1999)
[2] B. Charrier *et al.*, Phys. Rev. Lett. **78** (1997) 4637.
[3] S. Kashimoto *et al.*, Solid State Commun. **109** (1999) 63.
[4] T. Shimizu and T. Ishimasa, Jpn. J. Appl. Phys. **37** (1998) 5691.
[5] J. K. Lang *et al.*, J. Phys. F **11** (1981) 121.

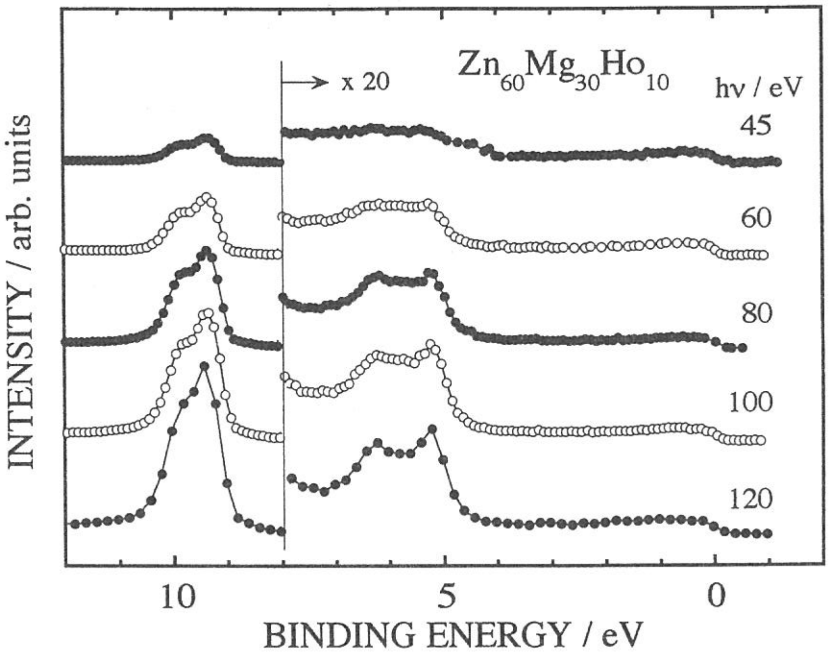

Fig. 1 Photoelectron spectra of an icosahedral $Zn_{60}Mg_{30}Ho_{10}$ quasicrystal.

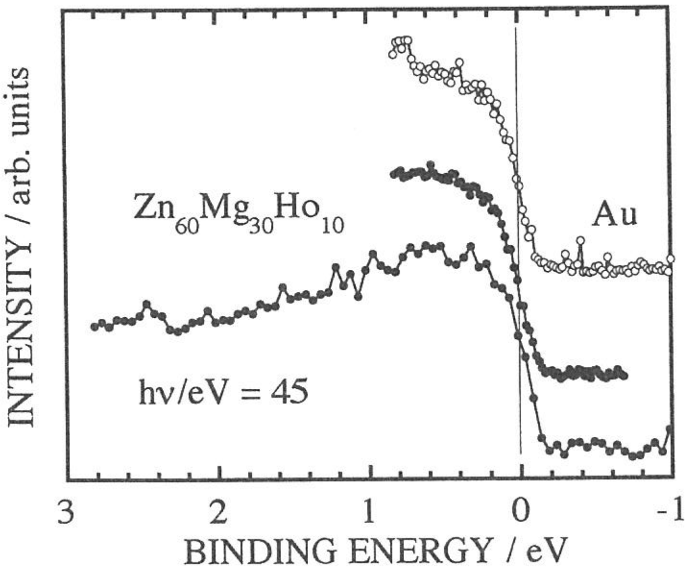

Fig. 2 Photoelectron spectra of an icosahedral $Zn_{60}Mg_{30}Ho_{10}$ quasicrystal near the Fermi level (closed circles) in comparison with that of Au (open circles).

(BL5A)

High-Resolution Photoemission Study of Si(111)-√3x√3-Ag Surface

Y. Yanagida, K. Soda, M. Kato, H. Takeda, D. Ishikawa,
J. Yuhara, K. Morita, S. Tanaka *, and M. Kamada *

Graduate School of Engineering, Nagoya University, Furo-cho, Chikusa, Nagoya 464-8603
** Institute for Molecular Science, Myoudaiji, Okazaki 444-8585*

Recent progress of the high-resolution photoelectron measurement is bringing one of the powerful techniques which elucidate the chemical bonding and local atomic arrangement of the complicated Si surface layers [1]. The structure of the Si(111)-√3x√3-Ag surface has been already studied by various techniques in surface science, and the honeycomb chained triangle (HCT) model proposed by Takahashi *et al.* [2] has been widely accepted. In the HCT model, the top layer is occupied by three Ag atoms in the √3x√3 unit cell, and the underlying Si atoms form a Si trimer layer as the missing-top layer model. According to the analysis of surface X-ray diffraction, the third and forth Si layers have large bucklings in the normal direction and the reconstruction ranges up to the seventh Si layer. In this report, we present the results of the high-resolution measurement of the Si(111)-√3x√3-Ag surface at temperatures T of 100 and 300 K.

Measurements were performed at the BL-5A of UVSOR. Silicon specimens used were mirror-polished n-type Si(111) wafers with a size of 5x9x0.5mm^3. The specimen was placed on a manipulator in a conventional ultrahigh vacuum chamber equipped with a hemispherical analyzer, a LEED optics, an AES one, and a Ag evaporation source. The Si(111)-√3x√3-Ag surface was produced by about 1 monolayer deposition of Ag onto the Si(111)-7x7 surface, prepared by repeated direct-current heating, and subsequent annealing at 700 K for 300 s. Clear √3x√3 LEED spots were obtained, and no contamination was observed by AES. The amount of deposited Ag was also checked by AES. The total energy resolution was estimated to be less than 70 meV.

Figure 1 shows Si2p core-level spectra taken at T=100 and 300 K with the photon energy $h\nu$ of 130 eV at the emission angles θe of (a) 60° and (b) 0°. The normal emission spectrum obtained at 300 K agrees well with the results reported by Herman *et al.* [3]. They have explained the spectrum by three surface components and a bulk one. However, we have found that another surface component (S2 in our notation), at least for the low-temperature, is needed to consistently explain all the low-temperature spectra taken at θe=0° and 60° with $h\nu$=110 and 130 eV. The decomposition into a bulk component B and four surface components S1-S4 is also shown in the figure, and the fitting parameters are summarized in Table 1, where the surface core-level shifts are referred to the bulk position. The relative intensities of the components are listed in Table 2.

The S1 component is assigned to the top-most Si layer bonding to the Ag atoms, since it is the most intense in the surface-sensitive spectra taken with $h\nu$=130 eV, in particular, at θe=60°. Because of its large intensity, comparable to the S1 component in the normal emission spectra, the new component S2 may be also attributed to another Si in the Si top layer, which is inconsistent with the HCT model. Recent theoretical calculation [4] suggests that an asymmetric structure might have lower total energy than the HCT arrangement. However, this structure appears to be incompatible with the observed intensity ratio of the components. Another possible interpretation within the HCT framework is that the large S2 peak might be caused by the diffraction of the photoelectron emerging from Si atoms in the deeper Si layer. Thus, further investigation on the low-temperature surface phase is necessary to solve this problem. The S3 and S4 components, whose chemical shifts of −0.25 and +0.51 eV are in accordance with the result reported by Herman *et al.* [3], are tentatively ascribed to Si atoms in the domain walls and those below the second Si layer.

References
[1] H. W. Yoem *et al.*, Phys. Rev. B 56 (1997) R15525.
[2] T. Takahashi *et al.*, Surf. Sci. 282 (1993) 17.
[3] G. S. Herman *et al.*, Surf. Sci. Lett. 290 (1993) L643.
[4] H. Aizawa and M. Tsukada, *unpublished.*

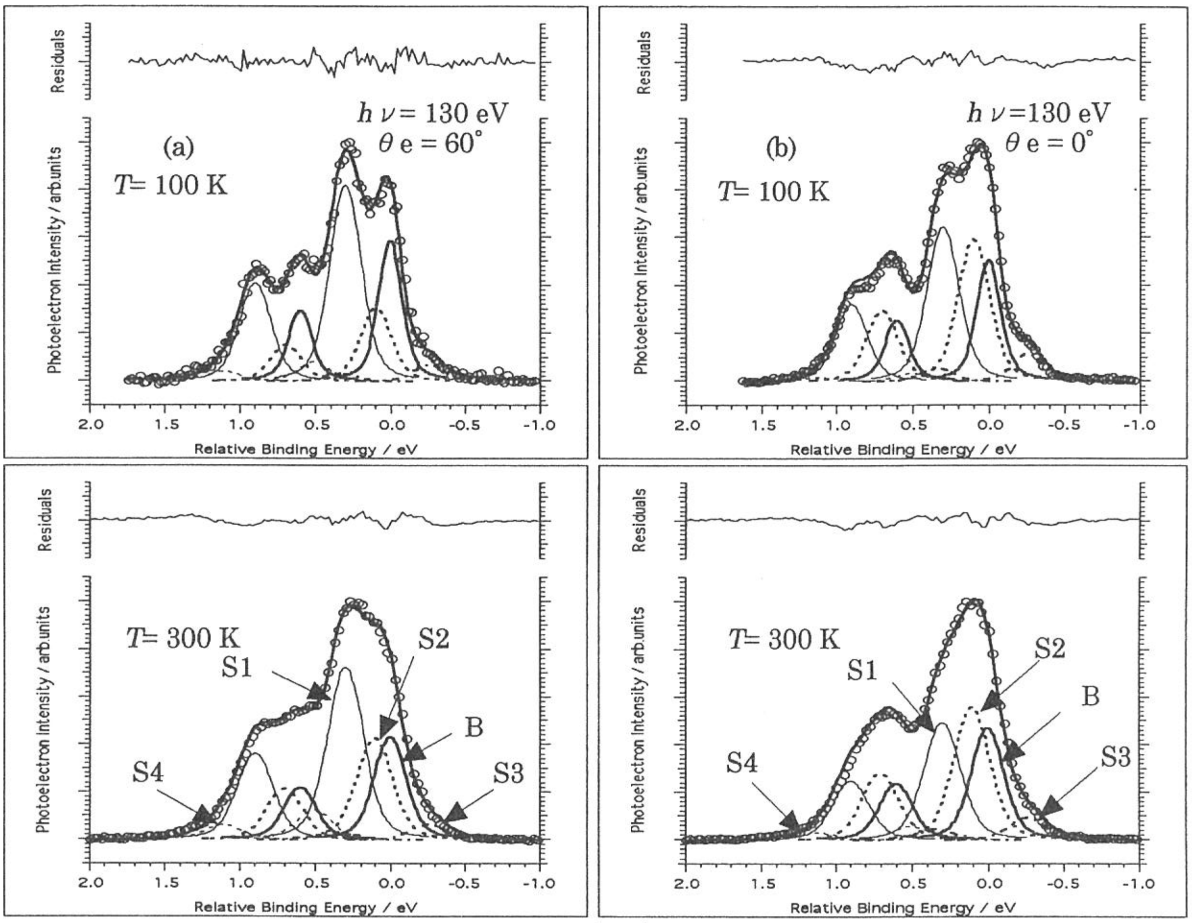

Fig. 1 Si2*p* core-level spectra of the Si(111)-$\sqrt{3}$x$\sqrt{3}$-Ag surface taken at the emission angle θ_{e} of (a) 60° and (b) 0° with a photon energy $h\nu$ of 130 eV at temperatures T of 100 K (top) and 300 K (bottom). The relative binding energy scale is referenced to the $2p_{3/2}$ line of the bulk component B. The decomposition of the spectra is also shown.

Table 1 Fitting parameters for the Si2*p* spectra. All energies are in eV. The Lorentzian and Gaussian widths refer to the full width at half maximum.

Spin-orbit splitting	0.600
Branching ratio	0.5
Lorentzian width	0.083
Gaussian width of a bulk compnent	0.136 (100 K) 0.204 (300 K)
Gaussian widths of surface components	0.199 (100 K) 0.235 (300 K)
Surface core-level shifts	S1: +0.301 S2: +0.104 (100 K) +0.112 (300 K) S3: −0.251 S4: +0.510

Table 2 Fraction of integrated intensity for the decomposed components measured at 100 K.

	$h\nu$=130 eV θ_{e}=60°	$h\nu$=130 eV θ_{e}=0°	$h\nu$=110 eV θ_{e}=0°
B	0.32	0.27	0.82
S1	0.44	0.34	0.09
S2	0.16	0.31	0.03
S3	0.04	0.06	0.06
S4	0.04	0.02	0

(BL5A) Photoemission Study of Initial Growth of Cu Layers on Si(111)-√3x√3-Ag Surface

Y. Yanagida, D. Ishikawa, M. Kato, K. Soda, H. Takeda,
J. Yuhara, K. Morita, S. Tanaka* , and M. Kamada*

Graduate School of Engineering, Nagoya University, Furo-cho, Chikusa, Nagoya 464-8603
** Institute for Molecular Science, Myoudaiji, Okazaki 444-8585*

The epitaxial growth of a Cu film on Si substrates has received intensive attention from the points of view of fundamentals and technology for epitaxial metallization in Si microdevices. Adsorbate Cu atoms have been considered to be reactive with the substrate Si ; a LEED pattern at the coverage higher than 10 monolayers (ML) suggests an fcc (111) lattice of Cu metal or α-phase Cu-Si alloy [1], and an η-Cu3Si interface between Cu layers and the Si substrate at the 100℃-deposition is proposed from X-ray diffraction measurements [2]. In addition to the research on the single adsorbate system, a binary adsorbate system has interest due to the possible modification of surface structure, which may assist the epitaxial growth. Ishikawa *et al.* studied the room-temperature Cu deposition onto the Si(111)-√3x√3-Ag surface by AES and RBS techniques, and proposed that Cu3Si is formed with Ag atoms kept at the top-most surface [3]. Here, we have measured the Si2*p* core-level spectra of Cu-deposited Si(111)-7x7 (Cu/Si(111)-7x7) and Si(111)-√3x√3-Ag (Cu/Si(111)-√3x√3-Ag) surfaces in order to clarify change in the chemical bond on the initial growth of Cu layers on the Si(111)-√3x√3-Ag surface.

Measurements were performed at the BL-5A of UVSOR. The silicon specimen was placed on a manipulator in a conventional ultrahigh vacuum chamber equipped with a hemispherical analyzer, a LEED optics, an AES one, and evaporation sources of Ag and Cu. After the preparation of the Si(111)-√3x√3-Ag and Si(111)-7x7 surfaces, Cu was deposited onto these surfaces at room temperature. The amount of deposited Cu was monitored by AES.

Figure 1 shows typical Si2*p* core-level spectra on the Cu deposition onto the Si(111)-7x7 and Si(111)-√3x√3-Ag surfaces, and their decomposed components. The decomposition was performed with use of measured bulk- and surface-sensitive spectra and Voigt functions representing a bulk and several surface components with the 2*p*1/2-2*p*3/2 branching ratio of 0.5 and the appropriate fitting energy parameters. The surface components S1-S5 obtained for the Si(111)-7x7 surface (a) are consistent with the result of Karlsson *et al.* [4], and S1*-S4* for the Si(111)-√3x√3-Ag surface (d) are referred to the spectrum measured at low temperature [5]. Spectra with increasing Cu desorption onto the Si(111)-7x7 and Si(111)-√3x√3-Ag surfaces are shown in (b)-(c), and (e)-(f), respectively. The abscissa is the relative binding energy whose origin is the energy position of the bulk component B, in order to cancel out the shift due to the band-bending.

As seen in the figure, the main peak of the Si2*p* spectra is shifted to the low relative binding-energy side for both surfaces, and the low-binding energy tail is enhanced with the Cu deposition increasing. For the Cu/Si(111)-7x7 surface, the spectral change is ascribed to decrease of the initial surface components S1-S5 and increase of the S3' and S4' components, which indicates that new Cu-Si bonds are formed on the Cu deposition. The increase of the Cu-Si bonds is also recognized in the panels (e) and (f) for the Cu/Si(111)-√3x√3-Ag surface. Furthermore, the S1* component corresponding to the Ag-Si bond is much reduced on the Cu deposition. These findings are consistent with the growth model proposed by Ishikawa *et al.* On the other hand, the S1 component persists in the panel (c), in accordance with its assignment of the pedestal atoms in the Si(111)-7x7 surface. The S2* component may be attributed to Si atoms in the third and forth layers rather than another type of Si in the first Si layer [5], because of its less sensitivity to the deposition and its small chemical shift from the bulk.

References
[1] F. Ringeisen *et al.*, J. Vac. Sci. Technol. B 1 (1983) 546.
[2] F. J. Walker *et al.*, Phys. Rev. Lett. 67 (1991) 2818.
[3] D. Ishikawa *et al.*, Surf. Sci. 357-358 (1996) 432.
[4] C. J. Karlsson *et al.*, Phys. Rev. B 50 (1994) 5767.
[5] Y. Yanagida *et al.*, *presented in this activity report.*

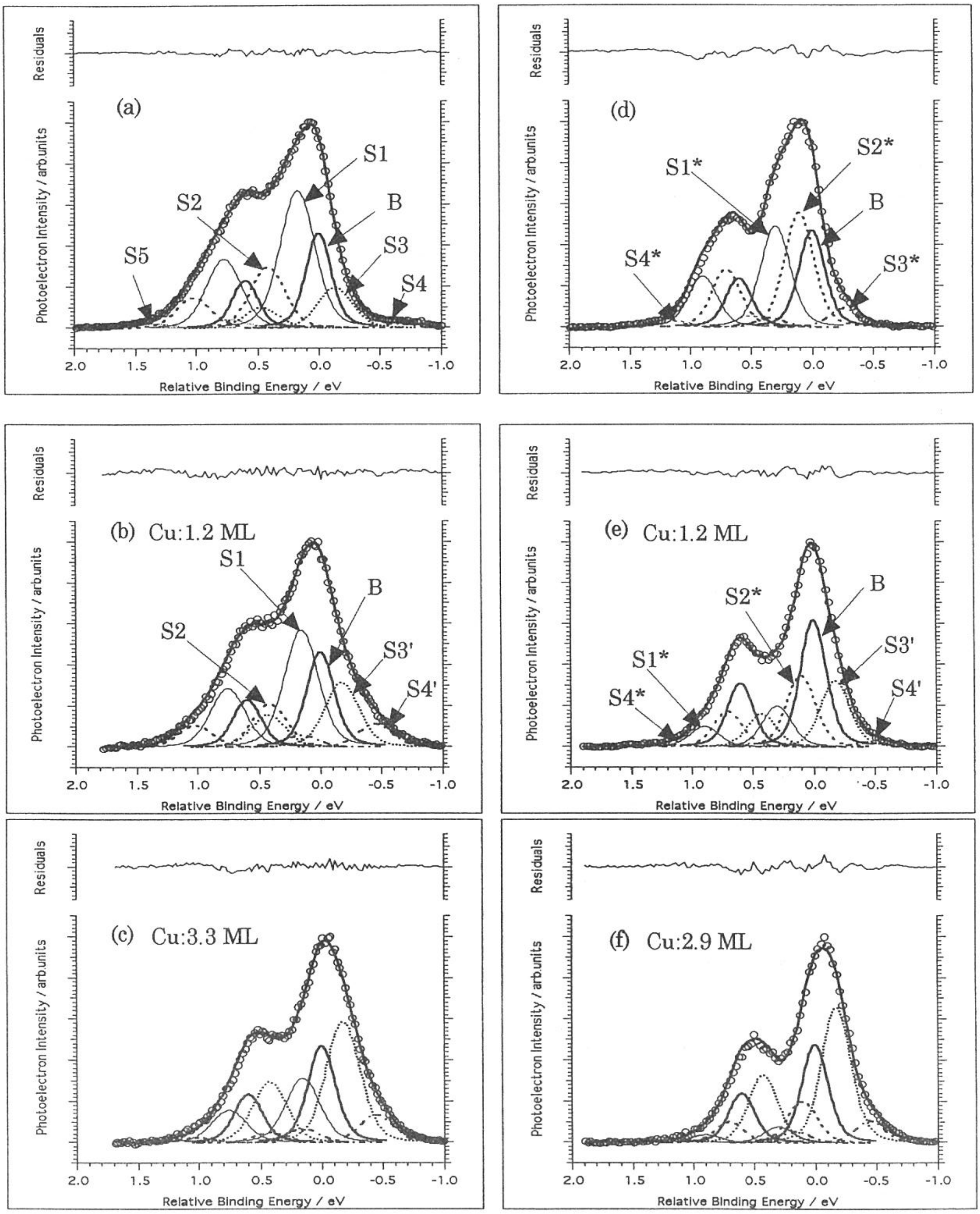

Fig. 1 Si2*p* core-level spectra and their decomposed components of Cu/Si(111)-7x7 surfaces (left panels) and Cu/Si(111)-√3x√3-Ag ones (right panels). These spectra were taken at the normal emission with a photon energy of 130 eV at room temperature. The initial Si(111)-7x7 and Si(111)-√3x√3-Ag surfaces are shown in the panels (a) and (d), respectively. The Cu coverages are indicated in the figure. The abscissa is the relative binding energy referenced to the 2*p* 3/2 line of the bulk component B.

(BL5A)

Core-level excitation and decay of multi-layered Xe film

Shin-ichiro Tanaka, Sam D. More and Masao Kamada

Institute for Molecular Science, Okazaki, 444-8585, Japan

The core-level excitation and decay of solids and solid surfaces has been extensively studied for these decades. The measurements of photo-absorption spectrum near the core-level edge and the Auger electron spectra taken at the photons of which energies corresponds to a specific excitation allow us to insight the detailed mechanism of excitation and decay. The Auger decay of the excited state created by the photons at the core-threshold is different from the Auger decay of normally ionized state created by the photons or electrons far beyond from the threshold energy. In the former situation, excited electrons stays during the Auger decay ("spectator" case) or take part in the Auger decay ("participator" case), so that the final state of the Auger decay contains 2 holes 1 electron (spectator) or 1 hole only (participant). Meanwhile, the final state of the normal Auger decay contains 2 holes. In the case of the isolated molecule or atoms, an excited electron can stay near the core hole long enough to survive during the Auger decay, and therefore, resonant Auger electron spectra, like the spectator or participant Auger described above, are observed usually. However, in the case of the metallic solid, the excited electron has only a short lifetime due to the charge transfer in the crystal, and the excited state decays to be ionized state before the Auger decay. Therefore, only the normal Auger electron spectra are observed taken at the photon energy of the threshold of the core excitation for the metallic solid. In this report, we made an investigation of the absorption spectroscopy and resonant Auger electron spectroscopy, at the 4d level of Xe layers produced on the Si(111) surface at 30K. We observed the surface core exciton, and observed the resonant Auger spectra of the surface and bulk core exciton of Xe film.

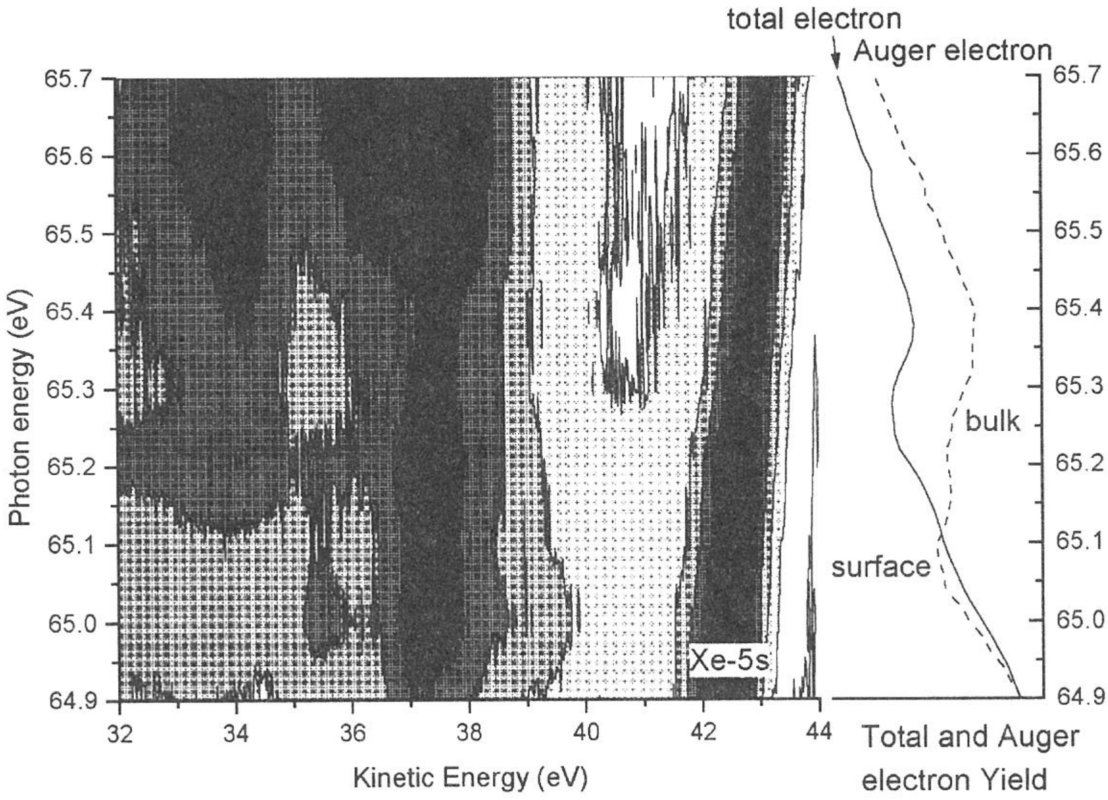

Figure 1

The right panel of the figure 1 shows the total electron yield (bulk sensitive) and Auger electron yield (surface sensitive). The kinetic energy of the electron was set to be corresponding to the Xe-NOO Auger emission. The bulk core exciton is observed at 65.28 eV, and the surface core exciton is observed at 65.08 eV. The left panel of the figure 1 shows the contour plot of the series of photoelectrons obtained by changing the photon energy in steps of 0.1 eV across the surface and bulk core exciton. Peaks observed near E_K=42 eV

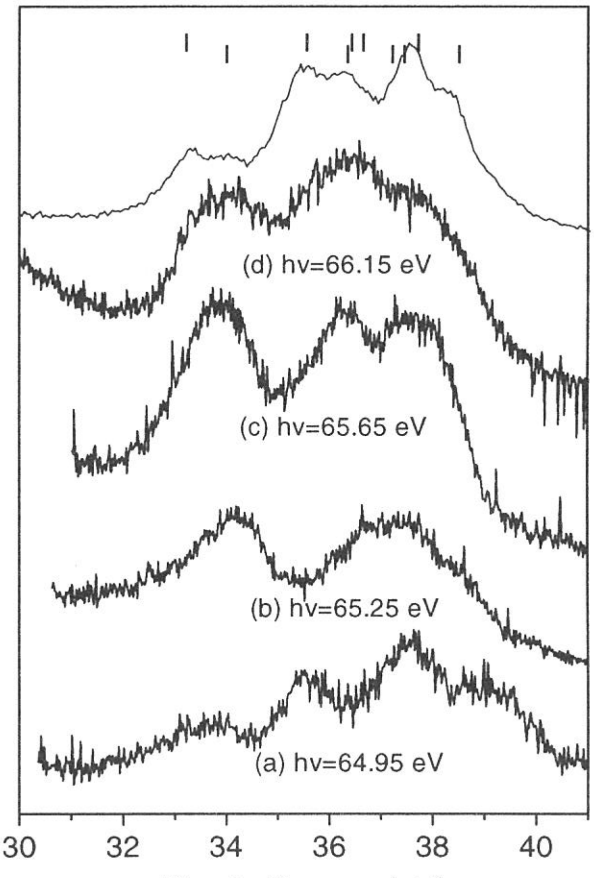

Figure 2

(hv=64.9eV) is the direct emission from the Xe-5s level, and is shifted as a linear function of the photon energy. The structures observed in 32-40 eV is attributed to the Xe-NOO Auger electron and the shake-up satellite of the Xe valence peaks. It is obvious that contour plot can be separated into 3 regions correspoiding to the surface core exciton (near hv=65.0 eV), to the bulk core exciton (near hv=65.2 eV), and to the higher photon energies (hv>65.5 eV). The spectra at hv>65.5 eV is considered to be mostly contributed by the normal Auger emission, which result in the 2 hole as the final state. The decay spectra of the surface and bulk core exciton were different from the normal Auger, which may mean that the resonant Auger spectra are observed. In order to investigate the resonant behavior of the decay spectra of the surface and bulk core exciton, we eliminate the contribution of the satellite peaks of the Xe valence level from the raw spectra. Results are shown in the figure 2.

Spectra (a) and (b) of the fig. 2 correspond to the decay spectra of the surface and bulk core exciton, respectively. Spectra (c) and (d) were taken at higher photon energies, and do not show significant differences from a top curve which is the normal Auger electron spectrum obtained at hv=90 eV. A shift to higher kinetic energies in the Auger electron spectrum is clearly observed for the decay of the surface core exciton [Fig.2 (a)]. Thus, it is considered that the lifetime of the surface core-exciton is long enough to survive during the Auger decay. The resonant behavior of the bulk core-exciton is not so clear as observed in the case of the surface core exciton [fig2.(b)]. The investigation of the system in detail is now under progress.

(BL5B)

Study of electronic structure and magnetic phase of Co film on oxygen-rich Cu(001)($\sqrt{2}$x2$\sqrt{2}$)R45°-O surface

Krishna G. Nath[1], Yuichi Haruyama[2] and Toyohiko Kinoshita[2]
[1]The Graduate University for Advanced Studies, Okazaki 444-8585
[2] UVSOR facility, Institute for Molecular Science, Okazaki 444-8585

In the present report, the magnetic properties and the reconstructed phase of ferromagnetic Co film on oxygen pre-adsorbed Cu(001) surface are shown. It is well known that the presence of molecules such as oxygen, sulfur etc. sometimes disturb to obtain the thin films with good quality. The reason may not be so clear, but disordered nature of the thin films and/or the substrates caused by the existence of the molecules probably seems to be one of the origins of the disturbance. It is interesting therefore to study the properties of ferromagnetic thin films grown on the ordered surface with the presence of the molecules. In order to study the magnetic stability of magnetic thin film on such substrate, we performed the LEED (low energy electron diffraction) and magnetic dichroism in photoemission spectroscopy experiments for the Co films grown on the oxygen adsorbed Cu substrate. The experiments were performed by using the modified XPS equipment; VG ESCALAB 220I-XL [1].

The Cu(001) substrate was cleaned by sputtering and annealing. Then the different amount of oxygen was exposed on the clean surface to obtain reconstructed surfaces. We observed two kinds of LEED patterns as a function of the amount of oxygen. At low amount (100L>) stage, the LEED pattern was not different from the clean 1x1 surface. At the higher amount (500L-1200L) stage, the superstructure Cu(001) ($\sqrt{2}$x2$\sqrt{2}$)R45°-O pattern was observed in accordance with the previous report [2]. However, no 'four-spot' or C(2x2) pattern reported previously [3] was observed in the present experiment. On these oxygen-rich Cu surfaces, 5ML of Co was evaporated.

Figure 1 shows the representative LEED photographs taken at different stages of experiment. As shown in the figure, the LEED is changed form ($\sqrt{2}$x2$\sqrt{2}$)R45° in (b) to c(2x2) in (c) upon depositing of 5ML Co. (d) shows the LEED pattern of the system O(3.2L)/Co(5ML)/Cu(001), where the oxygen was adsorbed on the clean Co film. The structures (c) and (d) seem to be same.

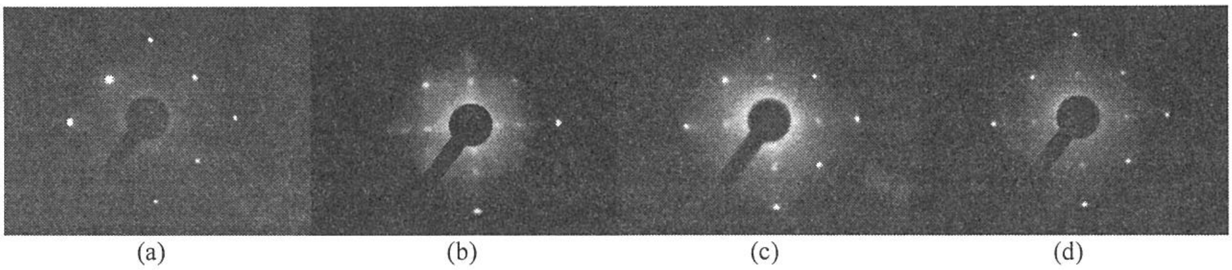
(a) (b) (c) (d)

Figure 1. LEED patterns of (a) clean Cu(001) at E_K=121eV, (b) O(1200L)/Cu(001), E_K=110eV, (c) Co(5ML)/O(1200L)/Cu(001), E_K=110eV, and (d) O(3.2L)/Co(5ML)/Cu(001), E_K=110eV .

Figure 2(a) shows the O 1s XPS spectra for the systems in Figs. 1 (b), (c) and (d), respectively. It is noticed that the binding energy between the Co/O/Cu (Fig.1(c)) and the O/Co/Cu (Fig.1(d)) is same in contrast to that of O/Cu (Fig. 1 (b)). It is concluded from the results of LEED and XPS that the oxygen in Co/O/Cu system comes out to the topmost of the surface from the substrate. The amount is estimated to be the same coverage as that for 1L-coverage on clean Co film system. Binding energy position indicates that the bonding between the Co and floated oxygen is stronger than that of Cu-O. In Fig. 2(b), the MUDAD (magnetic dichroism in angular distribution by unpolarized light, here excited by MgKα) result of Co2$p_{3/2}$ is shown. As described previously [4], two spectra (upper panel) for opposite magnetization direction give an asymmetry (down panel), $(I_{M+}- I_{M-})/(I_{M+}+I_{M-})$. The presence of asymmetry signal (3%) means that the magnetic film with good quality can be grown on the oxygen pre-adsorbed substrate, namely even on the microscopically inhomogeneous (different domain exist on the oxygen-rich Cu) Cu-surface [2].

References

1. T. Kinoshita et al., J. Electron Spectrosc. Relat. Phenom. 92 (1998) 165.
2. F. M. Leibsle, Surface Science **337**, 51 (1995).
3. T. Fujita *et al.* Phys. Rev. B **54**, 2167 (1996).
4. M. Getzlaff *et al.*,Phys. Rev. Lett. **73**, 3030(1994)

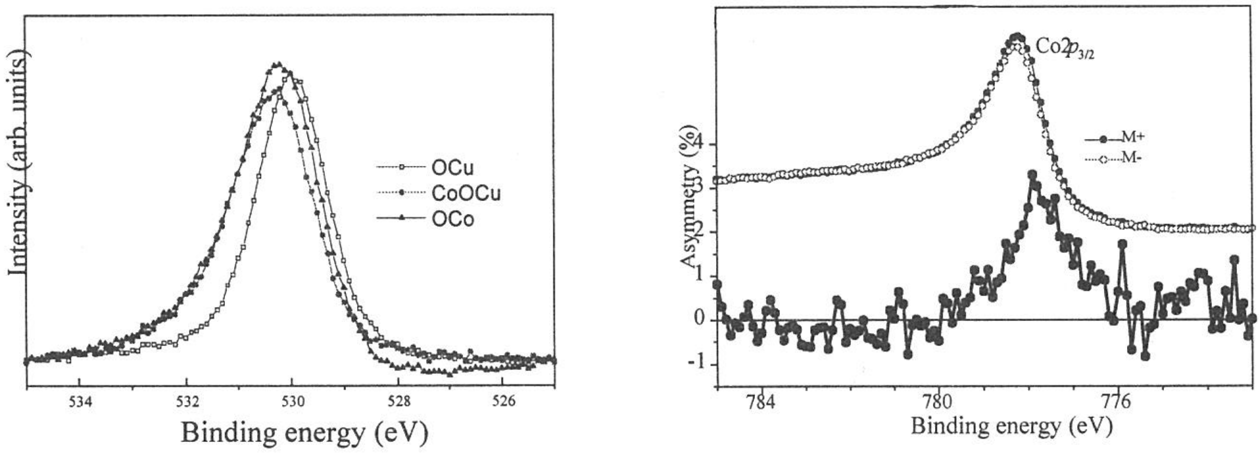

Figure 2. (a) O1s XPS spectra for three systems, O/Cu (open square), Co/O/Cu (solid circle) and O/Co/Cu (triangle). (b) MUDAD of Co2$p_{3/2}$ XPS for Co/O/Cu system.

(BL-5B)

Si-L Reflection Spectra of Si/CaF$_2$ Multilayers

Takeo EJIMA, Yuji KONDO and Makoto WATANABE

Research Inst. for Scientific Measurements, Tohoku Univ., Sendai 980-8577, JAPAN

Few years ago, we had measured total photoelectron yield (TEY) spectra of Si/CaF$_2$ multilayers around the Si-L edge changing angles of incidence. Recently, we have performed reflection measurements on the same samples. Preparation of the Si/CaF$_2$ multilayers are described in elsewhere [1]. The angle of incidence of the monochromatized light was changed from 0° to 88° in the measurements with its electric vector perpendicular to the plane of incidence.

The reflection spectra at angles of incidence between 60° and 88° for Si 185 Å /CaF$_2$ 70 Å /Si(111) multilayer are shown in Figure 1. In the figure, solid lines represent results of the measurements, and dashed lines are results of tentative simulation using optical constants of crystalline Si and crystalline CaF$_2$ [2,3]. At angles of incidence between 0° and 60°, obtained signals are weak, therefore we could not distinguish the signals from backgrounds. With an increase of the angle, the spectral shapes change around the Si-L edge (100eV). The simulation is not satisfactory one to reproduce the measured spectral shapes well. We are now trying to find the optical constants which are able to reproduce both reflection and TEY spectra.

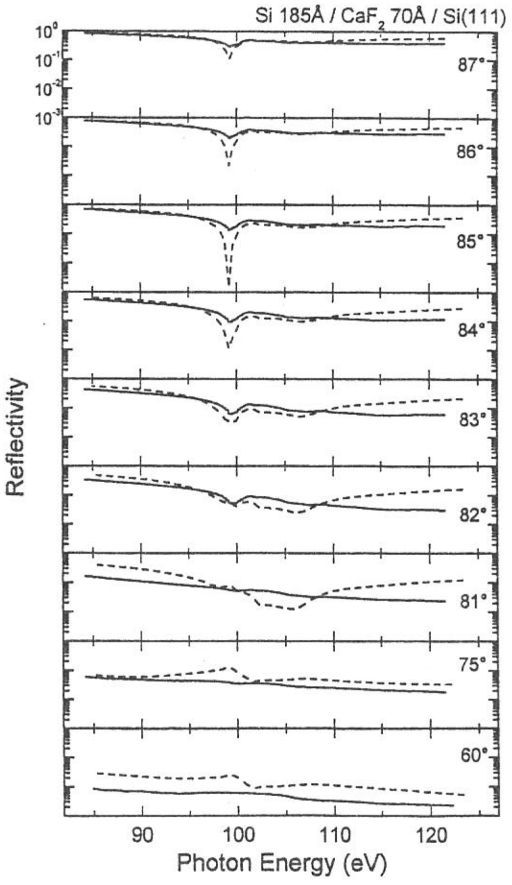

Figure 1: Reflection Spectra of Si 185Å /CaF$_2$ 70Å/Si(111).

References

[1] T. Ejima, K. Ouchi, M. Watanabe: *Proc. of the 12th Int. Conf. on Vacuum Ultraviolet Radiation Physics*, San Francisco, 1998, to be published in J. Electron Spectros. Rel. Phenom.

[2] *Handbook of Optical Constants of Solids*, ed. E. D. Palik (Academic Press, 1985).

[3] B. L. Henke, P. Lee, T. J. Tanaka, R. L. Shimabukuro, B. K. Fujikawa: At. Data Nucl. Data Tables **27** (1982) 1.

(BL5B)

Absolute yield of exciton induced desorption from the surface of solid Ne

T. Hirayama[A*], T. Adachi[A], I. Arakawa[A,B], K. Mitsuke[B] and M. Sakurai[B]

[A]*Department of Physics, Gakushuin University, 1-5-1 Mejiro, Toshimaku, Tokyo 171-8588*
[B]*Institute for Molecular Science, Myodaiji, Okazaki 444-8585*

We have been studying the desorption of excited particles from the surface of rare gas solids (RGSs) induced by exciton creation using photon- and electron- stimulated desorption (PSD and ESD) techniques[1]. The mechanisms for the desorption of exited atoms in the excitonic energy region have been well established in these 10 years by measuring the kinetic energy, angular distribution, and excitation energy dependence using a synchrotron radiation[2, 3]. Absolute desorption yield can be an essential information for the quantitative understanding for the desorption dynamics. Hirayama et al. [4] first reported the absolute yield for exciton induced desorption of the metastable atoms from the surface of solid Ne. In the present study, we present the results for the total absolute yield for exciton induced desorption from the surface of solid Ne.

Experiments have been done at the beam line BL5B in UVSOR. The experimental setup is similar to the one used in our previous work[3] equipped with a quadrupole mass spectrometer (QMS400, ULVAC) in order to detect Ne molecules desorbed from the surface of solid Ne. Briefly, the sample substrate is a Pt(111) attached to the head of a rotatable liquid He cryostat installed in an UHV chamber (base pressure ~ 5×10^{-9} Pa). Absolute desorption yield has been estimated by the increase of Ne partial pressure measured by the quadrupole mass spectrometer, which is calibrated by using an extractor gauge (Lybolt). Pumping speed of a turbo molecular pump and the cryostat has been experimentally determined to be 0.16 m^3/s. Absolute number of the incident photon was measured using a photoelectric yield of Au plate as described in [4].

Figure 1 shows a wavelength dependence of the absolute desorption yield from the surface of solid Ne whose thickness is about 35 atomic monolayers. Positions of the first and second order bulk excitons (B1, B2) and the band gap energy (E_g) are marked in the figure. Only peak of bulk excitons has been appeared. Yield at the surface exciton (first order surface exciton, S1: 72.3 nm, $2p^5 3p$-type surface exciton, S': 65.4 nm) are less than our detection sensitivity (~ 0.1 atoms/photon). A broad peak at around 80 ~ 90 nm, where the excitation energy is below the lowest energy of the exciton creation (S1: 72.3 nm), is attributed to the desorption induced by the secondary electrons emitted from the platinum substrate. Unexpectedly large desorption yield (order of unity) can be explained by such a mechanism that the bulk exciton created near the surface, namely, second or third layer, desorbs via cavity ejection mechanism together with some ground state atoms around the excited atom. Further analysis is in progress.

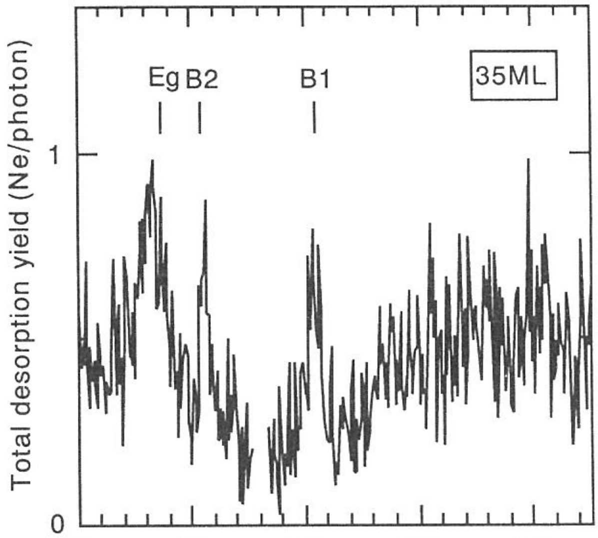

Fig.1. Excitation wavelength dependence of the absolute desorption yield from the surface of solid Ne.

References.

[1] I. Arakawa, in *Molecular Crystals and Liquid Crystals* (Gorden and Breach Science Publishers, New York, 1998), Vol. 314, p. 47.
[2] D. E. Weibel et al., Surface Science **283**, 204 (1993).
[3] I. Arakawa et al, Nucl. Instrum. Meth. Phys. Res. **B101**, 195 (1995).
[4] T. Hirayama et al., Surf. Sci. **390**, 266 (1997).

---

* Fax: 03-3987-6732, e-mail: takato.hirayama@gakushuin.ac.jp

(BL5B)

XUV radiation effects on back-thinned CCDs

S. Tsuneta, R. Kano, T. Sakao, K. Kobayashi[1], K. Kumagai

National Astronomical Observatory, 2-21-1 Osawa, Mitaka, Tokyo, 181, Japan
[1] *Department of Astronomy, School of Science, The University of Tokyo, Bunkyo-ku, Tokyo, 113, Japan*

Back-thinned CCDs have recently gained much attention as major detectors for astronomical applications, not only for ground-based observatories, but also for space-borne telescopes. For observations of the solar corona in the X/XUV wavelengths, back-thinned CCDs are well suited due to their high sensitivity to X/XUV light together with their high dynamic range.

As back-thinned CCDs started to be used in space, radiation hardness of back-thinned CCDs against incident X/XUV photons has become a major concern. EEV in UK and Site in US are only two major manufacturers currently producing large-format science-grade back-thinned CCDs. We have carried out experiments regarding XUV-radiation effects on several back-thinned CCDs purchased from EEV and SITe at UVSOR in the Institute of Molecular Science, Japan. Intense XUV beams from the synchrotron allows us to study, within a few days, effects of years of in-orbit XUV illumination from the sun. Systematic study on radiation hardness of back-thinned CCDs is done in the program for the first time.

We have illuminated both EEV and Site CCDs at 300 and 200Å. Fig. 1 shows the dark current level as a function of soft X-ray dose at 300Å. Fig. 2 shows the quantum efficiency (QE) with respect to the QE before the illumination. CCDs from EEV have turned out to be significantly robust against XUV photons at 200 and 300 angstroms. EEV CCDs show slight, or even marginal, increase in the dark current level after XUV illumination equivalent to several years of solar observations from space, while maintaining high quantum efficiency (higher than 0.5). On the other hand, Site CCDs have experienced significant increase in dark current level, and decrease in QE. We also performed the experiment at 50Å, and obtained essentially the same result.

The degradation both in dark current level and in the quantum efficiency is related to the sensitive back-surface of the CCDs. CCDs silicon substrate is mechanically and chemically etched to thickness of about 10 microns, and the silicon-silicon-dioxide layer has many intermediate traps. Although the degradation appears to be related to the intermediate states, polarization of the silicon-silicon-dioxide interface due to soft X-ray irradiation, and the resultant change in the internal potential profile, the physical mechanism is not completely understood, and is being discussed with the manufacturers. The difference in performance between EEV and Site is related to that in method of annealing. A full paper for the experiment is being prepared.

As a practical side, this experiment serves to choose the best possible CCD device for the Solar-B spacecraft. Solar-B is scheduled to be launched in the year 2004 by the Institute of Space and Astronautical Science (ISAS). The X-ray telescope (XRT) is developed under Japan-U.S. collaboration. The Japanese XRT team is responsible for the development of the CCD camera, together with associated electronics.

References (published in FY1998):

T. Sakao, R. Kano, K. Kobayashi, and S. Tsuneta, 1999, XUV radiation effects on back-thinned CCDs, in Proc. International Symposium on Solid State Detectors.

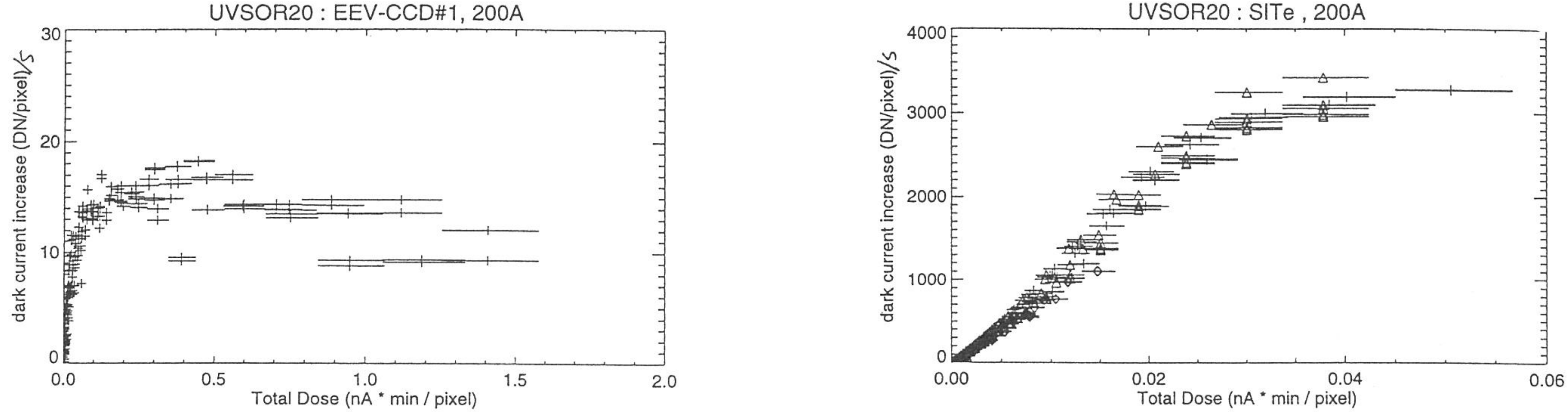

Figure 1: Dark current level as a function of the soft X-ray dose at 200Å; (left) EEV CCD, (right) Site CCD.

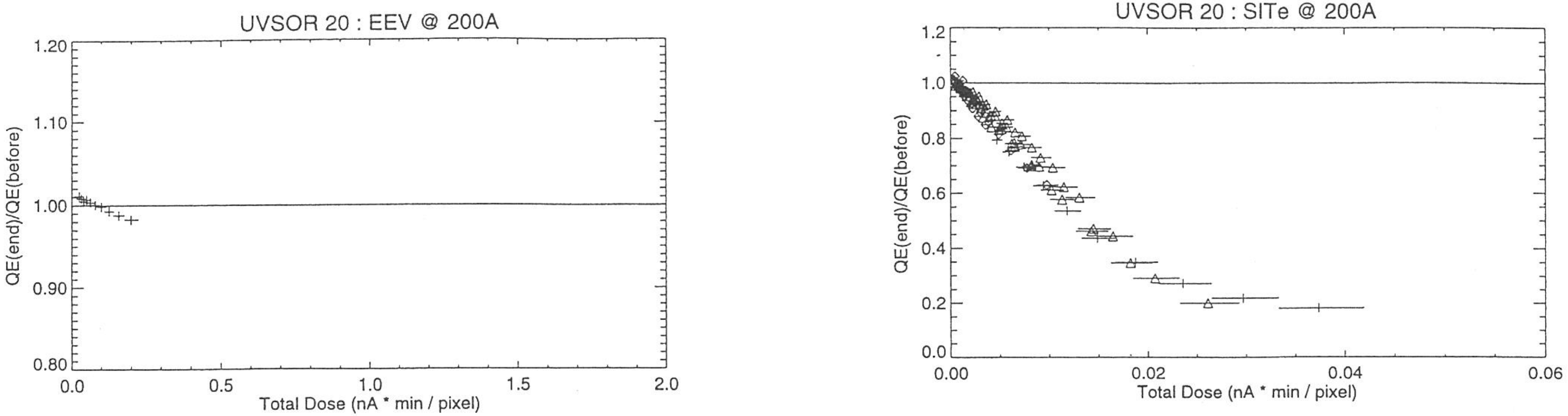

Figure 2: Relative quantum efficiency as a function of the soft X-ray dose at 200Å; (left) EEV CCD, (right) Site CCD.

(BL5B)

Electronic structures of organic salts (DI-DCNQI)$_2$M (M = Cu and Ag) using photoelectron spectromicroscopy

Yuichi Haruyama,^{A} Krishna G. Nath,^{B} Shin-ichi Kimura,^{C} Yüksel Ufuktepe,^{D}
Toyohiko Kinoshita,^{A,E} Ko-ichi Hiraki^F and Kazushi Kanoda^G

^{A}*UVSOR Facility, Institute for Molecular Science, Okazaki 444-8585, Japan*
^{B}*Department of Structural Molecular Science, The Graduate University for Advanced Studies, Okazaki 444-8585, Japan*
^{C}*Division of Structural Science, Graduate School of Science and Technology, Kobe University, Kobe 657-8501, Japan*
^{D}*Physics Department, University of Cukurova, 01330 Adana, Turkey*
^{E}*Institute for Solid State Physics, University of Tokyo, Tokyo 106-8666, Japan*
^{F}*Department of Physics, Gakushuin University, Tokyo 171-8588, Japan*
^{G}*Department of Applied Physics, University of Tokyo, Tokyo 113-8656, Japan*

The crystal structures of (DI-DCNQI)$_2$M (M=Cu, Ag), where DI-DCNQI is 2,5-diiodo-*N,N'*-dicyanoquinonediimine, are isostructural with a space group $I4_1/a$, whereas the physical properties are quite different from each other. In the electrical resistance [1], (DI-DCNQI)$_2$Cu (abbreviated DI-Cu) shows metallic conductivity down to low temperature, on the other hand, (DI-DCNQI)$_2$Ag (DI-Ag) shows semiconducting nature with a gap of 490K. The difference in the physical properties is considered to arise from the *d* band position of M ion. Although the photoemission is a direct method to investigate these electronic structures, the photoemission study for the single crystals DI-Cu and DI-Ag has not been performed so far. The reason is that the size of these single crystals is not large enough to carry out the photoemission experiments. However, photoelectron spectromicroscopy apparatus can do the experiment. Therefore, we have measured the photoemission spectra for DI-Cu and DI-Ag using the photoelectron spectromicroscopy [2].

Photoemission experiments were carried out by using a conventional UHV system (FISONS, ESCALAB-220i-XL) at a base pressure of 2×10^{-8} Pa [2]. Total instrumental energy resolution was 0.3~0.6 eV full width at half maximum (FWHM), depending on the photon energy ($h\nu$) in the energy range of 30~200 eV. Needlelike shaped single crystals of DI-Cu and DI-Ag were synthesized by electrochemical reduction [1]. Figure 1 shows the photoelectron image of DI-Ag excited by AlKα light of $h\nu$=1486.6 eV. The I $3d_{5/2}$ photoelectrons at E_B= 620 eV were collected. The typical sample size used here was less than $\phi100\times1000\mu m^2$. These samples were characterized by x-ray diffraction, electrical resistance, magnetic susceptibility and NMR measurements [1]. The clean surface was obtained by scraping the sample surface using an edge of a razor. The cleanliness was confirmed by x-ray photoemission spectroscopy for the absence of extra features arising from the contaminations.

Figure 2(a) shows the photoemission spectra of DI-Cu and DI-Ag, respectively. The detection area of the photoemission spectra was 50μm, which is smaller than the sample size. For DI-Cu, five features in this valence band region are observed at ~0.5, 3.2, 4.0, 6.5 and 9.0 eV labeled A, B, C, D and E, respectively. It is recognized that from the photon energy dependence of the photoemission spectra that the features A, C and D are predominantly derived from N and C 2*p* states, and the feature B is from Cu 3*d* states [3]. For DI-Ag, five features in this valence band region are observed at ~0.5, 4.0, 5.2, 6.6 and 9.0 eV labeled by F, G, H, I and J, respectively. The features F, G and I are predominantly derived from N and C 2*p* states, and the feature H is from Ag 4*d* states [3]. It is obvious that the Ag 4*d* states have much deeper than the Cu 3*d* states. In addition, as shown in Figure 2(b), the spectral feature above ~0.5 eV for DI-Cu is larger than that for DI-Ag. This is probably due to the contribution of the Cu 3*d* states. The tail of the Cu 3*d* states seems to reach near the Fermi level. These results indicate that the *pπ-d* hybridization at the Fermi level between the M ions and the N atoms of the DCNQI molecules for DI-Cu is large as compared with that for DI-Ag. The tendencies of the position of the metal M *d* states are consistent with the band calculation [4]. However, the position of features A and F assigned to the pπ orbitals (LUMO) is not consistent with the band calculation [4]. This shows the importance of the electron correlation.

References

[1] K. Hiraki and K. Kanoda, Phys. Rev. **B 54**(1996)17276.

[2] T. Kinoshita, K. G. Nath, Y. Haruyama, M. Watanabe, S. Yagi, S. Kimura, and A. Fanelsa, J. Electron Spectrosc. Relat. Phenom. **92**(1998)165; T. Kinoshita, K. G. Nath, M. Watanabe, S. Yagi, S. Kimura, and A. Fanelsa, UVSOR Activity Report 1996, p.154.

[3] Y. Haruyama, K. G. Nath, S. Kimura, Y. Ufuktepe, T. Kinoshita, K. Hiraki and K. Kanoda, Solid State Commun. in press.

[4] T. Miyazaki and K. Terakura, Phys. Rev. **B 54**(1996)10452.

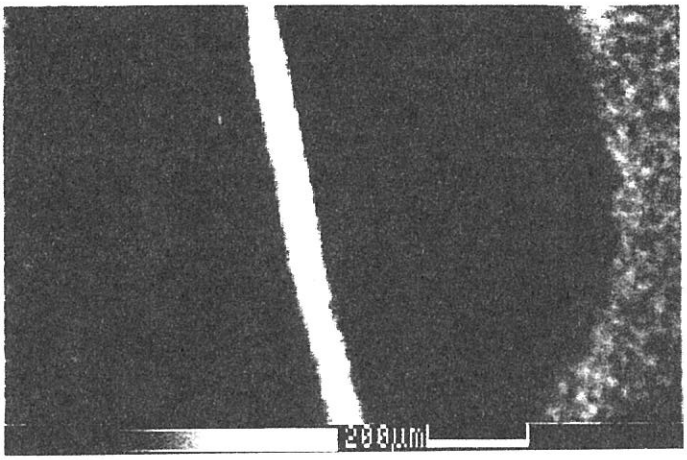

Figure 1. Photoelectron image of $(DI\text{-}DCNQI)_2Ag$ excited by AlKα light of $h\nu = 1486.6$ eV. The I $3d_{5/2}$ electrons at $E_B = 620$ eV were collected.

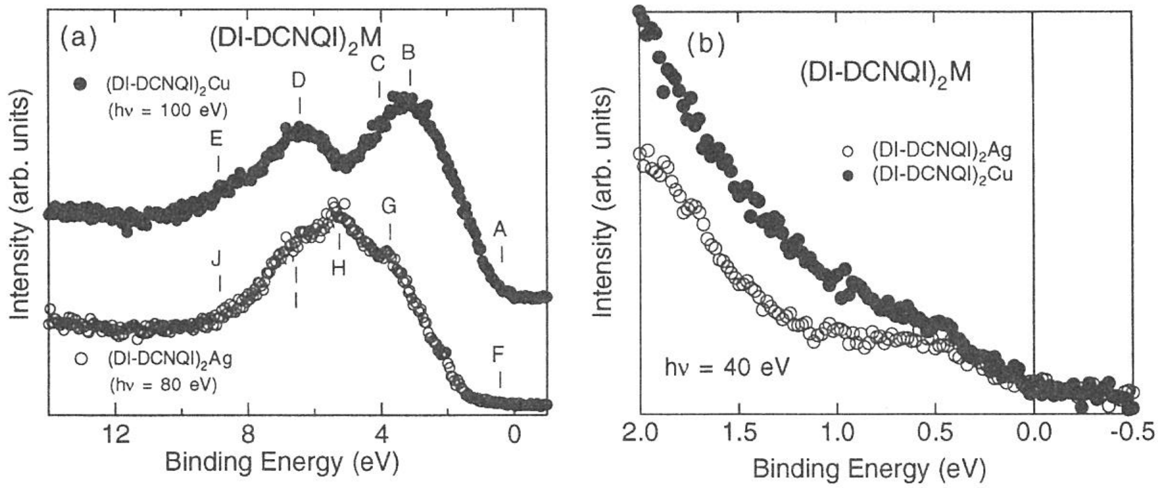

Figure 2. The photoemission spectra of $(DI\text{-}DCNQI)_2Cu$ and $(DI\text{-}DCNQI)_2Ag$ (a) in the whole valence band region (b) near the Fermi level. The detection area was 50μm.

(BL5B)

Measurement of absolute efficiency for MCP onboard Mars orbiter by using pure-calibrated EUV beam

Masato Nakamura[1], Yoshiyuki Takizawa[2], Ichiro Yoshikawa[3]
Atsushi Yamazaki[1], Kei Shiomi[1], and Etsushi Ohyama[1]
[1] *Department of Earth and Planetary Science, Univ. of Tokyo, Bunkyo-ku, Tokyo 113-0033*
[2] *The Institute of Physical and Chemical Research, Wako, Saitama 351-0198*
[3] *Institute of Space and Astronautical Science, Sagamihara, Kanagawa 229-8510*

As one of the calibrations for the sensitivity characteristics of the eXtreme Ultra-Violet Scanner (XUV) onboard the Mars orbiter *NOZOMI*, the object of this experiment is to measure the quantum efficiency of the same-type MCPs as XUV on flight at the 304Å line. For this purpose, during this whole machine time an Al/Mg/Al (744Å/3958Å/747Å) filter is installed on the SOR beam's entrance to eliminate the multi-order lines from the 304Å line with PGM35/36. As the usual detectors which are set on the outer rotation stage of the goniometer, we use our position-sensitive MCPs when using PGM36 and the photo diode when PGM35.

We investigate the purity of the 304Å line through the Al/Mg/Al filter in the following two ways. At first, we judge the purity from the consistency between the transmittance of an Al/Mg/Al (744Å/3958Å/747Å) filter and an Al/Sn (1608Å/500Å) filter for the continuous lines at UVSOR and that for the particular lines at the University of Tokyo EUV facilities. The latter is measured for the emission lines of the gas (He, Ne) with the discharge light source. Fig.1 shows the transmittance profiles of the two filters measured at UVSOR and University of Tokyo. It is clear that both profiles of each filter are consistent in the wavelength region of 250-500Å. Second, we investigate the dispersion of the 304Å line with PGM35 by using our grating for experiments on the X-Y stage of the goniometer. The result shows that no contamination of the 152Å line (the second-order line) and the 76Å line (the fourth-order line) exists. Not exactly, we seem that the contamination of the 38Å line (the eighth-order line) exists much a little.(Fig.2) But even if it should exist, the result of the transmittance analysis turn out that the degree of the contamination almost can be neglected. We interpret from the two results that the pure 304Å line can be introduced through the Al/Mg/Al filter by using PGM35/36.

With the available pure 304Å line, we measure the quantum efficiency of the XUV-type MCPs which are set on the X-Y stage of the goniometer, and our position-sensitive MCPs. The quantum efficiency is calculated by the rate of the MCPs count to the electron yield of the photo diode which is absolutely calibrated. Table1 shows that the quantum efficiency of the XUV-type MCPs is 11.3%(HV:-2.90kV). The position-sensitive MCPs is 9.2%.

As the next step, in addition to the 304Å line (He II emission), we plan to measure the quantum efficiency at the 584Å line (HeI emission), which is another observational object of XUV. Then the purity of 584Å line is essential, and must be investigated for the next machine time.

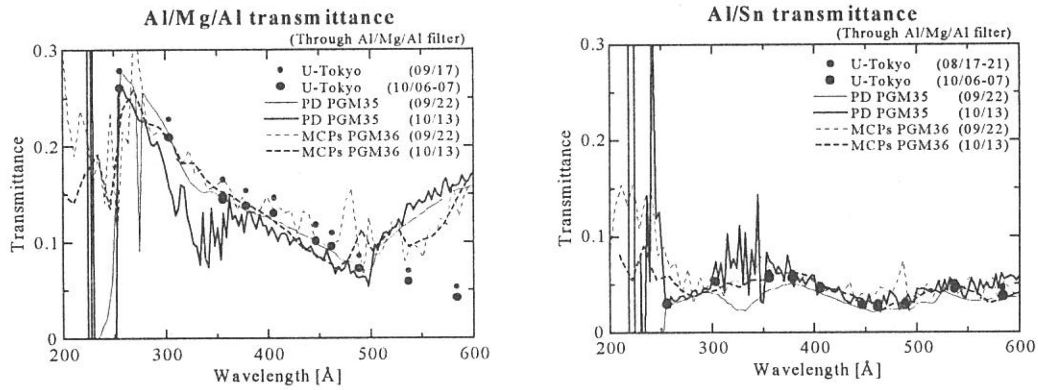

Fig.1 The transmittance profiles of an Al/Mg/Al(744Å/3958Å/747Å) filter and an Al/Sn(1608Å/500Å) filter. The solid and dashed lines show the measurement at UVSOR, and the solid circles show those at the University of Tokyo EUV facilities.

Fig.2 The dispersion of the 304Å line detected by the position-sensitive MCPs.

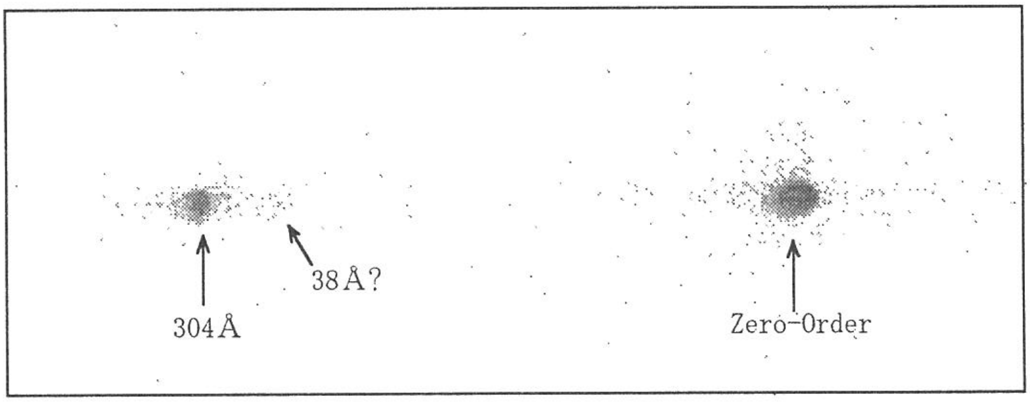

Table 1 The quantum efficiency of the XUV-type MCPs at the 304Å line.

High Voltage	The quantum efficiency
-2.65kV	9.1%
-2.70kV	9.9%
-2.80kV	10.8%
-2.90kV	11.3%
-3.00kV	11.7%
-3.10kV	11.9%

(BL5B)

Soft X-Ray Reflectances of Novel Oxide Multilayer Structures Fabricated by Atomic Layer Deposition

Hiroshi Kumagai, Katsumi Midorikawa, Hiroko Matsuyama[A], Hidehiko Asahi[A] and Minoru Obara[A]

Laser Technology Laboratory,
The Institute of Physical and Chemical Research (RIKEN),
2-1 Hirosawa, Wako, Saitama 351-0198, Japan
[A] *Electrical Engineering, Faculty of Science and Technology, Keio University,*
3-14-1 Hiyoshi, Kohoku-ku, Yokohama 223-0061, Japan.

Development of high-performance normal-incidence multilayer optics for the water-window wavelength region between the oxygen and carbon K absorption edges at 2.33 and 4.36 nm, respectively, where water is relatively transmissive and organic materials are absorptive, has been a technical challenge of great interest. The extremely small periods (1.2-2.2 nm) of soft-X-ray reflectors require very rigorous specifications to be met with respect to interface roughness and interlayer mixing, because interface roughness on an atomic scale has a substantial effect on soft-X-ray reflectance. Therefore, the reflectances achieved at these wavelengths are very low.

The authors have proposed the use of a novel metal oxide multilayer, whose material combination is the same as that used in free electron lasers, for soft-X-ray reflectors at water-window wavelengths,[1,2] because an oxide multilayer can prevent from forming an alloy at the interface, and the absorption of oxygen in oxides is negligible at the water-window wavelengths; moreover, the metal oxide multilayer can be fabricated by the atomic layer deposition or atomic layer epitaxy technique. These techniques can be used to control surfaces on an atomic scale by sequentially dosing the surface with appropriate chemical precursors and then promoting surface chemical reactions which are inherently self-limiting. We have found that the self-limiting adsorption mechanism works in the fabrication of oxide thin films such as aluminum oxide and titanium oxide.[3-5]

We report here on reflectance performances of novel metal oxide multilayers of titanium oxide and aluminum oxide using monochromatized synchrotron radiation (SR) from the beamline 5B of the 750-MeV electron storage ring located at the Ultraviolet Synchrotron Radiation Facility (UVSOR).

Figure 1 shows the experimental results of wavelength dependence on reflectances of the aluminum oxide/titanium oxide multilayer fabricated by the atomic layer deposition method of controlled growth with sequential surface chemical reactions. A high reflectance (s-polarization) of 33.4% at the wavelength of 2.734 nm and an incident angle of 71.8° from the normal incidence are demonstrated in the 20-period structure of d=4.43nm. A reflectance (s-polarization) over 15% at the wavelength of 2.734 nm and an incident angle of 58.5° from the normal incidence are demonstrated in the 40-period structure of d=2.62 nm.

Figure 2 shows comparisons between measured reflectances, calculations with and without surface roughness. In the cases of #2 and #3, experimental reflectances are almost the same as the calculations without roughness. For the case #1, whose period is 2.17 nm, the measured reflectance is close to the calculation with roughness. The descrepency between experimental and calculated reflectances might arise from the surface/interface roughnesses and interlayer mixing and so on.

This work was supported by the Joint Studies Program (1998) of the Institute for Molecular Science.

References
1) H. Kumagai, K. Toyoda, K. Kobayashi, M. Obara and Y. Iimura, Appl. Phys. Lett. 70, 2338 (1997).
2) H. Kumagai, M. Matsumoto, Y. Kawamura, K. Toyoda and M. Obara, Jpn. J. Appl. Phys. 33, 7086 (1994).
3) H. Kumagai, K. Toyoda, M. Matsumoto and M. Obara, Jpn. J. Appl. Phys. 32, 6137 (1993).

4) H. Kumagai and K. Toyoda, Appl. Surf. Sci. 82/83, 481 (1994).
5) H. Kumagai, M. Matsumoto, K. Toyoda, M. Obara and M. Suzuki, Thin Solid Films 263, 47 (1995).

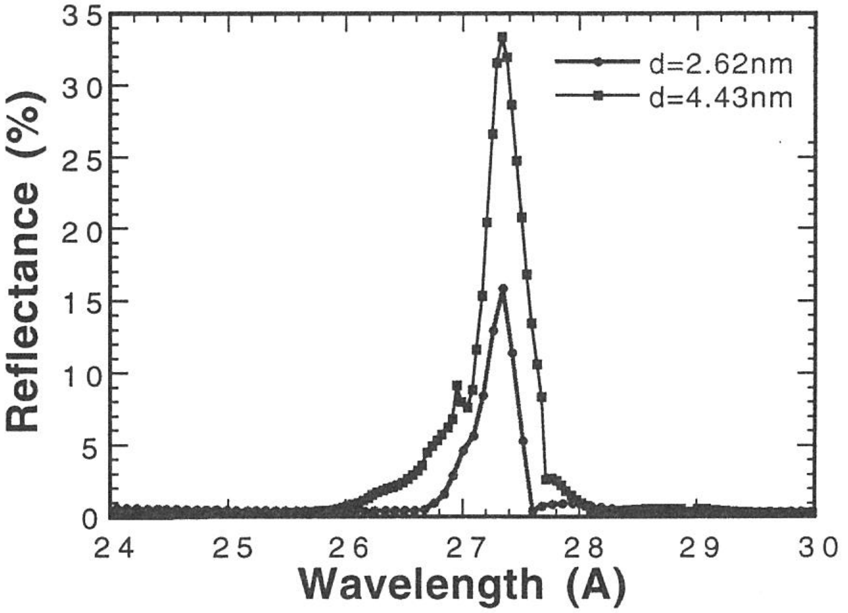

Fig.1 Plots of wavelength dependence on reflectances of the aluminum oxide/titanium oxide multilayer with different periods fabricated by the atomic layer deposition method of controlled growth with sequential surface chemical reactions.

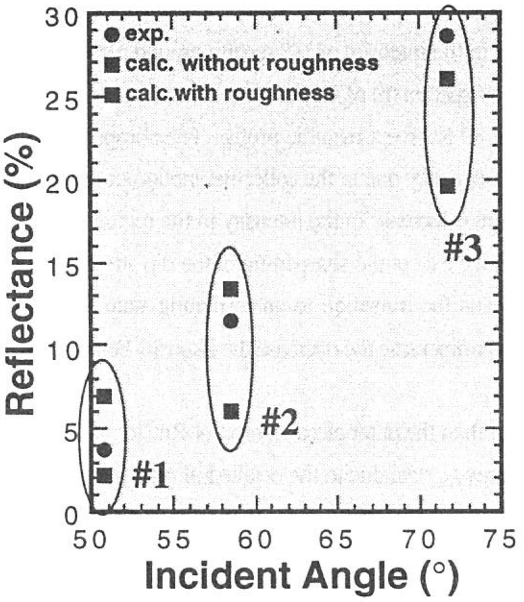

	#1	#2	#3
incident angle	50.8°	58.5°	71.8°
period	2.17nm	2.62nm	4.43nm
number of periods	40	40	20
roughness	0.37nm	0.37nm	0.373nm
substrate	Si(100)	Si(100)	Si(100)

Fig.2 Comparisons between measured reflectances, calculations with and without surface roughness. The wavelength is 2.742 nm which corresponds to Ti Lα.

（BL6A1）

Optical response of $PrRu_4P_{12}$ due to metal-insulator transition

Masato Hayashi[a],Masaya Nakayama[a] ,Takao Nanba[a], Itimin Shirotani[b], and Chihiro Sekine[b]

a Graduate school of Science and Technology, Kobe University, Nada-ku,
Kobe 657-8501, Kobe,Japan
b Muroran Institute of Technology, 27-1, Mizumoto,Muroran 050-0071, Japan

$PrRu_4P_{12}$ and $CeRu_4P_{12}$ are ones of ternary metal phosphides with the skutterudite structure ($CoAs_3$-type) which is represented as RT_4P_{12} (R=rare earth element and T=transition metal). Recently, their stable compounds have been successfully synthesized using a wedge-type cubic anvil high pressure apparatus under a high pressure of 4 GPa and high temperature of 1100 ℃[1] Most of them show an interesting physical properties at low temperature. According to the electric resistivity data, $CeRu_4P_{12}$ and $CeFe_4P_{12}$ are a semiconductor [1,2], $LaRu_4P_{12}$ shows a superconductivity, and $PrRu_4P_{12}$ show a metal-insulator transition with *Tc*=60K [3].

After the success of the synthesis, many experiments has started on these compounds but the optical measurements has not yet been done. We measured the reflection spectrum in order to know the electronic structure close to the Fermi energy level. In the present report the results of $PrRu_4P_{12}$ and $CeRu_4P_{12}$ are presented.

The temperature dependence of the optical reflection spectra of $PrRu_4P_{12}$ and $CeRu_4P_{12}$ were measured in the energy region of 5 meV-4 eV. A Michelson type of interferometer, Bruker 66v, was used with a suitable beam splitter in each available region combined together with a Si bolometer, a mercury-cadmium-telluride and a silicon photo-diode detector, respectively. The energy resolution was 4 cm^{-1} in the infrared region. The whole reflection spectrum at each temperature was obtained by connecting reflection spectra at different energy regions. The ordinate of the spectrum was calibrated by measuring the reflectivities by a few of He-Ne and argon ion laser lines. Finally the optical conductivity spectrum ($\sigma(\omega)$) was obtained from a Kramers-kronig transformation of the reflectivity spectrum.

Fig.1 shows the measured reflection (a) and the optical conductivity spectra (b) of $CeRu_4P_{12}$ at 300 K (dashed line) and 10 K (solid line). Both spectra showed a semiconductor-like behavior. We can see many phonon lines in the infrared region and the onset of the interband transition as the abrupt rise in the intensity of σ-spectra around 1000 cm^{-1} at a room temperature and 10 K. Fig.2 shows the reflection (a) and the σ spectra (b) of $PrRu_4P_{12}$ at 80 K (dashed line) and 10 K (solid line). The reflection and the σ spectra of $PrRu_4P_{12}$ at 80 K give a metallic profile. The abrupt rise in the reflection spectra below 2500 cm^{-1} corresponds to a so-called plasma frequency due to the collective motion of the free carriers. On the other hand, the reflection spectrum at 10 K showed a definite decrease in the intensity in the region below 1000 cm^{-1} although the position of the onset in the reflection does not change except the sharpening of the dip structure at 2500 cm^{-1}. The overall decrease in the intensity of the reflectivity means the transition to an insulating state from a metallic. In the σ spectra, the intensity around 200 cm^{-1} increases so as to compensate the decrease the intensity below 100 cm^{-1}.

The electronic configuration of $CeRu_4P_{12}$ is $Ce^{4+}[(Ru_4)^{8+}(P_{12})^{12-}]^{4-}$ and then the outer electron orbit of Ru^{2+}ion is $(4d)^6$. This configuration gives a semiconductor character because the lower energy t_{2g} state due to the octahedral crystalline field splitting is fully occupied and the upper e_g state is unoccupied. On the other hand, if the valence of the Pr ion of $PrRu_4P_{12}$ is Pr^{3+}, the valence of Ru ion has mixed valence of Ru^{3+}:$(4d)^5$ and Ru^{2+}:$(4d)^6$. The $(4d)^5$ configuration gives the partially unoccupied state of the t_{2g} state of Ru 4*d* orbit which gives rise to the metallic properties of $PrRu_4P_{12}$("valence fluctuation model"). However, the volume anomaly due to the metal(Pr^{3+})-insulator(Pr^{4+}) transition at 60 K has not been observed by the X-ray diffraction measurement. On the other hand, recent band calculation of $CeFe_4P_{12}$ pointed out the possibility of the gap formation due to the hybridization of the 4*f* state (Ce ion) with the 4*d* state (Ru ion) close at the Fermi level [4]. The peak at 200 cm^{-1} in the σ spectra of $PrRu_4P_{12}$ at 10 K may corresponds to the allowed transition between the mixed 4*f*-4*d* state.

References

[1] I.Shirotani *et al.*, J.Phys.Chem.Solids **57**, (1996)211. [2] G.P.Meisner, *et al.*, J.Appl.Phys.57, (1985)3073.

[3]C.Sekine, T.Uchiumi, I.Shirotani, and T.Yagi, Phys.Rev.Lett.79, (1997)3218.

[4] L.Nordström and D.J.Singh, Phys.Rev.**B53**, (1996)1103.

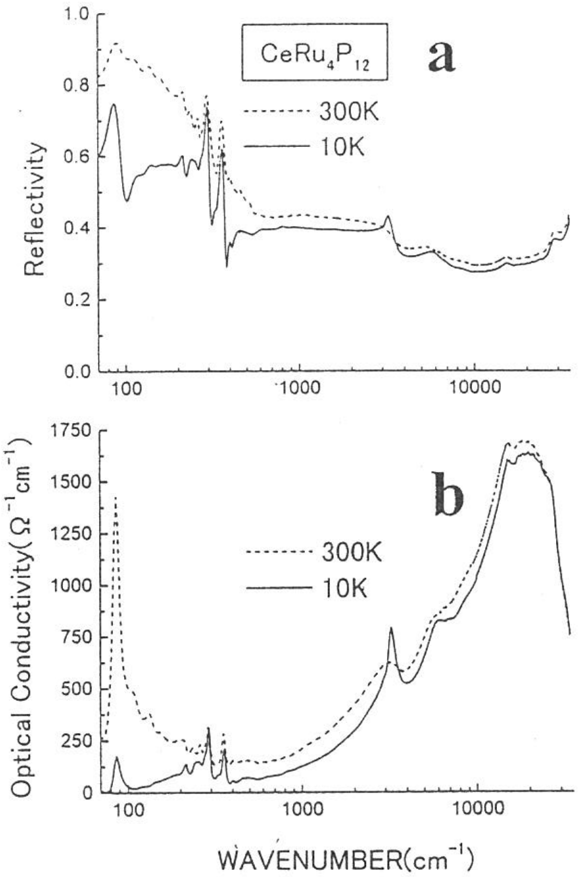

Fig.1 Reflection (a) and optical conductivity spectra (b) of $CeRu_4P_{12}$ at 300 K (dashed line) and 10 K (solid line).

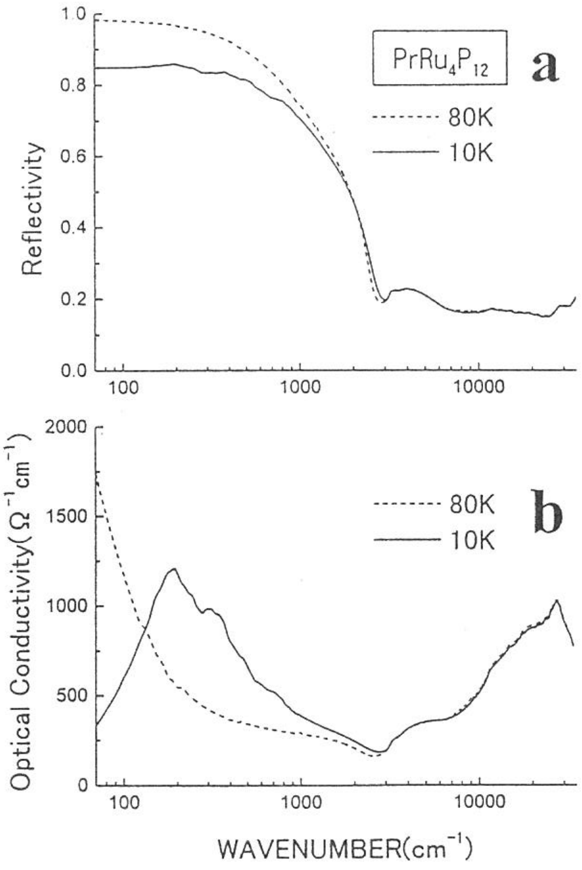

Fig.2 Reflection (a) and the σ spectra (b) of $PrRu_4P_{12}$ at 80 K (dashed line) and 10 K (solid line).

(BL6A1)

Reflection Measurements of Secondary Battery Substances $Li_{1-x}Ni_{1+x}O_2$ in the Millimeter Wave Region

Hitoshi OHTA, Shunsuke ONO, Atushi UEDA, Takao NANBA, Atushi HIRANO*
and Ryoji KANNO*

Department of Physics, Faculty of Science, Kobe University, 1-1 Rokkodai, Nada, Kobe 657-8501
**Department of Chemistry, Faculty of Science, Kobe University, 1-1 Rokkodai, Nada, Kobe 657-8501*

Recently $LiNiO_2$ has attracted much attention as an electrode material in Li ion secondary batteries. Although the composition of $LiNiO_2$ is very sensitive to the synthesis condition, especially the sintered temperature, and it can be easily lead to a decomposition of $Li_{1-x}Ni_{1+x}O_2$ which degrades the charge and discharge characteristics, Kanno *et al.* succeeded in synthesizing nearly stoichiometric $LiNiO_2$ and controling the concentration x.[1] We started our investigation to obtain the information about the diffusive motion of Li^+ ions in $LiNiO_2$ by observing "ionic plasmon" in the millimeter wave region because the mass of Li^+ ion is much heavier than that of electron. As we reported before,[2] we succeeded in observing an increase in a reflectivity of $LiNiO_2$ towards a low energy side in the millimeter wave region above 300K. In this study we tried to analize the data and also tried the measurement of non-stoichiometric sample to compare with the stoichiometric sample.

The reflection measurements of x=0.01 sample sintered at 650°C (sample A) and x=0.05 sample sintered at 850°C have been performed in the spectra region from 6 to 60 cm^{-1} using the beam line BL6A1 of UVSOR. For the measurement below 22 cm^{-1}, low pass filter was used. The temperature was changed from 79 K to 380 K for both samples. The gold plate was used as a reference and InSb detector was used as a detector. Figures 1 and 2 show our results for samples A and B. First we tried to analyze our data by simple Drude model but it turned out to be too simple to interpret our results. Therefore we employed the phenomenological model by Bruesch *et al.* [3] The fitted results are shown by dashed lines in Fig. 1 and the obtained plasma frequency turned out to be about 80 cm^{-1}. Therefore we need more measurements in higher wavenumber region in order to perform more accurate analyses. The temperature dependence of sample B shows similar behavior but higher reflectivity and the relaxation time in sample B seems to be shorter. More detailed x dependence measurements are still underway.

Acknowledgments: One of the authors (HO) is grateful to Kansai Research Foundation for technology promotion for the financial support.

[1] R. Kanno *et al.*: J. Solid State Chem. **110** (1994) 216.
[2] H. Ohta *et al.*: UVSOR Activity Report (1997) 128.
[3] Bruesch *et al.*: phys. stat. sol. (a) **31** (1975) 217.

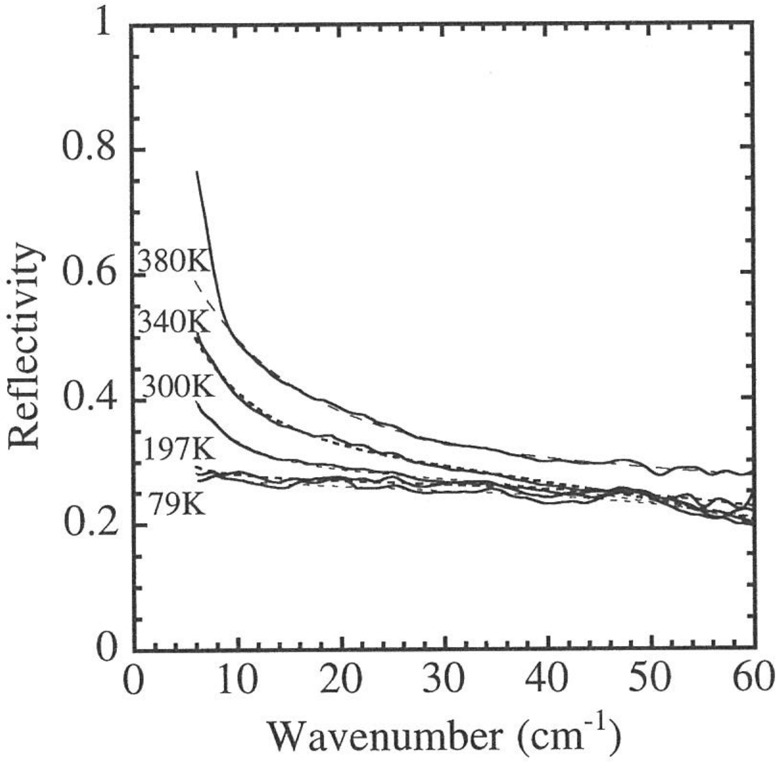

Fig.1 Reflection spectra of $Li_{1-x}Ni_{1+x}O_2$ sintered at 650℃ (sample A). x is about 0.01. Dashed lines are fitting curves.

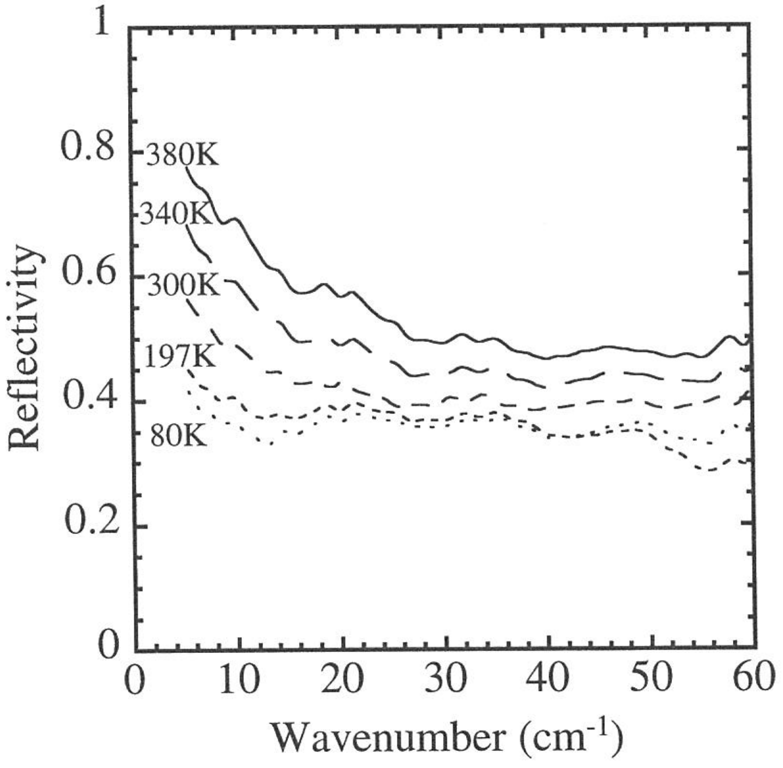

Fig.2 Reflection spectra of $Li_{1-x}Ni_{1+x}O_2$ sintered at 850℃ (sample B). x is about 0.05.

(BL6A1)

Electronic structure in magnetic ordered state of CeSb studied by magneto-optical spectroscopy in the infrared region

Shin-ichi Kimura[1], Hideaki Kitazawa[2], Giyu Kido[2], and Takashi Suzuki[3]
[1]*Graduate School of Science and Technology, Kobe University, Nada-ku, Kobe 657-8501*
[2]*Physical Properties Division, National Research Institute for Metals, 1-2-1 Sengen, Tsukuba, 305-0047*
[3]*Institute for Solid State Physics, The University of Tokyo, 7-22-1 Minato-ku, Tokyo 106-8666*

Materials in the magnetic ordered state shows the diversity of the physical properties in comparison with the normal state. Since the electronic structure in the ordered state should reflect the physical properties, the investigation of the electronic structure gives much useful information of the origin of the physical properties.

Cerium monopnictide (CeX; X = N, P, As, Sb, Bi) has complex magnetic phase diagram. In CeX series, CeSb is the material which has been studied very much. The famous neutron diffraction experiment has been done by Rossat-Mignod *et al.* and the complex magnetic phase diagram of 16 phases of CeSb was observed.[1] However the origin of the complex magnetic phase has been unclear yet. Our purpose is to understand the origin of the complex magnetic phase from the electronic structure in the magnetic ordered state of CeSb using optical reflectivity and magnetic circular dichroism measurement under magnetic field in the infrared region.

The CeSb sample was grown by a Bridgman method of a high-frequency furnace. The sample size for the optical measurement is about 4 mmϕ and 1 mm thickness. The sample was scraped along (100) plane in helium atmosphere and was mounted a closed cycle helium cryostat.

The magneto-optical experiment was done by using the infrared magneto-optical apparatus.[2] The measuring parameters of temperature, magnetic field and photon energy are 6.5 – 30 K, 0 – 6 T, and 0.05 – 2 eV, respectively. The optical measurement was done along the (100) plane and the magnetic field was applied to the <100> direction.

In this study, reflectivity spectra under magnetic field with unpolarized light (MR) and magnetic circular dichroism spectra of reflectivity with circularly polarized light (MCDR) were measured in the energy range of 0.05 – 2 eV. The optical conductivity spectra ($\sigma_{xx}(\omega, T, H)$) and the magnetic circular dichroism optical conductivity spectra ($\sigma_{\pm}(\omega, T, H)$) were obtained by the Kramers-Kronig transformation of the MR and MCDR spectra, respectively. Here, ± indicates the different selection rule of the magnetic quantum number of ±1. Below, the analysis is done by using the σ and $\sigma_{\pm}$ spectra.

Figure 1 indicates the temperature dependence of reflectivity spectrum from 6.5 to 30 K at 3 T. Above 20 K, the magnetic phase is assigned to be para-phase. The spectrum is very similar to those measured by Kwon *et al.*[3] and Pittini *et al.*[4] The spectra below the temperature change very much. The boundaries of the different spectra indicate the temperature of the magnetic or structural phase transition.

The parameters of temperature and magnetic field at which the MR spectra were measured are shown in Fig. 2. The same mark is the point of the same spectrum.

The boundary of the different marks indicates the phase transition point. The boundary is in good agreement with the magnetic phase diagram which was obtained by using the neutron scattering.[1] Therefore the result indicates that we can get the information of the magnetic phase transition from the MR spectra.

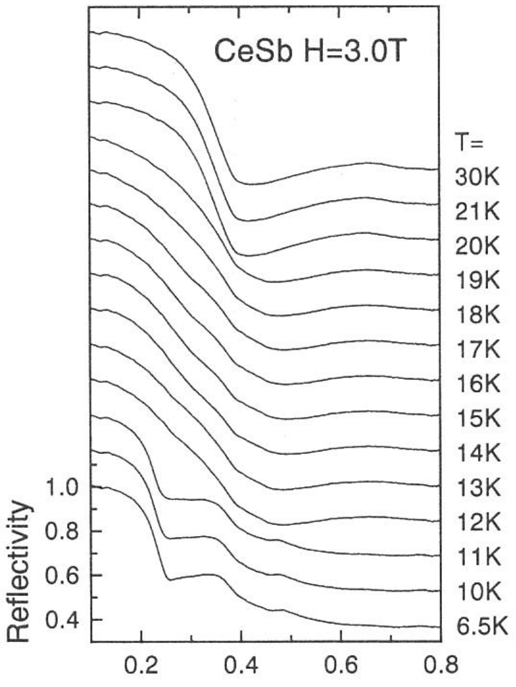

Fig. 1. Temperature dependence of the reflectivity spectrum of CeSb at 3.0 T as a function of the photon energy. Successive curves are offset by 0.2 for clarity.

The $\sigma_{xx}(\omega, T, H)$ spectra reflect the electronic

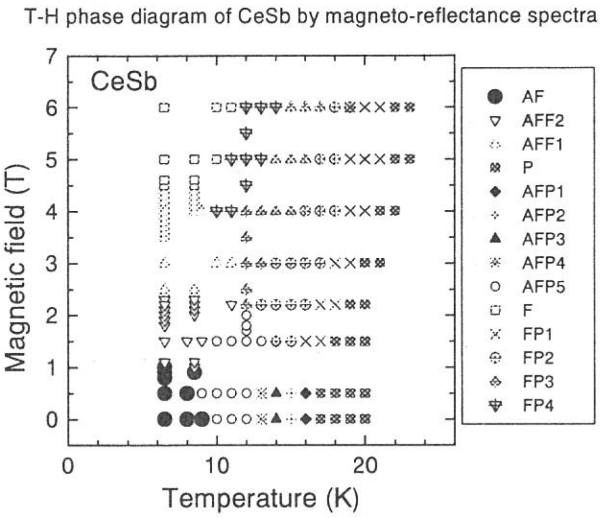

Fig. 2. Magnetic phase diagram determined by optical reflectivity measurement under magnetic field. The same marks indicate that the same spectrum has been obtained.

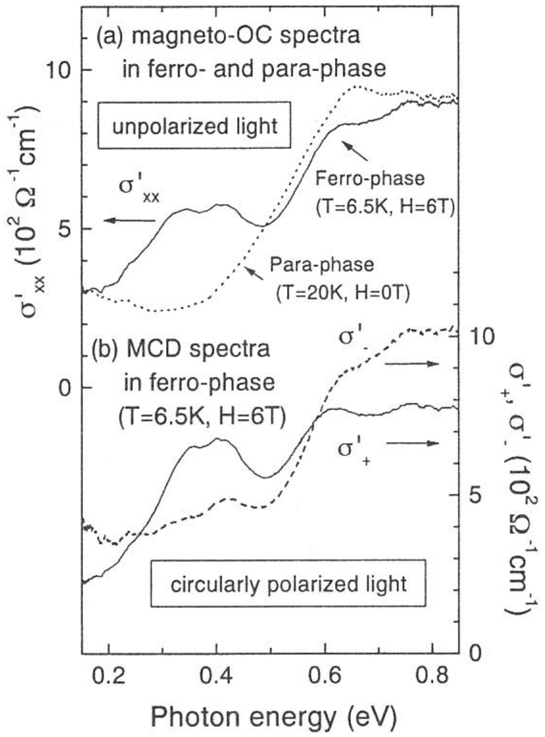

Fig. 3. (a) Optical conductivity spectra, σ'_{xx}, of the ferro-magnetic phase of CeSb at the temperature of 6.5 K and at the magnetic field of 6T (solid line) and that of para-magnetic phase at 20 K and at 0 T (dot line). (b) MCD optical conductivity spectra, $\sigma'_{\pm}$, of CeSb in the ferro-magnetic phase with the different selection rule of $\Delta m_j = \pm 1$, respectively.

structures in the magnetic phases. The optical conductivity observed in the energy range is due to the transition from the top of the valence band of Sb-*5p* to the bottom of the conduction bad of the Ce-*5d* bands according to the La*X* band structure. Then, the change of the $\sigma_{xx}(\omega, T, H)$ spectra reflect the change of these bands.

The change of the electronic structure is considered to originate from not only the band folding due to the appearance of the long periodic structure of the ordered magnetic state but also the shifting of the energy band, because the change of the $\sigma_{xx}(\omega, T, H)$ spectrum cannot be explained only by the band folding.[5]

We measured the MCDR spectra in the ferro-magnetic phase for the detail analysis of the electronic structure. Figure 3 (a) is the $\sigma_{xx}(\omega, T, H)$ spectra with unpolarized light and figure 3 (b) the $\sigma_{\pm}(\omega, T, H)$ spectra with circularly polarized light of the ferro-magnetic phase. Here, $\sigma_{\pm}(\omega, T, H)$ indicates the different selection rule of the magnetic quantum number of $\Delta m_j = \pm 1$. From the figure, we can understand that the double peak at 0.4 eV belongs to the $\Delta m_j = +1$ and the shoulder structure at 0.65 eV to the $\Delta m_j = -1$.

The *p* band of the magnetic ordered state is explained by the *p-f* mixing theory by Takahashi and Kasuya.[6] According to the theory, one *p* band shifts to 0.5 eV above the Fermi level and the others remain at the same energy of the para-magnetic state. The energy is almost equal to that of the double peak structure. However the optical transition from the *p* valence band to the shifted *p* band is considered to be weak even if the Sb *5p* - Ce *5d* mixing is strong. While, the Ce *5d* band should move close to the Fermi level in the ferro-magnetic phase. The electronic structure of the *5d* band is considered to be the origin of the anomalous physical property and the complex magnetic phase diagram. However, the theoretical study has never done before. Further theoretical study is required.

---

[1] J. Rossat-Mignod, J. M. Effantin, P. Burlet, T. Chattopadhyay, L. P. Regnault, H. Bartholin, C. Vettier, O. Vogt, D. Ravot and J. C. Achart; J. Magn. Magn. Mater. **52** (1985) 111.

[2] S. Kimura, Proc. SRMS-2 (to appear in Jpn. J. Appl. Phys. (1999)); UVSOR Activity Report 1996 (1997) 170; UVSOR Activity Report 1997 (1998) 60.

[3] Y. S. Kwon, T. Suzuki and T. Kasuya, Jpn. J. Appl. Phys. Series 8 (1993) 104.

[4] R. Pittini, J. Schoenes, O. Vogt and P. Wachter, Phys. Rev. Lett. **77** (1996) 944.

[5] S. Kimura, H. Kitazawa, G. Kido and T. Suzuki, preprint.

[6] H. Takahashi and T. Kasuya, J. Phys. C: Solid State Phys. **18** (1985) 2731.

(BL6A1)

Optical reflectivity study of the Kondo alloy system (Yb, Lu)B_{12}

H. Okamura, T. Inaoka, S. Kimura, T. Nanba,
F. Iga[A], S. Hiura[A], T. Takabatake[A], and J. Kleijn[A]

Department of Physics and Graduate School of Science and Technology,
Kobe University, Kobe 657-8501.
[A]Graduate School of Advanced Science of Matter,
Hiroshima University, Higashi-Hiroshima 739-8526

YbB_{12} is one of the strongly correlated electron systems known as "Kondo semiconductors".[1] Upon cooling below ~ 80 K, an energy gap of 10-15 meV develops, and also the magnetic susceptibility shows a large decrease. These unique behaviors are believed to arise from strong interactions between the localized Yb 4*f*-electrons and free carriers, but the microscopic mechanism is not precisely known yet. Previously, we reported the detailed temperature-evolution of the energy gap in the optical conductivity spectrum of YbB_{12}.[2] We also found a characteristic absorption in the mid-infrared region. This peak, referred to as the "IR peak", is likely to arise from Yb 4*f*-related optical transitions, but its microscopic origin was unclear.

In the present work we study the optical spectra of the mixed system (Yb, Lu)B_{12}, in order to see how the energy gap and the IR peak is suppressed as the Yb ions are replaced with Lu ions. An Yb^{3+} has 13 electrons and 1 hole in the 4*f* shell, while a Lu^{3+} has 14 electrons filling up the 4*f* shell. Hence, the substitution of Lu for Yb results in a decrease in the magnetic moment due to Yb^{3+}. Figure 1 shows the optical conductivity spectra in the gap region of (Yb, Lu)B_{12} at 8 K, normalized by those at 78 K. The clear energy gap seen for Yb 100 % sample is already much less clear for Yb 75 %, demonstrating a large effect of Yb replacement on the energy gap. It should be noted that the gap collapses by filing in from the bottom rather than becoming narrower, with the "shoulder" seen at ~40 meV nearly unshifted. Figure 2 shows the evolution of the IR peak for different Yb fractions. It is seen that, with decreasing Yb fraction, the IR peak red-shifts, becomes weaker and narrower, and finally merges into the Drude-like spectrum for the LuB_{12}. At lower temperatures (not shown here), the IR peak becomes narrower and slightly blue-shifts. Currently we are attempting to analyze these behaviors more quantitatively by fitting the spectra with Lorentz and Drude functions.

References

[1] T. Takabatake *et al.*, J. Magn. Magn. Mater. **177-181**, 277 (1998).

[2] H. Okamura, S. Kimura, H. Shionzaki, T. Nanba, F. Iga, N. Shimizu, T. Takabatake, Phys. Rev. B **58**, R7496 (1998).

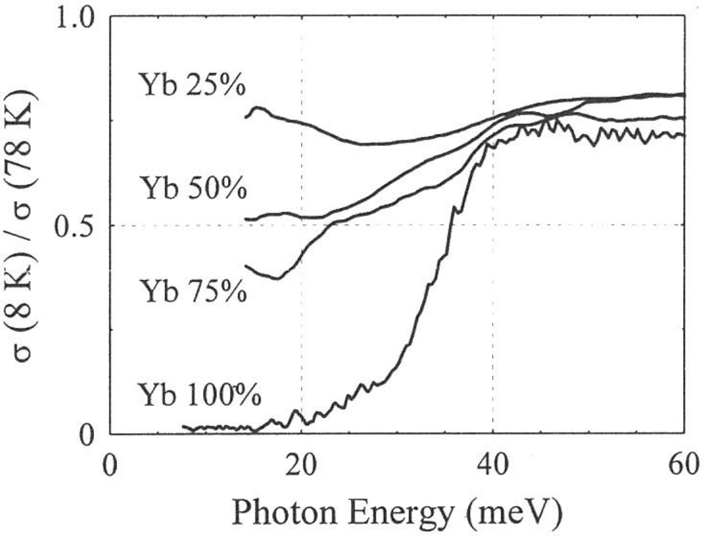

FIG. 1. Optical conductivity spectra of (Yb, Lu)B_{12} in the gap region at T=8 K normalized by those at 78 K.

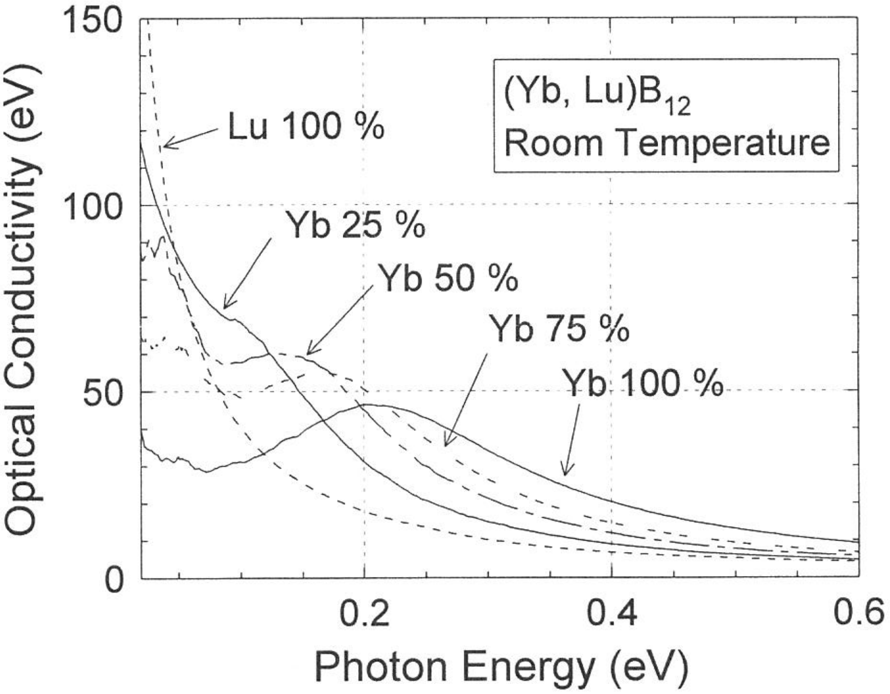

FIG.2 : Optical conductivity of (Yb, Lu)B_{12} at room temperature for (Yb, Lu)B_{12} with different Yb mole fractions.

(BL6A2)

Photoelectron spectroscopic study of core-exciton decay in BaF_2

Masao Kamada, Minoru Itoh,[A] and Yukinori Kiyota[A]

UVSOR Facility, Institute for Molecular Science, Myodaiji, Okazaki 444-8585
[A]Faculty of Engineering, Shinshu University, Nagano 380-8553

In recent decade, new luminescence, so-called Auger-free luminescence or cross luminescence, was discovered by the core-level excitations in the wide-band gap materials, where the band-gap energy (E_g) is larger than the energy difference (E_{VC}) between a valence band and an outer-most core level.1) The luminescence is attributed to the transition from the valence band to the core level. There is no Auger process when the condition $E_g>E_{VC}$ is satisfied, and then the Auger-free luminescence is so strong and useful for fast scintillation in the vacuum ultraviolet and soft x-ray regions. The Auger-free luminescence appears with the excitation of the core level. It is known that there are no exciton peaks in the excitation spectra, but the reason is not fully understood yet. The present work has been conducted to understand why core-exciton peaks are missing in the excitation spectra of Auger-free luminescence.

Experiments have been conducted at plane-grating monochromator beamline BL6A2 of the UVSOR facility, Institute for Molecular Science. Photoelectron spectra of BaF_2 were observed with an angle-resolved hemi-spherical energy analyzer. Specimens were prepared by evaporation in a preparation chamber and were transferred to an analyzing chamber. The base pressures of the preparation and analyzing chambers were $5x10^{-10}$ and $2.5x10^{-10}$ Torr, respectively, while the pressure was raised to $2x10^{-8}$ Torr during evaporation. Special cares were taken to make thin films of about 10 nm in thickness. No charging effects were observed in the present experiments.

Luminescence spectra of the same thin films were observed in the analyzing chamber by using a quartz lens and a Spex 270M monochromator with a princeton LN-532CCD detector. The luminescence and excitation spectra of single crystals were also measured for comparison. The luminescence spectra consist of two different luminescence bands, the Auger-free luminescence and the luminescence due to a self-trapped exciton. The energy positions of these luminescence bands in films are almost the same as those in the single crystals, but the intensity ratios are not the same between films and crystals.

Figure 1 shows a set of EDCs of a BaF_2 film which was obtained with excitation photon energies of 16.5-20 eV. The peak position and intensity of the valence band photoelectrons change drastically around the excitation photon energy of Ba-5p core exciton (17.1 eV). One of the present authors (M. K.) has been studying the decay process of the core-excitons in alkali halides by using photoelectron spectroscopy and proposed the following two non-radiative decay processes of the Li K-exciton in LiF; (1) direct-recombination process and (2) K_{ex}-VV Auger process.2) In the direct-recombination process, an excited electron and a core hole forming an core exciton recombine with one another, transferring the energy to a valence electron. This causes the resonant enhancement of the valence photoelectrons. The probability of the direct-recombination process can be estimated by using CIS and absorption (reflection) spectra. The obtained value is about 27-54 % for the Ba-5p exciton peak of BaF_2. It should be noted that the value is not 100 % , while there is no core-exciton peak in the excitation spectra of Auger-free luminescence. This indicates that there is another non-radiative decay of the core-exciton.

Previously kamada et al. proposed that in the K_{ex}-VV Auger process, a valence electron recombines with a core hole, transferring the energy to another valence electron. 2) This produces the two-holes and one-electron bound state consisting of two-holes in the valence band

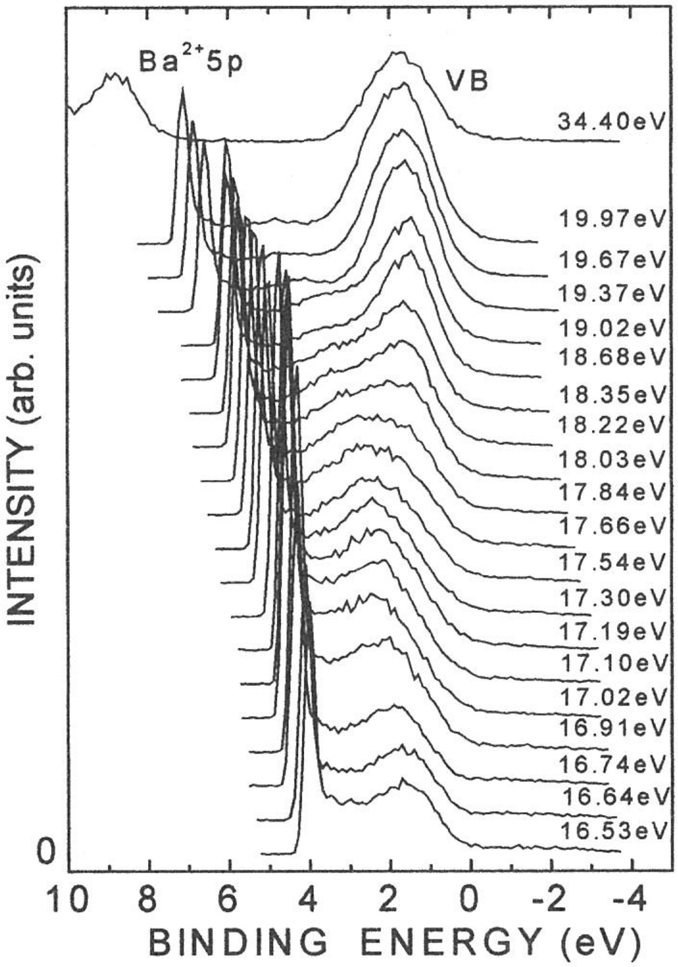

and an electron in the excited state, resulting in the resonant enhancement of the Auger electrons and the energy shift of the Auger electrons. The present material BaF_2 has an energy gap (E_g=10.8 eV) larger than the energy difference (E_{VC}=7.9 eV) between the valence band and an outer-most core-level. Therefore, in order to explain the present result, the two-holes and one-electron bound state may be produced at the final state of the core-exciton decay. The typical energy shift of the Auger electrons due to the two-holes and one-electron bound state is about 1.0 eV. Thus the kinetic energy of the Auger electrons produced at the final stage of the core-exciton decay is roughly estimated to be 8.9 eV. Since the exciton absorption band has a long tail down to 8.8 eV and also there are unknown bound states around 8 eV, the Auger transition may be possible, resulting in the suppression of the Auger-free luminescence at the excitation photon energy of the core-exciton.

It is also found that the resonance enhancement due to the core-exciton decay is large in the higher-binding energy part of the valence band. This fact indicates that the partial density of states of barium ions locates on the higher-binding energy side of the valence band or that the relaxed excited state of the core-exciton in BaF_2 is shifted by about 0.9 eV. The detailed analyses will be reported in near future.

References

1) S. Kubota, M. Itoh, J. Ruan(Gen), S. Sakuragi, and S. Hashimoto, Phys. Rev. Lett. 60 (1988) 2319.
2) M. Kamada, K. Ichikawa, and K. Tsutsumi, Phys. Rev. B 28 (1983) 7225.

(BL6A2)

Laser-induced core-level shifts in GaAs (100)

Masao Kamada, Jun-ichi Murakami[A], Senku Tanaka[B], Sam Dylan More,
Shuji Asaka[C], Minoru Itoh[A], and Yasuo Fujii[B]

UVSOR Facility, Institute for Molecular Science, Okazaki 444-8585
[A]Faculty of Engineering, Shinshu University, Nagano 380-8553
[B]College of Engineering, Osaka City University, Osaka 558-8585
[C]Equipment Develop Center, Institute for Molecular Science, Okazaki 444-8585

Electric potentials at semiconductor surfaces and interfaces are very important to understand a variety of electrical properties and phenomena of semiconductors and to control semiconductor devices. Lots of works have been conducted to know the equilibrium electronic states at the semiconductor surfaces and interfaces, but few works have been carried out to understand the dynamics of non-equilibrium charge distribution. Long *et al.* have first reported the transient surface photo-voltage on Si (111) using synchrotron radiation (SR) and laser pulses.[1)] They obtained non-equilibrium electron density induced by laser pulses in the space charge layer. An agreement between their experiments and theoretical simulations is good for a high power laser, but not for a low power laser. In recent years, Marsi *et al.* have conducted the similar experiment to study the transient surface photo-voltage on Si (111)2x1 and GaAs (110) surfaces,[2)] and reported the difference in dynamics between Si and GaAs surfaces. The purpose of the present work is to investigate the photo-induced carrier dynamics on GaAs (100), since this surface provides spin-polarized electrons after Cs- and oxygen treatments.[3)]

Figure 1 shows a schematic arrangement of the present experiments at BL6A2, where a plane-grating monochromator (PGM) and a hemi-spherical electron analyzer were installed. We used a mode-locked Nd:YAG laser with a pulse width of about 300ps, which was triggered with a signal from a master oscillator of the UVSOR storage ring. Second-harmonic light of the laser (photon energy 2.33 eV) was focused on the sample in a vacuum chamber, having a spot size of 2 mm, which covered well the SR spot size of 1 mm. The temporal overlap was also carefully adjusted by using a MCP-PM/TAC system. The energy distribution curves with and without laser excitation were measured in single scan by using an optical shutter. The clean surface of p-type GaAs (100) doped with Zn was prepared *in situ* using Ne-sputtering and thermal annealing procedures.

Figure 2 shows Ga-*3d* photoelectron spectra at 165 K. It is clearly observed that the Ga-*3d* level under laser excitation is shifted by about 0.33 eV to higher kinetic energy side. The As-*3d* level is also shifted by the same amount. Any change in spectral shape was not appreciable in both cases. Therefore, the present core level shift induced by laser excitation can be attributed to the transient photo-voltage effect. Namely, hot electrons and holes produced by laser pulses are separately distributed in the surface space-charge layer, and then their redistribution may change the band bending of GaAs. The dependences of the core-level shifts on the incident photon flux and the sample temperature are well explained by this idea.

This work was partially supported by a Grant-in-Aid from the Ministry of Education, Science, Culture, and Sports.

References
1) J.P.Long et al., Phys. Rev. Lett. 64 (1990) 1158.
2) M. Marsi et al., Appl. Phys. Lett. 70 (1997) 895.
3) N. Takahashi et al. Jpn. J. Appl. Phys. 35 (1996) 6314.

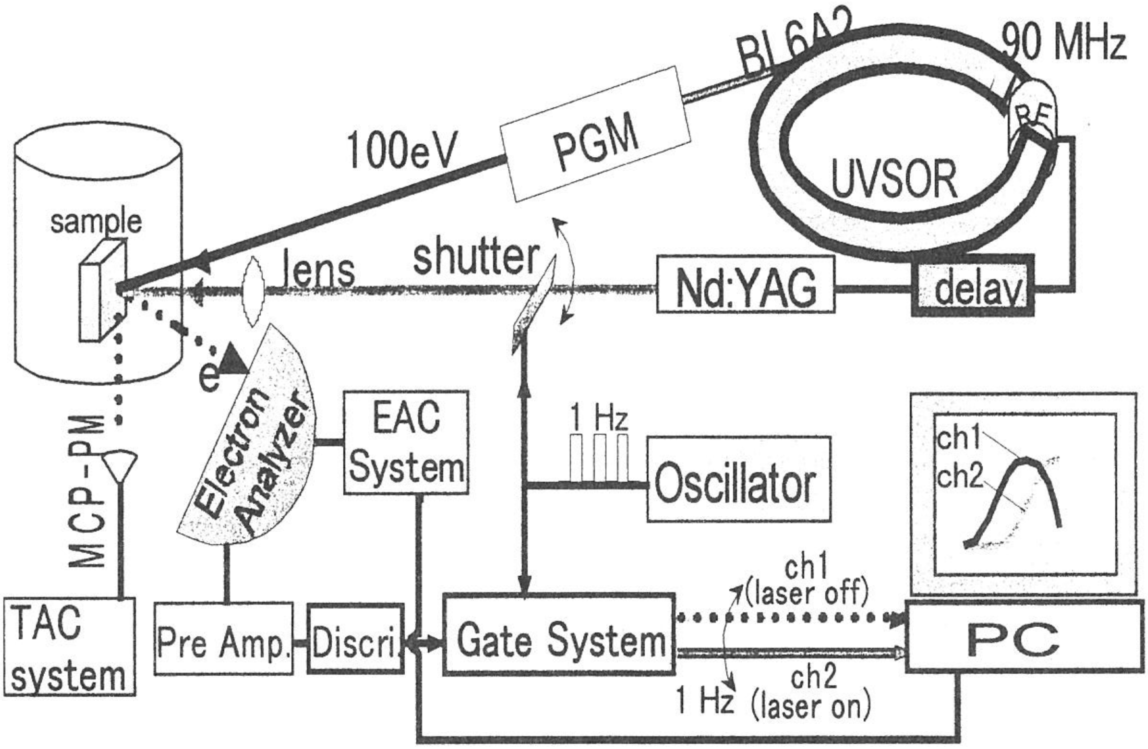

Fig. 1. Schematic experimental setup

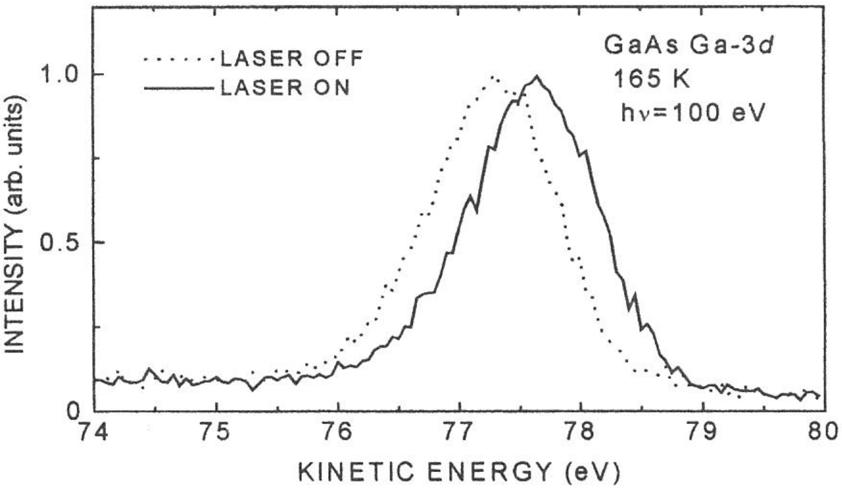

Fig. 2. Ga-3d photoelectron spectra with and without laser excitation.

(BL6A2)

Photoemission Studies on binary alloys $CrPt_3$ and $MnPt_3$

Hitoshi SATO, Shinya SENBA, Kozo TERAMOTO,
Masaki TANIGUCHI, Hiroshi MARUYAMA* and Masao KAMADA#

Fuculty of Science, Hiroshima University, Kagamiyama 1-3-1, Higashi-Hiroshima 739-8526
**Fuculty of Science, Okayama University, Tsushima-Naka 3-1-1, Okayama 700-8530*
#Institute for Molecular Science, Myodaiji, Okazaki 444-8585

Transition metal intermetallic compounds TPt_3 (T=V, Cr, Mn, Fe, Co) have Cu_3Au-type crystal structure and reveal a wide variety of magnetism. For VPt_3 and $CrPt_3$, the magnetic moments on the Pt sites align in an antiparallel direction to those on the T sites, forming a ferrimagnetic ordering. $MnPt_3$ and $CoPt_3$ are ferromagnetic compounds, while $FePt_3$ exhibits antiferromagnetism with a (1/2,1/2,0) magnetic reflection. In this study, we have carried out the photoemission experiments on $CrPt_3$ and $MnPt_3$ in the Cr and Mn 3p-3d excitation region.

Samples used for the experiments were prepared by the arc-melting method under an Ar atomosphere. Photoemission experiments were carried out on plane-grating monochromator beam line BL6A2. Photoelectrons were collected with a hemi-spherical analyzer. Clean surfaces were obtained by scraping with a diamond file under ultrahigh vacuum. All experiments were performed at room temperature.

Figure 1 shows a series of photoemission spectra of $MnPt_3$ in the Mn 3p-3d excitation region (~ 50 eV). The photoemission intensities have been normalized to the monochromator output. Binding energy is referred to the Fermi level. We notice that the Mn 3d and Pt 5d hybridization band spreads over the top 7 eV region of the valence bands. It is noted that the resonant enhancement is not observed clearly. This means that the Mn 3d electrons in $MnPt_3$ have extremely itinerant character and strongly hybridize with the Pt 5d states. However, a small amount of enhancement is observed around 3.2 eV as indicated by a bar in the figure. The Mn 3d states are considered to contiribute to the valence bands mainly around this energy. As for $CrPt_3$ also, the resonant enhancement was not observed (not shown here), but the energy position of the Cr 3d states seems to be just below the Fermi level.

In the Cr and Mn 3d excitation region, the photoionization cross-section of the Pt 5d states is larger than those of the 3d states. In order to separate more clearly the Cr/Mn 3d and Pt 5d partial densities of states in the valence bands, we plan to measure the photoemission spectra at the Cooper minimum in the Pt 5d cross-section.

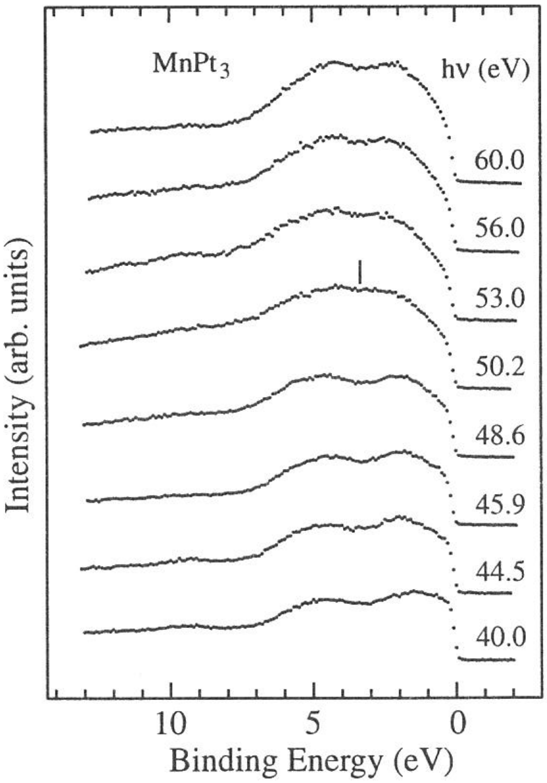

Fig.1 A series of photoemission spectra of $MnPt_3$ in the Mn 3p-3d excitation region.

(BL6B)

Far-Infrared Pump-Probe Measurement of an Organic Semiconductor β'-(BEDT-TTF)$_2$ICl$_2$ using Synchrotron Radiation Source

Akito Ugawa[†] and Tahei Tahara

Institute for Molecular Science, Myodaiji, Okazaki 444-8585, Japan

Time-resolved spectroscopy (TRS) provides decisive information about fast-decay phenomena in solid state as well as in liquid or gaseous state. The investigations for the phenomena observable in infrared-visible regions have been achieved in stages by the development of nano-, pico-, and femto-second pulsed lasers. For far-infrared (FIR) region, however, it is still difficult to carry out TRS because (1) suitable crystals that can generate short FIR pulses with non-linear optical process are not available and (2) the response of ordinary FIR detectors is too slow to trace the changes faster than nanosecond order. Synchrotron radiation (SR) affords picosecond optical pulses ranging from FIR to x-ray, pulses which enable a picosecond FIR-TRS over unlimited measurable ranges when we can induce detectable changes in a sample by irradiation of the picosecond laser pulses synchronized with the SR.

We have constructed a FIR-TRS system at UVSOR BL6B beamline, the schematic diagram of which is shown in Fig. 1. We employed a Bruker IFS 113v for FIR spectrometer. The pumping laser pulses and the probing SR pulses are focused and overlapped on a sample. The relative timing of the laser pulses to the SR pulses, which is variable through a phase shifter, was measured by a single-photon counting technique. The time resolution in the current system is about 1 ns, predominantly determined by the duration of the SR.

We chose in this study an organic semiconductor β'-(BEDT-TTF)$_2$ICl$_2$ as a candidate for the pump-probe experiment. Figure 2 shows the $\boldsymbol{E}||\boldsymbol{b}$ polarized conductivity of β'-(BEDT-TTF)$_2$ICl$_2$ obtained by a Kramers-Krönig transformation of the reflectance that was measured on a mosaic consisting of three single crystals aligned so as to make a large (001) face: the absolute reflectivity was obtained by normalizing the sample spectrum with the spectrum measured again after evaporating gold on the sample surface. The line width of each absorption band becomes narrower and consequently sharper at low temperature, and we choose the spectrum at 6.7 K for the band assignment (see the inset of Fig. 2). In the β'-type crystal, BEDT-TTF molecules are stacked along the *b*-axis, forming strongly dimerized chains. In such cases intermolecular electron density oscillations appear only as a result of totally symmetric (A_g) vibrations of the dimer forming molecule through electron-molecular-vibration (EMV) coupling[1].

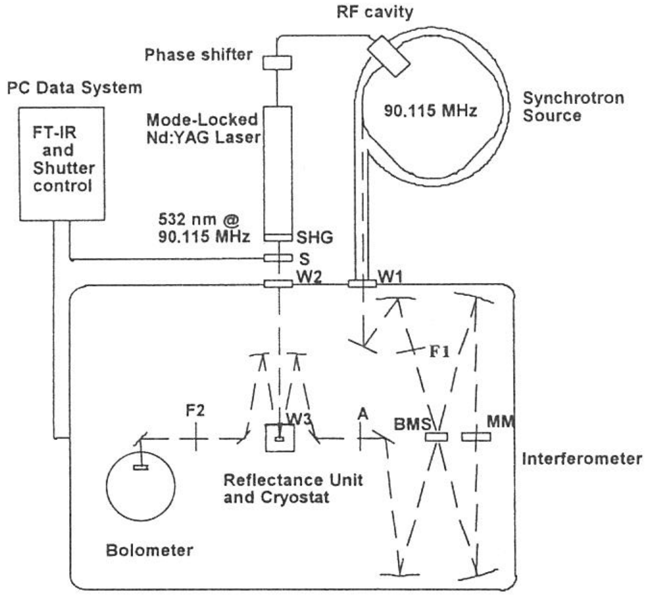

Fig. 1. Diagram of FIR-TRS system at UVSOR BL6B. All of optics are placed under the vacuum (~5 Torr) to exclude the influence of vapor water and carbon dioxide. W1: wedged silicon window; W2: quartz window; W3: white polyethylene-quartz hybrid window; F1, F2: black polyethylene filter; BMS: beam splitter; MM: moving mirror; A: aperture; S: solenoid shutter. Some mirrors are not drawn for simplicity.

[†] Present address: Department of Physics, University of Florida, Gainesville, FL32611-8440, U.S.A.

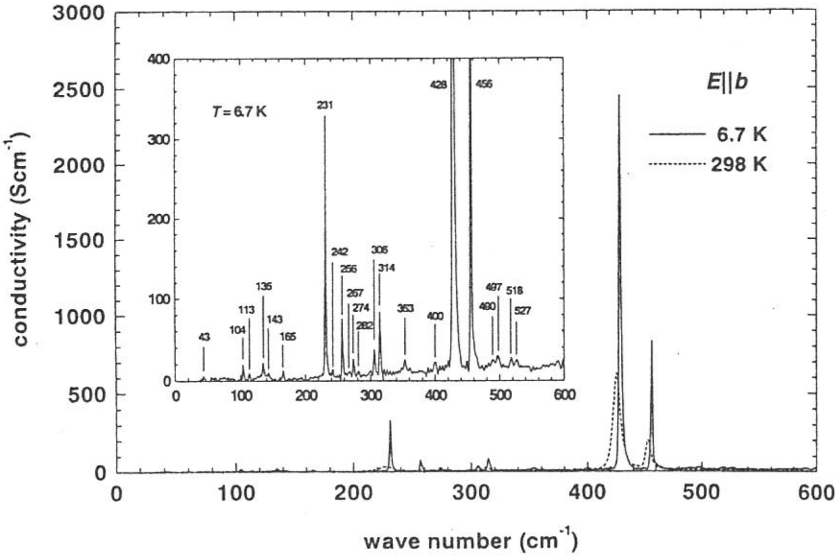

Fig. 2. Far-infrared conductivity of β'(BEDT-TTF)$_2$ICl$_2$ measured at 298K and 6.7 K with the $\boldsymbol{E}||\boldsymbol{b}$ polarization.

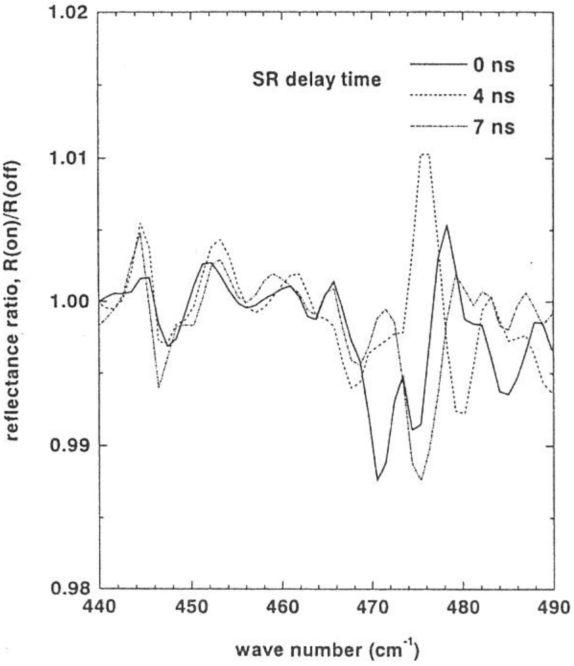

Fig. 3. Time-resolved difference spectra of β'(BEDT-TTF)$_2$ICl$_2$ measured at 8.3 K, with the probing SR delay time of 0 ns (solid), 4ns (dash), and 7ns (dash-dot).

More than twenty absorption bands are observed below 600 cm^{-1}, three of which are assigned to the normal modes of the counter anion ICl$_2^-$, at 231 cm^{-1} (angle distortion), 256 cm^{-1} (totally symmetric stretching), and 428 cm^{-1} (totally anti-symmetric stretching), respectively. We here concentrate on the A_g modes of BEDT-TTF^{+1}, some of which can strongly couple with the HOMO of BEDT-TTF$^+$ where an unpaired electron is located [2]. The band at 456 cm^{-1}, one of the A_g modes of BEDT-TTF molecule [2], demonstrates a very strong absorption intensity compared to the other bands, implying that this band is enhanced due to the EMV coupling. This band is expected to show some photo-induced features accordingly.

In Fig. 3 is shown the time-resolved difference spectra at 8.3 K at the probing SR delay time of 0, 4, and 7 ns, with the pumping laser power of 10 mW. The most prominent change was observed around 230 cm^{-1}, originating from the counter anion, but it did not depend on the delay time. However, we observed the delay-time dependent change around 475 cm^{-1}. Although the signal-to-noise ratio is not high, we believe that this time-dependent change is due to the far-infrared dynamic phenomenon relating to the A_g mode in this organic semiconductor.

We acknowledge D.B. Tanner for providing A.U. with the opportunity to carry out this experiment at IMS.

[1]N.O. Liparri, *et al.*, Int. J.Quantum Chem. **11**, 583 (1977).
[2]M.E. Kozlov *et al.*, Spectrochim. Acta. **45A**, 437 (1989).

(BL7A)

Soft X-ray Absorption Study of Al-based Quasicrystals and Alloys

M. MORI, T. MATSUKAWA‡, T. ONDA and M. FURUTA

School of Informatics and Sciences, Nagoya University, Nagoya 464-8601
‡ Naruto University of Education, Naruto, Tokushima

Since the discovery of an icosahedral phase (i-phase) in Al-Mn alloys by Shechtman *et al.* [1], there have been reported a large number of studies about the electronic properties of icosahedral materials in spite of remaining the arrangement of the atoms in an i-phase unclear. By intuition the pseudogap structure can be interpreted in terms of the nearly-free-electron-like energy gap inferred from the strong diffraction spots, which may be related to the stability of the i-phase. Friedel pointed out the possibility that the pseudogap structure can be enhanced by a crossing effect of 3d state with the nearly-free-electron-like state, and the stability would be augmented in an i-phase system containing transition metals by the crossing effect at about E_F which enhances the energy gap of the Brillouin zone. Recently a pseudogap-like anomaly in the DOS structure near E_F was directly confirmed with the photoemission study of an Al-Cu-Fe i-phase by Mori *et al.* [2]. A number of authors have reported about the structures of quasicrystals. But the final answers has not reported yet. More than half materials making quasicrystals has a Al element for the main component. We should have the information around a local structure around aluminum at least. But we dot know the EXAFS study of an Al element. We have already tried to study EXAFS about Al, but in the results many goast peaks appear.

The purpose is to observe soft x-ray absorption study to search the Al K edge and discuss about Al electron states and Al local structures on the stability of the i-phase. The sample – an Al-Pd-Mn i-phase quasicrystal – was an ingot prepared by the same method in ref. [3]. It was confirmed that the specimen used with this study consists of only *a usually-reported F-type i-phase* but does not contain the other phases. Photo yield studies were performed with a spectrometer on beam-line BL-7A. All measurements were carried out at room temperature. The clean surface of the specimen was obtained by scraping with a diamond file in a vacuum of $2 - 4 \times 10^{-8}$ Torr. A spectral dependence of incident radiation was determined from a photoelectric yield spectrum of gold.

At first, we try to get a yield spectra of pure aluminum ingot. But we cannnot have good data of aluminum K-edge.

[1] Shechtman D., Blech I., Gratias D. and Cahn J. W., 1984, *Phys. Rev. Lett.*, **53**, 1951

[2] Mori M., Matsuo S., Ishimasa T., Matsuura T., Kamiya K., Inokuchi H. and Matsukawa T., 1991, *J. Phys.: Condens. Matter*, **3**, 767 *ibid.*, 1992, *J. Phys.: Condens. Matter*, **4**, L157

[3] Ishimasa T. and Mori M., 1992, *Phil. Mag.*, **B18**, L175

(BL7A)

Zr L_3-Edge XANES analysis of Fe/SO_4^{2-}/ZrO_2 catalyst.

Tomomi Kosaka, Yoshiaki Takahashi, Ayako Matsuyoshi, Atsuyuki Miyaji and Sadao Hasegawa

Department of Chemistry, Tokyo Gakugei University, Koganei, Tokyo 184-8501

Introduction

Sulfated ZrO_2 was known as the solid superacid which has catalytic function of skeletal isomerization for alkane. Recently, an iron and a manganese ion were promoted to the sulfated ZrO_2 was found to be several times more active than unpromoted one by Hsu et al [1]. This catalyst was later studied by several researchers [2-5] and confirmed its remarkable activity. However, the effect of Fe and Mn promoters to the activity for skeletal isomerization was still unknown. In this work, we prepared sulfated Fe/ZrO_2 and investigated its electron structure using X-ray absorption near edge spectroscopy at Zr L_3-edges.

Experimental

The sample powder was obtained by the following procedure. Aqueous ammonia (25% NH_3) added slowly to a solution of $ZrOCl_2 \cdot 8H_2O$ until pH=8. After the precipitated $Zr(OH)_4$ gel was washed by a deionized water, dried at 383K for 24h. Fe/ZrO_2 was prepared in a solution of 3.74mol/l $Fe(NO_3)_2$ for 6h and dried, then calcined at 473～1073K for 2h in air. Secondary, the obtained powder was stirred in a solution of 0.5mol/l H_2SO_4 for 6h and dried at 383K for 24h in air, calcined for 2h in air at 100K below than the temperature Fe/ZrO_2 prepared, then sulfated Fe/ZrO_2 powder was obtained. In this report, the secondary calcination temperature was indicated on the case of sulfated Fe/ZrO_2.

Zr L_3-edge XANES analysis was carried out on the BL7A at UVSOR, Institute for Molecular Science, Okazaki, Japan. Spectra were recorded in a total electron yield mode at room temperature, using Ge(111) double crystal monochromator.

Results and Discussion

Fig.1 and 2 shows Zr L_3-edge spectra of sulfated ZrO_2 [6] and sulfated Fe/ZrO_2 calcined at different temperature. The two peaks (2221, 2223eV) which were correspond to transfer from $2s_{3/2}$ to t_{2g} and e_g of 4d orbital, observed in these spectra. As reported previously, sulfated ZrO_2 has a characteristic electron structure when it was most active for catalytic reaction[6]. A same phenomenon was observed in Fig.2. The spectra of sulfated Fe/ZrO_2 which calcined at 673K and 773K was similar one of sulfated ZrO_2 calcined at 873K. It was indicated that Zr atom has high oxidation state due to S atom in SO_4 ion was acted as electron acceptor when the highly activity for catalytic reaction was observed. Accordingly, we measured the conversion of sulfated Fe/ZrO_2 to skeletal isomerization for n-butane at 473K. As expected, the best conversion was observed in sulfated Fe/ZrO_2 which calcined at 673K. However, the calcination temperature for most active state was about 100～200K lower than that of sulfated ZrO_2. On the other hand, the absolute value of best conversion on sulfated Fe/ZrO_2 (about 4%) was considerably low compared to sulfated ZrO_2(about 20%). This low activity of sulfated Fe/ZrO_2 was caused by small surface area due to two times of the calcination. From these results, it was confirmed that the calcination temperature needs for high oxidation state, that is, most active state was decreased by Fe addition in this catalysis series. However, its generation mechanism of superacidic sites were still unknown.

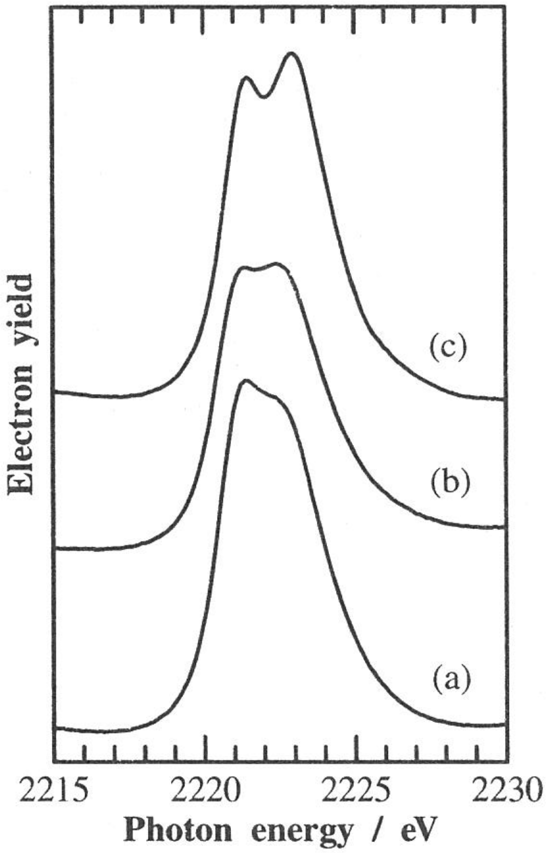

Fig.1 Zr L_3–edge XANES spectra on sulfated ZrO_2 calcined at (a)673K, (b)773K, (c)873K

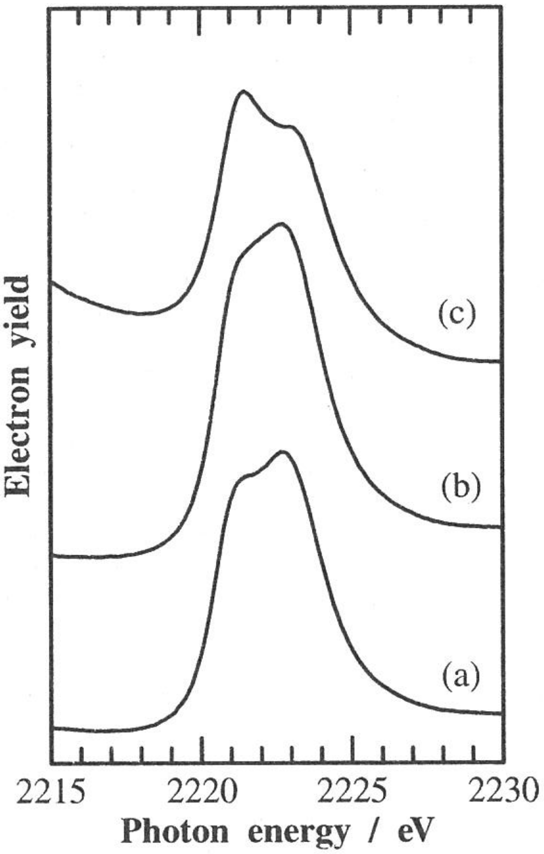

Fig.2 Zr L_3–edge XANES spectra on sulfated Fe/ZrO_2 calcined at (a)673K, (b)773K, (c)873K
Temperature is indicated the secondary calcination temperature.

References

[1] C. Y. Hsu, C. R. Heimbuch, C. T. Armes, and B. C. Gates, *J.Chem.Soc., Chem.Commun.*, 1645(1992).

[2] A. Jatia, C. Chang, J. D. MacLeod, T. Okubo, and M. E. Davis, *Catal.Lett.*, **25**, 21(1994).

[3] M. A. Coelho, D. E. Resasco, E. C. Sikabwe, and R. L. White, *Catal.Lett.*, **32**, 253(1995).

[4] V. Adeeva, J. W. de Haan, J. Jänchen, G. D. Lei, V. Schünemann, L. J. M. van de Ven, W. M. H. Sachtler, and R. A. van Santen, *J.Catal.*, **151**,364(1995).

[5] J. E. Tábora, and R. J. Davis, *J.Chem.Soc. Faraday Trans.*, **91**, 1825(1995)

[6] T. Kosaka, T. Ohnari, Y. Takahashi, and S. Hasegawa, *UVSOR activity report*, 164(1997)

(BL-7A)

Al K-edge XANES Study for the Quantification of Aluminum Coordinations in Alumina

Ken-ichi Shimizu, Yuko Kato, Tomoko Yoshida [A], Hisao Yoshida, Atsushi Satsuma and Tadashi Hattori [B]

Department of Applied Chemistry, Graduate School of Engineering, Nagoya University, Chikusa-ku, Nagoya 464-8603

[A] *Center for Integrated Reserch in Science and Engineering, Nagoya University, Chikusa-ku, Nagoya 464-8603*

[B] *Research Center for Advanced Waste and Emission Management, Nagoya University, Chikusa-ku, Nagoya 464-8603*

Transition aluminas, such as γ-Al_2O_3, formed by partial dehydration of aluminum hydrates have been of catalytic importance [1]. However, because of their poor crystallinity, an accurate structure of the transition aluminas is not known except for θ-Al_2O_3, in which Al atoms are equally distributed between tetrahedral and octahedral site of the spinel [2]. Although ^{27}Al MAS NMR can be used to distinguish several Al atoms with different local structures, its application to a quantitative structural analysis of amorphous alumina is difficult [3]. Recently, we reported that Ga atoms with different coordination symmetry can be estimated quantitatively by a deconvolution analysis of Ga K-edge XANES [4]. In this study, the Al K-edge XANES analysis is used to quantitatively determine the tetrahedral and octahedral Al atoms in the transition aluminas.

A series of alumina with various phases were prepared by calcining aluminum hydrate (boehmite) in air at various temperatures (673-1773 K) for 2 h. Mordenite-type aluminosilicate (JRC-Z-HM15, SiO_2/Al_2O_3 =15) containing Al atoms in the zeolite framework was supplied from the Catalysis Society of Japan. θ-Al_2O_3 was prepared by calcining γ-Al_2O_3 (JRC-ALO-4) at 1273 K for 12 h. Crystal phase of these samples was confirmed by X-ray diffraction and was noted in the caption of Fig. 1.

Al K-edge X-ray absorption spectra were measured on BL-7A at UVSOR with a ring energy of 750 MeV and a stored current of 70-220 mA in a mode of total electron yields. An YB_{66} double crystal monochromator was used, and the absolute energy scale was calibrated to a negative glitch due to Y L_3 peak of the YB_{66} at 2080.0 eV [5]. The step with of the monochromater scanning was 0.01° , which corresponds to about 0.3 eV at 1560 eV.

Fig. 1 shows the normalized Al K-edge XANES spectra of alumina samples together with those of some reference compounds of known structure. For the mordenite, which was employed as a model compound of the AlO_4 tetrahedra, a white line feature was appeared at 1566 eV. The sample calcined at 1773 K (α-Al_2O_3, corundum) and boehmite are regarded as model compounds for AlO_6 octahedra. The XANES spectrum of them exhibited a strong white line feature at 1568 eV, together with a broad peak at around 1571-1572 eV. The peaks at 1566 eV and 1568 eV in the spectra exhibited the same energy position as those previously reported for AlO_4 and AlO_6 model compounds, respectively [6], and thus they were assigned to octahedral and tetrahedral Al, respectively. A broad peak at around 1571-1572 eV is known to be due to AlO_6 octahedra [6]. This peak can include multiple scattering contributions [7], and thus it was not employed for the analysis in the present study. For the transition aluminas, which were calcined in the range 673 K to 1273 K, XANES spectra exhibited three distinguishable peaks due to AlO_4 (1566 eV) and AlO_6 (1568 and 1572 eV). It appears that the relative intensity of each peak differs from sample to sample.

To estimate the ratio of Al atoms in tetrahedral and octahedral sites in transition aluminas, the deconvolution analysis of XANES spectra [4] was carried out. Fig. 2 shows the deconvoluted spectrum of θ-Al_2O_3 as an example. The analysis was performed on the assumption that the XANES spectrum is composed of three Gaussian functions for white line peaks due to AlO_4 (1566 eV) and AlO_6 (1568 eV) and the third peak at around 1571-1572 eV and one arctangent function for continuum absorption. Thus, the best parameters, *i.e.*, the exact peak energy, the FMWH and the peak area of each Gaussian were determined so as to simulate the original spectra and were listed in Table 1. The positions of the first and the second Gaussian peaks were centered at 1565.5±0.1 eV and 1567.7±0.2 eV, which were almost identical to those of AlO_4 and AlO_6, respectively, within an experimental error. For θ-Al_2O_3, the ratio of the areas of 1566 eV peak and 1568 eV peak was determined to be 50/50, which is in good agreement with the value derived from X-ray diffraction analysis [2]. This suggests that the ratio of AlO_4/AlO_6 in the samples can be estimated quantitatively from the ratio of each Gaussian peak areas.

By using this method, the ratio of AlO_4 and AlO_6 was estimated for a series of transitional aluminas and plotted as a function of calcination temperature (Fig. 3). The result shows that the ratio of AlO_4 and AlO_6 is a function of the calcination temperature. For aluminum hydrate (boehmite), as expected, AlO_6 octahedra are predominant. As calcination temperature increases up to 1073 K, the fraction of AlO_4 increases up to the value of 36 %, and then it decreases at higher calcination temperature. For the sample calcined at 1773 K, which is classified as α-Al_2O_3, AlO_6 octahedra are predominant. Thus, this method is shown to be helpful for a better understanding of the effect calcination conditions on the local structure of the transition aluminas.

In conclusion, the deconvolution analysis of Al K-edge XANES is provided as a novel characterization method for the quantitative analysis of Al coordination states (tetrahedra and octahedra) in aluminum oxides. This method can now be used to determine the coordination states of unknown aluminum oxides.

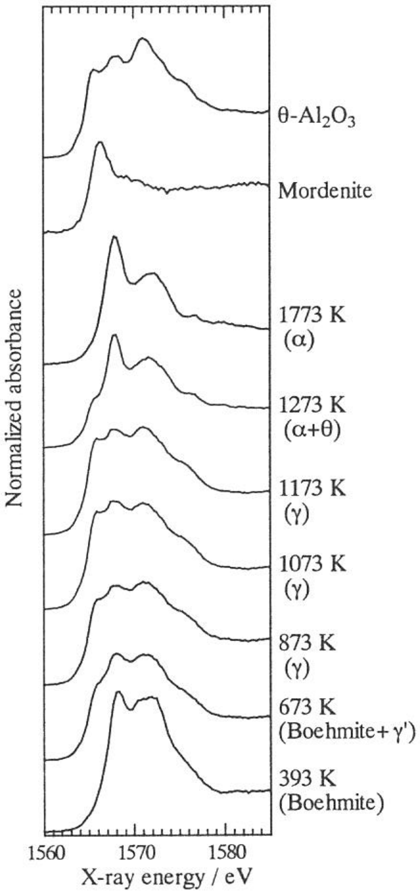

Figure 1 Al K-edge XANES spectra of alumina samples and reference compounds.

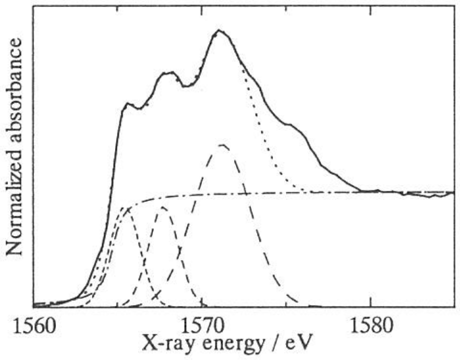

Figure 2 Al K-edge XANES spectrum of θ -Al_2O_3 (-) and the simulated spectrum (• • •), which is composed of three Gaussian (---) and one arctangent (-·-) functions.

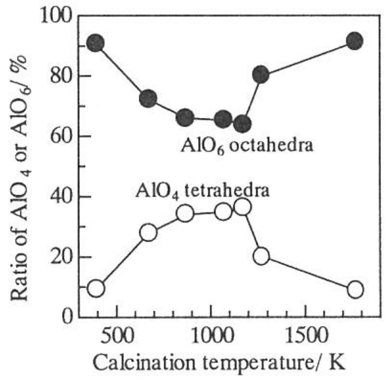

Figure 3 Ratio of AlO_4 tetrahedra (○) and AlO_6 octahedra (●) in alumina samples as a function of calcination temperature.

Table 1: Parameters of deconvoluted peaks in XANES spectra of aluminum oxides.

sample	AlO_4 tetrahedra / eV			AlO_6 octahedra / eV			third peak / eV			
calc. temp./K	position	FWHM	area	position	FWHM	area	position	FWHM	area	AlO_4/AlO_6
θ -Al_2O_3	1565.5	2.1	1.8	1567.8	2.1	1.8	1571.2	4.0	5.6	50/50
393	1565.5	1.8	0.5	1567.9	2.4	5.3	1571.5	5.0	13.5	9/91
673	1565.6	1.7	1.1	1567.7	2.6	2.9	1571.3	5.1	7.5	28/72
873	1565.6	1.7	1.3	1567.6	2.6	2.5	1571.3	5.0	6.3	34/66
1073	1565.6	1.7	1.9	1567.6	2.7	3.5	1571.3	5.1	8.4	35/65
1173	1565.5	1.7	1.9	1567.5	2.7	3.3	1571.2	4.8	7.7	36/64
1273	1565.4	2.0	0.7	1567.8	1.8	2.8	1571.5	5.1	6.1	20/80
1773	1565.4	1.7	0.5	1567.7	2.4	5.3	1571.8	4.4	5.7	9/91

References

[1] H. Knozinger, P. Ratnasamy, *Catal. Rev. Sci. Eng.*, 17 (1978) 31.

[2] R.-S. Zhou, R. L. Snyder, *Acta Cryst.*, B47 (1991) 617.

[3] G. Kunath-Fandrei, T. J. Bastow, J. S. Hall, C. Jager, M.E. Smith, *J. Phys. Chem.*, 99 (1995) 15138.

[4] K. Nishi, K. Shimizu, M. Takamatsu, H. Yoshida, A. Satsuma, T. Tanaka, S. Yoshida, T. Hattori, *J. Phys. Chem. B*, 102 (1998) 10190.

[5] T. Kinoshita, Y. Takata, T. Matsukawa, H. Aritani, S. Matsuo, T. Yamamoto, M. Takahashi, H. Yoshida, T. Yoshida, Y. Ufktepe, K. G. Nath, S. Kimura, Y. Kitajima, *J. Syncrotron Rad.*, 5 (1998) 726.

[6] G.A. Waychunas, G.E. Brown Jr., *EXAFS and Near Edge Structure III*; Springer-Verlag: Berlin, (1984) 336.

[7] D. Li, G.M. Bancroft, M.E. Fleet, X.H Feng, Y. Pan, *American Mineralogist*, 80 (1995) 432.

(BL7A)

Mg K-Edge XANES Study of Forsterite Precursor Prepared from Heterogeneous Alkoxide Solution and Crystallization

Takeshi SHIONO, Takushi MINAGI, Hirofumi ARITANI and Toshihiko NISHIDA

Department of Chemistry and Materials Technology
Kyoto Institute of Technology
Matsugasaki, Sakyo-ku, Kyoto, 606-8585, Japan

1 Introduction

Forsterite, Mg_2SiO_4 has good properties in dielectric loss and electric insulator at high frequency and at high temperatures. However, it is very difficult to prepare dense forsterite with high-purity and stoichiometric composition by a conventional method. Sol-gel method has been extensively studied because of high-purity and good homogeneity, low temperature processing and fabrication. These advantages are suitable for synthesizing fine and high-purity ceramic powder as a starting material. Author et al.[1)] prepared forsterite powder with good sinterability from heterogeneous alkoxide solution containing fine MgO successfully. However, the formation mechanism of forsterite was not clarified.

In the present study, the crystallization mechanism from forsterite precursor was investigated through Mg K-edge X-ray near-edge structure (XANES).

2 Experimental

Forsterite precursor was synthesized from tetraethyl-orthosilicate, TEOS and fine MgO powder with mean particle size of 10nm[2)]. MgO powder was added to partially hydrolyzed TEOS solution and subsequent addition of water promoted gelation of the solution. The precursor was dried and calcined at a temperature from 400°C to 1000°C in air. The crystalline phase of calcined powder was examined with XRD analysis. The thermal behavior was measured at a heating rate of 5°C by DTA.

Mg K-edge XAFS measurements were carried out on the BL-7A at UVSOR facility in the Institute of the Molecular Science, Okazaki. The spectra were recorded in a total electron yield, using a YB_{66} two-crystal monochromater. Ground samples were spread to carbon film on the first photodynode made of CuBe of the electron multiplier.

3 Results and Discussion

The forsterite precursor was recognized as a small amount of $Mg(OH)_2$ and amorphous phase from XRD analysis. $Mg(OH)_2$ in the precursor was transformed to MgO around 400°C. Forsterite phase was found to form at 800°C. These changes were also observed as endothermic and exothermic reactions, respectively. Figure 1 shows Mg K-edge XANES spectra of forsterite precursor and powders calcined at various temperatures. Figure 2 also shows Mg K-edge XANES spectra of some reference compounds. Spectra of $Mg_2Si_3O_8$ and $MgSiO_3$ in Fig.2 were measured by Yoshida et al.[3)]. At the temperature where the formation of MgO was recognized, the rest (amorphous phase) except MgO is inferred to consist of Si rich composition, compared with stoichiometric forsterite (Mg_2SiO_4). From Mg K-edge XANES spectra as shown in Fig.1 and 2, in fact, the local structure of calcined powder is found to be very similar to that of $Mg_2Si_3O_8$. Although this phase is amorphous and the long range order is not recognized by XRD analysis, the structure in short range is judge to be almost the same as that of $Mg_2Si_3O_8$. The exothermic reaction around 800°C would result from the formation of forsterite due to the reaction between

MgO and amorphous $Mg_2Si_3O_8$. In conclusion, the formation of forsterite from the precursor is found to be composed of two step, the transformation from $Mg(OH)_2$ to MgO and the transformation from the reaction between MgO and $Mg_2Si_3O_8$.

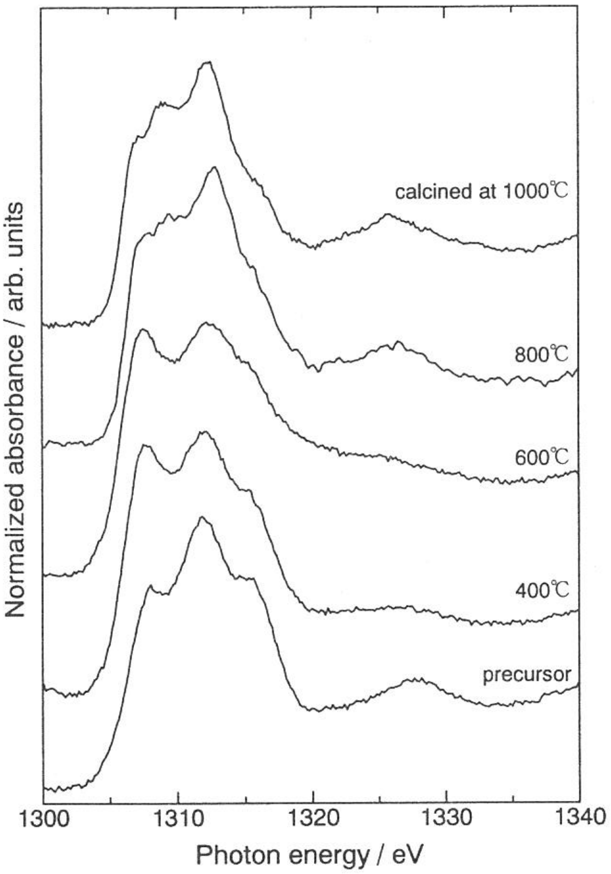

Fig.1.Mg K-edge XANES spectra of forsterite precursor and powders calcined at various temperatures.

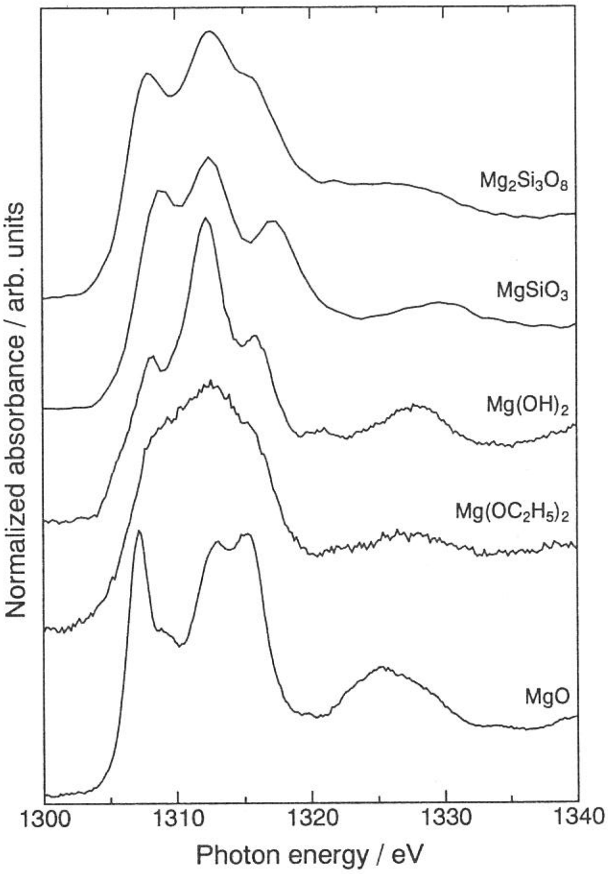

Fig.2.Mg K-edge XANES spectra of reference compounds.

References

1) T.Shiono, K.Miyamoto, Y.Sugishima, Y.Okamoto, K.Hayashi and T.Nishikawa, *J. Powder and Powder Metallurgy*, 41, (1994) 573-76.

2) T.Shiono, T.Nishida, Y.Okamoto, Y.Sugishima and T.Nishikawa, *Ceramic Transactions : Ceramic Powder Science IV*, **22** (1991) 69-74.

3) H.Yoshida, T.Tanaka, K.Nakatsuka, T.Funabiki and S.Yoshida, *Stud. Surf. Sci. Catal.*, **90** (1994) 473-78.

(BL7A)

Structural study of Al in a series of Aluminosilicate Minerals by X-ray Absorption Spectroscopy.

H. Ichihashi, T. Kurisaki, T. Yamaguchi, T.Yokoyama[1], and H. Wakita*
Department of Chemistry, Faculty of Science, Fukuoka University, Nanakuma, Jonan-ku, Fukuoka 814-0180, Japan
[1]*Department of Chemistry, Faculty of Science, Kyushu University, Hakozaki, Higashi-ku, Fukuoka 812, Japan*

Al *K* X-ray Absorption Near Edge Structure (XANES) spectra of a series of aluminosilicate minerals were measured on the BL7A at the UVSOR of the Institute for Molecular Science, and analyzed by a DV-Xα MO calculation method. The aluminosilicate minerals contain various oxygen coordinated Al(III), e.g. four-, five- and six- (1:1), and six-fold. In this study, the Al *K* XANES spectra of anorthite [$CaAl_2Si_2O_8$], andalusite [Al_2SiO_5] and kaolinite [$Al_2Si_2O_5(OH)_4$] were measured and analyzed in terms of the electron transition probabilities. Their coordination structures and their bond characters were also discussed. The results were compared with those of NMR measurements.

Keywords: Al-K XANES, aluminosilicate, molecular orbital calculation

1. Introduction

The electronic structure aluminosilicate minerals have not been studied in great detail. Recently, X-ray absorption spectroscopy, a powerful tool for structural analysis has been applied for studying the electronic property around the selected atom. Especially, XANES spectra contain the structural information, which is sensitive to the electronic state around the absorbing atom.

In this paper, we measured Al *K* XANES spectra for three aluminosilicate minerals with different Al types (environment) were analyzed by a DV-Xα MO calculation method and assigned the spectral features in terms of electron transition probability. The samples analyzed in this work are a series of aluminosilicalte minerals, anorthite [$CaAl_2Si_2O_8$: four- coordinated], andalusite [Al_2SiO_5 : five- and six-coordinated] and kaolinite [$Al_2Si_2O_5(OH)_4$:six-coordinated].

2. Experiment and calculation

The Al *K* XANES spectra were measured on the BL7A at the UVSOR of the Institute for Molecular Science (Okazaki, Japan), a crystal monochromater beam line with two YB_{66} crystals. The storage ring was operating at electron energy of 750 MeV. All of XANES spectra were measured by total electron yield method.

The DV-Xα molecular orbital calculations of these minerals were performed using the default values for well potential values for all atoms, and the transition state method.

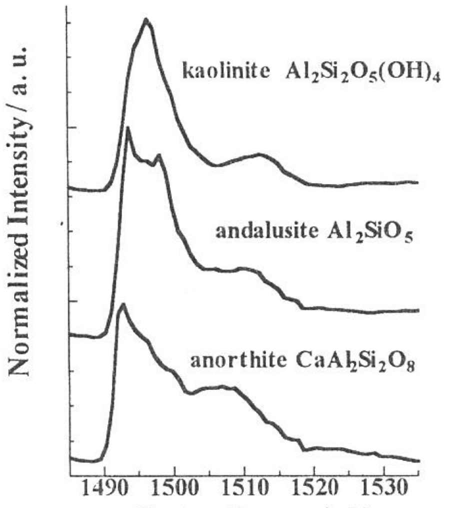

Fig.1 Al *K* XANES spectra of three aluminosilicate minerals

3. Results and discussion

Based on the Al *K* XANES spectral measurements of a variety of Al compounds, it was noted that the Al *K* edge shifts to the higher energy side with increasing of the coordination number around the aluminum atom[1),2)]. The Al *K* XANES spectra of aluminosilicate minerals containing Al with various coordination numbers are presented in Fig. 1. Energy shift in our measurements agrees well with the previous measurements. The model clusters for the use of the DV-Xα calculation contain up to the third coordinated shells. Presented in Figs. 2-4 show the measured and the calculated XANES spectra. As seen in these figures, the measured Al *K* XANES spectra agree well with the spectra calculated using the DV-Xα calculations. The Al *K* XANES are resulting from dipole allowed electron transitions from Al 1s orbital to the molecular orbitals mainly consisting of M 3p and M 3d orbitals [: M is a second shell atom.]. As seen in Fig. 1, the measured Al *K* absorption spectrum of andalusite is broader than the Al *K* absorption spectra of the other minerals, probably because andalusite has 5- and 6-coordinated Al, and the

5-coordinated Al in andalusite has a lower symmetry than the other minerals.

The DV-Xα M. O. calculation gives results of net charge and bond overlap population. The relationship between the coordination structure and bond characters for 4-, 5- and 6-coordinated Al can be interpreted from the difference in net charge and bond overlap population of anorthite and andalusite. The effective charge increases with increasing of the coordination number from 4 to 6, and the highest peak position shifts to the higher energy side. Furthermore, with the increases in coordination number of the Al, the Al-O distances in these aluminosilicate minerals increase, indicating that the Al-O bond becomes more ionic characters. By comparing the result of andalusite and kaolinite containing 6-coordinated Al, kaolinite shows lower net charge value than the net charge of andalusite and for the bond overlap population. Because the octahedral Al coordination structure of kaolinite is more distorted than that of andalusite.

The ^{27}Al MAS NMR method is also a powerful tool to probe the coordination structure of Aluminum. Fig. 5 shows the ^{27}Al MAS NMR measurements of three aluminosilicate minerals. These analytical results of Al in the aluminosilicate minerals (anorthite, andalusite$^{3)}$ and kaolinite) show good agreement with those of ^{27}Al MAS NMR measurements with our previous measurements $^{4), 5)}$ for the mullite and mullite precursors. Further, the ^{27}Al MAS NMR chemical shifts of three aluminosilicate minerals, which have 4, 5, and 6 coordinate aluminums, are in good agreement with the corresponding XANES spectral changes.

4. Conclusions

Al *K* X-ray Absorption Near Edge Structure (XANES) spectra of a series of aluminosilicate minerals were measured on the BL7A at the UVSOR of the Institute for Molecular Science (Okazaki, Japan). The measured spectra are in good agreement with the results from our DV-Xα MO calculations. The ^{27}Al MAS NMR chemical shifts of three aluminosilicate minerals, which have 4, 5 and 6 coordinate aluminums, are in good agreement with the corresponding XANES spectral change.

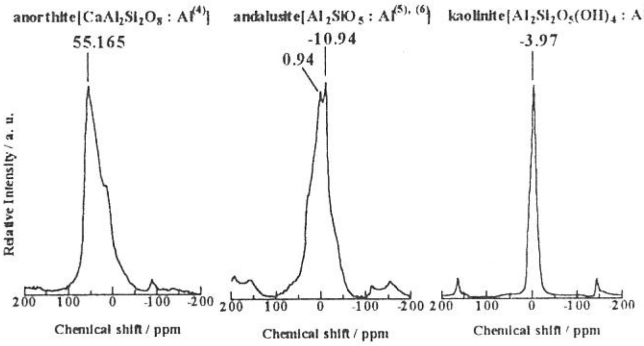

Fig. 5 ^{27}Al MAS NMR spectra of three aluminosilicate minerals.
Chemical shift range ; four-fold coordinated Al : 0-30 ppm
five-fold coordinated Al : 30-40 ppm
six-fold coordinated Al : 40-80 ppm.

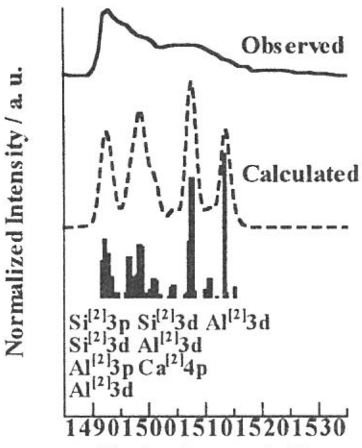

Fig. 2 Observed and calculated Al *K* XANES spectra of anorthite[CaAl$_2$Si$_2$O$_8$].

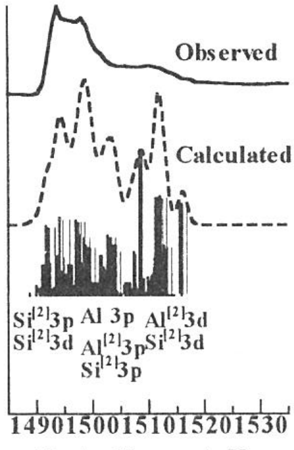

Fig. 3 Observed and calculated Al *K* XANES spectra of andalusite[Al$_2$SiO$_5$].

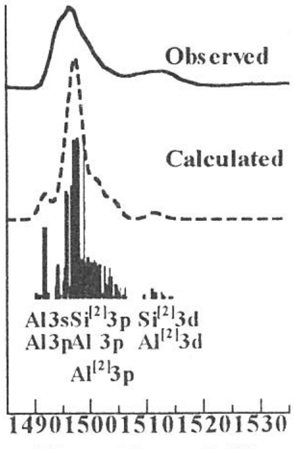

Fig. 4 Observed and calculated Al *K* XANES spectra of kaolinite[Al$_2$Si$_2$O$_5$(OH)$_4$].

References

1) Joe Wong, Z. U. Rek, T. Tanaka, etc., *Physica B* 208&209 220-222 (1995).
2) Joe Wong, G. N. George, etc., *Solid State Communication*, Vol. 92, No. 7, pp559-562 (1994).
3) Lawrence B., Alemany and Garry W. Kirker, *J. Am. Chem. Soc.*, 108, 6158-6162, (1986)
4) Y.Ikeda,T.Yokoyama, S.Yamashita, H.Wakita, Jpn.J.Appl. Pys. Vol32(1993)Suppl. 32-2, pp.670-672.
5) Y.Ikeda, T.Yokoyama, S.Yamashita, T.Watanabe, H.Wakita, Advances in X-ray Chem. Anal. Jpn.,27, 211-219(1995).

(BL-7A)

Influence of Ligands on Cu L XAS Spectra of Copper(II) Compounds

Ken-ichi Shimizu, Hajime Maeshima, Hisao Yoshida, Atsushi Satsuma, and Tadashi Hattori*

Department of Applied Chemistry, Graduate School of Engineering, Nagoya University, Chikusa-ku, Nagoya 464-8603, Japan.
Research Center for Advanced Waste and Emission Management, Nagoya University, Chikusa-ku, Nagoya 464-8603, Japan.

Recently, we have reported that Cu L_3 XAS is useful for the quantitative analysis of Cu(II) coordination states (tetrahedra and octahedra) in the copper-aluminate catalysts.[1] However, understanding of the influence of coordination state on XAS spectra is of empirical. We report herein the systematic XAS studies of a series of Cu(II) model compounds. The empirical regularity on the observed chemical shifts is first obtained, and then it is interpreted in terms of a basic crystal-field theory.

The copper(II) compounds studied in the present study were obtained as follows. CuO, $Cu(acac)_2$, $CuBr_2$, $CuCl_2 \cdot 2H_2O$, $Cu(OH)_2$, and phthalocyaninatocopper(II) ($[Cu(C_{32}H_{16}N_8)]$=[Cu(pc)]) were purchased commercially. $CuCl_2$ was obtained by the dehydration of the $CuCl_2 \cdot 2H_2O$. Copper(II) containing mixed oxide of stoichiometric spinel ($CuCr_2O_4$, $CuFe_2O_4$ and $CuAl_2O_4$) and copper aluminate with Cu content of 6 wt.% were prepared by a coprecipitation method [1]. Cu L XAS spectra were measured on BL-7A at UVSOR with a ring energy of 750 MeV and a stored current of 70-220 mA in a mode of total electron yields. A double crystal beryl monochromator was used, and the absolute energy scale was calibrated to the Cu $2p_{3/2}$ peak in CuO at 931.3 eV [2]. The intensity of the spectra have not been normalized because of missing of an adequate normalizing procedure. The electronic absorption spectra were measured using UV-VIS spectrometer (JASCO V-750) in a diffuse reflectance mode.

Figure 1a shows the L_3 XAS spectra of Cu(II) compounds. All the spectra exhibit a large white line feature, which is attributed to the transition from the $2p_{3/2}$ to the lowest unoccupied $3d$ state. The unoccupied 3d level of Cu^{2+} (d^9) compounds exists only at the highest 3d orbital. Thus, one symmetric absorption peak is present except for $CuAl_2O_4$, which contains two kinds of Cu(II) species (60% T_d and 40% O_h) [1]. It appears that the energy position of white line is characteristic to each compounds. Table 1 summarizes the positions of the peak in the order of increase in the energy. For Cu(II) compounds where Cu is octahedrally coordinated to six oxygen atoms, 6wt% Cu-Al_2O_3, $CuFe_2O_4$ and $Cu(OH)_2$, the peak position is 0.5-0.7 eV higher than those of the Cu(II) compounds containing tetrahedral CuO_4, $CuAl_2O_4$ and $CuCr_2O_4$. A further shift of the peak to the higher energy is observed for the compounds with strongly distorted octahedral symmetry and square planer symmetry. Within the compounds of the same symmetry, the peak tends to shift to higher energy with an decrease in the electronegativity of the bonding ligand as reported in an earlier report [3].

Figure 1b shows the Cu L_2 spectra, which exhibit a single $2p_{1/2} \rightarrow 3d$ transition peak. In the same manner as L_3 spectra, the position of the peak is shifted to the higher energies in the order of tetrahedra < octahedra < distorted octahedra < square planner.

On the basis of crystal-field theory, the crystal-field splitting ($10Dq$) increases in the order of tetrahedra < octahedra < distorted octahedra < square planner (spectrochemical-series). It is likely that the order of positive shift of the $2p \rightarrow 3d$ transition peaks corresponds to the crystal-field splitting. Table 1 includes the $10Dq$ value estimated from the d-d transition peak in UV-VIS spectra. By comparison with the XAS data, it is confirmed that the positive shifts in the $2p \rightarrow 3d$ transition peaks are systematically correlated to the increase in the crystal-field splitting. The energy position of these $2p \rightarrow 3d$ transition peaks should correspond to the energy difference between $2p$ level and the highest unoccupied level of the crystal-field, whose energy increases in the same order as $10Dq$. Therefore, it can be concluded that the positive shift in the absorption energies can be attributed primarily to an increase in the highest unoccupied level of the crystal-field, which is due to an increase in the crystal-field splitting.

In summary, the chemical shifts of the $2p \rightarrow 3d$ peaks in the Cu $L_{2,3}$ XAS spectra, which systematically correlated to the change in $10Dq$, was understood in terms of the basic crystal field concept. From the observed relationship, Cu L XAS can now be used to determine the crystal-field data and coordination environments of unknown Cu(II) compounds. Finally, the chemical shift concept obtained in this study will be useful for an improved understanding of X-ray absorption spectra.

References

[1] K. Shimizu, H. Maeshima, H. Yoshida, A. Satsuma, and T. Hattori, *Jpn. J. Appl. Phys.*, in press.
[2] M. Grioni *et al.*, *Phys. Rev. B* 39 (1989) 1541.
[3] A. S. Koster, *Molec. Phys.* 26 (1973) 625.

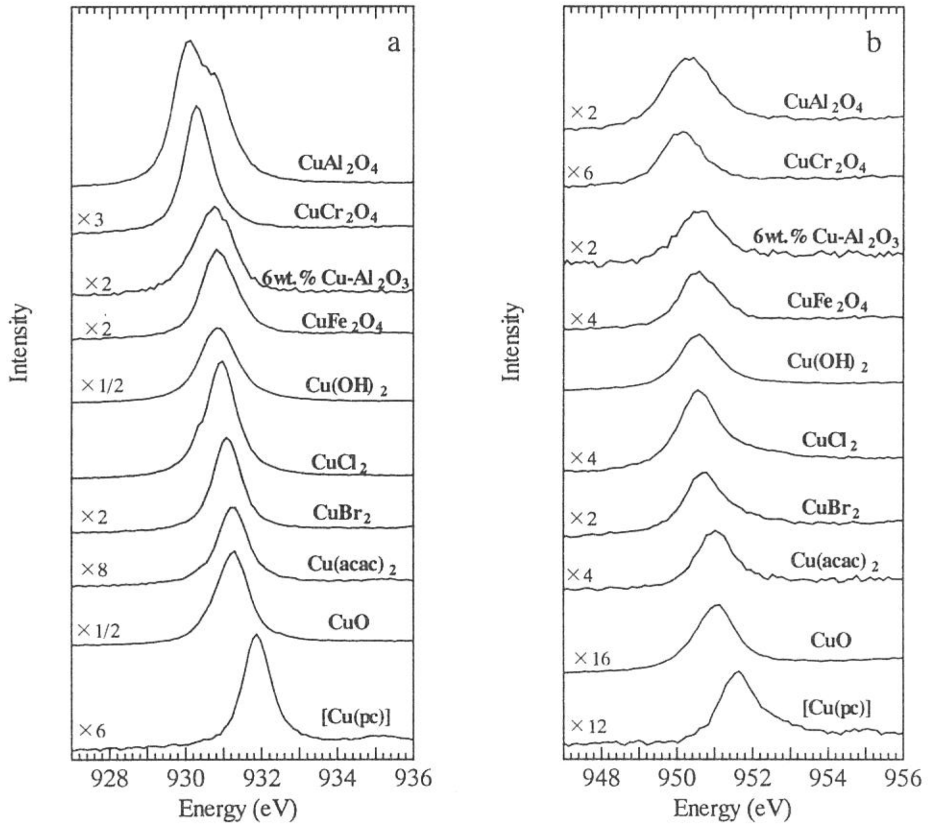

Figure 1. Cu L_3 (a) and L_2 (b) absorption spectra of a series of divalent Cu compounds.

Table 1: Characteristics of Cu $L_{2,3}$ XAS spectra and 10Dq data for Cu(II) compounds.

Sample	Symmetry	$2p_{3/2}\rightarrow 3d$ / eV	$2p_{1/2}\rightarrow 3d$ / eV	$10Dq^{a}$/ eV
CuAl$_2$O$_4$	T$_d$(O$_4$)+O$_h$(O$_6$)	930.1	950.3	0.8-0.9
CuCr$_2$O$_4$	T$_d$(O$_4$, c/a=0.92 ^{b})	930.3	950.2	1.0-1.1
6wt% Cu-Al$_2$O$_3$	O$_h$(O$_6$)	930.8	950.6	1.5-1.7
CuFe$_2$O$_4$	O$_h$(O$_6$, c/a=1.06 ^{b})	930.8	950.6	1.5-1.7
Cu(OH)$_2$	O$_h$(O$_6$, c/a=1.36 ^{b})	930.8	950.6	1.8
CuCl$_2$	O$_h$(Cl$_6$, c/a=1.28 ^{b})	931.0	950.6	1.5-1.6
CuBr$_2$	O$_h$(Br$_6$, c/a=1.33 ^{b})	931.1	950.7	1.5-2.1
Cu(acac)$_2$	D$_{4h}$ (O$_4$)	931.3	951.1	1.9-2.3
CuO	D$_{4h}$(O$_4$)	931.3	951.1	1.7-2.2
[Cu(pc)]	D$_{4h}$(N$_4$)	931.9	951.6	2.2-2.3

a) $10Dq$ was estimated from the d-d band of UV-VIS spectra.

b) The value c/a corresponds to the degree of distortion.

(BL7A)

Study on the local structure of hydrotalcite catalysts

Tomoko Yoshida,[a] Hisao Yoshida,[b] Kazuya Yamaguchi,[c] Kohki Ebitani,[c]
and Kiyotomi Kaneda[c]

[a] *Center for Integrated Research in Science and Engineering Nagoya University, Nagoya 464-8603*

[b] *Department of Applied Chemistry, School of Engineering, Nagoya University, Nagoya 464-8603*

[c] *Department of Chemical Science and Engineering, Graduate School of Engineering Science, Osaka University, Osaka 560-8531*

Introduction

The catalysis and basic property of hydrotalcite materials depend on the atomic ratio of Mg to Al in positively charged Brucite-like layer (1-3). The Al-Mg mixed oxides obtained by calcination of hydrotalcites also show the basic property which can be controlled by changing the calcination temperature as well as the Mg/Al ratio (4). The difference in the basic properties of these materials should be arisen from the different of the local structure around Mg cations. In the present work, we measured Mg K-edge XAFS of uncalcined and calcined hydrotalcites prepared with a variety of Mg/Al ratio, and analyzed the local structure around Mg ions.

Experimental

A typical example $Mg_6Al_2(OH)_{16}CO_3$ (Mg/Al = 3) was prepared as described elsewhere (2). To obtain the calcined hydrotalcite, it was heated at 673 K for 1.25 h in air. In the present work, the uncalcined and calcined hydrotalcite samples with various atomic ratio of Mg to Al (Mg/Al = 3, 5 and 8) were obtained . The hydrotalcite precursors with Mg/Al ratio were referred to as HT3, HT5, and HT8, and their corresponding calcined samples at 673 K were as cHT3, cHT5 and cHT8 hereinafter.

Soft X-ray absorption experiments were carried out on the beam line 7A at UVSOR, Institute for Molecular Science, Okazaki, Japan, with a ring energy 750 MeV and stored current of 80-200 mA. Mg K-edge X-ray absorption spectra were recorded using a beryl two-crystal monochromater. Data were collected in a total electron yield mode under high vacuum ($<10^{-7}$ Torr) at room temperature. The samples were put on the first photocathode made of Cu-Be of the electron multiplier by using adhesive carbon tape.

The curve-fitting analysis was performed for the Fourier-filtered EXAFS with the empirical parameters extracted from EXAFS of MgO calcined at 673 K.

Results and Discussion

Fig. 1 shows Mg K-edge XANES spectra of uncalcined hydrotalcite samples and $Mg(OH)_2$. The main features of the spectra were resemble, indicating that the local symmetry around Mg atoms in hydrotalcite samples was dominantly the same as $Mg(OH)_2$ phase. It is known that Mg ions are surrounded by six OH groups in the Brucite layer of hydrotalcites, and which was confirmed by these spectra. A detailed comparison of the XANES spectra led us to notice the slight difference between the spectra of uncalcined hydrotalcite samples and that of $Mg(OH)_2$, i.e., the peaks at 1305-1320 eV became broad by increasing Al content. This result supported that the incorporation of Al ions with Mg ions occurred over wide range of Mg/Al ratio in hydrotalcite (1) and indicated that the local structure around Mg ion was changed by the substitution of Al ions.

Fig. 2 shows Mg K-edge XANES spectra of hydrotalcites and MgO which were calcined at 673 K. In each spectrum of calcined hydrotalcite, the energy positions of the prominent peaks were the same as those for MgO, indicating that the dehydration of $Mg(OH)_2$ phase in hydrotalcites occurred during heat treatment and MgO phase was produced. However, it is noteworthy that the peak broadening around 1310 eV were observed for the XANES spectrum of cHT3. The XANES spectrum of cHT3 was indicative of the presence of different local structures other than MgO.

To elucidate this, Mg K-edge EXAFS spectra of the calcined samples were further analyzed. The overall patterns of EXAFS oscillations of the calcined samples were similar to that of MgO, although the amplitude became smaller with an increase of the Al content.

The radial structural functions (RSF, in Fig. 3) obtained from these EXAFS showed some differences. The peak appearing around 1.5 Å was assigned to the adjacent oxygen atoms to Mg ions, and the peak around 2.6 Å showed the presence of the second neighboring metal atoms. The magnitude of the peak around 1.5 Å was almost constant, while the peak position for the calcined samples shifted slightly to the shorter distance compared with that of MgO. Moreover, the magnitude of the peak around 2.6 Å was remarkably suppressed as the increase of Al composition.

Here, we performed curve-fitting analysis by using the parameters of Mg-O and Mg-Mg shells by the least-squares method. The results were summarized in Table 1. The interatomic distance of Mg-O in the calcined samples was evaluated to be slightly shorter than that of MgO. As for the second neighboring atoms around Mg in calcined samples, good fitting was obtained by use of one Mg-Mg shell for cHT8 sample, and the interatomic distance was estimated as 2.97 Å, which was the same value as Mg-Mg distance in MgO. On the other hand, the curve fitting was not completed with one Mg-Mg shell for cHT3, *i.e.*, the additional Mg-Mg bond with longer distance than 2.97 Å were required. These curve-fitting results clearly indicate that the interatomic distance between Mg and second neighboring metal atoms became variant by increasing the Al content. That is, the structure of MgO phase in the calcined samples of high Al content was clarified to be disordered due to the substitution of Al for Mg ions.

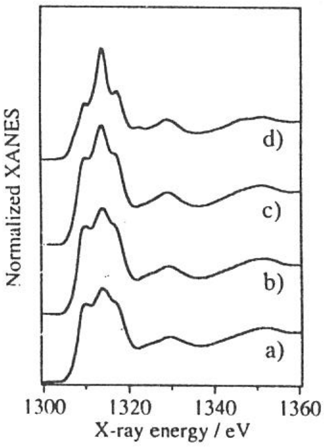

Fig.1 Mg K-edge normalized XANES spectra of a) HT3, b) HT5, c) HT8 and d) $Mg(OH)_2$.

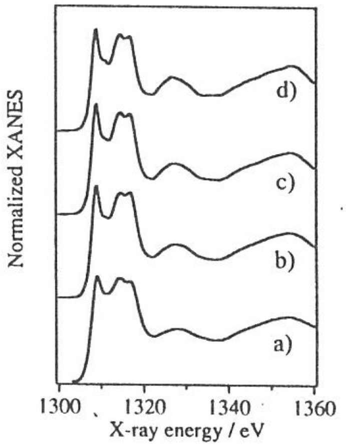

Fig.2 Mg K-edge normalized XANES spectra of a) cHT3, b) cHT5, c) cHT8 and d) MgO calcined at 673 K.

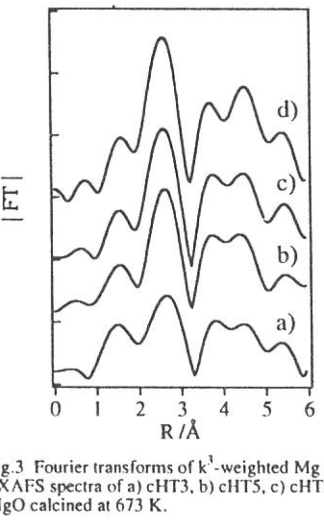

Fig.3 Fourier transforms of k^3-weighted Mg K-edge EXAFS spectra of a) cHT3, b) cHT5, c) cHT8 and d) MgO calcined at 673 K.

Table 1

Results of curve-fitting analyses.

Sample	shell	CN	R / Å	$\Delta\sigma^2$ a) / Å^2	RF b) /%
MgO c)	Mg-O	6.0	2.10	0	
	Mg-Mg	12.0	2.97	0	
cHT8	Mg-O	5.8	2.09	0.00199	
	Mg-Mg	11.0	2.97	0.00200	6.5
cHT5	Mg-O	5.7	2.09	0.00311	
	Mg-Mg	10.7	2.97	0.00378	4.2
cHT3	Mg-O	4.9	2.07	0.00395	
	Mg-Mg	7.5	2.98	0.00325	
	Mg-Mg	2.0	3.12	0.00062	4.5

The region of 1.0-3.4 Å in Fig. 4 were inversely Fourier transformed. The errors in CN and R are ± 10% and ± 0.02 Å, respectively.

a) $\Delta\sigma^2$ is the difference between the Debye-Waller factors of the sample and the reference sample MgO.

b) $RF = [(\Sigma (\chi(k) - \chi_{calc}(k))^2) / (\Sigma \chi_{calc}(k))^2]^{1/2}$

c) Mg-O and Mg-Mg shells were extracted from EXAFS of MgO.

CN: coordination number, R: interatomic distance

References

1) Cavani, F., Trifiro, F. and Vaccani, A., *Catal. Today*, **11** (1991) 173.
2) Kaneda, K., Ueno, S. and Imanaka, T., *J. Chem. Soc., Chem. Commun.* (1994) 797.
3) Ueno, S., Yamaguchi, K., Yoshida, K., Ebitani, K. and Kaneda, K. *Chem. Commun* (1998) 295.
4) Corma, A, Forn, V. and Rey, F, *J. Catal.* **148** (1994) 205.

(BL-7A)

Mg K-edge XANES Study of Li- and Mn- promoted MgO

Hirofumi Aritani,* Hiroyuki Yamada,* Takashi Nishio,* and Seiichiro Imamura,*
Sadao Hasegawa** and Tsunehiro Tanaka***
**Faculty of Engineering and Design, Kyoto Institute of Technology, Sakyo-ku, Kyoto 606-0962, Japan*
***Department of Chemistry, Tokyo Gakugei University, Koganei, Tokyo 184-8501, Japan*
****Division of Molecular Engineering, Graduate School of Engineering, Kyoto University, Sakyo-ku, Kyoto 606-8501, Japan*

Li-promoted MgO catalyst has been used and applied widely as a selective oxidation of alkanes. In particular, Li-MgO catalysts for oxidative coupling of methane (OCM) reaction have been studied by many workers in 1980s[1-3] because of high reactivity and C_{2+} selectivity. In addition, it is reported that Mn-based catalysts such as Li-Mn-MgO also effective for methane activation.[4,5] Catalytic active species of Li-MgO is recognized as unique oxygen-anion species which were characterized by means of ESR mainly. As for Li-MgO, Li^+-O^- centers which is in equilibrium with surface O^- centers via hole transport were responsible for activation of CH_4.[6] However, different oxygen-species such as O_2^- or O_2^{2-} are proposed as active centers on other OCM catalysts. Consistent active species for OCM reaction have not been decided. In fact, it would be difficult to characterize the active oxygen species in the reaction condition. On the other hand, it is accepted widely that vacant-hole sites such as F-center are generated onto MgO not only in the surface but in the bulk phase by promotion of Li^+ ions. Thus, the characterization of Li-promoted MgO is important for solving the generation of vacancy sites in the bulk phase. But direct observation of vacancy sites in MgO is difficult by means of several spectroscopic study. ESR study is only available for characterization of ESR-active oxygen anions. Although XRD study is available for characterizing the bulk phase on Li-MgO, cristallinity of MgO can only be evaluated. More information about the defect on Li-MgO is looking for. In this study, we applied the Mg K-edge XANES spectra for characterization of the local structure around Mg^{2+} ions of Li-MgO and Mn-MgO. For XANES measurement, total electron-yield mode is used in this study. In this method, a penetration range of XANES is less than 38 nm because a component of electron-yield is mainly low energy secondary electrons.[7,8] The structural information by XANES is reflected in "near-surface region". To compare between XANES and XRD results, the formation of vacancy sites and cristallinity of MgO can be discussed in both surface region and bulk phase.

A MgO sample was obtained by calcination of $Mg(OH)_2$ (Kojundo-Kagaku Kenkyusho Co.) at 873K for 3 h, and followed by cooling at ambient temperature for overnight. Li- or Mn-promoted MgO samples were obtained by impregnation of $Mg(OH)_2$ with aqueous solution of $LiNO_3$ or $Mn(NO_3)_2 \cdot 6H_2O$ (Nacalai Tesque Co.) at 343 K, and then evaporated excess water at 343K to form a paste. Then the paste was dried at 353 K for overnight and calcined at 873 K for 3 h. The Mg K-edge XANES spectra were collected on a facility of BL-7A station of soft X-ray beam line at UVSOR, in the Institute for Molecular Science, Okazaki, Japan, with 750 MeV of a ring energy and 120 - 220 mA of stored current. Each sample was mounted on a carbon-tape, and then attached on a beryllium-copper dynode which was set to the first-stage of electron multiplier placed into a vacuum chamber. After the chamber had been evacuated ($< 2.0 \cdot 10^{-7}$ Torr), the spectrum was recorded in a total electron yield mode at room temperature, using a beryl two-crystal monochromator ($2d$ = 1.5965 nm). The photon energy was calibrated by using Al metal-foil sample at Al K-edge (1559 eV).

Fig. 1 shows the XANES spectra of Li- and Mn- promoted MgO. In case of Li-MgO, the spectra in the range of 5.0 - 15.0 wt% loading reflect MgO-like structure mainly, indicating that cubic structure around Mg exists in the surface region. On the other hand, the spectrum in 2.5 wt%-Li includes another component (deconvoluted curve is shown in Fig 1, in right-bottom hand). It is different from $Mg(OH)_2$ or $Mg_2CO_3(OH)_2$, and rather similar to MgO. This result possibly indicates that MgO-like cubic structure with different Mg-O bonds from that of bulk MgO coexists in near-surface region. It suggests the generation of oxygen-vacancy sites such as F-center and/or substitution of Li^+ ions onto MgO cubic structure. From XRD results, a cristallinity of MgO cubic structure increased by Li promotion until 7.5 wt% loading. At high Li concentration, the vacancy sites may decreased because rich Li^+ cation gives little interaction for MgO. Thus, the vacancy sites generated in low Li concentration, which is localized in near-surface, may relates to the active species for OCM. The phenomenon mentioned above was also seen in case of Mn-MgO. In the region between 2.5 and 15.0 wt% of Mn loading, coexistence of MgO and another cubic structure was observed. At 25.0 wt% Mn loading, almost MgO cubic structure was seen. It suggests that substitutional existence of Mn ions onto MgO cubic structure was occurred because cristallinity of MgO was almost similarly in the whole Mn-MgO samples. In case of Ni-promoted MgO, the phenomenon mentioned above was not observed, as reported.[9] The reason of the difference between Mn-MgO and Ni-MgO has been studying now.

(1) Lee, J. S.; Oyama, S. T. *Catal. Rev. -Sci. Eng.* 1988, 30, 249. (2) Amenomiya, Y.; Birss, V. I.; Goledzinowski, M.; Galuskzka, J.; Sanger, A. R. *Catal. Rev. -Sci. Eng.* 1990, 32, 163. (3) Ito, T.; Lunsford, J. H. *Nature* 1985, 314, 721. (4) Keller, G. E., Bhasin, M. M. *J. Catal.* 1982, 73, 9. (5) Larkins, F. P., Nordin, M. R., *J. Catal.* 1991, 130,147. (6) Driscoll, D. J.; Lunsford, J. H. *J. Phys. Chem.* 1983, 87, 301. (7) Elam, W. T.; Kirkland, J. P.; Neiser, R. A.; Wolf, P. D. *Phys. Rev. B* 1995, 37, 2450. (8) Erbil, A.; Cargill III, G. S.; Frahm, R.; Boehme, R. F. *Phys. Rev. B* 1988, 37, 2450. (9) Yoshida, T.; Tanaka, T.; Yoshida, H.; Funabiki, T.; Yoshida, S.; Murata, T. *J. Phys. Chem.* 1995, 99, 10890.

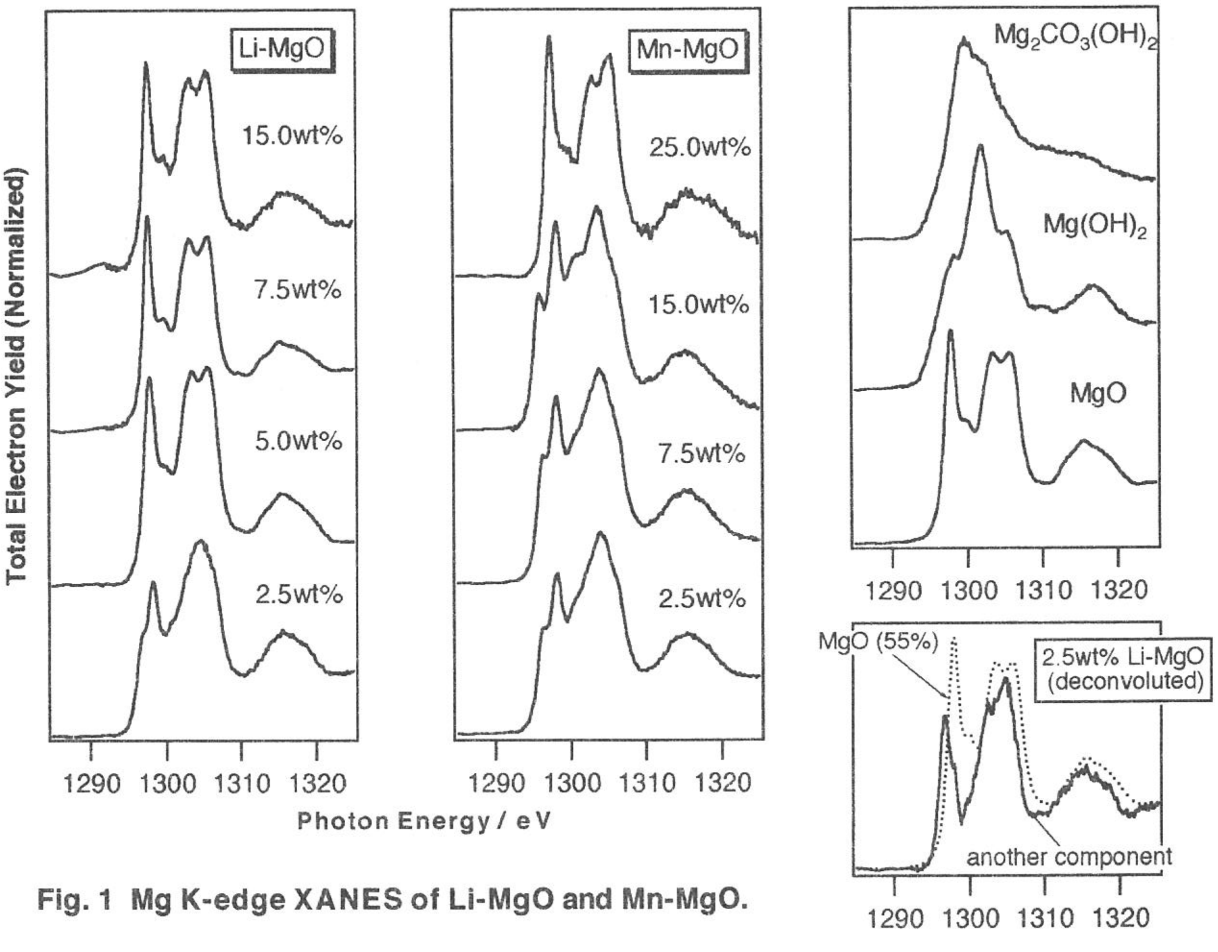

Fig. 1 Mg K-edge XANES of Li-MgO and Mn-MgO.

(BL7A)

Local structure around P atoms in the Ni-P plating films from total electron yield XAFS

Takashi WATANABE, Hisanobu WAKITA*, Tsutomu KURISAKI*, Shuji MATSUO*,
Hikoshiro ICHIHASHI* and Norimasa UMESAKI**
Division of Molecular Science, the Graduate School of Science and Technology, Kobe University,
Nada-Ku, Kobe 657-8501, Japan
**Department of Chemistry, Fukuoka University, Jonan-Ku, Fukuoka 814-0180, Japan*
***Department of Optical Materials, Osaka National Research Institute(ONRI), AIST, Ikeda,*
Osaka 563-8577, Japan

Introduction

The Ni-P plating film is using for titanium alloys of parts for industrial, automobile, and medical material parts by the purpose of corrosion resistance and the wear resistance improvement. In case of the deposition of the Ni-P plating film, it is important in the control of the physical properties of the film to analyse the deposition mechanism of intermetallic compound Ni_3P by the difference of the deposition processes.[1)] By the analysis of XRD , we have confirmed that the Ni-P films obtained at as deposited-200℃ are amorphous, those obtained at 250-300℃forms form intermetallic compound Ni_3P, and those obtained at over 300℃ form crystalline Ni and the precipitate of Ni_3P.

The purpose of this report is to clarify the deposition mechanism of Ni_3P from electroplating and electroless plating Ni-P films under various heating conditions by the use of total electron yield XAFS method and the spectral simulation technique.(Cerius^2, EXCURV92)

Experimental

The samples are those unheated of the deposition electroplating and electroless plating Ni-P films and those heated at 200℃, 250℃, 300℃, 350℃ and 400℃. The film thickness of all samples is 15 μm. The P *K*-edge XAFS data were collected on a facility of BL-7A station of soft X-ray beam line at UV-SOR. Each sample was prepared for measurement by putting on a beryllium-copper photo dinode which was attached to a first position of the secondary electron multiplier with a carbon tape. After the chamber had been evacuated ($<1.0\times10^{-7}$ Torr), the spectrum was recorded in a total electron yild XAFS method at room temperature, using InSb(111) double crystal monochromater. The XAFS analysis was applied to the obtained P *K*-edge spectrum, and P surroundings was analyzed the local structure and the electronic state. In addition, the result of the spectral simulation which used EXCURV92 with Cerius^2 was compared and examined with the experimental results.

Results and Discussion

As seen in Fig.1, the transition peak from *1s* state of the ground state of P to hybrid orbital state *3p/3d-4s-4p* is observed in P *K*-edge XANES spectra. The positions of A and B correspond to $1s\rightarrow\pi^*$ and $1s\rightarrow\sigma^*$, respectively. The peak of $1s\rightarrow\sigma^*$ becomes clearly as the heat treatment proceeds. Figure 3 shows the simulated radial distribution function (RDF) of P atom surroundings which is calculated from the tetragonal model of Ni_3P seen in Fig.2 and the RDF obtained from the experimental EXAFS signal $k^3\chi(k)$. Figure 3 indicates that the experimental RDF becomes to be similar to the simulated RDF from Ni_3P as the heat-treating temperature increases. The interatomic distances of P-Ni bond does not change into this with 2.28Å among local structural parameters obtained from least square fitting of the experimental value and the theoretical value concerning RDF 1st peak as listed in Table 1. It is supported from approaching by the coordination number of the first neighboring atoms of P advance to coordination number 9 of the first neighboring atoms Ni of P in Ni_3P as the heat-treating temperature increases.

These results give the conclusion that evenif as deposited samples, both of electroless plating and electroplating Ni-P films, are in the forms of quasi-compounds or crystallites of Ni_3P structure in Ni-P plating films. And the samples obtained from the heat treatment are in the forms of larger crystal grain of Ni_3P structure.

Table 1 Local structure parameters obtained from least-square fitting of the experimental value and Theoretical value concerning RDF 1st peak.

Samples		1st neiboring atom	interatomic distance(Å)	coordination number
Electroless plating Ni-P films	As depo.	Ni	2.28	7.9
	250℃, 2hr	Ni	2.28	7.9
	350℃, 2hr	Ni	2.28	8.9
	400℃, 2hr	Ni	2.28	9.0
Electroplating Ni-P films	As depo.	Ni	2.28	7.8
	250℃, 2hr	Ni	2.28	8.7
	350℃, 2hr	Ni	2.28	8.9
	400℃, 2hr	Ni	2.28	9.0

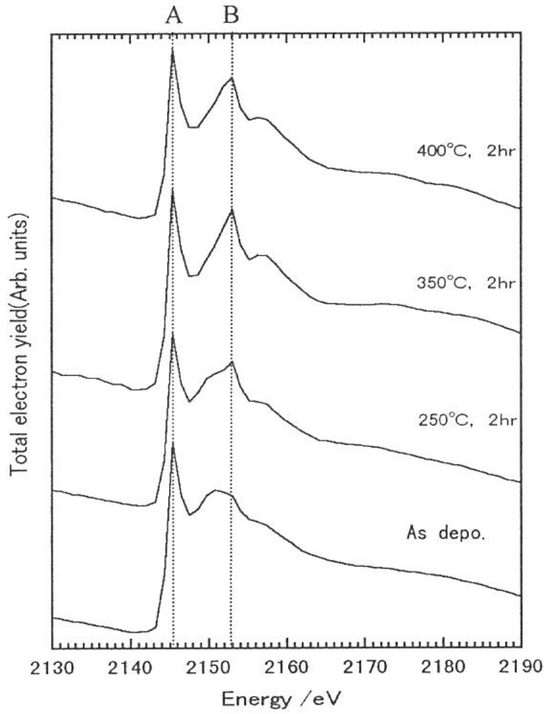

Fig.1. XANES spectra for P K-edge of electroless Ni-P films

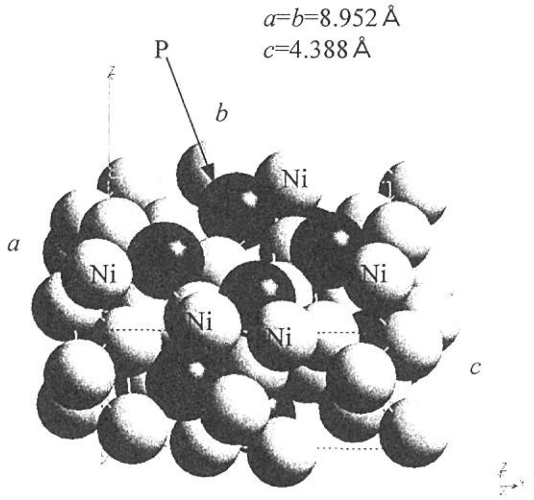

Fig.2. Tetragonal crystal structure of Ni_3P

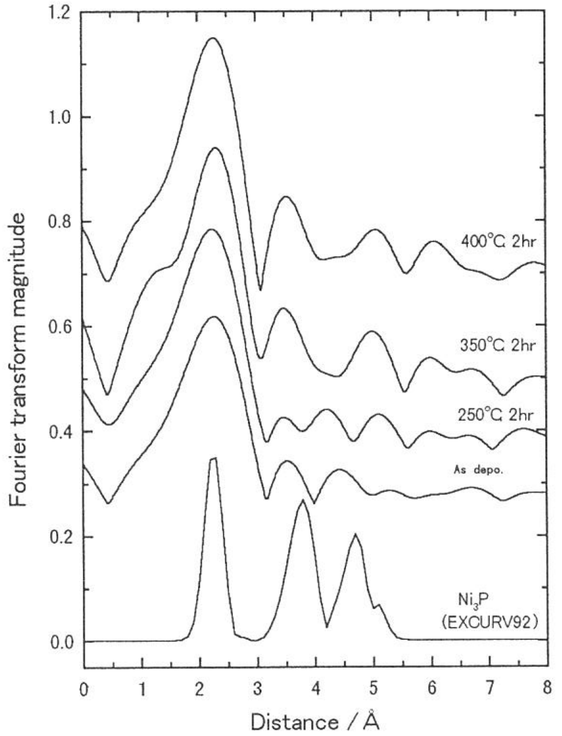

Fig.3. RDF around the P atom ofelectroless plating Ni-P films.

Reference

1) T.Nakayama, Y. Wada, H.Ido, "R&D" Kobe Steel Engineering Reports, **Vol.43**, **No.3**(1993)71.

(BL7A)

Si K-edge XANES Study of Neutron Irradiated Silica Glasses

Tomoko Yoshida[A], Hisao Yoshida[B], Mikio Sakai[C], Takanobu Hara[C] and Tetsuo Tanabe

[A]*Center for Integrated Research in Science and Engineering, Nagoya University,*
Furo-cho, Chikusa-ku, Nagoya 464-8603
[B]*Department of Applied Chemistry, School of Engineering, Nagoya University,*
Furo-cho, Chikusa-ku, Nagoya 464-8603
[C]*Department of Nuclear Engineering, Graduate School of Engineering, Nagoya University,*
Furo-cho, Chikusa-ku, Nagoya 464-8603

Introduction

Radiation effects of high energy particles on silica are one of the main concerns for their application as optical windows, insulators and optical fibers in nuclear environments. Defects in silica such as oxygen vacancy related ones and Si precipitates produced by energetic particles injection have been extensively studied mainly by optical techniques. Recently, it has been also revealed that such defects formation closely relates to electron excitation as well as lattice displacement under radiation.(1-3) However, it has been very difficult to observe directly the electronic and atomic structures of the defects due to their materials characters as amorphous and insulators which do not allow to use diffraction and electron probe techniques. In the present study, we applied X-ray absorption technique to observe the electronic state and the local structure of neutron irradiated silica glasses.

Experimental

Samples used were SiO_2 glasses of 15 mm diameter and 2 mm thickness produced by Toshiba Ceramics, Japan.

Neutron irradiation experiments were carried out at the nuclear reactor YAYOI at the University of Tokyo. During the experiments, YAYOI was operated with a power of 2 kW with an average neutron energy of 1.3 MeV. The fluence of neutron was 3.6×10^{15} n/cm^2.

X-ray absorption experiments were carried out on the beam line 7A at UVSOR, Institute for Molecular Science, Okazaki, Japan with a ring energy 750 MeV and stored current 80-200 mA. Spectra were recorded at room temperature in a total electron yield mode, using a two-crystal InSb monochromator. The sample was put on the first photocathode made of Cu-Be of the electron multiplier.

Results and Discussion

Fig.1 compares Si K-edge XANES spectra of a neutron irradiated silica with that of an unirradiated one. The XANES spectrum of the unirradiated silica sample showed a sharp and prominent peak at around 8 eV (relative to Si K-edge of pure silicon; 1838 eV). This absorption is assigned to atomic-like Si 1s to 3p transition.(4) In silica, a silicon atom occupies at a center of the regular tetrahedron of oxygen atoms. Therefore, Si 3p orbitals must be degenerated resulting in such a sharp absorption. The XANES spectrum of the neutron irradiated silica sample(b) was almost the same as that of the unirradiated one(a), indicating that SiO_4 structures around Si atoms are fundamentally maintained after irradiation. Because the neutron fluence was so small to produce heavy damages such as introduced by He^+ irradiation. Nevertheless, the main peak height was a little lower than that of the unirradiated one. Accordingly, as shown in Fig. 2, Radial structure functions (RSFs) which were obtained by Fourier transforms of k^3-weighted EXAFS spectra, exhibited a certain structural change. In RSFs, the first peaks appearing at around 1.5 Å are attributed to neighboring oxygen atoms (Si-O). By neutron irradiation, the intensity of the first peak was reduced without changing its FWHM (the full width at half maximum). This indicates the decrease in the coordination number of oxygen atoms due to the break of Si-O bonds or the formation of oxygen vacancies. In addition, the peaks at 2-3 Å in RSFs which are ascribed to Si atoms bridged by oxygen (Si-O-Si) became small and slightly shifted to short distance. This also confirms the existence of oxygen vacancy resulting in shorter Si-Si distance with changing the angle of Si-O-Si. Thus, XAFS should clearly reflect the structural change around Si atoms resulting from oxygen-vacancy formation.

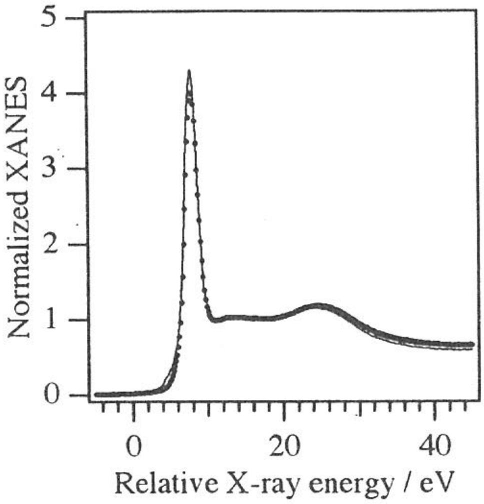

Fig. 1 Si K-edge normalized XANES spectra of a) an uniradiated silica glass (solid line) and b) its neutron irradiated sample (dashed line).

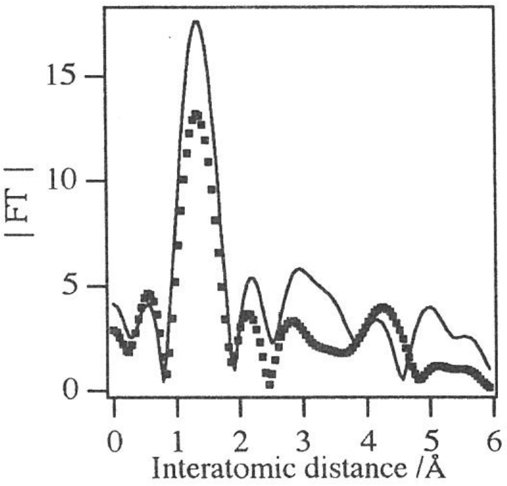

Fig. 2 RSFs obtained by Fourier transforms of k^3-weighted Si K-edge EXAFS of a) an irradiated silica glass (solid line) and b) its neutron irradiated sample (dashed line).

References

(1) M. Fujiwara, T. Tanabe, H. Miyamaru and K. Miyazaki, Nucl. Instr. and Meth. B, 116 (1996) 536.

(2) T. Tanabe, S. Tanaka, K. Yamaguchi, N. Otsuki, T. Iida and M. Yamawaki, J. Nucl. Mater., 212-215 (1994) 1050.

(3) T. Tanabe, M. Fujiwara, T. Iida, S. Tanaka, K. Yamaguchi and M. Yamawaki, Fusion Eng. Design 29 (1995) 435.

(4) T. Tanaka, S. Yoshida, R. Kanai, T. Shishido, H. Hattori, Y. Takata and K. Kosugi, J. Phys. IV France, 7 (1997) 913.

(BL7A)

X-ray Spectrum Measurement in the Range of keV by Ionization Chamber with Divided Electrodes

Tetsunori Taninaka, Masazumi Ishida, *Hironobu Matsuo, *Masayuki Fukao
Graduate School of Science and Engineering, Shizuoka Univ.
**Dept. of Electrical and Electronic Eng. Shizuoka Univ.*
Jouhoku 3-5-1 Hamamatsu 432-8561, Japan

Purpose

The purpose of experiment is to calibrate an Ionization Chamber with Divided Electrodes (ICDE) in the keV range by the monochromatic X-ray generated with 2 crystal spectroscopes of BL7A.

Items to be checked are ; (1)absolute sensitivity, (2)influences of other reactions besides photoelectric effect, (3)photoelectron crossing current among divided electrodes, (4)recombination effects of photoelectrons, and (5)distortion of photoelectron current distribution near photon entrance window.

Principle of Measurement

In the range of keV, the photoelectric reaction is dominant between photons and atoms[1], that is, an incident photon gives the energy to an electron by a single reaction. Therefore, by measuring the spatial distribution of photoelectrons along incident photon path in gas, the incident photon energy spectra can be estimated, since the photon mean free path is known as a function of the energy. The spatial distribution of photoelectrons can be obtained by measuring the current to electron collecting electrodes divided along the photon path. It must be considered that the photoelectrons have enough energy to ionize many gas molecules.

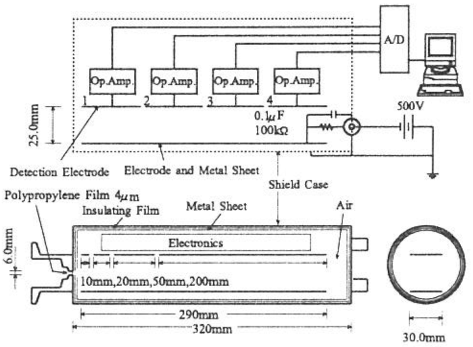

Fig.1 Ionization chamber with divided electrodes

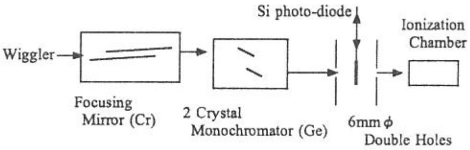

Fig.2 Experimental configuration

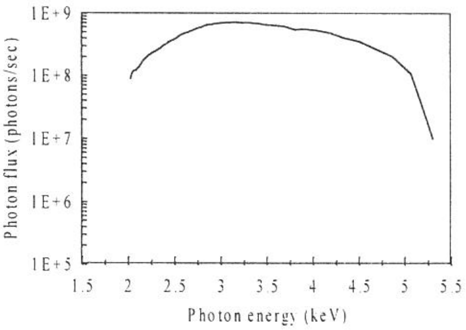

Fig.3 X-ray spectrum (beam current : 100 mA)

The constructed detector is shown in Fig.1[2]. In a metal cylinder case of 60 mm in dia. and 320 mm long, a pair of parallel plate electrodes are set in axial direction. While one side is of a piece, the other side consists of 4 pieces of 10, 20, 50 and 200 mm wide from the X-ray entrance window. The perpendicular width is 30 mm. The interval of electrode is 25 mm. Adjacent electrodes are separated by 2 mm gap. A thin cylinder is attached inside of and insulated by a thin film from the grounded cylindrical case. The common electrode and the inner cylinder are kept at -500 V. The divided 4 electrodes are connected to negative inputs of Op.Amps. with low input drift current and kept at the virtual ground potential, respectively. To minimize a distortion of electric field near the X-ray entrance window, the wall near the entrance hole is kept at -250 V. The Op.Amps. are installed inside of the cylinder and the output signals are extracted via feedthrough to a data acquisition system. The inside of chamber is kept in 1 atm. air. The X-ray entrance is of 6 mm in dia. and sealed with 4 μm polypropylene film. A swelling of the film due to the atmospheric pressure, which would change in size with temperature and pressurization cycle, made the boundary of sensing area ambiguous. It was improved by supporting the film with stainless steel mesh at the sacrifice of reduced photon flux. The current I_i into the i-th electrode is expressed as

$$I_i = \int_0^{E_a} \left(\exp(-z_{i-1}/\lambda(E)) - \exp(-z_i/\lambda(E)) \right) \frac{E}{W} T(E) S(E)\, dE \quad ,$$

where $S(E)$ is photon spectrum, E_a the maximum energy, $T(E)$ the transmission rate of the window film, z_i the distance from the entrance window to the far side boundary of the i-th electrode, W effective ionization energy. The E/W gives the number of electrons which are secondarily produced by a fast electron due to photoionization.

Experiment Results

The experimental configuration is shown in Fig.2[3)4)]. A pair of germanium crystals were used for monochromator. The X-ray was introduced through double holes of 6 mm ϕ each and 300 mm spacing, into the ICDE. The double holes are set against accidents such as the entrance film damage. Photon flux is measured by a Si photo-diode put between 2 holes as shown in Fig.2. The photon energy vs. flux measured by the Si photo-diode is shown in Fig.3. The flat photon flux was observed over 10^8 photons/sec from 2 keV to 5 keV. The ICDE was calibrated by 0.2 keV step in the whole energy range. Photon energy vs. currents into the four electrodes are shown in Fig.4(a), where the currents are normalized for 1×10^9 photon flux by using spectral curve shown in Fig.3. Theoretically expected curves are shown in Fig.4(b). Although each curve resembles other, there are some discrepancies. The experimental and the theoretical electrode currents normalized by the first electrode one are shown in Fig.5(a) and (b), respectively. Each curve agrees well with other.

The discrepancies observed between Fig.4(a) and (b) are considered to be owing to a shift of photon beam axis on rotating the double crystals to sweep energy. The spectrum of Fig.3 was observed in the middle of two holes, while the ICDE accepted the photons passing through the two holes. A small shift of position and/or angle of the beam axis would bring about serious changes in the energy spectra.

It would be concluded from this experiment about the items to be checked:

(1) Absolute measurement could not be confirmed because of the lack of photon profile in the cross section of photon beam and the beam axis shift on sweeping energy. The ICDE might be used for an absolute measurement from the simplicity of the principle.

(2)-(5) Since the experimentally observed current ratios are well fitted to the theoretical expectations which take account only of photoelectric reaction, it is concluded that there is no large influence of other reactions besides photoionizations. From the same reason, the effects of photo-electron cross currents among electrodes and recombination would be ignored. The electric field distortion near the photon entrance hole were not observed in this experiment so far as over 2 keV photons are introduced. In the case low energy photons are included, they interacts with gas near the entrance hole and might be accumulated in the vicinity and distort the electric field. This is beyond this calibration experiment.

In summary, it is concluded that the ICDE works well for measuring a broad spectrum of X-ray in the energy from 2 to 5 keV.

References

1) "Photon Cross Section from 0.1 keV to 1 MeV for Elements Z=1 to Z=94" Atomic Data 5, 51-111(1973)
2) M. Fukao, X-Ray Production in 1 keV Range and its Measurement: Journal of Plasma and Fusion Research, Vol. 73, No. 9(1997), pp. 912 - 922(in Japanese)
3) T. Murata et al., Soft x-ray beamline BL7A at the UVSOR: Rev. Sci. Instrum. 63(1), January 1992
4) T. Kinoshita et al., Focusing mirror system of the double crystal monochromator beamline Bl7A: UVSOR Activity report(1997)p. 62

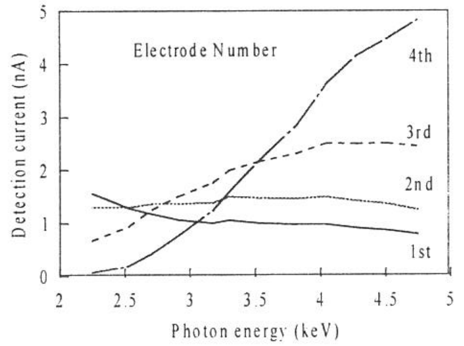

(a) observed

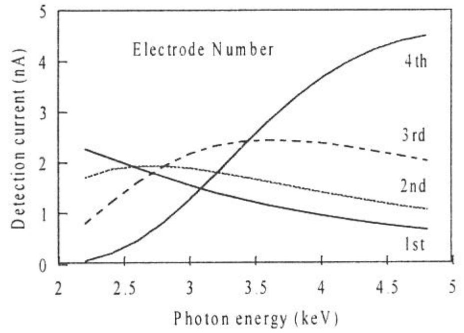

(b) theoretically expected

Fig.4 Photon energy vs. currents into the 4 electrodes
(beam current : 100 mA)

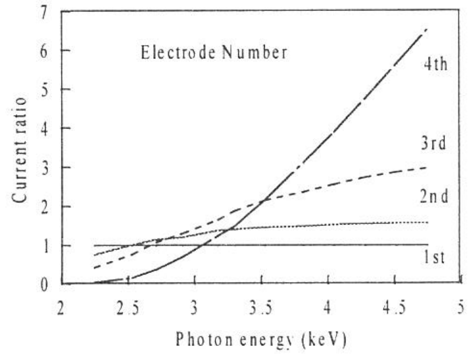

(a) observed

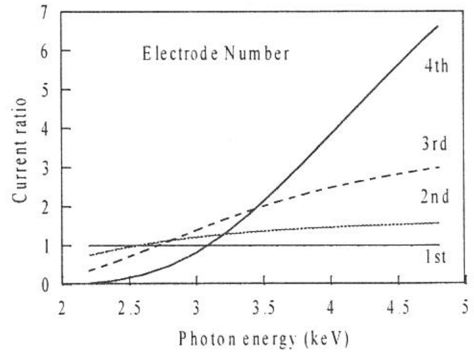

(b) theoretically expected

Fig.5 Photon energy vs. current ratios

BL-7A

Characterization of the Au and Pt replica mirrors for ASTRO-E

Kazutoshi Haga, Koujun Yamashita, Keisuke Tamura, Yasushi Ogasaka, Hideyo Kunieda, Yuzuru Tawara, Akihiro Furuzawa, Takashi Okajima, Harumi Takata, Seiji Takahashi, Satoshi Ichimaru, Yasuhiro Hidaka

Department of Physices, Nagoya University, Chikusa-ku, Nagoya 464-8602

X-ray astronomy satellite ASTRO-E will be launched in 2000. This satellite is equipment with five grazing incidence X-ray telescopes(XRT) coated with Au or Pt. X-ray imaging spectrometer(XIS) and X-ray spectrometer are installed on the focal plane, in order to observe the celestial objicts in the energy range 0.5 - 12keV.

XRT is made of 175 nested thin foil reflectors [1] per one telescope. The reflector is called "replica foil mirror " whose substrate is 0.15mm thick Al foil. The mirror is produced with replication of the gold or platinum sputtered on the glass mandrel with smooth surface.

The gold surface is a traditional material for total reflection and is prepared for XIS. On the other hand, Pt is used to extend the critical energy for the first time, because the density of Pt is higher than Au, the critical energy become larger in proportion to the square root of the density approximately.

Henke et al. reported the optical constants of various bulk materials including Au and Pt in 1982, 1993 [2,3]. But Owens et al.[4] reported that the M_V, M_{IV}, M_{III} edges of Au determined in reflecctivity measurements are about 30eV higher than Henke's value.

It is very important to know the optical constants of Au and Pt replica mirrors especially around the M edges in calculating XRT energy responces. Therefore the charactetization was carried out using monochromatized synchrotron radiation in the energy band 1.8 - 3.5keV including the M edges of Au and Pt.

Experiments were carried out in BL-7A. Incident beam was monochromatized by a double crystal monochrometer with InSn, and then introduced into the measuring chamber through the 0.2mmϕ pin-hole and filters to adjust the intensity and to calibrate the energies by using an absorption edge. The samples and the detectors(Proportional counter or Si detector) were mounted on the $\theta - 2\theta$ table in the chamber. First we measured the direct wavelength profiles in the energy range 1.8 3.7 keV. Next we obtained the reflected ones with the several incident angles.

Reflecivity of Au and Pt are shown in Fig.1, Fig.2. Energy calibration was carried out using K edge(3.2059keV) of Ar in the proportional counter, L edge(2.5202keV) of Mo in the filter, K edge(1.8389keV) of Si in the float glass reflector. These energies are refered from Henke's table.

Solid lines indicates the calculated value with rms roughness $\sigma = 5\mathring{A}$ which is defined as Debye-Wallar factor. It seems that absolute values of reflectivity are a little different from measured data. This is due to fluctuation of beam intensity within 0.2mmϕ pin-hole caused by the unstability of beam profile. For more accurate measurements in the future, we are considering a thin proportional counter of transparent type on the beam just in front of the sample, in order to monitor the incident flux.

From these measurements, M edge energies are determined as shown in Table.1 . Data summerized by Henke are also shown in Table.1 as a reference. These edge energies of Au in our measurements are similar to Owens's. As for Pt, the edge energy also has a tendency to be higher than Henke's as OWENS has listed. We would say that these results are very important and they shold be confirmed by other method such as transmission measurements.

material	M_V(eV)	M_{IV}(eV)	M_{III}(eV)
Au	2246±5(2205.7[3], 2241[4])	2331±5(2291.1[3],2329[4])	2747±5(2743.0[3],2756[4])
Pt	2160±5(2121.6[3],2154[4])	2235±5(2201.9[3],2234[4])	2641±5(2645.4[3])

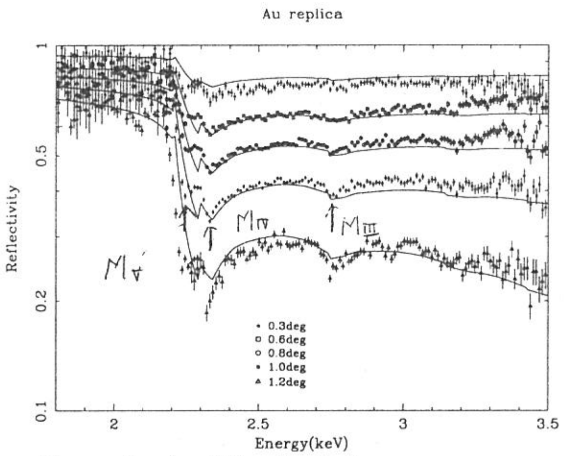

Figure 1: Au foil reflectivity: Solid line shows the calculated value. Measured data at the grazing angle of 0.3, 0.6, 0.8, 1.0, 1.2degree are shown.

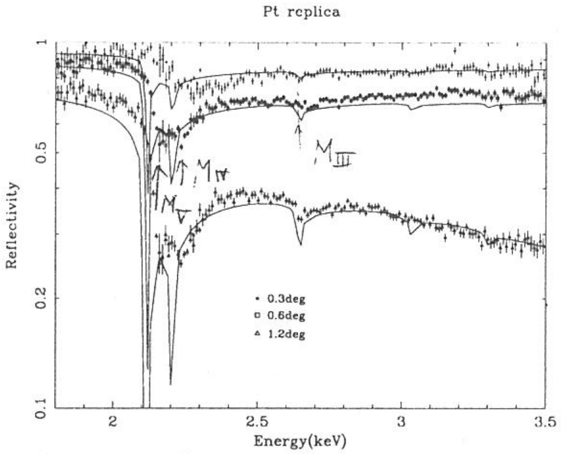

Figure 2: Pt foil reflectivity: Solid line shows the calculated value. Measured data at the grazing angle of 0.3, 0.6, 1.2degree are shown.

references

1) Peter J. SERLEMITSOS, et al. 1995, Publ. Astron. Soc. Japan 47, 105-114
2) HEKNE, B.L., et al. 1982, Atomic Data Nucl. Data Tables, 27, 1
3) HEKNE, B.L., et al. 1993, Atomic Data Nucl. Data Tables, 54, 1
4) OWENS, A., et al. 1996, ApJ, 468, 451

(BL-7A)

Structure of Impurity Si Atoms in α-Al_2O_3 Crystal by XAFS Spectroscopy.

Kohei Fukumi, Naoyuki Kitamura, Hiroshi Mizoguchi

Osaka National Research Institute, AIST
1-8-31, Midorigaoka, Ikeda Osaka, 563-8577 Japan

Optical properties of inorganic materials are much affected by impurities. In order to underdstand the optical properties of these materials, it is important to know the coordination structure and valence state of impurity atoms in the materials. In this study, the structure of Si atoms in α-Al_2O_3 has been investigated by XAFS spectroscopy.

α-Al_2O_3 single crystal including Si atoms as an impurity atom was used as a sample. β-SiC powder, α-Si_3N_4 powder, α-quartz type SiO_2 powder and Si single crystal were used as reference substances. The measurement of Si K-edge XAFS spectra of these samples was carried out on the beam line 7A at UVSOR facility, Institute for Molecular Science, Okazaki, Japan. The spectra of the Si-doped Al_2O_3 single crystal, silicon compound powders and Si single crystal were measured by electron yield, total electron yield and drain current methods, respectively. In addition, the Si K-edge XAFS measurement was carried out on the Si-doped Al_2O_3 single crystal with a photodiode(AXUV-100,IRD Inc.). All the spectra were measured at room temperature using an InSb double crystal monochromator.

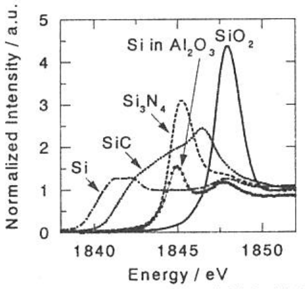

Fig.1 XANES spectra of Si in Al_2O_3, SiO_2, Si_3N_4, SiC and Si.

Figure 1 shows the Si K-edge XANES spectra of Si atoms in Al_2O_3 single crystal, SiO_2, Si_3N_4, SiC and Si. The edge energy shifted toward higher energies in the order of $Si<SiC<Si_3N_4<SiO_2$. This agrees well with the order of ionic charge of Si atoms. The edge of Si atoms in α-Al_2O_3 located at the energy of Si_3N_4, indicating that the ionic charge of Si atoms in α-Al_2O_3 is less than that of Si atoms in SiO_2.

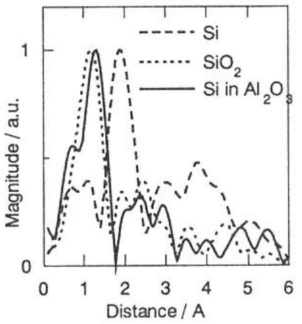

Fig.2 Magnitude of fourier-transform of $k\chi(k)$ of Si in Al_2O_3, SiO_2 and Si. Magnitude is normalized to unitiy.

Figure 2 shows the magnitude of fourier-transform of $k\chi(k)$ obtained from XAFS measurement. It can be seen that the most intense peak of Si atoms in α-Al_2O_3 locates at a position similar to that in SiO_2, indicating that Si atoms are mainly surrounded by oxygen atoms. The Si-O bond length in α-Al_2O_3 and SiO_2 was 1.67Å and 1.60Å, respectively, according to the fitting analysis in the region from 3.2 to 8.0Å^{-1}, although the k range of $k\chi(k)$ curves used for the fitting analysis was too narrow to discuss the bond length precisely. Oxygen atoms have the hexagonal closest packed structure to form tetrahedral sites and octahedral sites in α-Al_2O_3 crystal. It is deduced from the Si-O bond length that Si atoms occupy the tetrahedral site in α-Al_2O_3 crystal.

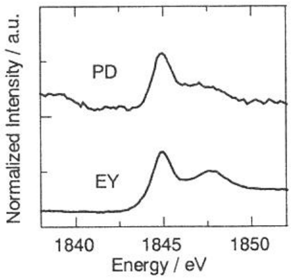

Fig.3 XANES spectra of Si atoms in Al_2O_3 measured by electron yield (EY) and photodiode (PD) methods.

Figure 3 shows that XANES spectra of Si atoms in α-Al_2O_3 measured by the electron yield method and the photodiode method. It was confirmed that XANES spectrum of dilute components can be measured by the photodiode method.

(BL8A)

Homoepitaxial growth of ZnTe by synchrotron radiation using metalorganic sources

Mitsuhiro NISHIO, Takeshi ENOKI, Yoshiaki MITSUISHI, Qixin GUO and Hiroshi OGAWA
Department of Electrical & Electronic Engineering, Faculty of Science and Engineering, Saga University, Saga 840-8502, Japan

Photo-excited growth using synchrotron radiation is promising as a new non-thermal technique. Actually, we have already demonstrated that the deposition of ZnTe using diethylzinc (DEZn) and diethyltelluride (DETe) occurs epitaxially on the (100) oriented GaAs substrate even at room temperature. However, it was very difficult to observe the photoluminescence from the ZnTe film grown on GaAs substrate, which suggests that the film exhibits inferior optical property. In this study, we have investigated homoepitaxial growth of ZnTe in order to improve optical property of the layer. We dealt with the effect of the transport rate of source materials upon the ZnTe growth using DEZn and DETe, since the partial pressure ratio of the alkyls is an important factor that not only gives valuable information on the associated growth process but also influences optical property of the layer. The experiments were carried out using the SR beam line, BL8A. The (100) orientated ZnTe wafers synthesized in our laboratory by Bridgman method were employed as substrates. The incident SR beam irradiates the sample surface perpendicularly. The deposition was carried out at a very low pressure of $\sim 10^{-5}$ Torr in the growth chamber. In Fig. 1, the relationship is shown between the growth rate and DETe transport rate. Here, the results obtained for DEZn transport rates of 0.1 μmol/min and 0.05 μmol/min are plotted in the same figure in order to investigate the effect of DEZn transport rate upon the growth rate. The growth rate increases sublinearly with increasing DETe transport rate and it becomes saturated, as shown for a DEZn transport rate of 0.1 μmol/min. The almost linear relationship between the growth rate and DETe transport rate means that rate limiting step is due to the supply of DETe. On the other hand, the saturated tendency of the growth rate indicates that the growth rate is limited by the supply of DEZn, in good agreement with the fact that the growth rate decreases with decreasing DEZn transport rate in this region. From the relationship between the growth rate and DEZn transport rate when DETe transport rate was kept at 1 μ mol/min, we have already shown that the growth rate increases rapidly with increaing DEZn transport rate and then it eventually becomes saturated beyond a very low transport rate of 0.1 μ mol/min (see fig.2). Thus, a significant difference can be found in the growth rate behavior between the results shown in figs.1 and 2. The growth rate of ZnTe will directly depend upon the adsorption coefficient of precursors, since the growth rate is decreased with increasing the substrate temperature due to the decrease of adsorption coefficient as shown in fig.3. The difference in the growth rate behavior under two conditions shown in fig.1 and fig.2 suggests that adsorption coefficient of DEZn is very high compared to DETe. We have measured the photoluminescence spectra at 4.2 K under 458nm Ar^+ laser excitation in order to assess the optical properties of ZnTe films. The penetration depth of the laser light is about one third of a μm. Therefore, ZnTe films with thickness between 1.5 and 2 μm were investigated in order to avoid influence from substrate. Figure 4 shows typical photoluminescence spectra of the ZnTe films. The excitonic emission (I_a) at 2.375 eV and the strong deep level emissions with two broad bands centered at around 2.1 eV and 1.85 eV were detected as the main feature of the spectrum (fig. 4(a)). The I_a line is attributed to shallow accepors, namely Li, Cu, Na. This peak is observed widely for undoped ZnTe grown by another growth methods. The deep-level luminescence obtained here can be found in the experimental results by Tews et al., who have attempted laser-induced diffusion in ZnTe with Cl. SR illumination looks to be effective in enhancing the decomposition of the impurity molecules such as Cl related compound. However, it is not at least difficult to suppress defects associated with the deep-level emissions by choosing a suitable growth condition. As shown in fig. 4(b), the deep-level emissions almost vanishes in the photoluminescence spectrum of epitaxial film deposited at a reduced growth rate (about 0.06 Å/mA·min). The spectrum was composed of strong I_a line and relatively weak donor-acceptor pair band. Although we have not yet attempted to optimize the various growth parameters to obtain the ZnTe film of high quality, it should be noted that near band gap luminescence can be observed even in the ZnTe epitaxial films grown at room temperature.

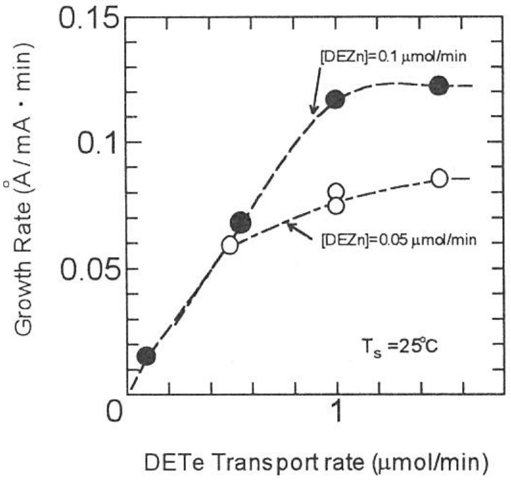

Fig. 1. Growth rate of ZnTe film versus DEZn transport rate.

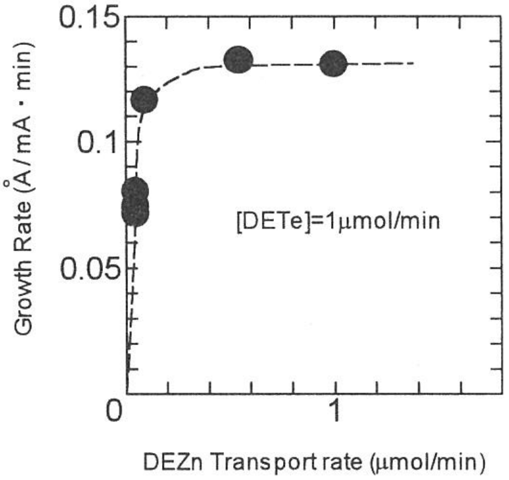

Fig.2. Growth rate of ZnTe film versus DETe transport rate.

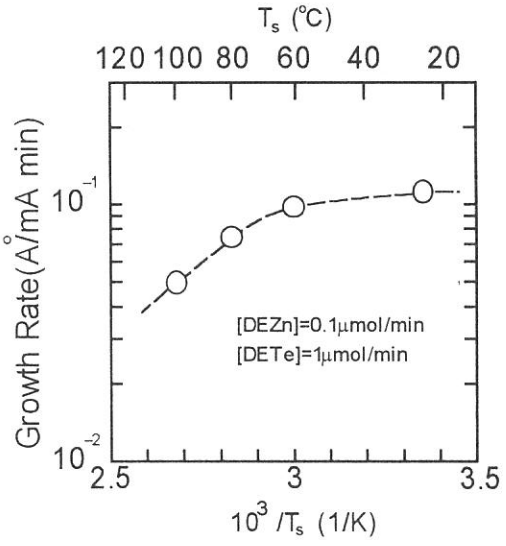

Fig.3. Growth rate of ZnTe versus substrate temperature.

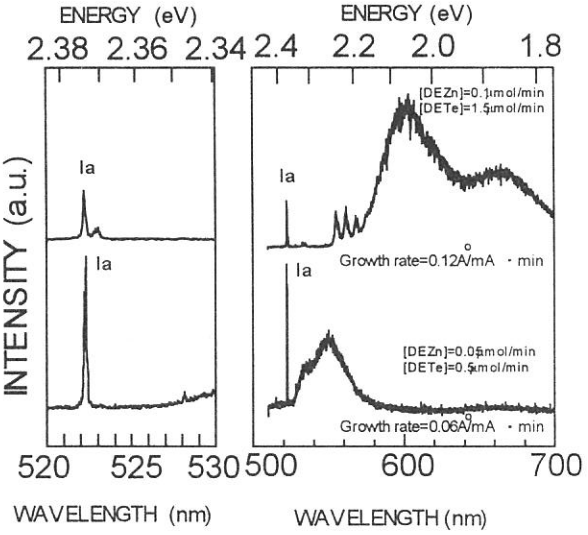

Fig. 4. Typical photoluminescence spectra of ZnTe films.

(BL8A)

Synchrotron radiation etching of diamonds

Eiji Ishiguro, Toshikazu Sugiura[1], Satoshi Nonoyama[1], Kosuke Shobatake[1],
Haruhiko Ohashi[2], and Tatsuo Gejo[3]

College of Education, University of Ryukyus, 1 Senbaru, Nishihara-cho, Okinawa 903-0213, Japan
[1] Department of Molecular Design and Engineering, Graduate School of Engineering, Nagoya University, Furo-cho, Chikusa-ku, Nagoya 464-0814, Japan
[2] Japan Synchrotron Radiation Research Institute, 323-3 Mihara, Mikazuki-cho, Sayo-gun, Hyogo 679 - 5198, Japan
[3] Institute for Molecular Science, Myodaiji, Okazaki 444-0867, Japan

Diamonds can be etched with the aid of synchrotron radiation(SR) excitation in the atmosphere of oxygen gas[1-2]. This is expected to become one of the potential techniques for micro-fabrication of diamonds.

The experiment was performed at the beamline BL8A of UVSOR which a reaction chamber with a differential pumping system was attached to. Etchant gas was filled in the chamber. NO_2 and H_2O were used as etchant besides O_2, because NO_2 is considered to be more reactive than O_2 for oxidization. The pressure of the gas in the reaction chamber was 0.1 torr and the diamond sample was kept in the room temperature. The etch rates for the three different etchants are listed in table 1. We see that the rate for H_2O is almost a half of that for O_2. Furthermore, no clear difference of the etch rate can be seen between O_2 and NO_2. This seems to show that atomic oxygen dissociated from the molecules may contribute to etching, but not the molecules themselves.

We can expect from the above result that a high concentration of atomic oxygen may result in a high etch rate of diamond. A radical generator by means of microwave discharge was attached to the reaction chamber in the direction perpendicular to SR. A nickel mesh mask was placed in the front of the sample. Oxygen gas was introduced into the radical generator operated in the power of 300 W. The surface of diamond taken by AFM is shown in Fig.2. The dose of SR was 10,000 mA·min and the pressure in the chamber was 1×10^{-4} torr. The temperature of the surface rose up to 80℃ because of irradiation of SR and heat from the radical generator, although the diamond sample was cooled by liquid nitrogen. We can see from the AFM micrograph that the surface irradiated by SR was etched with the depth of 160 Å. Thus, the each rate was estimated to be 0.16 Å/mA·min which is almost the same to those for the etchants of O_2 and NO_2 in the pressure of 0.1 torr. However, the etch rate in the former case is quite high comparing with those in the latter case, if the difference of the pressure in both cases is considered. This also indicates that oxygen radicals play an essential role on etching the diamond surface.

We would like to thank to Prof. M. Kamada for his valuable discussion on our experiment. The project was supported by a Grand-in-Aid from the Japanese Ministry of Education, Science, and Culture, for Scientific Research, No.09450021.

References

[1] H.Ohashi, E.Ishiguro, T.Sasano, and K.Shobatake, Appl.Phys.,**68**,3713-3715(1996)

[2] E.Ishiguro, H.Ohashi, T.Sasano, and K.Shobatake, J.Electron Spectrosc. Relat. Phenom., **80**,77-88(1996)

Table 1. Comparison of etch rates of diamond between the different etchant gases

Etchant	Etch rate(Å/mA·min)
O_2(0.1torr)	0.13
NO_2(0.1torr)	0.15
H_2O(0.1torr)	0.08

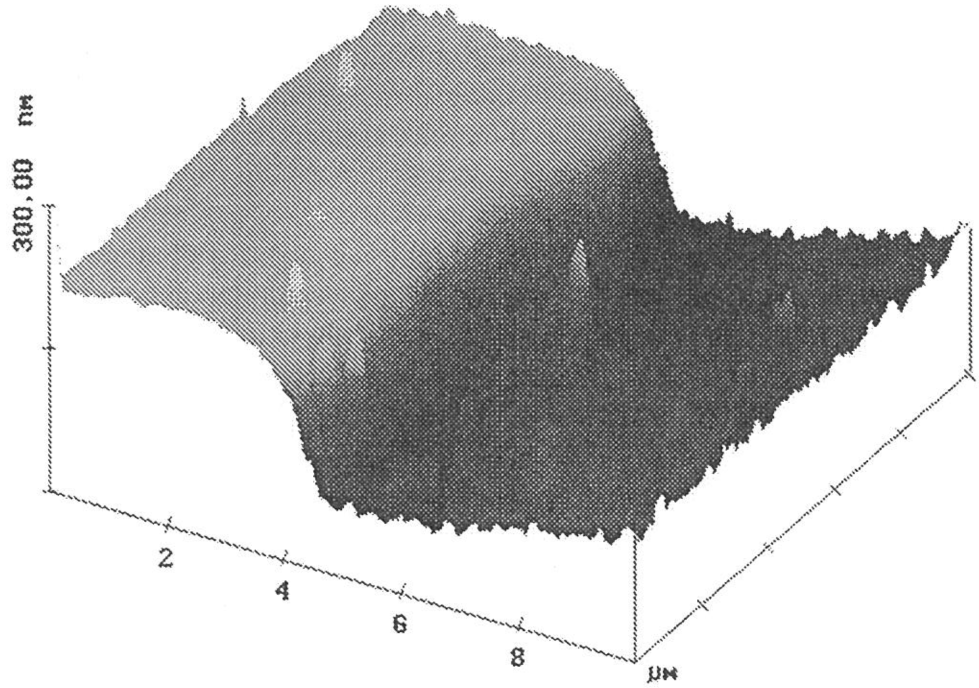

Fig.1. AFM micrograph of the diamond surface etched in the atmosphere of atomic oxygen generated by a microwave radical source. The depth of the etched surface was 16 nm. The dose of SR was 10,000 mA·min and the temperature of the surface on etching was 80℃.

(BL8A)

UVSOR Excited CF_4 Plasma Etching of Si Wafer Through LB Resist Film

Shinji Ogawa, Mohd Zalid Bib Harun, Girish J. Phatak* and Shinzo Morita
Deptt. of Electrical, Electronics and Information Engineering, Nagoya University, Nagoya 464 8603 Japan.
** Permanent Address : C-MET, Panchavati, Off Pashan Road, Pune 411 008 India.*

Introduction

In the series of UVSOR excited CF_4 plasma etching of silicon wafer, 50 nm line and space (L&S) pattern etching was realized in the previous work using a commercial resist SAL-601 (Shipley Far East Ltd), which is a negative tone chemically amplified resist [1]. However, this resist was developed for 100 nm pattern fabrication. Therefore, there is a need of a new resist for finer pattern fabrication. As an example of fine pattern fabrication resist, a fatty acid Langmuir Blodgett (LB) resist film was selected for the present experiments. It is reported earlier for LB resist films of PMMA that the these films show very low pin hole density of 10 cm^{-2} as compared to the conventional spin coated films of same thickness, which is more than 10^4 cm^{-2} [2]. It must be noted here that the proximity effect forces the use of resist film with thickness of same order of magnitude as that of the pattern dimension. In this respect also it is important to explore the suitability of LB resist films for fine pattern fabrication.

However, one problem of using LB resist film for fine pattern fabrication is the plasma etching resistivity of the LB resist films. The extreme low thickness of the films make the matter more difficult. Synchrotron Radiation Excited Plasma (SREP) is known for its low ion energy during plasma because the plasma is excited without any high electrical field. Another important aspect for this etching process is that because of the external energy source for plasma generation, the plasma parameters become independent of the gas parameters. Due to these aspects, this etching process is one of the attractive processes for nano scale pattern fabrication.

In the present work, we have continued the initial experiments of studying the etching characteristics of silicon. Further, we characterized the LB film etch rate with respect to that of silicon and finally carried out etching of fine pattern and obtained 100 nm L&S pattern successfully.

Experimental

The etching set up used for the present experiments was equipped along with beam line BL8A. Due to the requirement of high pressure during etching, the set up was arranged so that the maximum volume of gas is pumped through the rotary pump. The rotary pump used here was having pumping speed of 50 l/min. The CF_4 gas flow was controlled using a needle valve, and measured using a mass flow meter. In order to keep continuity with the earlier experiments [1], the gas pressure throughout the present experiments was kept constant at 130 mTorr. The CF_4 gas flow rate to maintain this pressure, was in the range of 60 sccm. The samples were arranged perpendicular to the incident radiation with the help of a micromanipulator, while being biased to –196 V with the help of a battery. We have earlier found that for CF_4 gas, the etching can be realized under negative bias voltage [1].

The etching experiments were done at a constant current of about 190 mA, and the dose was varied from 500 mA.min to 2500 mA.min. The samples were prepared by first coating 20 monolayers of stearic acid ($CH_3(CH_2)_{16}COOH$) on (100) oriented silicon samples using LB technique, followed by electron beam patterning at 50 kV with a dose of 5000 $\mu C/cm^2$. Two types of patterns were made. One was used for measuring the thickness of the patterns before and after etching. Because we used surface recorder for this purpose, these were big dimension L&S patterns having width of 5μm and length 4mm. These samples were exposed to varying dose as mentioned above. The other pattern was a fine pattern with different L&S patterns from 25 nm to 5 μm width and was exposed to a dose of 2000 mA.min.

Results and Discussion

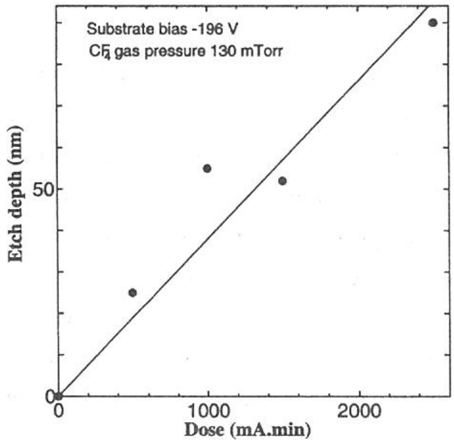

Fig. 1 :Etch depth dependence on dose

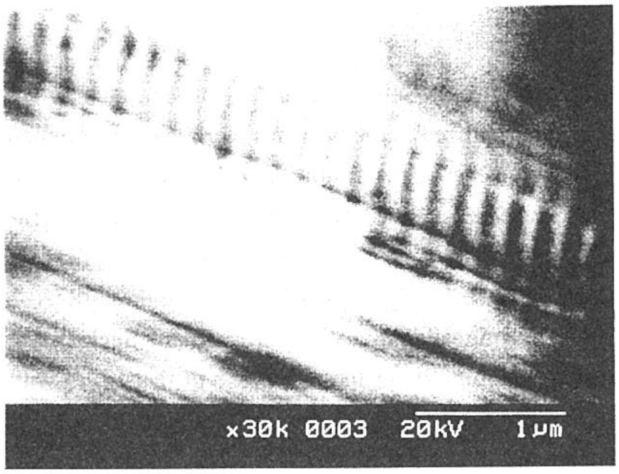

Fig 2. : SEM micrograph showing etched fine pattern

Figure 1 shows the recorded etch depth against the dose for the given experimental conditions. The etch depth obtained here for 2500 mA.min is found to be about an order lower than that obtained earlier [1] at about the same, -200 V substrate bias. This result is attributed to the possible difference in the gas flow rates, and thus the difference in the effective concentration of the etching species, as the pumping arrangement is different. Because in the present experiments a rotary pump has been used as compared to earlier, when a turbo molecular pump was used which has much higher pumping speed, the flow rates in the present experiments could be much lower. As developed and as etched 5 μm pattern were measured for their thickness using the surface recorder and the etch rate ratio of silicon and LB resist film was measured. It was found for all the dose conditions that the average etch rate ratio is 1. This may be either due to improper exposure of LB films while patterning or due to unsustainable ion energy during etching. All the patterns were found to be over etched. However, even at this etching ratio, fine patterns could be successfully transferred into silicon. Figure 2 shows the SEM micrograph of 100 nm L&S pattern after etching. Due to low height of the etched pattern, there was a considerable difficulty in obtaining an SEM micrograph. The present picture has been recorded at a an viewing angle close to 90°, and hence, a very small portion in the picture is actually focused.

Conclusions

Here we have conducted an initial study of silicon etching in SREP using extremely thin LB stearic acid resist films. A fine pattern of 100 nm L&S could be successfully transferred into silicon. However, it is found that the etch rate ratio between silicon and the LB resist film is only 1:1. Further optimization of the LB films preparation process and lowering of substrate bias is necessary to improve this etch rate ratio.

References

1. R. Inanami, T. Uchida and S. Morita, J Electrochem. Soc., **143**, 3754, 1996.
2. S. W. J. Kuan, R. F. W. Pease and C. W. Frank, in *Polymers in Electronics*, Ed. Y. Tabata, I. Mita, S. Nonogaki, K. Horie and S. Tagawa, Kodansha, Tokyo, p. 169. 1990.

(BL8A)

Velocity Distributions of the Desorbed Neutral Species Formed from the Ablation of Synchrotron Radiation-Excited Teflon

Toshikazu SUGIURA, Satoshi NONOYAMA, Hisashi KOTSUKA,
Haruhiko OHASHI[A], and Kosuke SHOBATAKE

Department of Molecular Design and Engineering, Graduate School of Engineering, Nagoya University,
Chikusa-ku, Nagoya 464-8603, Japan
[A]Japan Advanced Synchrotron Radiation Institute (JASRI), 323-3 Mihara, Mikazuki-cho, Sayo-gun, Hyogo
679-5198, Japan

Introduction A large body of information has been obtained for the state distributions of the ionic species formed from synchrotron radiation(SR) excited molecules and surfaces. However, detection of the neutral desorbed species formed in SR-excited processes has been rarely done, mainly due to the experimental difficulties in detecting neutral species. Y. Zhang, et al.[1] have found that the Teflon (commercial name for polytetrafluoroethylene, PTFE), $(-CF_2-)_n$ is quite easily ablated by irradiating SR upon it and Inayoshi et al.[2] have found that desorbed species formed by ablation of SR-excited Teflon can form Teflon-like thin films. Despite these findings the mechanisms of the SR-excited ablation of Teflon were not understood nor what kind of species are desorbed in the ablation process. The combination technique of GC/MS (gas chromatography /mass spectrometry) has been applied to determine the decomposition product from the pyrolysis of Teflon and it has been found that the major decomposition product formed at 750℃ is tetrafluoroethylene (TFE). Therefore from the thermal decomposition TFE moieties are chopped off from the end of the polymer chain. In the present project we have measured the velocity distributions of the desorbed neutral species formed from the ablation of SR-excited Teflon, to understand what species are formed in the ablation process and what mechanisms are applicable for the very fast ablation of Teflon.

Experimental The apparatus used for the present study was constructed for the measurement of the time-of-flight (TOF) spectra of the SR-excited surface reaction processes[3]. The TOF spectra of the desorbed species are measured using electron bombardment ionization mass spectrometry combined with a pseudo-random correlation chopper technique. The distance from the chopper to the ionization region was 31.1 cm. A TOF spectrum was measured as a function of the neutral flight time from the chopper to the ionizer region. The "white" focused SR was used for the experiment. The deflection angle of the focused light due to the Pt-coated mirror was 4 degrees. The intensity of the SR was adjusted using a filter made of layered Ni meshes and its intensity was monitored by photoelectric current (PEC) measurement.

Results and Discussion The TOF spectra were recorded at about 60 ion masses from *m*/e = 19 up to about 400. It is well known that organohalogen compounds are easily fragmented upon electron bombardment and thus daughter ions with masses much lower than the neutral mass are usually detected. The typical TOF spectra observed at masses, *m*/e = 19(F^+), 31(CF^+), 50(CF_2^+), 100($C_2F_4^+$), 129, and 382 are shown in **Figure 1**. The species arriving at the ionizer at earlier times have higher speeds. The TOF spectral profiles are not identical, which means that, for example, the neutral species detected at mass *m*/e = 19 (F^+) mostly originate from lighter species, such as F atoms as well as C_2F_4. To extract more information out of the spectra each TOF spectrum was analyzed assuming that it is a superposition of two or three velocity components, since none of them could be fitted to a single Maxwell-Boltzmann (MB) distribution. The MB distribution is characterized by a ratio, M/T, where M and T are the mass and a translational temperature of the desorbed neutral species. The translational temperature of the molecules desorbed from the surface by thermal desorption is known to be equal to the surface temperature, T_s. Thus the surface temperature was assumed to be equal to the translational temperature (T) of the Kr atom scattered to the direction normal to the surface when the effusive Kr beam was collided to the surface at an incident angle of about 45 degrees. T_s determined in this manner was adopted even when the SR is shone on the surface: T_s goes up when the SR is shone on it. In order to control the substrate temperature the Teflon plate was heated with a ceramic heater attached from the rear side.

Most of the data are fairly well fitted with two velocity components. Once the ratio, M/T, is determined from the fit the mass of the neutral species can be determined since T is set to be equal to T_s. However, there is one exception; for F atom desorption T for the fast component was found to be somewhat higher than T_s, especially when the light intensity was high. **Figure 2** illustrates T for the F atoms detected at mass *m*/e = 19 as a function of irradiation time on the same sample spot. The surface temperature was T_s = 405 K. One sees that

T is higher than the T_s by about 30% at the start of the irradiation. The F atoms formed are repulsed from the surface on a repulsive surface. **Figure 3** shows the neutral mass determined for the slower component detected at mass $m/e = 19$ and for $T_s = 405$ K as a function of irradiation time. The determined mass is almost equal to the mass number corresponding to a light molecule C_2F_3 or C_2F_4.

It is noted that the intensity of the desorption product is very low when the light intensity is very low (in the single bunch operation) and the surface temperature is kept low. After the irradiation under this condition the color of the sample surface turns light brown. Therefore it is concluded that the ablation does not proceed at a noticeable rate as long as the surface temperature is low and thus the sample was heated from the rear side to induce desorption. There is a tendency that heavier species are desorbed as the surface temperature is increased. **Figure 4** shows the masses of the desorbed species as a function of SR intensity and substrate temperature. The highest mass determined amounts to 833 amu. It is speculated that cleavages of C−F and C−C bonds are induced by inner core excitation of the constituent atoms followed by Auger processes and desorption of the imbedded fragments occurs after their diffusion to the surface by thermal motion. Although not shown here, the apparent desorption rate follows an Arrhenius rate form $k_{des}(T) = A \exp(-E_a/kT)$, implying the above mentioned notion.

(References)

1. Y. Zhang, et al., Appl. Phys. Lett. **67**, 872 (1995).
2. M. Inayoshi, et al., Jpn. J. Appl. Phys. **34**, L1675 (1995).
3. H. Ohashi and K. Shobatake, J. Electron Spectr. Related Phenomena, **80**, 77 (1996).

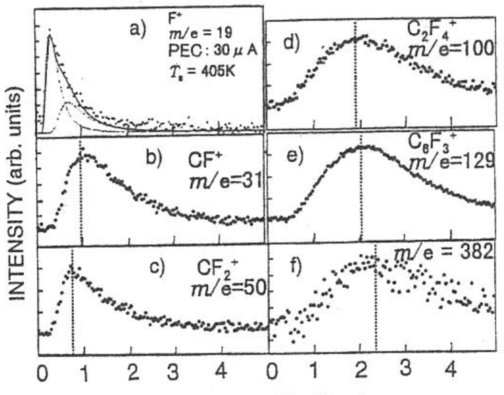

Figure 1. Typical TOF spectra of desorbed species detected at ion masses m/e = a) 19(F^+), b) 31(CF^+), c) 50(CF_2^+), d) 100 ($C_2F_4^+$), e) 129, and f) 382.

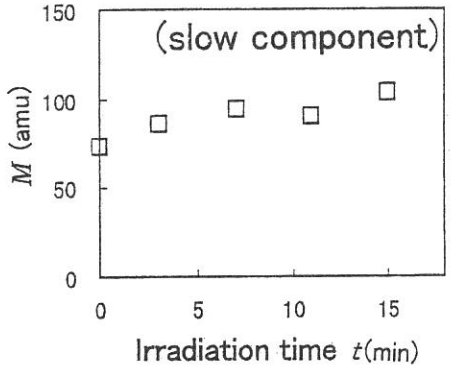

Figure 3. Irradiation time dependence of the translational temperature T for the slow component detected at F^+(m/e = 19) and at T_s = 405 K.

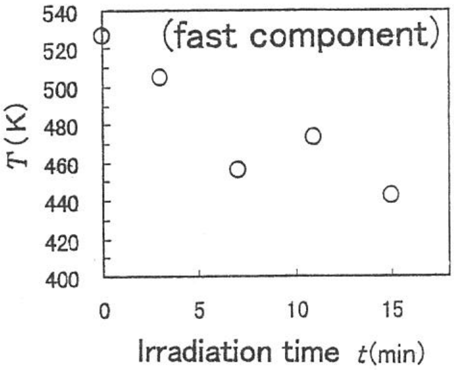

Figure 2. Irradiation time-dependence of the translational temperature T of F atoms (fast component) detected at F^+(m/e = 19).

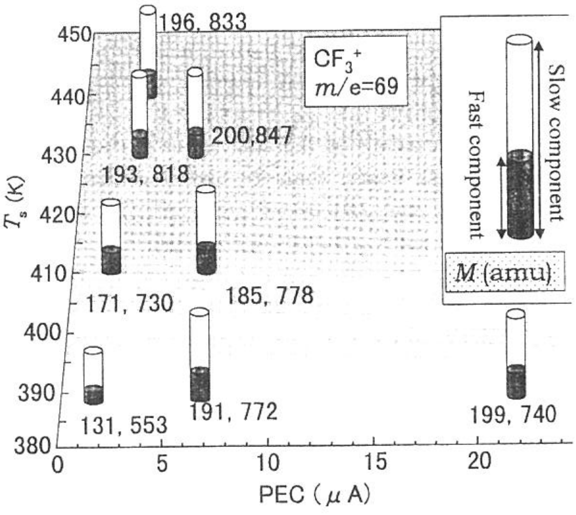

Figure 4. Surface temperature (T_s) and light intensity (measured by PEC) dependence of the mass of the desorbed species detected at mass m/e = 69 (CF_3^+). The height of the rod represents the molecular weight. The mass numbers are also indicated in the

(BL-8A)

Fabrication of Fluorinated Thin Films by SR ablation

JunKamiiisaka, Masafumi Ito, Masaru Hori and Toshio Goto
Department of Quantum Engineering, Nagoya University
Mineo Hiramatsu
Faculty of Science and Engineering, Meijo University

Introduction:

Teflon material is expected to use for the micro-machine fabrication. So far, we have successfully deposited Teflon materialssuch as PTFE, FEP and PFA and fabricated 19É m size pattern on them anisotropically at a high speed by using SR[1]. However, it has not been reported that the fine pattern of Teflon was fabricated on the curved surface to use this process further for maicro-machining.

In this study, we have formed $(CF_2)n$ films on the curved surface by using CF_2 radicals and fabricated them by SR ablation. Moreover, we have fabricated the metal fluoride thin films which was evaporated with electron-gun. On the basis of these results, we have proposed the total dry process of fabrication of fluorinated materials using SR.

Experiment and results:

The experiments were performed in BL-8A line in UVSOR.

CF_2 radicals which were considered as a precursor for the Teflon material were formed by the pyrolytic decomposition of HFPO gas. The $(CF_2)n$ thin films of 1.5μ m thickness were formed on 1/8 inch stainless tube and nichromium wire(0.5mm ϕ) by using the CF_2 radicals. The mesh mask was set on these samples and irradiated by SR at 10^{-4} Pa in vacuum and a room temperature.

Figure 1 shows the SEM images. The fine patterns were found to be fabricated on Teflon films deposited on the curved surface. In order to investigate the reaction mechanism of Teflon with SR, the wavelength irradiated on the Teflon surface is selected with the carbon and MgF_2/Carbon masks and thereby the ablation rate of films is evaluated.These results obtained are under analysis.

Furthermore, we have investigated the fabrication on the metal films as well as Teflon. AgF, MgF_2 and AlF_3 thin film of 50nm thickness were formed on Si substrate. These samples were irradiated through the mesh mask at 10^{-4}Pa in vacuum and a room temperature. We have successfully formed fine patterns on all films of AgF, MgF_2 and AlF_3 .

Figure 2 shows SEM image of 77μ m square patterns. Figure 3 shows the SR intensity dependence of etching rate. It was found that the etching rate increased linearly with increase of SR current and the etching rate was dependent on the materials which will be due to the evaporated pressure and SR absorption rate of materials.

Figure 4 shows SR duration dependence of etching rate. The etching rate was decreased as the SR duration was increased. The irradiated surface of AlF_3 pattern was investigated by XPS.

Figure 5 shows F/Al ratio of surface of films under-patterned by SR.The change of ratio was corresponding to the pattern area with and without SR irradiation. These results indicate the reaction mechanism where fluorine atoms were desorbed fast from metal fluoride surface by SR irradiation and the film structure is changed from fluoride rich surface to metal rich one with SR duration. Therefore, the etching rate is decreased with SR duration.

Summary:

The fine pattern fabrication of Teflon on the curved surface using SR was investigated for micro-machining process. The novel dry process using SR, where the $(CF_2)n$ films were formed on the curved surface of wire by using CF_2 radicals generated from pyrolytic decomposition and SR was irradiated on them through a mesh, was successfully demonstrated.

Furthermore, the fine pattern fabrication was investigated on metal fluoride films of AgF, MgF$_2$ and AlF$_3$ by using the dry process, where metal fluoride films were evaporated by electron gun and SR was irradiated on the films.We found the metal fluoride patterns were successfully fabricated by the SR dry process. The reaction mechanism of the ablation of fluoride films with SR irradiation was proposed.

[1]M.Inayoshi et.al.,Jpn.J.Appl.Phys.Vol.34,Pt.2,No.12B,pp.L1675-L1677,December 1995

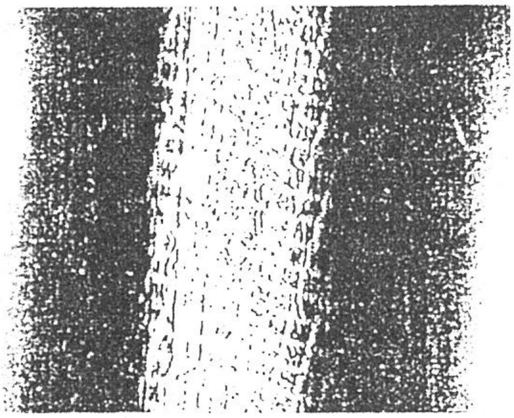

Figure 1:SEM photograph of the fine patterns created in Teflon film deposited on the curved surface

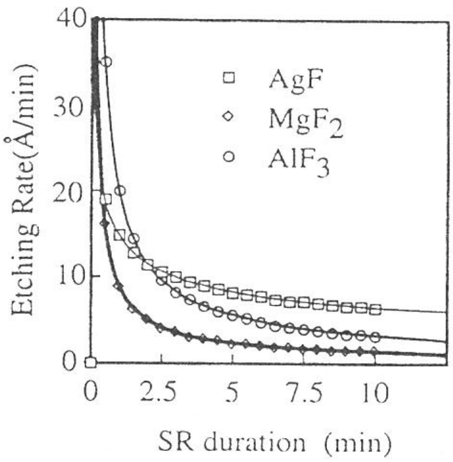

Figure 4:Etching rate of AgF,MgF2,AlF3 as a function of SR duration

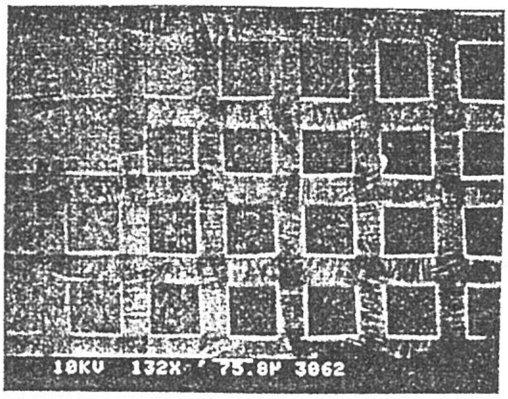

Figurre 2:SEM photograph of the fine 77μm square patterns created in MgF$_2$ film

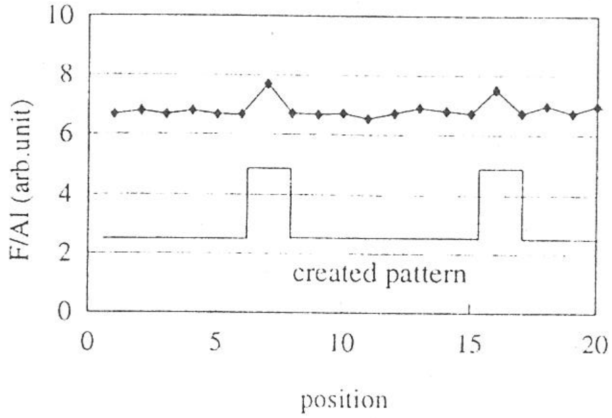

Figure 5:F/Al ratio of surface of films under-patterned by SR

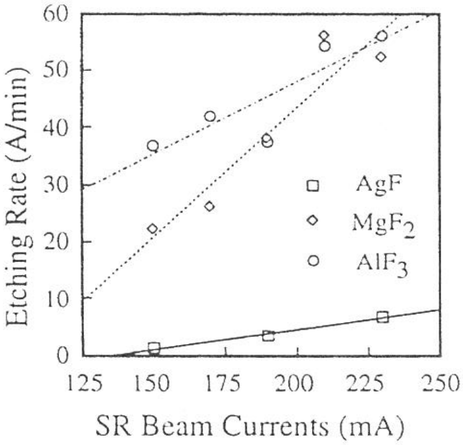

Figure 3:Etching rate of AgF,MgF2,AlF3 as a function of SR current

(BL8B1)

Pd $3p$ core level x-ray absorption spectroscopy of ordered Pd_3Fe

Takayuki MURO, Shin IMADA, Ki-Seok AN, Ran-Ju JUNG,
Takeshi KANOMATA[A], and Shigemasa SUGA

Department of Material Physics, Osaka University,
Toyonaka, Osaka 560-8531
[A]Department of Applied Physics, Faculty of Engineering, Tohoku Gakuin University,
Tagajo, Miyagi 985-8537

Series of Pd-Fe alloys have been extensively studied as typical transition metal alloys showing several interesting properties. One of the characteristic properties of Pd-Fe alloys is the large local magnetic moments on the Fe sites, especially in the Pd-rich region, up to 3 μ_B in comparison with 2.2 μ_B in Fe metal. Although Pd metal is not ferromagnetic, very small amount of Fe makes it ferromagnetic and the dilute PdFe shows so-called giant-moment as large as 12 μ_B per impurity [1].

The previously observed x-ray absorption (XAS) spectrum in the Pd $3p$ core region of Pd_3Fe showed anomalously large structures in the photon-energy (hν) regions of about 7.5 eV higher than the $3p_{3/2}$ and $3p_{1/2}$ main peaks. Similar structures were also seen in the Pd $3p$ XAS spectra of Ni-Pd alloys [2]. One possibility for the origin of the separations between the main peaks and the higher-energy structures is that the main peaks stem from excitonic states in the XAS final state. The binding energies (E_B) of the $3p_{3/2}$ and $3p_{1/2}$ levels were obtained as 532.3 and 560.1 eV, respectively, from the XPS measurement. If the hν at the $3p_{3/2}$ and $3p_{1/2}$ main peaks of the XAS spectrum are smaller than the E_B of the $3p_{3/2}$ and $3p_{1/2}$ levels, the XAS main peaks might be the excitonic states. Unfortunately, the photon energy of the previously observed Pd $3p$ XAS spectrum had not been corrected by any other references.

We have measured the Pd $3p$ XAS spectrum of Pd_3Fe again and corrected the hν by the O $1s$ absorption at the BL8B1. The corrected hν at the Pd $3p_{3/2}$ and $3p_{1/2}$ main peaks of the XAS spectrum are 535.0 and 563.0 eV, which are larger than the E_B of the Pd $3p_{3/2}$ and $3p_{1/2}$ core levels, respectively. Therefore, we conclude that the separations between the main peaks and the higher-energy structures are not due to the exciton effect.

References

[1] J. Crangle and W. R. Scott, J. Apple. Phys. **36**, 921 (1965).
[2] S. Y. Park, S. Muto, A. Kimura, S. Imada, Y. Kagoshima, T. Miyahara, T. Hatano, T. Hanyu and I. Shiozaki, J. Phys. Soc. Jpn. **64**, 934 (1995).

(BL8B1)

Photodissociation of ozone in the *K* edge region

Tatsuo GEJO, Kazumasa OKADA[A], Toshio IBUKI[B] and Norio SAITO[C]
Institute for Molecular Science, Myodaiji, Okazaki 444-8585, Japan
[A]Department of Chemistry, Hiroshima Univ., Higashi-Hirosima 739, Japan
[B]Kyoto Univ. of Education, Fukakusa, Fushimi-ku, Kyoto 612, Japan
[C]Electro technical Laboratory, Umezono, Tsukuba-shi, 305-0045, Japan

The inner-shell excitation of different atoms in a molecule leads to significant different photodissociation pathway. This effect is called site-specific dependence of fragmentation and has been observed in the *K* edge excitations of N_2O, CF_3CH_3 , CF_2CH_2, BF_3 and OCS. In view of this, it is of interest to investigate the dissociation of ozone in the *K* shell excited state. We have previously observed two distinct peaks around 529 and 536 eV in the ion yield spectra of ozone [1]. The first peak at 529 eV has been assigned as the $\pi^*(2b_1)\leftarrow O_T(1s)$ resonance transition of the terminal oxygen atom and the second around 536 eV as the excitation to the π^* level from the center O(1s) [1]. However, the latter has a wide bandwidth. Performing the molecular orbital (MO) calculations based on the SCF approximation, this band has been deconvoluted by two components: The calculation shows that one is the $\pi^*(2b_1)\leftarrow O_C(1s)$ transition, as we expected, and another is $\sigma^*(7a_1)\leftarrow O_T(1s)$ transition [1], where the O_C and O_T mean the terminal and center oxygen atoms, respectively. The excitation from these different 1s levels of ozone is expected to give different photodissociation or ionization pathway.

The time-of-flight (TOF) spectra measurement is a useful tool for investigating the pathway of ionic fragmentation of a molecule. In addition to this, angle-resolved measurement using the TOF apparatus provides information about electronic state of the decomposing molecule: The dipole transition probability depends on the molecular orientation with respect to the electric vector of polarized light. The *KVV* Auger decay or autoionization occurs within 10^{-14} s in the *K* shell excited molecule, while the rotational period of molecule is longer than 10^{-13} s. Hence the initial memory of the innermost core excited molecule may not be faded in fragmentation.

The TOF mass spectra were measured at 529.0, 535.7, and 544.6 eV for the $\pi^*(2b_1)\leftarrow O_T(1s)$, $\pi^*(2b_1)\leftarrow O_C(1s)/\sigma^*(7a_1)\leftarrow O_T(1s)$, and $\sigma^*\leftarrow O_C(1s)$ transitions, respectively. The detector axis was set at 0 degree (denoted as "horizontal") or 90 degrees (denoted as "vertical") with respect to the linearly polarized synchrotron radiation. Fig. 1 shows the TOF spectra at the vertical and horizontal positions excited at 529.0, 535.7 and 544.6 eV. In these spectra, the contribution from O_2 was subtracted. At the excitation energy 529.0 eV, the O^+ ion ejected to the vertical direction consists of three peaks with local maxima: The center one is presumably due to O^+ and O_2^{2+} with no kinetic energy. Two wing peaks should be O^+ fragments. On the other hand, the energy distribution obtained from the ions at the horizontal position shows the relatively narrow single O^+ peak. The difference of these two shapes arises from the fact that the O^+ fragment is preferably emitted to the vertical direction with some kinetic energy. Since the geometry of ozone in the ground state is bent (C_{2v}), this is consistent with our previous assignment that the 529 eV band is the $\pi^*(2b_1)\leftarrow 1s(2a_1)$ transition, whose transition moment lies perpendicular to the C_{2v} molecular plane. In contrast to this, at an excitation energy of 535.7 eV, the O^+ ion ejected both to the vertical and to the horizontal direction consists of three peaks. This implies that the O^+ fragment ions were ejected more isotropically.

Table 1 shows the appearance of fragments O_3^+, O_2^+ and O^+ and O^{2+} depending on the excitation energies. The main products observed were O_2^+ and O^+. Those fragments account for 85-90 % of products for these excitation energies. The parent O_3^+ was also produced. However, it is less than 8 % of total ions. In table 1 the fragment distributions are similar in the excitations of center O(1s) electrons at 535.7 and 544.6 eV, which means the effect of excitation energy on the fragmentation is not considerable. On the contrary, the O_2^+ fragment is preferably formed at the $\pi^*(2b_1) \leftarrow O_T(1s)$ excitation, especially 42% at the horizontal experiment. This enhancement of O_2^+ can be attributed to the atomic site selectivity of the relaxation processes following the initial excitation. That is, the core hole associated with the terminal oxygen produces the large yield of molecular O_2^+ fragment ion.

[1] T. Gejo, K. Okada and T. Ibuki, *Chem. Phys. Letters* 277 (1997) 497.

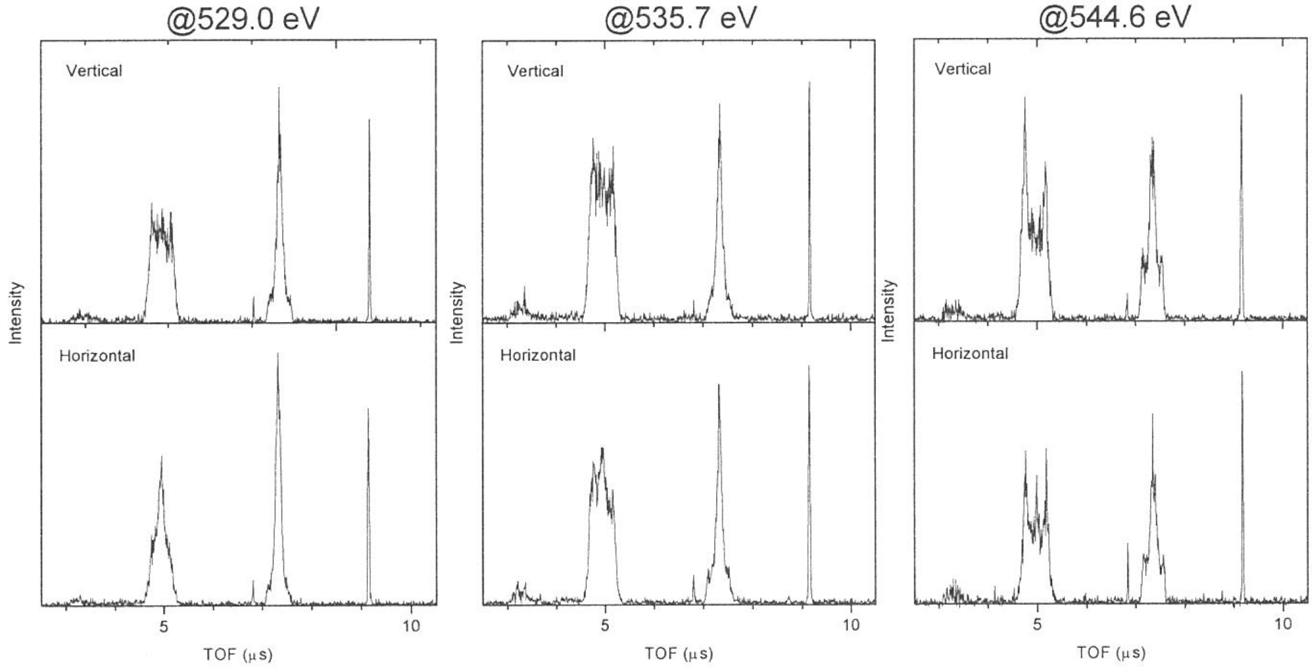

Fig. 1: TOF spectra obtainedwhen the detector is set to the horizontal and vertical to the direction of polarization of light.

Table 1: The branching ratios of ion photofragments observed at three energies.

	529.0eV (%)		535.7eV (%)		544.6eV (%)	
O_3^+	8(//)	6(⊥)	8	5	8	7
O_2^+	42	37	30	25	32	33
O^+	46	54	58	63	55	54
O^{2+}	4	5	5	6	5	5

Left values were measured when the polarization is set to horizontal position (//) while right ones were measured when it is set to vertical position (⊥).

(BL 8B1)

Characterization of the Catalysts for the Oxidative Cracking of n-Butane by O K-edge XANES

Sakae TAKENAKA*, Shoji KOBAYASHI*, Tomoko YOSHIDA**,
Ichiro YAMANAKA*, and Kiyoshi OTSUKA*

Faculty of Engineering, Tokyo Institute of Technology, Meguro, Tokyo, 152-8552
**Center for Integrated Research in Science and Engineering,
Nagoya University, Nagoya, 464-8603

1. Introduction

A promising area of light alkanes utilization is the conversion to unsaturated hydrocarbons. We have found that rare-earth metal oxide catalysts are effective for the oxidative cracking of n-butane to form ethene and propene. Furthermore, the addition of Li^+ ions to rare-earth metal oxide catalysts caused suppression of total oxidation of n-butane and increase in olefin yields. The addition of Li^+ ions to rare-earth metal oxides would bring about the change of chemical property of the lattice oxygen in Y_2O_3. In this study, we investigated the structural change of Y_2O_3 by the addition of Li^+ ions using O K-edge XANES spectroscopy and XRD, in order to obtain the information about active species for the oxidative cracking of n-butane.

2. Experimental

The Li^+-added Y_2O_3 was prepared by impregnating Y_2O_3 with an aqueous solution of Li_2CO_3, following by calcination at 1073 K under an air stream. The experiment for the oxidative cracking of n-butane was carried out using a conventional gas flowing system. The O K-edge XANES spectra of catalysts were recorded at room temperature in a total electron yield mode at BL-8B1 at UVSOR. In most measurements, the G2 grating and entrance and exit slits both of 20 μm width were utilized. The sample was put on a Cu-Be dinode which is attached to the first position of the electron multiplier.

3. Results and Discussion

Fig. 1 shows the changes of n-butane conversion and olefin yield by the added amounts of Li^+ ions in the oxidative cracking of n-butane over Li^+-added Y_2O_3 catalysts at 1023 K. The addition of Li^+ ions to Y_2O_3 catalysts resulted in the decrease of the n-butane conversion, however, the total oxidation suppressed and the olefin yields increased by the addition of Li^+ ions. This result indicates that the addition of Li^+ ions to Y_2O_3 brings about the formation of active sites on Y_2O_3 for the selective oxidation of n-butane to olefins.

Fig. 2 shows XRD patterns of Y_2O_3 and Li^+-added Y_2O_3 samples. The XRD pattern of Y_2O_3 was identical to that Li^+-added Y_2O_3. This result suggests that new phase was not formed by the addition of Li_2CO_3 to Y_2O_3.

Fig.3 shows O K-edge XANES spectra of Y_2O_3 and Li^+-added Y_2O_3 catalysts. In the XANES spectrum of Y_2O_3, two peaks were observed at ca. 534 and 538 eV. The first peak is assigned to the transition from O 1s to the hybridized orbital of the oxygen 2p and yttrium 4d (t_{2g}), and the other to e_g. By the addition of Li_2CO_3 to Y_2O_3, the feature of the XANES spectra changed. As the amounts of added Li_2CO_3 increased, the XANES spectra of Li^+-added Y_2O_3 got similar to that of Li_2CO_3. The XANES spectrum of Li^+(10 wt% as Li_2O)-added Y_2O_3 was identical with that of Li_2CO_3. This result indicates that Li^+-added Y_2O_3 was covered with Li_2CO_3 gradually, as the amounts of Li+ ions increased. In the XRD profile of Li^+-added Y_2O_3 catalyst, no peak due to Li_2CO_3 was found. Hence, Li_2CO_3 would be present on Y_2O_3 surface as thin layers. In Fig. 1, it is found that by the addition of Li^+ ions, the conversion of n-butane became lower and the selectivities to ethene and propene became higher. Therefore, the catalysts covered with Li_2CO_3 are effective for the formation of olefins.

Li^+-added Y_2O_3 was calcined at 1073 K, when the catalyst was prepared. During the calcination, CO_3^{2-} from Li_2CO_3 would be decomposed. Li_2CO_3 on the catalysts, which was observed in the XANES spectra of Li^+-added Y_2O_3, may be formed during the preservation in the air after the preparation. Because Li^+-added Y_2O_3 catalyst has a strong basic property, CO_2 in the air was adsorbed on the catalyst to form Li_2CO_3.

Li^+-added rare-earth metal oxide catalysts are also effective for the oxidative coupling of methane. It was reported that some lattice oxygen ions in these catalysts have O^- character[1]. The O^- was the active species to form methyl radical from methane. It is expected that the lattice oxygen with O^- character is also present on the surface of Li^+-added Y_2O_3. However, in the XANES spectra of Li^+-added Y_2O_3, the peak due to O^- species could not be seen. This would be due to adsorption of CO_2 on Li^+-added Y_2O_3. During the oxidative cracking of n-butane at 1023 K, the O^- species may be formed on Li^+-added Y_2O_3 catalyst. In order to investigate the presence of the O^- species, *in situ* measurements should be needed.

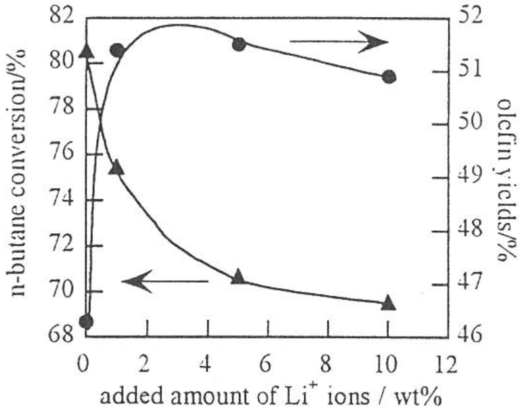

Fig.1 Change in n-butane conversion and olefin yield by added amounts of Li^+ ions.

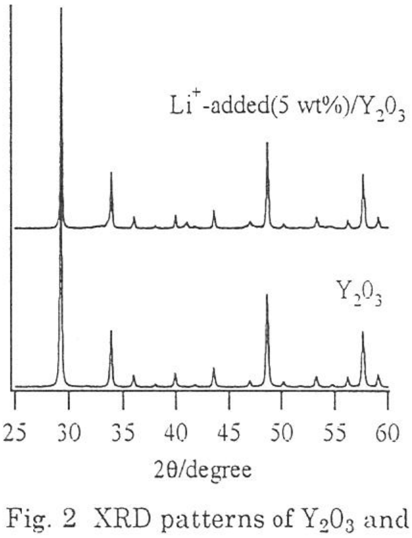

Fig. 2 XRD patterns of Y_2O_3 and Li^+(5 wt%)/Y_2O_3.

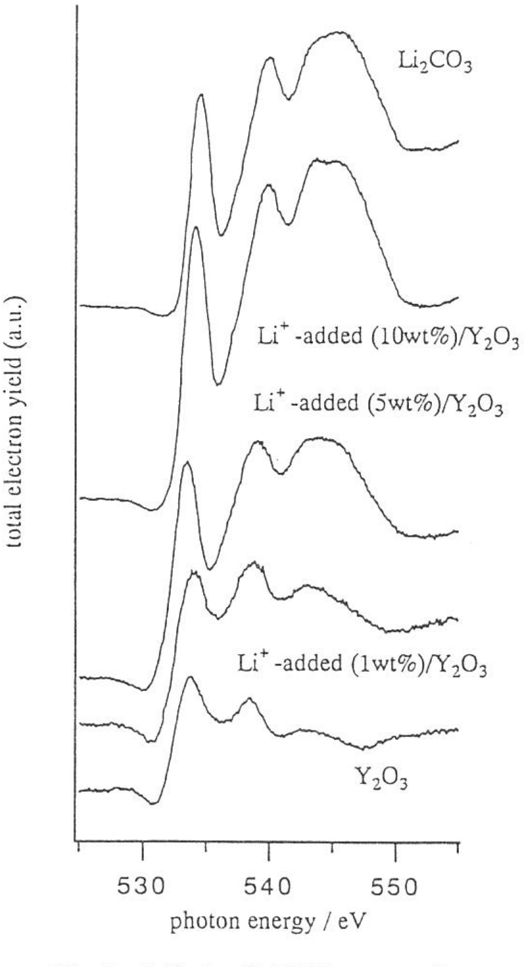

Fig. 3 O K-edge XANES spectra of Li^+-added Y_2O_3 catalysts and reference samples.

---

[1] T. Ito and J. H. Lunsford, *Nature*, 314, 721 (1985)

(BL8B1)

Study on Photodissociation of Core-excited CH_3CN and CD_3CN by Using a Reflectron-type Time-of-flight Mass Analyzer

Yasunori Senba, Hiroaki Yoshida, Tetsuro Ogata, Daisuke Sakata, Atsunari Hiraya and Kenichiro Tanaka

Department of Physical Sciences, Hiroshima University, Higashi-Hiroshima 739-8526, Japan

The angular dependent mass spectra of fragment ions for gas phase acetonitrile (CH_3CN) and acetonitrile-d_3 (CD_3CN) following nitrogen core excitation were measured at beamline BL8B1 [1]. The variable-angle reflectron-type time-of-flight mass analyzer named "VARTMAN" [2] was used as an experimental apparatus. Briefly, this apparatus is equipped with a reflectron-type time-of-flight mass spectrometer (RTOF-MS) which has higher mass resolution than the conventional linear-type TOF-MS. Also the detection axis of the RTOF-MS is variable from −20 to +110 degrees with respect to the electric vector of the linearly polarized soft X-ray without breaking the vacuum. In the present measurements, the detection angle of the RTOF-MS was set perpendicular or parallel to the linear polarization axis (horizontal) of the soft X-ray beam.

TOF spectra were measured at the resonant excitation N1s to the π^*. In order to subtract the contribution of valence bands excitation, mass spectra were also measured below the core excitation threshold. Intensity of these spectra were normalized by photon intensity and accumulation time prior to the subtraction.

Figure 1 shows mass spectra obtained for the resonant excitation $N1s \rightarrow \pi^*$ of CH_3CN with perpendicular and parallel detection angle. In addition to CHx^+ ($x = 0\sim3$), N^+ and C_2Hx^+ ($x = 0\sim3$) observed in these mass spectra, singly charged fragment ions H^+, H_2^+, $HxCN^+$ ($x = 0\sim2$) and $CHxCN^+$ ($x = 0\sim3$) were observed. Only one doubly charged fragment ion CH_2CN^{2+} was also observed. In these spectra, characteristic triad features are observed at mass number 13, 14, 15, 25, 26 and 27, while single peaks are observed at each mass number 12, 24 and 28. The triad features are due to a difference in the initial kinetic energy (KE) of ions released in dissociation process, and consist of a sharp central peak (KE~0) and two broad wings (KE>0). The central peak and the wings correspond to different dissociation processes. In brief, ions (KE>0) ejected in the direction towards RTOF-MS are arrive at the micro sphere plate in shorter time-of-flight than ions with almost zero kinetic energy, while ions with kinetic energy ejected in the opposite direction arrive in longer time-of-flight. Hence, we can estimate the initial kinetic energy of ions from flight time difference between the wings and the central peak. The initial kinetic energy of fragment ions at the maximum distribution observed for $N1s \rightarrow \pi^*$ are summarized in Table 1. The total kinetic energy release for each process in Table 1 was estimated to be about 4~6 eV by assuming the two-body dissociation process.

In the fragmentations with mass number 14, 15, 26 and 27, significant difference in the intensity ratio of wings to the central peak is observed between the mass spectra obtained with parallel and perpendicular detection angles. These differences are ascribed to the angular distributions of the fragment ions. The isotropically dissociated ions form the wings at both detection angles, while the anisotropically dissociated ions form the wings at only one detection angle. These two different types of wings are termed as isotropic and anisotropic wings, respectively. For instance, the wings at mass number 14 obtained with a perpendicular detection angle consisted of the isotropic and anisotropic wings. The contribution of the anisotropic wings to the whole wings was estimated to be 55 % from the integrated intensity of the wings obtained with perpendicular and with parallel detection angle. The orientation of molecules in space was defined by the electric vector of monochromatic light and the transition moment when molecules were excited. Thus the anisotropic wings indicate that fragment ions have "memory" of molecular orientation, since dissociation occurs more rapidly than molecular rotation.

Two ion species, CH_2^+ and N^+, correspond to mass number 14 (See Table 1). In order to estimate the contribution of each ion species, the mass spectra for CD_3CN was also measured. Figure 2 shows the comparison of mass spectra obtained for CH_3CN and CD_3CN. The mass number 14 observed for CH_3CN is formed by CH_2^+ and N^+, and indicates the larger ratio of wings to central peak than that of CD_2^+ observed for CD_3CN. The mass number 14 observed for CD_3CN is formed by CD^+ and N^+, and indicates the larger ratio of wings to central peak than that of CH^+ observed for CH_3CN. Assuming that the branching ratio of mass species for CH_3CN and CD_3CN are the same, the N^+ form the majority of the wings at mass number 14. The contribution of the N^+ to the wings was estimated to be 60 % from the integrated intensity of the wings at mass number 14 (CH_2^+, N^+) for CH_3CN and at mass number 16 (CD_2^+) for CD_3CN. This ratio is almost the same as the ratio between the anisotropic and the isotropic wings at mass number 14 for CH_3CN described above. Thus we concluded that the wings at mass number 14 consist of isotropic and anisotropic wings, and the latter is formed only by the N^+ contribution. The similar anisotropic wings were found at mass number 15 (CH_3^+), 26 (CN^+) and 27 ($C_2H_3^+$). The fragment ions of mass number 14 and 27, 15 and 26 are considered as counterpart ion pairs for the C≡N, C–C bond cleavage, respectively. This is also supported by the fact that the observed kinetic energies of counterpart ions are consistently explained by two-body dissociation. From these points of view, it is concluded that the cleavage of the C–C or C≡N bond following N1s→π* takes place faster than the molecular rotation period.

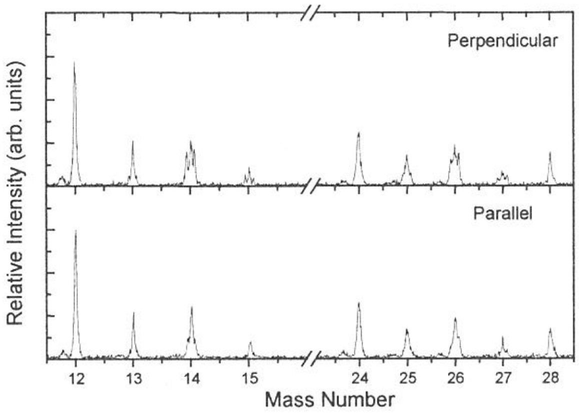

Figure 1. The mass spectra of acetonitrile (CH_3CN) following N1s→π* measured by perpendicular (top) and by parallel (bottom) detection axes.

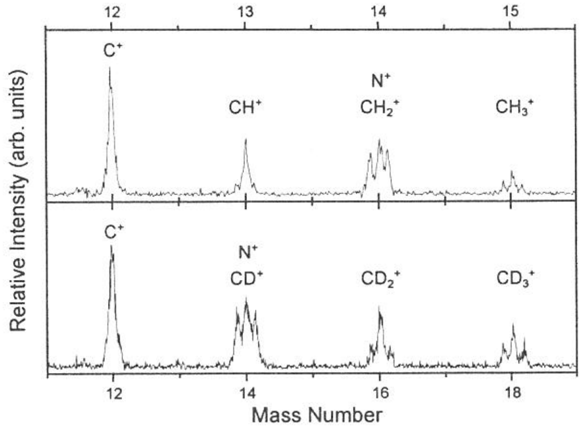

Figure 2. The mass spectra obtained for N1s→π* of CH_3CN (top) and CD_3CN (bottom).

References

[1] Y. Senba et al., J. Electron Spectrosc. Relat. Phenom. (1999), in press.

[2] A. Hiraya et al., J. Electron Spectrosc. Relat. Phenom. (1999), in press.

Table 1. The calculated initial kinetic energy of fragment ions observed for N1s→π* and the total kinetic energy release calculated by assuming the two-body dissociation process.

Mass number (Ion species)	Observed kinetic energy (eV)	Process of reaction	Kinetic energy release (eV)
13 (CH^+)	3.1 ± 0.4	$CH_3CN \rightarrow CH^+ + H_2CN$	4.5 ± 0.6
14 (CH_2^+)	2.6 ± 0.2	$CH_3CN \rightarrow CH_2^+ + HCN$	4.0 ± 0.3
14 (N^+)	4.3 ± 0.4	$CH_3CN \rightarrow N^+ + C_2H_3$	6.5 ± 0.6
15 (CH_3^+)	2.5 ± 0.2	$CH_3CN \rightarrow CH_3^+ + CN$	3.9 ± 0.3
26 (CN^+)	1.2 ± 0.1	$CH_3CN \rightarrow CN^+ + CH_3$	3.3 ± 0.3
27 ($C_2H_3^+$)	1.8 ± 0.1	$CH_3CN \rightarrow C_2H_3^+ + N$	5.3 ± 0.3
27 (HCN^+)	1.2 ± 0.1	$CH_3CN \rightarrow HCN^+ + CH_2$	3.5 ± 0.3

(BL8B1)

Faraday Rotation Measurement around Ni $M_{2,3}$ Edges Using Al/YB$_6$ Multilayer Polarizers

Tadashi Hatano, Weibing Hu, Katsuhiko Saito and Makoto Watanabe

Research Institute for Scientific Measurements, Tohoku University
2-1-1 Katahira, Aobaku, Sendai 980-8577

Magnetic circular dichroism (MCD) measurements in core absorption regions have been carried out explosively to investigate local magnetic states in ferro- and ferri-magnetic, alloy and multilayer systems, using circular polarization of synchrotron radiation. For easier sample preparation, the total photoelectron yield (TY) method with bulky samples or evaporated samples on thick substrates is usually employed [1] instead of the transmittance method with thin film samples [2]. However, the best performance of MCD measurements can not be brought out by the TY method in the studies of bulk materials or buried layers in multilayers, because the probing depth of the TY method is considered to be a few ten angstroms so that the obtained spectra are affected more or less with surface conditions. Furthermore, MCD measurements even including the transmission method would involve the ambiguity of the degree of circular polarization of incident monochromatized light, unless it were evaluated with an ellipsometric monitoring throughout the relevant energy range. The alternative approach to magneto-optical effects can be made by means of the Faraday rotation measurement. One can obtain the imaginary part of off-diagonal element of the dielectric tensor of the magnetized material by detecting the change of the azimuth of polarization ellipse between incident and transmitted lights (in principle, one can also obtain the real part by detecting the change of the ellipticity). In the core absorption regions, Faraday rotation measurements have been only performed by Kortright's group so far [3]. In our previous paper, we reported multilayer polarizers for use in the 55–90 eV region for Faraday rotation experiments around $M_{2,3}$ edges of 3*d*-transition metals [4]. In the present work, we constructed a polarimeter for Faraday rotation measurements, which consists of a multilayer polarizer, a multilayer analyzer and a magnetic circuit. Measurements were carried out on Ni film samples around the $M_{2,3}$ absorption edges, and the results were compared with the rotation angle obtained by Kramers-Krönig (K-K) transform of a measured MCD spectrum [1].

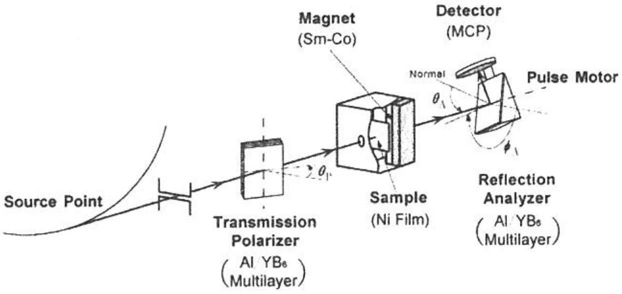

FIG. 1. Schematic illustration of the experiment at BL8B1.

The experiments have been performed at BL8B1. Schematic illustration is shown in fig. 1. Light incident to the sample was linearly polarized using the transmission polarizer between the post-focusing mirror and the sample chamber. The polarizer was a free-standing Al/YB$_6$ multilayer [4]. Three samples can be loaded on the sample holder at the same time. Samples are exchanged by linear motion of the sample holder. We will report the experimental results on four Ni samples in this paper. All samples were deposited on a collodion film supported with a copper mesh. The transmittance of the whole substrate (collodion and mesh) was about 35% in the spectral region of the present measurements. Samples #1 and #2 were made by magnetron sputtering to be 315 Å thick. Samples #3 and #4 were made by an evaporator of a BN composite boat and their thicknesses were 295 Å and 170 Å, respectively. Sample #4 was coated over in situ with a 330 Å thick aluminum by another evaporator to prevent surface pollution. Measurements were done at room temperature. The sample was magnetized in the Faraday configuration, in a magnetic field of 0.82 T generated by a magnetic circuit made of Sm-Co permanent magnet. The applied magnetic field of 0.82 T is stronger than the saturation magnetization of Ni (0.61 T at room temperature), though it is not obvious that the magnetization perpendicular to the film plane should be saturated. Rotation of polarization plane due to the magnetized sample was detected by rotating analyzer ellipsometry [5,6]. The analyzer was an Al/YB$_6$ reflection multilayer fabricated simultaneously with the transmission polarizer. When the the azimuthal angle of the analyzer ϕ_A is rotated, the detector's output changes in the form of $1 + P_L \cos 2(\phi_A - \Phi_0)$, where P_L and Φ_0 are the degree of linear polarization and the azimuth of polarization ellipse, respectively.

We measured the degree of linear polarization P_L of the light out of the monochromator first, because P_L was expected to be lower than unity owing to non-ideal alignment of the beamline optics [6]. The transmission polarizer was set at normal incidence and thus measured P_L was 0.80 at 65 eV. By adjusting the angle of incidence of the polarizer (41.5° at 65 eV), P_L was improved to 0.98. The polarizance of the transmission polarizer was evaluated to be 0.8 from the fact that P_L increased from 0.80 to 0.98. Then we introduced the magnetized Ni samples in the optical path and measured the shift of the azimuth of polarization ellipse which corresponds to the Faraday rotation angle.

In fig. 2, measured Faraday rotation angles for samples #1, #2, #3 and #4 are plotted by closed circles, open circles, squares and triangles, respectively, against the photon energy. The sign of Faraday rotation angle is defined in regard to the direction of magnetic field. It seems that the rotation angles per sample thickness were constant, which implies that samples do not suffer surface pollution and reflect bulk properties well. The thick line in fig. 2 means Faraday rotation spectrum for the sample thickness of 315 Å obtained by K-K transform of the MCD spectrum [1]. The MCD spectrum had been measured at BL-28A, Photon Factory using a helical undulator of which peak photon energy was 70 eV. The sample temperature was 140K and the applied magnetic field was 1.05 T. The absorption was measured by the TY method in arbitrary unit and was re-scaled into the unit of absorption coefficient (cm^{-1}) according to the published optical constants [7]. In the numerical calculation of K-K transform, the energy integral was carried out with limits of 40 eV and 90 eV practically. Since magnetization of Ni sample at 140K is considered to be larger than that at room temperature, this calculated value should be larger than the present experimental value. As seen in comparison of the calculated rotation angle with the measured ones, #1 and #2, however, the absolute value obtained by K-K analysis was almost the same as or smaller than those of the present measurement. Therefore it was found that the previous MCD experiment [1] has given smaller value than that of intrinsic one. At present, it is not clear that this is due to the surface pollution or the insufficiency of the degree of circular polarization. Anyway, the careful estimation of the degree of circular polarization of incident light [8] have been necessary in the MCD measurements. Our experiment shows that absolute values of measured MCD data can be easily corrected by Faraday rotation measurements.

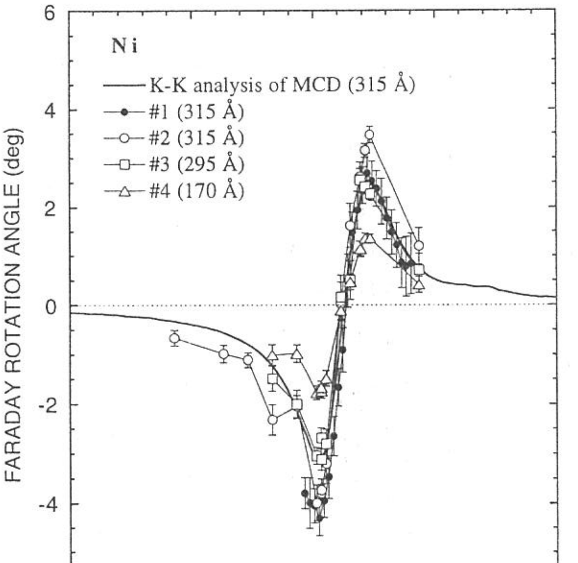

FIG. 2. Spectra of Faraday rotation angle measured at the present experiments and obtained by Kramers-Kröni g transform of an MCD spectrum [1].

References

[1] T. Hatano, S. Y. Park, T. Hanyu and T. Miyahara, J. Electron Spectrosc. Relat. Phenom. **78**, 217 (1996).

[2] S. Muto, Y. Kagoshima and T. Miyahara, Rev. Sci. Instrum. **63**, 1470 (1992).

[3] J. B. Kortright, M. Rice and R. Carr, Phys. Rev. B **51**, 10240 (1995).

[4] W. Hu, T. Hatano, M. Yamamoto and M. Watanabe, J. Synch. Rad. **5**, 732 (1998).

[5] T. Hatano, W. Hu, M. Yamamoto and M. Watanabe, J. Electron Spectrosc. Relat. Phenom. **92**, 311 (1998).

[6] T. Hatano, W. Hu, M. Yamamoto and M. Watanabe, UVSOR Activity Report 1997, 64 (1998).

[7] E. D. Palik (Ed.), Handbook of Optical Constants of Solids, Academic Press Inc., 1985.

[8] T. Koide, T. Shidara, T. Miyahara and M. Yuri, Rev. Sci. Instrum. **66**, 1923 (1995).

(BL8B1)

Polarization-Dependent Nitrogen *K*-edge Absorption of InGaN

Kazutoshi FUKUI, Ryousuke HIRAI and Akio YAMAMOTO
Faculty of Engineering, Fukui University, Fukui 910-8507, Japan
Fax +81-776-27-8749, fukui@fuee.fukui-u.ac.jp

The soft X-ray absorption (SXA) around nitrogen *K*-edge have been measured to investigate the electronic structure of the wurzite III – V nitrides, especially the structure of the unoccupied states. The N *K* absorption spectra of III – V nitrides near the N *K*-edge in principle represent the partial density of the final states with *p* symmetry according to the selection rule. Since the core levels are strictly localized in space, the N *K* absorption spectrum gives us the site-specific information. The N *K* absorption spectrum also gives us the information about the final states symmetry p_{xy} and p_z, because the incidence soft X-ray light is linearly polarized.

The experiments were carried out at BL8B1. Resolution power under the experimental conditions were about 0.5 eV at 400 eV. The soft X-ray absorption measurement was performed by using the total photoelectron yield (TY) method. Thin films were made by the MOCVD method at RIKEN on SiC substrates, at Fukui University on GaAs(111) surface and at Nichia Chemical on α-Al_2O_3 substrate. All films were cleaned with organic solvents just before the installation in the vacuum chamber. No specific surface cleaning of the samples was performed in the vacuum chamber. The TY measurements were carried out at room temperature in the range of 10^{-9} Torr. Sample holder was able to rotate in the vacuum chamber for the angular dependent measurement. The incidence angle θ is defined as the angle between the incident light and the normal axis of the sample surface, i.e., c-axis. The incidence angle dependent SXA measurements were performed under the *p*-polarization configuration which means **E** parallel to *c*-axis at $\theta \sim 90^\circ$, where **E** was the electric field of the incident light.

Figure 1 shows the N *K* absorption spectra of $In_{1-x}Ga_xN$. The energy scale is relative to the threshold energy which corresponds to the conduction band minimum. The labels A to G are corresponding to those for GaN in Ref. 1. The intensity of each spectrum is normalized at the peak B. The spectra features of GaN and InN are good agreement with the

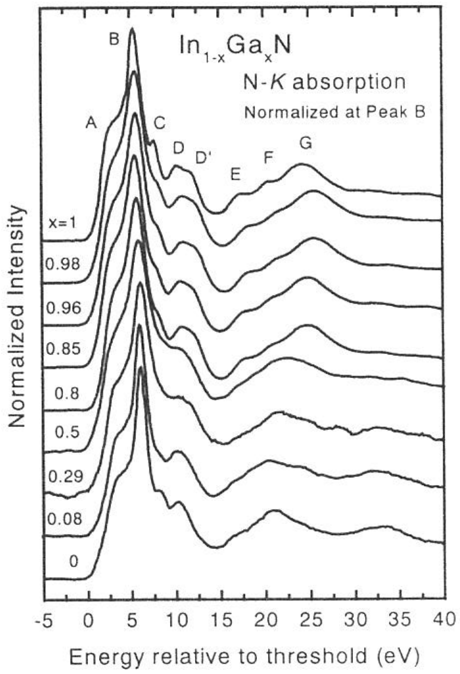

Fig.1 N K absorption spectra of InGaN. The energy scale is relative to the threshold energy.

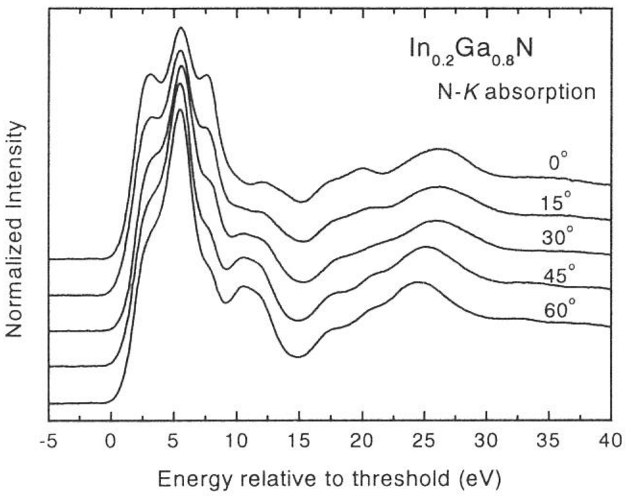

Fig. 2 N K absorption spectra of $In_{0.2}Ga_{0.8}N$ as function of angle which is defined as the angles between the incident light and the normal to the sample surface (c-axis).

previous works [1-3]. All spectra seem to be explained by the same labeling. It is suggested that the electric structures of the unoccupied states around nitrogen for III – V nitrides basically consist of the similar components. Figure 2 shows the N K absorption of $In_{0.2}Ga_{0.8}N$ as function of angle θ. All spectra are normalized at 34.5 eV. These types of angular dependence can be seen in all the samples. Each spectrum has angular dependent part and independent part, so that a numerical component analysis to separate the experimental spectrum into angular dependent and independent spectra has been performed under three assumptions as mentioned in Ref. 4. Figure 3 shows the partial spectra decomposed numerically from $In_{0.2}Ga_{0.8}N$ N K absorption spectra (Fig. 2). The three spectra labeled XY, Z and N correspond to p_{xy} , p_z, and angular independent components of the unoccupied p partial density of states around N-site, respectively. The spectrum labeled D represent the summation of the square residual error over whole spectra shown in Fig.2. The spectrum labeled M shows the calculated N K absorption spectrum at $\theta = 35.26°$. In case of hexagonal sample, the spectrum at this angle (Magic angle) loses its anisotropic information which means that it is easy to compare experimental results with calculated partial density of states.

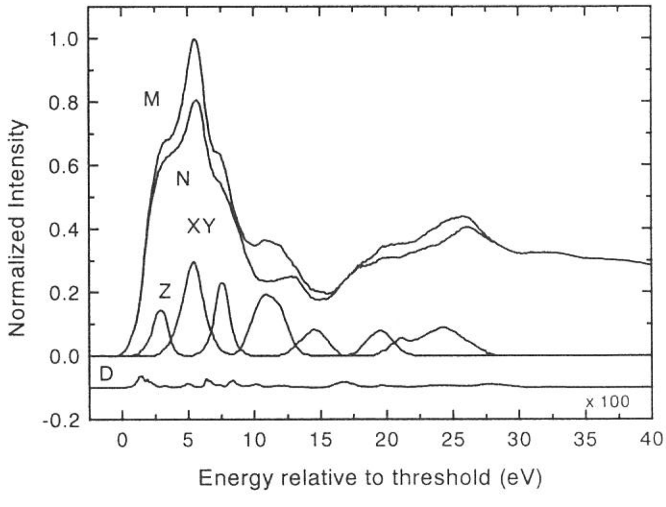

Fig. 3. Partial spectra decomposed numerically from N K absorption spectra of $In_{0.2}Ga_{0.8}N$. Three spectra labeled XY, Z and N correspond to in-plane, out-of-plane and angular independent components of the unoccupied p partial density of states at N-site, respectively. The spectra labeled M and D represent calculated K absorption spectrum at $\theta = 35.26°$ and the summation of the square residual error over whole spectra in Fig.2, respectively.

References

[1] W. R. L. Lambrecht, S. N. Rashkeev, B. Segall, K. Lawniczak-Jablonska, T. Suski, E. M. Gullikson, H. H. Underwood, R. C. C. Perera, J. C. Rife, I. Grzegory, S. Porowski and D. K. Wickenden, Phys. Rev. B **55** (1997) 2612.

[2] C. B. Stagarescu, L. -C. Duda, K. E. Smith, J. H. Guo, J. Nordgren, R. Singh and T. D. Moustakas, Phys. Rev. B **54** (1996) R17335.

[3] K. Fukui, M. Ichikawa, A. Yamamoto and M. Kamada, Solid State Electronics **41** (1997) 299.

[4] K. Fukui, R. Hirai and A. Yamamoto, UVSOR Activity Report 1997, 1998 p.184

(BL-8B1)

Measurement of Quantum Efficiency of the CCD Camera System

Atsuhiko Hirai[1], Kuniko Takemoto[2], Yasuyuki Nakayama[1] and Hiroshi Kihara[2]

[1] *Department of Physics, Ritsumeikan University, Kusatsu, Shiga 525-8577*
[2] *Physics Laboratory, Kansai Medical University, Hirakata 573-1136*

It has been realized that thinned back-illuminated CCD cameras without anti-reflective coatings are suitable as a detector of x-ray microscopy at water wavelength region [1, 2]. Since 1996, we have also been using a back-illuminated CCD (SiTe Ltd., SI502A) in our x-ray microscopy station [3], of which performance was measured as well as another type of CCD (EEV Ltd.) last year at UVSOR [4]. Contrary to our expectation, two CCD's show big difference in their quantum efficiency; the CCD of EEV showed quantum efficiency more than 20% from 1 to 10nm, whereas the other CCD of SiTe showed strong dependence on the wavelength and the quantum efficiency was less than 10% above 2nm. It was ascribed to the anti-reflective coating which should not be but was put accidentally. We, then, exchanged the CCD of SiTe to the new one without anti-reflective coating, and repeated the measurement of quantum efficiency of the SiTe CCD.

The CCD camera system consists of a CCD chip without the anti-reflective coating (SiTe Ltd., SI502-NAR), Astrocam CCD camera 4200 (liquid nitrogen cooling) and personal computer for camera controlling and data acquisition. The measurement system and the calculation system were basically the same with the last experiment with several improvements described below [4]. The scheme of the experimental arrangement is shown in Fig. 1. It consists of an aperture (6mm × 18mm), an Al attenuater (thickness, 2μm), a silicon photodiode (IRD AXUV-100) and the CCD camera system. In order to improve accuracy of the measurement, the number of incident photons were limited with the aperture and the attenuater. In the previous experiment, the absolute number of photons was measured by a drain current of an Au mesh, and was calibrated by the silicon diode (number of photons are counted by $n = h \cdot v/3.67$ eV) [4]. However, the drain current was a little too small to be measured with good accuracy. In the present experiment, then, the absolute number of photons was measured by the silicon diode directly. The number of detected photoelectrons was estimated from the CCD image [4].

The quantum efficiency of the CCD camera system thus estimated is shown in Fig. 2. The quantum efficiency decreases gradually with the increase of the wavelength. In water window region, the quantum efficiency shows a little higher than 20%. This result shows a quite similar tendency to the quantum efficiency of CCD (EEV Ltd.) [4].

There have been reports with quite different results. Aritome and his coworkers reported the quantum efficiency of CCD (EEV Ltd.) was c.a. 10% in water window region [5]; Wilhelm et al.

reported the quantum efficiency of CCD (SiTe Ltd.) was c.a. 55% in water window region [6]. It is not certain why the quantum efficiency are so different among the reports, but at least we can say the quantum efficiency of CCD would not depend on the fabrication company so much, as our measurements on CCD's of SiTe and EEV show similar results.

Acknowledgment

The authors are grateful for the help and encouragements from Prof. T. Kinoshita, Dr. T. Gejoh and other staffs of the Institute for Molecular Science.

References

[1] B. Niemann et al., X-ray Microscopy IV, eds. A. G. Michette et al. (Springer-Verlag, Berlin), 66 (1995).
[2] W. Meyer-Ilse et al., Synch. Rad. News 8, No.3 29 (1995).
[3] A. Hirai et al., UVSOR Activity Report 1995, 230 (1996).
[4] A. Hirai et al., UVSOR Activity Report 1996, 240 (1997).
[5] H. Aritome et al., SPIE 1741, 276 (1992).
[6] T. Wilhein et al., X-ray Microscopy IV, eds. A. G. Michette et al. (Springer-Verlag, Berlin), 470 (1995).

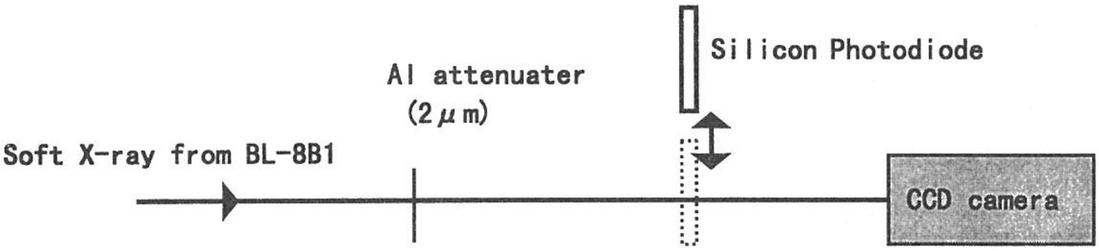

Fig. 1. Experimental setup arrangement.

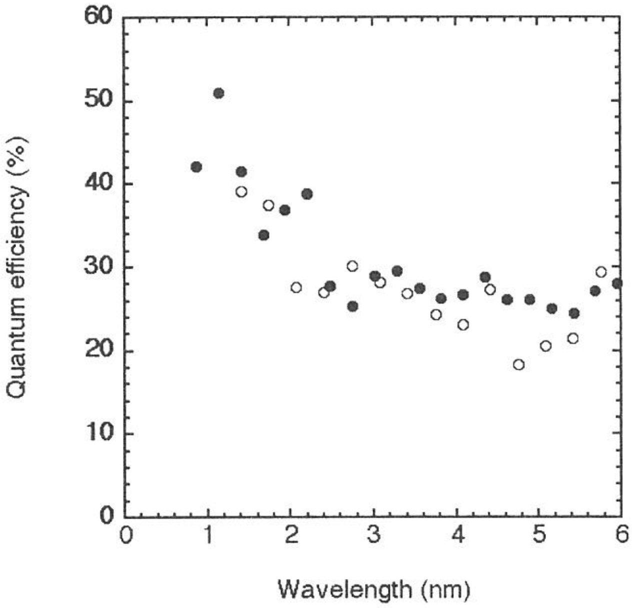

Fig. 2. Quantum efficiency of CCD camera system. ● is SITe CCD, and ○ is EEV CCD [4].

(BL8B1)

Oxidation States in $LiMn_2O_4$ Spinel Oxides from Transition Metal *L*-edge Spectroscopy

Yoshiharu UCHIMOTO, Takeshi YAO, Dan ISHIZAKI, and Taiji SASADA
Department of Fundamental Energy Science,
Graduate School of Energy Science, Kyoto University,
Yoshida, Sakyo-ku, Kyoto 606-8501, JAPAN

$LiMn_2O_4$ based spinel type oxides are one of the most promising cathode materials used in lithium ion batteries because their low cost, high theoretical energy density. In order to improve their cycle performance, several research groups have investigated the properties of manganese-substituted spinels of $LiM_yMn_{2-y}O_4$ (M=Cr, Ni, Co, etc.). These spinels show a decreased capacity on the 4.1 V plateau, however improved cycle life was reported for Co, Ni, and Cr doped spinels. Furthermore, recently Co, Ni, Cr, and Cu doped spinels show reversible redox processes at potentials above 4.5 V. (1, 2) It is important to clarify the structural change, valency change during charge and discharge process in order to understand their electrochemical properties. In the present study, transition metal doped spinels ($LiNi_yMn_{2-y}O_4$) were prepared. X-ray diffraction (XRD), X-ray Absorption Fine Structure (XAFS), and electrochemical studies were carried out. Especially, oxidation state of the transition metals in the $LiM_yMn_{2-y}O_4$ spinels were determined by using a measurement of Mn L_{23}-edge, Ni L_{23}-edge, and Oxygen K-edge X-ray Absorption Near Edge Structure (XANES). The Rietveld calculation was performed on the vector processor (Cray Y-MP2E/264) at the Institute for Chemical Research, Kyoto University, by using 'Rievec' computer program (3.4)

$LiNi_yMn_{2-y}O_4$ spinels were prepared from $LiNO_3$, $Mn(NO_3)_2$-$6H_2O$, $Ni(NO_3)_2$-$6H_2O$. The crystal structure of the product was determined by XRD using CuKα radiation. XRD pattern of $LiNi_{0.4}Mn_{1.6}O_4$ was indexed to an cubic lattice. The lattice parameters and other structural parameters were refined by the Rietveld method. Fig. 1 shows the results of the Rietveld analysis. The observed pattern agreed well with the calculated pattern. The obtained lattice parameters are given in Table 1. R_{wp}, R_F, and R_B are small enough to guarantee the reliability, and it was confirmed that $LiNi_{0.4}Mn_{1.6}O_4$ belonging to cubic *Fd3m* space group.

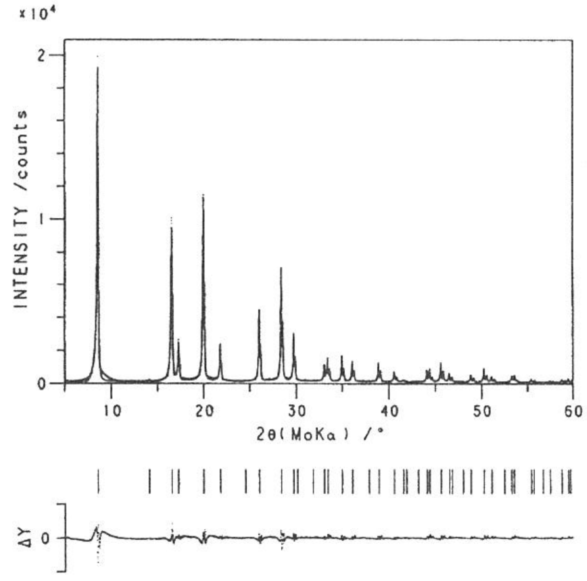

Fig.1 The observed (dot) and calculated (line) XRD patterns of $LiNi_{0.4}Mn_{1.6}O_4$. The difference between observed and calculated profiles is plotted below.

Table 1. Refined lattice parameters for $LiNi_{0.4}Mn_{1.6}O_4$

Cubic Spinel				
Space group : Fd3m				
Atom	site	x	y	z
Li	8a	0	0	0
Mn	16d	0.625	0.625	0.625
Ni	16d	0.625	0.625	0.625
O	32e	0.3875(1)	0.3875(1)	0.3875(1)

a = 8.17941(3) Å
R_{wp},R_F,R_B = 0.0837,0.0344,0.0321

Figure 2 shows a low rate discharge curve of $LiNi_{0.4}Mn_{1.6}O_4$. The $LiNi_{0.4}Mn_{1.6}O_4$ shows mainly 2 different plateau regions. Between capacity = 0 to -30 mAh g^{-1} (the first plateau), the discharge voltage was of 3.5 to 4.5 V and then the charging curve has a plateau of about 4.7 V. XANES analysis were performed to clarify the oxidation state of manganese and nickel for various x values in $Li_xNi_{0.4}Mn_{1.6}O_4$.

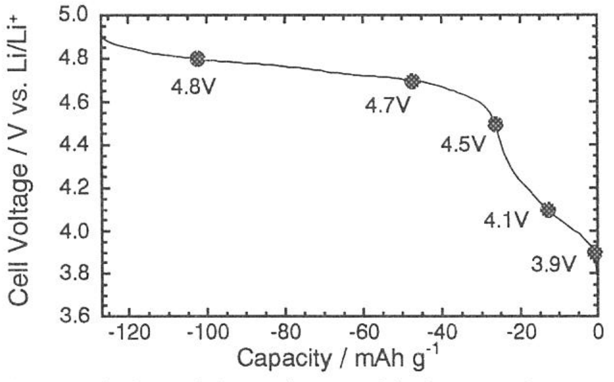

Fig. 2 Variations of electrode potential with capacity upon first charging of $LiNi_{0.4}Mn_{1.6}O_4$

Fig. 3 shows the Mn *L*-edge XANES of $LiNi_{0.4}Mn_{1.6}O_4$ at various potentials together with

MnO_2 (Mn^{4+}) and Mn_2O_3 (Mn^{3+}). The spectra correspond to $Mn2p^63d^n$ to $Mn2p^53d^{n+1}$ transitions. This figure shows that the Mn L_3 absorption edge of Mn_2O_3 was about 642.0 eV and that of MnO_2 was 643.4 eV. These results indicate that increasing the oxidation state of manganese, the Mn L_3 absorption edge shifted to higher energy. As shown in Fig. 3, the peak of $LiNi_{0.4}Mn_{1.6}O_4$ was a combination of peak of Mn_2O_3 and MnO_2. At low x value of $Li_xNi_{0.4}Mn_{1.6}O_4$ during the first plateau, contribution of Mn^{4+} increased. However, at the second plateau, the oxidation stage of Mn was 4+ and did not change.

Fig. 4 shows the Ni *L*-edge XANES of $LiNi_{0.4}Mn_{1.6}O_4$ at various potentials. The XANES spectra of $LiNi_{0.4}Mn_{1.6}O_4$ was in good agreement to that of NiO and did not change during the first plateau. At the second plateau, peaks at about 854.4 eV increased with increasing lithium deintercalation, however, the changes of the XANES spectra were very small. Fig. 6 shows O *K*-edge XANES of $Li_xNi_{0.4}Mn_{1.6}O_4$ at various potentials or x-values. The O *K*-edge XANES spectra of $LiNi_{0.4}Mn_{1.6}O_4$ did not change during the first plateau. At the second plateau, peak increased with increasing lithium deintercalation. This results shows that oxidations found to take place on oxygen 2p orbital. These results show that $LiNi_{0.4}Mn_{1.6}O_4$ was a charge transfer insulator and that oxidations found to take place not on nickel but on oxygen 2p orbital mainly.

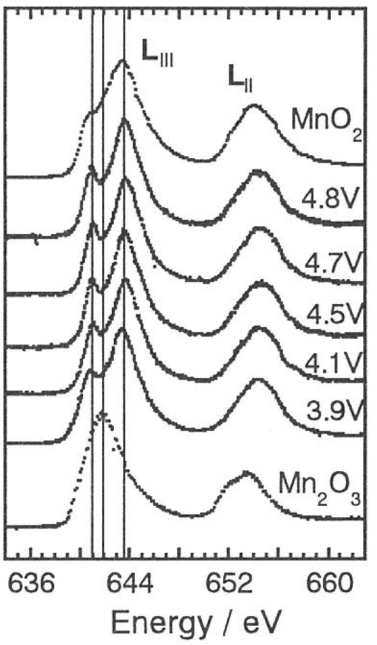

Fig. 3 Mn L-edge XANES of $LiNi_{0.4}Mn_{1.6}O_4$ at various potentials.

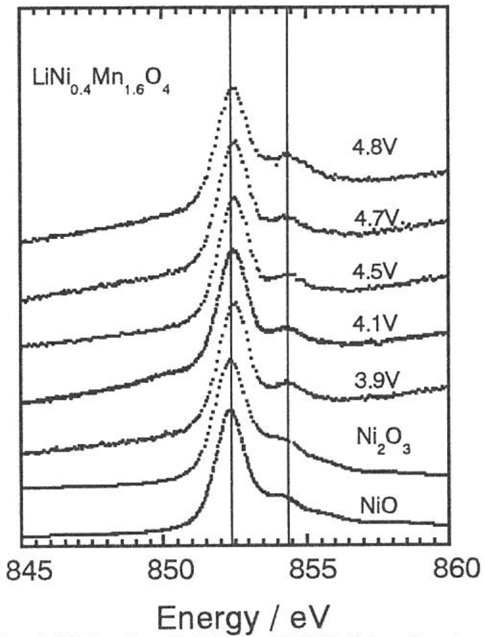

Fig. 4 Ni L-edge XANES of $LiNi_{0.4}Mn_{1.6}O_4$ at various potentials.

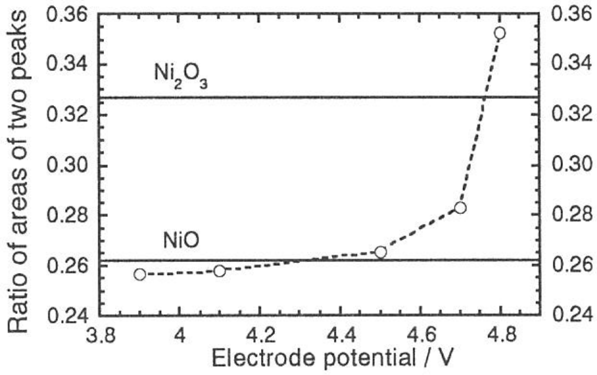

Fig. 5 Variations of peak ratio with electrode potential.

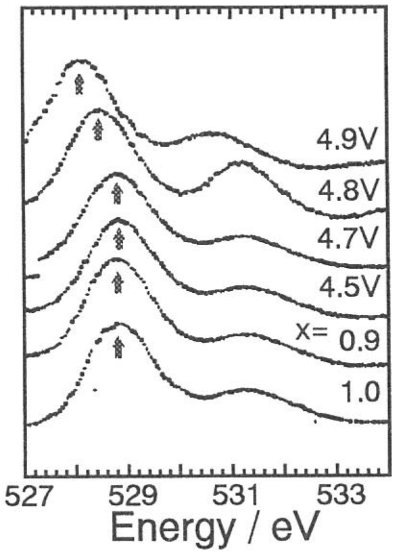

Fig. 6 O *K*-edge XANES of $Li_xNi_{0.4}Mn_{1.6}O_4$ at various potentials or x-values.

In conclusion, the average manganese valence in $LiNi_{0.4}Mn_{1.6}O_4$ was between 3 and 4 and the valence was increase during the electrochemical extraction of lithium at the first plateau. At the second plateau, manganese ions did not contribute to the oxidation reaction but the oxidations took place not on nickel but on oxygen 2p orbital mainly.

REFERENCES

1)Q. Zhong, A. Bonakdarpour, M. Zhang, Y. Gao, and J.R. Dahn, *J. Electrochem. Soc.*, **144**, 205 (1997).

2) Y. Todorov, C. Wang, and M. Yoshio, *Extended Abstract of 1997 ECS-ISE Joint Meeting*, **Vol. 97-2**, p. 94 (1997).

3) T. Yao, Y. Oka, and N. Yamamoto, *J. Mater. Chem.*, **32**, 331 (1992).

4) T. Yao, T. Ito, and T. Kokubo, *J. Materials Research*, **10**, 1079 (1995).

(BL8B1)

N and O *K* Shell Excitations of 5-Oxohexanenitrile

Toshio IBUKI
Kyoto University of Education, Fukakusa, Fushimi-ku, Kyoto 612-8522
Kazumasa OKADA and Ko SAITO
Department of Chemistry, University of Hiroshima, Higashi-Hiroshima 739-8526
Tatsuo GEJO
Institute for Molecular Science, Myodaiji, Okazaki 444-8585

It has been of great interest to control chemical bond fission of a free polyatomic molecule through a site selective core excitation followed by an Auger *KVV* process. In 1983 the C^+ and O^+ fragment ions were characteristically enhanced in the carbon *K* shell excited CH_3COCH_3.[1)] However, little evidence has been provided for the site or state selectivity of a core excited free molecule. In this study we observed a typical site dependent photofragmentation occurring in the N and O *K* shell excitations of 5-oxohexanenitrile, $CH_3COCH_2CH_2CH_2CN$, in which five carbon atoms separate the interesting N and O atoms.

The experiments have been performed at the BL8B1 soft x-ray beamline. The energy scale was calibrated using the major soft x-ray peaks appeared in the total ion yield spectra of N_2 and O_2.[2)] The total photoelectron-photoion coincidence spectra were acquired by using a reflectron type time-of-flight (R-TOF) mass spectrometer. The axis of the spectrometer was made at a magic angle with respect to the linearly polarized electric vector of the primary synchrotron radiation.

The total photoabsorption cross sections are shown in fig. 1a for the N and O *K* edge regions. The sharp peaks at 400.7 and 531.5 eV are assigned as the $\pi^*_{C\equiv N} \leftarrow$ N(1s) and $\pi^*_{C=O} \leftarrow$O(1s) excitations, respectively. The ionization potentials for $N(1s)^{-1}$ and $O(1s)^{-1}$ have not been reported so far as we know, and estimated to be ≈406 and ≈540 eV, respectively, from the analogs.

The R-TOF mass spectra are shown in figs. 1b and 1c for the $\pi^*_{C\equiv N} \leftarrow$N(1s) and $\pi^*_{C=O} \leftarrow$ O(1s) excitations, respectively. The fragment ions larger than m/e=60 were negligible. The most abundant fragment ion is N^+ generated by the strongest C≡N bond fission at the N *K* shell excitation, while it is CH_3CO^+ at the O *K* edge. That is, the photofragmentation basically occurs at the strongly limited area excited initially as has been expected. The second strongest CO^+ fragment formation in the N *K* edge, however, suggests a unique Auger process would dominantly take place. The HOMOs of $\pi_{C\equiv N}$ of 5-oxohexanenitrile are followed by the closely lying $\pi_{C=O}$ molecular orbitals (MOs). Thus, the electrons lying in the $\pi_{C=O}$ and $\pi_{C\equiv N}$ MOs may be released as the Auger electrons to generate CO^+ and N^+

fragment ions. The Auger electron-photoion coincidence measurement is required to get more detailed information. It is noteworthy to point out that intramolecular H atom migration is very fast since the H_2O^+ molecular ion is observed in both the R-TOF mass spectra excited at the N and O *K* shell.

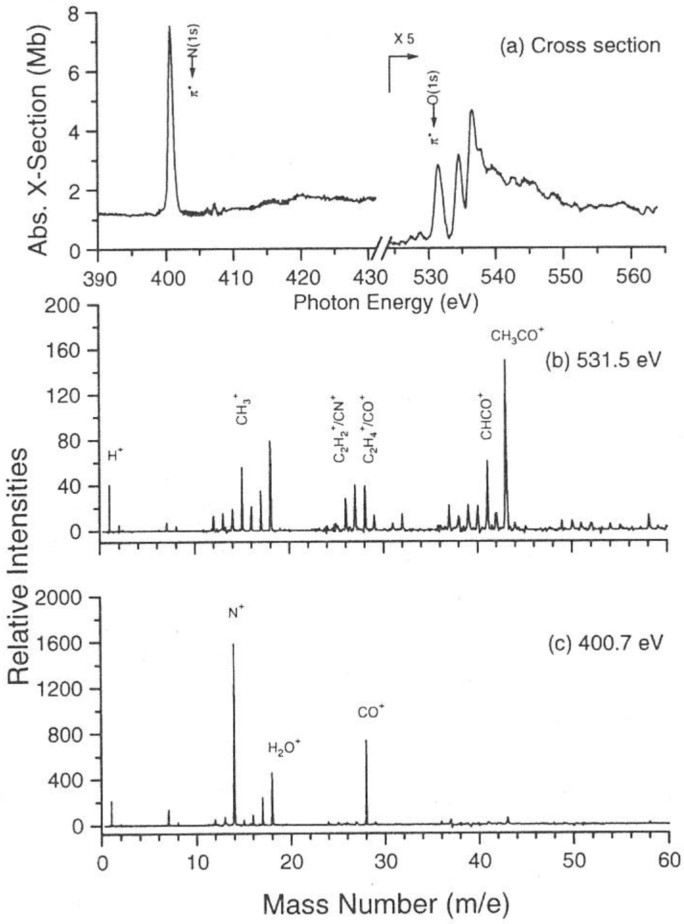

Fig. 1 Photoabsorption cross sections and R-TOF mass spectra at N and O *K* edges.
(a) Photoabsorption cross section, (b) $\pi^*\leftarrow$O(1s), and (c) $\pi^*\leftarrow$N(1s).

References

1) W. Eberhardt, T. K. Sham, R. Carr, S. Krummacher, M. Strongin, S. L. Weng, and D. Wesner, Phys. Rev. Lett. **50**, 1038 (1983).

2) K. Lee, D. Y. Kim, C. I. Ma, D. A. Lapiano-Smith, and D. M. Hanson, J. Chem. Phys. **93**, 7936 (1990).

(BL8B2) Photoelectron spectra of metallofullerene, Sc@C$_{82}$

Shojun Hino[a,b], Kazunori Umishita[a,b] Kentaro Iwasaki[a], Takayuki Miyamae[b,c],
Masayasu Inakuma[d] and Hisanori Shinohara[d]
[a] *Faculty of Engineering, Chiba University, Inage-ku, Chiba 263-8522 Japan*
[b] *Graduate School of Science and Technology, Chiba University, Inage-ku, Chiba 263-8522 Japan*
[c] *Institute for Molecular Science, Myoudaiji, Okazaki, Japan 444-8585*
[d] *Faculty of Science, Nagoya University, Chikusa-ku, Nagoya 464-8602 Japan*

Metallofullerenes have attracted a lot of attentions such as their structures including the position of the metal atom(s), their electronic structures as well as the amounts of transferred electrons from the metal atom(s) to the cage, their reactivity and so on. Photoelectron spectroscopy is a powerful tool to clarify their electronic structures. In this article, our recent results of the photoelectron spectroscopy on metallofullerene, Sc@C$_{82}$ are presented and its electronic structures are discussed.

Figure 1 shows the incident photon energy dependence of the UPS of the Sc@C$_{82}$ sublimed film. A clear intensity variation is observed in the UPS of Sc@C$_{82}$ as reported on other fullerenes [1-5]. Particularly, structures A and B vary their intensity drastically with the incident photon energy. Their intensities in the $h\nu = 20$ and 40 eV spectra are nearly equal, but in other spectra structure B is about one and half times more intense than A. A similar energy dependence is observed in the UPS of C$_{82}$ [2] and La@C$_{82}$ [1]. A close inspection reveals that structure N also changes its intensity as other structures.

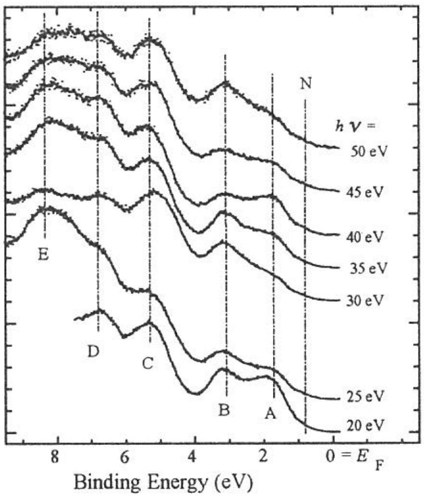

Fig. 1 The UPS of Sc@C$_{82}$

Figure 2 shows the UPS of Sc@C$_{82}$ and La@C$_{82}$ with that of empty fullerene C$_{82}$ obtained with 40 eV photon that gives the spectra having clear peak structures. These spectra look analogous; each of structures A – E have almost the same intensity and show one-to-one correspondence as indicated by chain lines. While significant shifts are observed in the energy positions of structures A and E, structures B – D have nearly identical binding energies. The shift of structure E may be due to a difference in the geometry of these fullerenes; C$_2$ for C$_{82}$ and C$_{2v}$ for these metallofullerenes. The troughs between the structures, such as those at about 4 and 6 eV, in the spectra of metallofullerenes are shallower than their counterparts in C$_{82}$. This may also be due to a difference in the geometry or to a change in the electronic structure caused by encapsulation of the metal atom to the cage.

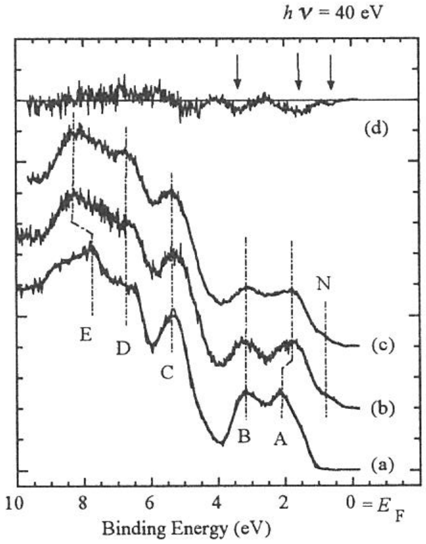

Fig. 2 The UPS of empty C$_{82}$ (a), La@C$_{82}$ (b) and Sc@C$_{82}$ (c) with difference spectrum (d) between (b) and (c).

The difference spectra obtained by subtraction of the 20 eV spectrum of empty C82 from those of metallofullerenes are shown in Fig. 3. There is a widely spread band between the E$_F$ and 2.2 eV (upper valence band region) in both spectra. There is no significant structure between 2.2 and 3.5 eV. Another evident band appears from 3.5 eV and deeper. This wide band is partly contributed from structure N that is not observed in the spectra of C_{82} and partly from the intensity difference in structure A. This band is considered to be due to the electrons transferred from the metal atom, since electrons from the Sc and La are expected to fill the LUMO of C_{82} and upwards. The band located beyond 3.5 eV is probably due to the intrinsic difference in the electronic structures of metallofullerenes and empty fullerene.

The peak area of the wide band in the Sc@C_{82} − C_{82} difference spectrum is smaller than that in La@C_{82} − C_{82}, and their ratio is about 2 : 3. This suggests that the amount of transferred electrons in Sc@C_{82} is about two thirds of that in La@C_{82}. Namely, two and three electrons are transferred from Sc and La to C_{82}, respectively. This is noteworthy, since both scandium and lanthanum are trivalent elements and their + 3 oxidation state is expected as the most stable one.

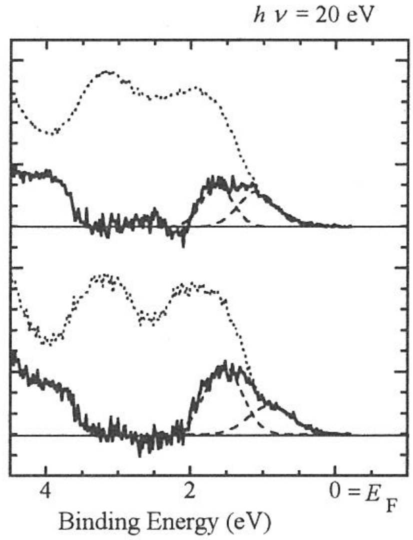

Fig. 3 Difference spectra Sc@C_{82} − C_{82} (upper) and La@C_{82} − C_{82} (lower).

References

1. S. Hino *et al.*, Phys. Rev. Letters 71, (1993) 4261.
2. S. Hino *et al.*, Phys. Rev. B 48, (1993) 8418.
3. J. H. Weaver *et al.*, Phys. Rev. Letters 66, (1991) 1741.
4. S. Hino *et al.*, Chem. Phys. Letters 190, (1992) 169.
5. S. Hino *et al.*, Phys. Rev. B 53, (1996) 7496.

(BL8B2)

Origin of the photoemission intensity oscillation of C_{60}

Shinji Hasegawa, Takayuki Miyamae, Kyuya Yakushi, Hiroo Inokuchi, Kazuhiko Seki[a], Nobuo Ueno[b]
Institute for Molecular Science, Myodaiji, Okazaki 444-8585, Japan
[a]*Department of Chemistry, Faculty of Science, Nagoya University, Nagoya 464-8602, Japan*
[b]*Department of Materials Science, Faculty of Engineering, Chiba University, Inage-ku Chiba 263-8522*

The photoemission intensities of the highest occupied molecular orbital (HOMO) and the next-HOMO (NHOMO) states for thin films, single crystals and gas phase of C_{60} exhibit remarkable oscillations with the incident photon energy in the range of hν= 10 – 120eV [1], and much attention has been paid to the phenomenon. From theoretical points of view, Xu *et al.* first reported two simple models to explain these oscillations [2]. They approximated the initial and final state wave functions with the radial and angular parts in the spherically symmetric potential of C_{60}, and calculated the energy positions of the cross section minima by using one of the allowed states ($l_f = l_i - 1$). They concluded that the oscillations originate from a specific ability of C_{60} to form a spherical standing wave of the final state by the interference inside the molecule. As mentioned by themselves, however, more detailed and quantitative studies are required to confirm the origin of the oscillations.

We measured the angle-resolved ultraviolet photoelectron spectra (ARUPS) of C_{60} thin films in the photon energy range of hν= 18 – 110 eV, and calculated the hν dependences of the differential photoionization cross sections by changing the degree of approximation for the final and initial states [3]. First we carried out the numerical calculations by the single-scattering approximation for the final state with the *ab-initio* molecular orbital (MO) calculation for the initial state, where the angular parameters for the incident light and the photoelectron momentum were identical with the experimental conditions. It is noted that such quantitative calculations considering the scattering effects, to our knowledge, have not been reported yet for C_{60}. Next we simplified only the final state, and calculated the photoionization cross sections by using the plane-wave final state. In Fig.1, the measured and calculated hν dependences of the intensity ratio, HOMO/NHOMO, are shown. Both calculated curves are based on the interference of photoelectron waves, since they are made up of a sum of the individual photoelectron wave from each atomic site with its phase difference. Therefore, the agreement between the calculated and measured results in Fig.1 suggests that the oscillation originates from the interference of photoelectron waves emanating from each atom constituting the C_{60} molecule, *i.e.*, the multi-centered photoemission from the MO state. Further, it should be noted that the calculated result by the simplest plane-wave approximation for the final state exhibits the similar oscillation as the measured one. This points out that the oscillation itself is independent of the accuracy of the final state. It should be ruled by a specific character of the initial state due to the molecular geometry of C_{60}.

In order to clarify this point, we approximated the MO initial state by a spherical-shell like state, and derived a simple formula for the differential photoionization cross section as [3],

$$d\sigma_n^{pw}(\mathbf{k}_n)/d\hat{\mathbf{r}} \quad \propto \quad \frac{h\nu}{k_n}\{\int \cos(k_n r + \alpha_{l_i} - \frac{l_i}{2}\pi)\Theta(r)r^2 dr\}^2. \tag{1}$$

To evaluate the eq.(1) by a simple analytical calculation, we approximate the radial part of initial state $\Theta(r)$ by step functions as,

$$\Theta(r) = \begin{cases} -\xi & \mathrm{R}_s - \Delta \le r \le \mathrm{R}_s \\ \xi & \mathrm{R}_s \le r \le \mathrm{R}_s + \Delta. \end{cases} \tag{2}$$

R_s and Δ stand for the radius of the node in the spherical shell and the half width of the shell, respectively. Consequently, the integral in eq.(1) is easily solved and the differential photoionization cross section at a given photon energy hν can be calculated. In Fig.2, the calculated hν dependences of the photoionization cross section for the HOMO and NHOMO states are plotted with E_k. The solid curves are the results by the spherical-shell like initial state and the plane-wave final state, where we used the parameters $R_s = 3.26$Å, $\Delta = 0.5$Å. The values are reasonable, since $R_s = 3.26$Å is close to 3.54Å of the radius of C_{60}, and $\Delta = 0.5$Å was referred to the average half thickness of the deep potential shell for carbon solids. The broken curves are the same results as shown in Fig.1 calculated by the STO-5G MO initial state and the single-scattering final state. Note that the broken curves represent the intensity oscillations for the HOMO and NHOMO states before deriving their ratio in Fig.1. In spite of the present rough approximations for the initial and final states, the simple calculations with eq.s(1) and (2) give the equal oscillations as obtained by the more sophisticated calculations in regard to the energy positions of maxima and minima for both states (Eq.(2) is too rough to discuss the exact photoemission intensities. This may be the reason for the intensity difference between the solid and broken curves.). It means that the simplest model contains an essential point for the oscillations, that is, the spherical-shell like initial state due to the specific structure of C_{60} dominates the oscillations.

In addition, the radius of the spherical shell is also important to observe the oscillations in the experimental hν range. We can roughly examine the eq.(1) for the following cases, (i) $\Theta(r)$ has a non zero value around $r = 3.5$Å and (ii) it has a non zero value around $r = 1.0$Å. The former is for the case of a large spherical-shell molecule like C_{60}, while the latter is for a smaller shell which may correspond to usual organic molecules. Since the oscillation derived by eq.(1) is due to the cosine term, $\cos(k_n \times 3.5 + const.)$ and $\cos(k_n \times 1.0 + const.)$ are picked out for the examination. In the experimental k_n range ($3 \sim 6$ Å^{-1}), the cosine term for $r = 3.5$Å decreases and increases across 0 and an oscillation will be observed in $d\sigma_n^{pw}(\mathbf{k}_n)/d\hat{\mathbf{r}}$. On the other hand, the cosine term for $r = 1.0$Å is hardly changed due to the longer period of the cosine term, and no oscillation will appear. Therefore, it is concluded that the essential factors for the oscillations are (1) the molecular structure of C_{60} like a spherical shell, and (2) the fairly large radius of the shell.

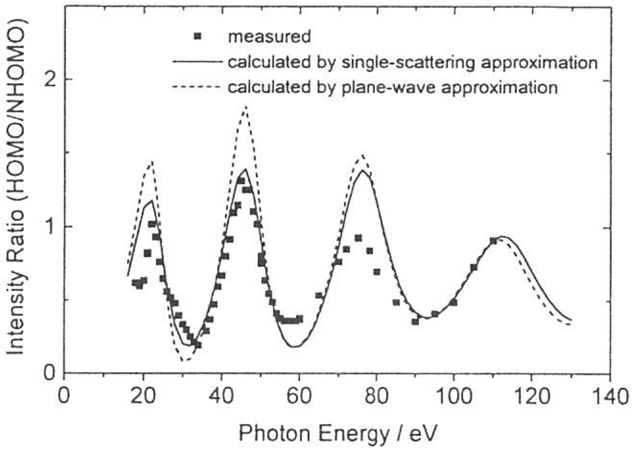

Figure 1 Photon energy hν dependences of photoemission intensity ratio of HOMO/NHOMO. The intensity oscillation of the measured results (solid squares) is in good agreement with the calculated curves. The solid line was calculated by the single-scattering approximation for the final state. The broken line was calculated by the plane-wave approximation for the final state.

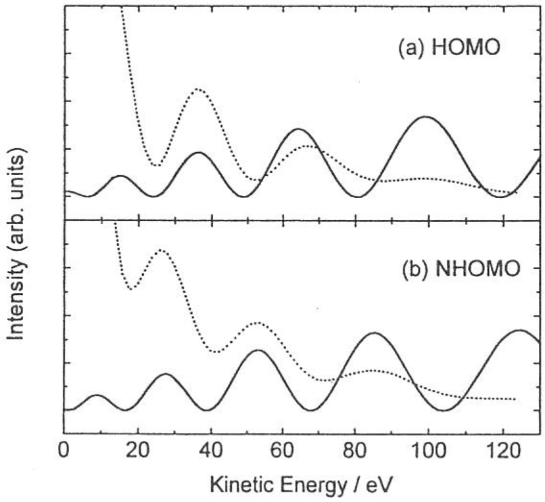

Figure 2 Calculated hν dependences of photoionization cross section. The solid curves were calculated with the spherical-shell like initial state and the plane-wave final state, where $R_s = 3.26$Å, $\Delta = 0.5$Å and $V_0 = -10$eV.

REFERENCES

[1] P. J. Benning *et al.*, Phys. Rev. B, **44**, 1962 (1991)., J. Wu *et al.*, Physica C, **197**, 251 (1992)., T. Liebsch *et al.*, Phys. Rev. A, **52**, 457 (1995).

[2] Y. B. Xu, M. Q. Tan, and U. Becker, Phys. Rev. Lett., **76**, 3538 (1996).

[3] S. Hasegawa *et al.*, Phys. Rev. B, **58**, 4927 (1998).

(BL8B2)

Angle-resolved UPS of Poly(2-vinylnaphthalene) thin films

K.K.Okudaira, Y.Azumai, K.Meguro, S.Hasegawa[A], K.Seki[B], Y.Harada[C], and N.Ueno[A]

Graduate School of Science and Technology, Chiba University, Chiba 263-8522
[A]Institute for Molecular Science. Okazaki, 444-8585
[B]Faculty of Science, Nagoya University, Nagoya 464-8602
[C]Department of Material Science, Faculty of Engineering, Chiba University, Chiba 263-8522

Thin films of pendant group polymers are the most promising candidates for practical use due to their stability and facility of preparation. Furthermore, their surface properties can be easily controlled by changing the pendant chemical group. However, in general the molecules in polymer solids are not ordered due to the large molecular-weight distribution and mixed tacticy, etc., and therefore it is believed that the pendant groups are also unoriented at the surface.

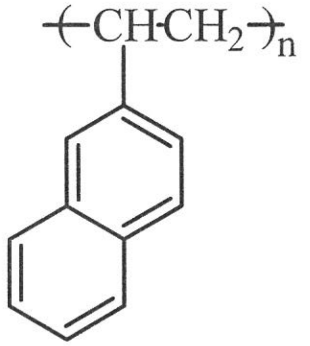

Figure 1 Molecular structure of Poly(2-vinylnaphthalene)

In this work the electronic structure and orientation of pendant groups of poly(2-vinylnaphthalene) (PvNp) (Fig.1) thin films were investigated by angle-resolved ultraviolet photoelectron spectroscopy (ARUPS) using synchrotron radiation. The ARUPS offers information on the geometrical structure of thin films as well as on their electronic structure. For example, we could determine the structure of thin films consisting of large organic molecule such as of 3,4,9,10-perylenetetracarboxylic dianhydride by the analyses of ARUPS intensities.[1] Furthermore we recently found that the orientation of the pendant group of polystyrene at the film surface depends on film thickness.[2]

ARUPS measurements were carried out at the beamline BL8B2 of the UVSOR at the Institute for Molecular Science. ARUPS spectra were measured at hν=40eV and at normal incidence (incidence angle of photon α=0°). Thin films of PvNp were prepared by spincasting on Au-evaporated Si(100) wafers from toluene solutions of 0.3wt/vol%. The film thickness prepared in this way is about 100Å.

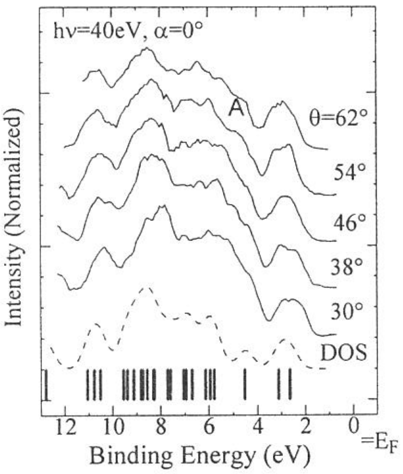

Figure 2 ARUPS of PvNp thin films spincasted from 0.3 wt/vol% toluene solution at hν=40eV and α=0° as a function of take-off angle (θ). The vertical bars show the molecular orbital energies calculated by *ab initio* MO calculation (STO-6G). The density of states (DOS) is represented by (– – – – –) (see text). The calculated binding energy scale was contracted by 1.35 and shifted to fit with the experimental results.

Figure 2 shows the ARUPS spectra of the PvNp thin film as a function of the take-off angle (θ). The intensity of top band A shows slight θ dependence. The calculated density-of-states (DOS) using molecular orbital (MO) calculation (STO-6G) is also shown in Fig.2. The MO calculation was performed for a model compound [CH_3-$CH(C_{10}H_7)$-CH_3] of the polymer unit, and the DOS was obtained by a Gaussian broadening (FWHM = 0.8 eV) of the MO levels. The agreement between the observed spectra and the DOS indicates that the electronic structure of PvNp is well simulated by that of the model compound. The band A in the spectra originates from two top π states at the pendant naphthalene, and hereafter we focus on the θ dependence of the intensity of the band A to determine the orientation of the pendant naphthalene groups at the surface.

In order to obtain the molecular orientation of the pendant naphthalene, we made the analyses of the θ dependence in the single-scattering approximation combined with molecular orbital (SS/MO) approximation.[3] The calculations were performed for the model compound. The phase shift and radial matrix element were calculated for all subshells of the atoms constituting the molecules using the Muffin-tin potential,[4] and the potential between the Muffin-tin spheres was assumed to be zero. In the present calculation we used the phenomenological electron mean-free path of 8 Å to calculate the damping factor.[3] We further assumed an azimuthal disorder for the rotational orientation of the pendant naphthalene groups with respect to the surface normal. For the calculation of photoelectron intensity, we introduced an inclination angle (β) of the molecular plane of pendant naphthalene groups with respect to the film surface.

In Figure 3 the observed θ dependence of the intensity of the band A is compared with calculated results, for (i) 3-dimensional isotropic orientation which gives a mean value of β (β_{mean}) of 58° shown in the inset of Fig.3, (ii) a uniform distribution of β ($\beta_{mean}=45°$), and (iii) a system where all pendant naphthalene groups tilt at 57°. It is seen that the calculated θ pattern for the case (i) gives the best agreement. The β_{mean} of 58° obtained by the analyses of ARUPS is in good agreement with the β of 57° determined by the NEAXFS study.[5] From these results we conclude that the tilt angle of the pendant naphthalene groups at the film surface have a distribution with a mean value of about 58°.

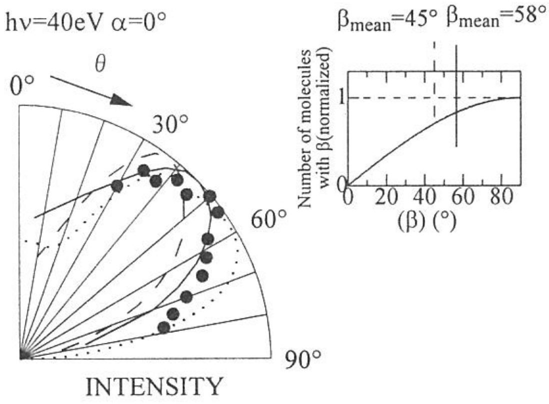

Figure 3 Comparison between calculated and observed (●) take-off angle (θ) dependences of the intensity of the band A. All calculations were carried out by the SS/MO approximation. The calculated result for 3-dimensional isotropic orientation shown in the inset is represented by (————). The calculated result for a uniform distribution shown in the inset is represented by (– – – – –). The calculated result for $\beta=57°$ is represented by (···········).

The ARUPS study offers the tilt-angle distribution as well as its mean value

REFERENCES

[1] Y. Azuma, T. Hasebe, T. Miyamae, K. K. Okudaira, Y. Harada, K. Seki, E. Morikawa, V. Saile, and N. Ueno, J. Synchrotron Radiation **5**, 1044 (1998).

[2] N. Ueno, Y. Azuma, M. Tsutsui, K. K. Okudaira, and Y. Harada, Jpn. J. Appl. Phys. **37** 4979 (1998).

[3] N.Ueno, A.Kitamura, K.K.Okudaira, T.Miyamae, S.Hasegawa, H.Ishii, H.Inokuchi, T.Fujikawa, T.Miyazaki, and K.Seki, J.Chem.Phys., **107** 2079(1997).

[4] D.Dill and J.L.Dehmer, J.Chem.Phys., **61** 692 (1974).

[5] K. K. Okudaira, E. Morikawa, D.A.Hite, S. Hasegawa, H. Ishii, M. Imamura, H. Shimada, Y. Azuma, K. Meguro, Y. Harada, V. Saile, K. Seki, and N. Ueno, J.Electron Spectrosc.Relat.Phenom, accepted

(BL8B2)

Electronic structure of poly(1,10-phenanthroline-3,8-diyl) and its K-doped state studied by ultraviolet photoelectron spectroscopy

T. Miyamae [a], Y. Saito [b], T. Yamamoto [b], S. Hasegawa [a], K. Seki [c], and N. Ueno [a,d]
[a] *Institute for Molecular Science, Myodaiji, Okazaki 444-8585*
[b] *Research Laboratory of Resources Utilization, Tokyo Institute of Technology, 4259 Nagatsuta, Midori-ku, Yokohama 226-8503*
[c] *Department of Chemistry, Faculty of Science, Nagoya University, Chikusa-ku, Nagoya 464-8602*
[d] *Department of Materials Science, Faculty of Engineering, Chiba University, Inage-ku, Chiba 263-8522*

Families of π-Conjugated polymers are receiving much attention because of their interesting optical and electronic properties. Also such studies of interaction between metal atoms and conjugated polymers can be regarded as a kind of model system of metal/polymer interface formed at the fabrication of organic electroluminescent devices. Poly(1,10-phenanthroline-3,8-diyl), denoted PPhen hereafter, exhibits n-type conducting properties due to the electron-deficient nature of phenanthroline.1) Its molecular structure is shown in Fig. 1. In this work, we report UPS studies of PPhen and discuss its electronic states. We also studied the changes in electronic structure upon *in situ* doping with potassium by UPS. In order to obtain deep understanding of the electronic states derived by doping, we simulated the UPS spectra of the model compounds using the single-scattering (SS) approximation combined with MO calculations.

The UPS spectra were measured with an angle-resolving UPS spectrometer at BL8B2 of UVSOR Facility. Thin films of PPhen were prepared on gold coated Si (100) substrates by vacuum. Potassium doping of PPhen was carried out *in situ* using a SAES K-getter source. The MO calculations were carried out with a MOPAC 6 program. The calculations of photoemission intensities with SS approximations were carried out on the IBM SP2 computer at the Computer Center of IMS.

The UPS spectrum of PPhen at $h\nu = 40$ eV is shown in Fig. 2. From the right-hand onset T, the threshold ionization energy (I_{th}) was found to be 6.0 eV. The value of I_{th} of PPhen indicates that acceptor doping to the polymer should be difficult due to the large I_{th}. This large value of I_{th} is consistent with the fact that PPhen is inert against p-type doping (oxidation).1)

The UPS spectra of K-doped PPhen for increasing doping levels are shown in Fig. 3. By a slight doping with potassium (Fig. 3, curve b), Fermi energy shifts to the lower binding energy side by 0.57 eV. At the intermediate stage of doping (Fig. 3, curves c and d), two new states BP1 and BP2 appear in the band gap region. With increasing the doping level, these peaks gradually grow up, and the position of the Fermi level is further shifted toward the vacuum level by 0.24 eV.

From the comparison with our previous UPS studies of K-doped PBPy,2) the two states BP1 and BP2 which appeared by the doping can be assigned to the formation of bipolarons. The gap state at 3.94 eV is assigned to the LUMO stabilized by geometric relaxation and filled by electron donation from K atom, while the 5.94 eV peak is the destabilized HOMO due to the geometry modifications to quinoid structure. In addition, the highest lying state in the undoped polymer, peak A, shows decrease of intensity with increasing K content, as illustrated in the Fig. 4 (a). This is consistent with the picture that the formation of bipolaron states leads to the removal of a state from the valence band edge of the neutral molecule to form new states within the band gap. The intensity of peak B also decreases with increasing K doping, indicating that the lone pairs of N atoms of phenanthroline units interact with the K cations. This suggests that the K dopants are preferentially located close to the N atoms of phenanthroline unit.

Next, we will discuss the changes in observed UPS spectra described above by using the simulated UPS spectra obtained by the combination of the MO calculations and the SS approximations. Since K doping of PPhen forms bipolaron bands and the dopant are probably located close to the N atoms of phenanthroline unit, we performed semiemperical MO calculations of phenanthroline-tetramer and its doped systems assuming simplified model systems. For K-doped PPhen, two K cations are located close to the two neighboring phenanthroline dianion units. Potassium-doped PPhen takes a quinoidal character at the inner two units, and the chain becomes nearly coplanar, the torsion angle changing from 44.2 ° to 0 ° in spite of its steric hindrance. We find from the total charge per unit that most of the charges donated from K is transferred to the inner units, only 6 % going to the outer units. The geometry of the outer units is almost the same as that in the undoped case. These results indicate that the charges transferred to the next nearest-neighbor units should be fairly small. After the MO levels of each model compound were obtained from MO calculation, the photoelectron spectra were calculated with the SS approximations. In this method, a random molecular orientation was assumed. In Figs. 4 (a) and 4 (b), we show the measured and calculated UPS difference spectra between K-doped and pristine PPhen in the most intriguing energy region from the vacuum level to binding energy E_{b} = 14 eV. A good correspondence is obtained between the measured and calculated results, well reproducing the observed positive peaks located at 4.96 eV and 6.65 eV, due to the formation of bipolaron bands, and the negative peak located at 8.02 eV due to the removal of the states from the valence band edge. The good agreement between the difference spectra confirms that the bipolaron states are generated by the K doping. The relative intensity of BP1 and BP2 is different between the observed and calculated spectra. The observed intensity of BP1 is about one third of the observed intensity of BP2. This disagreement can be reasonably ascribed to a smaller dopant concentration in the observed spectrum than in the calculated one, which corresponds to 50 % doping level.

REFERENCES

[1] Y. Saitoh and T. Yamamoto, Chem. Lett. 785 (1995).

[2] T. Miyamae, D. Yoshimura, H. Ishii, Y. Ouchi, K. Seki, T. Miyazaki, T. Koike, and T. Yamamoto, J. Chem. Phys. **103**, 2738 (1995).

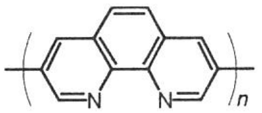

Figure 1. The molecular structure of poly(1,10-phenanthroline-3,8-diyl) (PPhen).

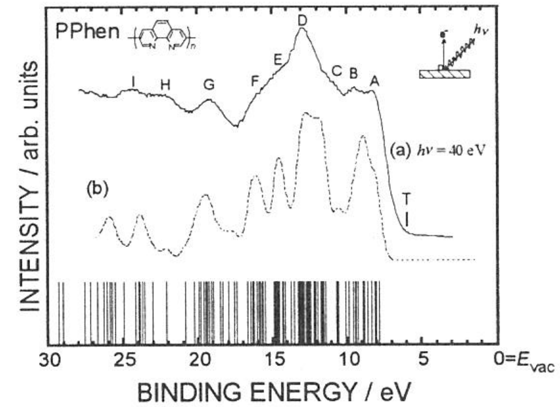

Figure 2. (a) UPS spectra of PPhen using synchrotron radiation of 40 eV. (b) The density of states derived MO calculation of phenanthroline tetramer. The vacuum level (E_{vac}) is taken as the origin of the energy scale. The vertical bars indicate the orbital energies. T denotes the threshold ionization energy.

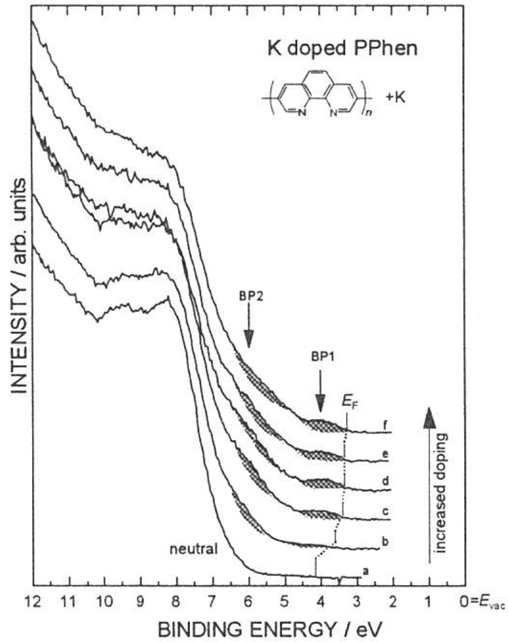

Figure 3. UPS spectra of neutral and increasingly potassium-doped PPhen.

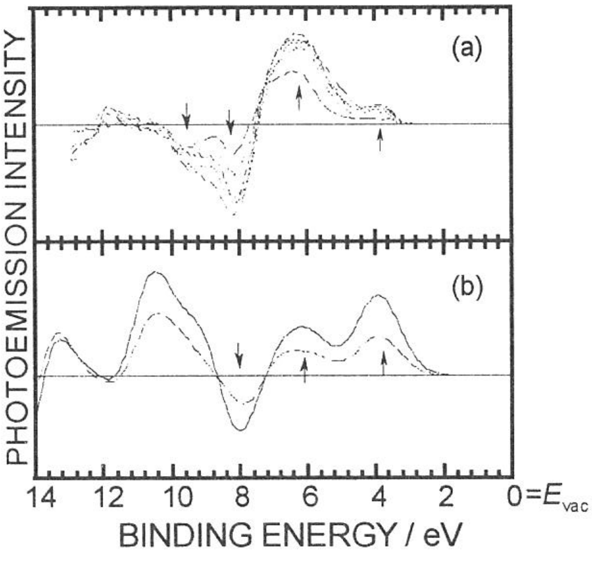

Figure 4. (a) Corresponding difference UPS spectra ($UPS_{doped} - UPS_{pristine}$) obtained by subtracting the spectrum of pristine PPhen from those of K-doped states and (b) corresponding difference UPS spectrum ($UPS_{doped} - UPS_{pristine}$) calculated for tetramer.

(BL8B2)

Ultraviolet Photoelectron Spectroscopy of Poly(anthraquinone)s; Their Electronic Structure and K-Doped States

T. Miyamae[a] , T. Yamamoto[b], Y. Sakurai[c], K. Seki[c], and N. Ueno[a,d]

[a] *Institute for Molecular Science, Myodaiji, Okazaki 444-8585*
[b] *Research Laboratory of Resources Utilization, Tokyo Institute of Technology, 4259 Nagatsuta, Midori-ku, Yokohama 226-8503*
[c] *Department of Chemistry, Faculty of Science, Nagoya University, Chikusa-ku, Nagoya 464-8602*
[d] *Department of Materials Science, Faculty of Engineering, Chiba University, Inage-ku, Chiba 263-8522*

π-Conjugated polymers have been the subjects of steadily growing interest in the past 20 years because of their unique and interesting structural and electronic properties. Recently we have found that poly(2methylanthraquinone-1,4-diyl (P(2Me-1,4-AQ), Fig. 1(a)) and poly(anthraquinone-1,5-diyl) (P(1,5-AQ), Fig. 1(b)) exhibit n-type conducting properties.[1)] In this work, we report experimental and theoretical studies of polyanthraquinones (PAQ)s, and discuss their electronic structures. We also studied the changes in electronic structure of PAQs upon doping with potassium by UPS

The P(2Me-1,4-AQ) and P(1,5-AQ) films were prepared by spin-coating from a solution of the polymer in CH_3Cl. The UPS spectra were measured by an angle-resolving UPS spectrometer at BL8B2. Potassium doping of PAQs was carried out *in situ* at 125 °C ± 5 °C using a SAES K-getter source.

The UPS spectra of P(2Me-1,4-AQ) obtained by synchrotron radiation of $h\nu = 40$ eV are shown in Fig. 2 (a). For comparison, in Fig 2 we also show the orbital energies obtained from the PM3 semiempirical calculations of anthraquinone-dimer by vertical lines, and the simulated spectra as the density of states (DOS). According to the calculation, the peak A is formed by the overlapping π and n bands derived from the uppermost-occupied orbitals of anthraquinone, where n denotes the lone pair orbitals of the O atoms. From the right-hand onset T, the threshold ionization energy (I_{th}), was found to be 6.4 eV. The value of I_{th} of P(2Me-1,4-AQ) indicates that acceptor doping of the polymers should be difficult due to the large I_{th}.

In Fig. 3, we show a series of UPS spectra of P(2Me-1,4-AQ) taken at different doping levels with potassium, at the steps from the pristine state to the heavily doping level. At the intermediate stage of doping (Figs. 3 c, d, e), only one new state appears in the energy gap region. Furthermore, no significant change of the work function (-0.24 eV) was observed at the whole doping region. In general, n-type doping of a conjugated polymer results in a decrease in the work function, i.e. a shift in the Fermi energy to lower binding energy, corresponding to the creation of new occupied states in the original energy gap region. The reason for the appearance of only one state and the absence of the change in the work function in K-doped P(2Me-1,4-AQ) may be that the polymer chain cannot take electrons from the dopants effectively to create the bipolarons. According to the electrochemical reduction of 2-methylanthraquinone, radical anion and dianion of anthraquinone are formed.[1)] In the case of P(2Me-1,4-AQ), the electron donation from potassium may lead to the formation of the reduced radical anion and dianion units. From the MO calculation of K-anthraquinone-dimer, each carbonyl group accepts c.a. –0.37 e extra charge at the doped state as compared to pristine polymer. This result indicates that the extra charges are localized at each carbonyl group of anthraquinone unit as radical anion or dianion. Thus we consider that K-doped P(2Me-1,4-AQ) contains the neutral, radical anion, and dianion units.

In contrast to the case of P(2Me-1,4-AQ), P(1,5-AQ) showed poor reactivity to the dopant (not shown). The difference between K-doped P(2Me-1,4-AQ) and K-doped P(1,5-AQ) may be caused by their conformational differences of polymer chain. Optimized geometries of these polymers, which are carried out with a molecular mechanics calculation, were illustrated in the inset of Fig. 3. From the molecular mechanics calculation, the polymer chain of P(2Me-1,4-AQ) has analogous structure with poly(*p*-phenylene), and its anthraquinone units protrude from the main chain, as shown in the inset of Fig. 3. In contrast to the case of P(2Me-1,4-AQ), the polymer chain of P(1,5-AQ) has rather helical structure. Thus we can summarize the P(1,5-AQ) show only a weak ability to coordinate with potassium presumably because of its helical geometry.

1. T. Yamamoto and H. Etori, *Macromolecules*, **28**, 3371 (1995).

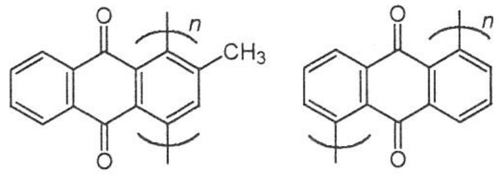

poly(2Me-antraquinone-1,4-diyl)
P(2Me-1,4-AQ)

poly(antraquinone-1,5-diyl)
P(1,5-AQ)

Figure 1 The molecular structure of P(2Me-1,4-AQ) (a) and P(1,5-AQ) (b),

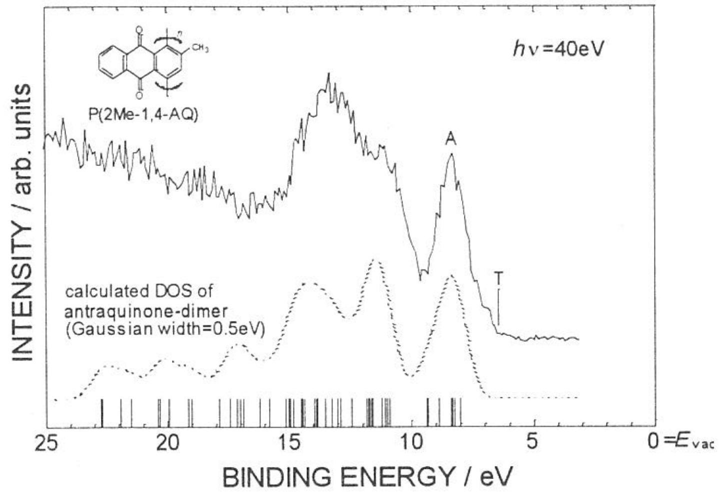

Figure 2 Observed (solid line) and simulated (dotted line) UPS spectra of P(2Me-1,4-AQ) film (a) and PPhen film (b). The vertical lines show the calculated orbital energies. T denotes the threshold ionization energy.

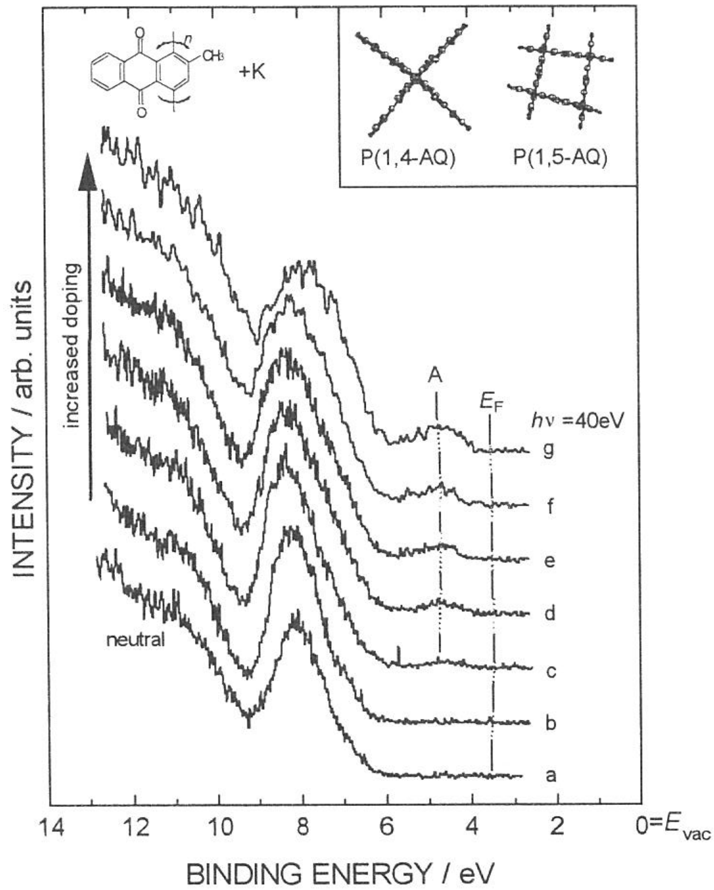

Figure 3 UPS spectra of neutral and increasingly potassium-doped P(2Me-1,4-AQ). The inset shows the projection along the chain axis for P(1,4-AQ) and P(1,5-AQ).

(BL8B2)

Electronic structure of Alq_3/insulator/Al interfaces studied by ultraviolet photoelectron spectroscopy.

T. Yokoyama[a), D. Yoshimura[a), E. Ito[b), S. Hasegawa[c), H. Ishii[a), and K. Seki[d),
a) Department of Chemistry, Faculty of science, Nagoya university, Nagoya 464-8602
b) Venture business laboratory, Nagoya university, Nagoya 464-8603
c) Institute of Molecular science, Myodaiji, Okazaki 444-8585
d) Research center of material science, Nagoya university, Nagoya 464-8602

Recently, organic electroluminescent (EL) devices have attracted much attention in close relation to the application to display technology. The interfacial electronic structure of such devices, which dominates the carrier injecting properties, is key issue for understanding and improvement of the performance of the devices. Very recently, the improvement of the device performance by the insertion of very thin insulating layer such as PMMA, LiF and aluminum oxide between a cathode electrode and electron-transporting layer (ETL) has been reported by several groups. In spite of the extensive studies, the mechanism of the improvement has not been well understood. The elucidation of the electronic structures of the cathode/ insulator and the insulator/ETL interfaces is indispensable for clarifying the mechanism.

In this work we investigated the electronic structure of tris(8-hydroxyquinolino)alminum (Alq3 (Fig1))/insulator (LiF and Aluminum oxide)/Al systems using ultra violet photoelectron spectroscopy (UPS) system at BL8B2 of institute of molecular science. The film thickness of Alq3 and LiF was measured with crystal oscillator. Aluminum oxide film was prepared by exposing the clean Al surface to the air for an hour.

Figs. 2(a)-(c) show the energy diagrams of Alq3/Al, Alq3/LiF/Al, and Alq3/Al oxide/Al interfaces obtained from the UPS results. In the case of Alq3/Al, the shifts of vacuum level(Δ) of -1.0 was observed. Because of this downward shift, lowest unoccupied molecular orbital (LUMO) is close to the Fermi level of the Al electrode, inducing the small barrier height for electron injection as shown in Fig.2(a). In the case of Alq3/LiF/Al, the vacuum level shifts of −1.0 and −0.2 eV were observed at Al/LiF and LiF/Alq3 interfaces, respectively. The total vacuum level shift between Al and Alq3 was −1.2 eV and were larger than that at Alq3/Al interface, suggesting the decrease of the barrier height for electron injection by LiF layer. Such decrease of the barrier height for electron injection is probably one of the possible origins of the improvement effect by insulating layer.

At Alq3/Al oxide/Al interfaces, the vacuum level shift of −1.0eV was observed at Al oxide/Al interface as in the case of LiF/Al and Alq3/Al interfaces, while no significant shift was observed at Al oxide/Alq3 interfaces. The total shift of −1.0 eV was similar to that at Alq3/Al interface. Thus we cannot expect the improvement of the device performance. This discrepancy can lead two possible explanations: first is that the other origin for the improvement effect rather than the decrease of the barrier height should be considered. Second is that the difference of the surface preparation between our experiment and the real device can change the barrier height. In order to clarify this point, the UPS measurement of the interface prepared in the real device condition should be performed.

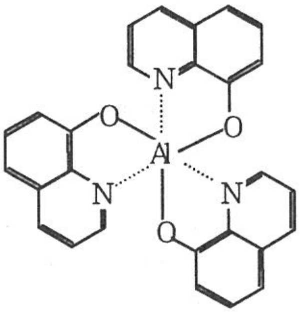

Fig1 Chemical structure of tris(8-hydroxyquinolino)alminum (Alq3)

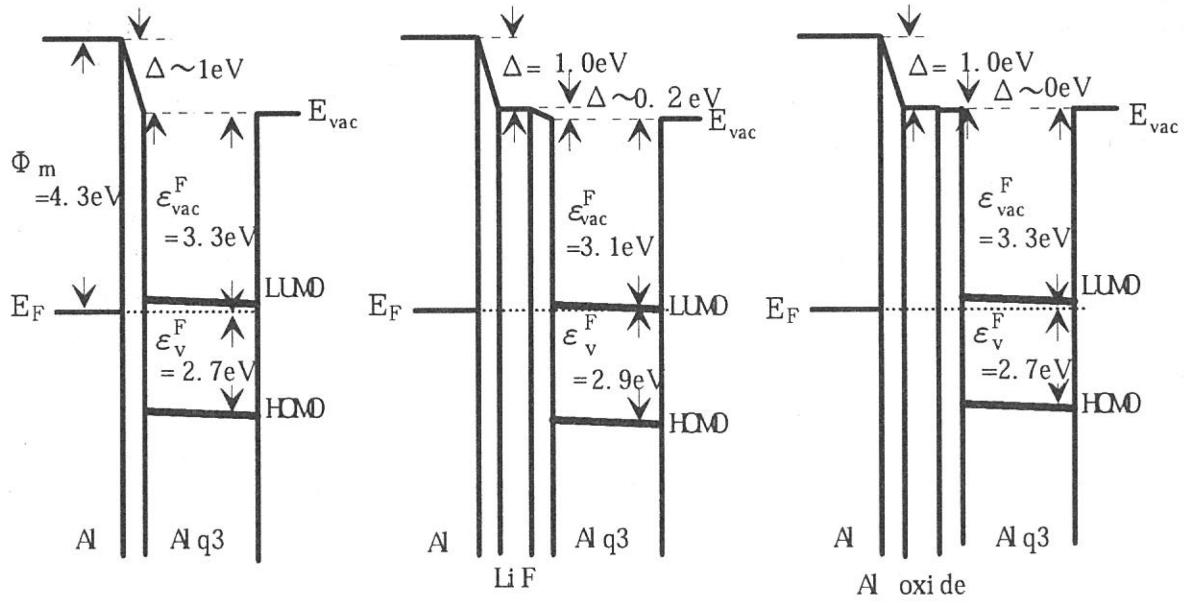

(a)Alq3/Al (b)Alq3/LiF/Al (c)Alq3/Al Oxide/Al

Fig2 Energy diagram of Alq3/insulator/Al interfaces

(BL8B2)

UV Photoelectron Spectroscopy of Polycarbosilane

Y. Sakurai[a], D. Yoshimura[a], H. Ishii[a], H. Isaka[b], H. Teramae[b],
N. Matsumoto[b], S. Hasegawa[c], N. Ueno[c], and K. Seki[d]
a) Department of Chemistry, Faculty of Science, Nagoya University, Nagoya 464-8602
b) NTT Basic Research Laboratories, Morinosato-Wakamiya, Atsugi, Kanagawa 243-0198
c) Iistitute for Molecular Science, Myodaiji, Okazaki 444-8585
d) Reserch Center of Material Science, Nagoya University, Nagoya 464-8602

Polysilane and polyethylene have homocatenated skeletons composed of silicon and carbon atoms, respectively. Polysilanes, whose electronic structure is characterized by σ-conjugation along the Si backbone, have attracted much attention as a new class of photoresists, conducting polymers, and emitting materials in organic light-emitting diode. While polyethylenes have also σ-conjugation along the C backbone, the σ-conjugation does not dominate the electronic properties of polyethylenes, because the ionization potentials of the σ-conjugated orbitals are quite larger. Electronic structure of polycarbosilane whose backbone consists of silicon and carbon is expected to differ from those of the homopolymers. In this work, by using ultraviolet photoelectron spectroscopy (UPS), we investigated the electronic structure of polycarbosilane which consists of repeating Si_2C units, and compared the observed electronic structure with those of polysilane and polyethylene.

The sample was synthesized at NTT. The samples used in the UPS measurements were prepared on a copper disk by spin coating of 0.2wt% toluene solution. UPS spectra were measured using angle-resolved UPS system at BL8B2 of UVSOR at Institute for Molecular Science. Ionization threshold energy was measured by the photoelectron spectrometer with a retarding field analyzer and a helium discharge lamp (hν = 21.2 eV) in Nagoya university.

The UPS spectrum of polycarbosilane $[(SiMe_2)_2CH_2]_n$ at hν=40eV is shown in Fig. 1(a). The abscissa is the binding energy relative to the vaccum level. The spectrum has four structures labelled by A, B, C and D. For comparsion, reported gas-phase UPS spectra of Si_2Me_6 and Si_4Me_{10}[1] with the peak assignments are shown in Fig. 1(b) and (c). The energy axes of gas-phase spectra were adjusted to align the SiC peaks with peak B in the UPS spectrum of polycarbosilane. From the comparsion among the spectra, we assigned feature A to Si-Si bond, feature B to Si-C bonds, feature C to C-H bonds, and feature D to C_{2s}. The peak due to Si-Si bond extends to lower binding-energy side than those of Si_2Me_6, and the lineshape is similar to that of Si_4Me_{10} in shape. This suggests that each Si-Si units, which are separeted by a carbon atom, still interact with each other, forming σ-conjugation of the backbone.

In Fig. 2 (a) - (c), UPS spectrum of polycarbosilane and the density of states (DOS) obtained from 3-21G *ab-initio* and PM3 MOPAC calculations. The calculated results agree well with the UPS spectrum. The analysis of the molecular orbital patterns demonstrated that the molecular orbitals due to the Si-Si bond are actually delocalized over the molecule. Such σ-conjugation is also supported by the observed ionization potential. The observed ionization potential of polycarbosilane was 6.4 eV. This value is between those of polysilanes (5.9eV)[2] and polyethylene (8.5eV)[3], indicating that the degree of σ-conjugation of polycarbosilane is smaller than those of polysilanes.

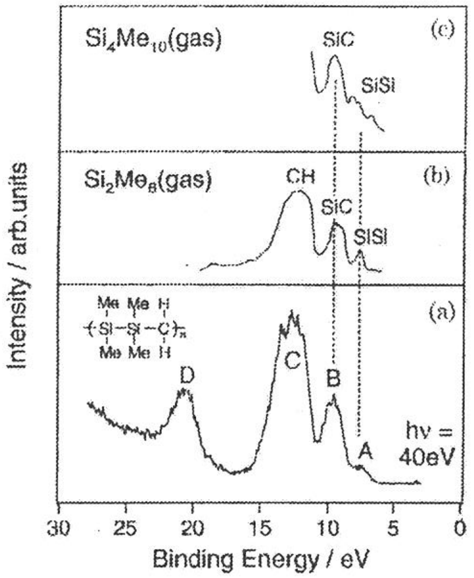

Figure 1. (a)UPS spectrum of polycarbosilane at hν = 40 eV, (b)UPS spectrum of gas-phase Si_2Me_6, (c)UPS spectrum of gas-phase Si_4Me_{10}.

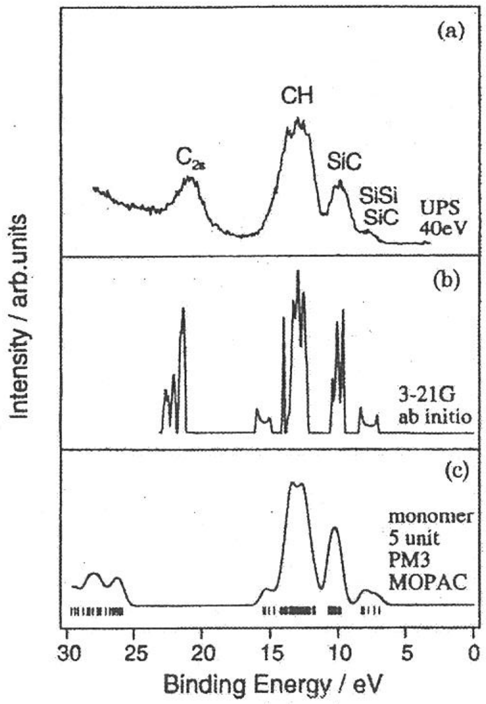

Figure 2. (a)UPS spectrum of polycarbosilane at hν = 40 eV, (b)the calculated density of states by 3-21G ab initio molecular orbital calculation, (c)the calculated density of states by PM3 MOPAC calculation.

References

1) H. Bock and W. Ensslin, Angew. Chem., Int. Ed. Engl., 10,404 (1971)
2) K. Seki, T. Mori, H. Inokuchi and K. Murano, Bull. Chem. Soc. Jpn., 61,351 (1988)
3) M. Fujihira and H. Inokuchi, Chem. Phys. Lett., 17, 554 (1972)

UVSOR

List of Publications

LIST OF PUBLICATIONS (1998)

O. Arimoto, S. Fujiwara, T. Tsujibayashi, M. Watanabe, M. Itoh, S. Nakanishi, H. Itoh, A. Asaka and M. Kamada
Combination of Synchrotron Radiation and Laser for Two-Photon Spectroscopy of BaF_2[1]
J. Electron Spectrosc. Relat.Phenom., **92** (1998) 219.

S. Asaka, S. Nakanishi, H. Itoh, M. Kamada, M. Watanabe, O. Arimoto, S. Fujiwara, T. Tsujibayashi and M. Itoh
Time-gated Photon Counting Method for Two-Photon Spectroscopy Using Synchrotron Radiation and Laser
Rev. Sci. Instrum., **69** (1998) 1931.

M. Fujita, M. Itoh, H. Nakagawa, M. Kitaura and D. L. Alov
Exciton Transitions in Orthorhombic and Cubic PbF_2
J. Phys. Soc. Jpn., **67** (1998) 3320.

K. Fukui, H. Nakagawa, I. Shimoyama, K. Nakagawa, H. Okamura, T. Nanba, M. Hasumoto and T. Kinoshita
Reconstruction of BL7B for UV, VIS and IR Spectroscopy with a 3 m Normal-Incidence Monochromator
J. Synchrotron Rad., **5** (1998) 836.

K. Fukui, M. Ichikawa, A. Yamamoto and M. Kamada
Photoemission and Core Absorption Studies of Indium Nitride
Solid-State Electronics, **41** (1997) 299.

Q. X. Guo, M. Nishio, H. Ogawa, A. Wakahara and A. Yoshida
Electronic Structure of Indium Nitride Studied by Photoelectron Spectroscopy
Phys. Rev. **B**, **58** (1998) 15 304.

Q. Guo, M. Nishio, H. Ogawa and A. Yoshida
Energy Loss Spectrum of AlN in the 6-120 eV Region
J. Crystal Growth, **189/190** (1998) 457.

H. Hama, M. Hosaka, J. Yamazaki and T. Kinoshita
Single-bunch Beam Property for FEL on the UVSOR Storage Ring
Nuclear Instruments and Methods in Physics Research, **B 144** (1998) 75.

S. Hasegawa, T. Miyamae, K. Yakushi, H. Inokuchi, K. Seki and N. Ueno
Comparison between Calculated and Measured Photoemission Spectra of C_{60} *Thin Films*
J. Elecctron Spectrosc. Relat.Phenom., **88-91** (1998) 891.

S. Hasegawa, T. Miyamae, K. Yakushi, H. Inokuchi, K. Seki and N. Ueno
Origin of the Photoemission Intensity Oscillation of C_{60}
Phys. Rev., **B 58** (1998) 4927.

T. Hatano, W. Hu, M. Yamamoto and M. Watanabe
Handling the Polarization of Soft X-Ray Using Transmission Multilayers.
A Case Study[1]
J. Electron Spectrosc. Relat.Phenom., **92** (1998) 311.

T. Hatsui, Y. Takata, N. Kosugi, K. Yamamoto, T. Yokoyama and T. Ohta
Ni 2p Excitation Spectra of Some Planar Ni Complexes
J. Electron Spectrosc. and Relat. Phenom., **88-91** (1998) 405.

T. Hatsui, Y. Takata, and N. Kosugi
Strong Metal-to-Ligand Charge Transfer Bands in Ni 2p Photoabsorption of $K_2Ni(CN)_4 \cdot H_2O$
Chem. Phys. Lett., **284** (1998) 320.

S. Hirose and M. Kamada
Time Response and Temperature Dependence of Photo-Stimulated Desorption of Sodium Atoms from Sodium Halides[1]
J. Elecctron Spectrosc. Relat.Phenom., **92** (1998) 109.

M. Hosaka, H. Hama, J. Yamazaki and T. Kinoshita
Study of Beam Property on a Storage Ring Operated with Negative Momentum Compaction Factor
Nucl. Instr. and Meth. in Phys. Res., **A 407** (1998) 234.

S. Hosokawa, Y. Hari, T. Kouchi, I. Ono, H. Sato, M. Taniguchi, A. Hiraya, Y. Takata, N. Kosugi, and M. Watanabe
Electronic Structures and Local Atomic Configurations in Amorphous GeSe and GeTe
J. Phys.: Condens. Matter , **10** (1998) 1931.

W. Hu, T. Hatano, M. Yamamoto and M. Watanabe
Transmission Multilayer Polarizers for Use in the 55-90 eV Region
J. Synchrotron Rad., **5** (1998) 732.

M. Ikeda, M. Inayoshi, M. Hori, T. Goto, M. Hiramatsu and A. Hiraya
Synchrotron Radiation Induced SiC Formation on Si Substrate Employing Methanol and H Radical
J. Vac. Sci. Technol., **A 16** (1998) 2252.

T. Inoue, S. Sasaki, M. Tokeshi and T. Ogawa
Photoionization Threshold of Perylene on Water Surface as Measured by Synchrotron Radiation
Chemistry Letters, (1998) 609.

H. Ishii, S. Hasegawa, D. Yoshimura, K. Sugiyama, S. Narioka, M. Seki, Y. Ouchi, K. Seki, Y. Harima and K. Yamashita
Electronic Structures of Porphyrins and their Interfaces with Metals Studied by UV Photoemission
Mol. Cryst. Liq. Cryst., **296** (1997) 427.

H. Ishii and K. Seki
Energy Level Alignment at Organic/metal interfaces Studied by UV Photoemission: breakdown of Traditional Assoumption of a Common Vacuum Level at the Interface
IEEE Trans. Electron Devices, **44** (1997) 1295.

H. Ishii, K. Sugiyama and K. Seki
Interfacial Electronic Structures of Organic/metal Interfaces Studied by UV Photoemission
Proc. SPIE-Int. Soc. Opt. Eng., **3148** (1997) 228.

H. Ishii, K. Sugiyama, D. Yoshimura, E. Ito, Y. Ouchi and K. Seki
Energy-Level Alignment at Model Interfaces of Organic Electroluminescent Devices Studied by UV Photoemission: Trend in the Deviation from the Traditional Way of Estimating the Interfacial Electronic Structures
IEEE J. Sel. Top. Quantum Electron., **4** (1998) 24.

H. Ishii, D. Yoshimura, K. Sugiyama, S. Narioka, Y. Hamatani, I. Kawamoto, T. Miyazaki, Y. Ouchi and K. Seki
Electronic Structure of 8-hydroxyquinoline Aluminum (Alq3)/metal Interfaces Studied by UV Photoemission
Synth. Met., **85** (1997) 1389.

M. Itoh
Valence-Band Structures of Lead Halides by Ultraviolet Photoelectron Spectroscopy
Journal of the Faculty of Engineering, Shinshu Univ., **80** (1998) 19.

E. Ito, H, Oji, T. Araki, K. Oichi, H. Ishii, Y. Ouchi, T. Ohta, N. Kosugi, Y. Maruyama, T. Naito, T. Inabe and K. Seki
Soft X-ray Absorption and X-ray Photoelectron Spectroscopic Study of Tautomerism in Intramolecular Hydrogen Bonds of N-Salicylideneaniline Derivatives
J. Am. Chem. Soc., **119** (1997) 6336.

M. Itoh, T. Shiokawa, K. Sawada and M. Kamada
Ultraviolet Photoemission Studies of Valence Bands in Lead Halides
J. Phys. Soc. Jpn., **67** (1998) 2140.

M. Kamada, Y. Q. Cai, N. Takahashi, S. Tanaka and D. A. Woolf
Circular Dichroism in the Angular Distribution of Core-level Photoelectrons from GaAs (111)
J. Electron Spectrosc. Relat. Phenom., **88-91** (1998) 219.

M. Kamada, S. Fujiwara, O. Arimoto, Y. Fujii and S. Tanaka
Simultaneous Measurements of Photoelectron and Luminescence of Barium Halides
J. Electron Spectrosc. Relat. Phenom., **88-91** (1998) 297.

S. Kimura, M. Kamada, H. Hama, K. Kimura, M. Hosaka, J. Yamazaki, X.-M. Marechal, T. Tanaka and H. Kitamura
Performance of a Helical Undulator of the UVSOR
J. Synchrotron Rad., **5** (1998) 453.

S. Kimura, Y. Ufuktepe, K. G. Nath, T. Kinoshita, H. Kumigashira, T. Takahashi, T. Matsumura, T. Suzuki, H. Ogasawara and A. Kotani
4d-4f and 3d-4f Resonant Photoemission of TmX (X=S, Se, Te)
Journal of Magnetism and Magnetic Materials, **177-181** (1998) 349.

S. Kimura, D. X. Li, Y. Haga and T. Suzuki
Magnetic Field Dependence of Low-energy Excitation of GdAs
Journal of Magnetism and Magnetic Materials, **177-181** (1998) 351.

T. Kinoshita, Y. Takata, T. Matsukawa, H. Aritani, S. Matsuo, T. Yamamoto, M. Takahashi, H. Yoshida, T. Yoshida, Y. Ufuktepe, K. G. Nath, S. Kimura and Y. Kitajima
Performance of the YB_{66} *Soft X-ray Monochromator Crystal at the Wiggler Beamline of the UVSOR Facility*
J. Synchrotron Rad., **5** (1998) 726.

T. Kinoshita, Y. Ufuktepe, K. G. Nath, S. Kimura, H. Kumigashira, T. Takahashi, T. Matsumura, T. Suzuki, H. Ogasawara and A. Kotani
Resonant Photoemission Studies of Thulium Monochalcogenides around the Tm 3d Threshold
J. Electron Spectrosc. Relat. Phenom., **88-91** (1998) 377.

J. Kikuma, K. Yoneyama, M. Nomura, T. Konishi, T. Hashimoto, R. Mitsumoto, Y. Ohuchi and K. Seki
Surface Analysis of CVD Carbon Using NEXAFS, XPS and TEM
J. Electron Spectrosc. Relat. Phenom., **88-91** (1998) 919.

N. Kitamura, K. Fukumi, H. Mizoguchi, M. Makihara, A. Higuchi and N. Ohno
Structure of Densified Lithium Silicate Glasses
Rev. High Pressure Sci. Technol., **7** (1998) 281.

M. Kobayashi, T. Nanba, M. Kamada and S. Endo
Proton Order-disorder Transition of Ice Investigated by Far-infrared Spectroscopy under High Pressure
J. Phys.: Condens. Matter **10** (1998) 11551.

N. Kosugi
Molecular Inner-shell Spectroscopy of Planar Ni Complexes
J. Electron Spectrosc. Relat. Phenom., **92** (1998) 151.

K. Mase, M. Nagasono, S. Tanaka, T. Urisu, E. Ikenaga, T. Sekitani and K. Tanaka
Auger Electron Photoion Coincidence Technique Combined with Synchrotron Radiation for the Study of the Ion Desorption Mechanism in the Region of Resonant Transitions of Condensed H_2O
J. Chem. Phys., **108** (1998) 6550.

T. Masuoka
Single- and Double-Photoionization of Surfur Dioxide
Mem. Fac. Eng., Osaka City Univ., **38** (1997) 147.

T. Masuoka, Y. Chung, E.-M. Lee and J. A. R. Samson
Dissociative Photoionization of SO_2 *from 16 to 120 eV*
J. Chem. Phys., **109** (1998) 2246.

H. Mekaru, T. Urisu, Y. Tsusaka, S. Masui, E. Toyota and H. Takenaka
Design and Perfoemance of a Multilayered Mirror Monochromator in the Low-energy Region of the VUV
J. Synchrotron Rad., **5** (1998) 714.

R. Mitsumoto, T. Araki, E, Ito, Y. Ouchi, K. Seki, K. Kikuchi, Y. Achiba, H. Kurosaki, T. Sonoda, H. Kobayashi, O. V. Boltalina, V. K. Pavlovich, L. N. Sidorov, Y. Hattori, N. Liu, S. Yajima, S. Kawasaki, F. Okino and T. Toubara
Electronic Structures and Chemical Bonding of Fluorinated Fullerenes Studied by NEXAFS, UPS, and Vacuum-UV Absorption Spectroscopies
J. Phys. Chem. A, **102** (1998) 552.

R. Mitsumoto, K. Seki, T. Araki, E, Ito, Y. Ouchi, Y. Achiba, K. Kikuchi, S. Yajima, S. Kawasaki, F. Okino, H. Touhara, H. Kurosaki, T. Sonoda and H. Kobayashi
Soft X-ray Absorption, UV Photoemission, and VUV Absorption Spectroscopic Studies of Fluorinated Fullerenes
J. Electron Spectrosc. Relat. Phenom., **78** (1996) 453.

R. Mitsumoto, H. Oji, I. Mori, Y. Yamamoto, K. Asato, Y. Ouchi, H. Shinohara, K. Seki, K. Umishita, S. Hino, S. Nagase, K. Kikuchi and Y. Achiba
NEXAFS Studies of Higher Fullerenes up to C_{96}
J. Phys. IV, **7** (1997) 525.

T. Miyamae, M. Aoki, H. Etori, Y. Muramatsu, Y. Saito, T. Yamamoto, Y. Sakurai, K. Seki and N. Ueno
Ultraviolet Photoelectron Spectroscopy of Poly(anthraquinone)s and Poly(1,10-phenanthroline-3,8-diyl); their Electronic Structure and K-doped States
J. Electron Spectrosc. Relat. Phenom., **88-91** (1998) 905.

M. Mizutani, H. Niikura, A. Hiraya and K. Mitsuke
Laser-induced Fluorescence Excitation Spectroscopy of N_2^+ *Produced by VUV Photoionization of* N_2 *and* N_2O
J. Synchrotron Rad. **5** (1998) 1069.

S. Nagaoka, K. Mase and I. Koyano
Site-specific Fragmentation Following Core-level Photoexcitation of Organosilicon Molecules in the Vapor Phase and on the Solid Surface
Chem. Phys., **6** (1997) .

S. Nagaoka, T. Fujibuchi, J. Ohshita, M. Ishikawa and I. Koyano
Fragmentation of $F_3SiCH_2CH_2Si(CH_3)_3$ *Vapour Follwing Si:2p Core-level Photoexcitation. A Search for a Site-specific Process in Complex Molecules*
International Journal of Mass Spectrometry and Ion Processes, **171** (1997) 95.

M. Nagasono, K. Mase, S. Tanaka and T. Urisu
State-selected Ion Desorption from Condensed H_2O *at 80 K Studied by Auger Electron-photoion Coincidence Spectroscopy*
Chem. Phys. Lett., **298** (1998) 141.

K. Nagayama, T. Miyamae, R. Mitsumoto, H. Ishii, Y. Ouchi and K. Seki
Polarized VUV Absorption and Reflection Spectra of Oriented Films of Poly(tetrafluoroethylene) $(CF_2)n$ *and its Model Compound*
J. Electron Spectrosc. Relat. Phenom., **78** (1996) 407.

K. Nagayama M. Seki, R. Mitsumoto, E. Ito, T. Araki, H. Ishii, Y. Ouchi, K. Seki and K. Kondo
Polarized NEXAFS Studies on the Mechanical Rubbing Effect of Poly(tetrafluoroethylene) Oligomer and its Model Compound
J. Electron Spectrosc. Relat. Phenom., **78** (1996) 375.

T. Nanba
High-pressure Solid-state Spectroscopy at UVSOR by Infrared Synchrotron Radiation (*)
IL NUOVO CIMENTO (Bologna), **20** (1998) 397.

T. Nanba, M. Muneyasu, N. Hiraoka, S. Kaga, G. P. Williams, O. Shimomura and T. Adachi
Phase Transition of CdS Microcrystals under High Pressure
J. Synchrotron Rad. , **5** (1998) 1016.

K. G. Nath, Y. Ufuktepe, S. Kimura, T. Kinoshita, H. Kumigashira, T. Takahashi, T. Matsumura, T. Suzuki, H. Ogasawara and A. Kotani
4d Core-level Resonant Photoemission Spectroscopy of Thulium Monochalcogenides Around the Tm 3d Threshold
J. Electron Spectrosc. Relat. Phenom., **88-91** (1998) 369.

H. Nishikawa, H. Fukui, E. Watanabe, D. Ito, K. S. Seol and Y. Ohki
Photoluminescence and Electron-spin-resonance Studies of Defects in Amorphous SiO_2 *Films*
Proceedings of 1998 International Symposium on Electrical Insulating Materials,Toyahashi, Japan, p59.

T. Noda, T. Nakane, K. Ozawa, K. Edamoto, S. Tanaka and S. Otani
Photoemission Study of the Oxidation of ZrC(111)
Solid State Comm., **107** (1998) 145.

H. Oji, R. Mitsumoto, E. Ito, H. Ishii, Y. Ouchi, K. Seki and N. Kosugi
Core Hole Effect in NEXAFS Spectroscopy of Aromatic Hydrocarbons: Chrysene, Perylene and Coronene
J. Electron Spectrosc. Relat. Phenom., **78** (1996) 383.

H. Oji, R. Mitsumoto, E. Ito, H. Ishii, Y. Ouchi, K. Seki and N. Kosugi
Core Excitonic Effects in the NEXAHS Spectra of Condensed Polycyclic Aromatic Hydrocarbons
J. Phys. IV, **7** (1997) 163.

H. Oji, R. Mitsumoto, E. Ito, H. Ishii, Y. Ouchi, K. Seki, T. Yokoyama, T. Ohta and N. Kosugi
Core Hole Effect in NEXAFS Spectroscopy of Polycyclic Aromatic Hydrocarbons: Benzen, Chrysene, Perylene, and Coronene
J. Chem. Phys., **109** (1998) 10409.

K. Ohtani, H. Doshita, M. Kohama, Y. Takamine , K. Asao, S. Tanaka, M. Kamada and A. Namiki
Physisorption Lifetimes of Cl_2 *on the Si(100) Surfaces Adsorbed with Cs and Cl*
Surface Science, **414** (1998) 85.

M. Sakurai, H. Okamura, M. Watanabe, T. Nanba, S. Kimura and M. Kamada
Upgraded IR Beamline at UVSOR
J. Synchrotron Rad., **5** (1998) 578.

N. Sanada, S. Mochizuki, S. Ichikawa, N. Utsumi, M. Shimomura, G. Kaneda, A. Takeuchi, Y. Suzuki, Y. Fukuda, S. Tanaka and M. Kamada
The (2×4) and (2×1) Structures of the Clean GaP (001) Surface
Surface Science, **419** (1998) 120.

M. Sano, Y. Seimiya, Y. Ohno, T. Matsushima, S. Tanaka and M. Kamada
Oriented Oxygen Admolecules on a Stepped Platinum(133) Surface
Appl. Surface Science, **130-132** (1998) 518.

K. Seki, E. Ito and H. Ishii
Energy Level Alignment at Organic/metal Interfaces Studied by UV Photoemission
Synth. Met., **91** (1997) 137.

K. Seki and H. Ishii
Photoemission Studies of Functional Organic Materials and their Interfaces
J. Electron Spectrosc. Relat. Phenam., **88-91** (1998) 821.

K. S. Seol, T. Futami and Y. Ohki
Concentration of Neutral Oxygen Vacancies in Buried Oxide Formed by Implantation of Oxygen
J. Appl. Phys., **83** (1998) 2357.

K. Sugiyama, K. Seki, E. Ito, Y. Ouchi and H. Ishii
UV Photoemission Study of Interfaces Related to Organic EL Devices
Mater. Res. Soc. Symp. Proc., **488** (1998) 719.

K. Sugiyama, D. Yoshimura, E. Ito, T. Miyazaki, Y. Hamatani, I. Kawamoto, H. Ishii, Y. Ouchi and K. Seki
Electronic Structure of Organic Carrier Transporting Material/Metal Interfaces as a Model Interface of Electroluminescent Device Studied by UV Photoemission
Synth. Met., **86** (1997) 2425.

K. Sugiyama, D. Yoshimura, T. Miyamae, T. Miyazaki, H. Ishii, Y. Ouchi and K. Seki
Electronic Structures of Organic Molecular Materials for Organic Electroluminescent Devices Studied by Ultraviolet Photoemission Spectroscopy
J. Appl. Phys., **83** (1998) 4928.

Y. Tanaka, T. Hatsui, and N. Kosugi
Ni 2p Resonant Photoelectron Spectra of Some Planar Nickel Complexes
J. Electron Specrosc. and Relat. Phenom., **88-91** (1998) 235.

Y. Takata, T. Hatsui, and N. Kosugi
Resonant Behavior in Ni 3d, 3p and 3s Photoelectron Spectra at the Ni 2p Excitation of Planar Molecular Complex, Nickel Dimethylglyoxime
J. Electron Specrosc. and Relat. Phenom., **93**, (1998) 109.

Y. Takata, M. Nakamura, N. Kosugi
Resonant Behavior of Satellite Photoelectrons in the Ni 3p and 3s Region at the Ni 2p Excitation of $K_2Ni(CN)_4$
Chem. Phys. Lett., **287** (1998) 35.

T. Tanaka, S. Yoshida, R. Kanai, T. Shishido, H. Hattori, Y. Takata, and N. Kosugi
Structural Change of Calcium Silicate, a New Type of Desulfurization Material, Studied by Si K Edge XAFS
J. PHYS. IV FRANCE, **7** (1997) C2-913.

Y. Taguchi, Y. Ohta, T. Katsumi, K. Ichikawa and O. Aita
Photoemission Study of Benzene Adsorbed on Si Surfaces
J. Electron Spectrosc. Relat. Phenom., **88-91** (1998) 671.

M. A. Terekhin, N. Yu. Svechnikov, S. Tanaka, S. Hirose and M. Kamada
High-density Effects Due to Interaction of Self-trapped Exciton with (Ba,5p) Core Hole in BaF_2 *at Low Temperature*
Low. Temp. Phys., **23** (1997) 349.

T. Tsujibayashi, K. Toyoda and T. Hayashi
Time-resolved Study of Free Exciton Luminescence in KI and RbI
Solid State Comm., **105** (1998) 681.

S. Uchida, K. Tabayashi, M. Tanaka, O. Takahashi, K. Saito, M. Kono and T. Ibuki
Photoabsorption and Fluorescence Excitation of Malononitrile in the Vacuum UV Region
Chem. Phys. Lett., **282** (1998) 375.

Y. Ufuktepe, S. Kimura, T. Kinoshita, K. G. Nath, H. Kumigashira, T. Takahashi, T. Matsumura, T. Suzuki, H. Ogasawara and A. Kotani
Resonant Photoemission Studies of Thulium Monochalcogenides around the Tm 4d Threshold
J. Phys. Soc. Jpn., **67** (1998) 2018.

K. Umishita, K. Iwasaki, S. Hino, T. Miyamae, K. Kikuchi and Y. Achiba
Ultraviolet Photoelectron Spectra of a Higher Fullerene C_{102} *and its Potassium Complex*
J. Electron Spectrosc. Relat. Phenom., **88-91** (1998) 843.

H. Yoshida and K. Mitsuke
Design of an 18 m Spherical-grating Monochromator at UVSOR
J. Synchrotron Rad. **5** (1998) 774.

D. Yoshimura, H. Ishii, S. Narioka, M. Sei, T. Miyazaki, Y. Ouchi, S. Hasegawa, Y. Harima, K. Yamashita and K. Seki
The Electronic Structure of Porphyrin/metal Interfaces Studied by UV Photoemission Spectroscopy
Synth. Met., **8 6** (1997) 2399.

D. Yoshimura, H. Ishii, Y. Ouchi, E. Ito, T. Miyamae, S. Hasegawa, N. Ueno and K. Seki
Angle-resolved UPS Study and Simulation with IAC Approximation for Oriented Monolayer of Tetratetracontane (n-$C_{44}H_{90}$) *on Cu(100)*
J. Electron Spectrosc. Relat. Phenom., **88-91** (1998) 875.

J. Yoshinobu, M. Kawai, S. Tanaka, K. Watanabe, Y. Matsumoto and M. Kamada
Electronic Structures in the Valence Region of Chemisorbed and Physisorbed Species on Pb(110)
J. Electron Spectrosc. Relat. Phenom., **88-91** (1998) 665.

J. Yoshinobu, M. Kawai, I. Imamura, F. Marumo, R. Suzuki, H. Ozaki, M. Aoki, S. Masuda, S. Tanaka, M. Kamada and M. Aida
Electronic Structure near the Fermi Level and STM Images of Pb(110)c(4×2)-Benzene
J. Electron Spectrosc. Relat. Phenom., **88-91** (1998) 997.

(Japanese)
T. Futami, K. S. Seol, T. Watanabe, H. Tseng, M. Ishii and Y. Ohki
Effect of Ion Implantation on the Photoluminescence in Hydrogenated Amorphous Silicon Nitride Films
DEI-97-147~155 p41.

H. Ishii and K. Seki
Electronic Structures of Organic/metal Interface Studied by UV Photoelectron Spectroscopy
Hyomen **3 4** (1996) 621.

K. S. Seol, H. Koike, T. Futami and Y. Ohki
Effects of Internal Oxidation on the Oxygen Deficiency and Dielectric Strength of Buried Oxide Formed by the Separation-by-implanted-oxygen (SIMOX) Process
Trans. IEE 118-A (1998) 826.

H. Hama, M. Hosaka, J. Yamazaki and T. Kinoshita
High-Energy Gamma Ray Production via Intracavity Compton Backscattering of Free Electron Laser on an Electron Storage Ring
OQD-98-16 p49.

K. Mitsuke, M. Mizutani, H. Niikura and K. Iwasaki
Pump-Probe Spectroscopy of N_2 *and* N_2O *by Using a Laser-Synchrotron Radiation Combination Technique*
The Review of Laser Engineerin **2 6** (1998) 458.

UVSOR

Workshop

UVSOR Workshop 1998

----Time-resolved measurements using the synchrotron radiation----

1998 November 18,19
IMS Conference Center

Nov. 18

13:30-13:40 Introduction

Nobuhiro Kosugi (Director of UVSOR, IMS)

13:40-15:40

Time structure of synchrotron radiation and it's application at the SPring-8
Haruo Okuma(SPring-8)

PF-AR Project – Application by using pulsed X-rays.
Hiroshi Kawata(KEK, PF)

Time structure of the VSX light source
Norio Nakamura (ISSP, Univ. of Tokyo)

"New-Subaru" and ultrafast spectroscopy
Yoshihiro Takagi (Himeji Institute of Technology)

16:00-17:45

Status and future of the studies in the ion desorption induced by the core-level excitation
Tetsuji Sekitani (Hiroshima Univ.)

Status of single bunch operation in UVSOR
Masato Hosaka (UVSOR)

Single bunch operation in UVSOR and other facilities
Masao Kamada (UVSOR)

Time-resolved measurement of photoluminescence in amorphous SiO_2 using synchrotron radiation under single-bunch operation.
Yoshimichi Ohki (Waseda Univ.)
Hiroyuki Nishikawa (Tokyo Metropolitan Univ.)

Nov. 19

9:00-10:40

Introduction of pulsed field ionization photoelectron spectroscopy at ALS
Koichiro Mitsuke (IMS)

ZEKE measurements using the synchrotron radiation

Yumio Morioka (Tsukuba Univ.)

Chemical reactions in gas phase as studied by pulsed synchrotron radiation
Noriyuki Kouchi (Tokyo Institute of Technology)

Ion pair formation from Freon molecules following soft X-ray absorption using the selective PIPICO technique
Isao Suzuki(Electrotechnical Laboratory)

11:00-12:15

Synchrotron radiation-laser combination studies of gaseous molecules.
Masakazu Mizutani (IMS)

Two-photon spectroscopy of condensed matters with synchrotron radiation and laser
Toru Tsujibayashi (Osaka Dental Univ.)

Time-resolved two-photon photoelectron spectroscopy
Susumu Ogawa (Hitachi)

13:30-15:10

Performance and usage of high-speed photon detectors
Takeshi Taguchi, Eiji Kume(HamamatsuPhotonics)

Availability of SR pulse light in solid state spectroscopy
Hideyuki Nakagawa (Fukui Univ.)

Time-resolved photoluminescence and laser damage toughnessof CaF_2 single crystals for VUV photolithography.
Mizuguchi Masafumi, Hideo Hosono (Tokyo Institute of Technology)

Core-luminescence studies under single-bunch operation of UVSOR
Minoru Itoh (Shinshu Univ.)

15:30-17:35

Time-resolved single photon counting of biological materials
Mieko Taniguchi (Nagoya Univ.)

Present and future of time-resolved infra-red spectroscopy using SR.
Eiichi Okamura (Kobe Univ.)

Electron ion coincidence spectroscopy and its time structure
Mitsuru Nagasono (IMS)

Time-of-flight measurement of photo-desorbed species from rare gas solids
Ichiro Arakawa (Gakushuuin Univ.)

Time-response of the photo-induced desorption
Masao Kamada (UVSOR)

UVSOR

Appendix

ORGANIZATION

Director

Nobuhiro Kosugi	Professor	kosugi@ims.ac.jp	

Accelerator Division

Hiroyuki Hama	Associate Professor	hama@ims.ac.jp	
Masahito Hosaka	Research Associate	hosaka@ims.ac.jp	
Shigeru Kouda	Research Associate	kouda@ims.ac.jp	(Aug. 98-)
Toshio Kinoshita	Unit Chief Engineer	kinoshita@ims.ac.jp	
Jun-ichiro Yamazaki	Engineer	yamazaki@ims.ac.jp	

Beamline Division

Masao Kamada	Associate Professor	kamada@ims.ac.jp	
Toyohiko Kinoshita	Associate Professor	toyohiko@ims.ac.jp	(-Mar. 98)
Shin-ichiro Tanaka	Research Associate	stanaka@ims.ac.jp	
Tatsuo Gejo	Research Associate	gejo@ims.ac.jp	
Osamu Matsudo	Section Chief Engineer	mastudo@ims.ac.jp	
Masami Hasumoto	Unit Chief Engineer	hasumoto@ims.ac.jp	
Tadanori Kondo	Engineer	kondo@ims.ac.jp	
Kenji Hayashi	Engineer	h-kenji@ims.ac.jp	
Suekichi Matsuo	Supporting Engineer	mastuo@ims.ac.jp	
Bunichi Kamimoto	Supporting Engineer	kamimoto@ims.ac.jp	

Guest Scientist

Hitoshi Tanaka	Associate Professor	tanaka@spring8.or.jp	(-Mar. 99)
Yuichi Haruyama	IMS fellow	haruyama@ims.ac.jp	(-Mar. 99)
Sam Dylan More	JSPS Research Fellow	more@ims.ac.jp	(Oct. 98-)

Secretary

Hisayo Hagiwara		hagiwara@ims.ac.jp	
Naoko Onitake		onitake@ims.ac.jp	

Graduate Students

Krishna G. Nath		nath@ims.ac.jp	(-Mar. 99)

STEERING COMMITTEE

(April 1998 – March 1999)

Nobuhiro Kosugi	UVSOR IMS	Chairperson
Masao Kamada	UVSOR IMS	
Hiroyuki Hama	UVSOR IMS	
Toyohiko Kinoshita	UVSOR IMS	
Hitoshi Tanaka	UVSOR IMS (RIKEN)	
Shuji Saito	IMS	
Kyuya Yakushi	IMS	
Koichiro Mitsuke	IMS	
Toshinori Suzuki	IMS	
Toshiaki Ohta	Univ. of Tokyo	
Inosuke Koyano	Himeji Inst. Of. Tech.	
Makoto Watanabe	Tohoku Univ.	
Kazuhiko Seki	Nagoya Univ.	
Motohiro Kihara	KEK	
Yukihide Kamiya	Univ. of Tokyo	
Takatoshi Murata	Kyoto Univ. of Edu.	

JOINT STUDIES

(Financial Year 1998)

Special Projects :3
Cooperative Research Projects :24
Invited Research Projects :2
Use-of-UVSOR Projects :156
Workshop :1
Machine Time for Users :39 weeks

People of UVSOR

Location

Ultraviolet Synchrotron Orbital Radiation (UVSOR) is located at Okazaki.Okazaki (population 320,000) is 260km southwest of Tokyo, and can be reached within 3 hours from Tokyo via the Tokaido Shinkansen and the Meitetsu line.

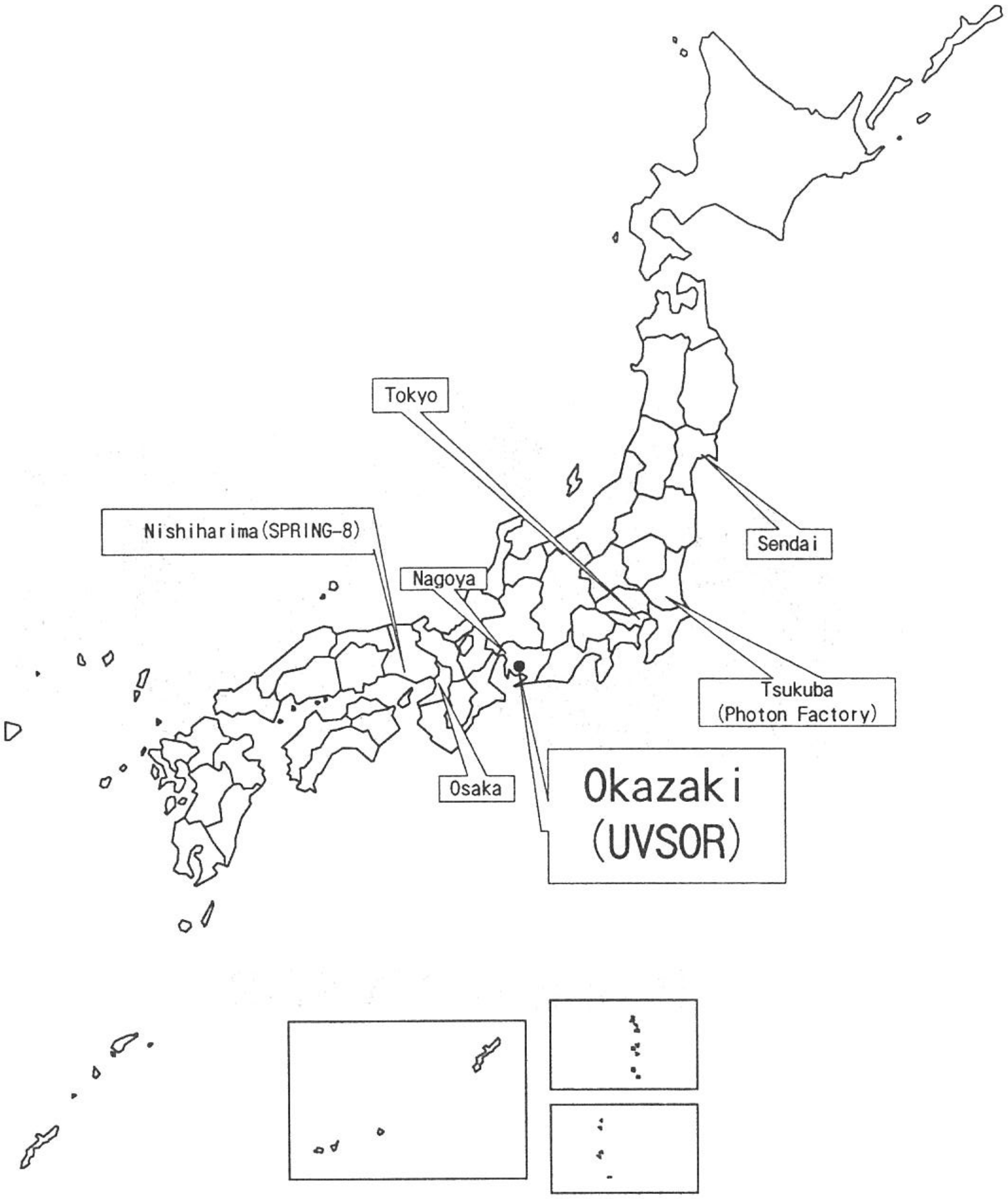

ADDRESS

UVSOR Facility
Institute for Molecular Science
Myodaiji, Okazaki, 444-8585, JAPAN

PHONE: +81-564-55-7402(Secretary)
+81-564-52-6101
FAX:+81-564-54-7079
Telex 4537475 KOKKEN J (IMS)
Homepage: http://www.uvsor.ims.ac.jp/